Complexity in lava flows: surface features and structural morphology

Presented for the degree of Ph.D. by

Louisa Jane Applegarth MESc (Oxon)

Department of Environmental Sciences
Lancaster University

October 2008

ProQuest LLC.
789 East Eisenhower Parkway
P.O. Box 1346
Ann Arbor, MI 48106 – 1346

Declaration

I, Louisa Jane Applegarth, hereby declare that the contents of this thesis result from my own work, and that no part of the work has been submitted in substantially the same form for the award of a higher degree elsewhere.

Abstract

Lava flows are complex phenomena, with the potential to cause severe damage to property and infrastructure. In order to accurately forecast the way in which lava will behave upon eruption, it is necessary to understand the complex processes that occur during emplacement. This thesis employs both analogue modelling, and observations of an active flow on Mt. Etna, to study the surface morphology of lava flows, aiming to relate this to their internal dynamics.

Analogue models were used to investigate the interaction between a viscous flow interior and a brittle crust, and the relationship between crustal thickness and flow advance and morphology. Using a high viscosity (10^4 Pa s) silicone gel, and a mixture of sand and plaster of Paris, the behaviour of rheologically stratified, channelised lava flows was simulated. The experiments were conducted on an inclined board with a reservoir constructed at one end. Silicone was released from the reservoir through a sliding gate, where it encountered a seed flow consisting of a silicone sheet topped with a crust of known depth and constrained by levées, in order to represent the influx of fresh lava into a channel.

Sequential digital images taken over the course of each experiment allowed marker points on the flow surface to be tracked, and these data were used to construct surface velocity maps. Several experiments were recorded using stereo imagery, allowing changes in the surface relief to be monitored. The observations showed that crustal thickness was a major control on surface morphology and flow behaviour. Thin crust flows were largely controlled by the fluid interior, and the crust rested passively on the surface of the silicone. Thick crusts were less easily deformed in compression at the channel head, but tensile fracturing at the flow front led to a greater degree of interaction between the crust and the flow interior than seen in thin crust flows, which has implications for cooling-limited lava flows.

The experiments were successful in reproducing structures seen on lava flows, but represented the emplacement of simple flow units. Compound `a`ā flow fields emplaced during long-lived eruptions often contain many complex features of enigmatic origin, whose significance needs to be evaluated. The 2001 flank eruption of Mount Etna (17th July – 9th August) provided an excellent opportunity to observe the emplacement of a compound lava flow field. Twenty three days of activity at a single vent on the southern flank produced the lower flow field, which reached its

maximum length in eight days and thereafter grew by the superimposition and juxtaposition of younger flow units, and break-outs from earlier channels. Several sets of data were collected during the eruption, and these have been used, together with detailed analysis of post-emplacement aerial photographs and field observations, to unravel the temporal and structural evolution of the flow field.

The surface morphology of the developing flow was examined, and it was possible to distinguish between features reflecting emplacement processes in individual units; those resulting from channel drainage, inflation, squeezing of lava from an older unit when overridden by a younger unit; and post-emplacement changes including the emergence of lava in a range of rheological states through flow surfaces, flow margins and levée-channel boundaries. This 'squeeze up' lava represents the latest stages of activity, and as such may provide information about the most advanced rheological state in which lava can flow.

Although no mature lava tubes were encountered during the field survey, there is clear evidence of preferential thermal pathways within stationary flow units. Had the eruption continued, there is a high probability that a tube system would have developed, as was the case during the 1983, 1991-3 and 2004 eruptions. This would have allowed the flow to extend significantly further, resulting in greater damage to property on this heavily populated side of the volcano. It is concluded that the widespread occurrence of the structures described indicates that the underlying processes responsible for their development are common and repeatable, and therefore amenable to inclusion in future models aiming to accurately forecast flow behaviour.

Acknowledgements

Despite the claims made in the declaration, it is clear that I wouldn't be in the position of submitting a thesis if it wasn't for the hard work of many other people. First and foremost, I would like to heartily thank my supervisors, Mike James, Harry Pinkerton and Ben van Wyk de Vries, for inducting me into the ways of volcanology, and being constantly on hand to offer advice and answer questions, even when the questions were a bit silly. I owe a huge debt of gratitude to Mike and Harry for introducing me to such exciting places as Etna and Montserrat, and to Harry for arranging for Etna to go off just at the right time... I'm also much obliged to Ben for showing me the ropes in the lab. at Clermont, and for not suggesting that I use the messier of the possible modelling materials. I cannot imagine having had better supervision, and for this I am very grateful.

Chapter six could not have happened without the help of INGV, and Sonia Calvari in particular, who very kindly let me have access to all the archived images they collected during the 2001 eruption of Etna.

Back in Lancaster, thanks go to Geoff and Phil in the workshop for lending me various bits of essential kit when I was trying to run models over here; and to Ian, for making videos into DVDs by magical means, so that I could catch up with the re-runs of 'Etna 2001'.

Lancaster would have been a much greyer place (metaphorically speaking) without the many unfortunates who have been compelled to share an office with me over the years, so I salute you all. To John and Matt for looking after me when I first arrived, showing me where to buy sandwiches, and instilling in me an almost religious awe for the ritual that is Volcanology Coffee. To Alistair, for providing the office with a mortal mascot, and giving me a page target that I could never hope to reach. To Rod, for setting an excellent example of how to finish one's Ph.D., and for the Costa Rican volcano I'm expecting in the post any day now... To Steve, for livening up/disrupting the office every time he deigns to visit, but not so much for leaving just as he's proved himself a master baker. To the Sauna Ladies, without whom I never would have found a use for the Spanish tape measure: Crop Circle Jo, for helping to feminise the office; Dr. Ruth for demonstrating that geology-chic is possible, and for being the cause of the new improved 'Geoscience Coffee', together with Captain Alex, to whom I am also indebted for cakes, spider shoes, getting the heating turned off and brownies. Less so the brownies. To Pear-shaped Adam, for putting up with the girliness and displaying his resignation with only mildly raised eyebrows. To Transient Mike, for his transience and magic tricks. You have all contributed muchly to making the Sauna a very nice place to work ☺.

I also need to pay tribute to those who, though not in Lancaster, have had to cope with the fallout of the frustrating times: Heather, for always being on the other end of MSN, and for providing the tent and trangia when we both needed to escape; and me Dad, for being exactly the right kind of parent.

Contents

List of figures

Chapter One

Chapter Two

Chapter Three

Chapter Four

Chapter Five

Chapter Six

List of tables

Chapter Two

Chapter Three

1. Introduction

The work presented in this thesis focuses on the study of lava flows, from simple, single cooling units, to complex groups of units, or flow fields. Lava flows are highly complex phenomena, and have the potential to cause considerable damage to property and infrastructure. As such, they have generated considerable interest for many centuries, with the earliest known ideas on the causes of volcanic eruptions dating back to the natural philosophers of Greece in the fifth century B.C. The first scientific expedition to study an eruption was famously (and fatally) carried out by Pliny the Elder during the 79 A.D. eruption of Vesuvius, Italy, and many detailed descriptive accounts of volcanic phenomena on Iceland survive from the likes of Snorri Godi (*c.*1000 A.D.), but the first field study of an active lava flow was carried out by Francesco d'Arezzo during the 1669 eruption of Mt Etna, Sicily (Guest et al. 2003). The favoured theory at that time was that lava consisted of molten sulphur, but d'Arezzo refuted this on the basis of two observations. Firstly, having carried out experiments burning sulphur, he noted that lava flows did not smell as strongly as the experiments, when due to their larger volume, the smell ought to have been far stronger. Secondly, upon trying to push a stick into molten lava, he noted that the consistency was very different from that of molten sulphur. This second experiment was probably the first rheological observation of active lava (Guest et al. 2003). Volcanology did not become established as a scientific discipline in its own right until the mid-eighteenth century, when Guettard and Desmarest studied volcanic deposits in the Auvergne region of France, and William Hamilton, who is credited with authoring the first modern text in volcanology, *Campi Phlegraei* (Macdonald 1972), monitored changes in the edifice of Vesuvius during the 1767 eruption (Sigurdsson 2000).

Although the underlying causes of volcanism were not understood at that time, the effects of volcanic phenomena were readily observed, as evidenced by the first recorded attempt to divert a lava flow away from a human settlement, during the 1669 eruption of Etna. Many recent accounts of the devastating effects of lava flows, and of more modern diversion attempts, are found in Macdonald (1972), Pinkerton (1987), and Barberi and Carapezza (2004), among others.

1.1 The problem

One of the principal aims of current work undertaken on lava flows is the provision of reliable and quantitative predictions of the rate at which a flow will advance upon eruption, the path it will follow, the length it will reach, and the area it can be expected to inundate. In order to describe such a complex process as emplacement quantitatively, it is necessary to be able to make accurate measurements of the many variable and interdependent physical parameters that control the behaviour of the flow. The wide range of possible pre-eruption processes means that lava can be extruded over a wide range of chemical compositions, temperatures, crystallinities and volatile and bubble contents, all of which intrinsic properties affect its rheology upon eruption. The problem of lava rheology, which is the manner in which the lava responds to applied stresses, is considered in more detail in section 1.3.1.

Lava is usually erupted as a three-phase flow of melt, crystals and bubbles. Upon eruption, it immediately begins to spread under the influence of gravity, and its advance depends on the above intrinsic properties, and the prevailing environmental conditions. The environmental parameters that affect behaviour include effusion rate, which has been observed in historical eruptions to span three orders of magnitude, the local topography, the presence or absence of water or ice and the ambient temperature.

As the lava spreads, it cools by radiation, convection and conduction, and the decrease in temperature, coupled with the resulting crystal growth, causes the viscosity of the lava to increase. Crystal growth, however, also releases latent heat and increases the water content of the melt, which counters some of the effects of surface cooling. Once the volume fraction of crystals is sufficient for crystal-crystal interactions to occur, the lava may develop a yield strength (Cashman et al. 1999b), and once the crystallinity has reached a critical value, estimated at 55 to 60% by volume (Marsh 1981; Lejeune & Richet 1995), it is no longer able to flow, and can be considered solid. The formation of solid material occurs first around the flow margins, forming a surface crust and stationary levées, and these insulate the still-viscous interior, reducing the rate at which heat is lost. The fraction of crustal coverage affects the cooling rate, as where the incandescent interior is exposed, the flow loses heat rapidly by radiation, while in areas covered by crust, it loses heat more slowly, by conduction. The texture of the surface crust may change with time, as discussed in section 1.3.2, and this variation in roughness affects how efficiently heat is lost from the surface, and hence the cooling rate. Interaction between the solid and fluid parts of the flow may result in solid fragments being incorporated into the fluid interior, and this entrainment results in a net cooling effect (Crisp & Baloga 1994). Meanwhile, as volatiles are lost from the lava through degassing, undercooling occurs (Sparks & Pinkerton 1978). Undercooling results from the adiabatic cooling of the magma system by decompression of the gas phase, and the fact that the anhydrous liquidus is higher than the hydrated liquidus, so the sudden loss of gas disturbs the equilibrium of the system. Sudden undercooling can lead to the pervasive growth of quench crystals, and so can have a much more profound effect on the rheology of the whole flow than surface cooling. The formation of bubbles as the volatiles exsolve can have variable effects on

the rheology, depending on bubble size (Cashman et al. 1999a; Manga & Stone 1994), but their influence is generally less important than that of crystals (Manga et al. 1998).

In addition to the problem of cooling-dependent rheology, observations of lava flow emplacement have documented the development of many structural complexities, such as lava tubes that can insulate the flow (e.g. Peterson & Swanson 1974; Guest et al. 1980; Greeley 1987; Calvari & Pinkerton 1999), and ephemeral vents that supply fresh hot lava to flows far from the vent (e.g. Polacci & Papale 1997; Calvari & Pinkerton 1998). While such structures are widely documented and broadly understood, their development is a consequence of the interaction between the intrinsic and the environmental parameters, and is difficult to reliably forecast. They are also able to significantly modify the behaviour of the flow, and therefore the hazard potential, and as such must be accounted for when attempting a comprehensive description of lava flow behaviour.

1.1.1 Numerical models of lava flow emplacement

For long, channelised basaltic flows, the inundation area can be considered of secondary importance in hazard assessment, and many attempts have been made to produce models for determining flow lengths and paths. Early empirical models related the length to which a lava could flow before being halted by cooling (its cooling-limited length) to effusion rate (Walker 1973), and to the total erupted volume (Malin 1980). The length-effusion rate relationship of Walker (1973) inferred that flows erupted at lower rates experience proportionally more cooling per unit length than those erupted at higher rates, and so attain a shorter length. While this is certainly seen to be the case, Pinkerton (1987) noted that the length-effusion rate correlation is

not well constrained, and the length of a flow can vary by a factor of seven for any given effusion rate.

The conductive cooling of lava can be characterised by the dimensionless Grätz number, Gz, which is the ratio of the depth to which cooling penetrates in a given time to a characteristic thickness scale, and can be written $Gz = d_e^2 / (\kappa t)$, where d_e is the equivalent diameter, defined as four times the cross-sectional area of the flow divided by its wetted perimeter, κ is the thermal conductivity of the lava and t is the time elapsed since the beginning of effusion (Knudsen & Katz 1958; Pinkerton & Sparks 1976; Pinkerton & Wilson 1994). While it has been found empirically that lavas reach their cooling-limited length when Gz falls to a value of approximately 300 (Pinkerton & Sparks 1976; Pinkerton & Wilson 1994), the use of Gz only accounts for heat loss by conduction, and thus cannot fully describe the dynamic evolution of the flow.

Pinkerton & Wilson (1994) suggested that parameters such as eruption duration, topography, and the rheological properties of the lava ought to be incorporated into models attempting to determine the final length of a flow. The topographic problem has been addressed through the use of probabilistic models, in which one-dimensional flows propagate from point sources, with flow being more likely down lines of steeper gradient (e.g. Macedonio et al. 1990; Favalli et al. 2005). While such models are useful in the rapid generation of hazard maps when the characteristics of the lava are unknown, they are unable to estimate the probable maximum length of a flow, which is the most important quantity when considering possible evacuation or lava diversion strategies. Deterministic models, which are capable of estimating this quantity by accounting for downflow rheological changes, are therefore preferable.

Many authors have conducted theoretical studies of lavas, attempting to determine the relationship between temperature, composition, crystallinity and rheology (e.g.

Pinkerton & Sparks 1978; Pinkerton & Stevenson 1992; Dragoni & Tallarico 1994, Pinkerton & Norton 1995), to model the heat loss from channelised flows and tubes (e.g. Crisp & Baloga 1990, 1994; Keszthelyi & Self 1998; Cashman et al. 1999b; Keszthelyi 1995; Sakimoto & Zuber 1998; Dragoni et al. 1995, 2002), and to model the formation of ephemeral vents (Dragoni & Tallarico 1996). The ability to describe these processes numerically is essential in the construction of deterministic flow models, and many such models exist, with varying levels of sophistication.

One simple model that describes both the path of a flow and its thermo-rheological evolution is FLOWGO (Harris & Rowland 2001; Rowland et al. 2005), which aims to incorporate all the possible parameters that can influence the advance of a lava, in a self-adapting model for one-dimensional channelised flow. FLOWGO includes a thorough treatment of the heat budget, but is severely limited by the assumption of one-dimensional, steady-state flow. Ideally, the problem of lava flow modelling can be tackled by solution of the Navier-Stokes equations of mass conservation, momentum and energy balance. However, these differential equations are difficult to solve for lava flows due to their non-Newtonian rheology, the free surface, and the problem of non-linear boundary conditions relating to heat loss in the energy equations (Costa & Macedonio 2005). The rheological and dynamic complexity of lavas has so far rendered accurate three-dimensional description by numerical models practically impossible, resulting in the development of simpler models designed to overcome the computational difficulties.

A number of models have been based on the use of cellular automata (CA), which consist of discrete dynamic systems (cells) that have one of a finite number of states. The state of each cell is updated according to an evolution function that depends on the properties of that cell and its local neighbours, which can be based on analytical or

numerical solutions to differential equations, or on empirical relations. Using these simple and local rules, the CA can produce very complex structures (Vicari et al. 2007). In such models, lava is added to one or more source cells, and is cycled through the cell network over time. The amount of lava added at the source can be varied with time, thus simulating changes in effusion rate. Cooling is calculated for each time step, and the resulting rheological changes, together with the relative altitude of the cells and the hydrostatic pressure, control subsequent distribution. Models based on CA, or similar systems, include those of Ishihara (1990) and Miyamoto & Sasaki (1997); SCIARA (Crisci et al. 1982, 1986; Barca et al. 1987, 1993; Avolio et al. 2006); and MAGFLOW (Del Negro et al. 2008; Vicari et al. 2007; Herault et al. *in press*). One model not based on CA is LavaSIM (Hidaka et al. 2005), which uses a computational fluid dynamic code that is capable of accounting for one important aspect of flow that cannot be described by any of the previously mentioned models, namely solidification. The ability to consider both liquid and solid phases means that complex structures such as tubes can be simulated, though currently the mechanical stability of tubes is not described, meaning that tube roofs sink upon drainage. The problem of ephemeral vent formation has also not yet been solved. This approach, however, represents the most comprehensive description of lava flow emplacement that has been achieved to date.

While these models have had some success in reproducing the inundation area of lava flows against which they have been tested, numerous problems still face lava flow modellers, even before the computational difficulties are considered, due to the fact that robust data from measurements on lava during eruptions is very scarce. The inability to accurately estimate input parameters seriously limits the viability of the model, as was observed by Del Negro et al. (2008) during their attempt to apply

MAGFLOW to the 2004-5 eruption of Etna. In this application, they tested three different empirical temperature-viscosity relationships, finding that the modelled inundation area was strongly dependent on which relationship was used. This relationship is only one of many model inputs, and uncertainties in the estimation of initial effusion rates, eruption temperatures and rheological parameters including viscosity, yield strength, crystallinity and gas content, are all expected to contribute to inaccuracies and errors in the model. In addition, the current inability to predict with confidence how these parameters depend upon each other, and how they vary in space and time, also needs to be addressed. The limitations are not restricted to rheological problems, as there are many processes that have been observed during lava flow emplacement that are not yet well understood, and even those that have been widely studied, such as the formation of tubes and ephemeral vents, cannot currently be accurately described by numerical models.

1.1.2 Analogue modelling of volcanic processes

Laboratory experiments provide an alternative method of modelling the behaviour of lava flows. Such an approach has become increasingly important in the study of volcanological processes in recent years, and provides a way in which highly complex dynamic processes can be investigated in controlled environments (Mader et al. 2004). Although experimental models necessarily simplify the natural systems they are investigating, they allow assumptions to be made that can bridge gaps in current knowledge, and so allow application of this limited knowledge to otherwise unfathomable systems (Middleton & Wilcock 1996). Experimental modelling provides systematic observations of scaled processes, which can be used to test hypotheses and computational models (Mader et al. 2004). Their major advantage is

their repeatability, and the possibility of varying initial (known) conditions to investigate the relative effects of different parameters on measurable outcomes.

While natural materials can be used in the experimental study of small-scale processes occurring in lavas, for example the bubble nucleation and growth experiments of Hurwitz & Navon (1994) and Mangan & Sisson (2000), their use in larger-scale dynamic processes can be difficult and expensive (Mader et al. 2004). To overcome this problem, models using analogue materials have been widely employed in the study of lava flow behaviour, as discussed in chapter two, as well as in many other geological problems, including volcanic spreading (e.g. Merle & Borgia 1996; van Wyk de Vries & Merle 1998), conduit processes (e.g. Lane et al. 2001; James et al. 2006), and granular flow with relation to the advance of pyroclastic flows, debris flows, avalanches and glaciers (e.g. Allen 1970; Carrigy 1970; Hutter et al. 1995; Roche et al. 2002, 2004, 2006; Doppler et al. 2007; Girolami et al. 2008; Valentino et al. 2008). Such processes can be simulated on a small scale if the rheological behaviour of the two systems can be shown to be similar, which is achieved through scaling of the experimental system, a problem considered in chapter three.

1.2 Aims and objectives

The problems discussed in section 1.1 illustrate that, currently, both our data on the physical properties of lava and our understanding of complex lava flow emplacement processes are somewhat limited. While the former problem is beyond the scope of this thesis, the work presented here attempts to address the latter. Kilburn (2000) notes that care must be taken when attempting to make inferences about flow dynamics from studies of inactive flows, as the preserved features often only provide insights into the latest stages of activity, and so may not reflect the conditions that prevailed during the

main phase of activity. The best prospects for extending our understanding of the processes at work during lava flow emplacement therefore lie in the use of analogue models, and the detailed observation of active lavas in the field.

This work employs both of these approaches, presenting a laboratory study of the development of simple flow units, and a complementary field study that extends the work by considering the emplacement of a compound lava flow field. The concept of a 'flow unit' was first introduced by Nichols (1936) to mean an individual body of lava that cooled as a single entity. This definition was used by Walker (1971), who introduced the terminology of a 'compound' flow, which can be separated into distinct cooling units, and a 'simple' flow, which cannot.

The use of laboratory experiments to model the emplacement of simple flows allows variation of the initial conditions in order to evaluate the relative influence of the parameters being tested. In this work, the effects of the surface crust thickness and underlying slope on the advance of a channelised flow and its resultant surface morphology are investigated. As has been discussed, the difficulty of describing solidification numerically has meant that it has not yet been incorporated satisfactorily into many computational models. It is highly likely that this process can be reproduced and described much more successfully through the use of analogue models, which may provide valuable insights into the relative influence of the crust and the fluid interior on the overall flow dynamics. A principal aim of the work, which would also validate the approach, is to produce surface structures analogous to those that have been observed on flows in the field, so that their modes of formation can be analysed. Comparison of the modelled morphologies with observations of flows of a range of compositions is used to evaluate the success of the approach.

The fieldwork component seeks to extend the understanding gained from the modelling of simple flow units. While theoretical and analogue modelling can produce realistic representations of simple flows units under straightforward conditions, the complex processes involved in the emplacement of compound flows are difficult to model, but can be fundamental in controlling the morphology of the resulting flow field. In this work, the emplacement of the compound lower flow field of the 2001 eruption of Etna is examined, using the wealth of data collected during and after the eruption. The flow field was emplaced during 23 days of activity, during which it initially advanced as a single channel, reaching its maximum length of 6.4 km in eight days. Thereafter, the flow grew by the juxtaposition and superimposition of flow units, as the main active lobes retreated upslope. Two auxiliary channels developed during the later stages of emplacement, one of which formed a major branch that advanced at an angle of approximately 40° to the original channel. Due to the threat posed to Nicolosi during the eruption (the flow advanced to within 3 km of the town), the activity was closely documented throughout the eruption. The work here has used all the available reports and images, together with my own recent field observations, to unravel the structural and temporal evolution of the flow field, distinguishing between a wide range of features representing early emplacement processes, and post-emplacement changes such as the inflation of units and the drainage of channels. In addition, many complex surface features were observed, which are interpreted to result from late-stage processes, but whose significance is unknown. These involve lava in a range of rheological states, and the insights provided by the examination of such features may provide valuable information about flow dynamics in the latter stages of emplacement. The study of the flow field morphology is supplemented by a

consideration of the significance of effusion rate changes, and the effect that these can have on the developing flow field.

1.2.1 Thesis structure

Following a brief consideration of rheology and lava flow morphology at the end of this chapter, the second chapter reviews previous work on the analogue modelling of lava flows and domes, and provides a justification for the materials used in the laboratory experiments undertaken in this work. Chapter three then presents the experimental work, detailing the experimental design, methods and materials, and including a scaling analysis to prove the validity of the modelling approach used. The data capture process, the quantitative measurements taken and the errors incurred during these measurements and the subsequent data processing are also considered. The final section of the chapter presents detailed qualitative observations of the developing flow models, and an assessment of the quantitative results. Chapter four then considers the morphological development of the experimental flows in more detail, focussing on how the resultant morphologies can be used to interpret the differences in behaviour of flows with different sets of initial conditions. A detailed analysis of all of the structures observed is presented.

Chapter five provides a bridge between the experimental and fieldwork components, beginning with the comparison of the structures seen in the experimental flows to those observed on natural flows of similar rheology, which include glaciers as well as lava flows. Having shown that the models are capable of faithfully reproducing structures seen to develop under simple flow conditions in the field, the focus moves to the emplacement of compound flow fields. First, the factors thought to contribute to the development of compound morphology are discussed, before specific

flow features common in compound flows are discussed. This discussion is tailored to the consideration of structures and processes that have been observed to be important during the emplacement of the 2001 lower flow field of Etna, which is considered in detail in chapter six. Chapter seven then draws together the main outcomes of the work, and summarises the contribution it makes to our understanding of lava flow emplacement processes, before looking ahead to the work that remains in this area of research.

1.3 Lava properties and behaviour

1.3.1 Lava rheology

As previously mentioned, rheology is the way in which a fluid or solid responds to the application of stresses (e.g. Eirich 1960; Reiner 1969; Scott Blair 1969), and the rheology of lava is one of the major controls on its behaviour after leaving the vent. A brief general introduction to rheology is given here, before considering the rheology of lava and magma.

Figure 1.1 shows three simple rheological models that can be used to describe the response of many materials to applied stress. In solids, the effect of applied stress is measured in terms of the resultant strain (figure 1.1 a), while in fluids it is measured by the resultant strain rate (figure 1.1 b). The dashed line in figure 1.1 (a) represents the behaviour of an ideal elastic solid which deforms instantaneously when stressed and recovers completely when the stress is removed. The solid line shows the behaviour of a plastic material, which does not deform at all below a certain yield strength, σ_y, above which it deforms permanently. In an ideal plastic, the applied stress cannot be increased above the yield strength as it is immediately relieved by flow.

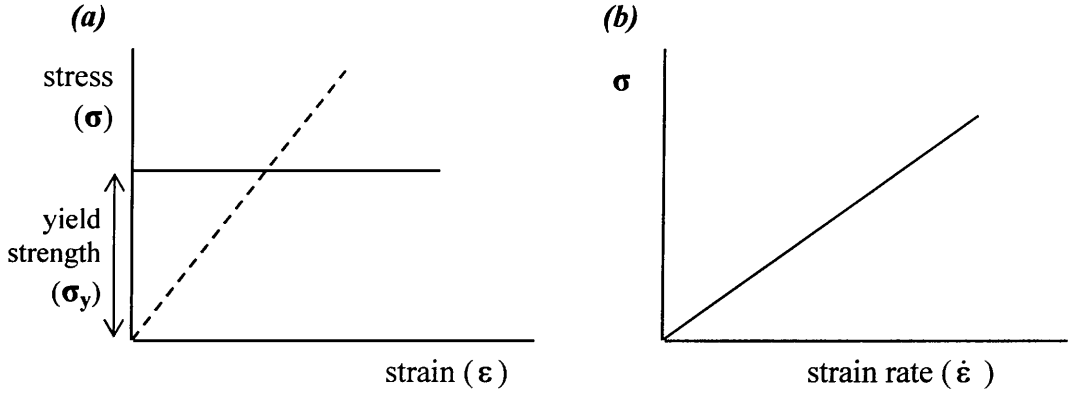

Figure 1.1. (a) Stress-strain plot for an ideal linearly elastic solid (dashed line) and an ideal plastic (solid line). (b) Stress-strain rate plot for a linearly viscous, or Newtonian, fluid. See text for details.

The model shown in figure 1.1 (b) is that of a linearly viscous fluid. Viscosity can be thought of as the internal resistance to flow, and linearly viscous, or Newtonian, fluids deform continuously under the application of a shear stress, no matter how small that stress is. Their behaviour contrasts with that of elastic solids, in that the deformation is permanent (like that of plastics), and contrasts with plastics in that deformation occurs at any stress (as for elastic solids). The relationship between shear stress and strain rate for a Newtonian fluid can be defined as:

$$\tau = \eta\dot{\varepsilon} \qquad (1.1)$$

where τ is the applied shear stress, $\dot{\varepsilon}$ the strain rate, and η the dynamic viscosity. The dynamic viscosity of a Newtonian fluid, i.e. the gradient of the line in figure 1.1 (b), is constant.

Combinations of these three simple models, and also of non-linear elastic and viscous models, can approximate the rheological behaviour of many natural materials. Figure 1.2 shows examples of non-Newtonian rheological models, which can be seen to incorporate various aspects of the three simple models seen in figure 1.1. A

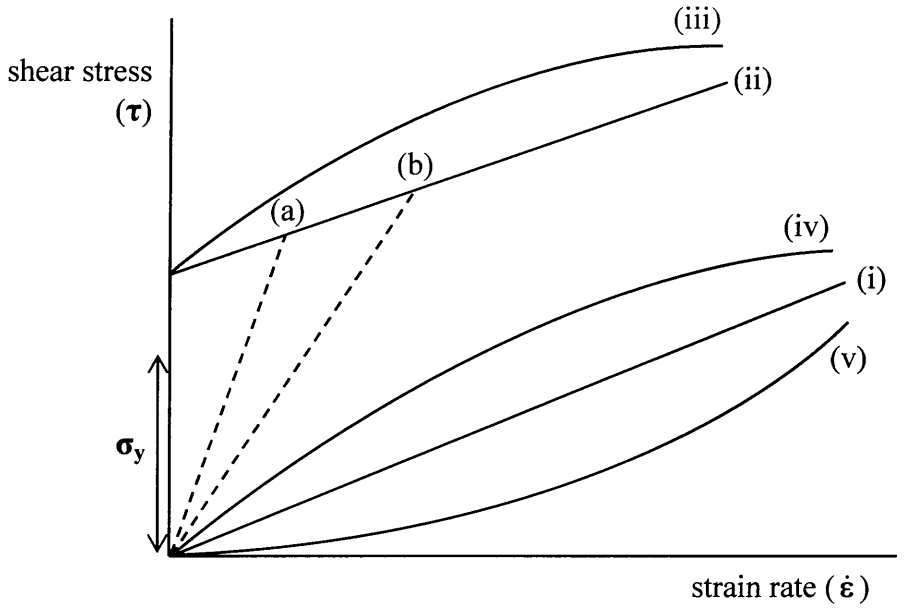

Figure 1.2. Common rheological models for fluids. (i) Newtonian fluid; (ii) Bingham fluid; (iii) viscoplastic; (iv) pseudoplastic; (v) dilatant fluid. The gradient of curve (i) gives the dynamic viscosity of the Newtonian fluid, and the gradient of curve (ii) gives the Bingham viscosity of that fluid. The gradients of the dashed lines give apparent viscosities of the Bingham fluid at points (a) and (b). See text for details.

Newtonian fluid, curve (i), is included for reference. Curve (ii) is a combination of linearly viscous and plastic models, and represents a special case of a viscoplastic material (curve iii), a Bingham fluid. Bingham fluids have yield strengths, and so do not deform at low applied stresses. Once the yield strength is exceeded, however, the resultant deformation is directly proportional to the applied stress. Curve (ii) can be described as follows, giving a value for the Bingham viscosity η_B:

$$\tau = \sigma_y + \eta_B \dot{\varepsilon} \qquad (1.2)$$

Curves (iv) and (v) depict shear thinning and shear thickening behaviour, respectively. Shear thinning, or pseudoplastic, behaviour involves the fluid becoming less viscous as the applied stress increases. By contrast, shear thickening, or dilatant, fluids

become more viscous as the applied stress increases. These rheologies can be described by the Herschel-Bulkley relation:

$$\tau = \sigma_y + \mathbf{K}(\dot{\varepsilon})^{\mathbf{n}} \qquad (1.3)$$

which is like that of a power law fluid ($\tau = \mathbf{K}(\dot{\varepsilon})^{\mathbf{n}}$), but with the addition of a yield strength. In this equation, **K** is the flow consistency index, and the exponent **n** is the flow behaviour index. In fact, all of the rheologies shown in figure 1.2 can be described using the Herschel-Bulkley or power law models, depending on the presence or absence of a yield strength respectively, as an exponent of $n < 1$ represents pseudoplastic behaviour, $n > 1$ represents dilatant behaviour, and $n = 1$ represents a linear stress-strain rate relationship.

The gradients of the dashed lines in figure 1.2 give the 'apparent viscosities' of the Bingham fluid at the stresses and strain rates given by points (a) and (b). The apparent viscosity can be defined as:

$$\eta_A = \tau/\dot{\varepsilon} \qquad (1.4)$$

and it can be seen that this value varies with the strain rate, whilst the Bingham viscosity, η_B, does not. Apparent viscosities can be defined for any non-Newtonian fluid, whilst Bingham viscosities are clearly only applicable to Bingham fluids.

Some fluids may also demonstrate time-dependent viscosities, which are not shown in the figures, whereby the viscosity increases or decreases with time as the fluid is subjected to a constant shear rate.

Lava behaves as a fluid, though the complexities outlined in section 1.1, including variable temperature, crystallinity, and volatile and bubble content, mean that it is a highly difficult task to characterise the rheology of a single flow, as the rheology varies in both space and time. Measurements of lava properties in the laboratory have shown that, above the liquidus, lavas exhibit Newtonian behaviour (Pinkerton & Stevenson 1992), and some proximal flows on Hawaii, where eruption temperatures are typically very high, have been found to have rheologies that are close to Newtonian (Rowland & Walker 1988; Walker 1989). Most lavas, however, are erupted at temperatures below their liquidus, and the added effects of cooling, crystallisation and degassing combine to produce a more complex rheology. The non-Newtonian behaviour of lava was first noted by Robson (1967), using the data of Walker (1967). Walker had attempted to find a relationship between the Newtonian viscosity of fluid lava, the thicknesses of solidified Etnaean lava flows and the slope angle on which they came to rest. Robson realised that if the lava was actually behaving as a Newtonian fluid, it would not have come to rest on a slope, but would have continued flowing until it ponded in a topographic low. He therefore surmised that lava behaves more as a Bingham material, at least when approaching the solid state.

Rheological measurements made on basaltic melts by Shaw et al. (1968) and Shaw (1969) supported the idea that lava cannot be treated as a Newtonian fluid. Shaw (1969) measured the viscosities of tholeiitic melts at temperatures between 1300 and 1120 °C, finding that the apparent viscosity increases by more than two orders of magnitude between 1200 and 1120 °C (0 to 25% crystallisation) for shear rates of around 10 s^{-1}. He found that pseudoplastic behaviour became extremely pronounced below around 1130 °C. Murase & McBirney (1973) and McBirney & Murase (1984)

also demonstrated the profound effects of cooling on viscosity and yield strength using laboratory studies, and the laboratory measurements of Pinkerton & Stevenson (1992) showed that once the yield strength of the lava is exceeded, it behaves as a pseudoplastic.

Cashman et al. (1999b) found that basaltic flows on Hawaii develop a yield strength once the crystal content has reached a critical threshold of around 45-50% crystals by volume. This is thought to correspond to the stage at which the relative motion of the crystals begins to be restricted by the fact that they overlap and interlock (Lister & Kerr 1991). Basaltic lavas from the 1975 eruption of Etna were found by Pinkerton & Sparks (1976) to have phenocrysts contents of 50-60% upon eruption, which is typical for historic Etnaean lavas (Tanguy 1973). Pinkerton & Sparks (1978) made rheological measurements on Etnaean lavas, finding that at 1086 ± 3 °C, the approximate eruption temperature, the lava had a yield strength of 370 ± 30 Pa, and displayed pseudoplastic behaviour. They also found that the yield strength increased by a factor of five over a temperature drop of 50 °C, implying a large difference in the rheological behaviour between the hot fluid interior of a flow, and the cooling margins and flow front. The shear thinning behaviour described by Shaw (1969), Pinkerton & Sparks (1978) and Pinkerton & Stevenson (1992) may possibly be due to the alignment of elongate crystals in the direction of shear, as the shear rate increases. The effect of bubbles is more complex, as small bubbles can behave rigidly due to their surface tension, and can increase the viscosity, while larger bubbles may deform more easily in shear, and can lead to pseudoplastic behaviour (Cashman et al. 1999a; Manga & Stone 1994).

It can be seen, then, that accurately describing the viscosity of a lava flow, only one of the many parameters needed to fully characterise the system, is a highly complex

task. Griffiths (2000) stated that if lava is viewed as a viscous fluid, then four different viscosity coefficients can be defined. These are the viscosity of the melt fraction alone (which may be Newtonian); the actual viscosity of the liquid-crystal-bubble mixture (Newtonian or otherwise, depending on the proportion of crystals and bubbles); and the apparent viscosity of this mixture (see figure 1.2), all of which represent the viscosity only at a single point in the flow; and the 'bulk' viscosity which is used to describe the whole flow in one parameter. The bulk viscosity is a highly inaccurate way of representing the rheology of the flow, as it averages over potentially very large spatial and temporal differences in the actual viscosity. Viscosity and yield strength have been found to increase markedly downstream (e.g. Booth & Self 1973; Pinkerton & Sparks 1978), and the estimates of Fink & Zimbelman (1990) suggest that these parameters increase exponentially with distance from the vent, calculating that their values changed by several orders of magnitude downflow.

1.3.2 Lava flow styles

The surface of a lava flow is commonly the only part that can be observed during emplacement, and surface morphology may be used to provide insights into flow dynamics. As has been discussed, large variations occur in the parameters controlling flow behaviour, and it is therefore perhaps surprising that lava flows evolve over only a few, clearly defined morphological trends. Lava 'flows' are distinguished from 'domes' by their extreme elongation downslope, but should not be considered as distinct entities, rather as end members of the broad spectrum of morphologies that can be produced when lava is extruded at the surface. Although lavas of most chemical compositions can produce flows that encompass a significant proportion of this spectrum, lava domes tend to form from more silicic lavas, which are highly

viscous and so pile up over the eruptive vent rather than easily flowing away. The surface morphology of domes varies greatly, and they range from smooth, axisymmetric edifices to collections of highly irregular lobes or spines.

Upon cooling, the surface of a flow increases in viscosity, develops a yield strength and eventually passes through the ductile-brittle transition. The morphology of the brittle crust is used to characterise terrestrial flows, which fall into three main categories: pāhoehoe, `a`ā and blocky. Pāhoehoe and `a`ā surfaces are usually restricted to basalts and basaltic andesites, whereas blocky flows are common in lavas with higher silica contents (basaltic andesites to rhyolites). Pāhoehoe surfaces are often smooth and usually continuous, while `a`ā and blocky surfaces are irregular and fragmented (figure 1.3, a to c). `A`ā and pāhoehoe categories can be further subdivided to provide more specific descriptions of surface texture. For example, pāhoehoe is commonly found to be 'ropy' (usually in more proximal parts of the channel), or 'slabby' (more distal); and `a`ā can have a 'cauliflower' (initial) or 'rubbly' (mature) aspect. A fourth type of surface texture has been described as 'toothpaste' lava (Rowland & Walker 1987), which is highly viscous material, squeezed out from a flow interior through cracks in the surface crust. This is inferred to have a significant yield strength, as it can retain grooves on the surface caused by irregularities on the edges of the source fracture (figure 1.3 d).

The variation in surface morphology gives some indication of the dominant processes at work during flow advance. As the flow cools, the relative influences of the developing chilled crust and the more mobile interior determine its morphological and dynamic evolution (Kilburn 1993). If the crust is able to deform continuously until its strength exceeds the applied stresses, then an unbroken surface forms; if the applied stress exceeds crustal resistance by an amount large enough to cause failure, a

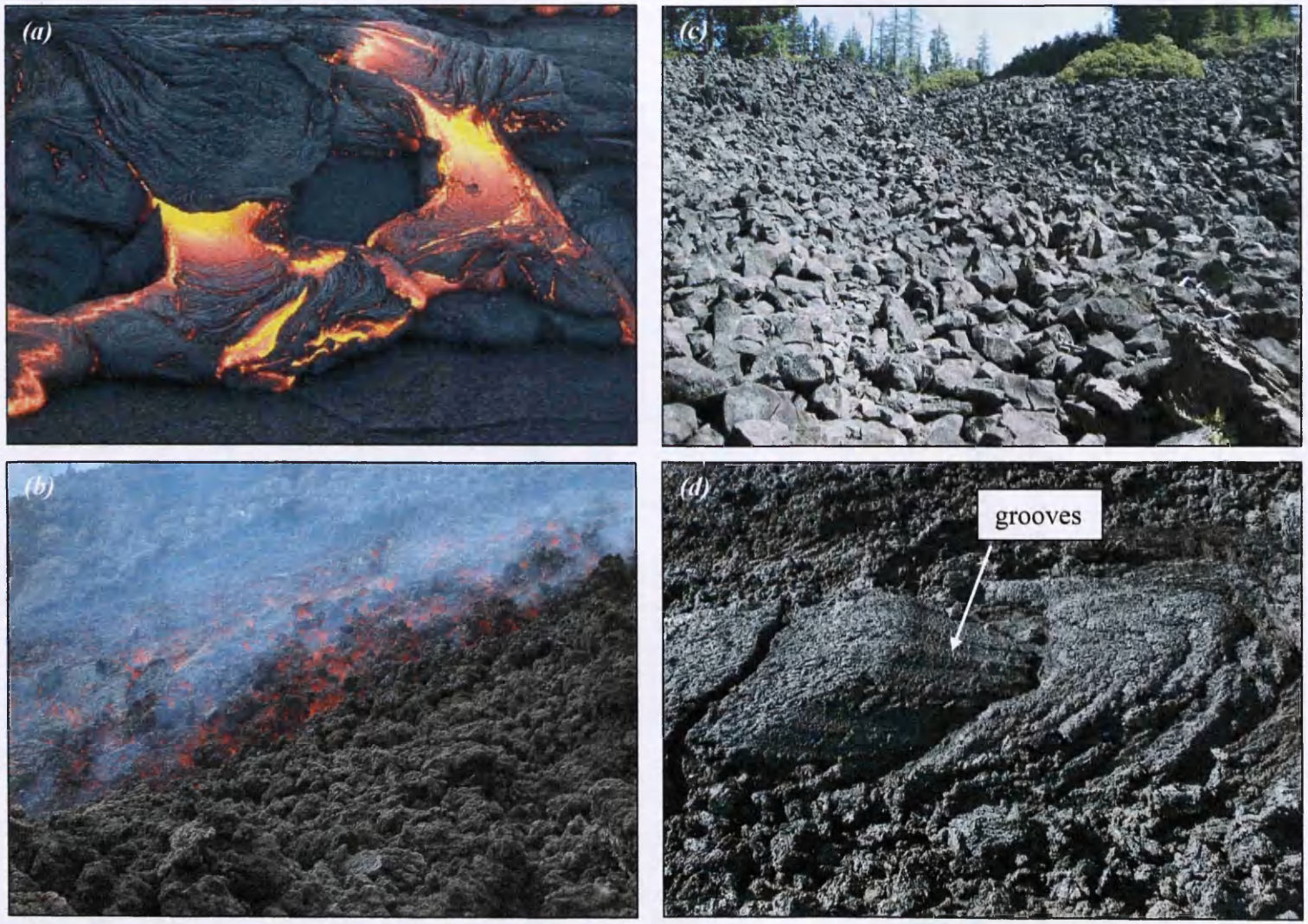

Figure 1.3. Examples of lava surface textures. (a) Pāhoehoe surface on basalt at Kīlauea, Hawai'i. Image by J. Alean, from www.swisseduc.ch (b) `A`ā texture on a basaltic flow, Etna, Sicily. Active channel is ~ 3 m wide. (c) Blocky andesite lava. The blocks are approximately 30 cm in diameter. Note the difference in texture, compared with the `a`ā, which has much rougher fragments. Image from www.fandm.edu (d) 'Toothpaste' lava, with grooves, in a basaltic flow field on Etna. Bocca is ~ 1 m wide.

fragmental surface is formed (Kilburn 1990). This effective resistance is determined by how quickly the broken crust can heal: slow healing leads to core dominated flow, while rapid healing leads to crust dominated flow (Kilburn 1993). The crust of `a`ā flows is fragmented because it is continuously ruptured during flow, and advance of an `a`ā flow involves rollover at the flow front, as the more rapidly advancing upper part of the flow cascades down the flow front, depositing crustal fragments in front of the flow. This fragmented crustal deposit later becomes a basal breccia, as the flow advances up and over it. Pāhoehoe flows commonly advance more slowly than `a`ā, and their flow front morphology is similarly controlled by the balance between crustal and interior influences. Since pāhoehoe flows are commonly thinner than `a`ā flows, they are more easily retarded by the strength of their crusts, which are continuous across the flow due to the slow advance. Pāhoehoe flows advance by oozing small lobes of lava through ruptures in the crust, and although rollover occurs in these tongues, they have no crust and so do not form a basal breccia. The presence or absence of a basal breccia is therefore a useful indicator of flow dynamics. While pāhoehoe advances as a series of toes, `a`ā and blocky lavas commonly advance as single units, due to the continuous disruption of their crusts, and often display channelised morphology.

The continuous disruption of `a`ā and blocky crusts means that flows with these surface textures cool more rapidly than better insulated pāhoehoe flows. Although pāhoehoe flows commonly advance more slowly than `a`ā flows, they can retain their fluid interiors for longer, and so can reach greater lengths than `a`ā flows of similar volume. Though many pāhoehoe toes stagnate after emplacement, others can remain interconnected, and form a network of tubes. Lava tubes also form in `a`ā flows, but the formation of established tube systems generally requires more time than in

pāhoehoe flows. Tubes are favoured by a large contrast between the fluidity of the flow interior and margins, so have not been documented in blocky flows, whose interiors tend to have a considerable strength.

While some flows maintain the same surface morphology throughout activity, in other cases pāhoehoe evolves into `a`ā (or `a`ā into blocky, for higher silica lavas). The transitions are not reversible, so pāhoehoe, `a`ā and blocky surfaces are therefore parts of a continuous spectrum of lava types. The pāhoehoe-`a`ā transition occurs at a certain critical relation between viscosity and strain rate, the 'transition threshold' (Peterson & Tilling 1980). If lava slows, cools and stops in response to a viscosity increase only, it remains pāhoehoe, but if it is forced to continue flowing after the transition threshold is reached, it will change to `a`ā. The enforced continuation may arise from either an increase in topographic slope, or the advance of more fluid lava from upslope. Hawaiian lavas tend to erupt at high temperatures, close to their liquidus, and as such are more fluid than, for example, Etnaean lavas, which have lower eruption temperatures, and tend to be more crystal rich upon eruption. These factors mean that while both pāhoehoe and `a`ā form in both volcanic settings, pāhoehoe is more common on Hawaii and `a`ā is more common on Etna.

1.4 Summary

The aim of this introduction, in addition to detailing the way in which the work is presented in the thesis, has been to provide some relevant background regarding the problems facing the accurate description of lava flow emplacement. The highly variable, cooling-dependent rheology is the major factor that must be considered in any attempt to described the emplacement of lava flows using analogue models, and the following chapter reviews the many ways in which this problem has been tackled

experimentally. This necessarily includes a discussion of the wide range of materials that have been used to simulate such complex rheology. As has been seen, the range of morphologies that can occur in lava flows is dependent on the external, environmental parameters as well as the rheology, and this aspect has also been considered in several of the experimental models that are discussed.

2. Analogue Modelling

2.1 Scaling and dimensional analysis

Analogue models can facilitate the study of complex geological phenomena, but the models must be capable of faithfully representing natural systems. Hubbert (1937) set out to derive the general theory of similarity between a model and its original for the mechanical case, and concluded that two systems can only be considered comparable if they are geometrically, kinematically and dynamically similar. Geometric similarity requires that all corresponding lengths in the two bodies are proportional, and all angles are equal; kinematic similarity that the times required for any given change of shape or position (i.e. the velocities and accelerations of corresponding points) are proportional; and dynamic similarity that the forces acting on corresponding elements of mass and volume must produce corresponding motions. In short, similarity requires that the masses of the model, point by point, are proportional to the corresponding masses of the original, and that the corresponding forces, point by point, have the same directions and proportional magnitudes. Dimensional analysis can include thermodynamic as well as mechanical relations, and although these were not considered by Hubbert (1937), they have been addressed by other workers since e.g. Fink & Griffiths (1990, 1992), Griffiths & Fink (1993).

The basis of dimensional analysis is simply that both sides of an equation must refer to the same type of physical entity, which means that they must have the same dimensions in terms of mass, length, time etc. (Middleton & Wilcock 1996). Dynamic systems can be described based on this prerequisite: if the main variables in the system are known, then based on their dimensions it should be possible to determine the form of the equations that relate the variables to one another. With respect to scale

models, dimensional analysis can also be used to show the conditions that are necessary for dynamic similarity between the model and the natural system. In a scale model, geometric similarity is relatively easy to reproduce, but establishing dynamic similarity can be more problematic, and involves careful consideration of the materials chosen. A fuller treatment of scaling is provided in chapter three, where these principles will be applied to the laboratory model used in this thesis, showing that the model is a very useful analogue for lava flows.

2.2 Background to analogue modelling

Many examples of scaled models of lava flows and domes appear in the literature, using a range of modelling substances (e.g. Hulme 1974; Hallworth et al. 1987; Fink & Griffiths 1990, 1992; Griffiths & Fink 1997; Osmond & Griffiths 2001; Buisson & Merle 2002, 2005; Lescinsky & Merle 2005; Balmforth et al. 2006). As discussed in chapter one, the rheology of lava between the liquidus and the solidus is best described using a pseudoplastic model (figure 1.2). It can, however, be usefully argued that the flow behaviour of a Newtonian fluid is similar to that of a Bingham fluid when its yield stress is exceeded, i.e. stress is proportional to strain rate, the gradient giving the Bingham viscosity. In turn, a Bingham model can approximate pseudoplastic behaviour over a small range of strain rates, so models incorporating any of these rheologies, as long as they are suitably scaled, can provide useful insights into the behaviour of lava flows. An additional problem, not considered in section 1.3.1, is that of solidification. Once the lava surface has cooled and solidified, it cannot be easily approximated by any of the rheologies considered in chapter one, and may behave as a brittle or rigid layer. This introduces an added complication for any analogue model. In all of the analogue modelling work reviewed in this chapter, the

authors have compared qualitative morphological observations and/or quantitative measurements of their models with similar studies of lava flows, and have often found agreement between the two data sets. This evidence suggests that even with rheological simplifications, useful results can be produced with analogue models.

The majority of models discussed in this chapter aim to investigate the effects of rheology and effusion rate, with or without the effects of slope and cooling, on the resultant dimensions and/or surface morphology of effusive products. 'Effusive products' covers the whole spectrum of morphologies from domes, through coulées, to long lava flows. A significant advantage of analogue models is that certain parameters or processes can be investigated in isolation, in order to elucidate the specific effects they have on resultant structures. Dimensions and surface morphologies are useful choices when examining flow dynamics, as dimensions can be measured from remote sensing images, and morphology can be observed during active flow. Many analogue models have been conducted to test theoretical models, while some theoretical models have also been inspired by analogue models, or are used to investigate specific structures which have been observed in analogue models. These approaches are relevant to the experimental work presented in the thesis, and are considered within the scope of this chapter. A summary of all the literature reviewed is presented in table 2.1.

Due to the complexity of lava flows, a large number of parameters and processes have been considered in the various modelling approaches, which include internal rheology of the flow interior (viscosity, yield strength); crustal rheology (viscosity, yield strength, tensile strength) and crustal thickness; effusion rate (increasing, decreasing, constant, pulsed); source geometry; cooling rate; slope; basal roughness; breakouts and internal thermal pathways; thermal erosion capabilities; convection;

channel irregularities; crystal concentration; surface morphologies (including folding, fracturing, lobe formation, the pāhoehoe-`a`ā transition, crustal distribution); internal strain, and crystal concentration. There is therefore a wealth of literature to assess, and this is presented in approximately chronological order, as earlier findings are built upon and improved in later work. Scaling arguments have shown that differing modelling approaches can represent flows of different rheologies and compositions. The whole spectrum of lavas, from fluid basalts to highly viscous rhyolites, can be represented within the wide range of modelling approaches, with some models applicable to a large range of compositions, and others to a narrower range.

It is useful to briefly consider the lava dome classification system of Blake (1990), before looking at the previous analogue modelling work. Blake classified lava domes on the basis of their morphology (figure 2.1), which is believed to be determined by the physical properties of the dome forming material. Starting with the most viscous, he defined 'upheaved plugs' (figure 2.1 a), which are too viscous or too strong to flow upon extrusion. They therefore grow vertically upwards from the source vent, and can reach heights exceeding their radii. Because they collapse easily, they are rarely observed. Material which is slightly less viscous, or has a lower yield strength, forms 'Peléean domes' (figure 2.1 b), which grow episodically and are characterised by spines and crags. Growth seems to be exogenous (Williams 1932), with magma being squeezed through cracks in the outer carapace to form new lobes, rather than being added to the interior, causing growth by inflation (endogenous growth). These domes are flanked by an apron of talus, which may or may not add support to the dome edifice. Less viscous magma forms 'low domes' (figure 2.1 c), which have smooth, gently rounded profiles, and grow endogenously. For a given radius, these domes are lower than Peléean domes, which is consistent with more fluid behaviour, and the

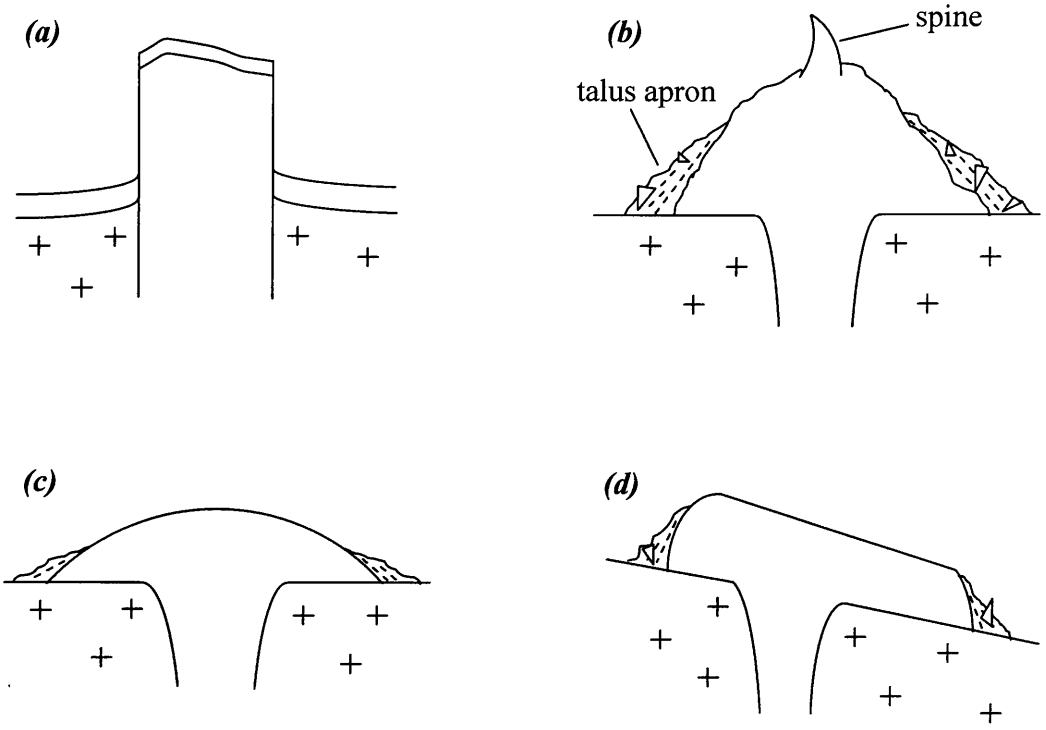

Figure 2.1. Sketches of the four dome types described in Blake (1990)'s classification. (a) Upheaved plug. (b) Peléean dome. (c) Low dome. (d) Coulée; note sloping ground. Redrawn after Blake (1990); figure 1. See text for details.

shape is governed largely by the rheological properties of the fluid interior, rather than by the mechanical properties of a talus apron. Finally, in considering more fluid material, he defined 'coulées' as stubby lava flows, whose morphology is influenced by slope as well as rheology, and which can flow down gentle inclines rather than building symmetrical domes (figure 2.1 d). Coulées can be considered intermediate between edifices strictly defined as 'domes', and extrusions which form extensive lava flows. All of the models discussed in this chapter can be considered to represent morphologies in the range from Peléean domes to extensive lava flows.

Table 2.1. Summary of the literature reviewed in chapter two.

Source	Fluid	Rheology	Cooling/ solidification? (C/S)	Aims and principal findings
Hulme (1974)	Kaolin-water slurry	Bingham	No	Levée formation explained by fluid's yield strength.
Greeley & Womer (1981)	PEG	Newtonian	C & S	Effusion rate and topography primary controls on resultant morphology.
Huppert et al. (1982)	Silicone fluid	Newtonian	No	Growth pattern similar to real lava domes, but high skin strength needed.
Olleveant (1983)	Kaolin-water slurry	Bingham	No	Reassessing model results of Hulme (1974)
Hallworth et al. (1987)	PEG	Newtonian	C & S	Flow morphology and distribution depends on how flow deals with solidification at flow front.
Bond (1988)	Kaolin-water slurry	Bingham	No	Explains discrepancies in models of Hulme (1974) by arcuate fracture zones.
Blake (1990)	Kaolin-water slurry	Bingham	No	Yield strength produces dimensions more comparable to lava domes. Surface slip lines seen.
Fink & Griffiths (1990)	PEG	Newtonian	C & S	Morphology dependent on relationship between solidification time and a timescale for lateral spreading.
Fink & Griffiths (1992a)	PEG	Newtonian	C & S	Source geometry does not disturb morphological classification of F&G 1990 significantly. Application to submarine flows.
Fink & Griffiths (1992b)	PEG	Newtonian	C & S	Application of results of F&G 1990 to planetary flows.
Stasiuk et al. (1993)	Glucose syrup	Newtonian	C	Highly temperature dependent viscosity changes shape of analogue flow: cooled margins slow spread.
Gregg & Fink (1995)	PEG	Newtonian	C & S	Very high slopes change regime boundaries of F&G 1990.
Gregg & Fink (1996)	PEG	Newtonian	C & S	Application of results of G&F 1995 to planetary flows.
Griffiths & Fink (1997)	Kaolin in PEG	Bingham	C & S	Yield strength a fundamental influence on developing morphologies.
Merle (1998)	Silicone gel	Newtonian	No	Examined strain in flow interiors.
Donnadieu & Merle (1998), Merle & Donnadieu (2000), Donnadieu (2000)	Silicone gel + sand & flour	Newtonian + brittle 'crust'	No	Investigated inflation of cryptodome intrusions by extruding silicone into a cone of sand and flour. Found that sector collapse occurred after initial period of endogenous inflation.

Blake & Bruno (2000)	PEG	Newtonian	C & S	Investigated the long term evolution of flow fields: crustal strength eventually dominates flow advance. Importance of eruption duration in controlling final morphology.
Gregg & Fink (2000)	PEG	Newtonian	C & S	Found increasing slope shifted regime boundaries in a more complex manner than that seen by G&F 1995.
Osmond & Griffiths (2001)	Kaolin in PEG	Bingham	No	Investigating effect of yield strength on final flow shape. Yield strength can be estimated based on flow shape and slope.
Buisson & Merle (2002, 2004)	Silicone gel	Newtonian	No	Examining the strain in dome interiors.
Griffiths et al. (2003)	PEG in channels	Newtonian	C & S	Found surface solidification to be strongly controlled by the pattern of thermal convection and the timescale for shearing.
Anderson et al. (2005)	PEG	Newtonian	C & S	Examined the way material flows in the flow interior, and suggested this could be governed by viscous fingering.
Buisson & Merle (2005)	Silicone gel + sand & plaster	Newtonian + brittle crust	No	Found thickness of brittle crust influences dome deformation. Thin crusts spread evenly; thick crusts undergo sector collapse.
Lescinsky & Merle (2005)	Silicone gel + different crusts	Newtonian + brittle or viscous crust	No	Investigated relationship between internal shear stresses and crustal rheology. Brittle crust models developed structures that resembled those seen on the surfaces of lava flows.
Lyman et al. (2005)	PEG or Kaolin in PEG in channels	Newtonian or Bingham	Isothermal or C & S	Looking at different spreading regimes based on the relative influence of solidification and yield strength.
Balmforth et al. (2006)	Corn syrup, Kaolin-water slurry	Newtonian, Herschel-Bulkley	No	Using analogue models to test numerical models of fluids flowing down inclined planes using asymptotic methods for shallow flow. Note that the model predicts the presence of 'pseudo-plugs'.
Cashman et al. (2006)	PEG in channels	Newtonian	C & S	Channel geometry, including changes in width, bends or floor roughness, has significant influence on resulting surface crust morphology.
Lyman & Kerr (2006)	PEG or Kaolin in PEG in channels	Newtonian or Bingham	Isothermal or C & S	Similar experiments to Lyman et al. (2005), but including the effects of slope.
Kerr et al. (2006)	PEG	Newtonian	C & S	Derived an expression for the final width of an unconfined flow on a slope. Demonstrated that the formation of channels was controlled by the yield strength of the growing crust.

2.3 Early work

2.3.1 Isothermal flow models of Hulme (1974)

The earliest example of a comprehensive analogue modelling approach in the literature is provided by Hulme (1974), who developed a theory for the unconfined flow of an ideal Bingham fluid on a slope, and tested this using kaolin-water slurries. Having noted that lava flows commonly come to rest on slopes as soon as the supply ceases, he reasoned that this was due to the presence of a yield strength rather than cooling, showing that the tensile strength of a thin solid skin would to be insufficient to resist the outward hydrostatic pressure of the still-liquid interior for anything other than small-scale flows. He used this argument to justify the use of an isothermal modelling approach for flows with high discharge rates, which, he demonstrated, would develop relatively thin skins during the emplacement time.

He predicted that the width of a flow would become fixed a small distance from the vent, due to the formation of stationary levées. This is commonly observed on natural flows, and was reproduced in his analogue models. During the early stages of an experimental model, the modelling fluid spread laterally as well as downslope, until the basal shear stress dropped to the yield strength, at the 'critical depth', the depth below which no flow occurs. At this point, stationary levées developed at the flow margins, fixing the flow width, and subsequent motion was concentrated in the downslope direction.

Hulme (1974) compared key dimensions from the experimental flows (total flow width, levée depth and width, channel centreline depth), with values predicted by the theory, and used them to calculate rheological parameters. However, this required accurate characterisation of the rheological parameters of the experimental fluid, which proved difficult due to the complex nature of the fluid and the primitive

equipment used. The discrepancies noted by Hulme between the measured and predicted values of the dimensions were attributed to this non-ideal behaviour, and he reasoned that the theory described the flow accurately enough to be used in the interpretation of natural flows, applying it to the study of some terrestrial and lunar flows. One of the primary applications of the theory was the use of levée dimensions to calculate the yield strength of the fluid. This calculated yield strength was then compared with estimates of viscosity, to estimate the effusion rates and compositions of the lunar flows. However, in applying these theoretical relationships between flow dimensions and rheological properties to the study of natural flows, some invalid assumptions were made. Firstly, Hulme noted from observations of his experiments that, in some cases, more than one set of levées could form, and stated that the use of the outermost set of levées would be most likely to give the best estimate of initial depth, and hence yield stress. This is indeed the case, but ensuring that a set of levées has not been modified since their formation is not a simple matter. While it is possible to verify for flows that are observed during emplacement, such an assumption cannot be justified on the basis of an image of an inactive flow alone. Even if only one set of levées is seen in the image, it cannot be assumed that they have not been modified by any further processes such as overflows or rubble accretion (e.g. Sparks et al. 1976). Secondly, in using the calculated yield strength and estimated viscosity to estimate the chemical composition and effusion rate of extraterrestrial flows, he did not take into account that the yield strength and viscosity of any given flow changes markedly as the lava cools and crystallises (e.g. McBirney & Murase 1984; Fink & Zimbelman 1990; Pinkerton & Stevenson 1992), so the relationship between yield strength, silica content and effusion rate is non-unique.

In summary, while the modelling approach produced a simple explanation for the formation of stationary levées and fixed channels, the significance of the theoretical predictions is questionable due to discrepancies between calculated and predicted values, and the large number of assumptions. The isothermal assumption can be considered reasonable close to the vent, or for deep, high effusion rate, high velocity flows, but will always break down given sufficient time, because all lavas eventually undergo significant cooling. It also seems to be in conflict with the assumption of a high aspect ratio (width >> depth), which will promote greater cooling than a more equant channel. Effusion rate was also assumed to be constant, which is rarely applicable (e.g. Wadge 1981), and did not seem to be achieved in the models judging by the development of nested levées in several runs. Whilst the overall assumption of a yield strength is appropriate for some flows, e.g. Etnaean basalt erupted at a low temperature, it cannot be applied to others e.g. proximal Hawai'ian flows, which are erupted at very high temperatures.

2.3.2 Reappraisals of the work of Hulme (1974)

Subsequent workers have aimed to reproduce the models of Hulme (1974) and have provided other explanations for the poor fit between his predicted and measured dimensions (e.g. Olleveant 1983; Heslop 1987; Bond 1988). They have also provided more detailed descriptions of some of the surface features observed on the experimental flows, which were only briefly mentioned by Hulme. The most comprehensive reassessment of the work was carried out by Bond (1988), who also attempted to fully characterise the rheology of the modelling substance, as rheology was assumed by Hulme to be the primary control on flow characteristics. Bond (1988) and Olleveant (1983) both note the development of compound levées, and of shear

Figure 2.2. Image illustrating the 'arcuate fracture zones' described by Hulme (1974), and Bond (1988), in their kaolin-water slurry models. Flow direction is left to right, and the flow is approximately 1 m long. Note that the flow has widened as it has travelled down the slope, facilitated by the action of the arcuate fractures. Compare the pattern of fractures in figure 2.3 (b). From Bond (1988); plate 5.7. See text for details.

fractures on the surfaces of the flows. These fracture planes (dubbed 'arcuate shear zones' by Bond (1988), figure 2.2) are remarked upon as being 'very common' by Hulme, then discussed no further. Bond, however, considers that they could be significant in causing the discrepancies which he observed between the theory and predictions. He found the levées to be consistently deeper than predicted, and the channels consistently shallower, suggesting that the action of the shear zones moved material from the centre of the channel to the margins, allowing levée formation at the flow front, and also allowing the flow to widen. The excess levée depth resulted in overestimations of yield strength, which highlights the importance of fully understanding all of the processes occurring in a model, before attempting to use models results as predictive tools.

It is significant that the flow equations of Hulme (1974) were two dimensional, accounting only for material flowing in the downslope or cross slope directions, but at no other angle relative to the channel. This would necessarily discount the possibility of considering the gradual flow of material towards the margins of the channel at the

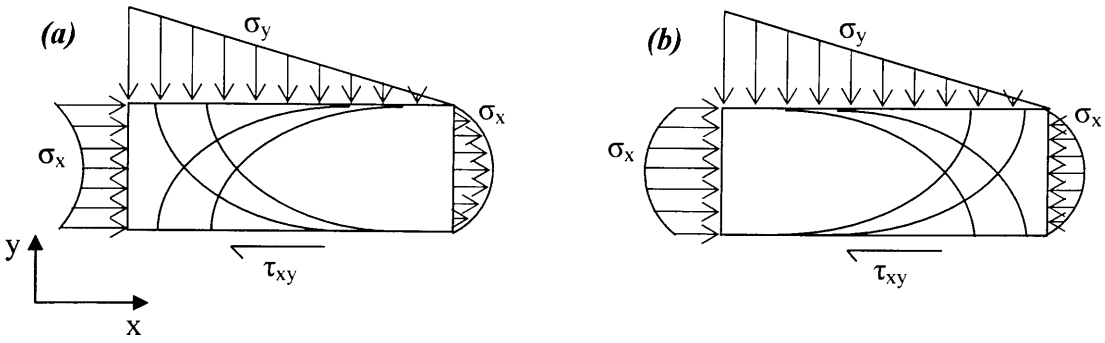

Figure 2.3. Stress distributions and resulting slip lines in a plastic pressed between two rough parallel plates. Flow direction is left to right. (a) Passive plastic state, where the plastic is squeezed out from between the plates, resulting in extension in the x-direction. (b) Active plastic state, where the horizontal compressive force causes the two plates to move apart, resulting in extension in the y-direction. The slip lines in the active plastic state resemble the arcuate fracture zones described by Bond (1988), see figure 2.2. Redrawn after Nadai (1950); figures 37-6 and 37-7.

flow front, thus preventing the description of the processes observed and considered important by Bond (1988). The geometry of the arcuate fractures is strikingly similar to the slip lines predicted to form in a plastic mass pressed between two rough parallel plates, by Nadai (1950), as shown in figure 2.3. Two states are represented in the figure: that of a passive plastic (a) and of an active plastic (b). The passive plastic state is produced by bringing the solid parallel plates together, forcing material out from between them in the x-direction, while the active state is governed by the horizontal compressive stresses, which tend to force the plates apart. The slip lines represent the directions of maximum shear stress. The fractures noted by Hulme (1974) and Bond (1988), shown in figure 2.2, resemble the slip lines in the active state, because of the presence of horizontal driving forces acting down the channel. The horizontal forces are greater than the confining forces, i.e. the basal shear stress, and so the channel widens, in accordance with Bond's interpretation (figure 2.2).

Bond (1988) also noted that drainage features could often be mistaken for levées, which would result in errors in the estimate of yield strength, and that basal sliding

could result in the flow being shallower than predicted, neither of which were discussed by Hulme (1974). Both Olleveant (1983) and Bond (1988) noted that viscosity and slope were the most important controls on flow length for isothermal flow, and that there was no relationship between flow length and effusion rate, such as those found by Walker (1973) and Wadge (1978). Such a relationship would not be expected in the absence of cooling, which shows that cooling cannot be ignored in a comprehensive flow model. Bond also found that changing effusion rates had a significant effect on the resulting channel width, and that assuming an average effusion rate for a situation in which the effusion rate changed could not predict the flow dimensions that developed. He concluded that the lack of agreement between experimental and predicted parameters could be attributed to the presence of arcuate shear zones.

2.4 Isothermal, axisymmetric 'low' dome models

Despite the early attempts of Hulme (1974) to incorporate a yield strength, many subsequent workers continued to use Newtonian fluids to model the growth of flows and domes. The Newtonian model can be justified for proximal pāhoehoe and `a`ā flows in Hawai'i, which have been shown to be close to linearly viscous through studies of crystal and vesicle distributions (Rowland & Walker 1988; Walker 1989). Such a model, however, is not valid for proximal flows of lava which have been erupted with a significant crystal content, or for medial and distal basaltic or andesitic flows (Pinkerton & Sparks 1978; Shaw et al. 1968). The most oft cited study of the spread of a Newtonian fluid is by Huppert et al. (1982), who presented a theoretical model of fluid spreading isothermally under its own hydrostatic pressure, thus assuming that viscosity is the key parameter in determining the shape and spreading

rate of a dome. Huppert et al. argued that even though dome-forming lavas are non-Newtonian, their yield strengths are lower than the basal stresses in large silicic domes, so the domes can be modelled as Newtonian. The model was tested by extruding a silicone fluid onto a horizontal plane at constant rate, and comparing its evolving shape and dimensions with the predictions of the theory, in a similar method to that of Hulme (1974). The evolution of the analogue model was found to fit well with the theory, but subsequent application of the theory to the growth of the basaltic andesite lava dome of the Soufrière, St Vincent highlighted some problems. While the changing shape of the dome was simulated quite well by the theory, in order to achieve this fit, an effective bulk viscosity for the dome of the order 10^{11} Pa s had to be assumed. This is several orders of magnitude greater than typical measured lava viscosities, and it was suggested that such a high value might reflect the presence of an extremely viscous 'skin', formed by marginal cooling, which constrained the flow of material in the dome to such an extent that it effectively dominated the dome behaviour. Since the laboratory model was isothermal, the growth of such a skin could not be reproduced, and neither could many of the behaviours associated with real domes: for example, since the fluid was Newtonian, the cessation of activity could not be modelled. Throughout the experiment, fluid was injected into the base of the dome to maintain the shape, so the dome was never in a state of static equilibrium but continually expanded. If the supply had been switched off, the fluid would have sagged into a flatter and flatter pile, spreading indefinitely until constrained by topography, or until surface tension effects became important. While sagging has been observed in real domes between episodes of extrusion (Mt St Helens, D. Swanson, in Iverson 1990), this does not result in indefinite spreading: when the supply ceases, the lava pile eventually settles into an equilibrium shape that remains dome-like, yielding

the features seen in the geological record. Secondly, since the fluid pressure in the model was everywhere hydrostatic, there was no build up of the excess pressure necessary to cause explosions or localised extrusions, both common in real domes (Iverson 1990).

With this in mind, other models were developed in an attempt to describe the evolution of natural domes more accurately. Blake (1990) again used an isothermal approach, but incorporated a yield strength into the theoretical model, using a kaolin-water slurry (a Bingham fluid, Hulme 1974) to test this. The Bingham approximation is considered appropriate for slowly growing domes, as the shear stresses will fall in a narrow range only slightly greater than the yield strength, so the effects of shear thinning are negligible. The spread of any dome involves driving (gravitational) and resistive forces, and the balance of these forces describes the equilibrium state of the dome (section 2.5). While the force balance for a Newtonian dome necessarily involves viscous shear, a dynamic process, the balance for a viscoplastic is achieved in a state of static equilibrium between gravity and the fluid's yield strength, and the dome grows from one state of static equilibrium to the next. Blake's method was similar to that of Huppert et al. (1982), effusing the slurry at a constant rate onto a horizontal plane, and measuring the changing dimensions over time. The measurements indicated that the weight of the dome (the gravitational driving force) is balanced by a basal shear force limited by the yield strength, so that dynamic growth was achieved by progression through successive states of static equilibrium. Alongside the measurements of dimensions, Blake presents morphological observations of the surface texture during growth, showing that the surface was divided into rhombohedral segments separated by two intersecting sets of spiral grooves (figure 2.4). The spacing of the grooves increased from the centre of the dome

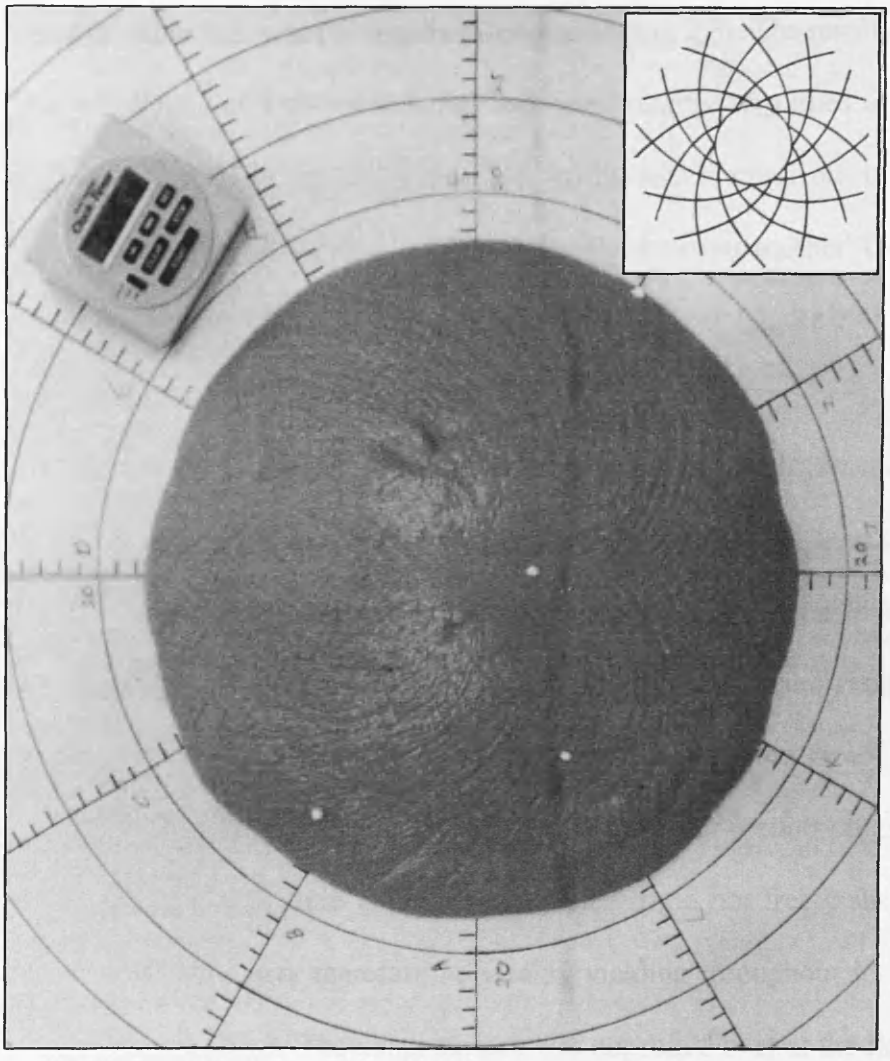

Figure 2.4. Image of a kaolin-water slurry dome, showing the slip planes that have developed across the whole dome surface. Spacing of concentric circles is 5 cm. From Blake (1990); figure 7. This pattern of slip planes closely resembles the logarithmic spirals described by Nadai (1950), shown in the inset. From Nadai (1950); figure 37-13. See text for details.

to its margins, and they are interpreted to be the traces of slip planes that cut through the dome allowing it to constantly adjust its shape, thus remaining in a stable configuration. The spirals remained smooth in trace even if extrusion was episodic or changed in rate, providing evidence that the dome was always in a state of static equilibrium. These spirals have also been observed in spreading isothermal viscoplastic models by Osmond & Griffiths (2001) and Balmforth et al. (2006). In his consideration of plastic flow, Nadai (1950) treated radial flow, as well as the flow

between parallel plates that was previously discussed (figure 2.3). The results from the study of the radial flow of a plastic material suggested that the slip lines in this case form two sets of logarithmic spirals (figure 2.4, inset), which spiral out in opposite directions from the centre of the flow, and are orthogonal to one another. Comparing Nadai's sketch and the kaolin-water slurry dome of Blake (1990) (figure 2.4), it can be seen that the patterns are indeed very similar.

The surface of Blake's domes were observed to stretch circumferentially and become compressed in the radial direction over time, suggesting that there is no true plug, though a vertical velocity profile may have shown plug flow near the margins. The slurry is, however, known not to be an ideal Bingham fluid, and Balmforth & Craster (1999) and Balmforth et al. (2000) showed that true plug flow is not always a valid assumption even for an ideal Bingham fluid. Instead, 'pseudo-plugs' occur, which are regions where the fluid is neither completely rigid nor freely shearing. In Blake's models, the fluid may therefore be weakly yielding throughout its depth to compensate for the expansion. The dome surface was not rolled over at the flow front, which contrasts with observations of `a`ā flow fronts, but is similar to the action of pāhoehoe surfaces with continuous crusts, as discussed in chapter one. Observations of the propagation of dome flow fronts are hampered by the presence of talus aprons, so it is unknown whether or not rollover occurs at the flow front, although the dome cross section shown in Huppert et al. (1982) does infer a basal rubble layer (figure 2.5). Blake (1990) also tested his growth model by comparison with the development of the 1979 Soufrière dome of St Vincent, and estimated a bulk yield strength for the dome material of the order 10^5 Pa, which is considered to be a significant overestimate, as material of this strength could not rise through conduits of realistic dimensions. The problem of overestimation is again due to the inability to account for

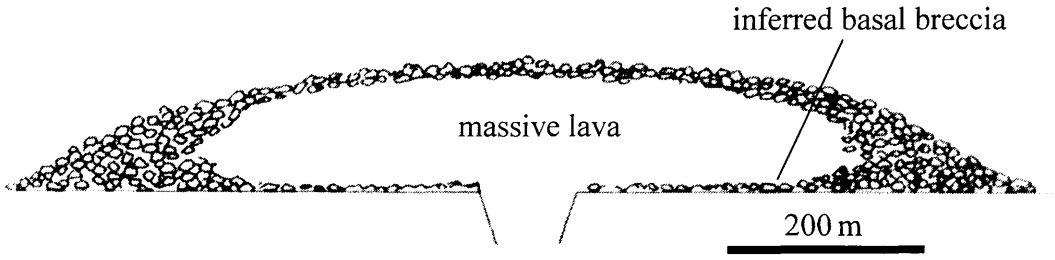

Figure 2.5. Schematic cross section through the 1979 lava dome of Soufrière, St. Vincent. The presence of a basal breccia is inferred. From Huppert et al. (1982); figure 14 (b).

the effects of the carapace, as was the case in the treatment of Huppert et al. (1982), and again illustrates that the carapace probably dominates the overall flow behaviour. The estimate of a bulk value to describe the overall rheology is necessarily unrealistic.

Despite the introduction of a yield strength, Blake's model failed to adequately describe the dome behaviour, although it provided the mechanism by which the dome can stop spreading after effusion ceases. As discussed with reference to the model of Huppert et al. (1982), the assumptions of hydrostatic pressure and rheological homogeneity are insufficient, and so the problem of the carapace needed to be tackled.

2.5 Theoretical treatment of surface crusts

Before moving on to the experimental treatment of surface crusts (section 2.6), it is useful to take a brief look at the theoretical approaches that have been employed in their study.

Iverson (1990) presented a theoretical two-layer model of a lava dome as a brittle shell enclosing pressurised magma. While not explicitly incorporating a cooling element into the model, the assumed rheological structure is a reasonable approximation of that which would develop in real domes due to the action of cooling. The model combined the carapace thickness and tensile strength, the unit weight of

the magma and the pressure head of the magma at the dome apex, to produce a single dimensionless parameter, D, which was argued to completely govern dome shape. Iverson noted that while the model of Blake (1990) incorporated a yield strength, this is a shear strength rather than strength in tension, while cooling and solidifying lava would be expected to develop a tensile strength. Growth of the dome was considered to proceed in a series of static equilibrium states, as described by Blake (1990) where equilibrium is defined as the carapace just containing the pressure exerted by the ductile core. If an increase in pressure occurred, the dome responded either by changing the equilibrium shape, or by a non-linear process such as tensile failure leading to an extrusion or explosion. A new set of values for the governing parameters would then be established, leading to a new equilibrium state. If the value of the parameter D stays the same during growth, the growth can be considered to be 'self-similar', so that the shape remains constant while the size changes. The model was compared with data from growing domes at Mt St Helens, which showed self-similar growth, and a good match between measured and predicted topographic profiles was found. A drawback of Iverson's model is that while the dome can exist in only one shape and size for fixed values of the four parameters which contribute to D, there is no way of knowing which parameters are changing, and how they change, during growth. This means that even though D values can be calculated for real domes, these cannot be used to provide information about the physical nature of the domes.

While the two-layer model of Iverson (1990) is still a simplification, since the rheological properties of a dome presumably vary continuously from core to carapace, it is an improvement on the models of Huppert et al. (1982) and Blake (1990), in that it supposes a distinct mechanical behaviour for the carapace, resulting from cooling. It also provides a mechanism for explosions and extrusions, which is tensile failure of

the carapace due to either an increase in pressure beyond the strength limit of the shell, or a decrease in its tensile strength under constant pressure. Denlinger (1990) noted accelerating endogenous growth of the Mt St Helens dome prior to the 1981 and 1982 exogenous extrusions, and attributed this to either a non-linear pressure increase in the interior, or progressive weakening of the carapace. He suggests that the progressive growth of cracks at velocities lower than those required to cause failure could provide an explanation for both possible mechanisms. Under constant pressure, progressive crack growth will reduce the tensile strength of the shell with time, while if the applied load is increased, crack growth rates will increase exponentially. The presence of pervasive fractures has been used to call into question the continuous carapace model (Stasiuk et al. 1993). While cracks obviously present a problem when trying to estimate the tensile strength of the carapace, the model can still be useful. If none of the cracks link directly from the fluid interior to the surface, then the dome will be in static equilibrium despite the lower-than-ideal tensile strength. If one of the cracks does subsequently result in failure, the response will be an explosion or extrusion which will release the excess pressure, allowing equilibrium to be restored.

Griffiths & Fink (1993) introduced the problem of cooling into their treatment of flow dynamics, and provided a broader range of possibilities for the rheologies involved. They point out that the carapace itself is likely to be rheologically complex, possibly incorporating brittle solid, ductile solid and cooled viscous melt, and that representing this complexity in a simple model consisting of a cooled crust and a uniform isothermal interior is somewhat problematic. The behaviour of any dome is controlled by force balances, and they defined a number of dynamic regimes, based on simple balances of the various forces involved. The forces available to drive the

spread of the lava result from inertia (which is negligible except at very small timescales), buoyancy (gravity-driven spread) and overpressure. The forces which resist spreading can result from the action of the hot interior or the action of the crust. The retarding forces from the interior may arise due to rate of strain, shear, shear strength or tensile strength, while the effect of the crust is more complex as the rheological heterogeneity means the effective mechanical properties are uncertain. The three simplest possibilities are considered: that where the crust is represented by an effective Newtonian viscosity (which may be much greater than the interior viscosity); by a plastic yield strength (again, which may be greater than that of the interior) or by a tensile strength. These options cover the range of rheologies previously considered by Huppert et al. (1982), Blake (1990) and Iverson (1990).

The scaling analyses of Griffiths & Fink (1993) indicate that a number of different dynamical regimes involving balances of the above forces can occur in the presence of surface cooling, and that they relate to the relative strength of the cooling. When cooling is slow and effusion rate high, the flow is effectively isothermal, and crust does not form close to the vent. In this case, the balance of forces is between gravity-driven buoyant flow and the viscous resistance of the fluid. At very high cooling rates or low effusion rates, crust forms almost immediately and the dynamical balance is between overpressure and tensile strength (Iverson 1990), but at longer times the driving force will become dominated by buoyancy. The relative importance of shear and tensile strengths in the crust is found to be unclear, and they consider that tensile strength is likely to dominate on small overpressurised lobes (Iverson 1990), but shear strength would become more important for larger, flatter domes and faster spreading flows with fragmented or deformable crusts. Intermediate cooling rates are therefore likely to be characterised by a balance between buoyancy and crustal shear strength.

An interesting prediction of the scaling analysis is that crustal rheology is dominant in resisting flow front advance when the ratio of crustal thickness (near the flow front) to flow length is greater than the ratio of the crust's shear strength to the basal shear stress exerted on the bulk of the flow. This means that, if the effective shear strength of the carapace is several orders of magnitude greater than the shear strength of the interior, flows with low to moderate cooling rates will be governed by the crustal strength once the crust reaches a thickness several orders of magnitude less than the length, for example, a 10 m thick carapace on a dome of radius 1 km is sufficient to control the spreading. Data from Mt St Helens and Soufrière, St Vincent, were found to support the hypothesis that the shape and spreading rate of these domes is controlled by crustal strength and not the stresses in the interior magma.

These theoretical approaches show that dome growth can be described more accurately if the rheological structure is not homogeneous, i.e. if the dome has a carapace whose properties are different to those of the interior, or ideally, whose properties vary continuously through the edifice. The rheological heterogeneity is, of course, due to the cooling and degassing of the lava upon extrusion, and so any analogue models attempting to fully describe the extrusion and evolution of a flow or dome before the point at which it ceases to advance, must incorporate cooling.

2.6 Cooling and solidification in analogue models

2.6.1 Cooling and flow dynamics

Stasiuk et al. (1993) incorporated the problem of cooling into models of low lava domes using glucose syrup, which is a Newtonian fluid with a strongly temperature-dependent viscosity. The syrup was effused at constant rate onto a horizontal plane beneath cold water in order to achieve realistic cooling rates, but it did not solidify

during the experiments. Initially, as the dome spread, its shape resembled that of the domes produced by Huppert et al. (1982) in the absence of any cooling. Over time, however, the cooling of the material at the flow front increased its viscosity to the point where it began to impede the spread of fluid behind, so the flow front became steeper and the surface behind flatter. The models show that, for a given eruption rate, cooled flows have steeper and thicker flow fronts than isothermal flows, which agrees with observations by Walker (1967) that lava flow fronts thicken with time. The scaling analysis performed by Stasiuk et al. (1993) shows that any calculated value for a bulk viscosity is heavily weighted towards the viscosity of the cooled crust (compared to the eruption viscosity), as inferred from the work of Huppert et al. (1982) and Blake (1990), so the bulk viscosity is much more sensitive to the effects of eruption rate and cooling than to the eruption viscosity. In order to estimate the bulk viscosity, therefore, they require a value for the skin viscosity, which necessitates being able to define what is meant by the term 'skin'. They argue that, while defining the solid crust as material below the brittle-ductile transition temperature is straightforward, this material has a negligible effect on dynamics due to the pervasive fracturing described by Denlinger (1990). In this case, the fluid layer which actually affects the flow behaviour must have a temperature higher than the brittle-ductile transition, and sit below the surface cover of solid blocks. This layer was subsequently identified in pāhoehoe flows by Hon et al. (1994), who describe it as the 'viscoelastic' layer and argue that it provides the strength that allows inflation. The top of the layer is defined by Hon et al. as lava that cannot be fractured in a brittle manner, and the base where it passes into lava with no strength. This more continuous rheological structure more closely agrees with the thermal structure expected in a cooling flow. Dragoni & Tallarico (1996) suggested that a similar layer could be present in `a`ā

flows, by modelling the timing of rupture of stationary `a`ā flow fronts using a deforming viscoelastic layer that eventually fails in response to overpressure in the core. The predicted times between cessation of flow and rupturing of the front compared well with failure times measured on Etnaean `a`ā flow fronts by Pinkerton & Sparks 1976.

Stasiuk et al. (1993) showed how cooling affects the dimensions and dynamics of the whole flow, with the thickness and rate of advance being coupled to the thermal structure. They also questioned the two-layer model of ductile interior and brittle crust as being too simplistic due to the limited strength of a pervasively fractured crust. While such a model is undoubtedly a simplification, and the identification of a cooled, yet still ductile, layer as fundamental in the control of flow dynamics is an important step, a solidified brittle crust is clearly a feature of all lava flows and domes. As such, its potential influence cannot be overlooked. In addition, the brittle surface crust is often the only part of the flow that can be observed, and so any major dynamic processes which occur in the interior of a flow must necessarily manifest themselves in an outward fashion through deformation of this crust. In addition to this, even if the brittle crust has negligible strength, the presence of an extra layer of blocks or clinkers must exert some influence on the flow, such as buttressing the flow front, and this layer will also contribute to insulation of the flow interior. As such, the significance of the brittle crust and its response to internal processes cannot be ignored.

2.6.2 Solidification and surface morphologies

2.6.2.1 The early use of PEG

The problem of solidification in flow modelling was considered by Hallworth et al. (1987), who cited the use of polyethylene glycol (PEG) wax in modelling attempts by

Hodgson (1969) and Greeley & Womer (1981). PEG has a temperature-dependent viscosity, though it is not as strongly temperature-dependent as glucose syrup (Stasiuk et al. 1993), and freezes over a narrow range of temperatures easily achievable in the laboratory. The fact that the viscosity is not too strongly temperature-dependent is advantageous, as this means the effects of the increasing viscosity in the surface layer are not easily confused with those of solidification (Griffiths & Fink 1997). The solidified crust is capable of deforming either by viscous flow, or by brittle fracture, depending on the strain rate (Fink & Griffiths 1992). Hallworth et al. (1987) were the first workers to use an experimental setup which effused the liquid wax into water rather than air, thus minimising the effects of surface tension, which are not important in real flows, and allowing more realistic cooling rates (Fink & Griffiths 1990). The aim of the models was to investigate the effects of effusion rate, temperature (hence viscosity) and slope on the morphology and distribution of the wax. This was achieved by extruding the wax from above onto a plane, and staining it with differently coloured dye during the run to allow easy observation of the distribution patterns. They found that high flow rates (i.e. high effusion rates, temperatures and slopes) led to simple flows consisting of straight, wide, open channels, while decreasing flow rates led to increasingly complex flows. Blockages in the channels became more common with decreasing flow rate, as the wax could solidify more easily, and the flow did not have enough momentum to push obstacles out of the way. Increased chilling of the flow front led to less uniform propagation, as the front would stop, inflate, then fail to produce breakouts in a similar manner to the advance of toey pāhoehoe.

Hallworth et al. (1987) concluded that flow morphology and distribution is dependent on the ability of the flow to deal with solidification at the flow front. The

strongly temperature-dependent purely viscous flows of Stasiuk et al. (1993) do not show the variety of qualitatively different behaviours seen in the solidifying purely viscous flows, which indicates that increasing viscosity is not the only factor affecting flow behaviour. It seems that although the surface layer of the models of Stasiuk et al. became increasingly viscous, it did not reach a sufficiently high viscosity or strength to be able to fail in the manner demonstrated by a viscoelastic layer. In addition, although a viscoelastic layer may provide the *strength* of the carapace, the presence of solidified brittle material is clearly influencing the resultant morphology by retarding the advance of the still-fluid wax.

The morphologies produced in the PEG models were phenomenologically comparable with those seen on real flows, such as the pāhoehoe-like propagation of toes and lobes of material at low flow rates, and the formation of levéed open channels at high flow rates. The process of material being moved from the centre of the channel to the margins was described, as observed by Bond (1988), indicating that materials with different rheologies can produce similar processes. The work of Hallworth et al. (1987) is important because it represents the first attempt to model the surface morphology of a flow, as opposed to just its overall dimensions, since Hulme (1974). As mentioned before, surface morphology can provide a useful insight into flow dynamics, and Hallworth et al. clearly demonstrated this outward manifestation of changing physical parameters.

2.6.2.2 Characterisation of the properties of PEG

The properties of PEG wax were characterised by Soule & Cashman (2004), who measured the tensile and shear strengths and the Young's modulus of solid PEG at temperatures and strain rates relevant to flow models. While Griffiths & Fink (1993)

found that flow geometry is best described using a balance of interior buoyancy forces and a crustal shear strength, Soule & Cashman (2004) found that the shear stress of solid PEG was four orders of magnitude smaller than the tensile strength. The effective shear strength observed in analogue models was therefore explained by the presence of a viscoelastic layer (Hon et al. 1994), whose rheological properties dominate the flow behaviour. The observed brittle behaviour of the crust in real and analogue flows is explained as a passive response to ductile deformation and subsequent failure of this viscoelastic layer, which is capable of retarding flow. It is likely that models using PEG wax are more appropriately scaled to pāhoehoe flows than large-scale `a`ā flows, since crustal thicknesses are lower, and the crust is capable of deforming continuously without fracturing, due to the low strain rates. Although in some high slope runs, Hallworth et al. (1987) recorded the presence of fragments of solid, and compared these to `a`ā surfaces, the viscosity-strain rate conditions (Peterson & Tilling 1980) in the models are insufficiently extreme to generate the continuous fracturing needed to produce `a`ā flow surfaces.

2.6.2.3 Scaled models using PEG: solidification time vs. spreading rate

Fink & Griffiths (1990, 1992) also used PEG models to simulate the growth of surface structures, but accompanied this with a scaling analysis that predicted that the resultant morphology will be controlled by the rate of the solidification of the crust. While this was implied by the results of Hallworth et al. (1987), they did not attempt to explain their observations with theoretical arguments. Fink & Griffiths (1990) argued that the experimental conditions could be described using two independent dimensionless parameters. The first parameter represented the amount of cooling required for solidification, and the second was a measure of the rate of lateral flow

compared to the rate of convective heat transfer from the wax to the overlying water. These could be combined to produce one single dimensionless parameter, Ψ, which was predicted to completely govern the dominant morphology observed on any flow. Ψ can be defined as the ratio of the solidification time to a timescale for lateral spreading of the viscous fluid in the absence of a crust (Fink & Griffiths 1992).

The models of Fink & Griffiths (1990), in which PEG was effused beneath an aqueous solution onto a planar base, investigated the effects of effusion rate, temperature difference, slope and basal roughness on the spreading rate and surface morphologies observed. All of these variables directly affect the rate at which the flow cools, hence also Ψ, and the experiments aimed to demonstrate that that this single parameter could be used to determine the character of the flow and the way in which it spreads.

For runs in which no solidification occurred, the flow spread uniformly with the radius being proportional to $\sqrt{t}$, where t is time, while for progressively cooler experiments, the radius at a given time decreases and propagation becomes less uniform (as documented by Hallworth et al. 1987). When a solid crust was able to form, the morphologies produced were indeed found to depend on the value of Ψ. For $\Psi < 0.65$, corresponding to the greatest cooling rates (i.e. the lowest effusion rates or greatest temperature contrasts), crust formed almost immediately over the vent, and the edifice inflated until failure occurred. Propagation then proceeded by progressive breakouts, like subaqueous pillow lava or subaerial toey pāhoehoe, as observed by Hallworth et al. (1987). As the cooling rate decreased (increasing Ψ), the morphologies progressed through rifted plates ($0.65 < \Psi < 2.8$); narrow radial strips of crust which underwent folding ($2.8 < \Psi < 6.4$); and 'levéed' flows, where crust was only produced in a single circumferential levée around the flow front ($\Psi > 6.4$)

(revised Ψ values from Gregg & Fink 1996). These morphologies are illustrated in figure 2.6. The flows usually showed one dominant morphology, and the well-defined ranges of Ψ values associated with the morphologies was consistent with the dependence of behaviour on the rate of crustal formation. These morphologies can be correlated with the dynamical regimes of Griffiths & Fink (1993), where strong cooling was predicted to result in a balance between overpressure and tensile strength (pillow regime); weak cooling in a buoyancy-viscosity balance (levée regime) and intermediate cooling in a buoyancy-shear strength balance (rifts and folds). Fine-scale structures, such as grooves on the pillows and `a`ā clinkers, were not seen in any of the experiments, and this was attributed to the fact that the strength of solid PEG does not scale directly to that of lava crust. Solid PEG is relatively stronger than lava crust, so would need higher strain rates than are produced in the models to continually fracture it. Despite this problem with scaling, the models produce repeatable morphologies which compare favourably to morphologies observed on real flows.

The morphological regimes were shown to be robust by varying certain parameters and observing any changes to the morphological sequence. Fink & Griffiths (1990) used two different effusion mechanisms, one delivering a constant flux, and the other a decreasing flux. When taking the average effusion rate in the second set of experiments, they found that the resultant Ψ value still consistently predicted the morphological regime. The pattern of effusion therefore appeared to have no effect on the developing morphology, in contrast to the observations of Bond (1988), though this may be due more to the fact that the timescales of the experiments were short, and so the gravity-driven decreasing effusion rate did not actually change much over the course of a simulation. Increasing the slope (up to 6.5°), which produced asymmetric flows, shifted the boundaries between the regimes to slightly lower values than would

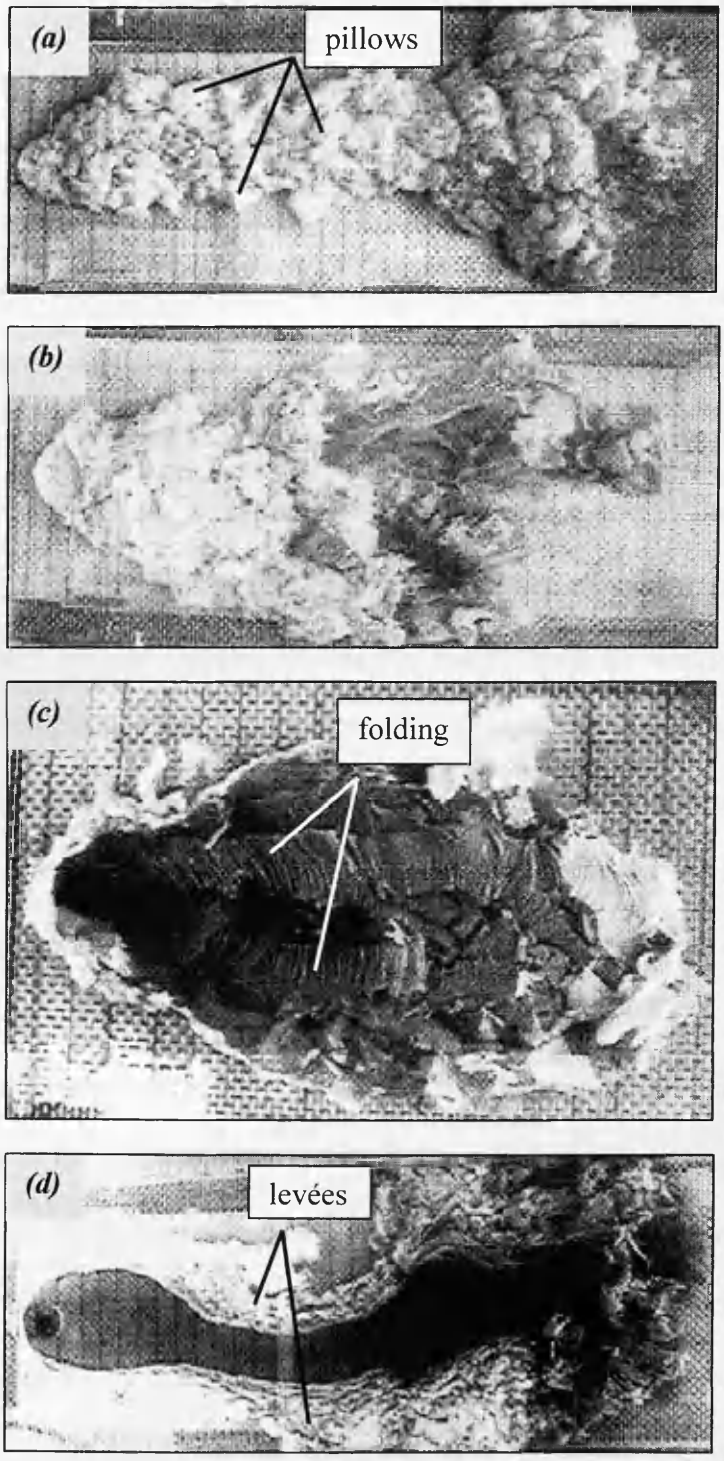

Figure 2.6. The four morphological regimes of Fink & Griffiths (1990), for the extrusion of a cooling and solidifying Newtonian fluid onto a slope. Flow direction is left to right, vent location can be seen in (d). Lines on the tank floor are 2 cm apart. From (a) to (d), Ψ is increasing. (a) Pillowed flow, $\Psi < 0.65$. (b) Rifted flow, $0.65 < \Psi < 2.8$. (c) Folded flow, $2.8 < \Psi < 6.4$. (d) Levéed flow, $\Psi > 6.4$. From Gregg & Fink (1996); figure 1. See text for details.

be expected from the measured conditions, because the higher slope effectively simulated higher effusion rates than were actually used. Increased basal roughness had the opposite effect, as it retarded the flow front by reducing sliding, and increased compressive stresses at the expense of tensile stresses. This expanded the folding regime, and also the pillow regime, as rifting requires large tensile stresses over the vent. A roughened base is probably a more realistic analogue, although the ratio of flow thickness to the vertical scale of roughness may be important (Gregg & Fink 2000), as a shallower flow will be more disrupted than a deeper one for the same amplitude of roughness. Fink & Griffiths (1992) looked at the differences between flows from point and line sources, finding that the differing geometry produced only small morphological changes. For line sources with smooth bases, no pillow regime appeared, which implies that concentric tensile stresses at the flow front are important in weakening the crust sufficiently to allow breakouts to occur. At higher Ψ values, a single rift developed over the source due to the lack of azimuthal tension; and folding occurred at slightly lower Ψ values than expected because of the fairly uniform compressional stresses compared with those in a radial flow from a point source, which decrease as the radius increases.

The robustness of the correlation between morphology and Ψ allows the theory to be applied to the interpretation of real flows with some confidence, and several applications to both terrestrial and planetary flows appear in the literature. Since the heat loss in the models is by convection in the overlying fluid, they are likely to be more applicable to submarine than subaerial terrestrial flows, but Griffiths & Fink (1997) argue that the role of Ψ is not expected to be governed by the heat transfer mechanism, so although subaerial lavas cool predominantly by radiation rather than convection, the results should be transferable. This argument is borne out by the

observations of Gregg & Fink (1996), who calculated that Ψ values of channelised Mauna Loa flows fall into the levéed regime, and that lobes on a Mt St Helens dacite dome have Ψ values in the rifting zone, which agrees with the morphological descriptions of crease structures presented by Anderson & Fink (1992). Gregg & Keszthelyi (2004) also applied the model observations to the study of subaerial flows, examining the emplacement of toey pāhoehoe. While they identified a morphological sequence that corresponded to changing Ψ and could be correlated to the models of Fink & Griffiths (1990), this was applicable only at the scale of individual lobes. It was found to be difficult to assign a single Ψ value to an entire pāhoehoe flow field on the basis of morphological type, as this depended primarily on the local effusion rate. The estimation of a total effusion rate from morphology is therefore difficult, unless there is good evidence for which parts of the flow field were active simultaneously. This is an important factor to be considered when trying to use the models for interpretation of complex flow fields.

Griffiths & Fink (1992a) applied the experimental results to the study of submarine flows, finding that calculated Ψ values for mid-ocean ridge basalt, using estimates of eruption temperature and viscosity, placed the predicted morphologies within the pillow regime for a large range of effusion rates. This is consistent with the observation that pillow basalts are the most common product of submarine eruptions. Gregg & Fink (1995) again considered submarine eruptions, but also extended the experimental work to include slopes of up to 60°. They found the same morphological sequence, but that increasing the slope shifts the regime boundaries to slightly lower Ψ values, in a similar way to increasing the effusion rate. This was later revised by Gregg & Fink (2000), who found that this effect was only seen on slopes of up to 30°, while above 40° there was a slight increase in transitional Ψ values. This was

attributed to the effects of gravitational forces becoming more important than the strength of the solid wax in controlling morphology. Gregg & Smith (2003) suggested that the higher tensile strength of the wax relative to lava (Soule & Cashman 2004) may be responsible for the predominance of levéed flows on high slopes. This observation questions the assumption that slope can be related directly between nature and experiment, though for slopes below 10° in the laboratory, the effects are not pronounced (Gregg & Fink 2000). The models may therefore only be readily applicable to flows on low slopes. Prior to these suggestions, however, Gregg & Fink (1995) made a comparison between experimental morphologies and those of submarine lavas, which are often emplaced on high slopes. They showed that, while the lava morphologies are not always identical to those seen in the models, obvious parallels can be seen, and the morphology again depends on the values of Ψ. The model was applied to an eruption on the Juan de Fuca ridge where the governing parameters (effusion rate, total volume, viscosity, eruption temperature, slope) were known, and the observed morphologies were found to correspond well with the calculated Ψ values, suggesting that, while the detailed relation of slopes may be difficult, the large scale behaviour of the flows remains largely comparable.

The experimental results have also been applied to the study of planetary flows on Venus, Mars, the Moon and Io by Griffiths & Fink (1992b) and Gregg & Fink (1996). Since Ψ is a function of eruption temperature, effusion rate, cooling rate, viscosity and gravity, it would be expected that the dominant morphologies observed on different planets and satellites are likely to be different. Given the lower gravity on Mars, the Moon and Io, and higher convection rates on Venus due to the dense atmosphere, Griffiths & Fink (1992b) predicted that faster effusion rates would be required on these bodies than (subaerially) on the Earth to produce the same morphologies, given

similar rheology. This would suggest that rifting and folding regimes should be more common on Venus and the Moon, given the same eruption parameters, which is consistent with the smooth lavas seen on these bodies, though their effusion rates are unknown.

Gregg & Fink (1996) took a more quantitative approach to the interpretation of planetary flows, first classifying flows on the basis of their morphology, assigning them a range of possible Ψ values, then (because the compositions were unknown) inserting a set of possible eruption parameters into the model, allowing effusion rates to be graphically determined. These eruption parameters (eruption temperature, viscosity, density) imply a composition by comparison with observed and estimated terrestrial eruption parameters. The calculated effusion rates were then compared to terrestrial values for lavas of similar compositions to assess the viability of the model results, and it was found that the existence of highly evolved compositions (dacite, rhyolite) on planetary bodies is not necessitated by the observed lava flow types.

2.6.2.4 Investigating the long-term evolution of a flow field

Blake & Bruno (2000) extended the work of Fink & Griffiths (1990, 1992), by examining the long-term development of flow fields, both theoretically and experimentally. They investigated the evolution of initially axisymmetric flows of PEG extruded from a point source onto a flat plane, concentrating on the development of the crust-dominated regime, in which deformation is focused on isolated weak spots in the crust, allowing breakouts of the hot interior to escape beyond the flow front. In all but the highest Ψ experiments, a complex field of many overlapping lobes developed, and breakouts occurred more frequently and at shorter times for lower Ψ flows. The theoretical predictions and experimental observations suggest that, given

sufficient time, any lava spreading over a flat surface will eventually attain the condition where the growth of the flow field is controlled by the yield strength of the chilled lava crust, rather than the viscosity of the hot flow core, assuming a simple two-layer rheological model. After this time, t_{crust}, instead of spreading axisymmetrically, the flow grows by breakouts of hot lava escaping from ruptures that develop at isolated weak spots in the retaining crust. Lava flows which cease before the breakout time is reached will retain a smooth outline, whereas those which last much longer will form a compound mass of overlapping lobes or toes. Blake and Bruno (2000) found that t_{crust} was proportional to the product of viscosity and effusion rate divided by the square of the crust strength:

$$t_{crust} \sim (g \Delta\rho \eta Q) / (\sigma^2 s^2 \kappa) \qquad (2.1)$$

where g is the gravitational acceleration, $\Delta\rho$ is the difference in density between the lava and its environment, η the viscosity of the hot lava core, Q the volumetric flux, σ the yield strength of cold crust, s is a constant of order 1 whose value depends on the details of the thermal exchange between the lava and its environment and the thermal boundary conditions, and κ is the thermal diffusivity of the lava. Assuming that the strength of cold crust is roughly similar for all flows, then compound lava flow formation is favoured by low viscosity and/or effusion rates. This is in agreement with the observations of Walker (1973) who noted that compound flows typically arise from the slow effusion of low viscosity lavas, while simple flows are the result of rapid effusion, or slow effusion of high viscosity lavas. The work of Blake & Bruno (2000) also indicates that the duration of the eruption is a critical factor in determining the final morphology. Once compound morphology is established, the flow from the vent becomes distributed to several regions, so breakouts are governed by local supply rates and viscosities. A large effusion rate, if sustained for sufficient time, can

therefore produce a mature compound flow with morphological elements representing a low flow rate. This argument is used to challenge the assumption of low effusion rates for flood basalts based on the evidence of compound morphology alone. Instead, the integrated effect of viscosity, eruption rate and time (or erupted volume) is found to be critical in determining morphology.

Anderson et al. (2005) carried out similar experimental work, but designed to study the manner in which material flows through the interior of a flow. This fluid flow pattern is a possible factor in the morphological evolution of a lava flow surface. Hon et al. (1994) and Self et al. (1998) suggested that sheet flows have a continuous molten interior whereas hummocky flows have discrete internal pathways, while Anderson et al. (1999) examined the fracture morphology on lava surfaces, inferring that both sheet and hummocky flows have continuous molten interiors but that the nature of the viscous fingering determined the final morphology. The experiments performed by Anderson et al. (2005) produced morphological progressions similar to those described by Fink & Griffiths (1990, 1992), with most runs demonstrating only part of the morphological suite, but some encompassing all morphologies. Over the course of any one run, there was a consistent progression from high to low Ψ morphologies. The wax used was dyed different colours as the models progressed, in order to trace different generations of internal pathways. Observations showed that the pathways became narrower, more numerous and better defined with time, and that in high Ψ runs, radial interior flow was maintained in crust free areas but many (>50) 'fingers' or narrow pathways occurred near the crusted margins. They suggested that the observations are consistent with the development of 'Saffman-Taylor instabilities', or viscous fingers. Saffman & Taylor (1958) found that low viscosity fluid propagated as fingers into higher viscosity fluids, as instabilities formed in response to viscosity

gradients. While viscosity gradients could not be measured in the models, they must exist along lines from the hot fluid core, through the viscoelastic layer, to the cool brittle crust. Anderson et al. argue for the possibility that natural lava flow interiors could develop similar viscous-fingering structures, based on the fact that Coussot (1999) showed Saffman-Taylor instabilities to be common in yield strength fluids, and lavas commonly demonstrate such rheologies. However, the possibility that these features are scale-dependent cannot be discounted. Also, Huppert (1982), when examining the flow of a viscous fluid down a slope, found that the fluid formed a 'wavy' flow front comprising many fingers, and that this could be explained solely in terms of the surface tension of the fluid, a property that is negligible in lava flows, but more significant in wax models.

2.6.2.5 Fractals as indicators of lava flow dynamics

Both Blake & Bruno (2000) and Anderson (2005) went further in their analysis and looked at the fractal properties of the lobate flow fronts produced in the experimental flows. 'Fractals' are objects that look similar at all scales: they are 'self-similar' or 'scale invariant' (Mandelbrot 1967; Bruno et al. 1992, 1994), and the fractal dimension D gives an indication of the deviation from linearity of a feature. A straight line has D = 1, and sinuosity increases as D approaches 2 (the maximum value). Fractals often represent non-linear or chaotic processes, and Bruno et al. (1992) found that lava flows from Hawai'i, Idaho, the Galapagos Islands, Venus, the Moon and Mars demonstrated fractal behaviour, implying that non-linear processes, possibly including Saffman-Taylor viscous fingering, are responsible for flow morphology. The results of Bruno et al. (1992) suggested that pāhoehoe and `a`ā could be distinguished by their fractal dimensions, with pāhoehoe appearing more sinuous than

`a`ā, therefore having a higher average fractal dimension, though they warned that the dynamics which give rise to the two types of morphology ought to be understood before their conclusions were applied without question. Bruno et al. (1994) subsequently showed that more silica-rich lava flows did not demonstrate fractal behaviour, which was attributed to the suppression of small scale features at the flow margins by the higher viscosity and yield strength of the lava. The fractal behaviour of basaltic lava was attributed to the core-dominated advance. Lipkaman & Gregg (2003) subsequently found that the fractal dimension does not reflect the *surface morphology* but rather the *flow emplacement mechanism.* Pāhoehoe and `a`ā are often, though not always, emplaced differently: `a`ā as single lobes or channels and pāhoehoe as networks of lobes, and this had previously been overshadowed by the more obvious differences in surface morphology. Lipkaman & Gregg (2003) found that the internal dynamics are more important than surface texture in determining flow margin morphology, so if a pāhoehoe flow is emplaced as a single channelised lobe, it can demonstrate `a`ā dimensions, and vice versa. The determination of fractal dimension can therefore be used to distinguish between flows that were emplaced as one continuous unit (probably due to 'high' effusion rates) or discontinuously ('low' effusion rates), though the fractal properties of lava flow margins break down at large scales.

Blake & Bruno (2000) found that the fractal dimension of any one of their models increased with time until reaching a steady state, implying that a growing wax field matures with time to reach a constant D value. Applied to lavas, this suggests that given sufficient time, any lava will become crust dominated, which fits with the suggestion of Lipkaman & Gregg (2003) that it is the emplacement style rather than the surface morphology which governs the fractal dimension.

Anderson et al. (2005) looked at the fractal dimensions of the exterior versus first interior margins of their flows, where the interior margin was defined as the boundary between the first and second dye colours. Interestingly, they found no systematic change in the dimensions of either boundary over time, in contrast to Blake & Bruno (2000), which they attributed to either the absence of any changes, analytical errors, or the experiments running for too short a time. They did find, however, that the dimension of the interior margin was consistently higher than that of the exterior margin. Many flows were seen to contain interior pathways with similar shapes to the exterior margin, plus some additional fingering, which leads to greater sinuosity, hence higher D. It is suggested that the higher D value in the interior results from internal paths 'remembering' flow paths present when the adjacent external margin was forming, with new instabilities forming additional fingers. Since fractals are self-similar, it has been suggested that processes controlling shapes at small scales are the same as those controlling shapes at large scales (Bruno et al. 1992). Since the internal and external margins in the experiments look similar, it suggests that similar processes (fluid instabilities) influence both when other variables (e.g. pre-eruption topography) are not dominant.

2.6.3 Long channelised flows and convection

The unconfined PEG models of Fink & Griffiths (1990, 1992), Blake & Bruno (2000) and Anderson et al. (2005), discussed earlier, produced a wide range of morphologies which have been shown to correspond to morphologies seen in terrestrial and planetary lava flows. However, the problem of understanding and predicting the behaviour of subaerial terrestrial basaltic flows, such as those of Hawai'i and Etna which commonly threaten property, requires a thorough

consideration of channelised flows. While the models of Fink & Griffiths (1990, 1992) can constrain the conditions under which channelised flows are able to form, and the experimentally tested theoretical models of Kerr et al. (2006) can predict the width of developing channels from eruptive and environmental parameters, neither of these approaches was concerned with the processes that can occur *within* channels. Griffiths et al. (2003) were the first workers to study these processes experimentally, addressing the problem of crustal stability by investigating the conditions that led to the formation and distribution of solid crust during channelised flow.

The surface coverage of incandescent lava affects the rate of heat loss and consequent rate of crystallisation, so the thermal (and rheological) history is very different for lava transport systems with or without continuous surface crusts. For example, Crisp & Baloga (1990) showed that the presence of a thin crust reduces the rate of cooling by introducing greater stability (less thermal overturn) at the surface, and it is known that the strength of cooling strongly influences the final length of long lava flows (e.g. Walker 1973; Crisp & Baloga 1994; Pinkerton & Wilson 1994). Any prediction of cooling rate, which can be an important input in theoretical models (e.g. Harris & Rowland 2001) therefore necessitates an understanding of crustal development and distribution.

Griffiths et al. (2003) investigated the effects of cooling and shear on the formation of solid crust, using PEG flows effused under water into pre-formed rigid channels of rectangular cross section. They found that two distinct regimes occurred, depending on the strength of cooling (Ψ), separated by a transitional regime which demonstrated elements of both end members. For high cooling rates (low Ψ), a rigid solid roof developed over much of the length of the channel, while flow continued beneath. This was defined as the 'tube' regime. For low cooling rates (high Ψ), the flow surface

along the centre of the channel was covered with solid fragments, but was carried along on the still molten material beneath. Open zones remained at the margins, and these were characterised by small fragments of a solid phase which could adhere to the sidewalls or the central raft. In these regions, the effects of shear outweighed those of cooling, so the surface solid was continually fragmented as is commonly observed in channelised lava flows. This was defined as the 'mobile crust' regime. Ψ values were calculated for each experiment, as were Rayleigh numbers, which indicate the relative importance of convection in heat transport within the models. Previously, the transfer of heat from the interior to the surface of the model flow had been assumed to be dominated by conduction, as for laminar flow, but convecting flow (though not turbulence) was considered in this treatment, requiring the definition of a new parameter:

$$\upsilon = \Psi (Ra / R_0)^{1/3} \qquad (2.2)$$

where Ra is the Rayleigh number and R_0 is a constant. The qualitative style of solidification in the experiments can be defined solely by the value of υ, with $\upsilon < 25$ leading to the tube regime, and $\upsilon > 25$ leading to the mobile crust regime.

The effects of cooling-induced thermal convection were also investigated, using dye tracers. In control runs without cooling, no movement of the dye traces was seen. When cooling did occur, the traces curved towards the channel walls, down the walls and back towards the centre of the channel, where they were carried far downstream. These traces were stationary with time, reflecting streamlines in the flow, but could be slightly disturbed by the presence of solid fragments. Solid fragments were observed to be transported down the sidewalls and across the base of the channel, which has implications for entrainment, and hence the final length of the flow (Crisp & Baloga 1994).

These experiments indicate that the surface solidification is strongly controlled by both the pattern of thermal convection and the horizontal velocity gradient. Both processes are important in maintaining open shear zones near the channel walls. Convection moves heat from the interior of the flow to the surface, where it decreases the rate of surface cooling (relative to that calculated by conduction alone) and extends the time taken for the surface to reach its solidification temperature. When convection is vigorous enough, the chilled surface is continually flushed away; if the flushing is too slow, the surface freezes and a tube develops. With regards to the horizontal velocity gradient, it is hypothesised that solid crust can develop only when the timescale for surface shearing (dependent on the velocity gradient) is sufficiently large compared to that for surface solidification.

General observations of lava flows show that the patterns of surface crust development are qualitatively similar to those in the models. These include observations that lava tubes are most common when effusion rates are low, and that central crusts are common features of open-channel flows. Values of υ can be calculated for lavas from basic flow parameters (velocity and depth) and thermal properties (temperature, thermal expansion, diffusivity), which provides a reasonable parameterisation for the extent of crust development on steady flows through uniform channels. Despite the qualitative agreement with observations of Hawai'ian and Etnaean channelised flows, the rheology is still assumed to be Newtonian, and channels are assumed to be uniform, both of which are simplifications of the natural system.

2.6.3.1 The importance of channel geometry

Cashman et al. (2006) extended the work on υ, seeking to investigate the effects of channel geometry on crustal behaviour. Again using PEG in pre-formed channels, they studied the effects of changing channel widths, sinuosity and basal roughness on crust formation and disruption, all of which affect local flow behaviour, and hence υ. The basic flow regimes identified by Griffiths et al. (2003) also describe flow through non uniform channels, but variations in planform geometry caused the value of υ to vary along the channel, thus allowing regime transitions despite steady effusion and a uniform slope. The transition between the mobile crust and tube regimes still occurred at $\upsilon \sim 25$. Whether widening or narrowing was smooth or abrupt affected the flow regime near transitional values, because of the rate at which the crust could adapt to the new channel conditions. Local flow acceleration produced by narrowing, bends or roughness disrupted the continuity of the crust, often causing the original central plug to fragment. These fragments could then cause blockages in the channel, which sometimes slowed the flow behind sufficiently to allow tube conditions to develop, due to the increased cooling of the slower flow. It was concluded that local changes in channel width, sinuosity and topography play an important role in the overall thermal evolution of lava channels, as the disruption of the crust causes variations in the proportion of incandescent material exposed at the surface, thus affecting local cooling conditions. This implies that, while the simple parameterisation of Griffiths et al. (2003) is applicable to defined flow conditions, tube versus open channel, it cannot account for changes in local geometry.

The solidifying PEG modelling approaches discussed here, and their applications to reasonably well characterised terrestrial flows, illustrate the usefulness of analogue

models as tools in discovering links between measurable parameters and observable features. Having validated the models, they can then be used to make informed estimates regarding the poorly constrained physical properties of terrestrial or planetary lavas whose emplacement has not been observed. However, the application of the Ψ model to natural lavas requires an assumption of Newtonian behaviour, which has previously been shown to be inappropriate for many basaltic and almost all more evolved lavas. While cooling and crystallisation undoubtedly imparts a yield strength to the behaviour of natural flows, Gregg & Keszthelyi (2004) argue that the morphologic and dynamic similarities between natural and simulated flows, coupled with the demonstrable applicability of Ψ values to natural basalt flows, shows that the non-Newtonian behaviour of natural basalts can be neglected in these cases. This applicability is, however, clearly limited. Laboratory models cannot represent the full range of complexities observed in real flow fields, which often depend on long emplacement times, and are, in large parts, governed by local flow conditions. In cases where only small parts of the flow field are observed, it is not possible to make any assumptions regarding overall vent behaviour. Similarly, experimental models have not produced the smaller scale features such as clinkery and blocky surfaces which are so common on basaltic andesite and more silicic flows. The presence of a solid crust has proved to be a substantial improvement in modelling terms, but still cannot fully represent the expected range of rheologies that can occur in natural lavas. Blake (1990) modelled features and processes in a yield strength fluid that have not been reproduced in Newtonian models, and Osmond & Griffiths (2001) argue that the effects of a yield strength may be important in resisting spreading before the effects of cooling become significant. It is also possible that, in some cases, the internal strength dominates over surface cooling. For example, in the large volume rhyolitic flows

studied by Fink (1978, 1980), the inferred eruption rates are much larger than those measured for domes today, and this high effusion rate (i.e. high Ψ) may have resulted in the flows only being weakly influenced by cooling over much of their emplacement history. Resultant morphologies may have depended much more strongly on the internal yield strength.

2.7 The incorporation of yield strength in addition to cooling

As discussed previously, isothermal Bingham flow models (Hulme 1974; Blake 1990), produced very different morphologies to models using isothermal (Huppert et al. 1982), cooling (Stasiuk et al. 1993) or solidifying (Fink & Griffiths 1990, 1992) Newtonian fluids. This causes uncertainties when attempting to assess the relative importance of cooling and yield strength in the overall dynamics of silicate flows: does one dominate the morphology, or are both important contributors depending on flow conditions? The problem was addressed through modelling by Griffiths & Fink (1997), who employed a similar method to Fink & Griffiths (1990, 1992), but used a slurry of kaolin in PEG that had a sufficiently large yield strength to ensure that the flows were dominated by their strength rather than the viscous stresses. While the study was primarily qualitative due to the complexity of the flows, the parameter Ψ was re-defined for a Bingham fluid, giving Ψ_B, which was expected to describe the effects of cooling in a similar manner to Ψ for solidifying Newtonian extrusions. In Newtonian models, if the rate of solidification was sufficiently rapid, advance of the flow was controlled by the yield strength of the cooled crust, while if the cooling rate was low, it was controlled by a buoyancy-viscosity balance (Griffiths & Fink 1993). In the models of Griffiths & Fink (1997), while the crust will still control flows that

are rapidly cooled, the flow at high Ψ_B values will be controlled by a buoyancy-interior yield strength balance.

The kaolin-PEG slurry was extruded from a point source onto a horizontal plane under water, and observations of the developing morphologies were compared with those of solidifying purely viscous flows, isothermal extrusions of kaolin-water slurries, and the predictions of the scaling theory. A range of morphologies was seen between low and high Ψ_B values, as expected, but these were very different to the morphologies seen in the purely viscous solidifying flows. For isothermal runs ($\Psi_B = \infty$), domes were axisymmetric with a rough surface texture close to the vent (where the strain rate was greatest), and the dome retained its shape after the supply ceased, indicating that growth involved a static balance between buoyancy forces and yield strength. These observations are in agreement with those of Blake (1990). For low cooling rates, growth remained endogenous and the flows were still largely axisymmetric except for 'scalloping' at the flow front. These structures developed in time as a result of the solidification of strong pieces of crust that tended to act as levées by inhibiting flow advance, but could also be displaced by the still-fluid wax. Spiral traces (Nadai 1950) like those described by Blake (1990) were noted. This morphological regime was dubbed 'levéed' or 'axisymmetric', and occurred at Ψ_B values greater than 15. As the cooling rate increased (Ψ_B decreased), the morphologies passed through 'platy' ($0.9 < \Psi_B < 15 \pm 5$), 'lobate' ($0.12 < \Psi_B < 0.9 \pm 0.3$) and 'spiny' ($\Psi_B < 0.12 \pm 0.02$) regimes, as shown in figure 2.7. 'Platy' domes still grew endogenously, with four to six rigid crustal plates developing, and the surface texture was rough. The divergent boundaries between the plates formed a star-like pattern, and the plates grew as rifting progressed. The surfaces of 'lobate' domes were solid from the outset of the run, and the domes grew asymmetrically. Initially, four to six

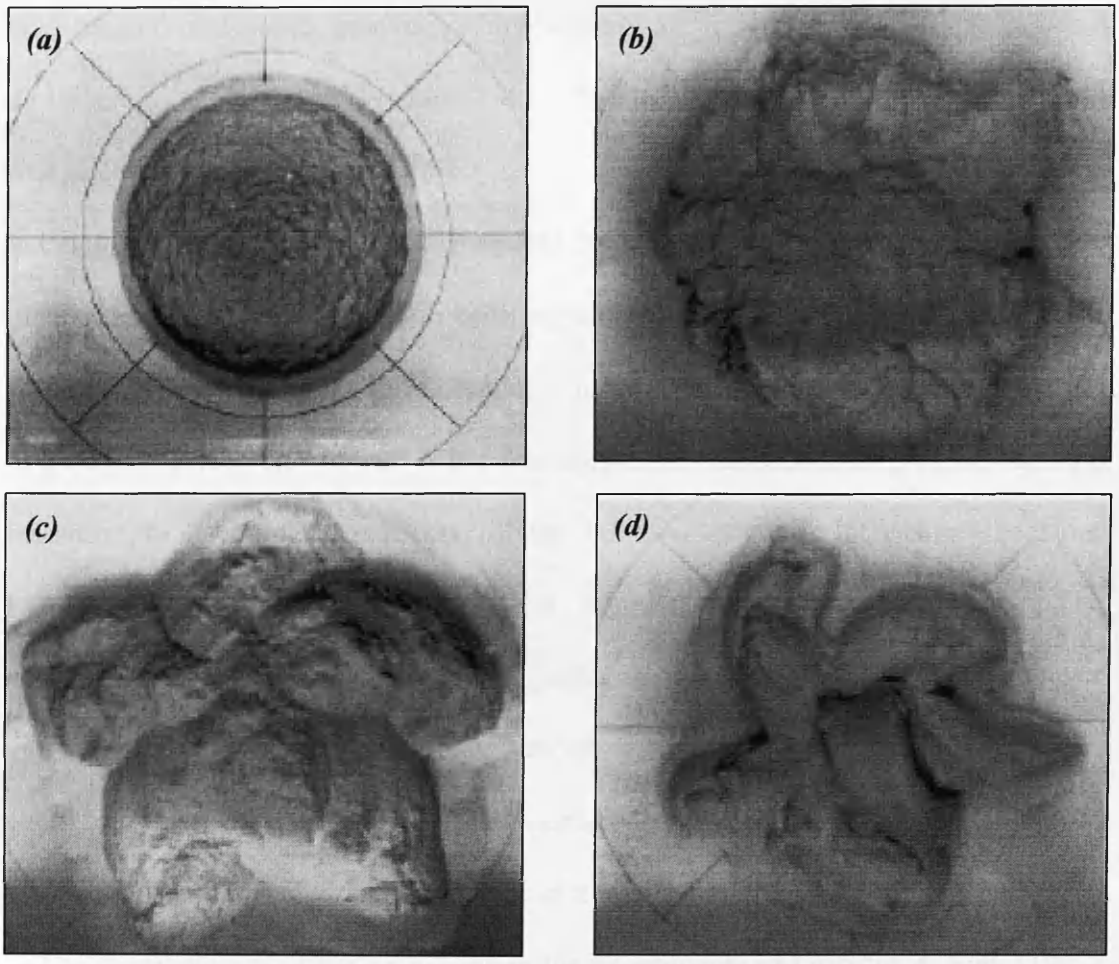

Figure 2.7. The four morphological regimes of Griffiths & Fink (1997), for a cooling and solidifying extrusion with a yield strength. The fluid is being extruded onto a horizontal plane. Vent is beneath the approximate centre of the resulting domes. (a) to (d) represent decreasing Ψ_B. (a) Axisymmetric flow, showing surface features which resemble the logarithmic spiral slip planes of Nadai (1950). (b) Platy flow. (c) Lobate flow. (d) Spiny flow. From Griffiths & Fink (1997); figure 2. See text for details.

lobes, showing distinct spiral curvature, grew simultaneously, but as the run progressed growth often became concentrated in one of these lobes at a time. The style of emplacement therefore varied between endogenous and exogenous, and the surface texture was again rough. The 'spiny' regime demonstrated purely exogenous growth, with only one extrusion growing at any time. First, a series of 4-6 extrusions built up in immediate contact with the base, then spines were added which came out of the top of the dome near the vent. The surface texture was dominated by smooth areas

that showed flow-wise grooves, which appeared similar to the toothpaste flows described by Rowland & Walker (1987). Similar features have been observed on recent flows at Mt Etna (figure 2.8).

Often, an initial period of axisymmetric inflation was observed, followed by the development of one of the morphologies above. This period of inflation became shorter as Ψ_B decreased, not appearing at all for $\Psi_B < 0.15$, and may represent a period of time where the yield strength is the dominant control on morphology, followed by a transition to a regime controlled by the solidifying crust. Increasing the floor roughness appeared to have no effect on the developing morphology. The observations are consistent with the hypothesis that Ψ_B is the primary parameter determining dome character for this given material, which conforms to expectations given the dependence of purely viscous extrusions on Ψ. The differences in observed morphology are attributed to the presence of a yield strength.

The morphologies of the extrusions in the experiments of Griffiths & Fink (1997) are also clearly different from the simple axisymmetric flows produced by experiments with isothermal yield strength fluids (Blake 1990, figure 2.4; Osmond & Griffiths 2001; Balmforth et al. 2006), and this can be attributed entirely to cooling and solidification. The obvious and important role of a strong crust therefore needs to be reconciled with the observation that the internal yield strength causes the major differences between solidifying viscous and Bingham extrusions for all values of Ψ_B. It is suggested that the internal yield stress in solidifying flows restricts the flow of material in the interior, thus limiting supply from the vent to the flow front (or other breakout point). Any new lobes or spines that form therefore originate close to the vent where the crust is thinner and weaker, and the flow can only feed one extrusion at a time. This pattern of flow development contrasts strongly with the prolific pillow

Figure 2.8. Squeeze-outs of plastic, 'toothpaste', lava at the front of the 1991-3 flow field, Mt. Etna, Sicily. Grooves can be seen on the lava surface, (picked out by arrows) indicating that it had a significant yield strength when it was extruded. The grooves, are believed to be analogous to those observed in the 'spiny' regime of Griffiths & Fink (1997), seen in figure 2.7 (d).

and lobe development in purely viscous flows, where the crust can be breached far from the vent. The role of the interior yield strength becomes more significant for more strongly cooled flows (smaller Ψ_B), because the development of a thicker crust leaves less room for the formation of interior channels. This may also lead to the overpressure driven regime becoming dominant over a greater range of Ψ_B. The models of Griffiths & Fink (1997) are considered to be more relevant to highly silicic lava domes than were the purely viscous models.

Fink & Griffiths (1998) compared the model domes of Griffiths & Fink (1997) with lava domes, and found that the experimental morphologies qualitatively correspond to Blake's classification, with 'axisymmetric' being 'low' and 'spiny' being 'Peléean'. However, they point out that assigning a single regime morphology to any of the lava

domes is problematic, as they rarely have effusion rates or properties that remain constant with time. The growth patterns of three of the lava domes studied were found to fit with a buoyancy-crustal yield strength balance. They argue that this demonstrates a basic dynamic similarity between the modelled and real domes, suggesting that if the morphology of a real dome can be classified, it may be possible to make inferences about its eruption rate and/or physical properties. On the strength of this argument they evaluate carapace strengths using a strong carapace model, arriving at estimates 10^3 times larger than strength estimates for the dome interiors, which is consistent with the dominance of the carapace in controlling dome height and lateral spreading. Lyman et al. (2005) and Lyman & Kerr (2006) examined the flow of solidifying Bingham extrusions (kaolin in PEG) in prescribed channels, with a view to assessing possible force balance regimes, and the relative importance of internal and crustal yield strengths in halting the spread of the flows. They observed that the yield strength of the extrusions increased with the proportion of kaolin, and that the strength of the surface crust increased systematically with that of the flow interior, always being much larger than that of the interior. They predict that a similar relationship between crustal and internal yield strength occurs in lava flows, where it is related to the volume fraction and microstructure of the crystals in the lava. This relationship between crustal and interior strengths is in agreement with the observations of Fink & Griffiths (1998).

2.8 Isothermal, rheologically stratified approaches

The above models using PEG have attempted to evaluate the relative importance of the surface crust, with or without an internal yield strength. While the use of PEG allows the formation of a strong surface crust, this crust is thin relative to the total

flow thickness, and is also relatively stronger than lava crusts. Both of these factors imply that PEG crusts are more appropriately scaled to pāhoehoe-like continuous crusts rather than more fragmented `a`ā and blocky crusts. Pāhoehoe crusts can deform continuously because they are only subjected to relatively low strain rates, while `a`ā crusts result from higher strain rates, and blocky crusts can often form even at low strain rates due to a high yield strength; but at laboratory scales, the model PEG crust is too stiff to break and create clinker. The kaolin-PEG slurries used in the solidifying yield strength models also tended to form continuous crusts, which again can be attributed to a combination of low strain rate and the strength of solid PEG, and the models have been shown to closely resemble real domes. While the solidifying viscous experiments are applicable to fluid basalt flows, and the yield strength solidifying flows are applicable to highly silicic domes, neither approach adequately describes the conditions which are likely to be present in long flows of basaltic andesite to rhyolite composition, with `a`ā or blocky textures. The PEG models also do not allow the thickness of the crust to be controlled, so that while Hallworth et al. (1987) found that more cooling, which presumably correlates to thicker crusts, led to increasing restriction of flow, this could not be easily constrained.

Recently, several workers have carried out experiments using isothermal but rheologically stratified models, to examine the roles of different crustal rheologies and thicknesses in controlling flow dynamics. This work simulated the ductile flow interior using silicone gel, which is a Newtonian fluid with an almost perfect dependence of stress on strain rate (Merle 1998). While the use of a Newtonian fluid might seem like a step backwards in the light of the models previously discussed, the advantage of silicone is its extremely high viscosity (of order 10^4 Pa s). There has been a long history of silicone use in modelling, with Merle & Borgia (1996) using it to

simulate weak rocks in experiments of volcanic spreading, and Merle (1998) and Buisson & Merle (2002, 2004) using it in their attempts to quantify strain in flow interiors. For the experiments of Merle (1998) and Buisson & Merle (2002, 2004), the measurements of strain were made by observing the deformation of a grid which is printed on the modelling substance, so a highly viscous material is required. Such an approach obviously precludes the use of materials such as wax or kaolin slurries. The modelled flows produced advance mechanisms (gravitational collapse and frontal rolling) and strain patterns that are similar to those observed and implied in real flows, which provides some justification for the use of silicone as a modelling substance, but the presence of a surface crust would be expected to modify the strain pattern near the crust/interior boundary. Merle (1998) argues that the deformation patterns of any viscous materials flowing over a rigid base present overall similarities regardless of rheology, based on the observation of similar structures in basalts, rhyolites and glaciers (e.g. Paterson 1981). Using scaling arguments he showed that the Reynolds number was small in the models, indicating that inertial forces are negligible compared to the viscous forces, which is the case for most lava flows (Merle & Borgia 1996). Previous studies of strain had been confined to the examination of inactive flows, which introduces uncertainty as to whether the features observed are characteristic of all phases of flow activity. The use of silicone models allowed the nature of the strain in different parts of an active flow to be observed, which is something that is impossible to achieve in the field.

2.8.1 Axisymmetric, rheologically stratified dome models

Following the demonstrated success of silicone as a modelling substance, Buisson & Merle (2005) looked at the patterns of endogenous dome growth in the presence of

a brittle carapace, in order to evaluate the influence of the brittle crust on dome behaviour. Their experiments focussed on the dramatic change in rheology between the crust and interior, and showed that the thickness of the crust plays a more significant role in the overall kinematics than had previously been assumed. As discussed in section 2.5, previous workers have argued that pervasive fracturing of the crust severely limits its strength (Denlinger 1990), and that all observed morphologies are a passive response to the behaviour of the viscoelastic layer (Stasiuk et al. 1993). However, the presence of a layer of brittle material must have some influence on the resultant morphology, even if this is due merely to weight rather than strength. As discussed by Iverson (1990), it is difficult to estimate the carapace thickness of domes, so the experiments of Buisson & Merle (2005) used a range of thicknesses, expressed as the ratio, λ, of carapace thickness to the total dome height.

Models of domes with a crust involved the extrusion of silicone from beneath onto a horizontal plane at a constant effusion rate. Once the height of the 'dome' was stable and all further growth occurred by lateral spreading, a cohesive crust of sand and plaster was poured onto the silicone to simulate the crust. In this way, the thickness is reasonably well constrained and a larger range of thicknesses can be investigated than would be produced if the crust had to grow by cooling, which is useful, as λ is known to vary greatly in nature. The range of λ values used was 0.065 to 0.5, with 'thin' crusts defined as having $0.065 \leq \lambda \leq 0.16$, and 'thick' crusts up to $\lambda = 0.5$.

Scaling the strength of the experimental crust to that of crusts on real domes is not straightforward, as real crusts are complex and highly heterogeneous (section 2.5). The tensile strength, or cohesion, of natural, massive, unfractured rocks has been shown to be around 10^7 Pa (Handin 1966; Hoek et al. 1995), and that of fractured rock

is estimated to be one or two orders of magnitude lower than this (Hoshino et al 1972; Schultz 1996). The crustal strength can be scaled by use of the hydrostatic equation:

$$\sigma = \rho g h \qquad (2.3)$$

where σ is the shear stress, ρ the density of the dome material, g the gravitational acceleration and h the height of the dome. The ratio of $(\rho g h)_{experiment}$ to $(\rho g h)_{nature}$, and therefore $(\sigma_{experiment} / \sigma_{nature})$, is approximately 0.5×10^{-4}, meaning that the analogue crust should be around 10^4 times weaker than the natural crust. A mixture of 20% flour and 80% sand has a cohesion of approximately 50 Pa, which provided the required ratio.

A continuous spectrum of morphologies was seen to develop between the thin and thick crust end members. Models of thin crust domes remained relatively flat in profile and developed symmetrical fracture patterns, with radial fractures dominating initially, and concentric fractures developing later. The intersection of these fractures created crustal blocks which slid away from the summit, and the size of the blocks increased with increasing λ. Over time, the fractures extended to the margins of the dome, producing petal-shaped blocks of crust (figure 2.9 a). These morphologies are similar to the blocky summit textures and logarithmic spiral slip planes (Nadai 1950) observed on the surfaces of domes modelled by Blake (1990), Griffiths & Fink (1997) and Osmond & Griffiths (2001). Spreading of the dome was accompanied by rollover at the flow front and basal breccia formation, as seen in `a`ā flows.

Thick crust morphologies differed significantly. Fracture evolution in these simulations was slower, and radial fractures only affected a small part of the dome as the thicker crust prevented lateral expansion. The growth of the dome was therefore limited to the vertical direction in the fractured summit region, which led to steepening of the dome margins and greater instability. Deformation was not

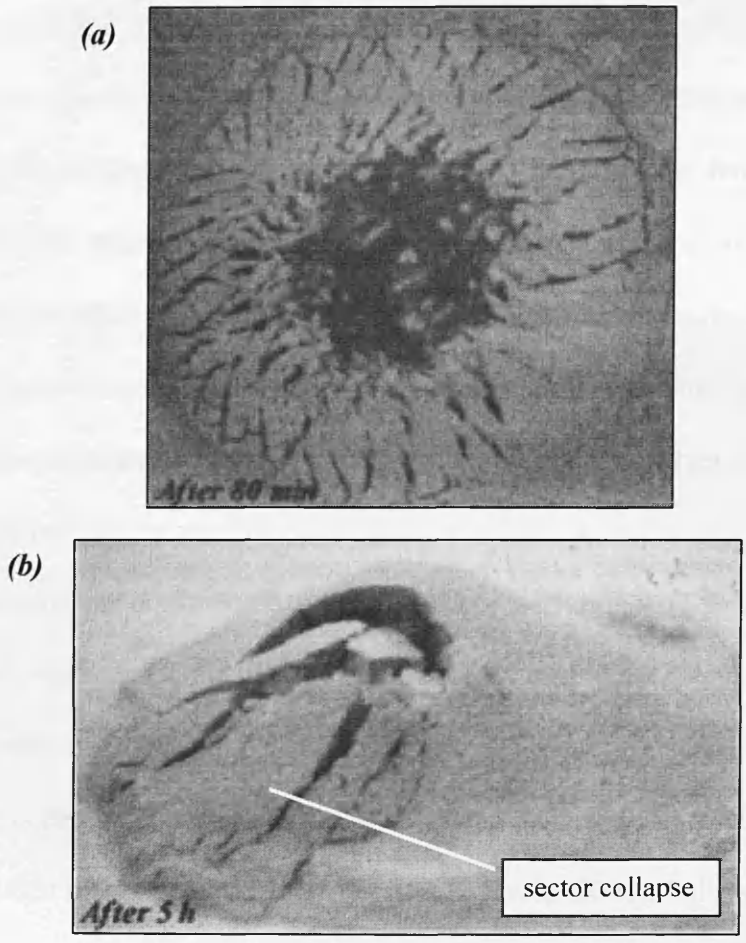

Figure 2.9. Fracture patterns in silicone and sand-and-plaster models of lava domes. Domes are approximately 20 cm in diameter. (a) Thin crust dome, showing symmetrical fracturing and petal-shaped blocks of crust. The fractures appear similar in shape to the logarithmic spiral slip planes described by Nadai (1950) and shown in figure 2.4. (b) Thick crust dome. Fracturing is only seen in one part of the dome, resulting in sector collapse. From Buisson & Merle (2005); figures 2 and 4. See text for details.

symmetrical, but limited to a small section of the dome, which eventually collapsed (sector collapse, figure 2.9 b). Transitional evolution was seen between the two end member morphologies, with increasing λ leading to an increasingly large undeformed section.

While other parameters are obviously at work in nature, all conditions except for the crustal thickness ratio were constant in the models. The significant variation in resultant morphology shows the basic influence that the thickness of the brittle crust

can have on dome dynamics. While the strength of the fractured brittle crust may be negligible compared to that of the underlying viscoelastic layer in a natural dome, the presence of a thicker carapace must necessarily affect how the dome expands due to the load on the interior material. The deformation patterns seen in the models were found to be similar to those documented for both thin (e.g. Pinatubo; Daag et al. 1996) and thick (e.g. Unzen; Nakada et al. 1995) crust domes, suggesting that the models are a realistic representation of natural dome growth, despite the structural and rheological simplifications.

Experiments on cryptodome intrusions were performed by Donnadieu & Merle (1998) and Merle & Donnadieu (2000), who used a similar experimental method, but extruded silicone beneath a pre-existing brittle cone of sand and flour. These experiments can be considered to have a λ value of 1, and the results were similar to the thick crust models described by Buisson & Merle (2005). Following a short initial period of radially symmetric endogenous inflation, a major shear fault propagated from the tip of the silicone to the surface, isolating a section in which all subsequent deformation was concentrated. The remaining part of the edifice was completely undeformed. An active ductile core remains a necessary condition for the processes described, because the ductile interface provides a decollement plane, so any study of potential hazard must include a consideration of the rheology. Failure of the carapace above a gas-rich interior could lead to explosive degassing and pyroclastic flow development, whereas if the interior magma is relatively fluid and degassed, fracture may lead simply to slow flow of the dome in that direction.

2.8.2 Long lava flow models

A similar approach was employed by Lescinsky & Merle (2005), though their scope was somewhat wider. They again used silicone as the modelling substance, since they were interested in the strain in flow interiors, but they specifically explored the relationships between internal shear stresses and surface crust rheologies, and the ways that these were affected by changing supply rates (increasing, decreasing or constant). As well as examining the strain distribution, they made observations of the developing surface morphology. Since the flows were isothermal, the cessation of flow advance could not be modelled and the processes and features observed are relevant to active flow advance. The crustal rheologies used were viscous (a second silicone fluid, more viscous than that used for the flow interior); rigid (Mylar sheets) and brittle (sand and plaster). The evolution of the surface crust rheology is known to be complex (section 2.5), and it probably initially behaves as a higher viscosity layer, later adopting a yield strength, and eventually passing through the ductile-brittle transition. With further cooling and thickening, since the resistance to brittle failure is a function of crustal thickness, thick crusts may become effectively rigid and unable to fracture during flow. As discussed in section 2.5 it is likely that a two-layer model of flow rheology is an oversimplification due to the continuous thermal structure and the presence of the viscoelastic layer, but for the purposes of the experiments the crusts were assumed to be rheologically homogeneous, since this results in significant simplification of the scaling, as well as the experimental set up.

Surface crusts play an important role in retarding flow advance as they impart a simple shear on the top of the flow interior. In flows with no surface crust, simple shear is at a maximum at the base of the flow, and decreases to near-zero at the surface. This results in a vertical velocity profile with the minimum (often zero)

velocity at the flow base and maximum velocity at the flow surface (Brun & Merle 1985), as shown in figure 2.10 (a). The formation of a crust slows the advance of a surface layer, and may eventually lead to the development of a reverse sense of shear (Merle 1998). For stationary rigid crusts, as in tubes, the shear is approximately symmetrical about a line of no shear strain at the flow mid-depth, resulting in a vertical velocity profile that is also symmetrical about the mid-depth (figure 2.10 b). While the viscous and rigid model crusts produced interesting shear patterns, the morphologies produced during the brittle crust experiments most closely resembled natural crusts, and only these results will be discussed here.

The brittle crusts were made from a mixture of sand and plaster. Quartz sand has been used as an analogue for brittle rocks in many previous experiments (e.g. Merle & Borgia 1996), and has negligible cohesive strength (Mourgues & Cobbold 2003). Dry plaster of Paris has a cohesion of a few tens of Pa (Fletcher 1976) and can be used to simulate cohesive brittle rocks. Both materials have an angle of internal friction of ~30°, and mixed together in different proportions, can simulate rocks of different cohesive strengths. Dimensional analysis suggested that the model crust strengths were appropriate for representing natural crusts, and that the experiments could be used to simulate a range of flow compositions and eruption conditions. Since geometric and force parameters combine such that rapid motion in a narrow channel is similar to slower motion in a wide channel, the dimensionless parameters were found to describe basaltic and rhyolitic flows equally well. The experiments are therefore considered to be applicable to high viscosity basalts, and lava flows of more evolved compositions, which is in contrast to the viscous PEG models that better represent lower viscosity basalts such as Hawai'ian pāhoehoe, and the kaolin-PEG models that correspond to highly silicic lava domes. The models investigated differing effusion

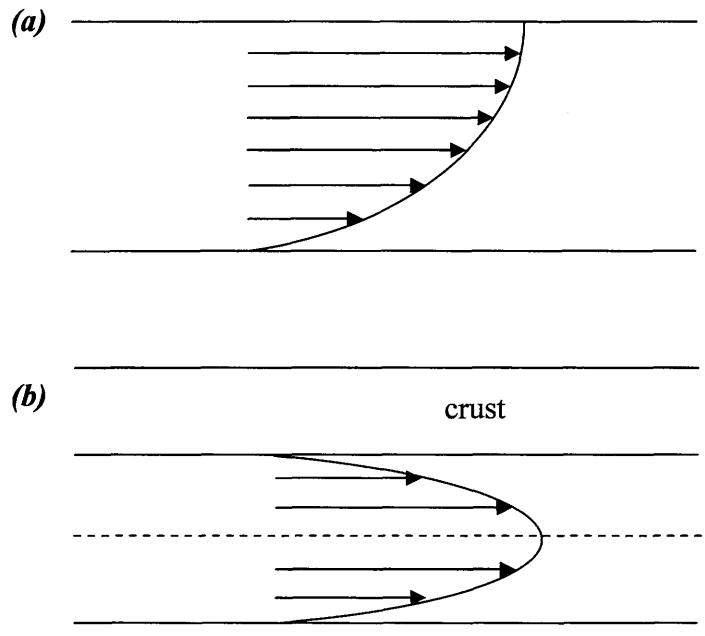

Figure 2.10. Vertical velocity profiles for (a) lava flows with no crust in open channels, and (b) tubed flow, assuming Newtonian rheology. In (a), the velocity is zero at the flow base and greatest at the flow surface, reflecting the fact that the shear stress is greatest at the flow base and zero at the surface. In (b), the roof of the tube is stationary, resulting in high shear at the top and base of the flowing lava. This results in a line of no shear at the mid-depth of the flow (dashed line), and the vertical velocity profile is symmetric, describing a parabola about this line of no shear.

rates, rheologies (pure sand to pure plaster) and crustal thickness ratios. Pure sand experiments used $0.036 \leq \lambda \leq 0.21$; pure plaster models, $0.2 \leq \lambda \leq 0.36$; and models using a mix of 80% sand to 20% plaster, $0.18 \leq \lambda \leq 0.5$. All models demonstrated advance by initial gravitational collapse and frontal rolling, producing basal breccias as the crust was overrun at the flow front. Measurements of strain in the flow interior showed a profile similar to that in figure 2.10 (a) with a maximum value of simple shear at the flow base, and no shear at the top of the flow interior. This indicated that there was no shear between the flow interior and the surface crust, or at least that there was not sufficient shear to be detected by the measurement methods employed.

Since the aim of the models was to measure interior strain, the experimental setup needed to facilitate these measurements. As such, a grid was printed on the sides of

the flow interior before each run, and in most of the models the walls of the channel were made of lubricated clear plastic to prevent sidewall effects from interfering with the strain measurements. The varying effusion rates were produced by having either a stationary (decreasing effusion rate) or moving (constant/increasing) back wall across the width of the channel. For constant effusion rates, the back wall was moved at the same rate as the flow front, while for increasing rates the back wall was moved more rapidly. This combination of conditions resulted in a state of shear which represented that in a single vertical plane down the centre of the channel. In real lava flows, the velocity profile across the channel is non-linear due to the effects of sidewall shear stresses. Velocity profiles across real channels are parabolic for the laminar flow of Newtonian fluids, and plug-like for yield strength fluids, and the absolute velocity at the channel-levée boundary is zero (figure 2.11). As a result of this, any short section of the channel would experience material entering at the upper end at different rates: faster in the centre and slowing towards the margins, unlike the uniform velocities achieved with the moving back walls in these experiments. The experimental methods are suitable for the investigation of internal strain, but the presence of a more realistic stress distribution in the flow would be expected to modify the nature of the structures produced. Direct comparison of surface morphology in the models to that of real flows must therefore be undertaken with care.

Despite the above limitations, many of the surface structures produced in these models resemble features seen on real flows, and this is argued to add confidence to the dimensional analysis, in providing extra evidence that the models are a reasonable reproduction of real flows. As the model flow front collapsed under gravity, the tensile stress experienced by the surface layer caused fractures to open up in the crust, perpendicular to flow direction. These fractures were closely spaced just behind

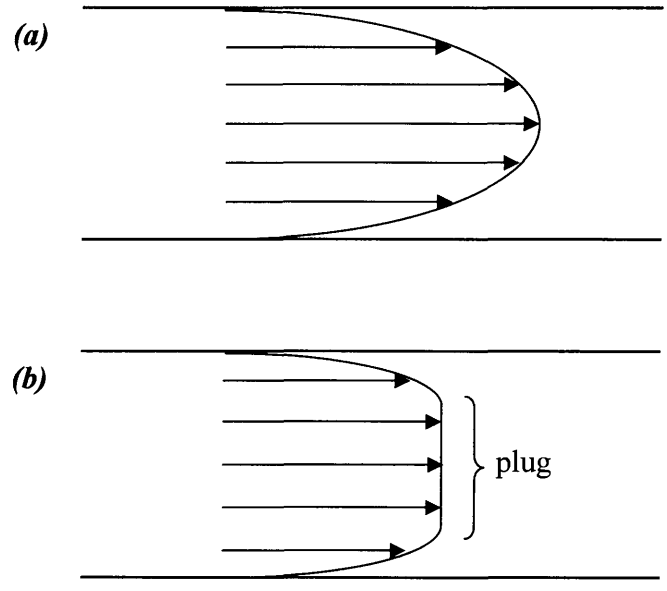

Figure 2.11. Cross-channel velocity profiles. (a) Parabolic profile demonstrated by a Newtonian fluid. (b) Plug flow profile demonstrated by a yield strength fluid. See text for details.

the flow front, with spacing increasing further up the flow. In weaker crusts (pure sand), the fractures developed as horst and graben structures that increased in width and complexity over time, while in stronger crusts (pure plaster) they formed as near vertical cracks that widened with time but did not show any structural variation. In experiments with lubricated sidewalls, the fractures were straight (figure 2.12 a), while the presence of lateral shear in the unlubricated runs caused the fractures to be slightly curved (figure 2.12 b). These fractures were convex downflow and curvature was greater further back from the flow front. Over time, new fractures were produced close to the sidewalls due to the effects of wrenching. Silicone welled up through the fractures over time as they widened, which could be easily seen if the crust was removed at the end of the run. Lescinsky & Merle suggest that the fractures can be likened to crease structures (Anderson & Fink 1992) and tension gashes seen in real flows.

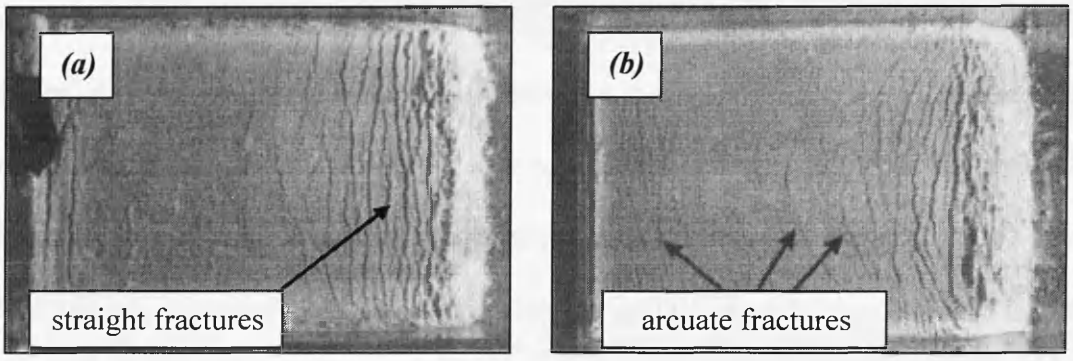

Figure 2.12. Tensile fractures in silicone and sand-and-plaster lava flow models. Channels are ~20 cm wide; flow direction is left to right. (a) Experiment with sidewall lubrication. Fractures are quite straight, perpendicular to flow direction. (b) Experiment without sidewall lubrication. Fracture shape is more arcuate, concave downflow, due to the action of sidewall shear. Fracture spacing increases back from the flow front in both examples, and curvature increases upflow in (b). From Lescinsky & Merle (2005); figure 6. See text for details.

For flows with increasing effusion rates, thickening of both the interior and the crust was noted at the rear of the channel, but no compression-related fold structures were produced. Fold formation is attributed to 'variations in the forward advance rate of surface crust', which result in the lead edge being thicker and moving more slowly, causing the thinner, faster moving crust behind to buckle. Lescinsky & Merle state that their models produce no folds because their crusts are uniform in thickness, which does not seem to answer to their reason for fold formation being velocity variation. Their increasing effusion rate models certainly involved velocity variations as the back wall moved more quickly than the flow front, so the reason for the absence of fold structures remains unresolved.

2.9 Summary

The above discussion has demonstrated how useful analogue models can be when attempting to reproduce processes and structures that occur in lava flows and domes, with a view to improving our understanding of flow dynamics. Many of these

processes are difficult to observe during eruptions, and also difficult to describe numerically, so the insight provided by analogue models is invaluable. One particular process which is poorly understood, and yet has a significant influence on both the thermal and structural evolution of a flow, is the interaction between the solid and fluid phases. This has been investigated in the solidifying PEG models of Fink & Griffiths (1990, 1992) and many subsequent workers, and in the silicone and sand models of Buisson & Merle (2005) and Lescinsky & Merle (2005). The two different approaches between them can simulate the development of lavas of basaltic to rhyolitic compositions, which necessarily covers a large range of flow sizes and thicknesses, and a large range of ratios between the crustal thickness and the total flow thickness. The models have been shown to behave in a similar manner to real lavas, indicating that the analogue experimental approach is valid. The work presented in chapter three is an extension of the isothermal, rheologically stratified approaches of Buisson & Merle (2005) and Lescinsky & Merle (2005). As discussed in section 2.8.1, the study of the passive influence of crustal thickness on the development of domes by Buisson & Merle (2005) provided interesting observations, suggesting that the thickness of the brittle crust is important in controlling flow development, with thicker crusts being increasingly influential in the flow dynamics. This contradicts the idea that, because of their negligible strength, brittle crusts simply sit passively on the flow and respond to the behaviour of the viscoelastic layer and viscous fluid beneath (Stasiuk et al. 1993). The varying rheologies of the crusts in the models of Lescinsky & Merle (2005) were shown to affect strain in the flow interiors in different ways, and the brittle crusts produced some interesting surface structures, which are the main observable features of lava flows. However, as discussed, their experimental setup was an unrealistic representation of the stress conditions that would be experienced by

a lava flow, and some of their interpretations of the surface structures produced are questionable. In the light of this, the work carried out in the following chapters has attempted to combine the two approaches, investigating how the thickness of a brittle crust affects the behaviour of channelised lava flows. Chapter three describes a new analogue experimental approach that endeavours to more realistically reproduce natural flow conditions, and aims to explore the relative influences of the crust and the flow interior in governing both the advance and the developing surface morphology of a lava flow.

3. Laboratory Experiments

The analogue modelling work undertaken here involves an investigation of the interactions between a flow core of silicone fluid, and a surface layer of mixed sand and plaster. These interactions are then scaled to lava flows possessing a fluid core and a solid crust. The experimental apparatus was designed to subject the analogue flow to stress conditions that resembled as closely as possible those experienced by a channelised lava flow. A full description of the rationale behind the modelling design is presented in section 3.1. In order that the results of the analogue experimental models can be confidently applied to the study of lava flow in the field, the models must be scaled, and scaling arguments are presented in section 3.1.1. The apparatus and modelling substances used are described in section 3.2, together with details of the ways in which the experiments were monitored. This includes an assessment of the errors associated with the measurement techniques, and a full list of experimental conditions is also provided. Finally, section 3.3 presents the results of the experiments in detail, including both qualitative descriptive observations, and quantitative measurements. An in-depth analysis of the experimental results then follows in chapter four.

3.1 Experimental design

Surface rheology begins to change as soon as lava is erupted and starts to cool, as outlined in chapter one. Cooling leads to the development of a thermal boundary layer, which is initially very thin, and whose rheology varies only slightly from that of the interior of the flow. Over time, the layer thickens and its viscosity increases. It first develops a yield strength, and later passes through the ductile-brittle transition,

behaving as a Mohr-Coulomb material (Lescinsky & Merle 2005). This brittle crust will fracture to produce a surface cover of `a`ā clinker if the viscosity-strain rate conditions are appropriate (Peterson & Tilling 1980). Cashman et al. (1999) suggested that, rather than requiring certain viscosity-strain rate conditions, the groundmass crystallinity must be high enough that a yield strength equivalent to the applied stress develops, and that this combined with a sufficient strain rate will lead to clinker formation in an open channel. Whether it is a threshold in viscosity or yield strength, or both, that must be reached, it is clear that, given sufficient time, the thermal boundary layer in a channelised lava flow will cool to such an extent that it can no longer behave in a ductile manner at the strain rates experienced, but must fracture.

The laboratory experiments presented in this chapter simulate the flow of lava into a channel that already contains a flow with a cooled, brittle crust. As described in chapter two, many previous analogue modelling approaches have simulated the emplacement of pāhoehoe-like flows, with thin, mechanically continuous crusts. Here, following the work of Buisson & Merle (2005) and Lescinsky & Merle (2005), a brittle crustal rheology is employed, resulting in a better representation of basaltic `a`ā and more silicic flows, as can be seen in the scaling arguments presented in the following section. The simulations aim to further our understanding of the effects of crustal thickness and topographic slope on the pattern of advance and the surface morphology of a flow, which will allow inferences to be made regarding the relative roles played by the solid and fluid phases. The use of an idealised channel geometry follows that of Merle (1998) and Lescinsky & Merle (2005), but there are important differences between their work and that described here. Firstly, there is no sidewall lubrication in the simulations presented here, so that a realistic velocity profile is produced across the channel due to the no-slip condition at the sidewall generating

lateral shear stresses. Secondly, instead of a solid back wall that can be moved to simulate different effusion rates, fluid is introduced at the channel head. These differences ensure that the shear and velocity conditions experienced in the experimental flows mimic natural flows as closely as possible.

3.1.1 Scaling

The scaling used here is very similar to that of Lescinsky & Merle (2005), due to the similarity of the experimental design. The experimental system can be described by eleven variables with three dimensions, which according to the Buckingham-pi theorem can be combined into eight independent, dimensionless parameters that completely describe the system. The variables are listed in table 3.1, along with experimental values and representative ranges of values for natural basaltic and rhyolitic systems from the literature.

Following the Buckingham-pi theorem, since the number of dimensions is three (length [L], mass [M] and time [T]), three variables are selected which have 'independent' dimensions. This means that no one variable can be expressed as a power product of the other two. These three are then combined with the remaining variables to make them dimensionless. In this instance, the chosen variables are total flow depth, D, with dimensions of length [L], the silicone density, ρ_f [ML^{-3}], and time, t [T]. For certain of the parameters, it may be more appropriate to use T rather than D, or ρ_c rather than ρ_f, but since the dimensions within these two pairs of variables are the same they can be readily substituted. Each of the other variables is treated in turn to produce eight dimensionless parameters, and various of the resultant dimensionless parameters are then combined to produce relationships between sets of forces.

Table 3.1. Variables describing natural and model systems.

Variable		Units	Dimensions	Value		
				Basalt	Rhyolite	Exp't
D	total flow depth	m	L	10^0 - 10^1*	10^1 - 10^2*	10^{-2}
T	crust thickness	m	L	10^{-2} - 10^0	10^0 - 10^1	10^{-3}-10^{-2}
W	flow width	m	L	10^0 - 10^2	10^1 - 10^2	10^{-1}
α	basal slope	(°)	-	<<1 - >35	<<1 - >35	4, 8, 12
ρ_f	density of fluid	kg m^{-3}	ML^{-3}	2700*	2200*	1400
ρ_c	density of crust	kg m^{-3}	ML^{-3}	2200$	1800$	1400
μ	viscosity of fluid	Pa s	$ML^{-1}T^{-1}$	10^0 - $10^{3\#}$	10^5 -$10^{10\#}$	10^4
c	cohesion of crust	Pa	$ML^{-1}T^{-2}$	10^4 - 10^{6}&	10^5 - 10^{6}&	10^2
g	grav. acceleration	m s^{-2}	LT^{-2}	9.8	9.8	9.8
t	timescale for viscous deformation§	s	T	10^{-4} - 10^{-2}	10^{-1} - 10^4	10^2
φ	angle of internal friction	(°)	-	30	30	30

**Values from Kilburn (2000). $From fluid density values, with 20% vesicles. #Values are at atmospheric pressure for volatile contents of 0-3 wt %. Basalts at temperatures of 1080-1400 °C; rhyolites at temperatures of 800-1000 °C (e.g. Friedman et al. 1963; Shaw et al. 1968; Shaw 1972; Pinkerton & Sparks 1978; Hess & Dingwell 1996). This evidently covers the range of possible eruption temperatures, while after eruption the viscosities will increase by several orders of magnitude before cessation of flow. The thermal structure is assumed constant. &Cohesion of massive rocks ~10^7 Pa (Handin 1966; Hoek et al. 1995), but that of fractured rock is one or two orders of magnitude less (Buisson & Merle 2005). This agrees with heating experiments of Vesuvian basalt (Rocchi et al. 2004). §Defined on p. 96.*

The dimensionless parameters that are used to compare the experimental and natural systems are shown in red. Table 3.2 shows ranges of values for these dimensionless parameters for natural flows compared to the range in the analogue experimental flows.

(1) Crustal thickness, T. T has dimensions [L], so only requires combination with D to become dimensionless. This gives the ratio of the crustal thickness to the total flow thickness: T/D

(2) Flow width, W, dimensions [L]. This gives the inverse aspect ratio.

W/D

(3) Slope, α, is already dimensionless. α

(4) Crust density, ρ_c, has dimensions [ML^{-3}]. ρ_c/ρ_f

(5) Angle of internal friction, φ, is already dimensionless.

$$\varphi$$

(6) Viscosity, μ, has dimensions $[ML^{-1}T^{-1}]$, so needs to be combined with all three chosen variables to become dimensionless. The process is shown below. μ needs to be multiplied by a combination of the three chosen variables so that it becomes dimensionless, and in this case, it is necessary to raise the variables to appropriate powers so that, when multiplied together, the dimensions all cancel out:

variables: $\mu^1 \cdot D^a \cdot \rho_f^b \cdot t^c$

dimensions: $[M L^{-1} T^{-1}][L]^a[M L^{-3}]^b[T]^c = 0,$

giving, $a = -2, b = -1$ and $c = 1,$

to result in a dimensionless quantity: $\mu D^{-2} \rho_f^{-1} t$

which rearranges to give: $\mu t / (D^2 \rho_f)$

(7) Cohesion, c, has dimensions $[ML^{-1}T^{-2}]$, so again is combined with all three variables:

$c^1 \cdot D^a \cdot \rho_f^b \cdot t^c$

$[M L^{-1} T^{-2}][L]^a[M L^{-3}]^b[T]^c = 0$

$c D^{-2} \rho_s^{-1} t^2$

$c t^2 / (D^2 \rho_f)$

(8) Gravity, g, has dimensions $[LT^{-2}]$. $g^1 \cdot D^a \cdot \rho_f^b \cdot t^c$

$[L T^{-2}][L]^a[M L^{-3}]^b[T]^c = 0$

$g D^{-1} t^2$

$g t^2 / D$

These last three dimensionless parameters can be combined to give more meaningful relationships between sets of forces. For example, the dimensionless gravity, (8), and dimensionless viscosity, (6), can be combined to give the ratio between the gravitational and viscous forces:

$$(g t^2 / D) / (\mu t / D^2 \rho_f) = g t^2 D^2 \rho_f / (D \mu t)$$
$$= g t D \rho_f / \mu$$

Since $D = (T + F)$, where F is the thickness of the silicone layer, this ratio would be more accurately written as: $(F \rho_f + T \rho_c) g t / \mu$. This is still a dimensionless quantity, but provides a better description of the flow, as it accounts for the possibility that the crust and flow interior have different densities, rather than assuming that the whole flow can be represented by the density of the fluid interior.

The second combination describes the ratio between the cohesive and viscous forces, (7) and (6) respectively:

$$(c t^2 / D^2 \rho_f) / (\mu t / D^2 \rho_f) = c t^2 D^2 \rho_f / (D^2 \rho_f \mu t)$$
$$= c t / \mu$$

The ratio between the inertial and viscous forces can be represented by the Reynolds number (Re), which is the inverse of the dimensionless viscosity defined above. The Reynolds number is generally small for lava flows, and the flow regime is laminar:

$$\mathrm{Re} = \rho_f D^2 / (\mu t)$$

Finally, in considering the crustal rheology, the frictional resistance to failure, under compressive stresses, can be described using the Mohr-Coulomb criterion. While the process of 'failure' can be an instantaneous loss of cohesion in a rock

sample, it can also be continuous, and occur progressively once the uniaxial compressive strength of the material has been exceeded. Criteria of failure attempt to describe the point at which failure *initiates* under general conditions. The Mohr-Coulomb criterion predicts that failure occurs when the applied shear stress, less the frictional resistance associated with the normal stress on the failure plane, becomes equal to a constant of the rock, its cohesion. This is written:

$$\tau = c + \sigma \tan\varphi$$

where τ is the shear stress across the plane of failure; c is the resistance to failure that exists even when the stress is zero, i.e. the cohesion; σ is the normal stress across the failure plane and φ is the angle of internal friction. This can be simplified if the material under question is assumed to have no inherent strength, i.e. no cohesion, which would be applicable in the case of clean, dry sand, so that:

$$\tau = \sigma \tan\varphi$$

This quantity can be also non-dimensionalised using the three chosen variables. From the hydrostatic equation, it is known that σ is equal to the product of density, gravitational acceleration and depth, which is conventionally written $\rho g h$, but can be more appropriately written $\rho_c g T$ in the notation used in this chapter when considering the crust. This quantity has dimensions $[ML^{-1}T^{-2}]$ and so the dimensionless form of the frictional forces is derived as follows:

$$\rho_c g T \tan\varphi \cdot T^a \cdot \rho_c^b \cdot t^c$$

$$[M L^{-1} T^{-2}][L]^a[M L^{-3}]^b[T]^c = 0$$

$$g T^1 t^2 \tan\varphi$$

$$g t^2 \tan\varphi / T$$

Taking the ratio of the frictional to viscous forces gives:

$$(g t^2 \tan\varphi / T) / (\mu t / T^2 \rho_c)$$

$$\rho_c g T t \tan\varphi / \mu$$

A timescale, t, for the models can also be calculated (table 3.1), using $t = \mu / \sigma$, where μ is the viscosity, and σ is the gravitational driving stress. As previously suggested, σ could also be represented by $\rho g D$, hence:

$$t = \mu / \rho g D \sin \alpha$$

for slope α, which is the timescale for viscous deformation, and can be written t_μ. The use of this timescale reflects the assumption that viscous deformation of the core will provide the dominant resistance to motion in the analogue flows.

Table 3.2 shows the ranges of values for the dimensionless parameters calculated for basaltic and rhyolitic lava flows, and for the analogue experimental flows, using the ranges of values given in table 3.1.

Table 3.2. Approximate values of the dimensionless parameters in natural and analogue flows.

Dimensionless parameters		Value		
		Basalt	Rhyolite	Experiment
crust/total flow thickness	T/D	10^{-2} - 10^{-1}	10^{-1}	10^{-2} -10^{-1}
inverse aspect ratio	W/D	10^{0} - 10^{2}	10^{1}	10^{0}
crust/fluid density	$\rho_c \rho_f$	10^{0}	10^{0}	10^{0}
slope	α	<<1 - >35	<<1 - >35	4 - 12
grav./viscous forces	$(F\rho_f + T\rho_c)gt_\mu/\mu$	10^{1} - 10^{2}	10^{1}	10^{1}
cohesive/viscous forces	Ct_μ/μ	10^{-1} - 10^{2}	10^{-1} - 10^{1}	10^{1}
inertial/viscous forces	$\rho_f D^2/\mu t_\mu$	10^{-5} - 10^{2}	10^{-8} - 10^{-1}	10^{-8}
frictional/viscous forces	$\rho_c g T t_\mu \tan\varphi/\mu$	10^{-1}	10^{-2} - 10^{-1}	10^{-1} - 10^{0}

Ranges of values reflect possible ranges in table 3.1, and also where viscosity is used, possible viscosities for basalts up to several orders of magnitude greater than those quoted in table 3.1, which only considered the viscosity upon eruption.

The values of the dimensionless parameters for the analogue experimental flows are similar to those for the basaltic and rhyolitic flows, suggesting that the flow behaviour in the analogue and natural systems is similar. The values of the force ratios suggest that while gravity dominates over viscosity, resulting in the flows advancing downslope, the roles of cohesion and friction in retarding flow advance are less easy to distinguish from the role of viscosity. This suggests that the systems can be

sensitive to small changes in conditions, and that behaviour may be dominated by either the viscous flow core or the brittle crust. The role of inertia is negligible in most flows, excepting very low-viscosity basalts, where the flow regime may be approaching turbulent, rather than laminar, flow. The similarity in values of the parameters suggests that the analogue flows can simulate the behaviour of lava flows ranging in composition from high-viscosity basalts to rhyolites, and that any observations of flow behaviour from the analogue models should be applicable to lava flows within this compositional range.

3.2 Experimental methods

3.2.1 Apparatus

As described in section 3.1, the experiments simulate the flow of fresh lava into a channel that contains a flow with a cooled, brittle crust. This was achieved using the apparatus shown schematically in figure 3.1, which consists of a reservoir with a sliding gate mounted at one end of a smooth flat basal board. The slope was changed by elevating the reservoir end of the apparatus, and slopes of 4, 8 and 12° were used. Before the experimental work began, the slope was established, then the reservoir was filled with fresh silicone fluid and allowed to stand until the surface was level and all large bubbles had escaped. The volume of silicone in the reservoir was then calculated by measuring the depth from the top of the reservoir walls to the top of the silicone. Subtracting the volume of space from the known reservoir volume gave the volume of silicone. The volume of silicone remaining in the reservoir was measured at the end of each run, before the reservoir was topped up with clean silicone in preparation for the next experiment.

During the course of a few trial runs, the experimental procedure was refined, and the method of setting up the initial flow remained the same from experiment six onwards. This procedure is illustrated in figure 3.2, which shows a series of images taken from vertically above the apparatus during the construction of the initial flow. To prepare the flow interior, silicone was pressed into a wooden frame of the desired dimensions (350 x 127 mm) and allowed to settle for several hours until it had attained a depth of 15 mm, and all the air bubbles had risen and escaped. 127 mm was the width of the sliding gate in the reservoir wall, and 350 mm was judged to be sufficiently short to leave room for significant flow to occur beyond the channel, but long enough that features within the channel would have time and room to develop

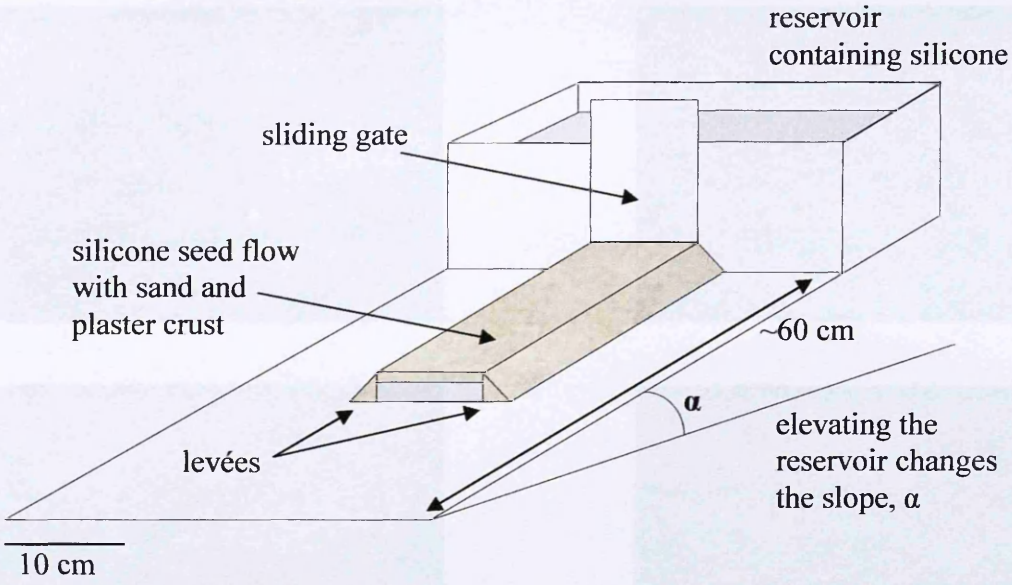

Figure 3.1. Sketch of the experimental apparatus as seen at the beginning of a run. Silicone is indicated by the grey shading, and can be seen in the reservoir and making up the flow interior. The sand and plaster mix is shown by the brown shading, and made up the surface crust of the seed flow, and the levées. The basal board is approximately 60 cm long, while the seed flow is 35 cm long. The manner in which the seed flow was constructed can be seen in figure 3.2. See text for details.

before being overrun by the silicone flowing in from the reservoir (hereafter referred to as the 'influx'). The sliding gate was then opened to a depth of 15 mm, and the silicone sheet was placed on the board with one end in contact with the silicone in the reservoir. The sand and plaster mix was poured from a jug to construct levées down each side of the silicone sheet (figure 3.2 a), in order to restrict lateral spreading, and thus simulate channelised geometry. A crust of predetermined depth was then added to the silicone flow by sieving the sand and plaster through a 400 μm sieve (figure 3.2 b). In order to achieve as even a covering as possible, point measurements of the crust depth were taken several times during the sieving procedure, using a wire probe with millimetric divisions. The depth of the crust could be measured with an accuracy of ± 0.5 mm.

Crust was added as a proportion of the silicone thickness, and the ratio $\chi = T / D$ is defined, where T is the thickness of the brittle crust and D is the total flow thickness.

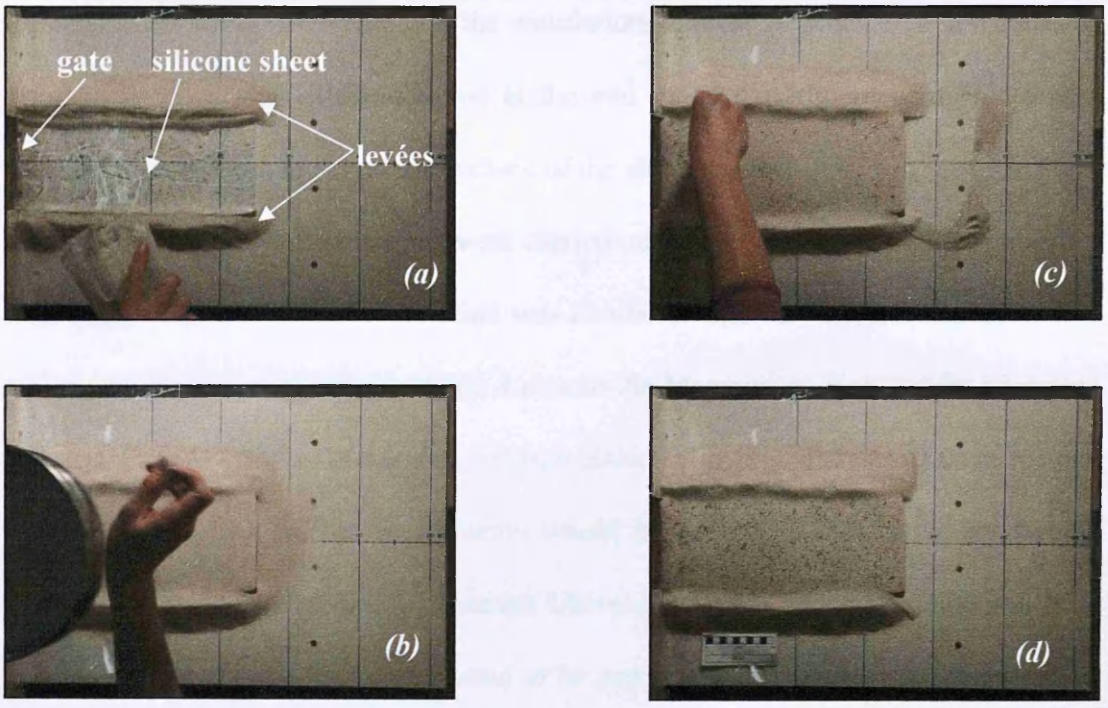

Figure 3.2. Images from vertically above the apparatus, showing the construction of a seed flow. The sliding gate can be seen at the left hand edge of the image, and the reservoir is beyond the left of the image. See text for details. (a) Approximately 6 minutes before the start of the simulation, the silicone sheet was placed on the board, and levées were constructed. (b) Crust sieved on. (c) Markers added. (d) Excess sand brushed away and scale bar added. This is the first image in the monitoring sequence.

Two experiments were conducted without crusts ($\chi = 0$), but for the experiments with crusts, χ ranged from 0.063 ± 0.03 to 0.5 ± 0.01. In nature, variations in parameters such as composition (i.e. thermal conductivity), effusion rate and effusion temperature lead to a range of χ values being observed, and spatial and temporal variations in χ are also seen within a single flow due to the effects of cooling. Once the crust had been added, black markers of silicone carbide or mustard seeds (section 3.3.3) were sprinkled over the surface (figure 3.2 c) and the experiments were left to proceed. Although the process of setting up the initial flow took between five and ten minutes, the high viscosity of the silicone meant that no appreciable movement of the flow occurred within that time, as can be seen in figure 3.2 (d), which shows a completed initial flow. The 'end' of an experiment depended on the experimental conditions and

the structures being produced, and the simulations ran for between five and fourteen hours. The crust was often removed at the end of an experiment using a vacuum cleaner or soft brush, to reveal the surface of the silicone fluid.

In total, thirty eight simulations were carried out, which are numbered two to thirty nine following an unrecorded test that was numbered one. Of these, numbers two to twenty four were carried out at the Laboratoire Magmas et Volcans in Clermont Ferrand, France, during February and March 2006. Following analysis of these results, it was decided that further experiments would be desirable, and so twenty five to twenty nine were carried out at Lancaster University between October 2006 and June 2007. Conditions were, however, found to be unsuitable in Lancaster, as discussed in section 3.3.1, and so the final simulations, thirty to thirty nine, were again carried out in Clermont Ferrand, in October 2007.

3.2.2 Flow structure

A cross section through a lava flow would reveal a complex internal structure, as sketched in figure 3.3 (a). The upper layer of brittle clinker graduates down into the fluid interior through a mixed layer of clinker and fluid. This structure results in a strong layer between the brittle surface cover and the viscous interior, the viscoelastic layer, as discussed in chapter two. Due to the rollover of crustal material at lava flow fronts, in addition to autobrecciation of the lower, cooled layers of the flow, lavas advance over a basal layer of clinker (the basal breccia), so there is a second mixed layer of fluid and clinker between the breccia and the fluid interior. While the lava flow interior continues to cool, the rate of heat loss through conduction once the crust has formed is significantly lower than the initial rate of heat loss through radiation. As such, the lava flow interior can be considered isothermal over short time intervals. The

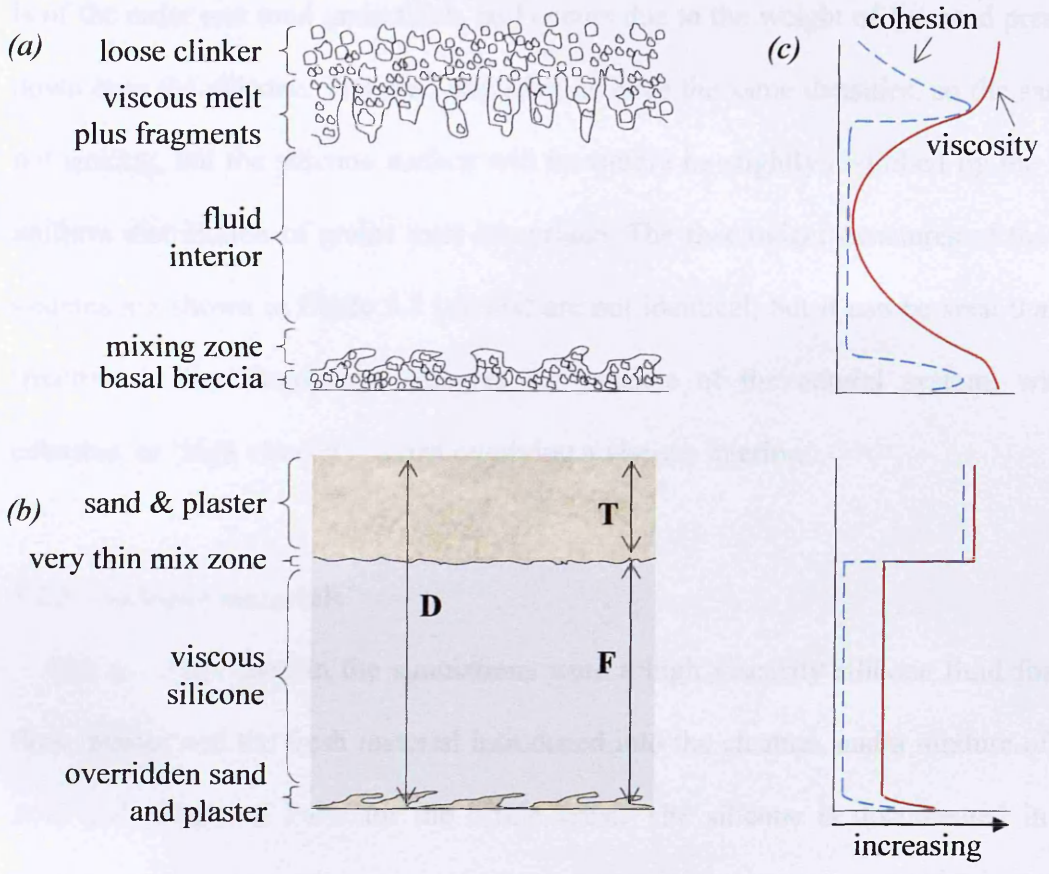

Figure 3.3. (a) Schematic cross section through a basaltic `a`ā lava flow, compared to the structure of an active model flow (b). The three geometric parameters T, D and F are shown. Model depth ~ 2.5 cm; lava depth 1-20 m. (c) Indication of relative viscosities (red) and cohesions (blue) as a function of depth for each system, not to scale. See text for details.

cross-sectional structure of the analogue models (figure 3.3 b) is necessarily simplified from the natural system, being represented here by a uniformly cohesive, brittle analogue crust overlying a purely viscous analogue flow interior. Figure 3.3 (b) represents a model in progress. A cross section through the initial analogue flow would be similar to that through a lava flow, but lacking the basal breccia layer. In the analogue models, a thin layer of overridden sand and plaster, which forms by rollover of crustal material at the flow front, as observed in lava flows, only develops downslope of the original flow front after the flow has started to advance. The thin 'mixing' zone shown between the analogue crust and the flow interior in figure 3.3 (b)

is of the order one sand grain thick, and occurs due to the weight of the sand pressing down onto the silicone. The sand and silicone have the same densities, so the sand is not sinking, but the silicone surface will inevitably be slightly disturbed by the non-uniform distribution of grains over its surface. The rheological structures of the two systems are shown in figure 3.3 (c), and are not identical, but it can be seen that the structure in the simulations captures the essence of the natural system, with a cohesive, or 'high viscosity', crust overlying a viscous interior.

3.2.3 Analogue materials

The materials used in the simulations were a high viscosity silicone fluid for the flow interior and the fresh material introduced into the channel, and a mixture of dry sand and plaster of Paris for the brittle crust. The silicone is documented in the literature as behaving like a true Newtonian fluid, with a viscosity of 10^4 Pa s (Merle 1998; Lescinsky & Merle 2005). Pure, dry quartz sand is known to have a negligible cohesion (Mourgues & Cobbold 2003), and has been used as an analogue for brittle rocks in many experiments (e.g. Hubbert 1951; Buisson & Merle 2005; Lescinsky & Merle 2005). Dry plaster of Paris has a cohesion of a few hundred Pa, and when mixed with sand can be used to simulate cohesive brittle clinker (e.g. Lescinsky & Merle 2005). The first four models (two to five inclusive) were carried out using a mixture of 90% sand to 10% plaster. Model six was carried out using 80% sand and 20% plaster, and the increased cohesion was found to increase the clarity of the structures produced, because fracture edges remained intact. Thereafter, all experiments were conducted this higher proportion of plaster.

3.2.4 Measurements

During the course of each experiment, sequential digital images were taken, to record the morphological evolution of the flows. For experiments two to twenty five, either an Olympus E-20 or a Canon EOS Rebel was used (table 3.3). In both cases, the integral timer of the camera was used to control the time interval between the images, and this was approximately 90 seconds for the E-20 and 60 seconds for the EOS. Camera specifications can be found in Appendix A. During these simulations, monoscopic images were taken from vertically above the models (figure 3.4 a), and the surface markers used were angular black silicon carbide grains, of the order 0.5 to 1 mm in diameter. While visual examination of the images allowed the qualitative

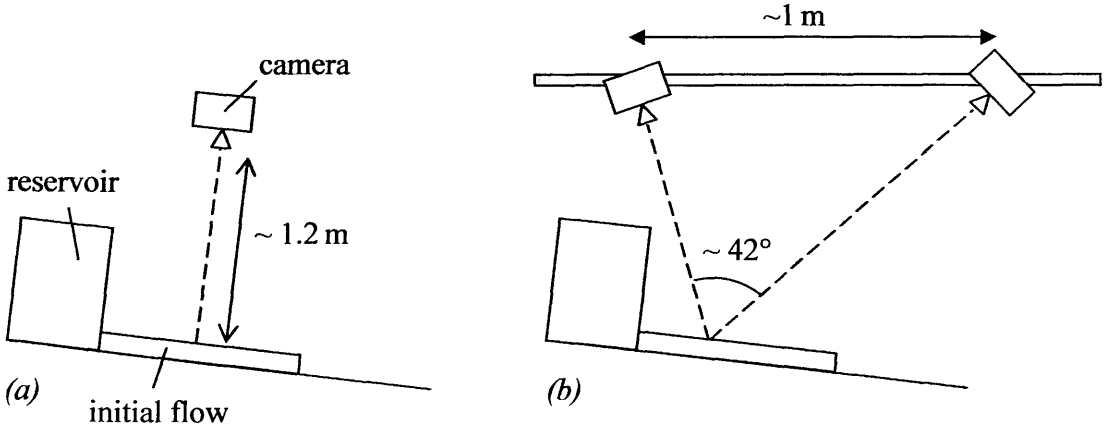

Figure 3.4. Schematic sketch showing data capture in (a) monoscopically and (b) stereoscopically monitored experiments. The cameras were fixed so that the centre of the field of view focussed on the centre of the seed flow. For monoscopic images, the camera was directly above the seed flow and viewing orthogonally. For stereo images the cameras were arranged so that the angle between the viewing angles was as great as possible while still allowing the whole seed flow to be seen. See text for details.

description of morphological changes, the tracking of surface markers using imaging software allowed a more quantitative approach to monitoring the crustal deformation.

In order to reconstruct the flow surface in three dimensions and hence to detect changes in surface relief, experiments twenty six to thirty nine were monitored using

stereo imagery, as illustrated in figure 3.4 (b), with image pairs taken every two minutes. The two cameras used, a Canon EOS 300D, and an EOS Rebel, were mounted on a horizontal strut above the experimental apparatus, and their fields of view were centred on the simulated flow. The camera setup and the errors of the measurement techniques are discussed further in the following section. For the analysis used, the marker points needed to be as close to spherical as possible, and approximately five to ten pixels in diameter in the images. This ruled out the use of the silicon carbide grains, which were irregular in shape, too small and too reflective. After some testing of various beads and seeds, black mustard seeds, which have matt surfaces, were found to be the most suitable markers, and these were approximately 2 mm in diameter.

3.2.5 Analysis techniques and errors

3.2.5.1 2-D processing

Tracking of the marker points through the image sequence was carried out using *Pointcatcher*, a correlation-based point tracking programme written in MATLAB by M. James. To run *Pointcatcher*, first a sequence of images is loaded into the software, and 'points of interest' are identified in the first image (figure 3.5 a) using a Harris interest operator (Harris & Stephens 1988). These are locations that are sufficiently different to their immediate surroundings as to provide a good chance of being identified in subsequent images. In the silicon carbide seeded flows, interest points were predominantly associated with the margins of the black carbide grains, which are in strong contrast with the pale sand beneath. Using the x-y coordinates of each interest point identified in the initial image, *Pointcatcher* searches for the same points within limited search windows in the subsequent image. For each point, the position

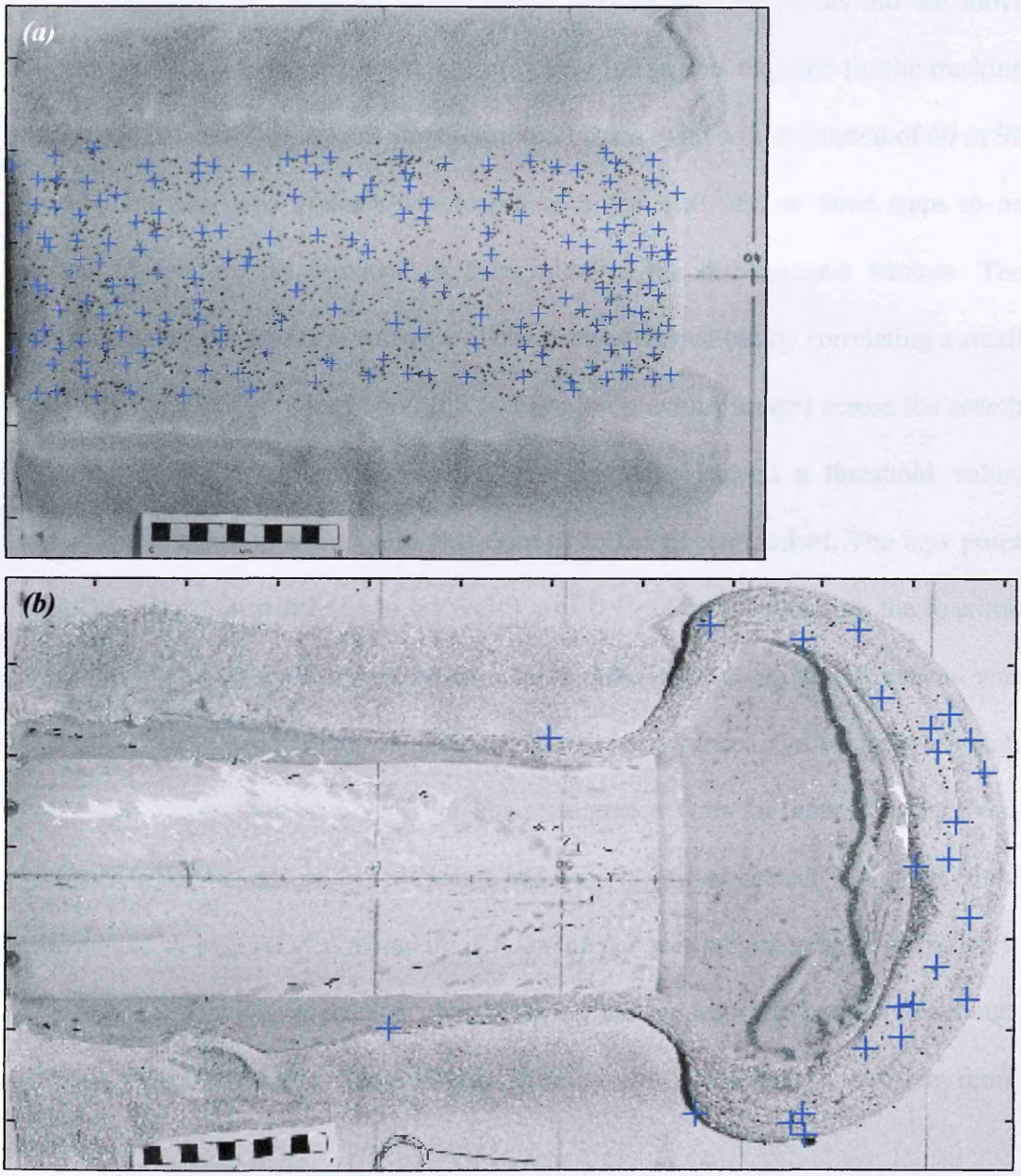

Figure 3.5. Experiment 19, χ = 0.167. (a) Initial and (b) final images of a Pointcatcher *sequence. The blue crosses indicate the points that are tracked through the image sequence, and it can be seen that a large number of points are lost during the course of a simulation, largely due to rollover at the flow front. See text for details.*

of the search window defaults to the position of the point in the previous image. However, if the point has been successfully tracked between the preceding two images, then the search window position is offset by the preceding displacement vector, essentially using the preceding displacement as an initial estimate of the

current displacement. Since the flows moved very slowly, the points did not move very far between the images, and hence not every image was required for the tracking procedure. The first two images were used in all cases, with a time interval of 60 or 90 seconds, and this was gradually increased over the next two or three steps to an interval of five or six minutes, to help initialise the displacement vectors. The identification of the points in subsequent images was carried out by correlating a small template image of the point region (taken from the previous image) across the search windows. If the maximum correlation was found to exceed a threshold value, generally set at 0.6, then the point was deemed to have been tracked. The new point coordinates were then refined to a precision of 0.1 pixels by obtaining the maxima coordinates of a surface fitted to the correlation data. If the correlation threshold was not reached then the point was not deemed to have been tracked. For each experiment, after *Pointcatcher* had been run, the image sequence with the interest points was closely examined to ensure that all points had been identified correctly. A point could be discarded or repositioned manually if *Pointcatcher* was judged to have identified it incorrectly, which was a problem that became more widespread later in the image sequence, when velocities were higher and the surface structure became more complex.

The output of the tracking procedure was a 'points' file, listing the pixel coordinates of all points in each image, and a 'displacement' file listing the displacement in pixels of each point between each consecutive pair of images. Since the time intervals between each image pair was known, these displacements could easily be converted into velocities, and surface velocity maps could be created for each time interval. Examples of these are shown in section 3.3.2.1. The use of velocity maps was confined to the early stages of the experiments, the first hour to ninety

minutes, and so illustrated the early deformation of the crust. As the simulations progressed, the increasing deformation became too complex to be accurately recorded by a small number of discrete points, and the points themselves were often lost as the surface markers were rolled over at the flow front, or fell into fractures. This is illustrated in figure 3.5 (b), where the number of points remaining at the end of an experiment can be seen to be rather small. This monitoring method, however, was very useful in the elucidation of early channel processes in the experiments.

The positional errors in the tracking method mainly stemmed from inaccurate manual redefinition of interest points that were lost by *Pointcatcher*, and were estimated to be less than ± 2 pixels. This is illustrated in figure 3.6, using data from experiment 20. Figure 3.6 (a) shows the initial image in a point tracking sequence, with six interest points identified on the surface, and 3.6 (b) shows the tracks of these points through a sequence of 30 images at the same scale as (a). The axes are in pixels. The points in blue are markers that *Pointcatcher* successfully tracked through the sequence, while those in red had to be manually replaced several times. A close up of the tracks is shown in part (c), where the replaced points are also indicated with arrows. It can be seen that at this scale, it is difficult, if not impossible, to tell whether the repositioning is resulting in any error. Part (d) therefore plots the x- and y-components of the displacement between each image pair for the three points that were repositioned, with displacement on the y-axis against the interval number on the x-axis. The x-component is shown in red, and the y-component in blue, and displacements are in pixels. The sharp increase in the x-displacement over the first two intervals reflects the increasing time interval over the beginning of the image sequence. Again, the stages at which the points were replaced are indicated by arrows, and it can be seen that while this often results in a slight departure from the prevailing

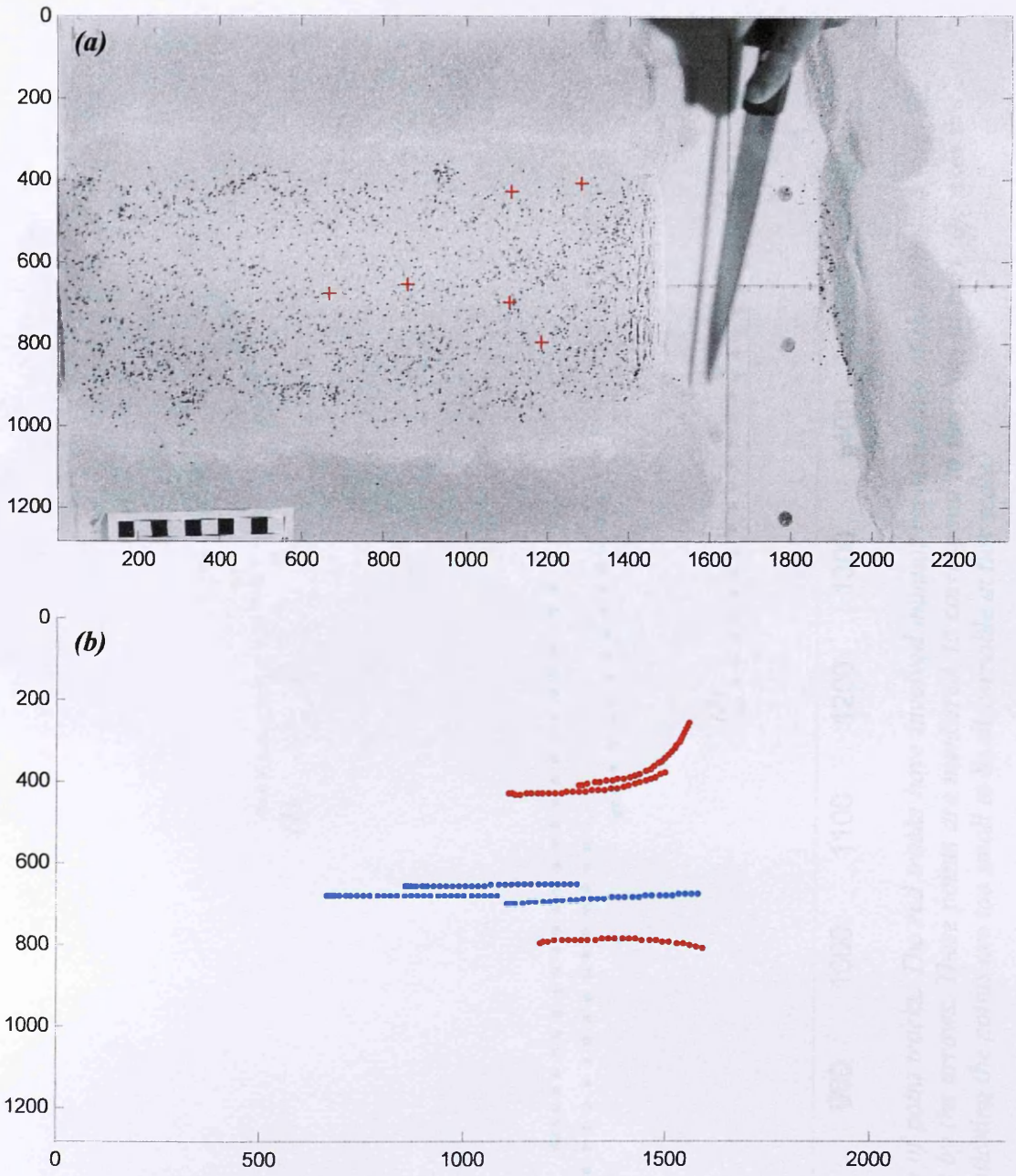

Figure 3.6. (a) Initial image in a sequence of 30, showing 6 points to be tracked through the sequence. Axes are in pixels. Scale bar is 10 cm long. (b) Plot showing the same area as the image in (a), with the image tracks picked out. The three blue tracks did not need any points repositioning, while the red tracks did need several manual readjustments.

trend, the magnitude of the departure is usually substantially less than one pixel, and in most cases results in only a very minor deviation (a small amount of noise) in the overall trend of the point movement. Point 3, however, is replaced several times

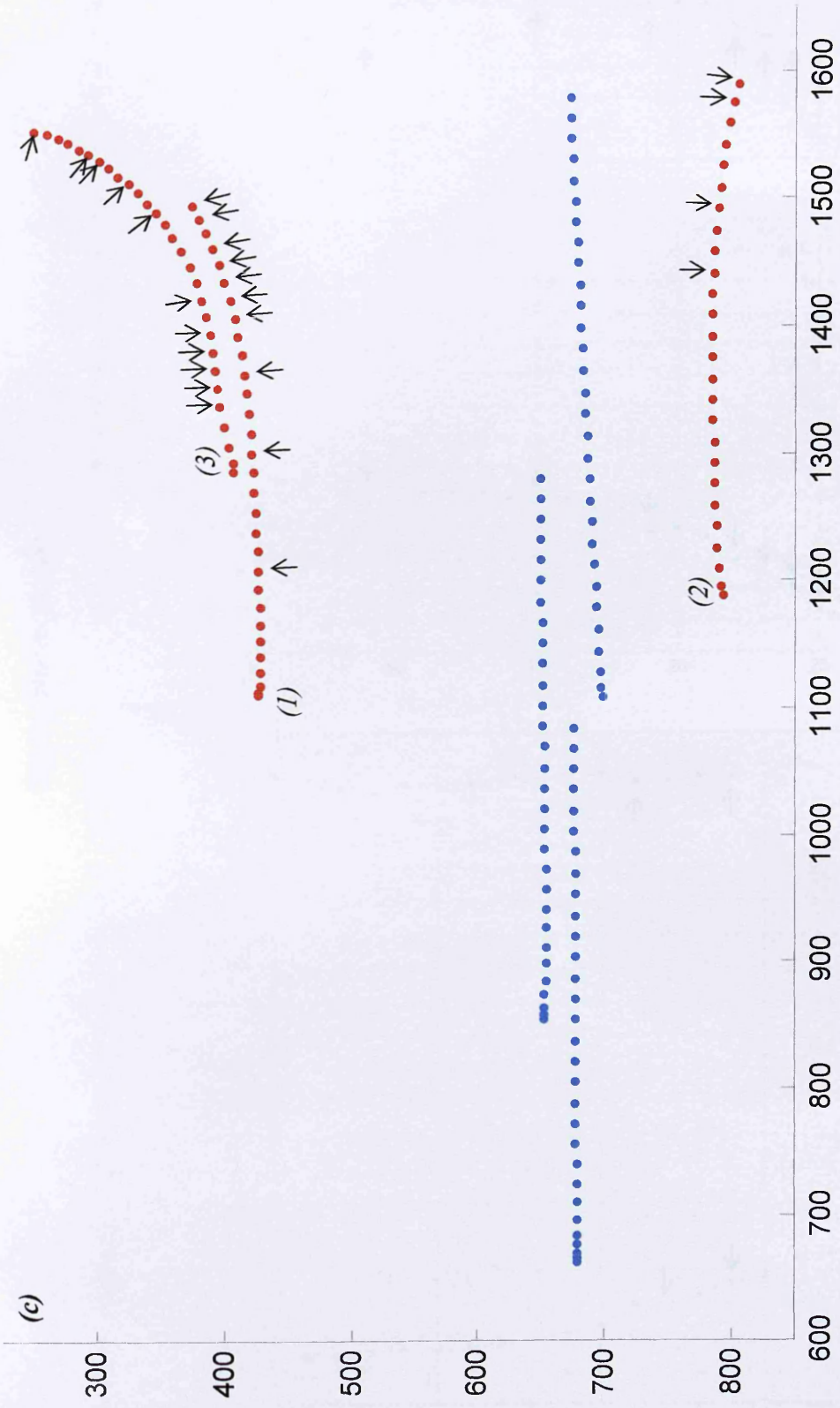

Figure 3.6 cont'd. (c) Close up of point tracks. The red tracks have involved manual repositioning of the points at several times, and these are picked out by the arrows. These points are numbered, to correspond to the plots in part (d). Axes are again in pixels. Errors in repositioning the points are too small to be discernable at this scale.

(d) ***Point (1)***

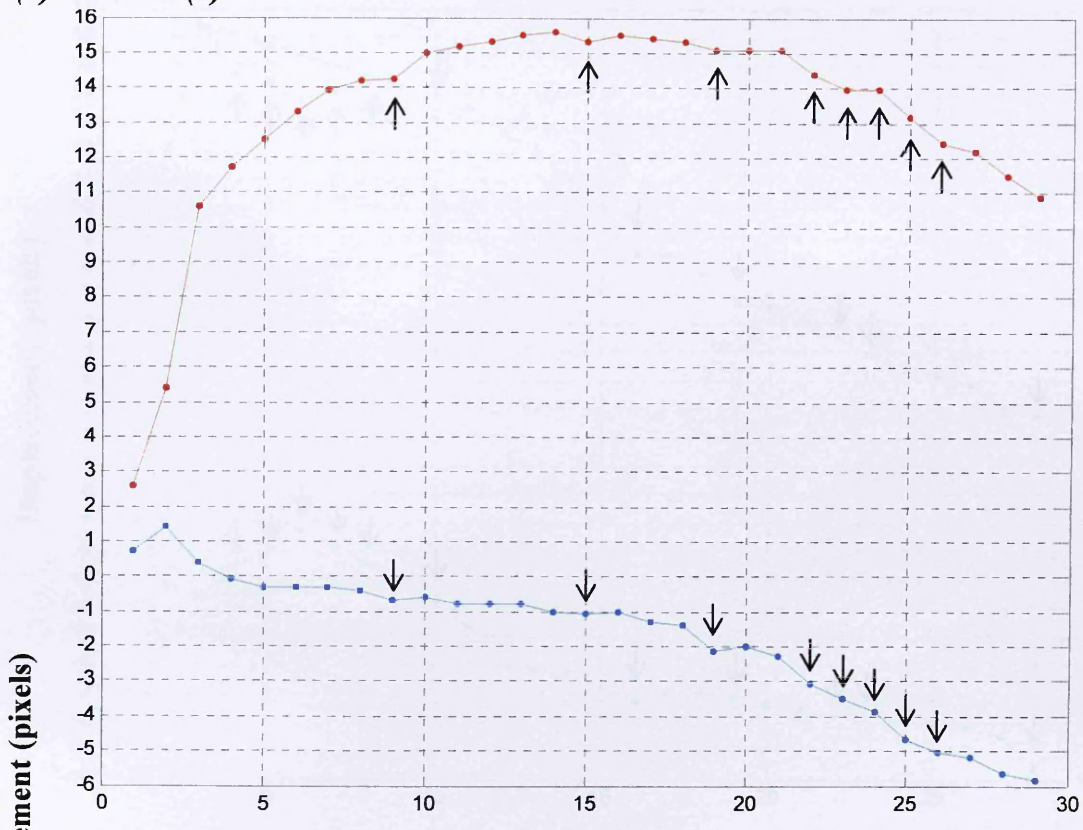

Point 2

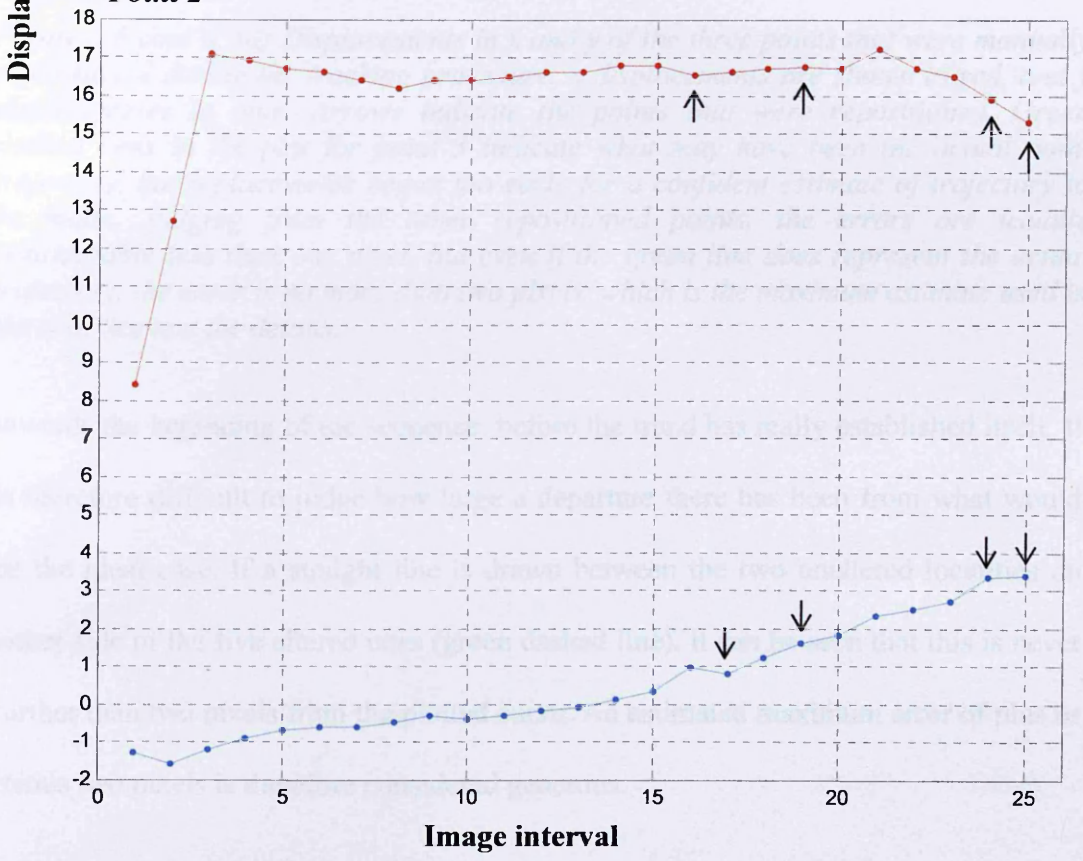

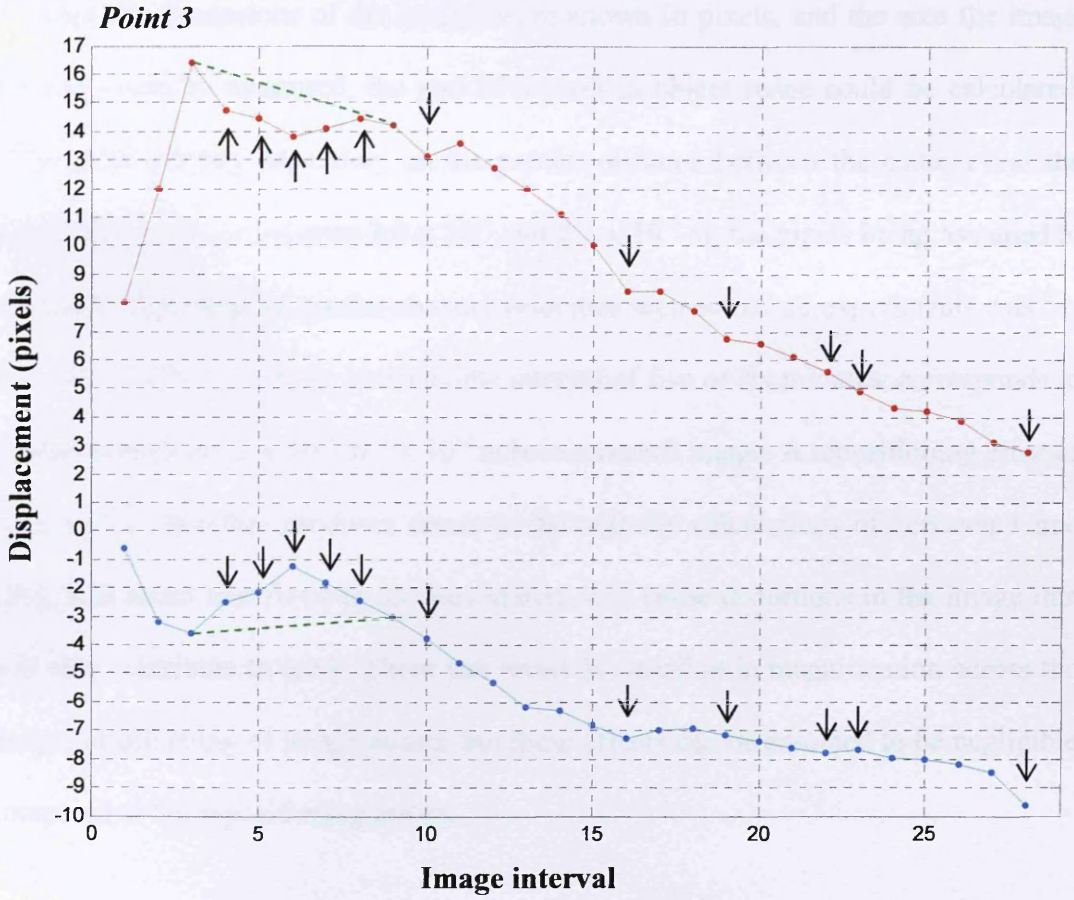

Figure 3.6 cont'd. (d) Displacements in x and y of the three points that were manually repositioned during the tracking procedure. x displacements are shown in red, and y displacements in blue. Arrows indicate the points that were repositioned. Green dashed lines in the plot for point 3 indicate what may have been the actual point trajectory, but replacements began too early for a confident estimate of trajectory to be made. Judging from the other repositioned points, the errors are usually considerable less than one pixel, but even if the green line does represent the actual trajectory, the error is no more than two pixels, which is the maximum estimate used in the text. See text for details.

towards the beginning of the sequence, before the trend has really established itself. It is therefore difficult to judge how large a departure there has been from what would be the ideal case. If a straight line is drawn between the two unaltered localities on either side of the five altered ones (green dashed line), it can be seen that this is never further than two pixels from the plotted curve. An estimated maximum error of plus or minus two pixels is therefore considered generous.

Since the dimensions of the images were known in pixels, and the area the image covered could be measured, the size of a pixel in object space could be calculated. This varied slightly depending on the precise distance between the camera and the simulation, and was between 2.0 x 10^{-4} and 2.5 x 10^{-4} m, the pixels being assumed to be square. The range of medial channel velocities seen across all experiments was 5 x 10^{-6} to 5 x 10^{-5} ms^{-1}, which, given a time interval of five or six minutes, corresponds to a displacement of ~2 x 10^{-3} to 2 x 10^{-2} m between each image. A repositioning error of ~2 x 10^{-4} m therefore produces errors in the velocity calculations of between 1 and 10%. It is noted that flaws in the lens system will cause distortions in the image that will also contribute to error. These can result in variation in magnification across the image, or offsetting of image points, but these effects can be assumed to be negligible compared to the repositioning errors.

3.2.5.2 3-D processing

Experiments twenty six to thirty nine were analysed using photogrammetric techniques, which allow the derivation of metric information about an object through measurements made on images of that object (e.g. Atkinson 1996, Mikhail et al. 2001). This involves imaging the object, in this case the experimental flow, from two viewpoints (figure 3.4 b). In order to be able to reconstruct the 3-D coordinates of points in object space from the corresponding 2-D coordinates of the points in image space, it is necessary to establish the geometric relationship between the images and the object. This involves firstly determining the physical parameters which describe the cameras (the interior orientation), and secondly the relative positions and orientations of the cameras (the exterior orientation). The interior orientation is determined for each camera during individual calibrations.

Individual camera calibration

The determination of the interior orientation involves the description of what happens to a bundle of light rays from the object that pass through the camera lens and onto the image plane. In an ideal system, this process can be described mathematically as a pin-hole camera, according to optical laws (Atkinson 1996), but, in reality, flaws in lenses mean that these laws can only be used as a good approximation. Lens distortions, which can be radial or tangential, cause flaws in the resulting image. Radial distortion relates to the variation in magnification with angle of incidence, while tangential distortion is the displacement of an image point caused by the imperfect alignment of lens elements. While these effects were deemed negligible in the two-dimensional processing, as only one camera was used, when trying to relate two images from different cameras with different flaws, they need to be accounted for. The distortions can be modelled by a set of parameters that describe their effect on the images, and these parameters are then used to remove the distortion effect, thus improving the object model derived from the images. Other parameters that are used to describe the interior orientation are the principal distance (equal to the focal length at infinite focus); the offset of the principal point (the location on the image plane of the direct axial ray passing through the centre of the lens) from the centre of the image plane; the orthogonality of the pixels (how close to 90° the angles between intersecting sides are) and the affinity of the pixels (how close to square the pixels are).

The determination of these intrinsic parameters is achieved through the calibration of the camera. The individual calibrations of the two Canon EOS cameras with fixed 28 mm lenses were carried out by M. James. Camera calibrations require the use of a calibration target, which in this case was a flat board with a series of dots of known

geometry. The dots are numbered, and their approximate positions are stored in a target file. While the use of a two dimensional board is not ideal, it was sufficient for the accuracies required here. A more rigorous characterisation of the cameras would require a three dimensional calibration structure.

For each camera, the calibration procedure involved a number of images (approximately twelve or more) being taken of the calibration target from a wide range of angles. This series of images was then loaded into Vision Measurement System, a photogrammetric software package written by S. Robson and M. Shortis, together with the target file containing the approximate locations of the target points. Four target points were identified in each image, after which VMS found all the other targets in the image using their approximate locations from the target file, and each image was resected. The process of resection determines the image's position and orientation with respect to the object space coordinate system, and the output gives the six exterior orientation parameters. These are the three object space coordinates of the camera centre and the three angles describing the orientation of the object space coordinate system with respect to the image space coordinate system. Following the individual resections, the positions of the targets in object space can be determined by the intersection of image rays from all images in which the targets appear. The final stage in the process is a self-calibrating bundle adjustment, which establishes the position and orientation of each bundle of rays using information both from the bundles and from the target control information. During this process, all parameters, including the interior orientation parameters, are adjusted to optimise the description of the system, and any target observations which are identified as outliers are automatically rejected from the optimisation procedure.

The output of the calibration procedure is an updated target file (.tar), with more accurate target positions; a photo file (.pho) with the exterior orientation parameters for each camera position; an observation file (.obs) with the x-y positions of each target in each image, and the calibration file (.cal) with the calculated interior orientation parameters and their associated precisions. The calibration data for each camera is shown in Appendix B.

Dual camera calibration

Once the two cameras have been mounted on the strut prior to an experiment being run, they need to be calibrated as a pair in order to establish the geometric relationship between them (figure 3.4 b). During this stage, it is only the exterior geometry that is determined: the interior orientations that were found during the individual calibrations are held constant. The dual calibration only needed to be done once for each suite of experiments, as, providing care was taken when the data cards were removed, the cameras were not disturbed during the dismantling and setting up of experiments. The procedure was very similar to that for the individual calibrations, with simultaneous images of the target board taken by the two cameras. Since the cameras were fixed to the strut, the board was moved to achieve the range of angles required. The two sets of images were then loaded into VMS with the individual calibration files and the target file. Again, the targets were identified in each image, followed by individual resections, intersection and the bundle adjustment. The resulting .pho file contains the information about the positions and orientations of the two cameras with respect to the origin on the target board. A log file is produced during the bundle adjustment, which includes an estimate of the overall precision of the network. The dual calibration .pho and network log files for the Lancaster and Clermont Ferrand experiment suites are

shown in Appendices C to F. The precision of the Lancaster network was found to be 1 in 5000, which corresponds to about three tenths of a millimetre, while that of the Clermont network was 1 in 59000, which is approximately twenty microns. As is discussed in section 3.3.1, a number of problems were encountered with the experiments carried out in Lancaster, and so they are not given the same weight of consideration in the analysis. The lower precision is not therefore considered to be a problem, as the conclusions that are drawn from the 3-D work are based solely on the results of the simulations performed in Clermont.

During the simulations, the experimental apparatus was placed on the calibration target board, so that a frame of reference was provided by the calibration targets visible in the image sequences captured.

Accounting for geometric considerations, to maximise the accuracy of the photogrammetric measurements, the angle between the two camera viewing angles should ideally be as close to 90° as possible. As shown in figure 3.4 (b), the angle used in this work was ~42°, which was the maximum possible considering the practical requirements of the setup, and is considered to be highly convergent for standard photogrammetric setups. Due to the fixed focal length of the cameras, and the need for the whole calibration target to be seen in each field of view, the cameras needed to be mounted approximately 1.2 m above the experimental apparatus. The horizontal strut used was made of Dexion bars, which were bolted in the centre to a substantial camera floor stand. Despite several bars being used, there was still some flexibility in the frame. In order to stabilise the system, wooden pillars were wedged between the floor and the bar at each end, and bolted to the bar. This resulted in a frame of the order 1.5 m square, and it was judged unfeasible to use a longer bar, both due to space constraints in the laboratory, and the increased flexibility that this would

introduce into the system. The cameras were therefore bolted to the frame approximately 1 m apart, resulting in the 42° separation between the viewing angles.

Post-experiment processing

After each experiment, the initial pair of images was loaded into VMS, with the .cal and .tar files. The camera positions were established by identifying four control targets on the board in each image and performing resections. Unlike the 2-D experiments, where *Pointcatcher* identified and numbered the points that would be tracked, VMS was used here to locate the centre of each of the spherical markers, and to assign the same number to each marker in the two corresponding images. When all points were identified, the .obs file was saved. Transferring these observation data to MATLAB provided *Pointcatcher* with initial point coordinates to track in the initial images of the two sequences, after which each sequence was run as for the 2-D experiments. The two 'points' output files together with the dual calibration information and the exterior orientation data from the .pho file were used to perform the intersections in MATLAB, which resulted in the final positions of all the points in each image, in 3-D object space. Error assessment is carried out during this stage, and the results are presented in the form of histograms of the residuals associated with the point position data. Residuals are always greater in the y-direction (cross flow) than the x-direction (downflow) because the x vectors are in the plane of the optic axes, while the y vectors are orthogonal to this plane. This results in the very accurate calculation of the x components of the marker positions, but a lower accuracy for the y components. In order to remove poor matches, points with residuals greater than 0.5 pixels (~ 4 μm) were removed. The residual histograms for experiment 38 are shown in Appendix G. The final point position data was used to create maps of the changes

in the surface relief experienced by the flows, and examples of these are shown in section 3.3.2.2.

The repositioning errors with respect to the z-coordinate can be examined in a similar manner to the x and y errors seen in figure 3.6. This was done by tracking several points through a 3-D sequence, some of which were repositioned, and plotting the z-coordinates of the repositioned points. Figure 3.7 (a) shows the point positions of markers that were tracked through the sequence of fifteen images, including one control point on the calibration board. The tracks of these points are shown in 3-D in figure 3.7 (b), with three tracks that involved repositioning highlighted in red. The control point is shown in green. Figure 3.7 (c) plots the z-coordinate against the image number for each repositioned point (red) and the control point (green). The image

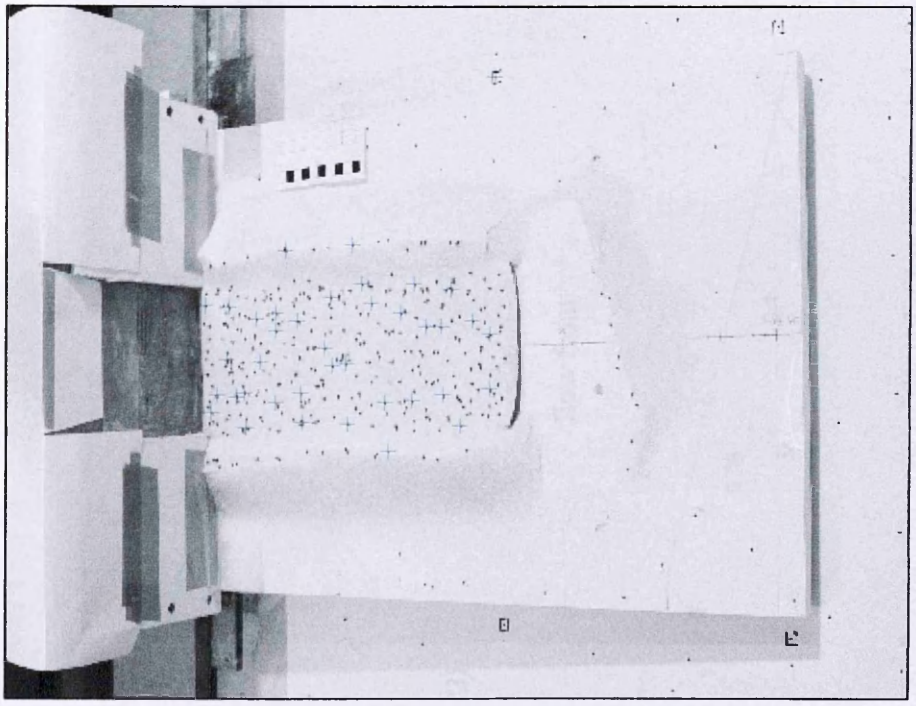

Figure 3.7. (a) Initial image in a sequence of 15 showing 40 points to be tracked through the sequence, including one control point on the calibration board beneath the apparatus. View is from the right hand camera in the stereo set up.

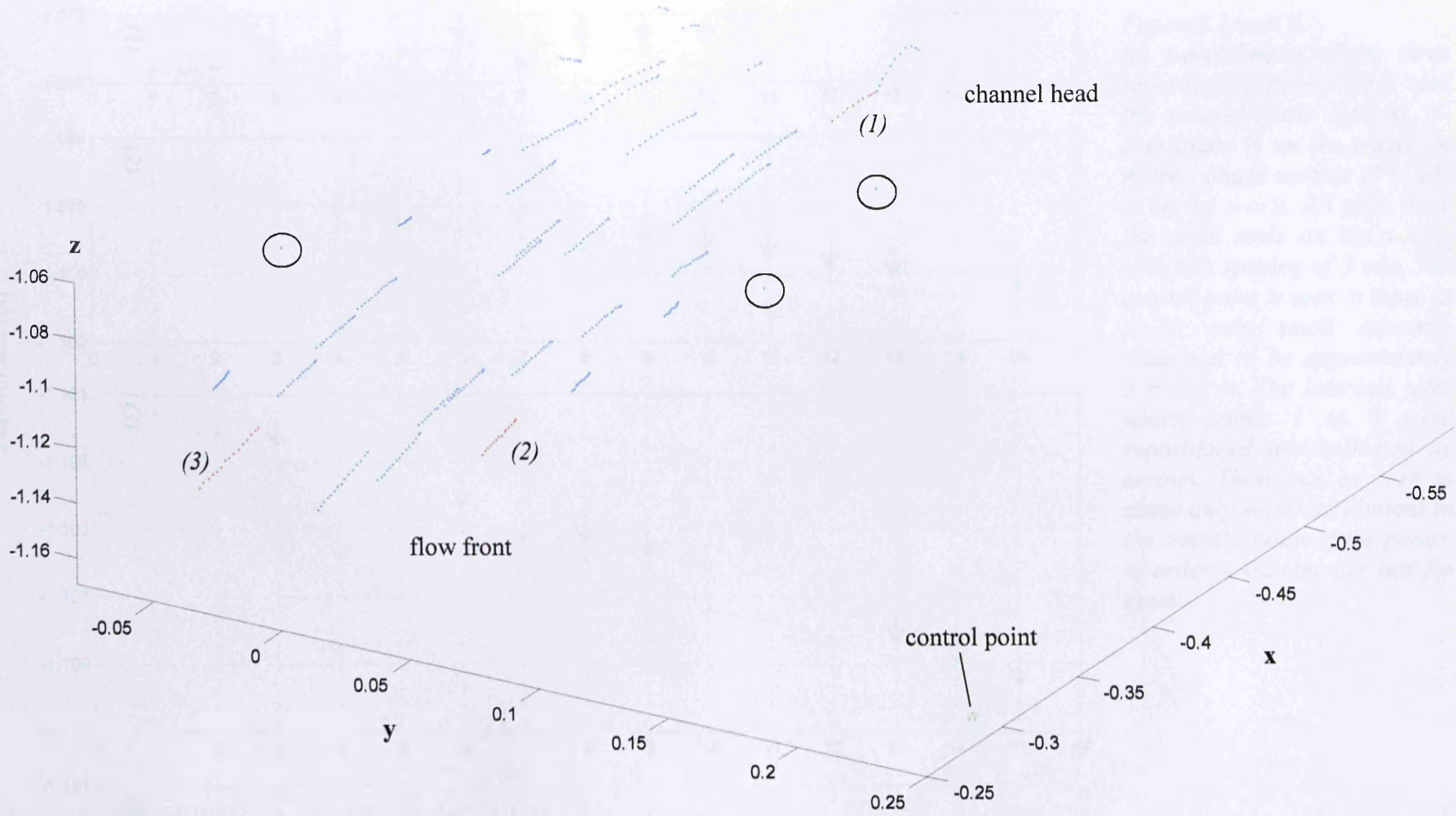

Figure 3.7 cont'd. (b) Perspective view of the point tracks through the image sequence, in 3-D. Axes are in metres. The flow is from top right to bottom left, and the perspective is similar to that in figure 3.1. Points in red are those that were repositioned during the tracking, and these are numbered for comparison with (c). Circled points are those that were on the levées, and so did not move during the tracking.

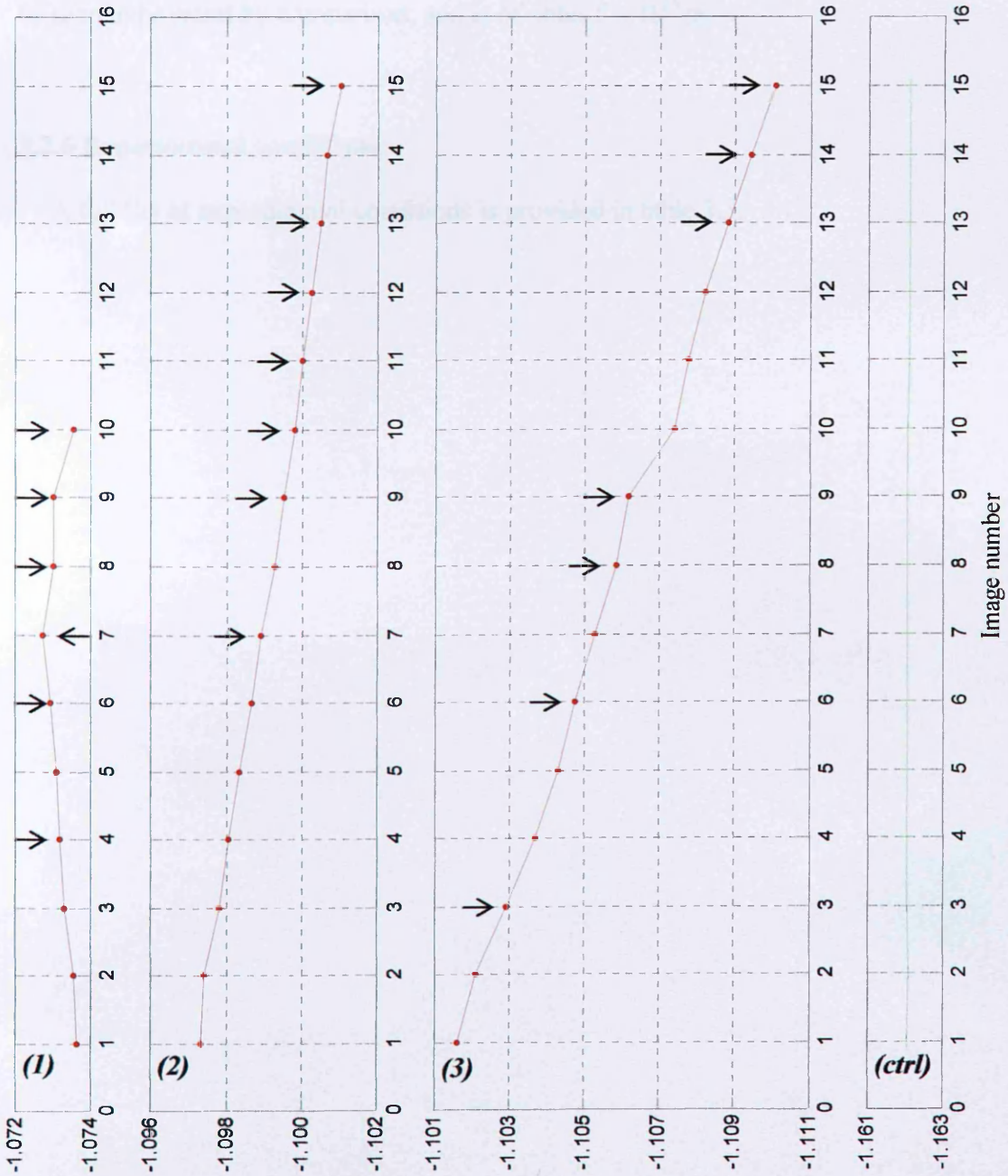

Figure 3.7 cont'd.
(c) z-coordinates of the three repositioned points (red) and the control point (green). z-coordinate is on the y-axis, in metres. Image number (1 to 15) is on the x-axis. All plots have the same scale on the y-axis, with tick spacing of 2 mm. The control point is seen to move in z by only small amounts, measured to be approximately 5 x 10^{-5} m. The intervals after which points 1 to 3 were repositioned are indicated by arrows. These can be seen to cause only minor oscillations in the overall trends of the points, of order < 0.5 mm. See text for details.

number is plotted on the x-axis and the z value in metres on the y-axis. All four sub plots have the same scale on the y axis, with tick spacing of 2 mm. Arrows indicate the points which were repositioned in one or both of the image tracking sequences. It can be seen that while repositioning can result in some inaccuracy, this is generally very small compared with the overall trend, and is of order 5×10^{-4} m. The variation in the z-coordinate for the control point, which can only reflect errors in the processing, can be seen to be small by comparison, and is of order 5×10^{-5} m.

3.2.6 Experimental conditions

A full list of experimental conditions is provided in table 3.3.

Table 3.3. Experimental conditions.

Exp. no.	Location	Date	Silicone flow dimensions (mm)			$\chi = T/(T+F)$	Slope (°)	Images	Camera(s)	No. images	Image interval (s)	Time (s)
			Depth	Length	Width							
2	CF	15/02/06	130	-	127	-	4	M	E-20	350	90	29390
3	CF	16/02/06	200	240	127	-	4	M	E-20	259	90	22374
4	CF	21/02/06	180	350	127	0.286	4	M	E-20	361	90	30530
5	CF	22/02/06	180	350	127	0.375	4	M	E-20	279	90	27758
6	CF	27/02/06	150	350	127	0.444	4	M	E-20	394	90	33134
7	CF	02/03/06	150	350	127	0.286	8	M	E-20	398	90	33464
8	CF	04/03/06	150	350	127	0.444	8	M	E-20	396	90	33288
9	CF	05/03/06	150	350	127	0.167	4	M	E-20	501	90	41756
10	CF	06/03/06	150	350	127	0.167	12	M	Rebel	540	60	32830
11	CF	07/03/06	150	350	127	0.167	8	M	E-20	401	90	33726
12	CF	07/03/06	150	350	127	0.286	12	M	Rebel	507	60	30628
13	CF	08/03/06	150	350	127	0.500	8	M	Rebel	507	60	30628
14	CF	10/03/06	150	350	127	0.375	8	M	Rebel	601	60	36316
15	CF	11/03/06	150	350	127	0.167	8	M	Rebel	431	60	26020
16	CF	12/03/06	150	350	127	0.286	8	M	Rebel	608	60	36726
17	CF	13/03/06	150	350	127	0.286	4	M	Rebel	651	60	39326
18	CF	14/03/06	150	350	127	0.375	4	M	Rebel	608	60	36710
19	CF	15/03/06	150	350	127	0.167	4	M	E-20	393	90	33564
20	CF	16/03/06	150	350	127	0.500	4	M	E-20	395	90	32798
21	CF	17/03/06	150	350	127	0.286	4	M	E-20	350	90	33204
22	CF	18/03/06	150	350	127	0.444	4	M	E-20	259	90	32344
23	CF	19/03/06	150	350	127	0.375	12	M	E-20	400	90	26800
24	CF	30/03/06	150	350	127	0.063	4	M	E-20	390	90	33090
25	LU	24/10/06	150	350	127	0	4	M	Rebel	321	60	38660
26	LU	18/05/07	150	350	127	0.444	4	S	Rebel/300D	394	120	18436
27	LU	05/06/07	150	350	127	0.444	4	S	Rebel/300D	640	120	40006

28	LU	06/06/07	150	350	127	0.286	4	S	Rebel/300D	154	120	39404
29	LU	07/06/07	150	350	127	0.167	4	S	Rebel/300D	333	120	36632
30	CF	12/10/07	150	350	127	0	4	S	Rebel/300D	328	120	47598
31	CF	13/10/07	150	350	127	0.167	4	S	Rebel/300D	305	120	40730
32	CF	14/10/07	150	350	127	0.286	4	S	Rebel/300D	396	120	32776
33	CF	14/10/07	150	350	127	0.375	4	S	Rebel/300D	339	120	45188
34	CF	15/10/07	150	350	127	0.167	4	S	Rebel/300D	273	120	31572
35	CF	15/10/07	150	350	127	0.444	4	S	Rebel/300D	376	120	49406
36	CF	16/10/07	150	350	127	0.375	4	S	Rebel/300D	263	120	38320
37	CF	16/10/07	150	350	127	0.444	4	S	Rebel/300D	411	120	42054
38	CF	17/10/07	150	350	127	0.167	4	S	Rebel/300D	319	120	28318
39	CF	17/10/07	150	350	127	0.286	4	S	Rebel/300D	350	120	49888

CF = Clermont Ferrand; LU = Lancaster University. M = Monoscopic and S = stereo images. E-20 = Olympus E-20 camera; Rebel = Canon EOS Rebel; 300D = Canon EOS 300D. Camera specifications can be found in Appendix A.

3.3 Results

As discussed previously, the simulations ran for between five and fourteen hours, and several hundred images were taken during each experiment (table 3.3). To illustrate the general pattern of development of a flow, figure 3.8 shows seven images of experiment 19, taken at intervals of approximately 100 minutes. Flow direction is left to right, and the reservoir of silicone is to the left hand side of the images.

As soon as a flow is set up, the flow front collapses under the influence of gravity, resulting in an initially high flow front velocity that gradually decays with time. The flow front velocity decreases further as the flow advances beyond the ends of the levées, and begins to spread laterally across the slope as well as downslope (figure 3.8 c to g). The reservoir silicone also begins to flow through the sliding gate into the head of the channel, as can be seen in figure 3.8 (b). It is evident that in this particular experiment, the influx of silicone is travelling more rapidly than the flow front from the very start of the simulation, which is resulting in crustal deformation at this early stage. Following the image sequence, it can be seen that the area of crust, i.e. the area of the initial flow visible at the surface, gradually decreases, and that it has almost all disappeared by (g). As discussed in chapter one, in `a`ā basalt and higher-silica flows the basal shear stress produces a vertical velocity profile with a maximum velocity at the flow surface and a minimum, often zero, velocity at the flow base. Because of this, the higher velocity upper part of the flow cascades down at the flow front, carrying crust with it and depositing it in front of the flow, a process known as 'caterpillar' flow. The flow then overruns this fragmented crustal deposit, producing a basal layer of sand and plaster, analogous to a basal breccia, and this process is sketched in figure 3.9. This advance mechanism was observed in all of the analogue flows, resulting in

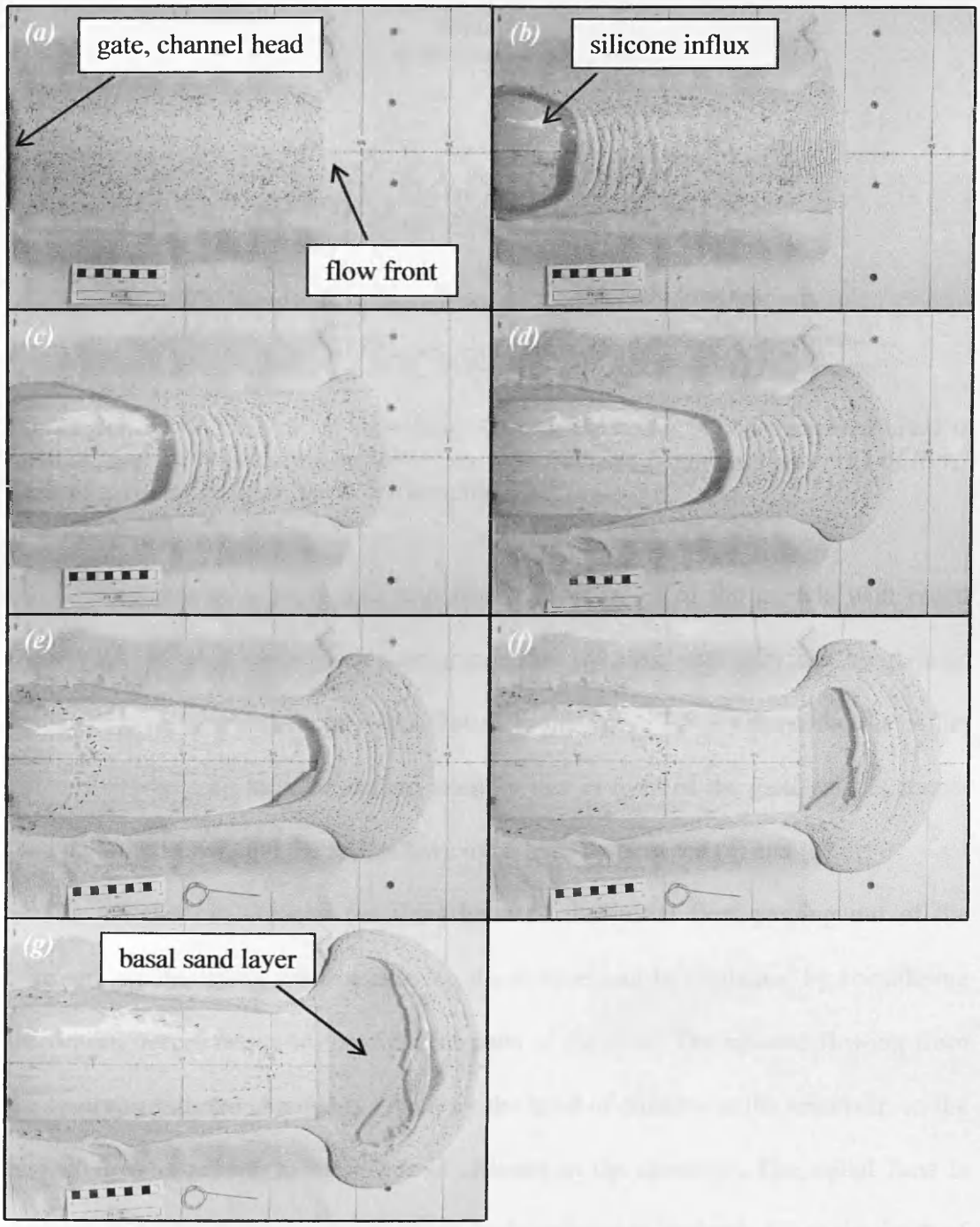

Figure 3.8. Experiment 19, χ = 0.167. Series of images, (a) to (g) illustrating the development of an experimental, and some of the terminology used throughout the flow descriptions. Scale bar is 10 cm. Images are at intervals of approximately 100 minutes. The reservoir is to the left of each image, and silicone can be seen to flow into the channel through the sliding gate. In this case, the crust is progressively deformed ahead of the silicone influx. The front of the flow is spreading out beyond the levées. By the end of the experiment (g), the silicone influx has almost reached the flow front, and the basal sand and plaster layer, the rolled over crust, can be seen through the flow. See text for details.

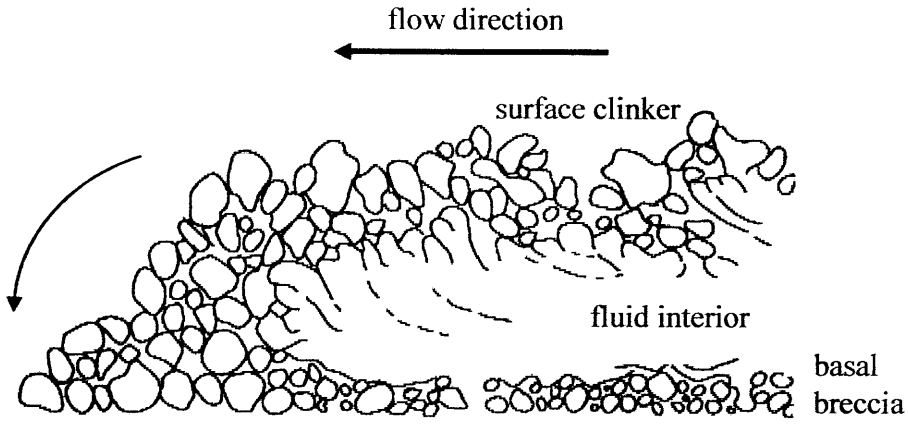

Figure 3.9. Flow front of an 'a'ā lava showing the rollover of fragmented crust to form a basal breccia layer beneath the massive interior. From the University of North Dakota's teaching pages, www.volcano.und.edu.

the development of a basal sand and plaster layer in all of the models with crusts (figure 3.8 g). This gives extra reassurance that dynamic similarity can be claimed between the models and active lava flows. From figure 3.8 (c) onwards, the influx silicone can be seen to be spreading laterally just in front of the gate, as it is deeper than the initial flow, and the levées have to be built up between (c) and (d).

The variation in velocity (or flux) between the initial flow passing out of the channel, and the influx silicone entering the channel can be explained by considering the driving forces acting in the different parts of the flow. The silicone flowing from the reservoir into the channel is driven by the head of silicone in the reservoir, so the rate of flow is related to the depth of silicone in the reservoir. The initial flow is draining from the channel at a rate which is also related to its depth. Since the depth of silicone in the reservoir is five to ten times that of the initial flow in the channel, silicone is supplied to the channel at a greater rate than the channel is drained. Once the silicone has flowed into the channel, its drainage is controlled by its own depth rather than that in the reservoir, so a thick influx builds up in the upper part of the

channel. This can be seen in Figure 3.8 (c), as the influx threatens to overtop the levées.

The surface velocity of a flow can be related to the basal shear stress and the viscosity through the Jeffreys equation (Jeffreys 1925):

$$u_{max} = \rho g h^2 \sin\alpha / n\eta \qquad (3.1)$$

where u_{max} is the centreline velocity of the flow surface, ρ is the density, g the gravitational acceleration, h the flow depth, α the slope, η the fluid viscosity and n is a constant whose value varies from 2 to 4 depending on the geometry of the channel. It can be seen that, all other things being equal, a greater flow depth will result in a greater velocity. In summary, the head of silicone in the reservoir causes silicone to be supplied to the channel at a volumetrically greater rate than the initial flow can drain, and the higher basal shear stress of the resulting deeper influx means that the influx advances at a greater velocity than the initial flow. These effects, combined with the slower advance of the initial flow once it begins to spread beyond the levées, and the retarding influence of the crust on the seed flow, result in the influx gaining on the flow front during the experiments, as illustrated in figure 3.8.

3.3.1 Morphological observations

The resultant surface morphology observed in the model flows was seen to strongly depend on the thickness of the original crust, but only weakly on the topographic slope. A continuous spectrum of morphologies developed between thin and thick crust end members, and the models have been divided up into broad thickness categories based on the structures which were observed forming. In this classification, 'thin' crust models are defined as those having $0 < \chi \leq 0.17$, intermediate as having $0.17 < \chi \leq 0.3$, and thick as having $\chi \geq 0.3$. Below are presented the observations of the

development and resultant morphologies of typical flows in each of these categories, as well as for flows with no crusts, together with illustrative images. Table 3.4, found at the end of the chapter, summarises the structures observed in all of the experiments. The development of individual structures is analysed in detail in chapter four, where the effects of slope are also considered.

It was previously noted that experiments twenty six to twenty nine were carried out at Lancaster University during the summer of 2007. The conditions in the Lancaster laboratory were found to be unsuitable for the reproduction of morphologies seen in the earlier simulations, which were carried out in Clermont Ferrand. This was attributed to the very high humidity that was experienced during that wet summer, which caused the plaster to stick together, increasing the cohesion of the crust. This problem may also have been compounded by the use of different sand, as variability in the roundness of the grains may also have contributed to differences in cohesion. Due to these differences, the later simulations (thirty to thirty nine) were again carried out in Clermont, and were found to reproduce the results seen in the previous experiments. While the observations of the Lancaster simulations are included in table 3.4 for completeness, the results of the photogrammetric analysis are not considered, and all conclusions from this part of the work are based on the results from simulations carried out in Clermont.

3.3.1.1 No crust, $\chi = 0$

For experiments with no crust, the surface of the silicone remained smooth throughout the runs. Initial extension at the flow front could be observed by the relative motion of the markers, but this was not accompanied by the development of any discontinuities in the flow surface. At the head of the channel, where the influx

enters from the reservoir, shortening of the surface was observed, again from the relative motion of the markers, and the flow was seen to thicken. Over time, the thickening produced a gradual increase in surface height from the flow front to the gate, and initially the join between the seed flow and the reservoir silicone, the 'influx horizon', could be observed, though this became indistinct with time. The influx horizon demonstrated a parabolic profile (figure 3.10 a), as would be expected due to the effects of shear at the channel-levée boundary. Although no basal sand layer could form due to the absence of crust, the rolling motion of the flow front could be seen as the surface markers travelled down the flow front to be deposited in front of the flow. The silicone then advanced over the markers, which could be seen clearly through the flow behind the influx horizon (figure 3.10 b), and which were observed to remain stationary at the flow-base plate boundary, supporting the zero-velocity assumption for this boundary.

3.3.1.2 Thin crusts, $0 < \chi \leq 0.17$ ($\chi = 0.063$ & 0.167)

For all crusts except the thinnest ($\chi = 0.063$), the initial gravitational collapse of the flow front was accommodated in the brittle crust by the development of fine, closely spaced, straight tensile fractures, parallel to the flow front (figure 3.11). These formed initially just behind the flow front, and propagated back up the flow with time. The fractures further back up the flow did not extend the full width of the channel, but began to open in the channel centre, propagating out only a short distance towards the margins. This behaviour produced a zone of obvious fractures which was parabolic in outline, as picked out by the dashed blue line in figure 3.11. Fracture spacing increased slightly upflow, and the fractures widened with time. No such fractures were seen for $\chi = 0.063$. As χ increased, the spacing and width of the fractures increased,

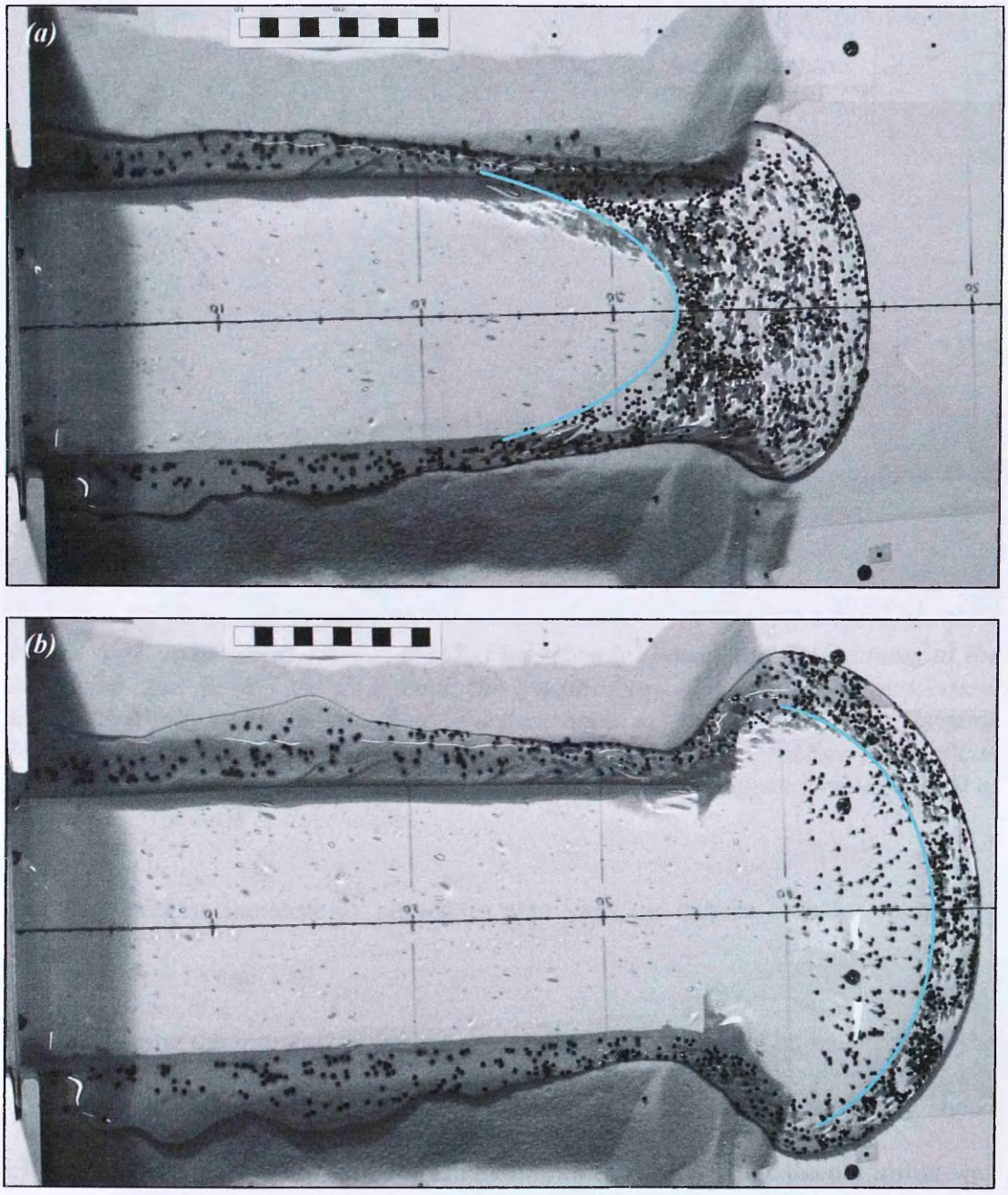

Figure 3.10. Experiment 35, $\chi = 0$. (a) The velocity profile across the channel is illustrated by the parabolic influx horizon, highlighted in blue. (b) The influx horizon is again picked out in blue. Markers that were originally on the flow surface can be seen to have been rolled over at the flow front, and along the levées as the flow thickened, and are now visible through the flow, to the left of the blue line.

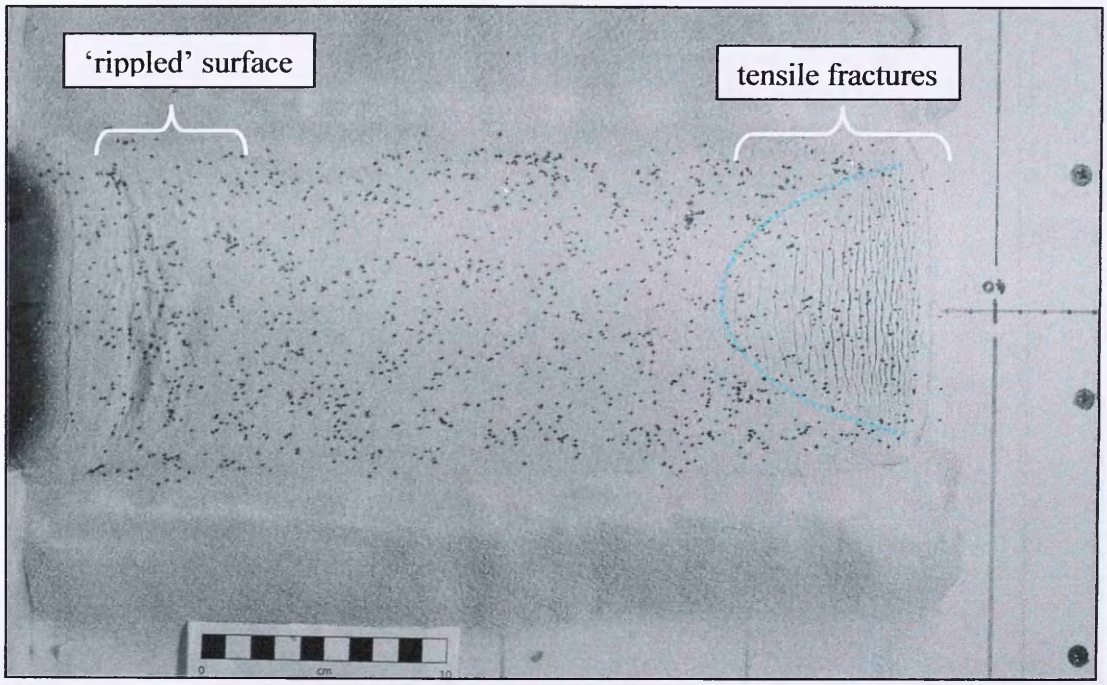

Figure 3.11. Experiment 19, χ = 0.167. Fine, closely spaced, tensile fractures at the flow front. Just behind the flow front, the fractures are almost straight, and extend nearly the full width of the flow. Further back up the channel, they become increasingly curved and only develop in the centre of the flow. Fracture spacing can be seen to increase upflow. Irregular surface 'ripples' can be seen forming ahead of the influx at the back of the channel.

and they became increasingly curved in plan view, as can be seen by comparing figures 3.11, 3.16 and 3.19.

Shortly after the initial flow was set up, the fresh silicone could be seen to enter the channel from the reservoir, compressing and deforming the crust immediately ahead of it. This deformation involved the shortening of the crust, as the deeper influx was advancing more rapidly than the initial flow, and at first produced a mottled surface texture with the crust appearing rippled on a small scale (figure 3.11). Over time, these irregular 'ripples' developed into laterally continuous, regularly spaced transverse ridge structures, which were deformed by the velocity profile of the flow to become curved in outline (figure 3.12 a). In cross section the ridge crests showed smooth, open profiles, separated by sharp, cuspate troughs. The ridges were

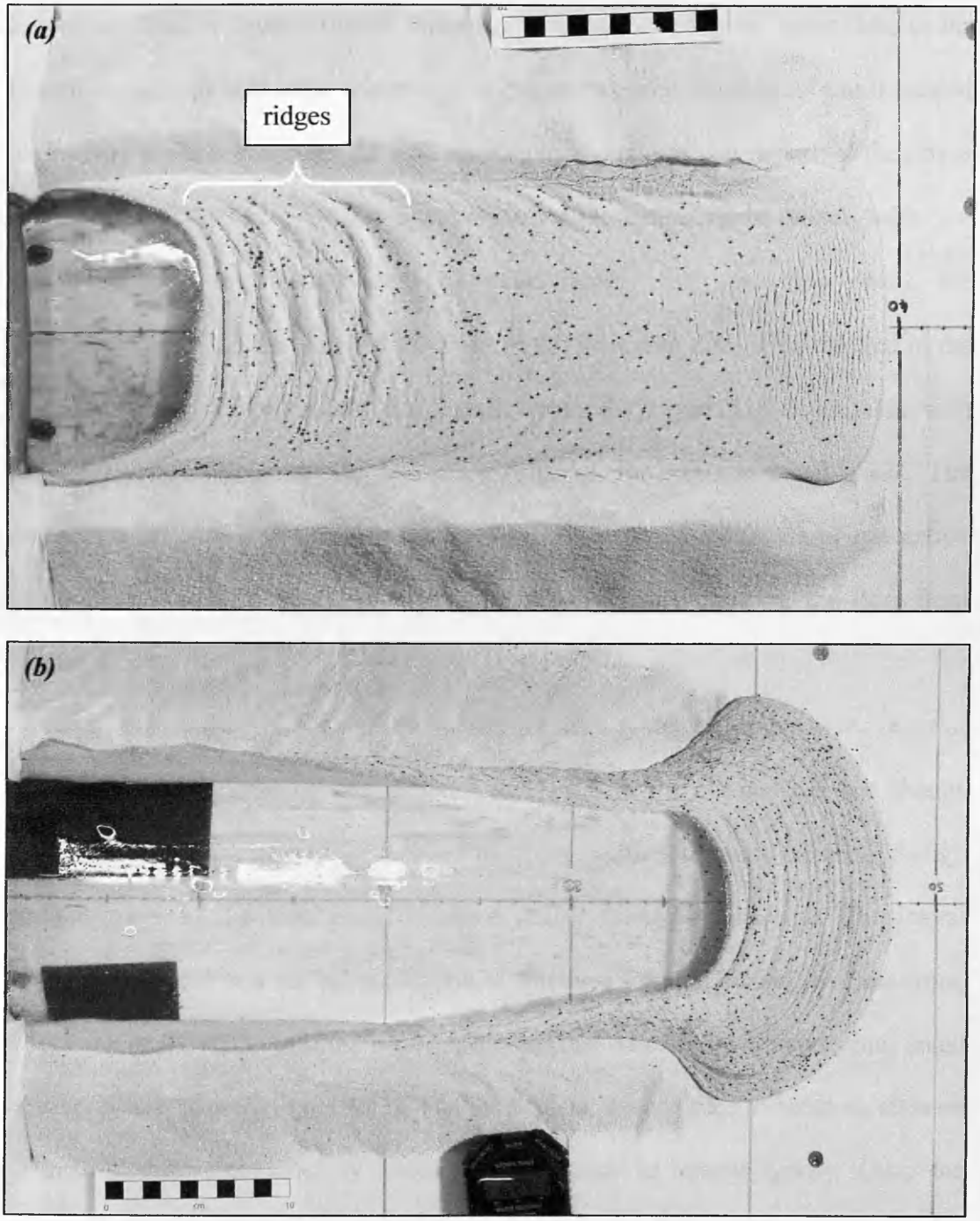

Figure 3.12. (a) Experiment 9, χ = 0.167. Irregular ripples have developed into regular wavelength ridges that are being deformed by the velocity profile of the influx. The ridges can often be seen to extend further down the channel at the margins than at the centre, and are more pronounced on the left hand side of the channel in this example, though this may be a lighting artefact. (b) Experiment 24, χ = 0.063. Ridges have reached the flow front, as a result of propagation and translation. Note that the thinner crust results in ridges of much shorter wavelength than in seen in (a).

commonly seen to extend further down the flow in the marginal zones than in the channel centre, though often where central ridges appeared these could not be traced all the way to the margins (figure 3.12 a). As χ increased, the wavelength of the ridges increased, and they became less regular. No ridges were seen in models with $\chi >$ 0.286. Because the influx advanced more rapidly than the flow front, the compressional stresses were felt further down the flow with time. This resulted in the fold structures propagating down the channel during the course of an experiment, with new folds developing at the downflow end of the compressional zone. The compressional zone was also translated downflow, and a combination of translation and propagation resulted in the fold structures eventually reaching the flow front (figure 3.12 b).

As the flow exited the channel, the flow front velocity decreased due to the onset of lateral spreading. However, the material remaining in the channel did not change velocity, and the rearmost of the tensile flow front fractures began to close up, though surface traces of the front ones remained visible throughout the run. The lateral spreading resulted in a second generation of fractures forming behind the flow front, which broke the strips of crust between the original extensional fractures into small equant crustal 'plates' (figure 3.13). The term 'plate' is used here to mean an element of crust which is bounded by fractures and appears to behave rigidly. Once the rearmost extensional fractures passed beyond the end of the channel, the lateral spreading was accommodated by conjugate pairs of fine fractures which propagated upflow from behind the rearmost extensional fracture as the flow advanced, but never extended into the channel, producing a cross-hatched pattern as they broke the crust into small plates (figure 3.14). In thin crusts, they were often difficult to discern as they were so faint, but when seen, the two sets were seen to intersect at approximately

60° (lower image, figure 3.14). The spacing of these conjugate fractures increased as the crustal thickness increased, as can be seen by comparing figures 3.14, 3.17 and 3.25.

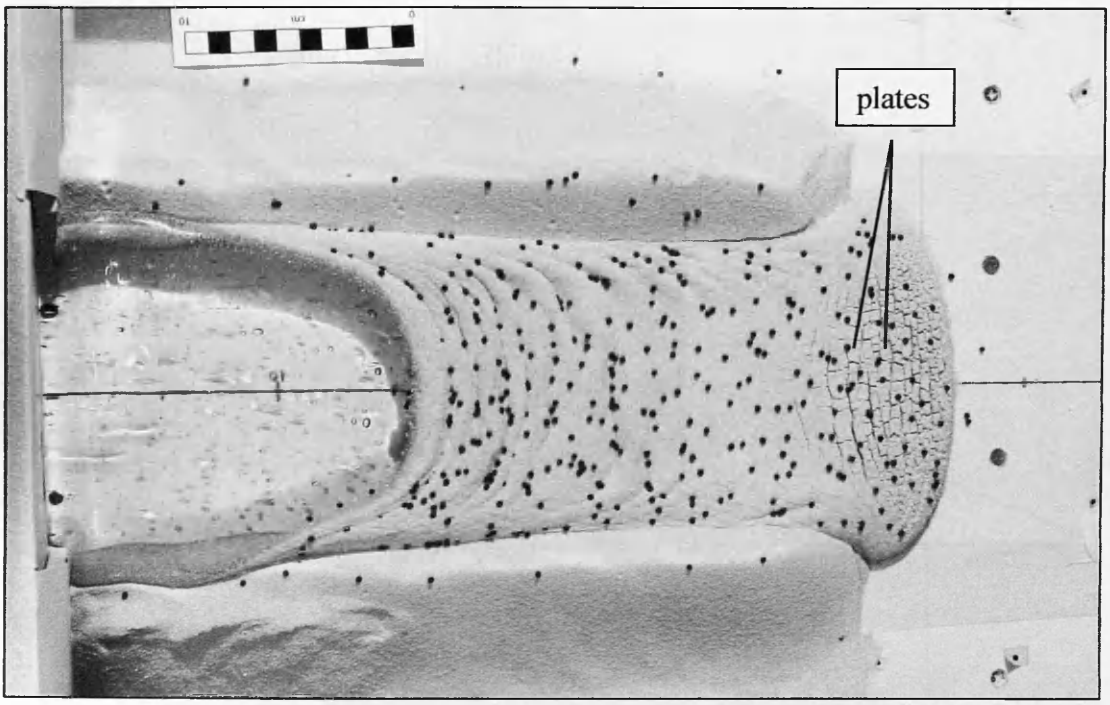

Figure 3.13. Experiment 34, $\chi = 0.167$. Equant plates of crust developing behind the flow front in response to the lateral spreading beyond the levées. As in figure 3.12 (a), ridges can be seen to extend further down the margins of the channel than in the centre.

At the end of a thin crust experiment, the flow front was observed to be smooth in outline and symmetrical about the centre line of the flow, with compressional ridges extending across the remainder of the crusted surface, parallel to the flow front (figure 3.15 a). No obvious variations in crustal thickness could be seen, and no clean silicone (flow core) was exposed through the original crusted region. In plan view, the folds could often be traced from one side of the channel, downflow around the influx horizon, and back up the other side of the channel, forming marginal ropy structures that were typically oriented at around 20 to 30° downflow in towards the channel

centre (lower image, figure 3.15 a). Cutting a vertical section through the flow front at the end of a run revealed a simple vertical structure, with little or no mixing between the crustal covering and the silicone, and a discrete basal layer of sand underlying the silicone interior. The ridge structures could be seen to extend a few millimetres into the top of the silicone layer (figure 3.15 b).

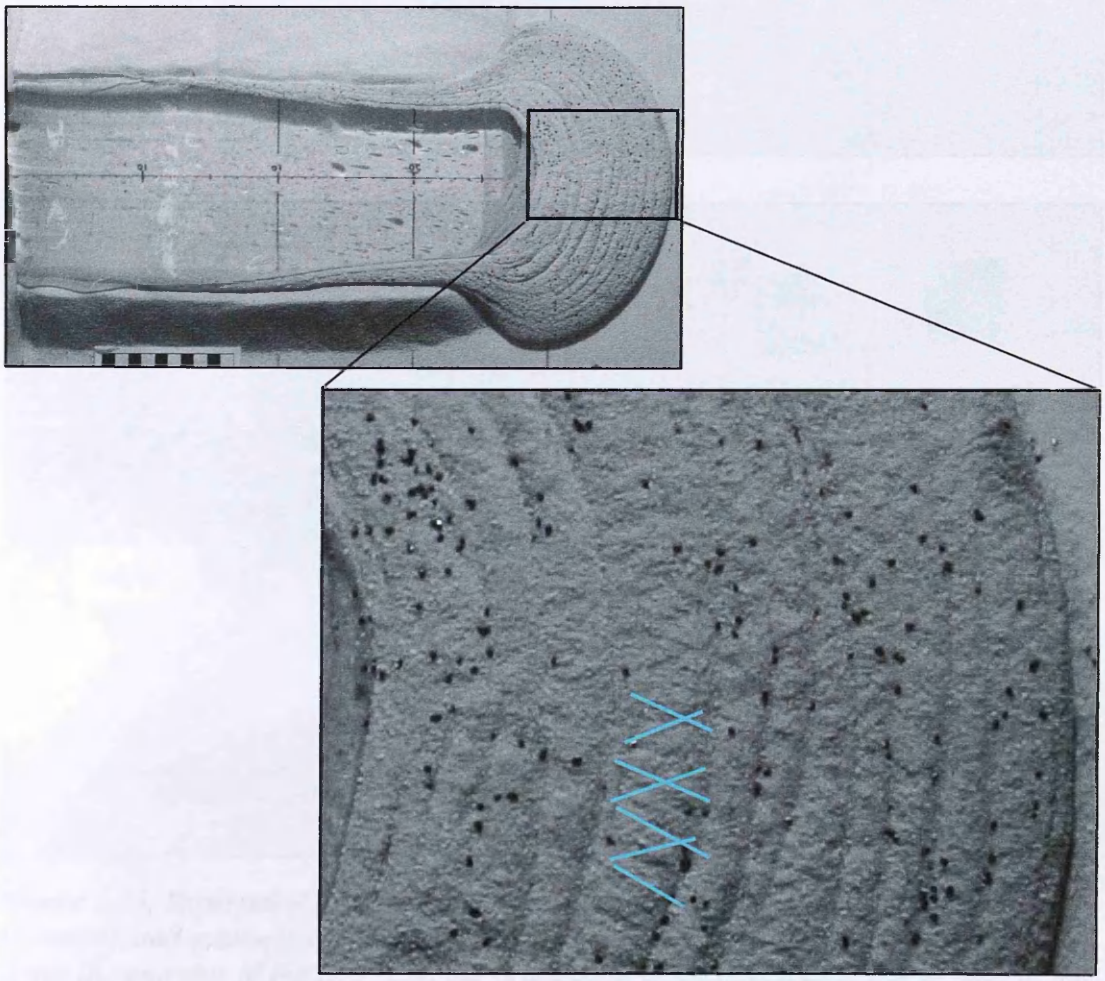

Figure 3.14. Experiment 15, χ = 0.167. As the flow spreads out past the levées, conjugate sets of fractures develop across the entire crusted surface of the flow. These create a cross-hatched texture, and the orientations of the fractures are picked out in the lower image.

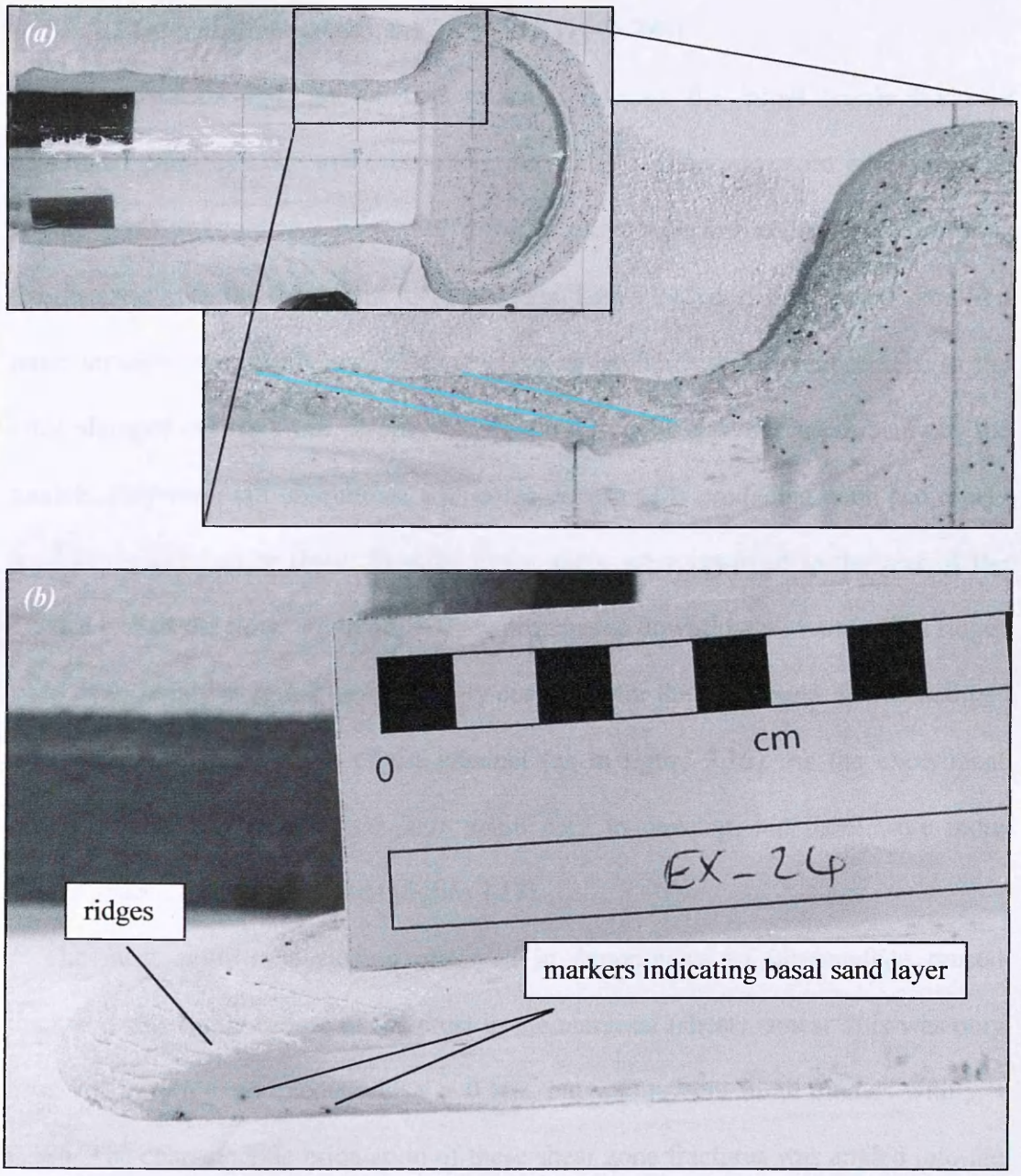

Figure 3.15. Experiment 24, $\chi = 0.063$. (a) At the end of a thin crust run, the flow front is smooth and symmetrical about the centreline of the flow. Ropy structures develop down the margins of the flow, and the orientation of these is picked out in blue in the close up image. (b) Cross section through the flow front after removal of the crust. The ridge structures can be seen to extend a few mm into the silicone fluid. Marker points can be seen underneath the flow where the crust has been rolled over to form a basal sand layer. Note that no crustal material has been incorporated into the fluid interior.

3.3.1.3 Intermediate crusts, $0.17 < \chi \leq 0.3$ ($\chi = 0.286$)

In experiments with intermediate crustal thickness, the initial tensile fractures developed more quickly, and were more curved in outline and more widely spaced (figure 3.16). It could also be seen that the fractures were increasing in curvature as the distance from the flow front increased. The larger thickness of crust resulted in a more unstable flow front, and discrete zones of avalanching were observed, as the crust slumped off the front. While fold structures could be observed in some of the models, they were not ubiquitous, with some experiments producing none and others producing only two or three. In some cases, these were confined to the rear of the crusted part of the flow, but in others they propagated downflow with time. The ridges were often highly irregular, not smoothly curved as for the thin crusts, and sometimes did not span the full width of the channel (as in figure 3.16). As the experiment progressed, conjugate fractures were again seen to develop, but these were more widely spaced than in thin crusts (figure 3.17).

The most significant process observed in experiments of intermediate crustal thickness was brittle failure of the crust in the marginal (shear) zones. This was only observed in two experiments with $\chi = 0.167$, but was present in all models with $\chi = 0.286$. The characteristic orientation of these shear zone fractures was angled into the levées downflow at around 15 to 20° (figure 3.18), though they could often be seen to curve slightly into the channel, becoming more sub-parallel to the margin. The length of the fractures did not change over the course of an experiment, remaining of order two to three centimetres long. Relative motion along the fractures could be seen by observing the markers on each side of a fracture, and the crust closest to the channel centre moved more quickly, which agrees with the velocity profile expected across a channel with lateral shear.

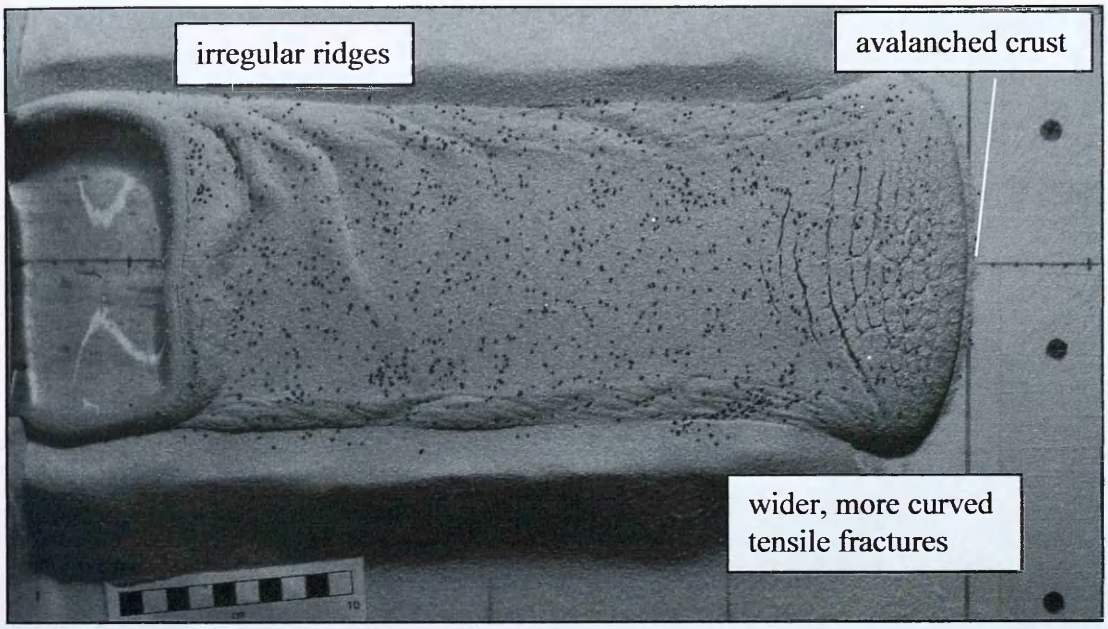

Figure 3.16. Experiment 16, χ = 0.286. Tensile fractures become wider and more widely spaced as crustal thickness increases. At the rear of the crust compressional ridges are longer wavelength and more irregular, but marginal ridges can be seen down either side of the channel. Crustal material is avalanching off the flow front.

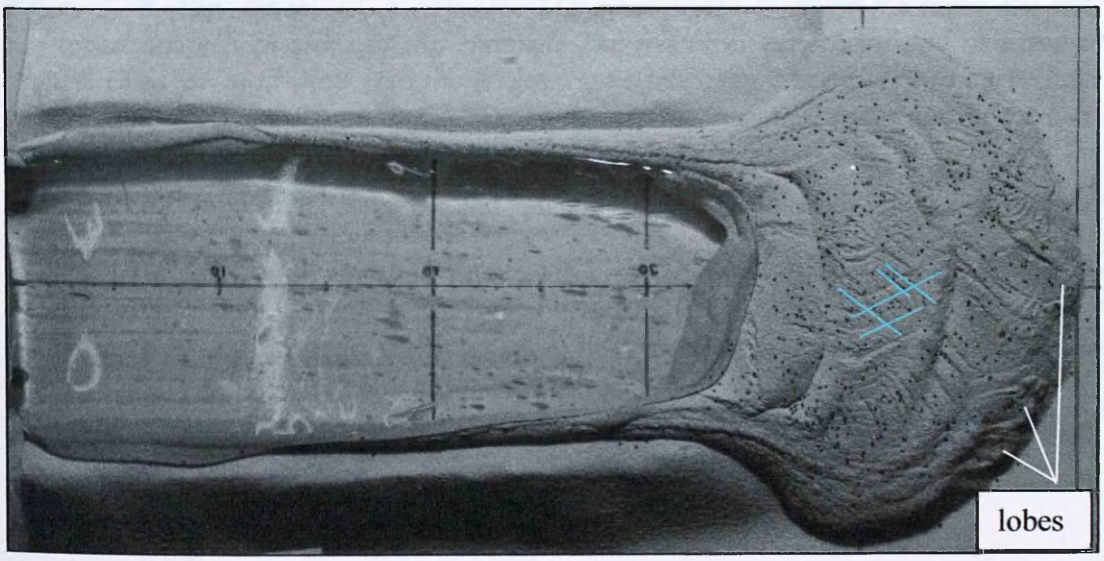

Figure 3.17. Experiment 16, χ = 0.286. The spacing of conjugate fractures is greater for intermediate than for thin crustal thicknesses, meaning the interstitial crustal plates are larger. Fractures intersect at angles of ~60°. Irregular wavelength ridges can be seen, which have reached the flow front. The positions of the crustal plates are influencing the advance of the flow front, causing the development of small lobe structures.

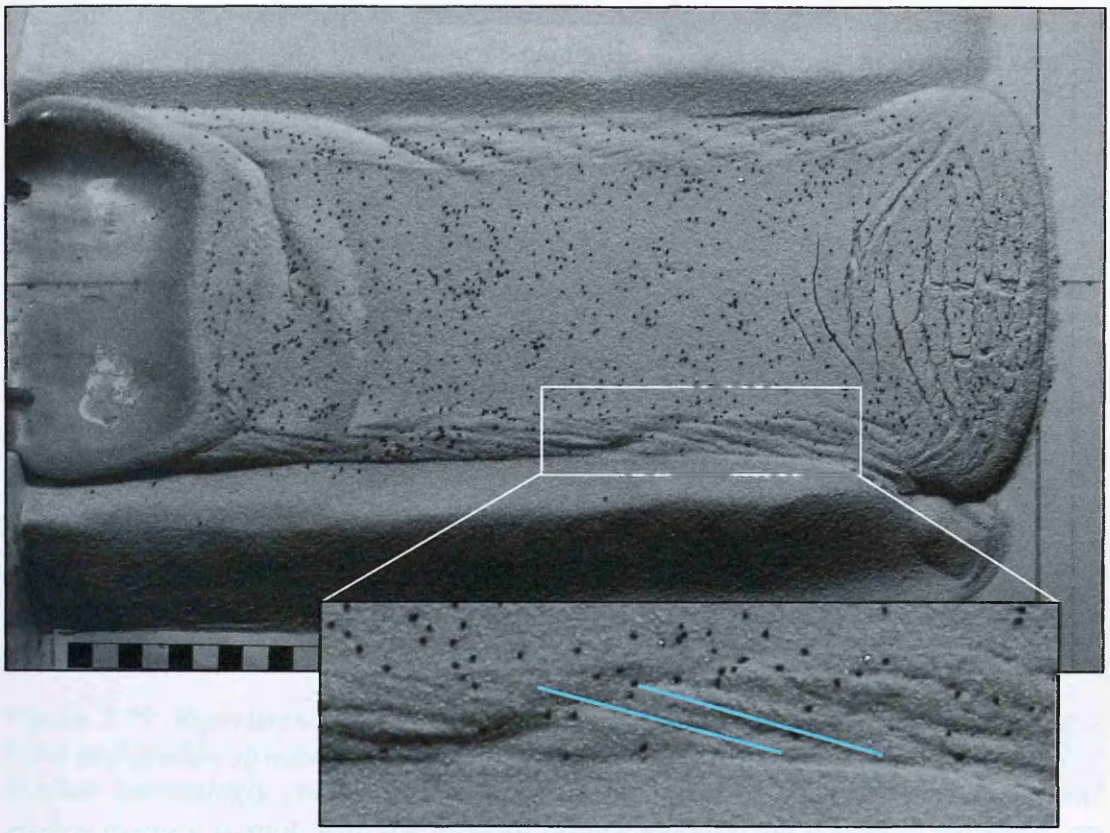

Figure 3.18. Experiment 17, χ = 0.286. Marginal zones of shear fractures are well developed down both sides of the channel. The fractures are short, and oriented at around 15 to 20° downflow into the levées. Some fractures can be seen to curve back up the channel. Again, irregular folds and ridges in the marginal zones can be seen.

A second important change seen in the intermediate crust models was the development of an irregular flow front as the run progressed. The irregularities took the form of lobate structures, the locations and sizes of which correlated with the distribution of the surface crustal plates, and therefore the distribution and spacing of the conjugate fractures (figure 3.17).

3.3.1.4 Thick crusts, $\chi \geq 0.3$ (χ = 0.375, 0.444 & 0.5)

For thick crust experiments, initial collapse of the unstable flow front resulted in the deposition of a large amount of crustal material in front of the flow (figure 3.19). The extensional fractures which formed were very wide, widely spaced features,

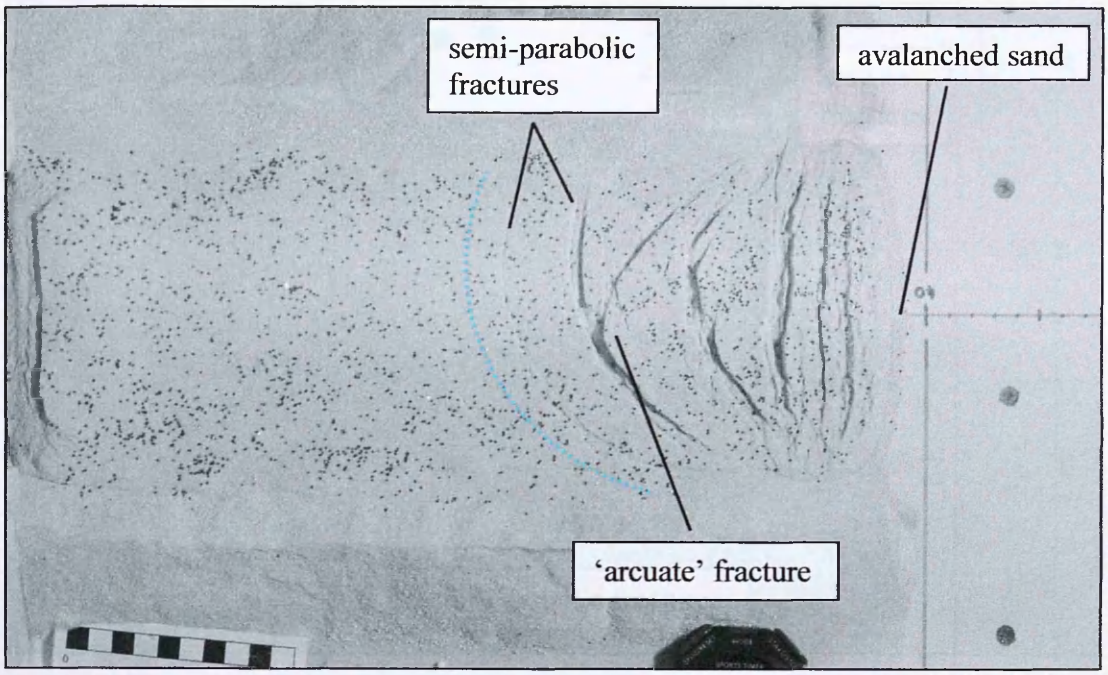

Figure 3.19. Experiment 20, $\chi = 0.5$. Flow front fractures are wider, often showing a horst and graben structure. Fractures are still almost straight near the flow front, but become increasingly curved further back up the channel. The rearmost horst and graben fracture is split, with the forward branch marking out a smooth parabola: an arcuate fracture. The rear branch of this fracture and the faint fracture behind both show a parabolic trace at the right hand side, but meet the left hand margin at approximately 90°, producing a trace that dubbed 'semi-parabolic'. This shape is picked out by the blue dashed line behind the faint rear fracture.

which showed horst and graben type structures for the higher χ values. These fractures were generally straight and parallel to the flow front just behind the front, becoming more widely spaced and more curved upflow. The rear fractures in the thickest crust experiments were parabolic in trace, concave downflow, and will hereafter be referred to as 'arcuate'. A small number of experiments also produced fractures that were 'semi-parabolic' at the rear of the fracture zone. These showed a similar pattern to the parabolic fractures at one side of the channel, but instead of curving back round towards the flow front, carried on to meet the margin at ~90° (figures 3.19 and 3.20). The fractures were usually observed to originate in the centre of the channel, unzipping' out towards the margins, which resulted in them being widest in the channel centre and narrowing towards the margins (figure 3.21).

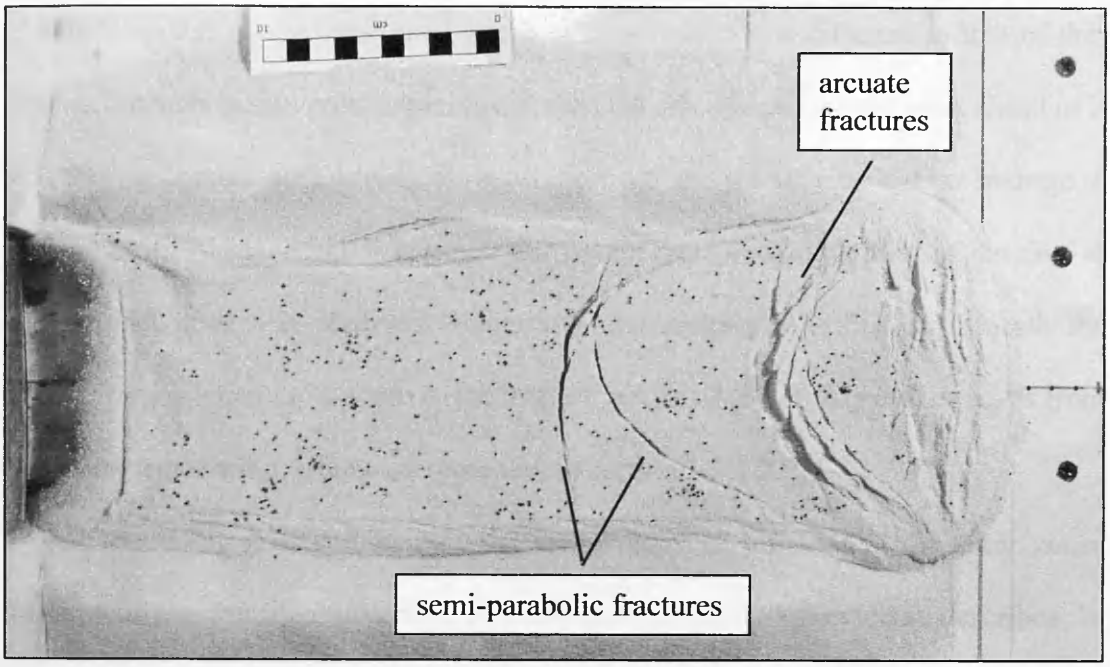

Figure 3.20. Experiment 8, χ = 0.444. Semi-parabolic fractures developing behind the zone of arcuate fractures. The shear zone fracture morphology is also changing, with long, oblique fractures on the right hand side, and a single fracture on the left hand side of the channel.

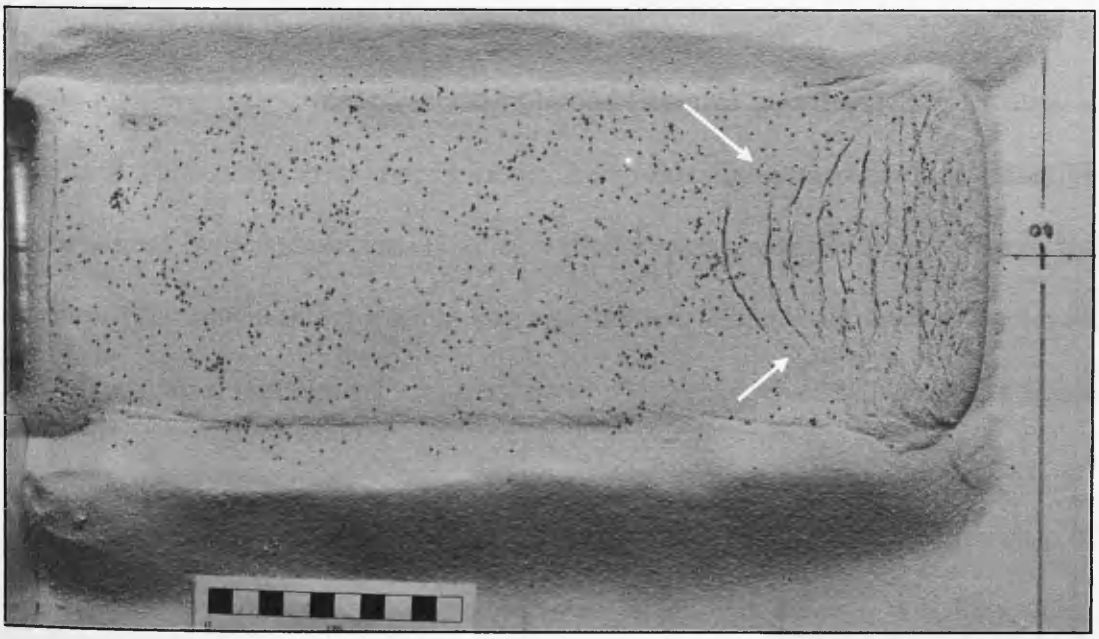

Figure 3.21. Experiment 14, χ = 0.375. The rearmost arcuate fracture has opened first in the centre of the channel, and is widest here. Faint extensions curving forwards can be seen, picked out by arrows, showing how the fracture is 'unzipping' towards the margins.

The response of the thick crust to the silicone influx was different to that of thin crusts. Whereas in thin crust experiments, the new silicone pushed the crust ahead of it and formed compressional folds, during thick crust runs the silicone did not manage to deform the crust in the initial stages of thick crust runs. Instead, doming of the flow at the channel head was observed, suggesting that material was flowing beneath the crust. This is difficult to discern in the images, but shows up clearly in the results from the stereo monitoring, which are presented in section 3.3.2.2.

For increasing crustal thickness, the morphology of fractures in the shear zones began to differ from that observed in intermediate crusts. As previously described, in intermediate crusts, the shear zone fractures developed a fixed length early on in the run, and were not observed to change thereafter. With increasing crustal thickness, the oblique fractures initially became longer and more widely spaced (figure 3.22 a), sometimes showing faint up- and downflow extensions that were more closely parallel to the margins. Over time, these long oblique fractures joined together, creating a sinuous fracture in the shear zone (3.22 b). This eventually resulted in a single fracture being present in each shear zone (3.22 c), with the crust moving as a slab between the fractures. The fractures were commonly oriented very slightly out towards the levée, so that the crustal slab tapered towards the rear of the channel, as can be seen in figure 3.22 (c).

The shear fractures usually had well defined, steep margins, with a narrow strip of lower relief, thinner, crustal material between them. This material was fragmented crust, and could be seen to deform. Oriented fractures like those in the intermediate thickness shear zones were commonly observed in the strip (3.22 c), though these usually became indistinct with time. Although clean silicone was never observed through these fractures, probing the zone with a wire showed that slight upwelling was

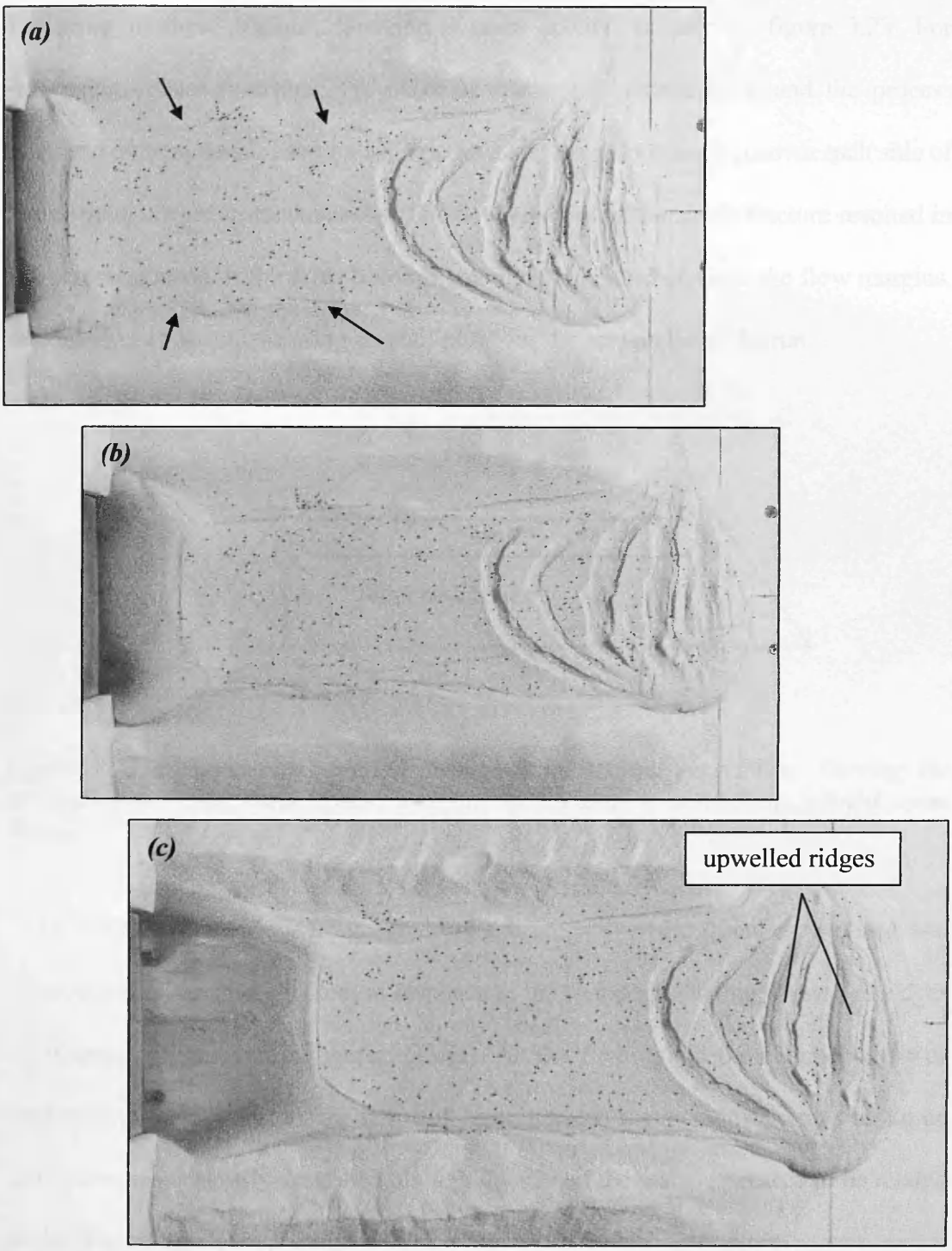

Figure 3.22. Experiment 6, $\chi = 0.444$. (a) Fractures in shear zones can be seen to be longer than for intermediate crust experiments (compare figure 3.18), and much more widely spaced. These are indicated by the arrows. (b) The long oblique fractures are joining together creating a sinuous fracture down each margin. (c) The single fractures are established, with the margins of the tapering slab clearly defined. Faint oblique fracture traces can be seen within the fracture down the right hand margin. Upwelling of silicone through the arcuate fractures can be seen in (c). See text for details.

occurring in these regions, inferring a cross section as seen in figure 3.23. For increasing crustal thickness, the onset of fracturing became later, and the process occurred quite suddenly, so that a single fracture seemed to develop down each side of the channel almost instantaneously. The development of the single fracture resulted in the central portion of the crust becoming completely detached from the flow margins, and moving as an undeforming crustal 'plug' for the remainder of the run.

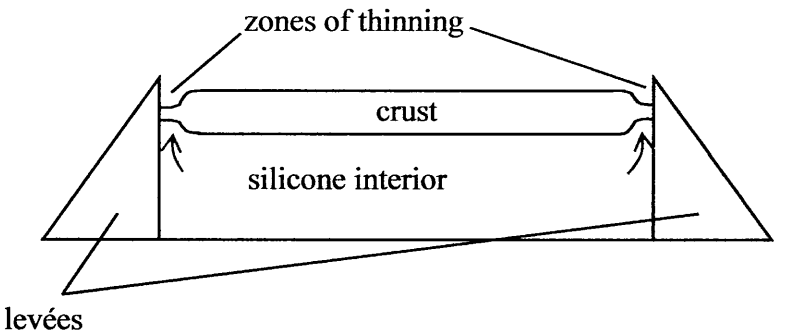

Figure 3.23. Inferred cross section through a thick crust experiment, showing the thinned crust in the shear zones, and silicone welling up into these thinned zones (arrows).

Over time, as the flow front extended, the arcuate tensile fractures widened and silicone welled up through them in response to the change in loading. Upwelled ridges of silicone can be seen in figure 3.22 (c). As the flow exited the channel and was subjected to lateral tension, the strips of crust between the arcuate fractures broke up into plates as previously described, though the size of the plates appeared to be related to the original fracture spacing, so thicker crusts produced larger plates.

As the flow front spread beyond the levées and slowed down, compression was seen to occur due to the channelised region of the flow continuing to move more quickly. In the thinner crust experiments, this simply caused the original extensional fractures to close up. For thick crusts, however, the ridges of silicone which had

upwelled through the fractures were compressed, and rolled over forwards, as the fractures began to narrow. This resulted in complex flow surfaces, as seen in figure 3.24. Upwelling was not observed so frequently through the secondary fractures which resulted from lateral tension, as these tended to be narrower than the original arcuate fractures.

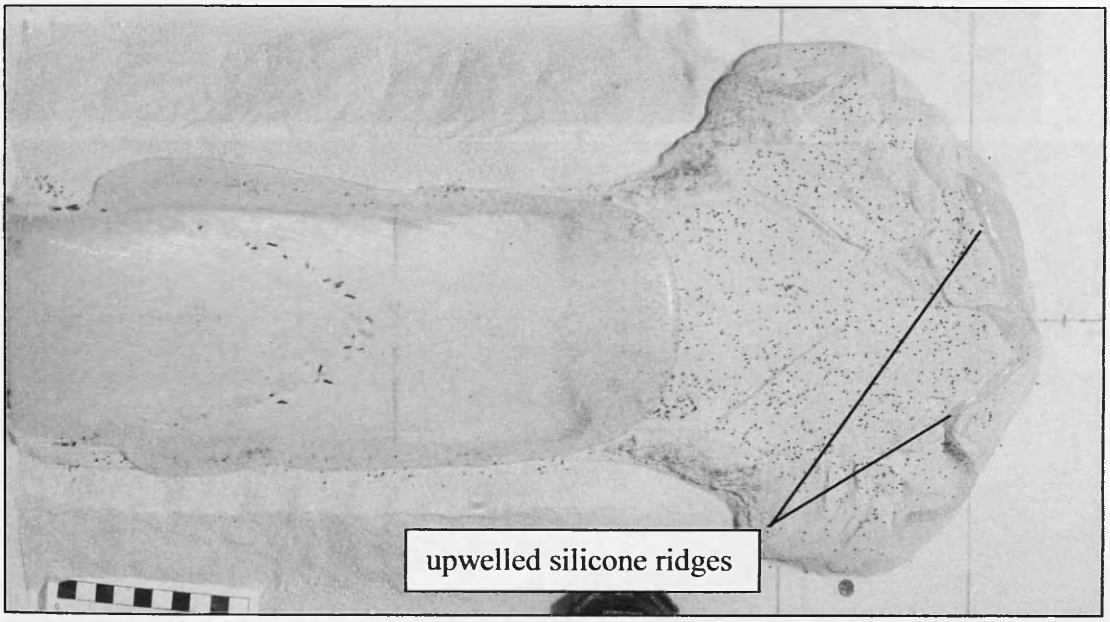

Figure 3.24. Experiment 20, χ = 0.5. As the experiment progresses and the influx advances on the flow front, ridges of silicone that welled up through the initial arcuate tensile fractures are deformed by the action of plates around them. The markers on the silicone influx illustrate the parabolic velocity profile across the channel.

Conjugate fractures again developed behind the original arcuate fractures, but these were much more widely spaced for thick crusts, and commonly only one orientation developed on either side of the centreline of the flow, forming an arrow-head shaped slab in the flow centre. The orientation of the fractures was around 30 to 35° downflow in towards the channel centre (figures 3.24 and 3.25 a), resulting in at intersection between the two sets at angles of 60 to 70°. The central slab moved more quickly than the frontal and lateral portions of the flow, and 'bulldozed' the smaller

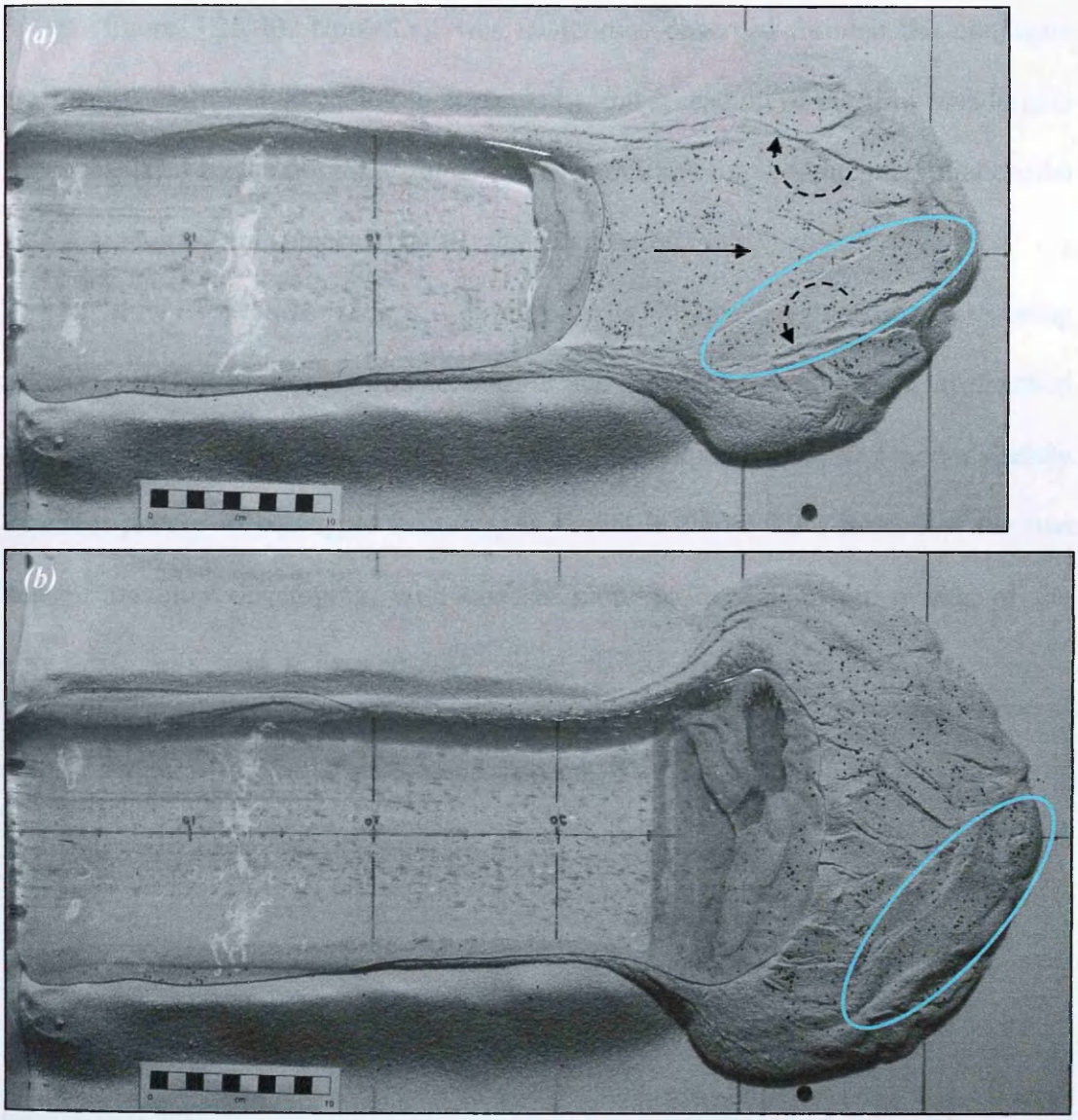

Figure 3.25. Experiment 14, $\chi = 0.375$. (a) Conjugate fractures can be clearly seen, breaking the crust into large plates. Plate location is influencing lobe development. Arrows indicate the directions of plate movement (solid) and senses of rotation (dashed). (b) Approximately 3 hours after (a), earlier plates can be seen to have been pushed towards the margins, and rotated (compare ringed plates). Later generations of conjugate fractures have formed. The plates have also been tilted towards the flow front, causing thickening of the flow.

crustal plates towards the margins, often introducing an element of rotation into their displacement (figure 3.25), and tilting them towards the flow front, causing crustal thickening. Progressive generations of conjugate fractures developed as the experiments continued, with the former central crustal slab being broken into large

plates (figure 3.25 b). Upwelling was sometimes observed through the conjugate fractures if sufficient spreading took place. Lateral spreading of the flow was largely accommodated by the fracturing, and once fractures had formed, the interstitial crustal plates were often not subject to further deformation.

The flow front was seen to develop in a highly irregular manner, being characterised by a strongly lobate outline and substantial amounts of avalanched crustal material (figures 3.24 and 3.25). One of the experiments developed a slightly different pattern of conjugate fractures, as shown in figure 3.26. Instead of the two sets of fractures developing, with one set more prominent on either side of the

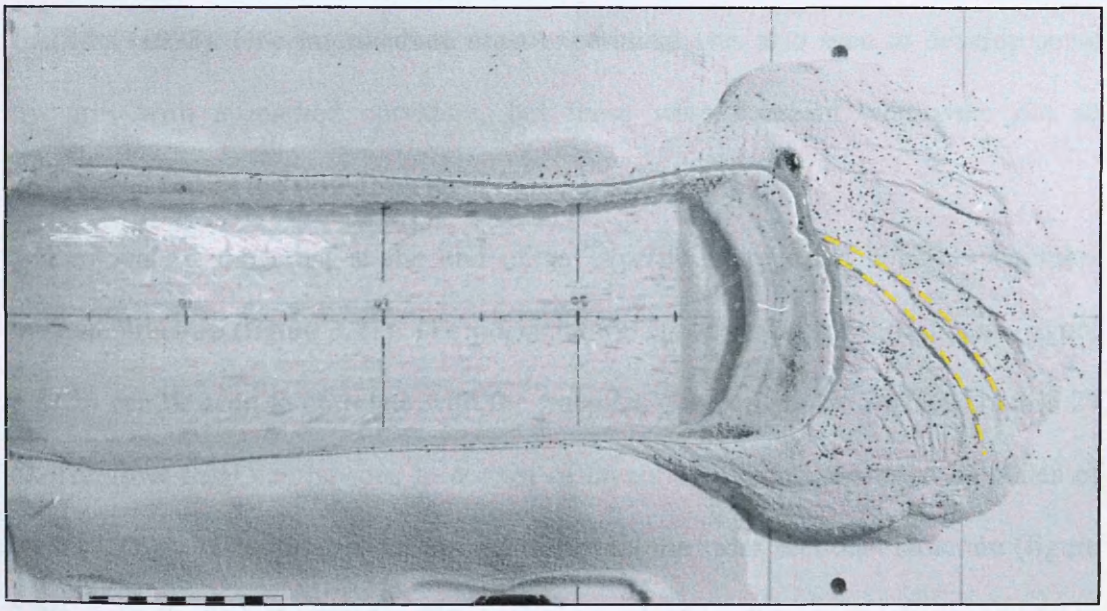

Figure 3.26. Experiment 23, $\chi = 0.375$. Flow front showing the predominance of one of the conjugate fracture directions, and the fact that the fractures are showing a marked curvature (yellow dashed lines). The curvature may be developing due to the fact that the flow front is slightly domed in shape, compared to the flatter fronts seen in figures 3.24 and 3.25 (a). These structures may be showing the transition in morphology between the linear conjugate fractures observed in the majority of the experiments described here, and the spiral slip planes observed in the kaolin slurry models of Blake (1990) and Osmond & Griffiths (1998). The changing morphology is inferred to reflect the change in surface shape rather than any change in formation mechanism.

centreline, and the fractures being straight, figure 3.26 shows that only one of the sets was well developed, and that these had a marked curvature. Some fracturing of the interstitial plates indicates the partial development of the second set of fractures. The fractures were convex downflow, and broadly parallel, though an increase in spacing can be seen towards the flow front in some areas. The experiment in which the fractures developed in this manner seemed, in the light of merely qualitative observations, to have a flow front that developed more dome-shaped topography than is seen, for example, in figures 3.24 and 3.25 (a). It is possible that this curved topography is influencing the fracture shape, causing them to more closely resemble the slip plane morphology seen in the models of Blake (1990) and Osmond & Griffiths (1998). One intermediate crust experiment was also seen to develop some fractures with a marked curvature, but these were transient, and were not so widespread across the flow front as in figure 3.26.

Removal of the crust at the end of an experiment revealed a highly complex internal structure (figure 3.27). The ridges on the upper surface of the silicone (figure 3.27 b) can be seen to correlate with the fractures observed in the surface crust (3.27 a). The flow front can be seen to consist of layers of silicone separated by plates of crust (3.27 c). If the flow is cut through to reveal the cross sectional structure (figure 3.28), it can be seen that the layered structure results from the progressive overrunning of upwelled silicone ridges. The ridges, which upwelled through the tensile flow front fractures, were folded over in the direction of flow as the faster moving influx encroached on the flow front, and sandwiched crustal plates between them. Early examples of this process are preserved at the base of the flow, as small, sand-filled cracks, dipping down in the direction of flow.

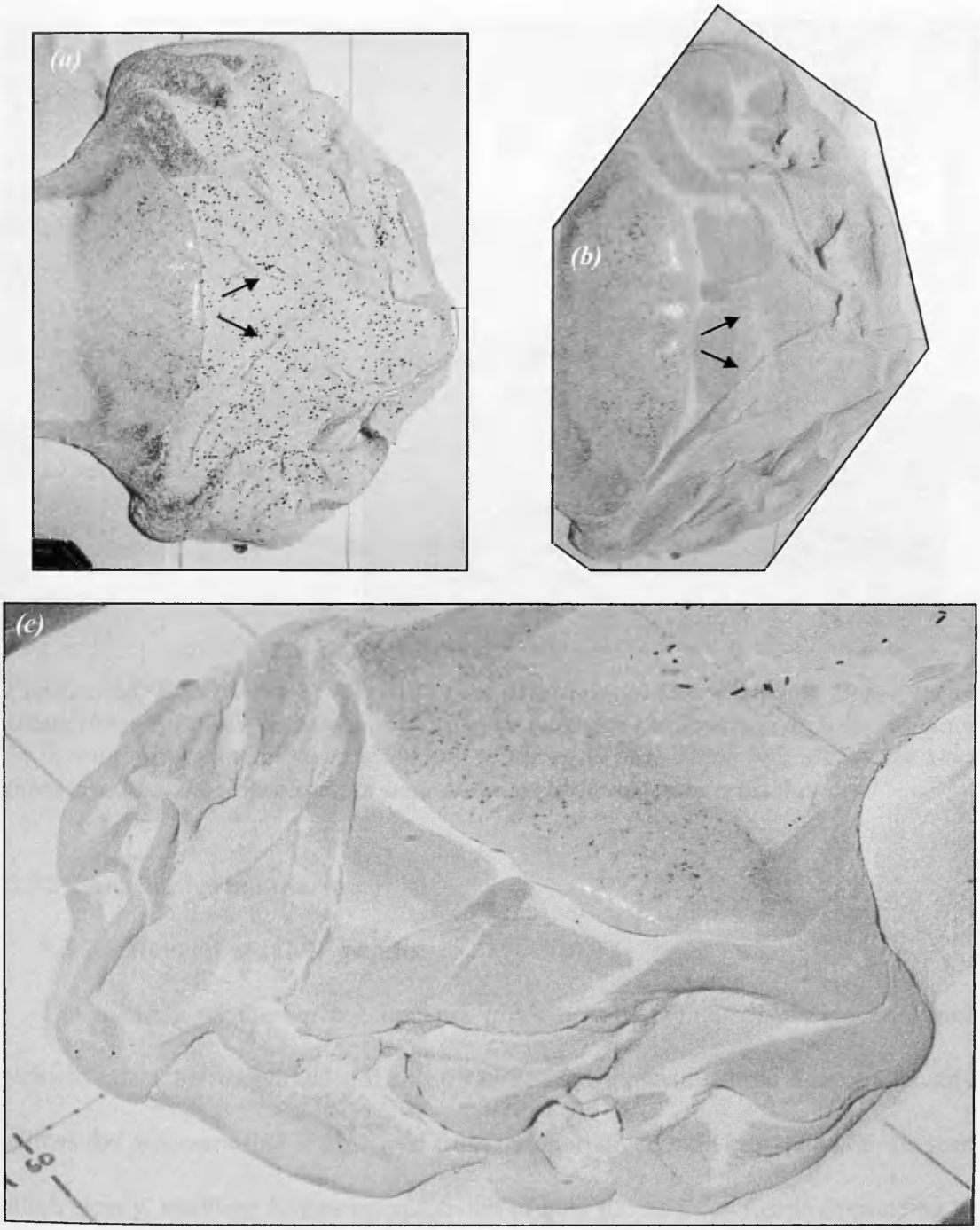

Figure 3.27. Experiment 20, χ = 0.5. (a) End of experiment, showing conjugate fractures (marked by arrows),lobes and crustal plates. (b) Flow front after removal of crust. Arrows indicate ridges of upwelled silicone that correspond to the conjugate fractures in (a), though no upwelling was visible through the crust. (c) The flow front consists of layers of silicone interleaved with pockets of sand, representing progressive generations of upwelled silicone ridges that have been deformed, trapping crustal plates between them. Scale is given by lines drawn on the basal board, which are spaced 10 cm apart.

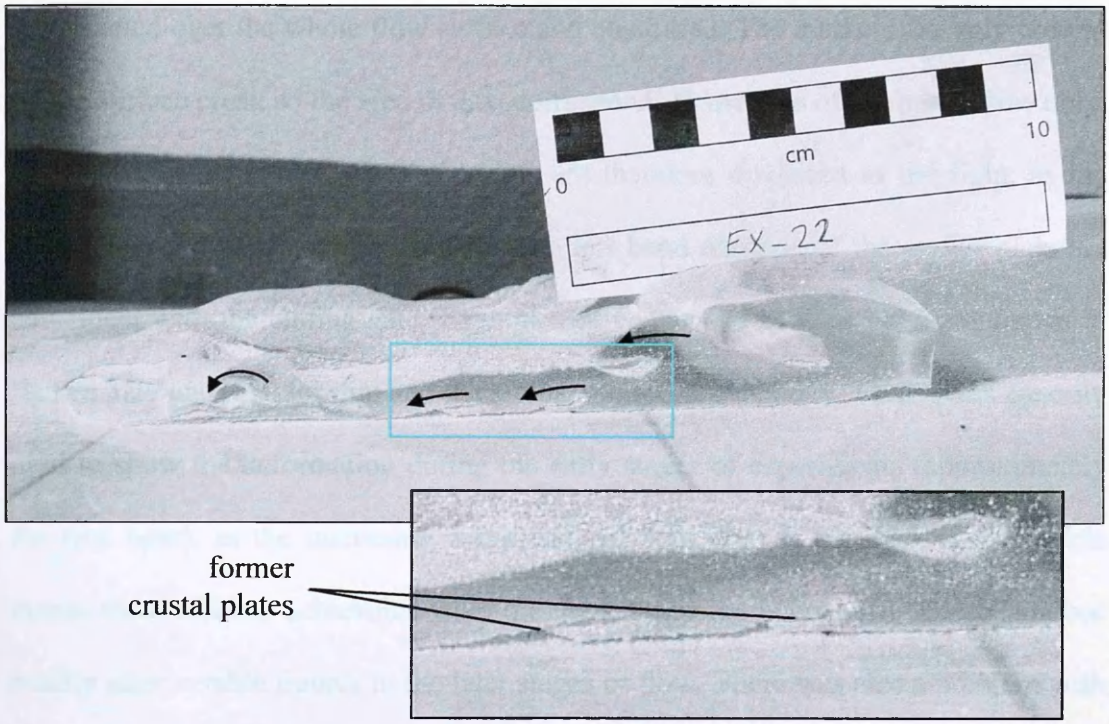

Figure 3.28. Experiment 22, χ = 0.444. Section through the flow front. Upper image shows the progressive deformation of silicone ridges in the direction of flow, indicated by arrows. Lower image, corresponding to the area in the blue box, shows the sand filled cracks at the flow base that indicate the prior location of crustal plates.

3.3.2 Quantitative monitoring

3.3.2.1 Monoscopic (2-D) results

The tracking of the surface markers gives near-horizontal displacement, hence velocity, data for individual points on the crust. Displaying these data graphically allows the processes that are inferred from the morphological observations to be seen more clearly, enabling further interpretation of how the surface crust is responding to the applied stresses. The presentation of the data in different ways can highlight different aspects of the deformation. The results are presented as both vector and contour plots (figures 3.29 and 3.30). In the vector plots, each marker on the flow surface is represented by an arrow, the length of which is proportional to the average velocity of that marker over the time period indicated. In the contour plots, the markers are represented as crosses, but the velocities of the discrete points are

interpolated over the whole flow surface and contoured. The markers are only present on the surface crust, so the area of data corresponds to the area of the initial flow only, not including the levées. The later plots are therefore displaced to the right, as the initial flow moves down the channel. The left hand margins of the earlier plots are coincident with the sliding gate. Examples of vector and contour plots are shown in figures 3.29 and 3.30 for thin and thick crust models respectively. These plots are only used to show the deformation during the early stages of experiments (approximately the first hour), as the increasing complexity of structures in the thick crust models means the resolution achievable from the marker spacing is not sufficient to produce readily interpretable figures in the later stages of flow. There was also a problem with markers rolling off the steepening flow front, or being lost through small collapses within the zone of tensile fracturing. In thin crust models, the growth of folds at the head of the channel resulted in marker points being lost by rolling down from the ridge summits into the cusps.

In all experiments, initial extension was observed at the flow front, as it collapsed under the influence of gravity, and this can be seen in (a) of figures 3.29 and 3.30 as longer vectors (higher velocities) at the flow front, and in (c) as arcuate contours. The contours are concave downflow, showing that the highest velocities are seen in the channel centre. Comparing (a) and (c) in the two figures, it can be seen that the velocity gradients at the flow front are initially steep, though steeper for the thick crust, and that this gradient dies off with time (compare a and c with b and d). The contours can be seen to extend further up the channel for the thick crust, showing that a greater area of the crust is being affected by deformation, as was observed by the larger region of arcuate fractures seen in the images.

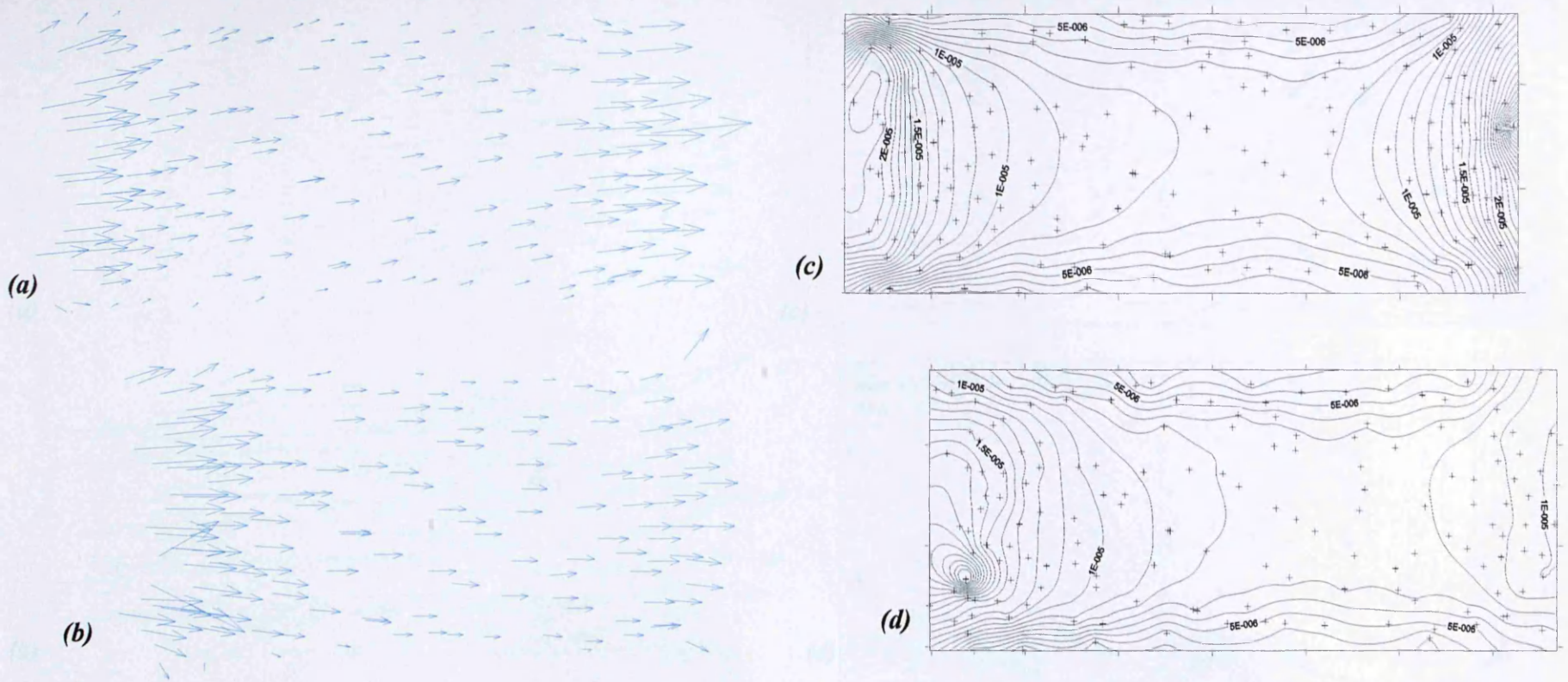

Figure 3.29. Velocity vector (a & b) and contour (c & d) plots for experiment 19, $\chi = 0.167$. Flow direction is left to right. Contour spacing is 1 x 10^{-6} m s^{-1}. Arrows in vector plots and crosses in contour plots indicate locations of data points. Arrow lengths are proportional to velocities. (a) and (c) show velocities for the time interval 0-3 minutes; (b) and (d) for 37-42 minutes. Since data is only available where markers are, figures (b) and (d) are offset to the right as the crust has travelled down the channel in the intervening time. Large velocities at the head of the channel and the flow front induce compressional and tensile stresses respectively. See text for details.

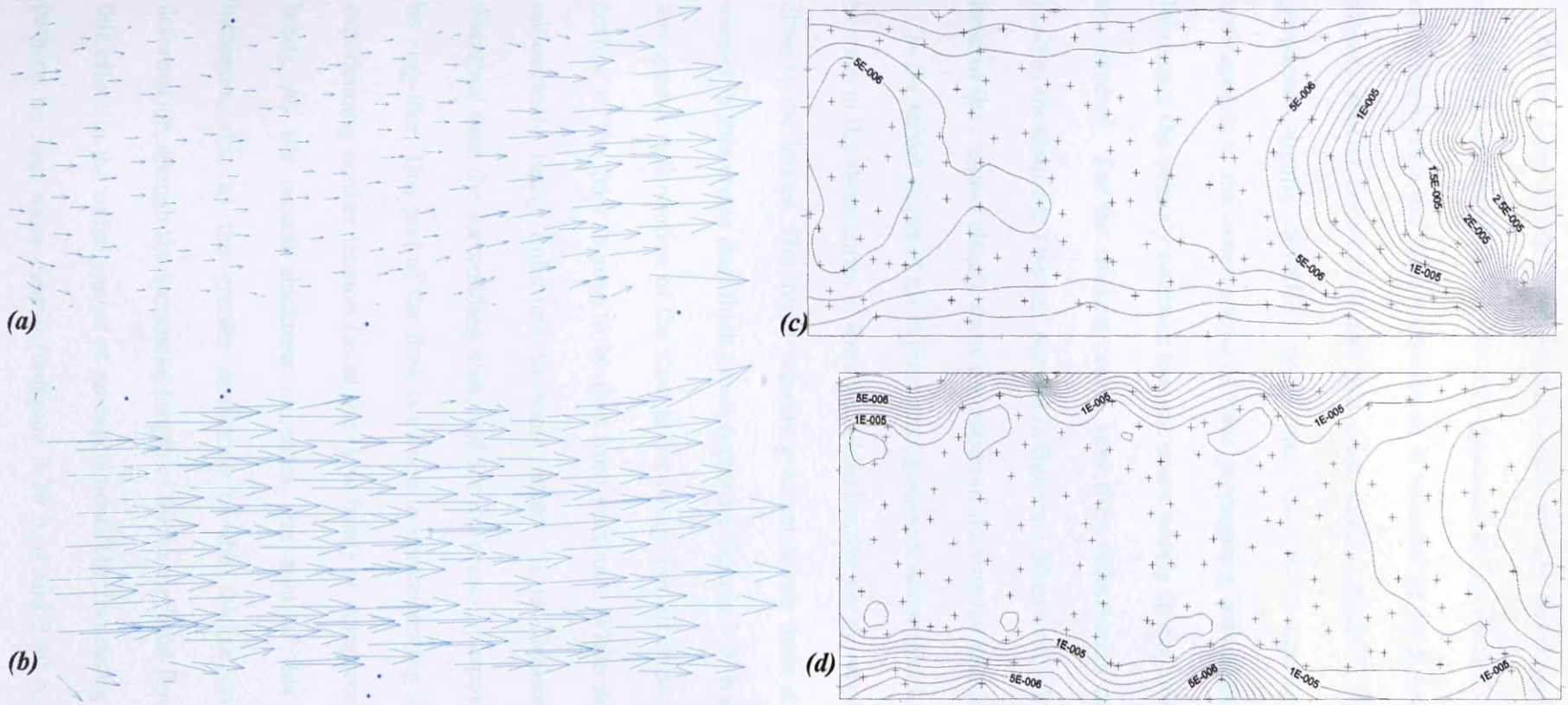

Figure 3.30. Velocity vector and contour plots for experiment 20, $\chi = 0.5$. Flow direction is left to right. Contour spacing is 1 x 10^{-6} m s^{-1}. (a) and (c) show velocities for the time interval 0-3 minutes; (b) and (d) for 35-40 minutes. Comparing figure 3.29, the crust can be seen to resist deformation at the channel head, as shown by the low velocities in the earlier time interval. The crust has not travelled far down the channel between the earlier and later intervals, though the velocity has increased significantly. The velocity distribution has changed dramatically between the two time intervals, and a steep velocity gradient is seen across the channel margin in the later time interval (b, d). See text for details.

At the head of the channel, thin crust models developed compressional ridge structures, whereas thick crusts only appeared to be affected by doming during the early stages of a run. This compression is reflected in the plots by longer vectors and closely spaced contours in the thin crust results (figure 3.29 a, c). The contours propagate slightly downflow with time, seen by comparing (c) and (d), which corresponds to the observations of folds propagating downflow. As crustal thickness increases, the velocity contours become more widely spaced and extend less far down the channel. For the thickest crusts, very little deformation can be discerned at the head of the channel. This can be seen in figures 3.30 (a) and (c). In (c), contours at the head of the channel clearly show the region of doming noted in section 3.3.1.4.

In the initial stages of all experiments, contours subparallel to the flow margins can be seen in the shear zones of the channel, indicating the slower movement of the crust close to the levées. The initial velocity gradient across these shear zones tends to be steeper in thin crusts than thick crusts (compare figures 3.29 b and 3.30 b), indicating that greater deformation of the crust is occurring. For all crustal thicknesses a medial portion of the flow is seen to be free from contours. While the contour-free area is undoubtedly being deformed to some extent, it is obviously considerably less disturbed than the surrounding area, and for the present purposes will be assumed to be plug-like. This part of the flow is closest to demonstrating steady-state behaviour, experiencing neither tension (as at the flow front) or compression (as at the channel head). As the crustal thickness increases, the area of this plug zone generally increases, due to the greater resistance of the thicker crust to compressional deformation, though the increasing length of the extensional flow front zone can mask this effect in the initial stages of an experiment. The increasing width of the slab can perhaps be seen more clearly (compare 3.29 b, d and 3.30 b, d). The plug zone is

always eventually affected by deformation in the later stages of a model as the flow spreads out of the channel, but, as previously mentioned, these plots are most appropriate for elucidating processes in the early stages of a model before the structure becomes too complex.

Comparing the early development of thin and thick crusts for the same slope, it has already been mentioned that the initial velocity gradient across the shear zones is steeper. It can be seen that this is due to the initial velocity of the plug being greater for thin than thick crusts (compare figures 3.29 a and 3.30 a). This can perhaps be seen more clearly in the vector plots than the contour plots, and remains the case for approximately the first 30 minutes of the experiments. At around 30 minutes, a sudden increase in slab velocity occurs (compare figures 3.30 a and b), and distinct, narrow shear zones develop, over which there is a strong velocity gradient (figure 3.30 d). Hereafter, the slab velocity is significantly higher for thick crusts than thin crusts, reflecting the higher crustal mass (compare figures 3.29 b and 3.30 b). The sudden velocity increase corresponds to the development of the long, single shear zone fractures which were described in section 3.3.1.4, after which the slab moved freely.

The distribution of contours illustrates a change in the behaviour of the flow as a whole as the crustal thickness increases. For thinner crusts, although plug flow is occurring in the medial channel, contours just upflow of this region are curved, indicating a cross-channel velocity profile that is approaching parabolic (figure 3.29 c, d). By contrast, plug flow is occurring throughout the upper and medial channel in the thick crust example (figure 3.30 d). The curved contours in the upflow part of the thin crust experiment indicate that the surface crust is reflecting the behaviour of the silicone fluid beneath. As the crustal thickness increases, the size (width and length) of the plug increases, showing that the crust is behaving as if it has an increasingly

large yield strength. This change in behaviour is indicative of the crust playing an increasingly important role in the flow dynamics, by forming a boundary for the fluid beneath.

If the locations of all the marker points are plotted for all time intervals, figure 3.31, it can be seen that the flow direction is not everywhere parallel to the direction of maximum slope. This is due to the advance of the deeper 'wave' of silicone from

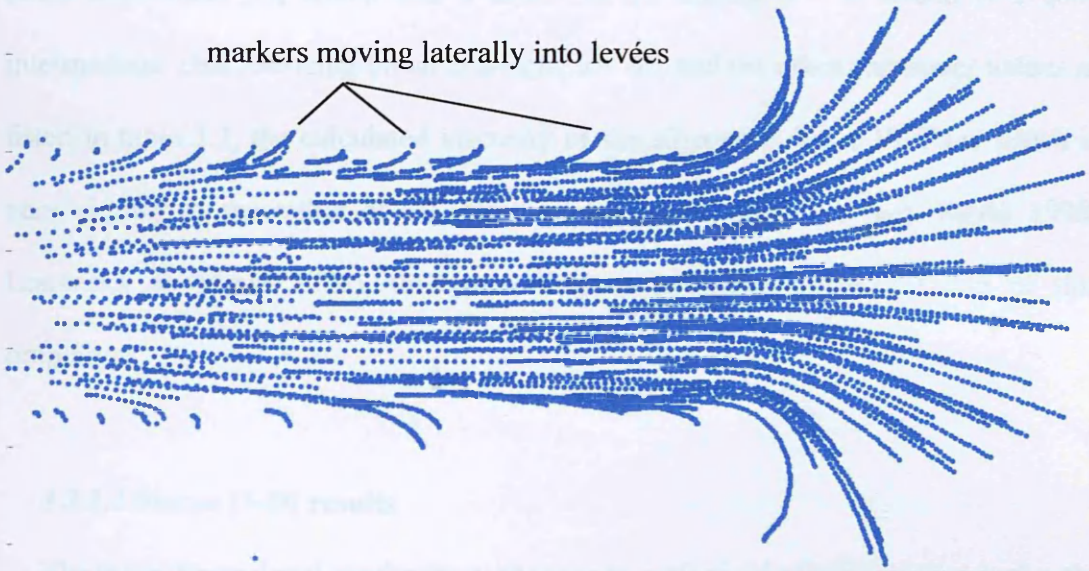

Figure 3.31. Experiment 19, χ = 0.167. Flow direction is left to right. Marker locations for all images. Towards the margins of the channel, markers can be seen to move into the levées, and slow down. At the very margins of the flow front, flow can be seen to occur back up slope slightly.

the reservoir, which causes an increase in the surface height in the channel, and hence the advance of the markers up the sloping levée walls. The marker tracks become increasingly oblique to the downslope direction over time, because the velocity slows as the points move further out towards the levées.

The velocities measured from the tracking of markers can be used as an independent check on the viscosity of the silicone, with the use of the Jeffreys equation (Jeffreys 1925). This was defined in equation 3.1:

$$u_{max} = \rho g h^2 \sin\alpha / n \eta$$

where ρ is the density of the silicone, g the gravitational acceleration, h the depth of the flow, α the slope, η the fluid viscosity, and n a constant. This equation was used to calculate the viscosity based on the measured maximum velocity of a flow without a crust, experiment 25, which was 3×10^{-6} m s^{-1}. Taking n = 3, which is a good intermediate, characterising broad channels, $\alpha = 4°$, and the other parameter values as listed in table 3.2, the calculated viscosity of the silicone is 2.4×10^4 Pa s, which is very similar to the value of 10^4 Pa s quoted in the literature (e.g. Merle 1998; Lescinsky & Merle 2005), thus providing an independent confirmation of this property.

3.3.2.2 Stereo (3-D) results

The three dimensional results show changes in surface relief which occur during the early stages of a flow's development. Again, during the later stages of the experiments, there were problems with points rolling around on the crust, and these were somewhat more pronounced than for the silicone carbide grains used in the 2-D models, as the mustard seed markers were almost spherical. Despite these difficulties, useful results were produced, some examples of which are shown in figures 3.32 and 3.33. Firstly, it needs to be noted again that the plots represent an orthogonal view of the flow, and that as the crust moves downflow, the data are shifted to the right. Here, though, the surface distribution of markers sometimes includes points on the levées, which is indicated in the figure caption. The figures indicate vertical displacements

between two images, and the time interval between the images is indicated in the figure captions. Each figure was created using two sets of point location data, one for each of the two images. For each set, interpolation of the height coordinate of the data points was carried out to produce a mesh. The earlier mesh was then subtracted from the later mesh to give the changes in relief, which are plotted against the x-y coordinates of the flow. Areas of no vertical change are shown in green, areas of positive change in reds and yellows, and areas of negative change in blues. The magnitude of the change is shown on the colour bar.

Figures 3.32 and 3.33 show results for thin and thick crust models respectively, over four time intervals spanning the first 36 minutes of the experiments. The same broad features can be picked out as were seen in the 2-D results, with the area of tensile fracturing being represented by the sinking zone at the flow front, and the area of compressional folding or doming of the crust causing the surface to increase in elevation at the head of the channel. Comparing figures 3.32 and 3.33, it can be seen that the area of sinking is larger, and the sinking is greater in magnitude, in thick crusts than thin crusts, due to the increased mass of the crust. The morphology at the head of the channel also differs between the thin and thick crusts, with the thick crusts developing domes that generally have smooth outlines (figure 3.33). The channel head results for the thin crust models are more complex, clearly showing the growth of fold structures, and the propagation downflow of these folds. In the earliest plot in figure 3.32, there is a single narrow strip of elevated crust at the very head of the channel, but after 35 minutes, three distinct bands of red can be seen, indicating the growth of three distinct folds.

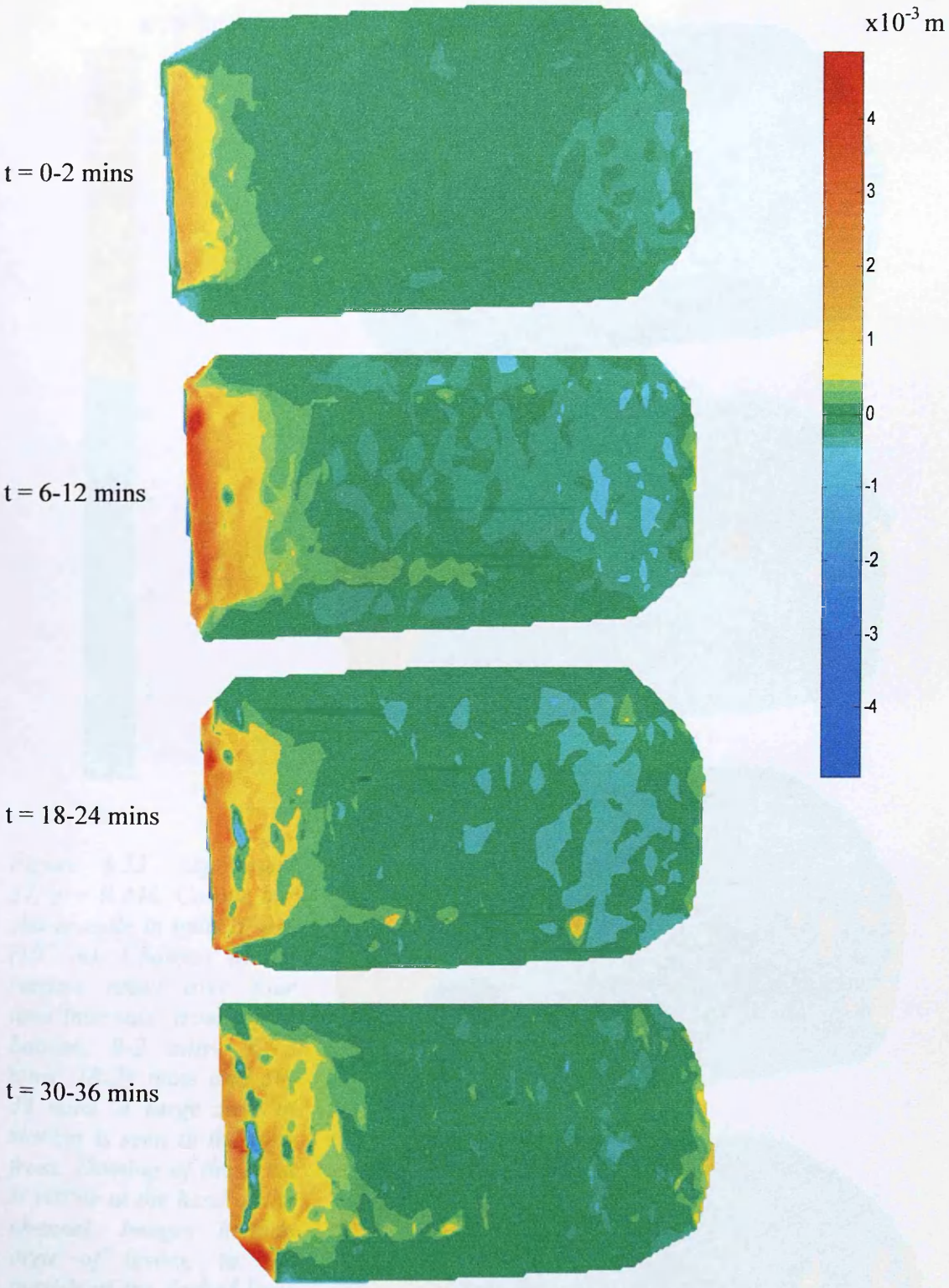

Figure 3.32. Experiment 34, χ = 0.167. Flow direction is left to right. Changes in surface relief over the four time intervals indicated. Blue indicates negative changes in relief, green no change and red positive change. Sinking due to tensile fracturing can be seen at the flow front, and ridges can be seen to grow at the head of the channel. Colour bar shows scale in units of mm (10^{-3} m). Images include narrow area of levées, and the approximate channel-levée boundaries are indicated by the black dashed lines in the top plot. See text for details.

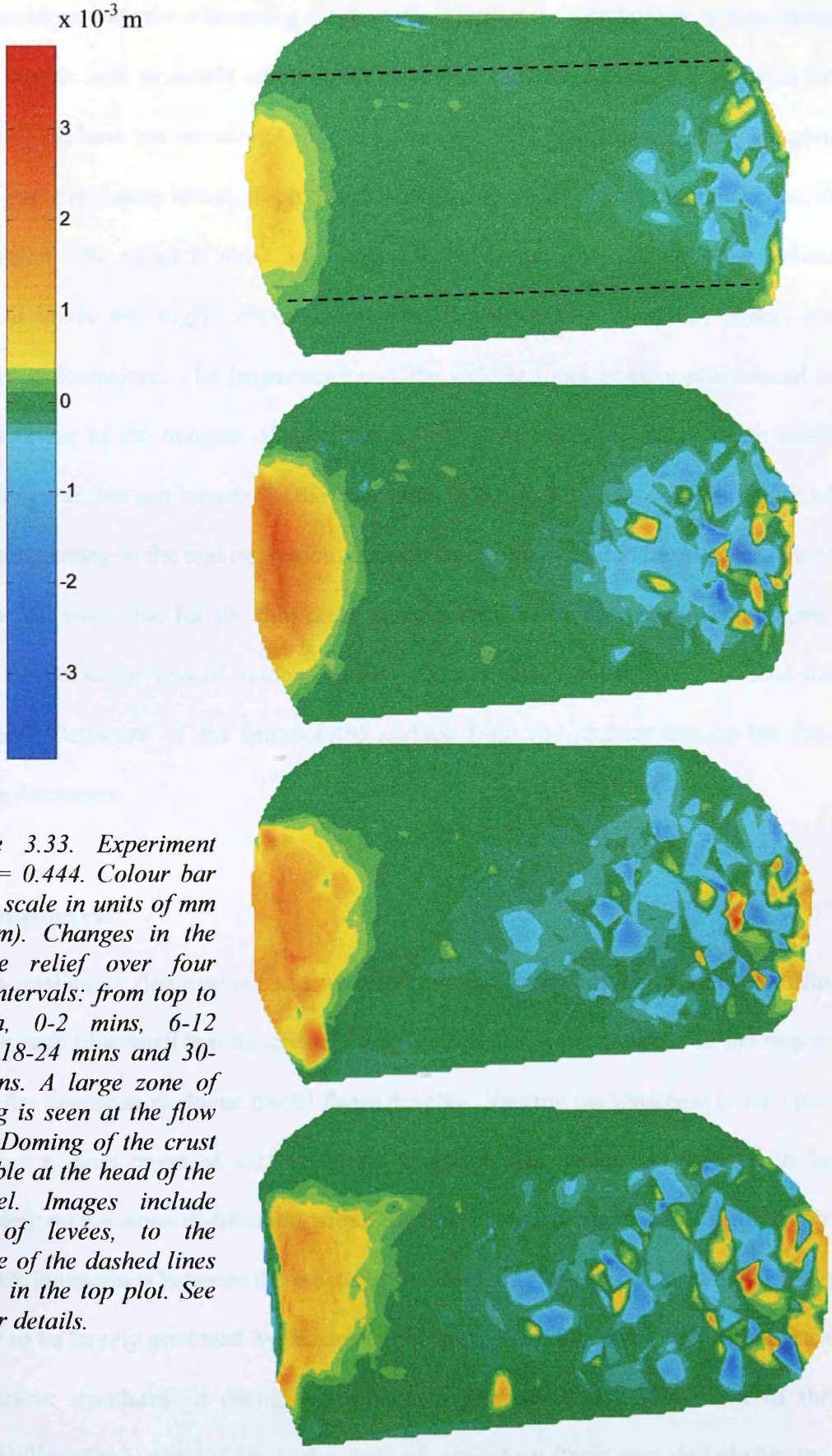

Figure 3.33. Experiment 37, $\gamma = 0.444$. Colour bar shows scale in units of mm (10^{-3} m). Changes in the surface relief over four time intervals: from top to bottom, 0-2 mins, 6-12 mins, 18-24 mins and 30-36 mins. A large zone of sinking is seen at the flow front. Doming of the crust is visible at the head of the channel. Images include area of levées, to the outside of the dashed lines shown in the top plot. See text for details.

A problem with the subtracting mesh method is that the whole flow is translating downslope as well as locally changing in elevation. This means that it is possible for points which have not actually changed in elevation, if they are moving into a region which was previously lower, to produce an artificial signature indicating elevation in that region. The effect is most pronounced in the extensional sinking zone, where strips of lower and higher elevation material (fractures and interstitial plates) are translating downslope. The fragmentation of the sinking zones is more pronounced in thicker crusts as the margins of the fractures are more unstable and prone to small collapses, and this can be seen in the later plots in figure 3.33 as localised regions of yellow occurring in the sinking region. In contrast, the zone of doming becomes more fragmented over time for the thin crust models, because of the crustal deformation, which results in the loss of markers as they roll around on the surface, and thus the increasing departure of the interpolated surface from the real surface as the data density decreases.

3.4 Summary

The qualitative descriptions and quantitative monitoring results presented in this chapter have illustrated that the crustal thickness has a significant effect on the way in which the two-layer analogue model flows develop. Varying the thickness of the crust produced a wide range of surface crustal morphologies, which are inferred to be dependent on the stress distribution within the flow. The experiments also showed that complex interactions between the crust and the fluid interior can occur, and that these appear to be largely governed by the crustal thickness. The following chapter analyses the surface structures in detail, while chapter five contains a discussion of the applicability of the model flows to the study of active lava flows, and also of glaciers.

Table 3.4. Summary of the structures observed in all experiments. (Abbreviations are listed below the table).

γ	Exp't	Slope (°)	Folds (F) Ropes (R)	Flow front fractures	Shear zones	Conjugate fractures	Lobes
0	25	4	None.	None.	No features.	None.	None.
	30	4	None.	None.	No features.	None.	None.
0.063	24	4	F: Well developed, short λ, regular. R: Down channel margins and on edges of ff.	None.	No fractures, ridges.	None.	None.
0.167	9	4	F: Well developed, regular λ . R: Down channel margins and on edges of ff.	Very fine, very closely spaced. Rear fractures close with time.	No fractures, ridges.		None.
	19	4	F: Well developed, regular λ. R: down channel margins and on edges of ff.	Fine, closely spaced. Rear fractures close with time.	No fractures, ridges.		
	31	4	F: Well developed, regular λ. R: Run length insufficient.	Fine, closely spaced.	No fractures, ridges.		None.
	34	4	F: Well developed, regular λ, R: Down channel margins and on edges of ff.	Fine, closely spaced. Rear fractures close with time.	No fractures, ridges.		None.
	38	4	F: Irregular λ but well developed.	Fine, closely spaced. Rear fractures close with time.	OB and ridges.		Slightly irregular ff, no discrete lobes.
	11	8	F: Irregular, longer λ. R: Down channel margins and on edges of ff.	Fine, closely spaced. Rear fractures close with time.	No fractures, ridges.		None.
	15	8	F: Short λ. R: Down channel margins and on edges of flow front.	None.	No fractures, ridges.		

0.167	10	12	F: Regular λ. Do not propagate far down channel. R: Down channel margins and on edges of ff.	Fine, closely spaced. Rear fractures close with time.	OB and ridges.		Irregular, 'wavy' ff at centre. Plates/avalanching.
	29	*4*	*F: 3-4, very poorly developed.* *R: Down channel margins.*	*Initially fine, closely spaced. Upwelling later.*	*No fractures, ridges.*	*Upwelling.*	*Small lobes associated with plates.*
	21	4	F: 2-3, long λ, very irregular R: At end of channel at margins and on edges of ff. Poorly developed	Fine, closely spaced.	OB and ridges.	1/2 curved fractures: slip planes? 1 direction only.	'Wavy' irregular ff. Influenced by avalanching.
0.286	17	4	F: Long λ, very irregular. R: Down channel margins and on very edges of ff.	Fine, closely spaced.	OB and ridges.		Small lobes aligned with plates.
	32	4	F: Irregular, 2-3. R: On edges of ff.	Fine. Widen with time-upwelling through a few.	RHM: OB. LHM: LO.		Associated with plates.
	39	4	F: None. Thrust fault ~1/3 way down channel. R: Down channel margins and on edges of ff.	Fine, Widen with time, upwelling through a few.	OB, becoming LO with time.		Small lobes, associated with plates.
	7	8	F: None. R: Down channel margins and on edges of ff.	Fine, closely spaced. Upwelling possibly through one fracture.	OB, becoming LO with time.	Upwelling.	Uneven ff, initially controlled by avalanching. Once CFs develop, plates more important.
	16	8	F: Irregular at first, develop better with time (extend round ff at end). Longer λ. R: Down channel margins	Fine, closely spaced.	OB and ridges.		Aligned with plates. Over time plates disintegrate, and ff becomes less lobate.

0.286	12	12	F: None. R: Down channel margins and wide zones at edges of ff.	Slightly irregular.	OB and ridges.	Small amount of upwelling.	Much avalanching. Clear correlation with plates near centre of ff.
	4	*4*	*F: None.* *R: Down channel margins and on edges of ff. Associated with thinning crust.*	*Few, wide fractures, though not well defined. H&G. Upwelling later.*	*RHM: OB and ridges; LHM: LO becoming wavy SF.*		*Associated with plates.*
	28	*4*	*F: None.* *R: Edges of ff*	*Wide. Upwelling.*	*LO.*		*Associated with plates.*
0.375	18	4	F: None. R: Edges of ff.	H&G. Slightly asymmetric/discontinuous. PP. Some upwelling,	OB, becoming LO then SF. Upwelling.	More upwelling than through ff fractures.	Clearly associated with plates. Much avalanching.
	33	4	F: None. Thrust fault ~ 1/3 way down channel. R: Edges of ff.	Wide, some H&G. Upwelling.	LO becoming SF.		Associated with plates.
	36	4	F: None. R: Edges of ff.	Wide, some H&G. Upwelling.	LO becoming SF.		Associated with plates.
	14	8	F: None. R: Down channel margins and edges of ff, poorly developed.	Wide, H&G. Upwelling through rear fracture.	OB becoming LO.		Clearly associated with plates.
	23	12	F: None. R: None.	H&G. Irregular, discontinuous. Cross-cutting linear and arcuate. Upwelling.	OB becoming LO.	Curved fractures: slip planes?	Small, associated with plates.
	5	*4*	*F: None.* *R: Down channel margins, associated with upwelling. Edges of ff. Crustal thinning.*	*Wide, irregular, H&G. PP. Upwelling.*	*OB becoming SF. Upwelling.*		*Wide, around whole ff. Associated with plates.*

0.444	6	4	F: None. R: Edges of ff, clearly associated with thinning.	Very wide. H&G. Upwelling.	LO becoming sinuous SF; OB within. Upwelling.		Wide, associated with folded over silicone ridges.
	22	4	F: None. R Edges of ff, poorly developed.	Wide, H&G. Upwelling.	LO becoming SF.		Associated with plates.
	35	4	F: None. R: Edges of ff.	Very wide, H&G. Upwelling.	LO becoming SF.		Clearly associated with plates.
	37	4	F: None. R: None.	Very wide, H&G, plus PP.	SF, without any obvious precursors.	Upwelling.	Associated with plates.
	8	8	F: None. R: Down channel margins and on edges of ff.	Linear just behind ff, H&G; arcuate further back; PP even further back. Upwelling.	RHM: LO becoming SF. LHM: SF.		Clearly associated with plates and deformation of upwelled ridges.
	26	*4*	*F: None.* *R: None.*	*Very wide, upwelling.*	*LO becoming SF.*		*Affected by plates and avalanching.*
	27	*4*	*F: None.* *R: Edges of ff.*	*Very wide, upwelling.*	*LO becoming SF.*		*Affected by plates. Lots of clear silicone squeezed out at ff.*
0.5	20	4	F: None. R: Very edges of ff.	H&G. PP. Upwelling.	Initially LO. Crustal slab develops but fractures indistinct.		Layered due to folding over of upwelled ridges. Associated with plates.
	13	8	F: None. R: Very edges of ff, margins at end of channel.	H&G. Upwelling.	LO quickly becoming SF. OB within SF.		Avalanching. Layered lobes from upwelled silicone ridges, lobes aligned with plates.

?	2	?	*F: One fold in front of influx. No propagation* *R: Down channel margins.*	*Small fractures orthogonal to ff at ff. OB symmetric about centre line over whole surface.*	*OB. Upwelling.*		*Pronounced in centre of ff, associated with plates/avalanching.*
	3	?	*F: Initial rippled texture, develops into 2 folds but do not appear to propagate.* *R: none.*	*Fine.*	*OB.*		*Small, in centre of ff. Aligned with plates. Avalanching..*

Experiments 2 to 5 were carried out before methods were finalised, and had a less cohesive crust. Experiments 25 to 29 were carried out in Lancaster, where high humidity affected the crustal material. The observations from these experiments are shown in italics.
Abbreviations: ff = flow front; H&G = horst and graben; λ = wavelength; PP = fractures shaped like the passive plastic spreading scenario described by Nadai (1950), figure 2.3 a; RHM = right hand margin; LHM = left hand margin; OB = short oblique fractures oriented at ~20° downflow into levées; LO = long oblique fractures, more widely spaced, which become more closely parallel to the margin over time; SF = long single fracture down channel margin; CF = conjugate fractures. See text for details.

4. Structural Analysis

This chapter focuses on the analysis of the structures described in chapter three, and how these resultant morphologies can be used to interpret the different behaviours of the experimental flows. Each group of structures is discussed separately, and the results of the analysis are combined into an overall description of how an experimental flow behaves, and how this can be related to the behaviour of natural flows of lava and of ice.

The structures that form in the crust are a function of the distribution of stresses in the channel, which is modified by crustal thickness and slope, and also by the strength of the crust. The strength of a material refers to the stress at which it begins to deform permanently rather than elastically. This deformation process is continuous, and occurs progressively through the brittle failure region once the (tensile or compressive) strength of the material has been exceeded (Jaeger & Cook 1969; Johnson 1970). While the strength is scale-independent in terms of the material itself, the strength of the experimental crusts can be considered in terms of the unit strength. In the same way that it is more difficult to snap a thick twig than a thin one though they are made of the same material, a thick experimental crust can be considered to be a 'stronger' unit than a thin crust.

An experimental flow experiences both normal and shear stresses as it moves through the channel, and the directions of the three principal stresses σ_1, σ_2, and σ_3 (major, intermediate and minor respectively) depend on the interaction of the normal and shear stress components. Figure 4.1 shows a schematic sketch of the frame of reference used hereafter when discussing the various stresses felt in the channel. The flow surface is assumed to be planar, with the x-axis in the surface and positive in the

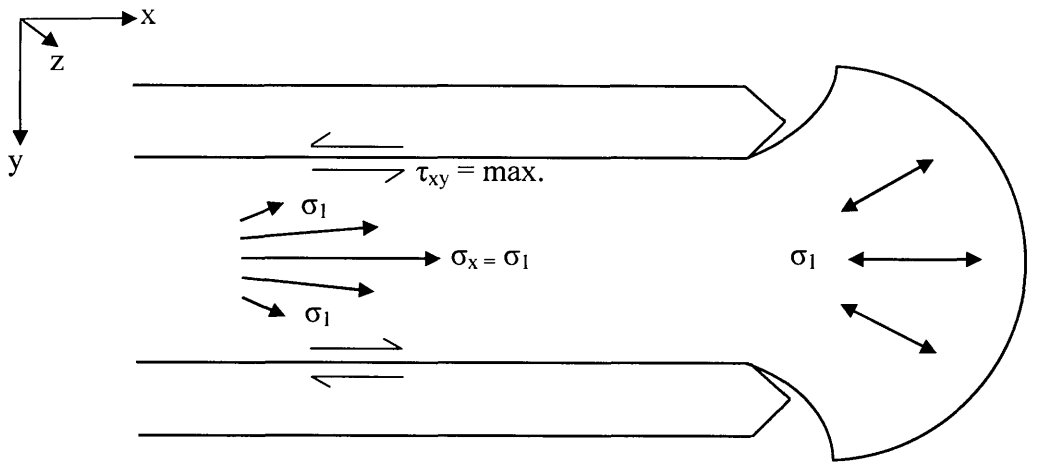

Figure 4.1. Sketch showing the frame of reference used when referring to stress directions. σ_x is the down channel normal stress, σ_1 is the maximum principal stress and τ_{xy} is the shear stress exerted on the flow by the levées. $\sigma_1 = \sigma_x$ at the centreline of the channel where the velocity is greatest and τ_{xy} is zero, but becomes increasingly influenced by τ_{xy} towards the channel margin and so is directed out towards the levees. At the margin, the down channel normal stress is zero, and the shear stresses are at a maximum. See text for details.

downslope direction, the y-axis in the surface and transverse to the downslope direction, and the z-axis normal to the surface. This convention differs to that found in the literature pertaining to glaciers, which is used in this chapter, in which the y-axis is normal to the flow surface and the z-axis is in the surface, transverse to the downslope direction. All notation taken from glacier literature is therefore changed, to bring it into line with the more common convention of the z-axis being vertical. The convention of tensile stresses being defined as positive and compressive stresses as negative is, however, adopted here. The normal stress components are σ_x, σ_y and σ_z, and the shear stress components, τ_{xy}, τ_{yz} and τ_{xz}. Since τ_{xz} and τ_{zy} are zero at the surface, σ_z is one principal stress component, σ_2. The other components are the roots σ_1 and σ_3 of:

$$\sigma^2 - (\sigma_x + \sigma_y)\sigma + (\sigma_x \sigma_y - \tau^2_{xy}) = 0 \qquad (4.1)$$

(Paterson 1981). Since τ_{xy} is zero in the centre of the channel, $\sigma_1 = \sigma_x$ down this line. The magnitude of σ_x decreases from a maximum at the centreline of the channel to

zero at the margins, due to the velocity profile. Conversely, the magnitude of τ_{xy} increases from zero at the channel centreline to a maximum at the margin. The interaction of σ_x and τ_{xy} means that σ_1 becomes inclined at an increasingly oblique angle to the x-axis, pointing out towards the levées, as the margin is approached (figure 4.1).

As covered briefly in the morphological descriptions, the longitudinal stress, σ_x, varies in magnitude along the length of the channel, and can be compressional, tensile, or zero. The initial collapse and extension at the flow front results in an increase in σ_x, which becomes tensile near the surface in the front portion of the channel, while the flow of material into the channel from the reservoir results in a decrease in σ_x, so that compressional stresses are felt at the head of the channel. Initially, between these regions is a zone where $\sigma_x = 0$, though this diminishes rapidly with time. Once the flow exits the channel, it begins to spread in a more radial fashion, though the slope ensures it will spread more rapidly in the x-direction, and the constraining marginal wall stresses vanish. As the influx catches up with the flow front, σ_x becomes everywhere compressional. The following sections discuss the different morphological features that result from these varying stress distributions in more detail.

4.1 Tensile flow front fractures

The initial zone of fractures developed behind the flow front in all but the thinnest crust ($\gamma = 0.063$) and the crust free experiments, and the shape, spacing and nature of the fractures were found to be dependent on the crustal thickness. In thinner crusts, the fractures tended to be straighter, more closely spaced and narrower, while in thicker crusts they became increasingly curved (parabolic) in plan view, more widely spaced

and wider, sometimes showing a horst and graben type structure. In all models, fracture spacing increased upflow, which can be attributed to a decrease in the differential stresses, and hence strain, which corresponded to the decrease in velocity gradient back from the flow front, as seen in figures 3.29 and 3.30. This fracture development is a transient effect, due to the collapse of the flow front, but simulates the behaviour that would be expected should a flow experience a local increase in velocity, for example if it were to encounter an increase in slope.

4.1.1 Fracture shape

The problem of fracture, or crevasse, development was considered in the context of glaciers by Nye (1952a). He initially tried to describe glacier flow assuming a pseudoplastic rheology with a yield strength (figure 1.2). This was accomplished only for the case of laminar flow, where all surfaces of differential shearing are parallel to the flow bed, and the three normal stresses are equal in magnitude. This was inadequate when attempting to explain crevasse formation, for which at least one tensile principal stress is needed, thus requiring an imbalance in the normal stresses (specifically an excess of longitudinal stress). Nye found it problematic to account for this using a pseudoplastic rheology, and so simplified the problem by assuming a plastic model instead (figure 1.1), finding that this was still a reasonable representation of the natural system. Negligible drag was assumed at the valley sides, which is a reasonable assumption for a very wide flow, but the results were considered to be applicable on the vertical axial plane of any valley glacier. The analysis showed that it is possible to have either compressive or extending flow. In the compressive regime, the longitudinal normal stress (σ_x) is everywhere compressive, and always more compressive than the vertical normal stress (σ_z). In extending flow, the

longitudinal normal stress is compressive at depth, but tensile in an upper layer, and is always more tensile than the vertical stress. Transverse crevasses would be expected to form in the upper layer of the extending flow, but not in the compressive flow. At the base of the tensile layer, the pressure from the weight of the ice above, plus the atmospheric pressure, exceeds the horizontal pressure, causing the crevasse to close up comparatively quickly. An additional factor is that above a critical depth, the shear stresses are smaller than the yield strength of the ice, which prevents closure.

The theory of crevassing in compressive and tensile flow regimes follows that of Hopkins (1862). The patterns that crevasses make can be deduced from the directions of the principal stresses (Nye 1952a), which are determined from the combination of the normal and shear stress directions. Crevasses will form only at places where one of the principal stresses in the plane of the surface is tensile, and only if this tensile stress exceeds the tensile strength of the ice. The crevasses will open up perpendicular to the tensile stress. Nye considered a glacier of constant width and assumed that σ_x (the longitudinal normal stress, figure 4.1) had the same value across the whole glacier. While this assumption is a simplification, as the effect of the sidewall shear stresses will be to slow flow near the margins, it is more appropriate for a plastic rheological model, in which the longitudinal normal stresses are at least constant across the plug region, than it would be for a Newtonian rheological model, in which the cross flow velocity profile is parabolic.

For the theoretical case of purely laminar flow, where σ_x is assumed to be zero (i.e. no tension or compression), τ_{xy} is the only non-zero stress component acting in the plane of the surface. In this case, the principal stress components are a tensile stress of magnitude τ_{xy} and an equal compressive stress, each inclined at 45° to the x-axis. This

is shown in figure 4.2. The crevasses therefore develop normal to the tensile principal stress, but die off towards the centre of the glacier as τ_{xy} tends to zero.

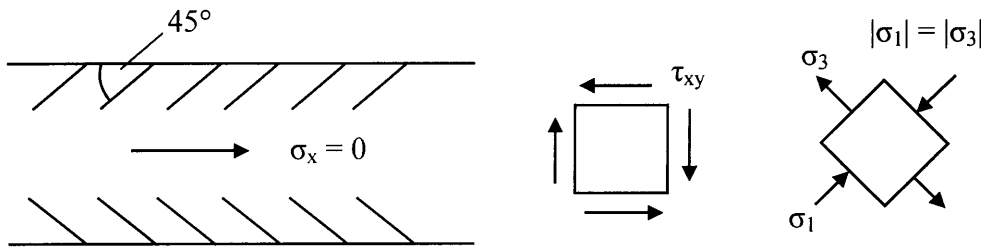

Figure 4.2. Crevasse patterns which develop in a valley glacier if $\sigma_x = 0$, so τ_{xy} is the only non-zero stress component at the surface. The principal stresses in this case are a tensile stress of magnitude τ_{xy}, σ_3, and a compressive stress of equal magnitude, σ_1, each inclined at 45° to the valley margin. The crevasses open up perpendicular to the direction of the tensile principal stress. From Nye (1952a); figure 9.

The case of interest with regard to the tensile fractures forming at the flow fronts in the experiments is that of extending flow, in which the longitudinal normal stress component, σ_x, is tensile. At the centreline, this normal longitudinal tensile stress is the principal stress σ_3, so crevasses open up transverse to the downslope direction, i.e. parallel to the y-axis. Towards the flow margins, the combination of σ_x with the increasing τ_{xy} component is equivalent to a large tensile principal stress (σ_3) inclined into the centre of the channel at more than 45° to the x-axis, and a small compressional principal stress (σ_1) orthogonal to this (figure 4.3). The increasing influence of the shear stress component means that the angle made by the principal tensile stress with the x-axis *increases* towards the margin, and hence the angle made by the fractures with the margins *decreases* as the margin is approached (angle measured upflow from the fracture to the levée). This results in curved fractures which are concave downflow, as shown in figure 4.3. In the absence of a sidewall shear stress, e.g. in the lubricated sidewall models of Lescinsky & Merle (2005), the tensile fractures would everywhere be perpendicular to the x-axis, and so would make angles

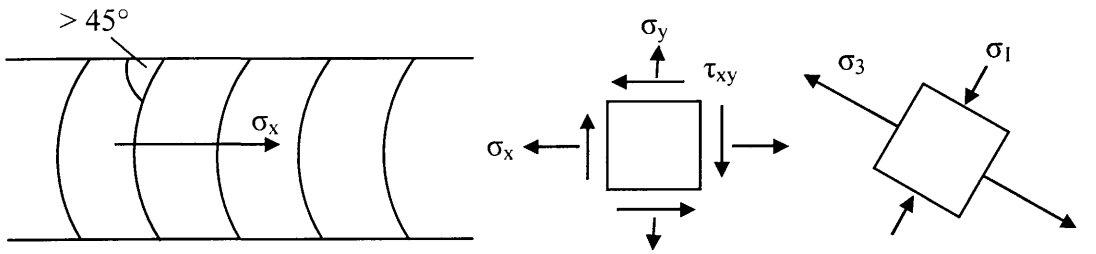

Figure 4.3. Crevasse pattern in a valley glacier if σ_x is tensile. In this case, the combination of σ_x and τ_{xy} gives a large tensile principal stress inclined at more than 45° to the valley margin, and a small compressive principal stress perpendicular to this. From Nye (1952a); figure 9.

of 90° with the margins (figure 2.12 a). It is the presence of shearing stresses that causes the fractures to be curved. Nye's model assumed a constant tensile stress along the length of the channel considered, which resulted in parallel fractures, as shown in figure 4.3. Longitudinal variations in the magnitude of the stress would result in a change in shape of the fractures. As the magnitude of the tensile stress decreases, the angle the fractures make with the margin would be expected to decrease, tending towards the case where $\sigma_x = 0$ (figure 4.2). In the experiments described here, tensile stress is at a maximum at the flow front, decreasing upflow as the flow has less freedom to collapse downslope, and the influence of the influx is increasingly felt. In addition, the shearing stresses felt at the flow front are lower, due to the termination of the levées at the flow front. As such, the fractures at the very flow front are straight, and increase in curvature further upflow. The case in which σ_x is compressive will be considered in section 4.2.

4.1.1.1 Comparing the rheological structure of glaciers and lava flows

The rheological model assumed in Nye's analysis, that of an ideal plastic, is obviously in contrast to that of the models described in chapter three, which have a bimodal rheology. In lava flows, the same material forms the crust as well as the

interior, but a vertical temperature gradient induces the vertical rheology gradient. In glaciers, again the material is the same throughout the flow, but it can be argued that the stresses and strain rates experienced in the different parts of the flow induce different behaviours that could be seen as analogous to a rheological stratification. If this is the case, then Nye's glacier analysis can be more comfortably applied to the study of lavas.

At small stresses and strain rates, ice deforms elastically (recoverably); at large stresses and small strain rates, it deforms permanently by creep, while at large strain rates, it will deform by fracturing. Variation in the fabric of ice is likely to occur with depth due to the increasing pressure experienced in the lower reaches of the flow. Ice near the surface will probably have randomly oriented crystals, while at depth it will have recrystallised so that many of the crystals are favourably oriented for deformation in the direction of the shear stress. The deeper ice is therefore more easily deformed, i.e. the strain rate increases for a given stress, and will also be subjected to greater shear stresses due to the weight of the overlying material. Paterson (1981) discusses the measurement of vertical velocity profiles in glaciers, and shows data from Athabasca Glacier, Canada, which seems to reflect these inferences. In figure 4.4, it can be seen that the velocity does not vary substantially in the upper part of the ice, but that the gradient increases rapidly towards the base. This is very similar to the vertical velocity profile that would be expected in a rheologically stratified lava flow with a thick crust showing 'plug' flow, as expected for a plastic rheology. Any changes in the fabric with depth would be expected to amplify this behaviour, as the recrystallised ice can be deformed more easily than the more isotropic surface layer. It seems that, despite having uniform rheologies, glaciers can demonstrate behaviour similar to that of a bimodal system. Regarding the velocity profile of a lava flow, for

thinner crusts the uniform gradient would occur over a smaller region of the flow, but the overall shape of the profile would remain similar.

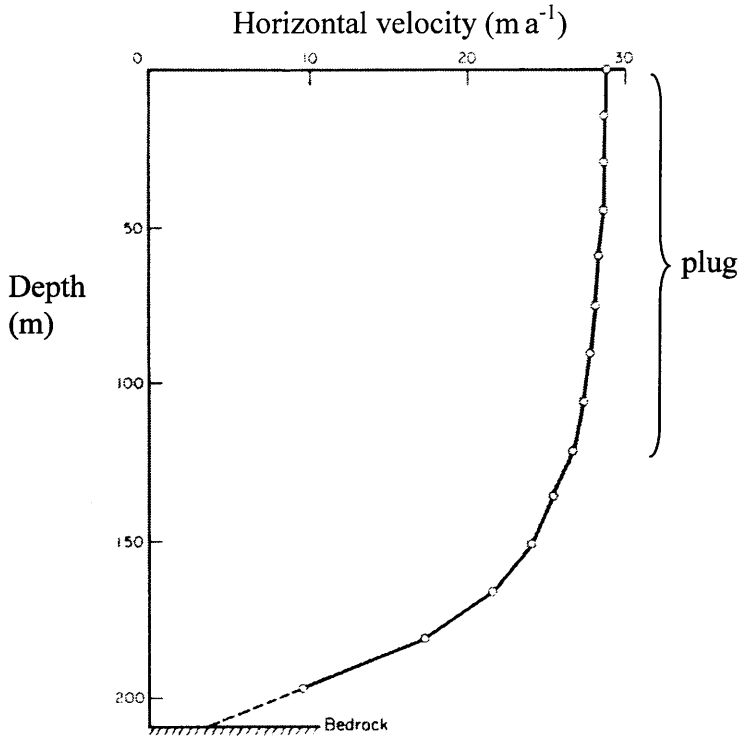

Figure 4.4. Variation in the horizontal velocity with depth for the Athabasca Glacier, Canada, using data from Savage & Paterson (1963). The upper part of the flow, indicated by the bracket, is experiencing little or no shearing, while the lower part is being strongly sheared. This velocity profile is representative of plug flow. From Paterson (1981); figure 5.4.

The depth of a crevasse is controlled by the balance of horizontal and vertical stresses, and the maximum depth attainable represents the stage at which the horizontal pressure can no longer balance the vertical pressure exerted by the weight of the overlying material. Crevasses will therefore be limited to the upper layer of a glacier. From these observations it appears that glaciers can behave like lava flows with crusts, or like the experiments presented in this work, with an upper layer that travels at a uniform velocity and is able to fracture, and a lower layer that 'flows' and behaves in a more ductile manner. Deformation is therefore dominated by ductile,

perhaps viscous, processes in the lower layer and brittle processes in the upper layer, thus allowing comparison between glacial and lava flow fractures to be undertaken with a reasonable degree of confidence.

4.1.2 Fracture growth

In the experimental flows, opening of the arcuate fractures is not instantaneous, but begins at the centre of the channel, progressing to either side over time, so that the fractures appear to 'unzip' from the channel centre towards the margins. In thinner crusts, the rearmost fractures rarely fully achieve this unzipping, remaining as short fractures in the channel centre, which results in a parabolic region of fracture behind the flow front (figure 3.11). In thick crusts, variation in the widths of the arcuate fractures can be seen, and they are wider in the centre of the channel, narrowing towards the margins (figure 3.21).

The unzipping of the fractures, and the dependence of their shape on the velocity profile can be illustrated graphically. Figure 4.5 shows steady-state parabolic Newtonian velocity profiles for different channel centre velocities, on a plot of cross-channel distance versus velocity. The velocity is calculated using the following equation:

$$u = (\rho g \sin\alpha / 3\eta)(a^2 - r^2) \qquad (4.2)$$

where u is the velocity, ρ the density, g the gravitational acceleration, α the slope, η the viscosity, a the radius of the channel and r the distance across the channel.

Figure 4.6 shows velocity profiles for an *accelerating* flow for two different velocity gradients, which mimics the conditions prevailing at the flow front in the experiments. The original velocity profile is shown towards the left hand side, and then repeated in the direction of flow (towards the right) with profiles for increasing

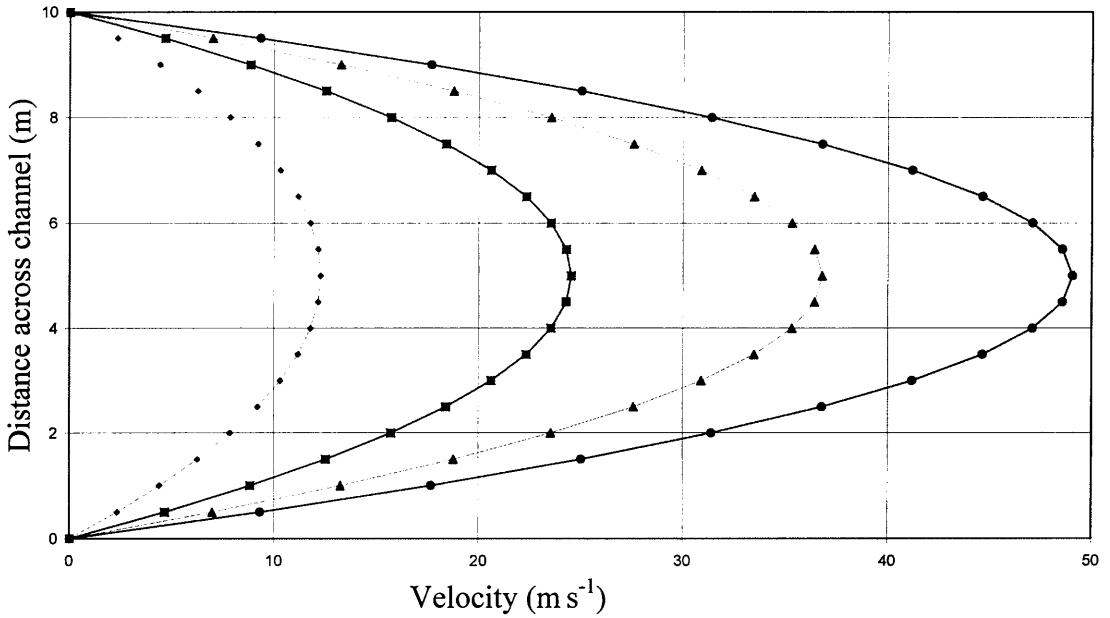

Figure 4.5. Plot showing velocity profiles across a channel for different gradients, calculated using equation 4.2. $\rho = 2000\ kgm^{-3}$, $g = 9.81\ ^{m\ s\text{-}1}$, $n = 4$, $\eta = 1000\ Pa\ s$. Sin α (sine of the slope) values for the curves, from left to right are 0.1, 0.2, 0.3 and 0.4.

velocity superimposed on each of the repeats. It is assumed that fracturing occurs when the flow is strained to a threshold value, and that this critical strain can be represented by a distance ε_{crit} between the original profile and the new profile for that locality. It can be seen that this distance is achieved first at the centre of the flow where the velocity is greatest, so the fracture will open first in the centre. As the velocity increases, ε_{crit} is achieved further out from the centre towards the margin, so the fracture propagates towards the margins of the flows, growing symmetrically. This explains the observed growth of the fractures in the models, and the fact that the fractures are widest at the centre and narrowest at the margins. Contrasting figures 4.6 (a) and (b), it can be seen that as the velocity gradient increases, the fractures become less curved, as ε_{crit} is achieved more quickly across the whole width of the flow. This explains the observations that the curvature of the fractures increases further back from the flow front, as the velocity gradient decreases upflow from the flow front.

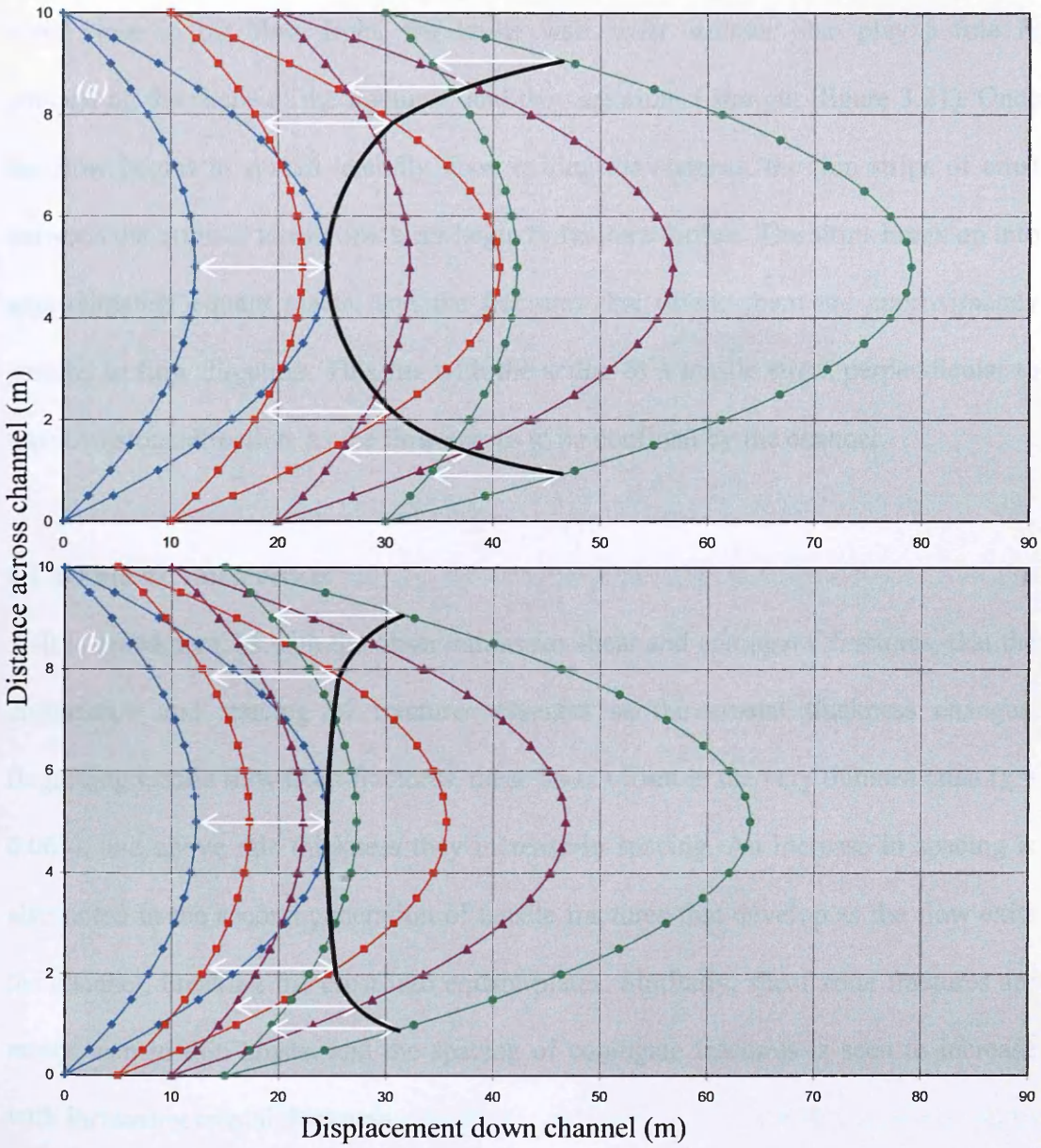

Figure 4.6. Velocity profiles of accelerating channelised flow. Displacement down the channel in m is on the x-axis, and distance across the channel in m on the y-axis. The different curves represent velocity profiles across the channel at different time steps. (a) Velocity profiles for a slowly accelerating flow. Blue, red, purple and green curves represent four different time intervals, and for each interval the original velocity profile is shown (left hand curve of the pair), together with a new one for the new velocity at that time (right hand curve). (b) Velocity profiles for a rapidly accelerating flow, with the same colours representing the same accelerations occurring over a shorter distances and times. Velocities are calculated using equation 4.2, with the same values of the parameters as used in figure 4.5. The sin α values are changed to simulate increasing velocity, with pairs of values used as follows: 0.1 & 0.2 (blue); 0.1 and 0.25 (red); 0.1 and 0.3 (purple); 0.1 and 0.4 (green).The distance between the two blue curves at the channel centre is defined as ε_{crit}. This strain is achieved further out towards the channel margins at later time steps, as indicated by the white arrows. The black curves indicate the shape of the fracture that develops. This is more curved for more slowly accelerating flows.

Very close to the flow front, the lower wall shear stresses also play a role in controlling the shape of the fractures, and they are almost straight (figure 3.21). Once the flow begins to spread laterally upon exiting the channel, the thin strips of crust between the original tensile fractures begin to fracture further. The strips break up into approximately equant plates, and the fractures that divide them are approximately parallel to flow direction. This fits with the action of a tensile stress perpendicular to the downslope direction, as the flow ceases to be confined by the channel.

4.1.3 Thin vs. thick crusts

It is noted here, as with the observations for shear and conjugate fractures, that the appearance and spacing of fractures changes as the crustal thickness changes. Regarding tensile flow front fractures, these do not form in the very thinnest crust (χ = 0.063), and above this thickness they increase in spacing. An increase in spacing is also noted in the second generation of tensile fractures that develop as the flow exits the channel, breaking the crust into equant plates. Similarly, shear zone fractures are rarely seen in thin crusts, and the spacing of conjugate fractures is seen to increase with increasing crustal thickness.

The slower flow front collapse in thinner crust models results in lower velocity gradients, and hence lower strain rates being experienced behind the flow front than in thicker crust models. As discussed above with reference to glaciers, it is strain rate, as well as total strain, which largely governs the ability of the crust to fracture, and it would appear that the strain/strain rate experienced during the initial extension of the thinnest crust flows did not reach sufficient levels to induce fracture formation. It is possible that the stretching and thinning of the very thin crusts can be accommodated by effective 'creep' in the crustal material, with small movements of the sand grains

being able to keep pace with the extension of the underlying material. This creep mechanism may also be operating in the shear zones of thin crusts, when the stresses are insufficient to cause fracture.

The increase in fracture spacing with crustal thickness may relate to how fractures propagate through the crust. It is possible that once the point of failure is reached in any crust, many fractures are initiated, but that in thick crusts only a small proportion of these manage to propagate through the whole thickness of the crust. In thinner crusts, it is easier for a fracture to develop through the whole crust, and so the majority of initiated fractures appear at the flow surface. A larger number of fractures also means that each fracture must accommodate only a small part of the total deformation, as so displacement across fractures in thin and intermediate crusts is less obvious than in thick crusts. This may, however, be influenced to a large degree by the smaller amount of deformation that needs to be accommodated by the slower moving thinner crust models.

4.2 Shear zone fractures

The morphology of shear zone fractures was seen to change with changing crustal thickness. Fractures were only observed in the marginal zones of the channel for two thin crusts, which suggests that, in the majority of cases, the stresses could be accommodated by creep of the sand grains, as discussed in the previous section. As the crustal thickness increased, the velocity and hence the shear stresses increased, until the accommodation of stress in this way was unsustainable, and the stresses and/or strain rates experienced were sufficient to cause fracturing. The fractures in intermediate crusts were short, linear, discrete features, regularly spaced and oriented at around 15 - 20° downflow into the levées (figure 3.18). As the crustal thickness

increased, these became longer, more widely spaced and less linear, with oblique extensions developing in up and down channel directions, which were more closely parallel to the flow margins. These began to merge in thicker crusts, forming a single fracture down each side of the channel (figure 3.22), and, for the thickest crusts, the development of the single fracture was rapid, and the intermediate stage was not always visible in the image sequences. Observations of point movements indicate that strike-slip motion occurs along the fractures, suggesting that they may be shear fractures. However, the crevasse studies of Nye (1952a) suggest that there may also be a tensile element to the stresses in this region.

As discussed with reference to the tensile fractures, the stress distribution in the channel determines the pattern of fractures that forms, and the reader is referred back to figure 4.1 for a sketch of the general stress distribution. Considering the case in which the longitudinal normal stress σ_x is compressive, as it will be in the upper reaches of the channel from the very start of the experiment, extending further down the channel over time, σ_1 will be a maximum in the channel centre, where it is parallel to the x-axis. Towards the margins, as the magnitude of σ_x decreases and that of τ_{xy} increases, the orientation of σ_1 becomes increasingly oblique to the x-direction, pointing outwards towards the levées. At the channel-levée boundary, the value of σ_x is zero, and so σ_1 will be oriented at 45° downflow into the margins, as it is influenced only by the shear stresses (figure 4.2). According to the Mohr-Coulomb hypothesis, the orientation of shear fracture surfaces to the direction of σ_1 within a compressive stress regime is at an angle, θ, equal to $\pm (45° - \varphi / 2)$, where φ is the angle of internal friction of that material being fractured. For the sand and plaster mix, φ is ~30°, and so θ is ± 30° to σ_1. Considering the orientation of σ_1 close to the margins, the shear fractures should be inclined at a fairly small angle to the levée (~15°), as is observed.

Note that only one of the possible orientations is developed, which is that closest to the orientation of the τ_{xy} direction.

As the crust becomes thicker, the velocity of the channelised flow increases, so the velocity profile across the channel becomes steeper. While the magnitude of σ_x will be much greater in the centre of the channel, it is still fixed at zero at the margins, and so its magnitude close to the margins cannot be expected to be significantly greater than for intermediate crusts. The magnitude of the shearing stresses, however, will be much greater than in intermediate crusts. The change in fracture behaviour suggests that the shear stresses are causing the angle made by σ_1 with the margin to decrease, as the fractures become more closely parallel to the flow margin, with angles of less than 10° being observed for the single fractures seen in thick crusts (figure 3.22). It is possible that the stage between oblique fractures and single fractures (oblique fractures with levée-parallel extensions up- and downflow) reflects the initial formation of oblique fractures under conditions of lower compressional stress, but as the stresses increase due to the build up of material behind the crust, the compressional stresses experienced at the margins increase, causing the change in fracture orientation. Another possibility is that once the crust has produced oblique shear fractures, it is weakened, allowing fracture growth in directions more closely parallel to the directions of the shear stresses.

In addition to the explanation of the fracture orientations solely in terms of shear fracture development, a possible tensile contribution to growth can be considered. In his consideration of glaciers, Nye (1952a) showed that close to the margins, the combination of a compressive longitudinal normal stress and the marginal shear stresses results in a large compressive principal stress, σ_1, oriented downflow into the margins at $\leq 45°$ (figure 4.7), and a small tensile principal stress, σ_3, perpendicular to

this. At the channel-levée boundary, the angle that σ_1 makes with the boundary will be 45°, but it will decrease rapidly into the channel. Tensile fractures open up perpendicular to the direction of σ_3, making angles of less than 45° with the margin, which die off towards the centre of the channel. This tensile element to the problem may be another reason why only one of the shear fracture directions is developed in the models: as well as being closest to the τ_{xy} direction, this orientation is also closest to the normal to the tensile stress direction.

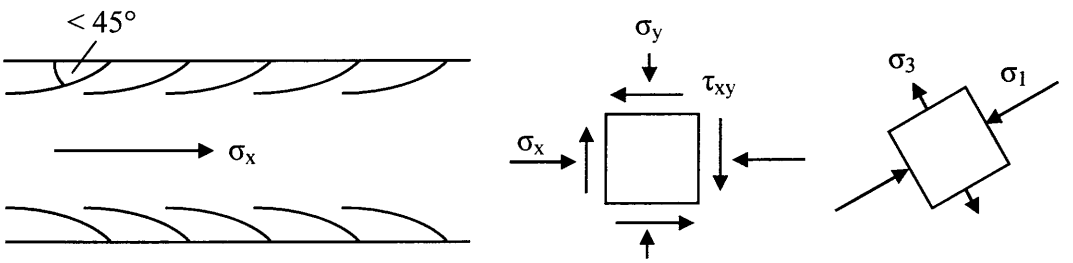

Figure 4.7. Crevasse pattern in a valley glacier if σ_x is compressive. The combination of σ_x and τ_{xy} gives a small tensile stress inclined at less than 45° to the valley margin, and a large compressive stress perpendicular to this. Fractures are oriented at less than 45° to the channel margin and die off towards the channel centre as the shear stresses tend to zero. From Nye (1952a); figure 9.

It was initially unclear from the monoscopic image sequences whether the change in fracture morphology represented a change in crustal failure mechanism associated with the different behaviour of intermediate and thick crust flows. While the oblique fractures in the intermediate crust could be explained in terms of the shear stresses in the channel, the single fractures that developed late in the thick crust models, defining a central crustal slab, bore a resemblance to marginal fractures that form in inflated pāhoehoe flows on Hawai'i (described in Hon et al. 1994). Due to the obvious bulge which forms underneath the crust at the head of the channel in thick crust models, it was known that silicone could flow under the crust, and so it was postulated that perhaps the whole flow could be inflating slightly, resulting in the marginal fractures.

A second possibility that was also considered was that the material flowing out at the front of the channel was draining the flow behind and causing sinking of the surface, which led to the fracturing. Since such a contribution to the fracturing process of widespread inflation or sinking could not be resolved in the 2D data, the experiments using stereo imaging were undertaken, to monitor the changes in surface relief. These results are shown in figures 3.32 and 3.33. As previously mentioned, red indicates areas of increasing relief, green shows areas of no change, and blue, areas of sinking. Fourteen experiments were conducted, covering all crustal thicknesses, using a slope of 4°. Figure 3.33 shows a thick crust model with $\gamma = 0.444$, covering four time intervals which span the time over which the single fractures develop. It can be seen that while the area of sinking behind the flow front is very large, and that a bulge is forming at the head of the channel, in the medial reaches of the channel, there is no change in surface relief that delineates the crustal slab from the marginal crust which remains on the outer side of the fractures, or the levées. A similar situation can be seen in figure 3.32 for the thin crust example. These observations allow more confidence in the shear fracture/tensile fracture explanation given above for the marginal shear zone features, as no other potential contributing processes can be distinguished in the data. It is therefore concluded that although the fracture morphology changes with increasing crustal thickness, the formation mechanism remains the same. A second reason for suggesting that inflation or sinking could be the predominant factor in changing behaviour is the late onset of fracturing in thick crusts compared to intermediate crusts. It was thought that perhaps the flow of silicone underneath the crust would take time, causing the onset of fracturing to occur later. Instead, it is now thought that the increasing thickness results in increased resistance to the stresses in the channel because of the greater unit strength, and possibly the increased time

required for fractures to propagate through the whole crust. The result is that the crust initially does not move in response to the flow of silicone beneath or the compressional stresses exerted by the influx from the reservoir. Instead, silicone flows under the crust at the rear of the channel, causing the bulging, and silicone flows out at the front of the channel, partially draining the flow behind. As the tensile fractures develop at the flow front and propagate up the channel, large plates of crust break off from the crustal slab, leaving a shorter region attached to the flow margins. Eventually, the friction between the crust and the levées is not sufficient to resist the compressional stress exerted by the influx silicone, and shear fractures do develop in the marginal zones. In several cases it was observed that the long shear fractures initially are not quite linear, but seem to be made up of several, slightly oblique, *en echelon* fractures, which rapidly join up to completely separate the crustal slab from the margins. These then smooth out by collapse, so that in later images the fractures appear almost straight.

4.3 Conjugate fractures

As the flow passes out of the channel, it begins to spread laterally as well as downslope. This causes downslope advance of the flow front to slow, and the initial tensile stresses that caused the arcuate fractures begin to diminish. As the influx from the reservoir advances down the channel, encroaching on the flow front, the stress regime in the flow front changes from tensile to compressional, as was illustrated by the gradual closing of the arcuate fractures with time. A second effect of the compressional stresses felt beyond the channel is the development of conjugate sets of crustal fractures across the whole flow front. These form in models of all crustal thicknesses, though their appearance changes with χ. The fractures develop as soon as

the flow passes out of the channel, and, after their formation, they advance without significant change in shape or orientation, until the latter stages of influx encroachment. The crustal plates appear to behave as rigid entities, with deformation taken up by relative motion or rotation of the different plates. This process is clearer in thick crust models, as the fractures are more distinct and there is a smaller number of larger plates. For thin crusts, the fractures are very fine, closely spaced features, producing an even, cross-hatched texture across the whole flow front, while for thicker crusts, the spacing increases and one orientation is commonly developed on either side of the flow centreline. For all crustal thicknesses, the fractures have orientations of ± 30° to the centreline of the flow. Stress directions in the flow front region are shown in figure 4.8, with σ_1 being everywhere parallel to flow direction, and compressional. The orientation of the fractures is in agreement with the Mohr-Coulomb hypothesis as discussed in section 4.2, forming at $\pm (45° - \varphi / 2)$ to the σ_1 direction, which is ± 30° as observed.

The fractures in thin crusts are very closely spaced (a few millimetres) and very fine, and no relative motion of the small crustal plates could be observed. As the size of the crustal plates increased, the fractures became more clearly defined, and different parts of the crust could be seen to move at different speeds. As would be expected from the cross-flow velocity profile, central plates move more quickly than marginal plates, and this caused rotation and lateral movement of the plates towards the edges of the flow (figure 3.25). In thicker crusts, the arrow-head shaped indenter can often be seen to produce a protruding flow lobe at the flow front. The differential motion of plates across the width of the flow may have implications for levée formation near the flow front, as the slower moving material near the margins is

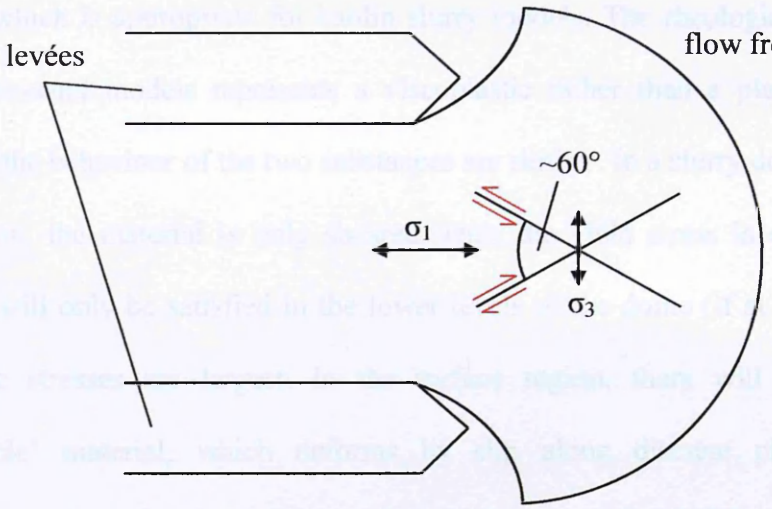

Figure 4.8. Stress distribution in the flow front, indicating the direction of the maximum principal stress, and the orientations of the maximum shear stresses. The fractures open up in these directions, at ± 30° to the σ_1 direction, meaning that the angle between the two sets of fractures is 60°. See text for details.

pushed towards the sides where it is likely to stagnate and stop moving (cf. rubble levées, Sparks et al. 1976).

The orientation and general appearance of the conjugate fracture suggests that they may be of a similar origin to the 'spiral slip planes' documented in the dome models of Blake (1990), Osmond & Griffiths (1998) and Balmforth et al. (2006) (figure 2.4), and the thin crust fractures of Buisson & Merle (2005) (figure 2.9). Similar features were observed and described by Bond (1988), in kaolin slurry flows on a slope, who dubbed them 'arcuate fracture zones' These were discussed in chapter two (section 2.3.2). While these examples involve the spreading of domes or unconfined flows, the flow front in my channelised models can be crudely thought of as representing half a dome, albeit on a slope and being fed from upslope. The stress conditions in the flow front due to the lateral spreading will be similar to those in spreading domes. As discussed in chapter two (section 2.4), the slip lines of Blake (1990) bear a remarkable resemblance to logarithmic spirals, which were described by Nadai (1950) for radial and laterally confined flow. Nadai's analysis involved the spreading of plastic

material, which is appropriate for kaolin slurry models. The rheological structure of the silicone-sand models represents a viscoplastic rather than a plastic, but some aspects of the behaviour of the two substances are similar. In a slurry dome of uniform composition, the material is only sheared when the yield stress is exceeded. This condition will only be satisfied in the lower levels of the dome (if at all), where the hydrostatic stresses are largest. In the surface region, there will be a plug of 'unshearable' material, which deforms by slip along discrete planes. This is comparable to the behaviour of a stratified model in which a brittle crust overlies a viscous interior, in that the crustal layer is essentially a plug, while the material below can be deformed. Although the behaviour of the deformable layer in the two materials is different, the deformation of the surface plug may be considered analogous in the two cases, thus allowing the comparison of the conjugate fractures with the logarithmic spiral slip planes. One significant point to note is that the two sets of slip planes in Nadai's analysis for radial flow are expected to be orthogonal, while it has already been shown that the conjugate fractures observed in my experimental flows meet at approximately 60°. Nadai's spirals also curved around the flow, whereas my conjugate fractures, in all but two experiments, appear straight. These discrepancies can perhaps be explained on the basis of the different geometry and composition of my flows, which have minimal curvature of the surface, and which are also fed by material flowing from upslope. As such, the σ_1 direction in the flow front region is in the direction of maximum slope at the centreline and everywhere else angled slightly out towards the margins. It will, however, always be influenced by the slope direction, and so will be a poor representation of a half-dome. The flat flow surface means that

the fractures will be straight, while the influence of the slope direction, coupled with the granular nature of the material results in angles of less than 90°, according to the Mohr-Coulomb hypothesis .

4.4 Compressional ridges

The flow of material into the channel was driven by the head of material in the reservoir (ρ_f g h sinα), while the downflow movement of material in the channel was initially driven only by its own weight, (ρ_f g F + ρ_c g T) sinα, where ρ_f and ρ_c are the fluid and crustal densities respectively, g the gravitational acceleration, h the depth of material in the reservoir, F the depth of the fluid in the channel, T the crustal thickness, and α the slope of the basal board. Since h >> (T + F), the material in the channel moved much more slowly than that draining from the reservoir. In thin crust models, this resulted in a bulge developing behind the crusted flow, as material entered the channel more quickly than it could be drained. The increased flow depth at the back of the channel resulted in a velocity gradient developing down the channel, as was seen in the 2-D surface velocity results (figure 3.29), hence the development of a compressional stress regime. The strain accompanying this compressional stress was accommodated by the crust buckling into ridges. In thick crusts, no buckling was seen, and silicone accumulated underneath the back of the crust instead, forming a bulge.

The wavelength of ridges was related to the crustal thickness, with smaller thicknesses producing shorter wavelengths. As the folds grew, they were subjected to differential stresses related to the velocity profile across the channel, and so developed a curved aspect with time. They also propagated down the channel with time. Often, ridges could be seen further down the channel in the marginal shear zones rather than in the channel centre, which possibly indicates the importance of boundary effects, as

folds have been observed to form as a result of wrenching along flow margins (Coward & Potts 1983; Odonne & Vialon 1983; Ridley & Casey 1989). It may also indicate that the crust is thinning in the marginal regions due to the shear, and so the stresses are able to produce folds here more easily than in the channel centre. The orientation of the marginal ridges can be seen to reflect the orientation of the principal stresses in the channel, as discussed in section 4.2 with reference to shear fractures. The major principal stress, σ_1, is oriented at an oblique angle downflow into the levée, resulting in a shear fracture oriented at around 15 to 20° downflow into the levée. The compressional ridge will be oriented orthogonal to the direction of σ_1, which was shown to be approximately 45° downflow into the levées in figure 4.2, which should result in the ridges being oriented at around 45° upflow into the levées. This is in fact somewhat larger than the observed angle, which ranged from approximately 20° to 40°. The discrepancy between the expected and observed angles may indicate that the folds are being influenced by the shearing in the marginal regions, or are being stretched out in the direction of flow. While the fractures and folds would be expected to intersect at approximately 60°, the observed angle of intersection is actually around 45° (figure 4.9).

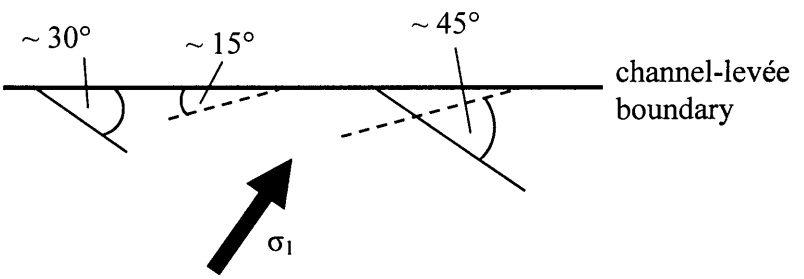

Figure 4.9. Orientation of structures at the channel-levée boundary (heavy line). Fracture orientation is shown by the dashed lines, and marginal fold orientation by the faint solid lines. The σ_1 direction is indicated. Folds and fractures intersect at more than 45°.

Regularly spaced surface ridges of varying scales have been observed on lava flows of all compositions, and examples of these are shown in chapter five. Surface ridges are most well known from pāhoehoe flows, which have been extensively documented on Hawai'i (e.g. Wentworth & Macdonald 1953; Macdonald 1972), and many other volcanoes. These ridges appear as laterally continuous arcuate structures, symmetrical about the centreline of the flow, with open ridge crests separated by tight cuspate troughs (figure 4.10). Observations of active and solidified flows

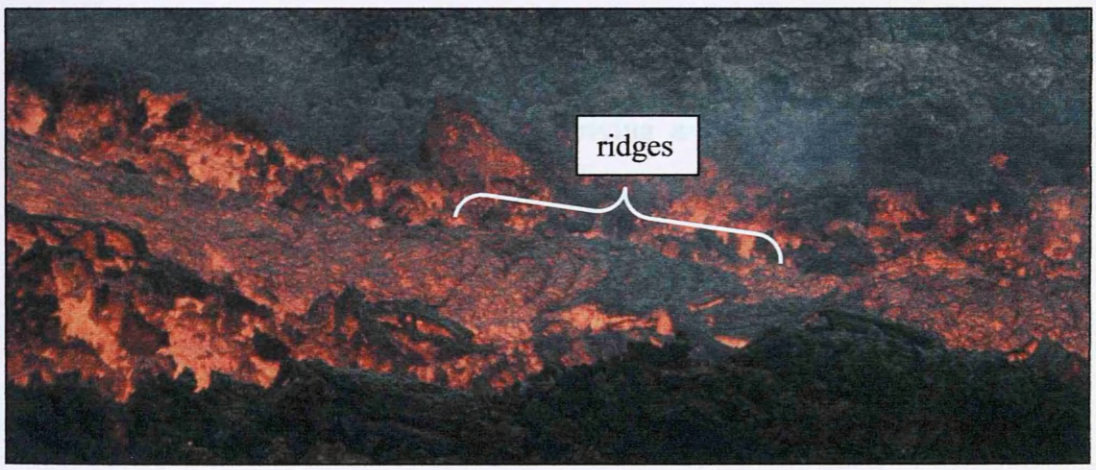

Figure 4.10. Surface ridges on pāhoehoe lava, showing smooth curved anticlinal summits and synclinal cusps. The ridges are forming in response to a decrease in the local slope. Channel is approximately 1 m wide.

indicate that the ridges develop in regions of shortening within the channel, where the velocity of the lava decreases, for example, due to breaks in slope (Fink & Fletcher 1978). Once the ridges have formed, they move downstream, taking on a parabolic shape in response to the velocity profile. As the flow cools further and the crust thickens, they eventually stop being deformed, though if a new region of shortening is encountered, a second phase of folding can occur. Due to the increased thickness of the thermal boundary layer, this second generation will have a longer wavelength, as is observed with increasing crustal thickness in the experiments.

The folding process in pāhoehoe is described by Fink & Fletcher (1978) as 'one in which the initially perturbed surface of a fluid whose viscosity decreases with depth is shortened, causing a certain wavelength of the perturbation to be selectively amplified into folds'. The fundamental point to note is that folding will not occur without a decrease in viscosity with depth. Fink & Fletcher (1978) analyse the folding process using a linearly viscous fluid (Newtonian) which is subjected to uniform shortening in the flow direction across its whole depth, dealing with the initial stage of the process in which the arc length of the folds is established. The viscosity structure is approximated by a thin surface layer within which the viscosity decreases exponentially as a function of depth, overlying a fluid half-space in which the viscosity is uniform (figure 4.11, curve b). These assumptions are deemed appropriate because the temperature of a flow decreases rapidly across a thin boundary layer from the nearly uniform interior value, and because the length scale of the folds is small compared with the total flow depth.

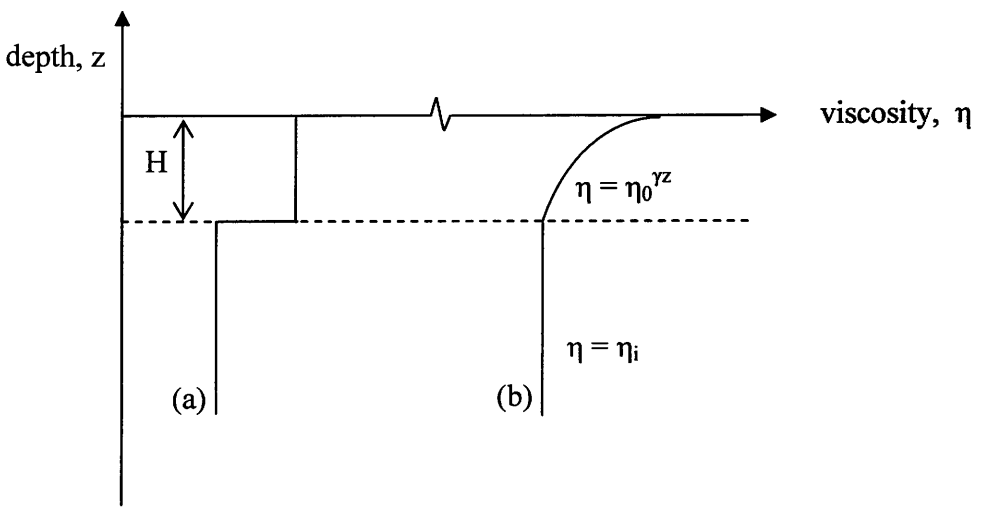

Figure 4.11. Viscosity structure in the analogue models (a), compared to that used in the folding analysis of Fink & Fletcher (1978) (b). The depth of the thermal boundary layer is H. See text for details.

The rheological structure of the fluid can be described by the following equation :

$$\eta(z) = \begin{cases} \eta_0 \exp(\gamma z) & -H \leq z \leq 0 \\ \eta_i & z < -H \end{cases} \qquad (4.3)$$

where η_0 is the viscosity of the surface layer, η_i the interior viscosity, z the depth measured from the flow surface, H the thickness of the surface layer, and γ a parameter which affects how quickly the viscosity decreases with depth. A small γ indicates a low viscosity (temperature) gradient across the thermal boundary layer, while a large γ indicates a high gradient. If the interior viscosity is the same in all cases, decreasing γ values will represent decreasing surface viscosities, η_0. The viscosity at the base of the thermal boundary layer must equal that of the interior, hence:

$$\eta_i = \eta_0 \exp(-\gamma H) \qquad (4.4)$$

In order to be able to describe the folding process, the viscosity must be known both in the interior and at the surface. The rheological structure of the experimental flows presented here can be approximated on the same plot as the structure used by Fink & Fletcher (1978), as shown by curve (a) in figure 4.11. However, while the interior viscosity can be quantified, that at the surface cannot, save to say that its effective viscosity is much greater than that of the interior. Moreover, there is no viscosity gradient over the surface layer, and so γ could not be defined for the experimental flows. This precludes the application of the folding analysis employed by Fink & Fletcher (1978) to this work, though is has been successfully applied to analogue models using solidifying PEG extrusions, by Gregg et al. (1998).

Despite the difficulties with the quantitative comparison between the theory for lava and for the experiments described here, the qualitative results suggest that the folding process that occurs in the experimental flows is similar to that described by

Fink & Fletcher (1978). It was noted in the discussion of thin crust morphologies (section 3.3.1.2) that the surface of the flows often took on an uneven texture during the early stages of the experiment, which was described as 'rippled', before continuous folds developed. Figure 4.12 (a) shows an example of this texture, 35 minutes into an experiment, while 4.12 (b) shows the results of the three-dimensional surface tracking for a period of 6 minutes immediately before this image was taken. Although no folds are visible in (a), the plot of vertical displacements shows three distinct bands of positive change, indicating that the folds are already forming. This suggests that the mechanism for fold formation may be similar to that described by Fink & Fletcher (1978), despite the different rheological structure. Due to a mechanical instability (Biot 1961), initially small perturbations of the surface are selectively amplified or quashed, according to their wavelength, and a single wavelength becomes dominant in the folds that eventually develop. Although Fink & Fletcher's model was originally developed for the surface folding of basaltic pāhoehoe, it has subsequently been applied to lavas of more evolved compositions. Fink (1980) studied rhyolitic obsidian flows at Glass Mountain, Minnesota, and concluded that the morphological similarity between pāhoehoe ropes and the rhyolitic ridges suggested a similar mode of formation. Although estimating physical properties for rhyolitic flows is more difficult, the use of estimated ranges for these parameters was found to fit with the measured ridge spacing well. While ridges on pahoehoe are commonly found in regions of slope decrease or where the channel narrows or becomes blocked, ridges on rhyolite flows can develop because the brecciated flow fronts have effective viscosities some orders of magnitude greater than the bulk flow viscosity (Friedman et al. 1963) and therefore retard the advance of the more fluid

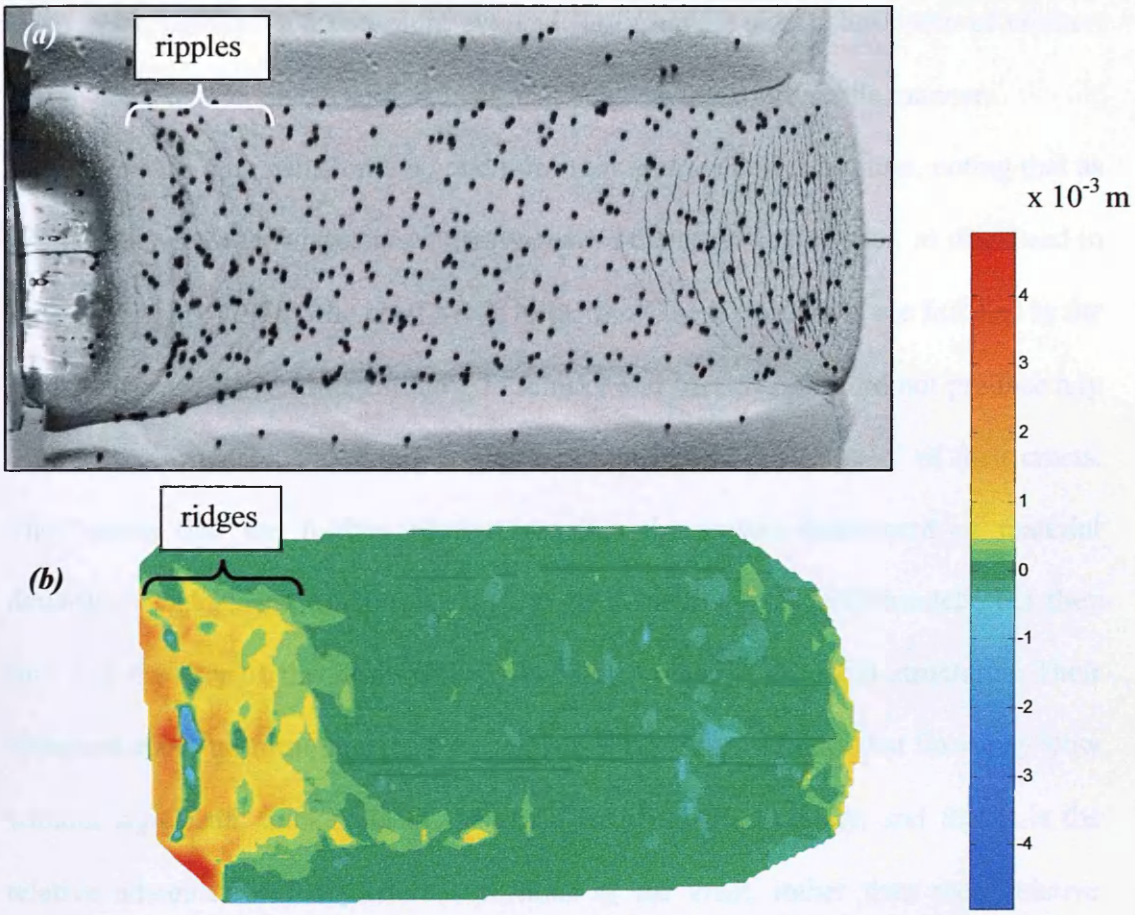

Figure 4.12. Experiment 34, χ = 0.167. (a) Image taken 35 minutes into the experiment. Flow is approximately 35 cm long. (b) Changes in surface relief during the 6 minute period immediately before the image was taken. Plot is aligned with the area of the flow it is representing, i.e. the crusted region. Colour bar shows relief changes in mm (10^{-3} m).

material behind. The application of the theory of Fink and Fletcher (1978) to active lava flows is considered further in chapter five.

As previously mentioned, ridge structures are commonly documented on flows of all compositions, and it is probable that the rheological structure of more evolved flows is more similar to that in my models than to that of pāhoehoe. Pāhoehoe surfaces are unfragmented, and the rheological conditions that lead to folding are probably quite well described by Fink & Fletcher's model in which the viscosity decreases exponentially through the boundary layer and is constant beneath this layer.

In contrast, basaltic `a`ā and more evolved flows have a significant cover of clinker, and so are likely to have a surface layer that behaves in a more brittle manner.

Fink (1978) comments on the conditions required for fold formation, noting that as well as the necessary viscosity contrast between the crust and interior, as discussed in Fink & Fletcher (1978), the crust needs to be thin. These conditions are fulfilled in the models presented here. Interestingly, Lescinsky and Merle (2005) did not produce any folds in their models, which they attributed to the 'uniform thickness' of their crusts. They noted that the folding process requires the slower movement of material downflow, and indeed do simulate this in their moving back wall models, but they find that the rear of the flow thickens without producing any fold structures. Their comment about uniform thickness does not consider the possibility that flow may slow without significant thickening of the crust occurring immediately, and that it is the relative advance rates of different portions of the crust, rather than their relative thicknesses, that induce conditions favourable for folding. Indeed, the crustal thicknesses used in the experiments presented here are uniform, and folds are still produced. The conditions in Lescinsky & Merle's experiments at first glance appear to be favourable for folding, but examination of their flow conditions may help explain why none were produced. Of a total of thirty six experiments, seven were conducted using moving back walls, and of these, only three used crusts, all of which had a brittle rheology. These three experiments had χ values in the range 0.162 to 0.189, which places them in the thin to lower-intermediate crust range, according to the classification used in this work, and so it is perhaps surprising that none of them produced folds. However, it is unclear from the article whether these experiments, which all recorded the same value for back wall velocity, had simulated constant or increasing effusion rates. It may be assumed that folds will only be produced if the

effective effusion rate is increasing. If it is assumed for the sake of argument that the simulated effusion rates *were* increasing, another explanation must be found for the absence of folds. Examination of their flow dimensions can also shed some light on the important factors controlling experimental morphologies. Although the χ values of the flows were in the thin to intermediate crust range, their total flow thickness was considerably greater than in the experiments presented here (36-37 mm compared to 16-18 mm respectively), and their crusts were 6-7 mm thick rather than 1-3 mm. It therefore seems that it is not merely the *ratio* of crustal thickness to the total flow thickness which is important, but the *absolute* thickness of the crust, as suggested by Fink (1978). It should also be noted that not all of the simulations presented here with crustal thicknesses of 6 mm (χ = 0.286) produced folds, and that the models of Lescinsky & Merle were conducted on a slope of 6°, which is higher than that in the majority of my models, and could possibly dampen the tendency to produce folds, as is discussed in section 4.7. With such a small number of models, it cannot be definitively concluded that the model conditions used by Lescinsky & Merle would never produce folding.

4.5 Marginal ropes

As the thin crust experiments progressed, the folds propagated downflow, eventually reaching the flow front, where they could be traced from one side of the channel, around the influx, to the other side. This resulted in the formation of marginal ropy fold structures which were oriented at a small angle (± 20°) to the downslope flow direction. These structures were also seen, though over a more limited area, in thicker crusts, when they could not be linked to earlier folding events (figure 4.13). The wavelength of the ropes was very small ($\leq$ 2 mm), suggesting that they form in

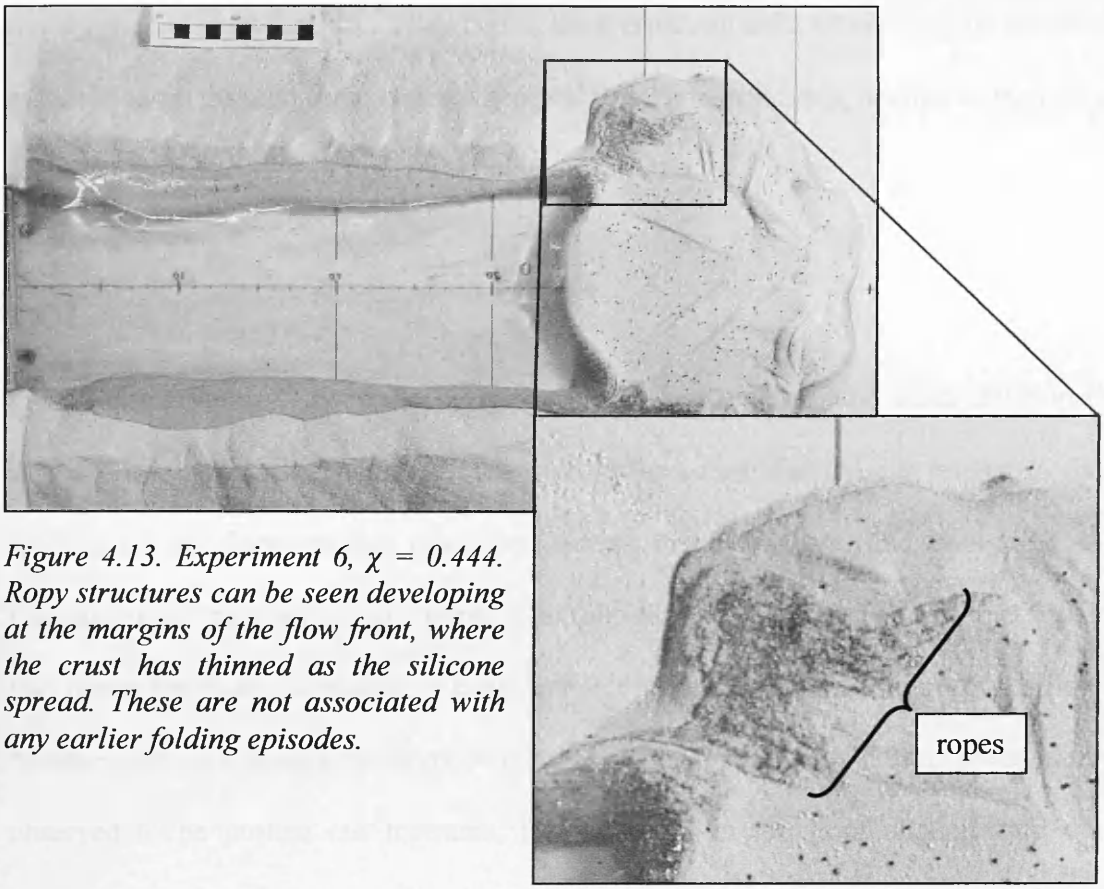

Figure 4.13. Experiment 6, χ = 0.444. Ropy structures can be seen developing at the margins of the flow front, where the crust has thinned as the silicone spread. These are not associated with any earlier folding episodes.

areas of thinning crusts. This is more obvious in the thicker crusts examples, where the ropes develop close to the margins of the flow, at the ends of the levées. In figure 4.13 it can be seen that the silicone is becoming visible through the crust in these regions. It is likely that stretching is a maximum in these regions, as the flow rounds the end of the levées and begins to flow back up slope slightly, as well as merely spreading across the slope, as was seen in figure 3.31. In thick crusts, thinning can only be seen in these small regions; elsewhere, deformation is accommodated by fracturing and the crustal plates maintain their rigidity. In thinner crusts (figure 3.15), ropes can be seen to extend for a significant distance along the channel margins, suggesting that thinning of the crust occurs in the shear zones also. This has already been suggested when considering the fact that compressional ridges extend further down the flow in the marginal zones than in the centre of the channel. The thinning of

the shear zone crust was also described in thick crusts models, where silicone was felt to be rising up through these zones when probing them with a pin, leading to the cross sectional structure seen in figure 3.23 being inferred.

4.6 Lobes

The observations showed that flow front lobe structures became better developed as the crustal thickness increased. The size of the lobes was closely related to the spacing of the fractures that developed across the flow front, and two different mechanisms were observed to contribute to lobe formation. Firstly, as the crust broke into plates due to the formation of conjugate fractures, the viscous interior of the flow became unevenly loaded. Regions of the flow front topped with crustal plates were observed to be pushed out forwards, leaving clefts in the front aligned with the interstitial fractures (figure 3.17). This accounts for the observed correspondence between lobe size and plate size or fracture spacing. Lobes were rarely observed in thin crust experiments, which may be due to the weight of the crust being insufficient to press the front out into lobes. However, a second mechanism was also seen to contribute to lobe development: as the flow advances, crust is rolled over at the flow front, and if this builds up in sufficient quantities (obviously related to the crustal thickness), it can affect the advance of the flow. In thin crust experiments, the amount of crust being rolled over is very small, and, combined with the very small crustal plates that are separated only by very narrow fractures, this generally results in no lobes developing. As the fracture spacing and width increases, then the amount of crust avalanching off the front, as well as increasing, becomes more unevenly distributed, causing differential retardation of the flow front, and hence lobes.

4.7 Effects of slope

As previously mentioned, the resultant surface morphology was found to depend predominantly on the thickness of the brittle crust, rather than the topographic slope. Some observations, however, indicated that a high slope can result in structures appearing at lower χ values than would be expected: in essence, the slope seems to change the bounding χ values for the thin, intermediate and thick crust morphological categories. For example, experiment 10, which had $\chi = 0.167$ (classed as a 'thin' crust) and a slope of 12°, developed oblique shear zone fractures which were only seen in one thin crust experiment, with a low slope (experiment 38). Experiment 38 was also found to develop an irregular flow front. It is possible that the structures are very sensitive to crustal thickness, and that the crust in this experiment was slightly thicker than intended. Experiment 10 also developed a slightly more uneven flow front than was usually recorded for a thin crust.

Other anomalous examples include experiments 7 and 12, which had $\chi = 0.286$ and slopes of 8° and 12° respectively. In these models, silicone was observed to well up through the tensile flow front fractures, a phenomenon that was not observed below $\chi = 0.375$ for slopes of 4°. However, experiment 16, which also had $\chi = 0.286$ and a slope of 8° did not show any evidence of upwelling. Interestingly, this experiment developed compressional ridges, whereas experiments 7 and 12 did not. This discrepancy, with two supposedly identical models (experiments 7 and 16) displaying thick and intermediate crust morphologies respectively suggests that the morphologies are very sensitive to small changes in crustal thickness, and also possibly that the critical value of χ delineating the regime change is very close to 0.286. If this is the case, then a small inaccuracy in the measured crustal thickness when adding the crust could produce an observable change in morphology.

The phenomenon of thinner crusts appearing 'thicker' can be attributed to the faster advance of the flow, hence the greater stresses in the channel, and the greater instability of the flow front. Regarding the shear zone fractures that developed in experiment 10, a thin crust model, the greater velocity would have resulted both in a larger compressive stress down the channel and larger sidewall shear stresses, which enabled the fractures to open up. The higher slope also resulted in increased instability of the flow front, causing more crust to avalanche off the front, and producing conditions conducive to the development of lobes. The more rapid collapse of the flow front would also allow the tensile fractures to open at a greater rate, making it easier for upwelling to occur, as was observed in the intermediate crust experiments 7 and 12. A higher slope effectively produced similar conditions to those induced by increasing crustal thickness: larger channel velocities, greater velocity gradients across the channel, and greater shear stresses at the sidewalls.

4.8 Discussion

As discussed in chapter two (section 2.5) the flow of lava down a slope is controlled by the balance between driving and retarding forces. In the case of the experimental flows, the driving force is gravity, and the retarding forces are the silicone viscosity, the frictional effects of the levées acting on the flow margins, and whatever stresses are exerted on the viscous flow core by the brittle crust. Initially the advance of the flow front is driven only by gravitational forces acting over the depth of the seed flow, but over time, the influence of the deeper influx is increasingly felt. The velocity of the influx itself will decrease over time as the level in the reservoir drops, and so the flow in the channel initially experiences an increasing 'effusion rate', which then dies off with time. Although this is not precisely controlled or

measured, the general pattern described above is similar to that described by Wadge (1981), in which an eruption is characterised by an initially rapidly increasing effusion rate, followed by a gradual decrease. This is a gross simplification of the situation, as eruptions are commonly found to have fluctuating effusion rates, producing surges and pulses interspersed with periods of either waning or relatively constant flow rate. In any case, a set of eruption conditions for a suite of models must be decided upon, and no model can capture the full range of behaviour of the natural system. The experiments in their entirety are indeed a simplification of conditions prevailing during an eruption, as previously discussed, but while they are unable to represent the conditions that would be experienced throughout an entire flow field, it is hoped that as well as being a useful method of studying surface morphology, they can provide insights into the dynamics of single lobes that develop during an eruption, for example marginal overflow lobes. In these cases, it is likely that the effusion conditions are more directly comparable, as overflows commonly form during surges in flow down a main channel, so they initially experience an increasing supply ('effusion') rate, which decreases and is cut off as the level in the main channel again drops below the height of the levées.

All observations have indicated that the experimental flow models are a useful analogue for the emplacement of lava flows, and also glaciers. One of the key outcomes of the simulations is that thin and thick crusted lava flows respond very differently when subjected to similar stress regimes. This has implications for lava flows where progressively thicker crusts represent increasing amounts of cooling and thus increasingly distal channels. The spectrum of crustal thicknesses, i.e. morphologies, in the simulations therefore reflects a range of stages in flow

emplacement. Thin crusts, corresponding to the conditions prevailing in proximal channels, deform easily under compression, with the entire carapace being affected. At the beginning of a flow simulation, the crust of these flows begins to respond as soon as the fluid from the reservoir comes into contact with the seed flow. In addition, the parabolic nature of the folds that are produced, and the surface velocity profiles generated from the 2-D monitoring indicate that the crust is unable to resist the drag forces of the viscous flow beneath. The inferred vertical velocity profile is shown in figure 4.14 (a), and in these flows no shearing is thought to occur between the crust and the viscous interior. By contrast, in flows with thicker crusts, the carapace is more resistant to compressive deformation and shearing, so initially does not respond to changes beneath it. This is shown by the absence of contours at the head of the channel, and by very low velocities in the upper and medial parts of the channel. Instead, silicone flows under the back of the crust causing the flow to inflate, and silicone flowing out at the front of the channel partially drains the flow behind, causing a large region of tensile fractures to develop. The crustal thickness does not affect the development of tensile fractures to the same extent as it affects morphology at the head of the channel, as increasing crustal thickness produces some increase in compressive strength, while leaving the tensile strength unchanged.

For any crustal thickness, the carapace is stronger in compression and shear than in tension. The inferred vertical velocity profile for the early stages of a thick crust flow at the head of the channel (figure 4.14 b), shows that the crust is probably retarding the flow of silicone beneath, at least at the start of the experiment, resulting in a reverse sense of shear in the top of the viscous flow. Eventually, however, the progressive collapse of the flow front weakens the resistance of the crust, and it begins

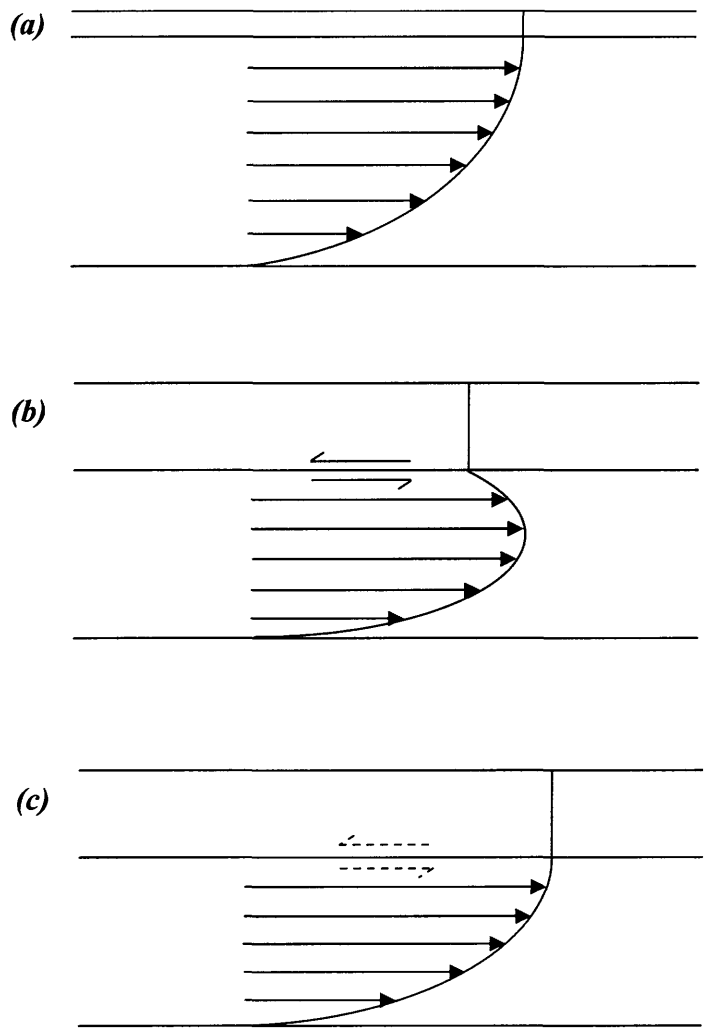

Figure 4.14. Inferred centre-channel vertical velocity profiles. Arrows indicate flow direction. (a) Thin crust. Crust sits passively on flow, exerting no shear on the core. This is equivalent to a very thin plug. (b) Early stages of a thick crust experiment. The crust is stationary, with the silicone moving beneath, and so there is shearing at the crust-core interface. This is similar to the profile that would be expected for a flow in the early stages of tube formation. Once a tube is fully established, the profile in the core would be parabolic, constrained to zero velocity at the base and the crust-core interface, and symmetrical about a centre line of no shear. (c) Later stages of thick crust flow, after the shear zone fractures have formed. The crust is again sitting more passively on the flow core, though some shearing is inferred to explain the plug flow surface profiles when the flow interior is Newtonian. Comparing (a) and (c), it can be seen that increasing the crustal thickness is similar to increasing the yield strength, as it results in a greater plug depth. After Merle 1998; figure 1.

to shear down the channel margins, leading to the velocity profile shown in figure 4.14 (c). This initial resistance to movement, however, suggests that although a self supporting roof does not form in any of the models, increasing crustal thickness,

corresponding to more distal channels, leads to conditions that are closer to tube flow. It is highly unlikely that tube flow could ever be reproduced in models such as these as the cohesion, or strength, of the crust is not great enough.

Once the marginal shear zones have developed, it is probable that the vertical velocity profile reverts to one more like the thin crust model. One distinct difference between the thin and thick crust end members is that some shear must occur either within the crust or between the crust and interior, or that the fluid velocity profile must be modified by the presence of the crust, for the thick crust models (figure 4.14 c). This is because while the cross-channel velocity profile must be parabolic in the underlying silicone, the profile recorded at the flow surface is one of plug flow. The shape of the velocity contours in figures 3.29 and 3.30 can therefore be used to illustrate which part of the flow is more influential as regards the movement of the surface. Parabolic contours indicate that the fluid has the greater influence and is deforming the crust, whereas if the crust is more influential, the contours would be expected to show a greater degree of plug flow. The increasing crustal thickness has been shown to result in flatter contours at the channel head, while the contours at the flow front remain parabolic (figure 4.15). This indicates that while the fluid is always more influential at the flow front, the crust becomes increasingly influential at the head of the channel, and this can be attributed to the fact that the crust is stronger in compression than in tension.

The problem of representing lava flow rheology in isothermal models using Newtonian fluids was discussed in chapter two, and the results of previous modelling attempts have been used to argue that such approaches can still produce useful results. Having analysed the experimental structures presented here, and compared the flow conditions and resultant structures with analyses of natural flows of lava and ice, this

argument still stands. However, it is interesting to note that despite the two component viscous-brittle structure of the simulations, the 2-D surface velocity results and inferred vertical velocity profiles show that the models in fact also represent the flow of a viscoplastic material. For thinner crusts, the cross-channel surface velocity profiles are indeed close to parabolic, but as the crust thickens, the profiles increasingly resemble plug flow profiles (figure 4.15). For all experiments with crusts, the vertical velocity profiles are likely to show plug flow, with the thickness of the crust corresponding to the thickness of the plug, hence thicker crust experiments represent increasing compressive yield strengths (as seen in figure 4.14). While real flows would not necessarily be expected to have a linearly viscous layer beneath the unsheared plug, if the rheology is thought of as Bingham, or pseudoplastic and subjected to a small range of strain rates, the stress-strain rate behaviour of the sheared layer could be adequately described using a Newtonian model.

Another significant difference between the analogue models and lava flows concerns the viscoelastic layer. This layer, described by Hon at al. (1994) and Cashman et al. (2006), and discussed in chapter two, has been inferred to be the primary control on flow advance, with limited importance attached to the influence of the brittle carapace. However, the experiments presented here are known to have no viscoelastic layer, which indeed would be difficult to scale to a natural system, and yet have produced structures which can be compared to those on real flows, further examples of which are presented in chapter five. From these results, it may be argued that while the viscoelastic layer is a very important area of future investigation, both in field work and modelling approaches, the influence of a purely brittle crust certainly cannot be ignored, and has been shown to be a significant control on the structures produced during flow advance. The combination of a Newtonian fluid with

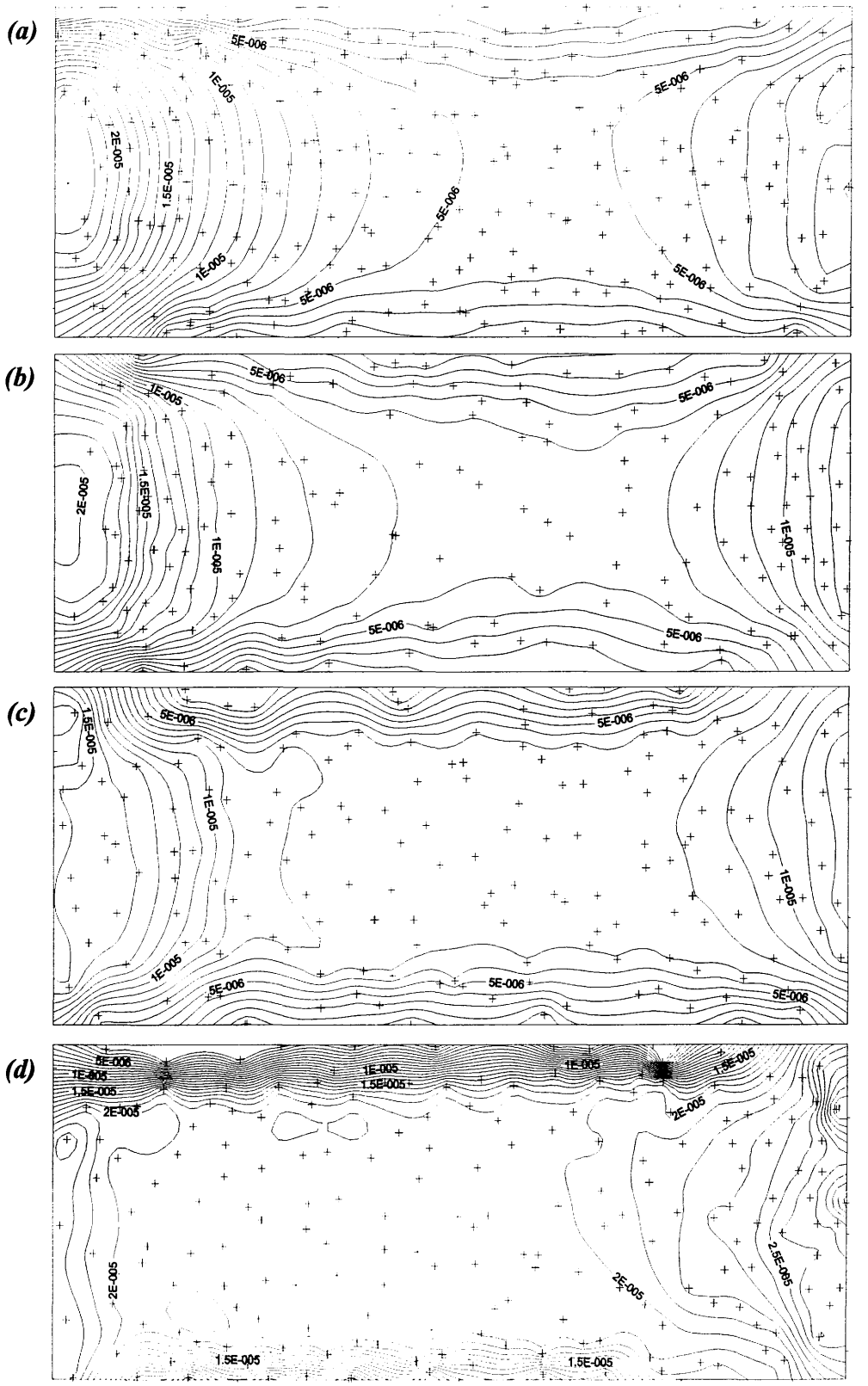

Figure 4.15. Contoured velocity plots for the time interval ~7-12 minutes in four different experiments. (a) χ = 0.63; (b) χ =0.167; (c) χ = 0.286; (d) χ = 0.375. Contour spacing is 10^{-6} m s $^{-1}$. The contours at the head of the channel can be seen to become increasingly flattened as the crustal thickness increases, while those at the flow front do not differ significantly. See text for details.

a brittle crust is therefore widely applicable in simulations of natural flows, and can be used with confidence in the modelling of cooling lava flows and glaciers, with possible extension to other flows of similar rheology such as debris flows.

The resulting morphologies observed in the experiments indicate that a thicker crust plays an increasing role in controlling the advance of a flow. This is in agreement with the results of dome modelling experiments by Griffiths & Fink (1997), discussed in chapter two, who showed that thin crust domes are controlled by the viscous flow interior, and thick crust domes by the resistance of the carapace. It is noted that despite the isothermal nature of the experimental flows described here, the influence of a thick brittle crust at the flow front can produce morphologies similar to those of the cooling flow fronts of Griffiths & Fink (1997). In the thick crust experiments presented here, flow fronts are observed to thicken over time as the flow front is retarded (dammed) by the avalanched crust in front. Material arriving from upslope causes crustal plates to be tilted forwards and piled up around the slower-moving front. Interstitial silicone ridges can then be squeezed out in the direction of flow, and override crustal plates downflow. These processes are never observed in thin crusts, and produce very complex internal structures in thick crust models, as shown in figures 3.27 and 3.28. Observations of solidified flow fronts, and predictions from analogue models of cooling flows (e.g. Anderson et al. 2005) have shown that complex internal structures can develop in lava flow fronts with time, perhaps due to the viscosity gradients present. Anderson et al. (2005) showed that 'viscous fingering' could take place in a cooling flow, whereby hotter, less viscous fluid penetrates into the cooler, more viscous frontal portion of the flow. Inferred internal structures of solidified flows and domes frequently show a simple three layer structure in the more

proximal parts of the flow, with basal breccia overlain by a massive flow interior that is in turn covered with clinker and blocky rubble (e.g. figure 3.8), while the flow front structure is expected to be considerably more complex (e.g. figure 4.16). The structures described from the experimental models agree with these observations and predictions, as behind the flow front the structure remains relatively simple, while the flow front itself incorporates plates of crust within the flow interior, and squeeze outs

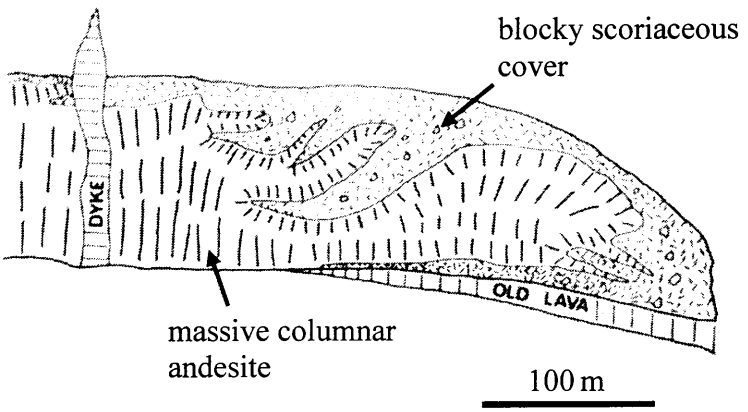

Figure 4.16. Section through an andesitic lava dome exposed in the crater wall of Soufriere volcano, St. Vincent, showing the complex relationship between the massive interior and the scoriaceous surface cover. From Huppert et al. (1982); figure 14 (a).

of interior material through fractures in the crust.

It has been noted in this work that thicker crusts, i.e. cooler flows, lead to a greater degree of interaction between the crust and the flow interior. Observations of model development showed that thicker crusts were more easily and permanently disrupted at the flow front, resulting in upwelling through the arcuate and conjugate fractures, and the incorporation of crustal material into the flow interior. Fractures that developed in thin crusts did not widen to the same extent due to the lower velocity, and the flow interior was therefore subjected to less exposure to the ambient environment. The entrainment of crustal material into the interior of active flows has been observed by Crisp & Baloga (1994), who noted that entrainment enhances flow

cooling by advection, and is therefore important when considering the heat budget of a flow. The experiments indicate that as the crustal thickness increases, the greater disruption results in increased entrainment of crustal fragments. Although it might be expected that thicker crusts would lead to the greater insulation of a flow, and thus a lower cooling rate, the results presented here suggest that there may actually be a positive feedback mechanism operating in the flows. In this scenario, cooling results in fractures which are more difficult to heal, and so exposure of the flow interior increases. Added to the greater amount of entrainment observed in thicker crusts, this would suggest that increasing crustal thickness could in fact lead to an increased rate of cooling, therefore reinforcing the tendency of the flow front to cease moving. The increased resistance of thicker crusts to the flow of material behind could also result in surface flows, as the flow front is overrun by hotter material, which could result in fracturing and entrainment of underlying crustal material. These observations could be important in understanding the cessation of cooling limited flows.

4.9 Concluding remarks

While this chapter has concentrated on the analysis of the structures produced in the experimental flows described in chapter three, the following chapter moves towards the consideration of lava flows in the field. After first drawing parallels between surface structures seen in the models and features observed on lavas and glaciers, the problem of increasing flow complexity is addressed. The simulations presented here have allowed the modelling of simple flow lobes, while the emplacement of lavas rarely involves a single channel and flow front, and the factors that can cause the complex morphologies commonly described in the field are briefly

discussed, before chapter six presents a comprehensive study of the emplacement of a compound flow field.

5. Scaling Up: From Experiments to Field Studies

The observations and interpretations of surface morphologies produced in the analogue experiments have provided insights into the behaviour of rheologically stratified flows, and the interactions that can occur between the fluid interior and brittle crust of a two-phase flow. In order to apply the experimental results to the interpretation of naturally occurring flows with confidence, it is necessary to make comparisons between the surface morphologies observed in the two systems. The first part of this chapter provides examples of natural flows, of both lava and ice, which exhibit structures closely resembling those that developed in the experimental flows. This resemblance provides support for the assumption of dynamic similarity between the analogue and natural systems. However, as discussed in chapter four, the analogue models are considered to be representative of the emplacement of individual flow units, while lava flows are commonly observed to demonstrate compound morphology, consisting of many overlapping units. The structure of complex flow fields is therefore introduced in the second part of the chapter, which considers both the factors that result in compound morphology, and the types of structures that can develop within flow fields. While the remarkable similarity between analogue and natural flows indicates that the usefulness of analogue models in illustrating the importance of individual processes is beyond doubt, their limitations are necessarily highlighted by these observations. The final section of the chapter considers the many gaps that still exist in our understanding of lava flow emplacement, highlighting the importance of continued field observations, which form the basis of the following chapter.

5.1 Natural flows with straightforward morphologies

While the experimental work presented in this thesis is focussed primarily on the interpretation of lava flows, some of the analysis in chapter four used results that were derived from the study of glaciers. As discussed in that chapter, the rheological structure of glaciers can be compared with that of lava flows, as the surface of a glacier can fracture in a brittle manner, while at greater depths it is more likely to flow in a viscous or pseudoplastic manner. The experimental rheology is therefore capable of representing the flow of a viscous or viscoplastic material, provided that the flow geometry is similar, i.e. it is confined within a channel, and so the simulations are useful analogues for both channelled lavas and laterally confined glaciers. Figure 5.1 (a) shows a valley glacier which is laterally confined between mountains in its upper reaches, while figure 5.1 (b) shows piedmont glaciers which spread out into wide lobes as they leave their confining valleys. The morphological similarity between glaciers and lava flows was used by Johnson (1970) to imply similar rheology, and can also be used to imply similarity between these two naturally occurring flow types and the analogue models. Geometric similarity results in analogous stress distributions, which is the reason why many structures widely documented on glaciers and lavas can be reproduced by the experiments. An advantage of studying glaciers in addition to lava flows is that their surfaces are commonly observable, whereas those of `a`ā and more silicic lavas are often obscured by the blanketing layer of clinkers and blocks, which means that surface structures can be more easily identified on glaciers.

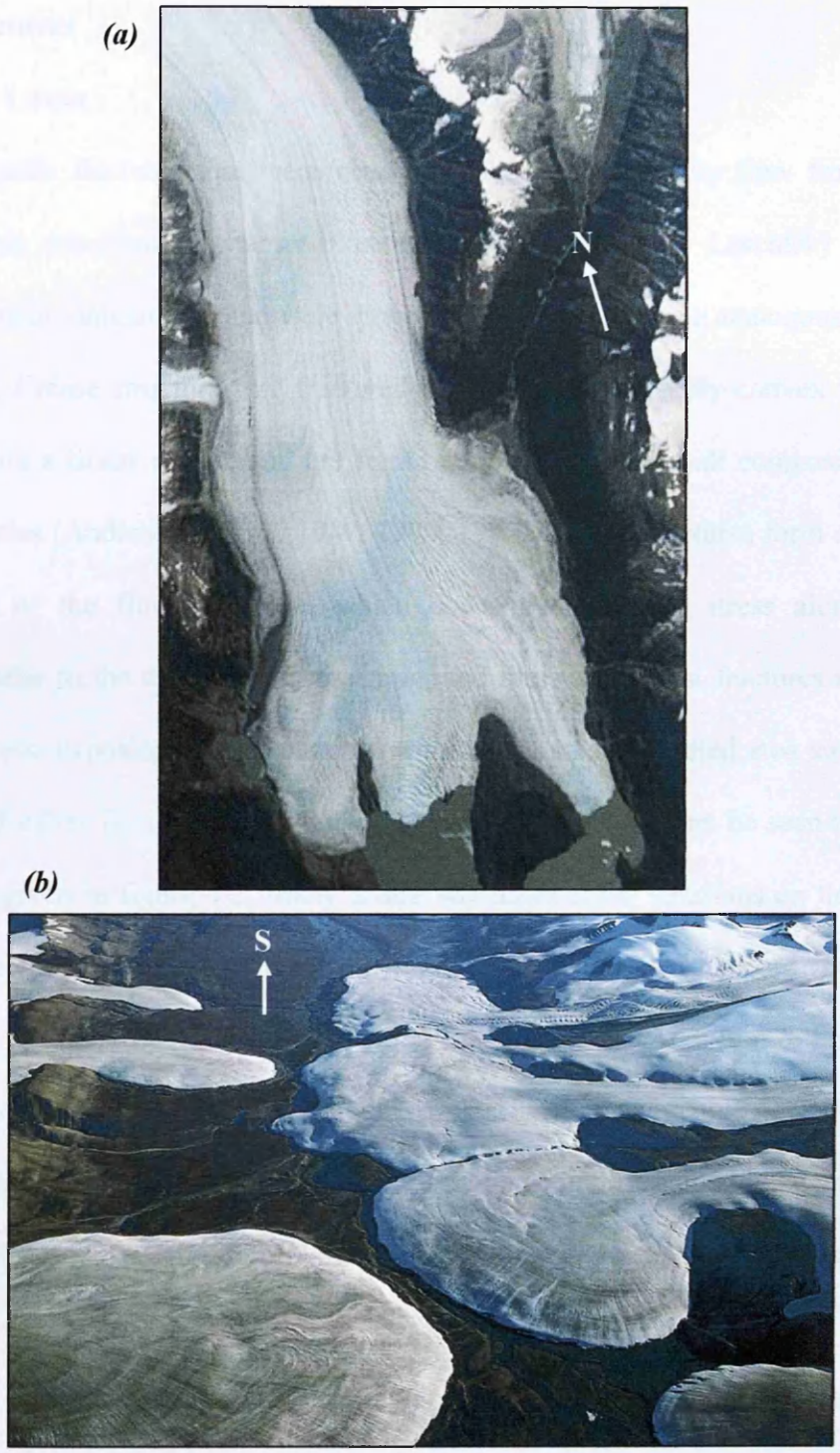

Figure 5.1. (a) Valley glacier: Glacier Grey, Torres del Paine National Park, Chile. The glacier is approximately 4 km wide in the upper part of the image. Image: NASA (ISS004-E-7058, 30.1.2002). (b) Piedmont glaciers: Axel Heiberg island, Canadian Arctic. These form when a glacier which was initially laterally confined spreads out beyond the confining valley. The valley into which the glaciers are flowing is approximately 5 km wide. Both piedmont and valley glaciers show geometry that is similar to the experimental flows described in this thesis, being confined in their upper reaches, and spreading laterally near the flow front. Image: J. Alean, 1977, from http://www.swisseduc.ch/glaciers/glossary/piedmont-glacier-en.html

5.1.1 Fractures

5.1.1.1 Lavas

The tensile fractures that were observed to form behind the flow front in the experiments described in chapter three were also observed by Lescinsky & Merle (2005) in their simulations, and were interpreted by them as being analogous to crease structures. Crease structures are fractures with smooth, outwardly convex walls that extend from a linear valley, and are found on flows of nearly all compositions and crystallinities (Anderson & Fink 1987, 1990, 1992). These structures form due to the spreading of the flow or dome, which concentrates tensile stress along a line perpendicular to the direction of spreading, and the cooled crust fractures along this line of stress, exposing the hot material within. The smooth-walled area surrounding the central valley is commonly observed to be lens-shaped, as can be seen in the two examples given in figure 5.2. Many crease structures show striations on their walls, parallel to the orientation of the valley, which are believed to record incremental fracturing, as the crust fractures, heals, then fractures again (Anderson & Fink 1992). In the sense that the tensile fractures in the thick crust models involve upwelling of the fluid interior through them, the process of formation can be regarded to be similar, but true crease structures will not form on the silicone-sand models as the interior does not solidify.

Crease structures, as they appear in figure 5.2, have not been described on the surfaces of channelised flows in the field in a manner that can be considered directly comparable with the experiments. However, tensile fractures that are arcuate in plan view have been described, and an example is shown in figure 5.3. This image, taken shortly after the 2001 eruption of Mt. Etna, shows a channelised flow approaching a break in slope, and therefore experiencing an acceleration. The tensile stresses in the

Figure 5.2. Crease structures. (a) December 1980 dacitic dome lobe at Mt. St. Helens. The crease is the smooth surfaced area at the summit of the lobe. Lobe is ~150 m in diameter. Image: from Anderson & Fink (1992); figure 6b (U.S. Geological Survey). (b) Crease structure on the surface of a basaltic overflow lobe in the 2001 lower flow field, Mt. Etna, Sicily. Arrow indicates flow direction. Structure is ~5 m long down the central axis.

channel have caused arcuate fractures to open up across the channel in a manner analogous to the fracturing in thick crust experiments described in chapter three (e.g. figure 3.19). In cross section, Pinkerton (pers. comm. 2007) noted that the fractures

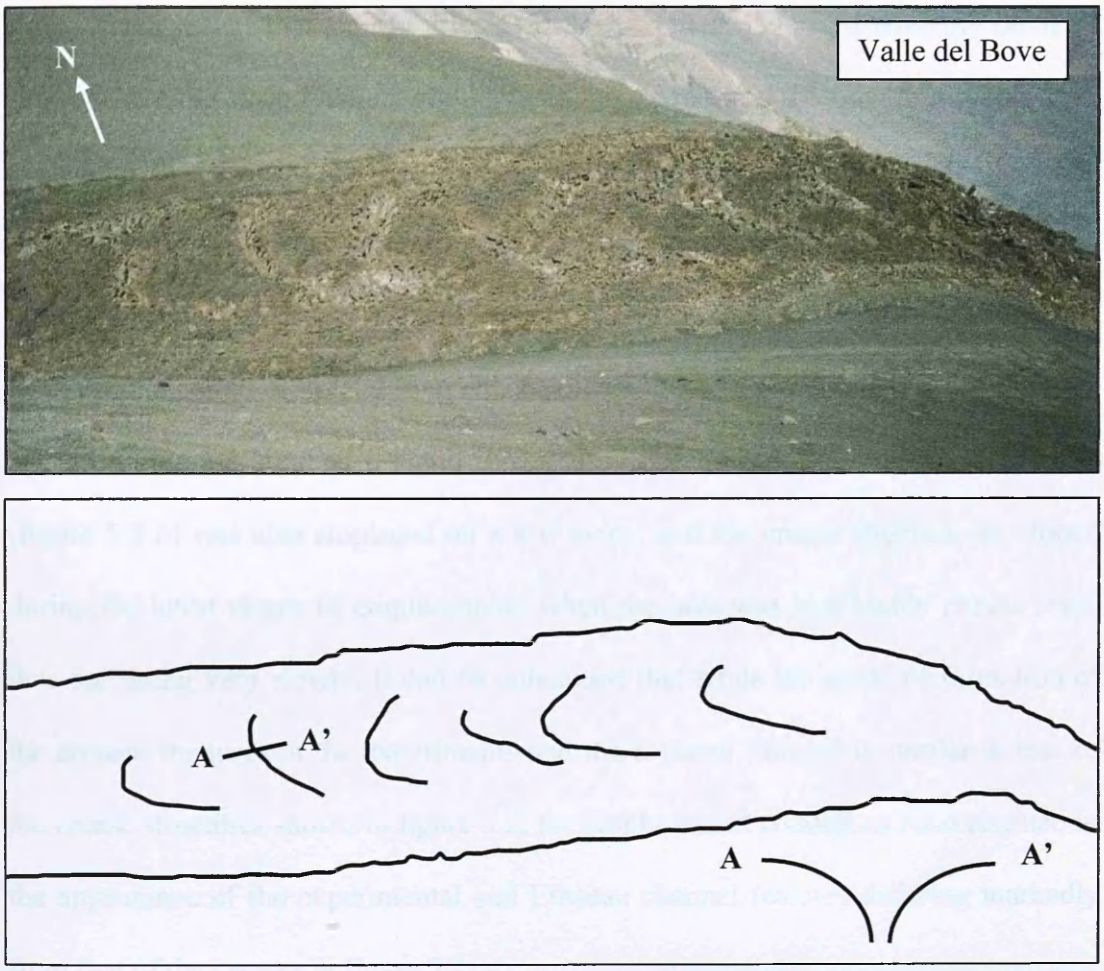

Figure 5.3. (a) Channelised lava flow in the upper flow field of the 2001 eruption of Mt. Etna, Sicily. Channel is approximately 15 m wide. The flow is approaching a break in slope, the headwall of the Valle del Bove, and responding to the tensile stresses by developing arcuate fractures. Image: H. Pinkerton. (b) Schematic illustration of the image in (a), highlighting the arcuate shape of the fractures. The approximate cross-sectional structure through a fracture is also shown. Distance A-A' is 1 to 2 m.

have outwardly convex walls, shown schematically in figure 5.3, as observed on the structures described by Anderson & Fink (1992). However, comparing figures 5.2 and 5.3, it is clear that in plan view the structures look very different. The tensile fractures in the Etnaean channel have a very low width/length ratio, where A-A' represents the width, in contrast to that of the dacitic and basaltic creases shown in figure 5.2. While the structures may have developed in a similar manner, those in the Etnaean channel were clearly active for a shorter time. This was due to the continuing advance of the

flow, which meant that shortly after a fracture formed, it moved over the break in slope, where the steep gradient and high strain rate reduced the flow to a rubbly rock avalanche. In contrast, the Mt. St. Helens dacite dome (figure 5.2 a) was emplaced on a very low slope, and this, coupled with the high silica content and high crystallinity, meant that the lava was spreading very slowly. The dome was active for a considerable period of time, during which spreading was approximately axisymmetric, and so the crease attained a significant width. The Etnaean basaltic overflow lobe (figure 5.2 b) was also emplaced on a low slope, and the crease structure developed during the latest stages of emplacement, when the lava was in a highly plastic state, thus spreading very slowly. It can be concluded that while the mode of formation of the arcuate fractures in the experiments and the Etnaean channel is similar to that of the crease structures shown in figure 5.2, the emplacement conditions have resulted in the appearance of the experimental and Etnaean channel features differing markedly from that of the creases in figure 5.2.

Observations of shear and conjugate fractures in lavas are rare, which may be due to the common occurrence of a surface layer of clinkers. An example of what may be shear fractures is shown in figure 5.4. Figure 5.4 (a) shows the Nesjahraun tholeiitic lava flow field, to the south western side of Þingvallavatn, south west Iceland, which was emplaced 1880 ± 65 years B.P. (Saemundsson 1992). The flow field consists of a number of different flows, one of which is picked out by the box in figure 5.4 (a), and enlarged in (b). This flow, outlined in (b), can be seen to have similar geometry to the experimental flows, with its proximal part confined in a channel that is approximately 300 m wide, and its distal reaches spreading laterally beyond the end of the channel. Two areas along the left hand margin of the flow are highlighted, and these are

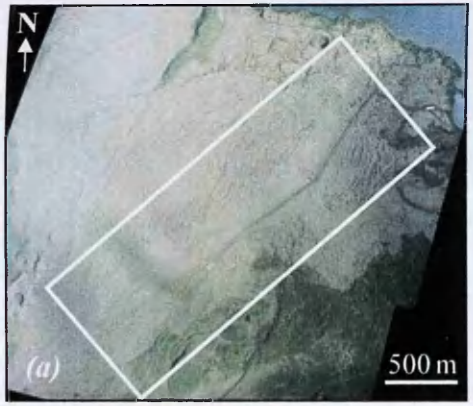

Figure 5.4. Example of shear fractures. (a) Shows the area of interest, the Nesjahraun tholeiitic lava flow field on the south western side of Þingvallavatn, south west Iceland. The lake can be seen in the upper right hand corner of the image. (b) Enlarged view of the boxed area in (a). This shows a channelised lava flow, the boundaries of which are sketched in white. Dashed lines indicate areas where the boundary is difficult to discern. The flow is geometrically similar to the experimental simulations, in that it was laterally confined during the earlier stages of emplacement, and spread out when it reached flatter topography. Two regions along the left hand margin of the flow are boxed, and these are enlarged in (c) and (d), on the following page. Note also the compressional ridges which developed behind the flow front.

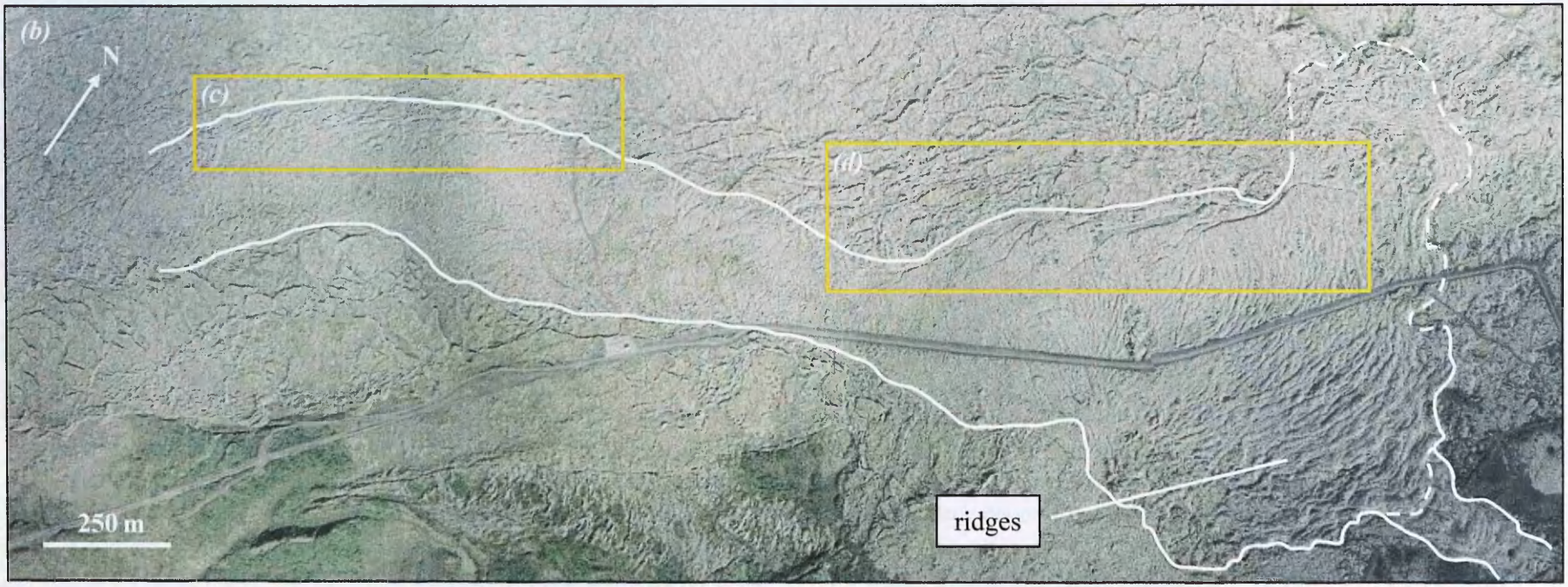

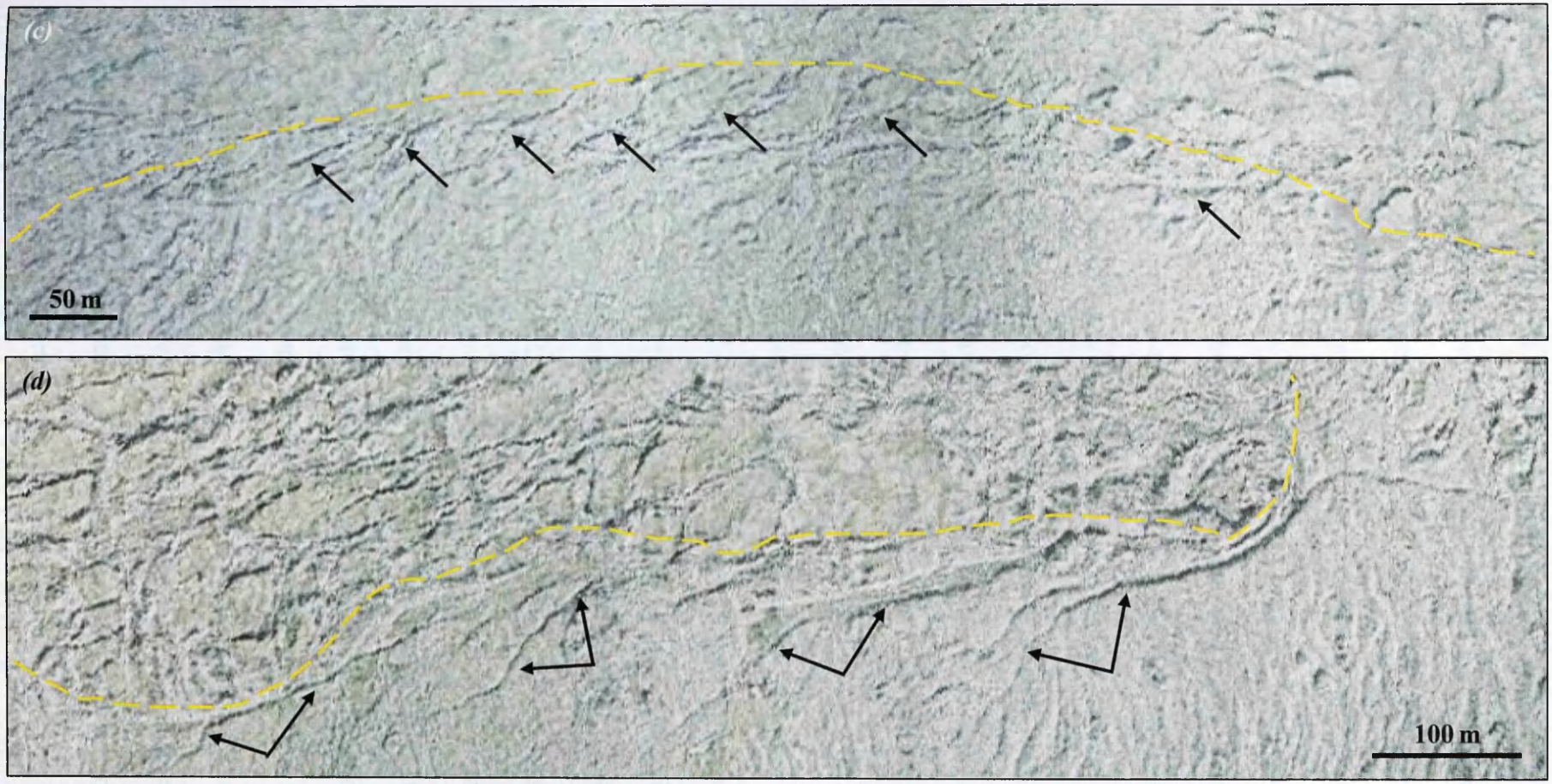

Figure 5.4. cont'd. Enlarged views of boxes in 5.4 (b). Flow direction is left to right, dashed lines indicate flow margins. (c) Flow margin in the upper part of the channel. Fractures are visible, directed downflow into the margins at a small angle, which appear similar to those described in intermediate crust experiments. Compare figure 3.18. (d) Closer to the flow front. Fractures are longer, more widely spaced and have the more uneven shape of oblique fractures (left hand arrow or each pair) with flow-parallel extensions (right hand arrow), as described for the thick crust experiments. Compare figure 3.22. See text for details. All images: NERC Airborne Research and Survey Facility, 2007.

enlarged in figures 5.4 (c) and (d). In the upper, narrower part of the channel, short (~50 to 100 m) fractures can be seen, which are oriented downflow into the channel margins at angles of approximately 15 to 30° (figure 5.4 c). The fractures are quite closely spaced, and although more sinuous in trace, bear a resemblance to the oblique shear fractures observed in the intermediate crust experiments described in chapter three (figure 3.18). Closer to the flow front, where the channel is widening, the shear fractures have a quite different morphology (figure 5.4 d). They are longer (up to 200 m), more widely spaced than those in (c), and commonly display two different orientations. The upflow part of the fracture is usually oriented oblique to the flow direction, angled downflow into the flow margins, as described for the fractures in (c) and the intermediate crust experiments, while the downflow part is sub-parallel to flow direction. This is indicated by the pairs of arrows in figure 5.4 (d), where the left hand arrow indicates the oblique part of the fracture and the right hand arrow the sub-parallel part. In some cases, a sub-parallel extension can also be seen at the upflow end of the fracture. This morphology closely resembles that described for shear fractures in thick crust experiments (the 'long oblique' fractures described in section 3.3.1.4 and shown in figure 3.22), which were interpreted to be an intermediate stage between the short oblique shear fractures and the single parallel fractures which extended down the whole channel margin. If the interpretation of the fractures on the Nesjahraun flow is correct, and they can be considered analogous to the fractures observed in the laboratory experiments, their morphology suggests that when the crust fractured in these regions, it was thinner in the proximal part of the channel than in the distal part. This is borne out by the lobate flow front, which also suggests the presence of a thick crust. These observations are in agreement with expectations, as the flow would have cooled more the further it travelled from the vent.

A possible example of conjugate fractures occurs in the 2001 flow field of Mt. Etna, on an overflow lobe, and is shown in figure 5.5. The lobe was channelised for approximately 250 m before spreading out on encountering a decrease in slope (figure 5.5 a), and its geometry is very similar to that of the laboratory experiments. The surface of the flow is characterised by dark, near-linear features, indicated by arrows,

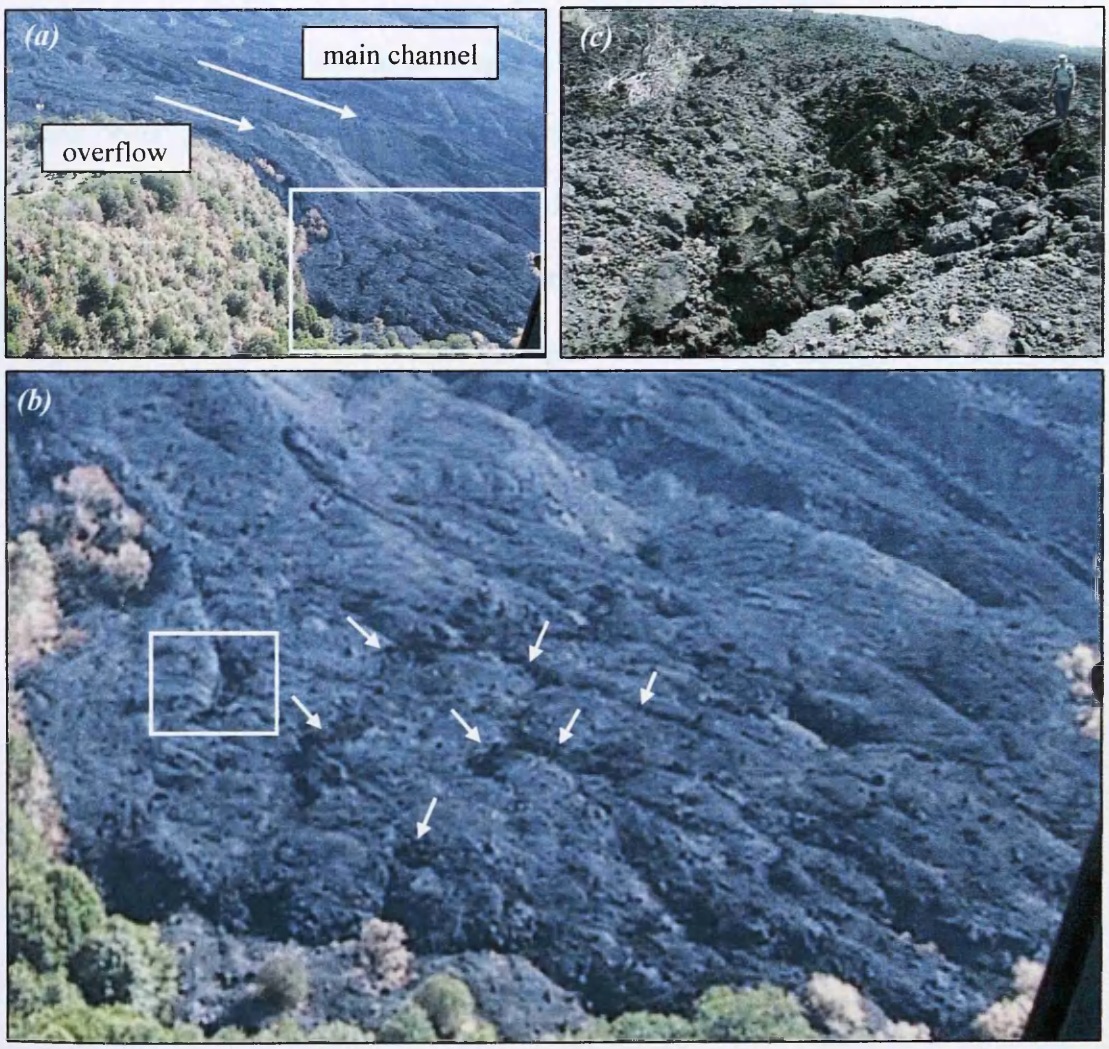

Figure 5.5. (a) Overflow lobe in the lower flow field of the 2001 eruption, Mt. Etna. The lobe is channelised for ~250 m, flowing parallel to the main channel, before spreading out into a broader flow front on reaching lower gradient topography. Flow front is ~170 m wide. The boxed area is enlarged in (b), where arrows indicate the locations of the dark, linear squeeze-ups. The distribution of these squeeze ups may be controlled by conjugate fracturing of the flow surface. Image: INGV Catania. (c) An image of the boxed area in (b), taken from the ground, showing a squeeze up of plastic lava. Compare figures 3.14, 3.17 and 3.24.

where the flow interior is squeezing up through fractures in the crust. While the oblique view makes estimation of the relative orientations of the features difficult, the squeeze ups seem to be aligned in two dominant directions, and as such, may reflect conjugate sets of shear fractures, as described forming on experiments with $\chi > 0.063$ (e.g. figures 3.14, 3.17, 3.24). If the squeeze ups had not been present, it is probable that the fractures would have been less prominent due to the clinker cover, and so it is the flow conditions in the latter stages of emplacement that have resulted in them being observable. Squeeze ups, as is discussed further later in this chapter and in chapter six, occur when the interior of the flow becomes pressurised above local static levels, if, for example, supply continues once the flow front has stopped moving. The stagnant interior is then forced out through breaches in the crust, as can be seen in figure 5.5 (c). Since the fractures would have developed while the flow was spreading, i.e. relatively early in its emplacement, they provided loci of weakness that could then be exploited when the pressure in the flow built up later in its history. If the overpressure had not developed, then the squeeze ups would not have occurred, and the orientation of the fractures would not have become so clear.

5.1.1.2 Glaciers

As discussed in section 4.1, the models can be considered applicable to glaciers as well as to lava flows, as their rheological structures are broadly similar (Johnson 1970; Patterson 1981). Spectacular arcuate and shear fractures have been recorded on many glaciers, and examples of these are shown in figures 5.6 and 5.7. The two glaciers shown in figure 5.6 both have very well developed arcuate tensile fractures, comparable to those seen in the Etnaean channel (figure 5.3), indicating the influence of the marginal shear stresses. The radius of curvature of the fractures can give an

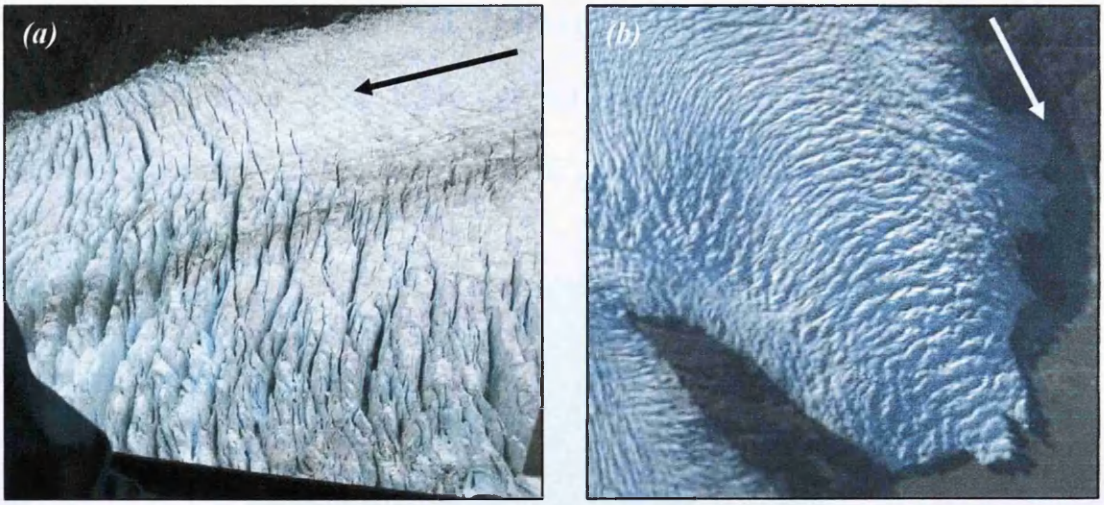

Figure 5.6. Arcuate crevasses in glaciers. Flow direction is indicated by the arrows. (a) Oblique view of the Franz Josef Glacier, South Island, New Zealand. Glacier is ~500 m wide. Image courtesy of S.P. Hayden. (b) Central toe of Glacier Grey, Torres del Paine National Park, Chile. See also figure 5.1 (a). Toe is ~2 km wide. Image: NASA ISS-015-E-10699. See text for details.

indication of the velocity gradient over the fractured zone, as discussed in section 4.1.2, and the high radius of curvature of the fractures in (a) suggests that the velocity gradient in this region is relatively high. The fractures in figure 5.6 (b) increase in curvature back from the flow front, as was observed in the experiments, indicating that the velocity gradient is decreasing up the toe. Figure 5.1 (a) shows a much larger region of Glacier Grey, and if the central toe is examined in this figure, it can be seen that the arcuate fractures die off completely some distance behind the flow front. (Note that the field of view in figure 5.6 (b) does not stretch this far).

An example of shear fractures is shown in figure 5.7, which shows a section of the Tasman Glacier, New Zealand. The left hand margin of the glacier is to the right of the image, but the right hand margin cannot be seen. The darker area to the top left of the image is a second, debris covered, glacier that has merged with the cleaner glacier. Along the left hand margin of the clean glacier, shear fractures can be seen intersecting with the margin at angles of around 45°, then curving back up the flow at

shallower angles of ~15 to 30°. The shear experienced by the clean glacier at the right hand margin is lower, as the debris covered glacier is also moving, which probably explains why shear fractures, though visible, are less prominent in this area.

Figure 5.7. Shear fractures in the Tasman Glacier, South Island, New Zealand. Flow direction is indicated by the arrow. The non debris-covered part of the glacier is approximately 650 m wide. Image: Google Earth. See text for details.

5.1.1.3 Shear and conjugate fractures on Mars

A potential example of shear fractures on Mars can be seen in figure 5.8, which shows what has been interpreted to be a channelised deposit. This deposit forms part of the ejecta blanket that was emplaced after the impact which created the Tooting crater (figure 5.8 a). While the nature of the deposit is uncertain, it is very unlikely to be a lava flow. It is more probably a flow of either country rock melted by the impact, or water-rich sediment from the melting of ice in the frozen substrate. In either case, it

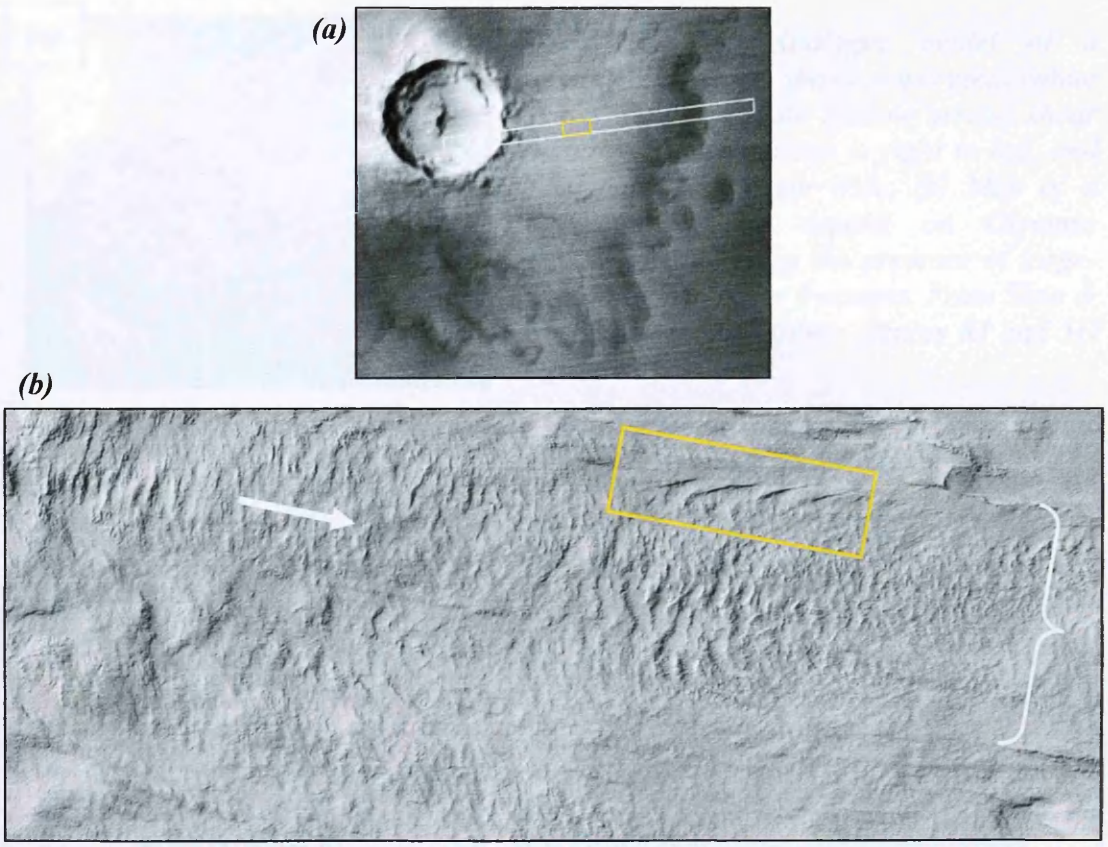

Figure 5.8. (a) Tooting Crater, Mars, and part of its associated ejecta blanket. The area shown in (b) is boxed in yellow. (b) Image of what may be a channelised deposit, with the flow direction indicated by the arrow. The channel, spanned by the bracket, is approximately 1 km wide. The yellow box picks out features which have a similar orientation to the shear fractures observed in the intermediate crustal thickness experiments, and which may be formed in an analogous manner. See text for details. Image: http://www.msss.com/moc_gallery/m13_m18/images/M13/M1301995.html

is probable that as the deposit flowed, it cooled rapidly due to the very low ambient temperature on Mars, and so developed a solidified or frozen crust. As such, it is again probable that the vertical rheological profile through the deposit is similar to that in my models, with a brittle surface layer underlain by more viscous material. Since the channelised geometry is also similar to the models, it is plausible that the structures observed are shear fractures.

Shea & van Wyk de Vries (2008) modelled rockslide-avalanches using the slide of granular material down smooth curved ramps, producing marginal shear and conjugate shear fractures that appear very similar in morphology to those features

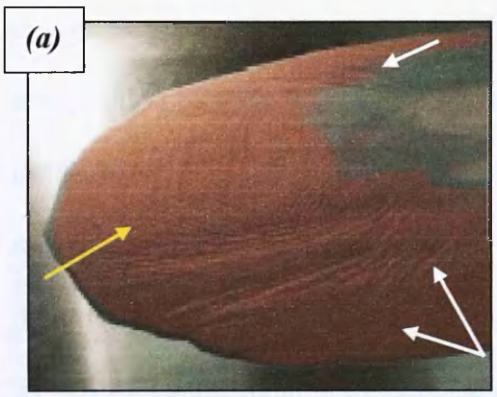

Figure 5.9. (a) Analogue model of a rockslide-avalanche, showing marginal (white arrows) and conjugate (yellow arrow) shear fractures. Flow direction is right to left, and the deposit is ~20 cm wide. (b) Map of a rockslide-avalanche deposit on Olympus Mons, Mars, inferring the presence of large-scale conjugate shear fractures. From Shea & van Wyk de Vries (2008); figures 8J and 5D respectively.

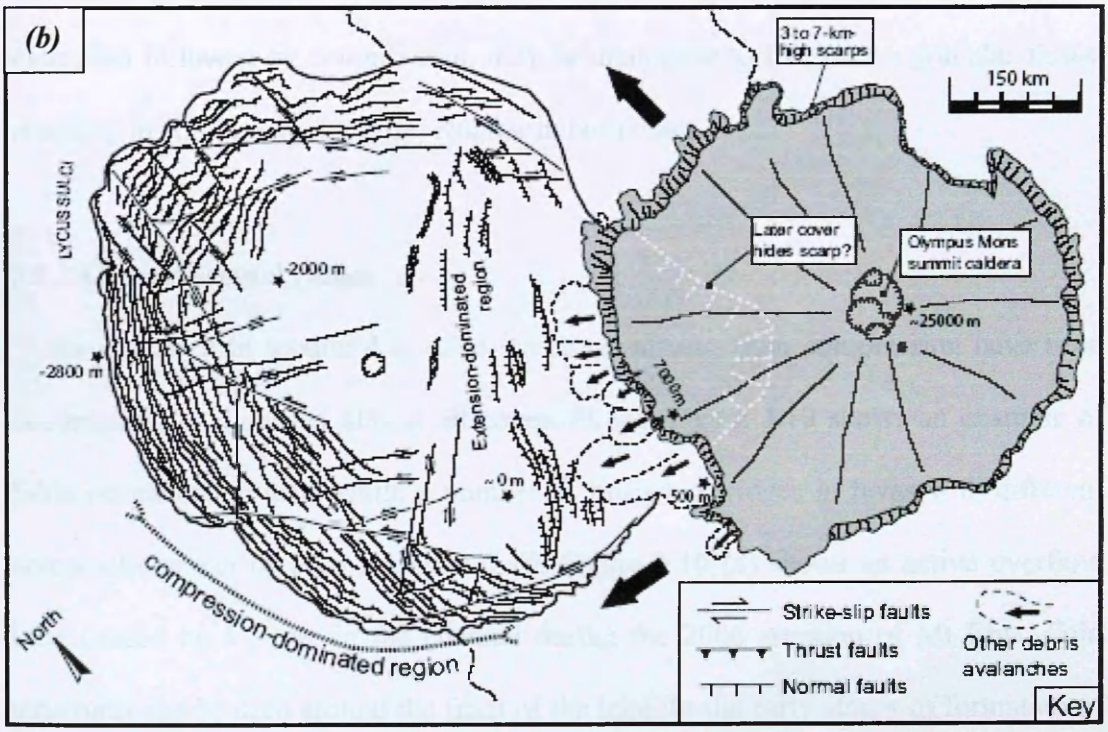

described in the two-layer viscous-brittle models presented here. An example of one of their granular flows is shown in figure 5.9 (a). In addition to their experimental work, Shea & van Wyk de Vries mapped the morphological and structural features of several natural rockslide-avalanche deposits, including one large deposit on Olympus Mons. Their map is reproduced in figure 5.9 (b). It can be seen that the presence of large-scale (lengths and spacings of several tens to hundreds of kilometres) conjugate shear fractures has been inferred, particularly towards the north of this deposit, which intersect at angles of 60 to 90°. These features appear similar to those described in the

experiments presented here, and by Shea and van Wyk de Vries (2008). Although the composition of rockslide-avalanches is different to that of the experiments described in this work, consisting largely of granulated breccia, it is possible that the interiors of rockslides become fluidised by shear during transport, which may result in a similar rheological structure. Even if this is not the case, the behaviour of the brittle crusts in the experimental models upon being subjected to similar conditions, namely initial extension followed by compression, may be analogous to that of the granular flows, resulting in similar structures developing in both cases.

5.1.2 Compressional ridges

As discussed in section 4.4, ridge structures arising from compression have been documented on flows of almost all compositions. Figure 4.10 shows an example of folds on pāhoehoe lava, while a number of images of ridges in lavas with different compositions can be seen in figure 5.10. Figure 5.10 (a) shows an active overflow lobe caused by a surge in the channel during the 2006 eruption of Mt Etna. Fold structures can be seen around the front of the lobe. In the early stages of formation of the lobe, the thermal boundary layer would have been thin, and the supply rate would have probably exceeded the flux at the lobe front, thus creating conditions favourable for folding. The folds would initially have formed in the main body of the lobe, but as cooling progressed and the lobe advanced, conditions soon became unsuitable for folding, and the surface solidified to produce a rigid crust. The folds would have been pushed to the flow front by the advancing crustal plates, in a manner analogous to the experimental influx pushing the ridges to the flow front (figure 3.8), and they are preserved only around the very margins of the flow.

Figure 5.10. Ogives on lavas of different compositions. In all cases, flow direction is indicated by the arrows. (a) Short wavelength ogives around the flow front of a basaltic pāhoehoe overflow lobe at Mt. Etna, 2006. Main channel is ~2 m wide. (b) Ogives in a basaltic `a`ā channel, during the 2001 eruption of Mt. Etna. Image: INGV Catania. (c) The Chao dacite flow, northern Chile. The flow is ~14 km long, and the ogives have wavelengths and amplitudes of order 100 m and 30 m respectively. Note that the ogives are curved near the flow front, but flatter in plan view further back up the flow. Image: from de Silva et al. (1994); figure 3a. (d) Three comendite (rhyolite) flows on San Pietro Island, Sardinia, showing very well developed ogives that are parabolic in plan view. Image: Google Earth.

Fink & Fletcher (1978) successfully described the surface ridges on pāhoehoe lava using a folding model, but the term 'fold' cannot be implied with impunity to all

examples of surface ridges, as there is a genetic connotation which needs to be verified in each case: there are other mechanisms by which surface irregularities that bear a resemblance to folds can arise. While the term 'ridges' has previously been used in this work, this is rather non-specific. Instead, the term 'ogive' is preferred, and will be used from now on to describe compressional ridges on basaltic `a`ā lavas, and those of more evolved composition. This term originally came from glaciology, but found its way into volcanological terminology following the observations of Thorarinsson (1953), who noted that 'waves' on the surface of lava flows formed in similar situations, and had similar morphology, to glacial ogives. The term 'ogives' describes the sinusoidal flow surface profile, and also the commonly curved aspect of the flow features in plan view, without implying a formation mechanism. Examples of ogives on lavas of varying composition are shown in figure 5.10 (b-d).

Fink (1980) used measurements of the dimensions of ogives on the Big Glass Mountain rhyolite, California, and the Chao dacite, Chile, to determine whether they could be explained by the folding model of Fink & Fletcher (1978). The models was indeed found to be appropriate. This method was also successfully applied to the Nesjahraun basaltic flow shown in figure 5.4 by M. Cassidy (pers. comm. 2008). The method of Fink (1980) allows the calculation of viscosities which may not be estimable by other methods, and this is attempted below for the `a`ā flow shown in figure 5.10 (b).

5.1.2.1 Folding analysis for an Etnaean channelised basalt

The analysis of Fink & Fletcher (1978) showed that three dimensionless parameters related to the properties of the lava and the geometry of the channel could be defined, and that if the values of these parameters fell within certain ranges, the presence of a

strong folding instability could be confirmed. These parameters are R, the ratio of the surface to interior viscosities, η_0 / η_i; S, the ratio between the damping stress due to the weight of the lava and the compressive stress that favours folding; and $L_d\gamma$, a dimensionless form of the ridge spacing. For the folding instability to be sufficiently great, $R > 35$, $S < 0.02$ and $L_d \gamma > 28$ (Fink 1980).

The rheological structure of the flow with respect to the vertical axis, z, can be described by the following equation, which was also equation 4.3:

$$\eta(z) = \begin{cases} \eta_0 \exp(\gamma z) & -H \leq z \leq 0 \\ \eta_i & z < -H \end{cases} \qquad (5.1)$$

in which η_0 is the viscosity at the surface; η_i is the interior viscosity; H is the thickness of the surface layer and γ is the exponential decay parameter for the viscosity decrease. This viscosity distribution is shown schematically in figure 4.11 (curve b), and describes a surface layer in which the viscosity decreases exponentially, below which is the flow interior, in which the viscosity is constant. Although this viscosity distribution is a simplification of that in an active lava flow, Fink & Fletcher (1978) argue that the folding process will be relatively insensitive to the details of the distribution.

Fink (1980) estimated the interior and surface viscosities of the Big Glass Mountain rhyolite, California, using measurements of the ridge spacing and amplitude, and estimates of the strain rate. The amplitude and wavelength of the ogives on the `a`ā flow seen in figure 5.10 (b) were estimated in the field to be ~ 1 m, and ~ 3 m respectively. In order to estimate the strain, the initial distance between the crests of the incipient ogives needs to be known, which was found empirically by Fink & Fletcher (1978) and Fink (1980) to be approximately 1.5 times the wavelength, hence 4.5 m for this flow. The analysis indicates that for a sufficiently large folding

instability to exist, the dimensionless ridge spacing, $L_d \gamma$ must be greater than 28. L_d can be approximated by the arc length, which is 4.5 m, which provides the constraint $1/\gamma < 0.16$. From the viscosity distribution (equation 5.1), $H = (1/\gamma) \ln R$. Assuming $R = 10^4$, a value used by Fink & Fletcher (1978) for pāhoehoe, and by Fink (1980) for obsidian and dacite flows, the limit $H < 1.47$ m is obtained. This is consistent with the amplitude of the ogives being ~ 1 m.

The stress ratio, S, can be expressed as:

$$S = \rho g H / (4 \ln R \dot{\varepsilon}_{xx} \eta_0) \qquad (5.2)$$

where $S < 0.02$, $\rho = 2700$ kg m^{-3}, $g = 9.81$ m s^2, $H = 1.47$, and $R = 10^4$. The strain rate $\dot{\varepsilon}_{xx}$ can be estimated from the known shortening, and the estimated time over which this shortening occurred. The arc length is taken as 1.5 times the final wavelength, so the shortening was 33%, and the ogives are known from field observations to have formed within a 24 hour time frame (H. Pinkerton, pers. comm. 2007). Assuming then, that the shortening occurred within a period of between one and twenty four hours, strain rates of between 9.2×10^{-5} and 3.8×10^{-6} s^{-1} are obtained. Equation 5.2 can then be used to calculate the possible surface viscosities, giving values of between 3.9×10^8 and 9.4×10^9 Pa s. Using these values of strain rate and surface viscosity, S is constrained to be smaller than 0.02, thus proving compatible with the folding analysis. Assuming $R \sim 10^4$, this gives interior viscosities of between 3.9×10^4 and 9.4×10^5 Pa s. Estimation of the lava viscosity in this part of the flow at this point in the eruption is carried out by a different method in section 6.3.2, and gives similar values, suggesting that the method used here has produced plausible results. The three criteria for surface folding, $R > 35$, $S < 0.02$ and $L_d \gamma > 28$, have been satisfied by the ogive geometry, indicating that ogive growth can be explained by such a folding process.

While the previous examples of ogives have been shown to form by the folding process described by Fink & Fletcher (1978), the ogives on San Pietro (figure 5.10 d) are rather more enigmatic. As discussed in section 4.4, the folding analysis requires a relatively thin, high viscosity surface layer underlain by a lower viscosity interior. As such, folds are expected to occur in the surface layer, and only extend a short distance into the flow interior. The comenditic flows, however, have been shown to be folded throughout their whole depth (Cioni & Funedda 2005), suggesting that the folding model of Fink & Fletcher (1978) is not applicable in this case. This indicates that while ogive growth can be explained by the folding model, it should not be considered universally applicable to all examples of ogives without being tested. Though the San Pietro flows could not be analysed here using the method of Fink (1980) due to a lack of field data, Cioni & Funedda (2005) cite the explanation of Dragoni et al. (1992) for large scale folding. In their model, compression related to thermal-induced downflow rheological changes in the body of the lava (Newtonian to Bingham rheology) causes a sharp change in the compressive strain rate acting on the lava flow, so triggering fold formation.

5.1.3 Marginal ropes

Marginal ropes were identified on the model flows both closely associated with channel-wide folding, and in isolated small patches in experiments that showed no other evidence of folding. The examples in figure 5.10 (a, c and d) show that fold structures do indeed get stretched out in the direction of flow, ending up sub-parallel to the flow margins. In the case of the overflow lobe (figure 5.10 a), initial ductile deformation of the crust led to folding, and subsequent thickening of the central part

of the crust beyond its ability to fold resulted in the early folds being marginalised to produce morphology similar to that observed in the thin crust experiments.

Another possible example of such features is seen in figure 5.11, which shows the margin of a small channelised pāhoehoe flow from the 1991-3 flow field on Etna. This flow clearly had a rather longer lifespan than the lobe shown in the previous figure, and as such had well developed levées. The levée can be seen in the lower right of the image, and the smooth flow surface in the upper left. Flow direction is lower left to upper right. At the channel-levée boundary, there is a narrow zone characterised by structures which may be analogous to the ropes seen in the models. The geometry of the example suggests that if they are analogous, they formed under conditions similar to those seen in the thin crust models, where ropes are the marginal extents of the fold structures which originally traversed the channel. As the folds were carried downflow, the marginal extents were constrained to remain stationary due to the velocity profile across the channel, and they were gradually stretched out in the direction of flow, becoming ever more closely parallel to the flow margins. Since the ropy structures in this image were not observed forming, and solidified flows only show the latest stages of emplacement, so cannot be inferred to be representative of conditions prevailing during the majority of active flow, it is not certain that they are truly analogous to the experimental structures. An additional reason for caution is the observation of features that may be shear fractures, parallel to the ropes, which are picked out by arrows in figure 5.11. Again, since the emplacement of this flow was not observed, it is unknown when the fractures formed relative to the ropes: they may represent later activity, once the flow surface had attained a significant strength.

An alternative explanation can also be suggested following observation of the experimental flows. As was seen in the thick crust experiments, once the long shear

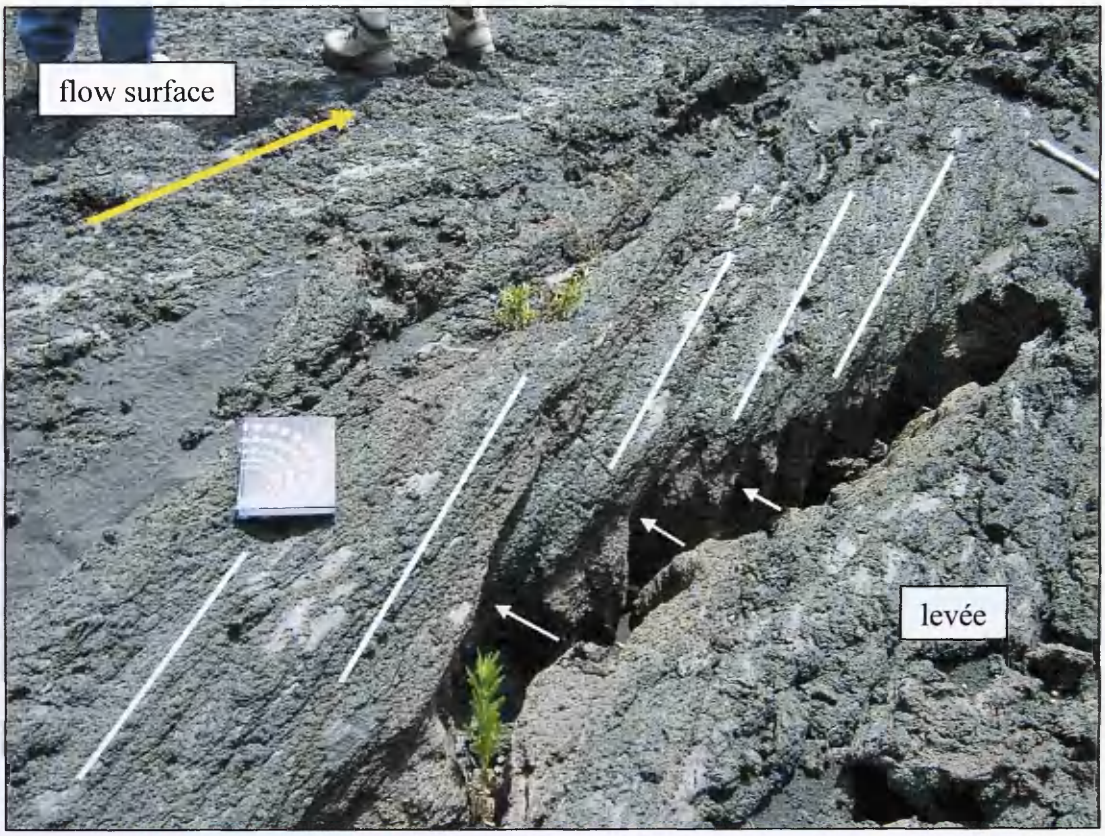

Figure 5.11. Possible ropy folds down the margin of a small pāhoehoe flow in the 1991-3 flow field, Mt. Etna. Flow direction is indicated by the arrow. The ropes can be seen to have developed between the levée and the flow surface proper. They are oriented in a similar fashion to those seen in the experiments, at a small angle downflow into the channel, as picked out by the white lines. Possible shear fractures are indicated by arrows. See text for details.

zone fractures have formed, the upwelling and subsequent compression of material in this region of thinned crust can result in the development of ropy structures. The morphology of the ropes shown in figure 5.11, and the fact that they have a regular 'wavelength' certainly suggests that compression played a role in their formation, and one of the two mechanisms described above may explain the way in which they formed.

5.1.4 Lobes

Lobe structures are frequently observed in lavas of all compositions. In flows of basaltic pāhoehoe, they are easily observed forming, and can be seen to develop by progressive inflation and failure of earlier lobes, which allows the advance of a new toe of molten lava which itself soon cools and begins to inflate, ready for a new cycle. The mode of lobe formation is less obvious in `a`ā flows, again due to the ubiquitous clinker cover and the fact that lobe development often takes place over longer timescales. While breakouts from `a`ā flow fronts are certainly observed (as is discussed in section 5.2), it is questionable whether the large-scale lobate structure of single flow fronts emplaced in short time intervals can be interpreted using a similar mechanism to that of pāhoehoe advance. This is discussed further in chapter six. Figures 5.4, 5.5, 5.10 (c) and 5.12 show that the structure of basaltic `a`ā and more siliceous flow fronts closely resembles that of the experimental flow fronts. From observing the experiments, it is known that mechanisms other than crustal rupture can result in lobes, as the cohesion of the experimental crust is not sufficient to retard the flow interior to the extent of generating overpressure. If is it possible for lobes to form by other mechanisms in the models, and it has been shown that the models are comparable to active lava flows, then by extension it is possible that these other processes are also occurring in lava flows. In section 4.6, two mechanisms of lobe formation were discussed, involving, firstly, the differential loading of the fluid interior by crustal plates, and, secondly, the differential retardation of the flow front by heterogeneous avalanching of crustal debris. It is clear that the second mechanism could be operating in `a`ā flows, as they are well documented to advance by the rollover of brecciated surface material. The first mechanism, however, requires the formation of crustal plates, and hence conjugate surface fractures, which are

Figure 5.12. Flow front of the 2001 lower flow field, Mt. Etna. The `a`ā flow front is ~20 m thick, and ~200 m in width. Lobate structures are seen, and appear similar to those observed in the thick crust laboratory experiments. See text for details. Image: INGV Catania.

themselves somewhat enigmatic, as discussed previously. Figure 5.5, which shows a possible example of conjugate fractures, cannot provide much enlightenment, as the inter-plate squeeze ups are restricted to areas some distance behind the flow front, and so squeeze up (i.e. fracture) distribution cannot be related with any confidence to the flow front lobe distribution.

Nonetheless, is it interesting to note that alternative lobe forming mechanisms could be at work in `a`ā and more siliceous flows that do not require the presence of a coherent, continuous crust with a tensile strength, or pre-existing topographic irregularities. The mechanisms observed in the models are clearly applicable only to

a`ā flows, as pahoehoe flows have continuous crusts, and also do not experience avalanching and overriding of crust at the flow front.

5.2 The emplacement of compound flow fields

Comparison of the analogue models with examples of lava and other natural flows has shown that the models successfully reproduce many of the processes and surface structures observed during the emplacement of single, channelised flow units. Although analogue models are invaluable for providing insights into certain processes, and elucidating the influence of individual parameters on the development of a flow, the development of compound morphology, as illustrated in both pāhoehoe and `a`ā flows in figure 5.13, is dependent on many factors, and there is no universal model scaled to include all the possible conditions that prevail during the emplacement of such flows. Fieldwork must therefore play a major role in improving our understanding. The problem of increasing flow complexity is considered in this part of the chapter. The factors that may contribute to the transition from simple to compound morphology during a single eruption are discussed in section 5.2.1, and examination of recent flows on Etna that were closely observed during emplacement illustrates the importance of these controlling factors. Sections 5.2.2 and 5.2.3 describe the development of tubes and ephemeral vents respectively, which are commonly observed during compound flow emplacement. These can have a considerable impact on the way in which a flow field develops. The surface features that can arise from inflation, and the information that these features can provide about internal flow dynamics, are discussed in section 5.2.4.

A truly comprehensive consideration of all the aspects of compound flow morphology is beyond the scope of these discussions, which are intended as an

overview to provide background for the following chapter. Chapter six considers in detail the structural and temporal evolution of a compound `a`ā flow field emplaced during the 2001 eruption of Etna. The descriptions of features in this chapter are partly tailored to the consideration of processes that were observed during the emplacement of that flow.

5.2.1 Simple vs. compound flow emplacement

Simple and compound morphologies are observed at basaltic volcanoes, during the eruption of both pāhoehoe and `a`ā. Simple, channelised flows can develop during the emplacement of either type of lava, though are more commonly associated with `a`ā. Laterally extensive sheet flows, in which levées do not develop, can also form during eruptions of pāhoehoe or `a`ā, but these are generally short lived during `a`ā eruptions, as lava rheology causes flow to rapidly become confined to well-developed channels. In both pāhoehoe and `a`ā, the development of compound flow fields is dominated by superimposition and juxtaposition of many flow units, and the formation of tube systems and ephemeral vents. Compound pāhoehoe flows (figure 5.13 a) are made up of toes, or tongues, of lava, up to a few tens of centimetres in size. These are emplaced individually, forming as small tongues of liquid lava advance, chill, inflate and rupture to allow hot fluid from the interior to advance once more. The scale of flow units is commonly much greater in `a`ā flows, and these can result from breaches in and breakouts from stagnating channels and flow fronts (Figure 5.13 b).

The conditions that determine whether a flow field demonstrates simple or compound morphology are the same for pahoehoe and `a`ā flows, and can be illustrated by considering the emplacement of four `a`ā flow fields during three different eruptions of Mt. Etna.

Figure 5.13. (a) Advancing toey pāhoehoe flow on Hawai'i. Each toe originates as a breakout from an earlier toe. Fractures in the chilled surface crust expose the incandescent flow interior, as can be seen to the left of the image. Image: J.D. Griggs, from http://volcanoes.usgs.gov/Products/Pglossary/pahoehoe.html. (b) Aerial image of the 1983 flow on Mt. Etna, during its emplacement. The flow is made of many units of different ages, with younger units appearing darker. Darker material can clearly be seen along the western margin, where a new flow unit has been emplaced alongside older flows, increasing the width of the flow field. Towards the flow front, branches of darker material appear to emanate from within the flow field, as indicated by the arrow. This indicates where new material has been transported in subsurface supply systems, breaking out from an ephemeral vent in an earlier flow front. Image courtesy of INGV Catania.

5.2.1.1 Effusion rate

Guest et al. (1987) examined the emplacement of the 1981 and 1983 flows, which were emplaced over different periods of time and had very different morphologies, but reached similar lengths. The 1981 eruption lasted for only three days, had an average effusion rate of 128 m^3 s^{-1}, and developed predominantly simple morphology. By contrast, the 1983 flow lasted for 131 days, had an average effusion rate of ~ 8 m^3 s^{-1}, though short term fluctuations in effusion rate were observed by Frazzetta & Romano (1985), and developed compound morphology. Calvari et al. (2002) described the emplacement of two lava flow fields on different sides of the volcano during the 1999 eruption, which had different final morphologies. Ten months of effusive activity at predominantly low flow rates from fissures located on the South East Crater (SEC) resulted in the emplacement of the thick, compound eastern flow field. The western flow field arose as a result of several overflows of lava from the Bocca Nuova (BN), which produced discrete, short-lived periods of high flow rate over a period of about one month. This flow field consisted of several thin, simple flows. While the longest flow in the western flow field reached a length of approximately 4 km, the longer lived eastern flow field only reached around 2.7 km in length. Measurements of effusion rate showed fluctuations during the emplacement of both flow fields, but those relating to the western flow field were much larger in magnitude (Calvari et al. 2002).

Absolute effusion rates, and fluctuations in effusion rate, can be seen from these examples to be important in determining final morphology. Frazzetta & Romano (1985) argued that fluctuations alone were the cause of the compound nature of the 1983 flow field, but the observations of Calvari et al. (2002) show that fluctuations can also result in the emplacement of several simple flows. It appears instead that it is

the absolute effusion rate, coupled with the magnitude and frequency of fluctuations, that determine the morphology. In both of the 1999 flow fields, if supply ceased for more than 24 hours, active flows stopped advancing, and new flows formed when the vents reactivated (Calvari et al. 2002). In the western flow field, the discrete, high flow rate episodes were short lived, resulting in several simple, volume-limited flows. By contrast, the effusion rate, though subject to small fluctuations, was lower and more steady in the eastern flow field, which developed as a thick sequence of cooling-limited flow units. As was also seen by comparison of the 1981 and 1983 eruptions (Guest et al. 1987), high effusion rate favours the development of simple flows, while compound flows are generally the result of sustained, low flow rate eruptions. The cessation of supply at any time can interrupt the development of either type of flow field, resulting in the emplacement of new flows when supply resumes, but the effusion rate will determine the morphology that forms during each period of supply. In compound flows, the effusion rate as defined by the flux from the main vent is not necessarily the appropriate parameter to use when considering individual parts of the flow. 'Local supply rate' may perhaps be preferable, as the main supply is usually divided between several channels, tubes or lobes. It is the local supply experienced by any part of the flow field that determines its morphology

The link between effusion (or supply) rate and morphology can also be seen in Hawai'ian pāhoehoe flows. At low effusion rates the characteristic toey morphology is observed. However, if the cooling rate is low, generally favoured by a high effusion rate, then the tongues can coalesce, and re-melt their chilled skins, forming a simple sheet flow with a continuous fluid interior. This sheet then inflates as one body, with uniform uplift of the stationary crust (Hon et al. 1994). At very high effusion rates, channelised pāhoehoe flows can develop. Such a link between effusion rate, or

cooling rate, and morphology has also been demonstrated by analogue models using PEG wax (e.g. Hallworth et al. 1987; Fink & Griffiths 1990, 1992).

5.2.1.2 Topography

A second factor that can result in compound morphology is variation in the local topographic slope. Polacci & Papale (1999) observed that flows commonly increase in complexity upon encountering a decrease in the local slope. This was seen during the 1983 eruption of Etna, in which the flow initially advanced down a steep slope, before negotiating a break in slope. The proximal part of the flow was characterised by a well established open channel during the earlier part of the eruption, which later roofed over to form a master tube. As the slope shallowed, however, downslope advance slowed and the flow began to spread laterally to conserve mass. The surface of the flow on the shallow slope became stationary within ten days (Duncan et al. 2004), after which the flow thickened by inflation, and a major system of branching tubes became established.

Such a link between morphology and slope is again documented during the development of pāhoehoe flows on Hawai'i, in which channelised morphology is more commonly observed on high slopes. Simple sheet flows and compound toey flows are observed to form at high and low flow rates, respectively, on low slopes ($\leq$ 1°). If the slope is slightly higher (> 1-2°, Hon et al. 1994), then toe coalescence to form sheet flows is hindered, and the toes become elongated in the downslope direction. This favours the formation of a tube system, within which localised inflation can occur, leading to the development of hummocky morphology (Hon et al. 1994). In the case of thin pāhoehoe flows, microtopography can also be important in hindering toe coalescence.

5.2.1.3 Eruption duration

The duration of the eruption is another major control on basaltic flow field morphology. If an eruption is brief, the resulting flow may find its supply cut off while it is still advancing, as was the case during the 1981 eruption of Etna, and the emplacement of the 1999 western flow field. In these examples, the flows were volume-limited (Guest et al. 1987; Calvari et al. 2002), and retained simple morphology. If, however, supply is sustained beyond the point at which the rheological changes arising from cooling and degassing have caused the flow front to cease advancing, in which case the flow is cooling-limited, continued supply is likely to result in increasing complexity. This can occur in several ways. If the proximal reaches of the channel are still open when the flow front ceases to advance, continued supply may result in the level in the channel rising and overtopping the levée to form breakouts. The increased level in the channel will result in a higher pressure being exerted on the levées, which may cause failure, producing a new branch. Continued supply may allow this channel to propagate until it reaches its cooling-limited length, after which the formation of breakouts and branches may be repeated. Alternatively, during continued advance of a branch, stochastic processes such as levée collapse may cause blockages of parts of the channel, leading to 'accidental' breaches (Pinkerton & Wilson 1994). The longer the duration of an eruption, the more chance there is of such stochastic processes having an influence on flow field development. Finally, supply to a cooling-limited flow front can result in the failure of its chilled crust to form an ephemeral vent, and the development of a tube along the path of the original channel. Tubes and ephemeral vents are considered in the following sections.

5.2.1.4 Composition and rheology

While these three factors, effusion rate, slope and eruption duration, are the dominant controls on the final morphology of basaltic flows, it is worth briefly considering the emplacement of more silicic flows. Long flows of dacite and rhyolite are common in the geological record, and are believed to have been erupted at very low effusion rates over long periods of time. For example, the 26 km^3 Chao dacite of northern Chile has been estimated to have been emplaced over a period of 100 to 150 years, at an average rate of approximately 5 m^3 s^{-1} (de Silva et al. 1994), and yet it demonstrates very simple morphology (figure 5.10 c). While this particular example was emplaced on a steep slope (up to 20°, de Silva et al. 1994), almost all long silicic lava flows show simple morphology, regardless of the local topography. Such flows are observed to have blocky morphology, indicating their advance was achieved through autobrecciation (e.g. Macdonald 1972; Kilburn 2004). This gives an insight into another important control on simple versus compound morphology, which is a high contrast in fluidity between the flow interior and the chilled margins (Kilburn 2000). If no such contrast exists, then the development of breaches, and therefore tubes, cannot occur, as the interior cannot become overpressured. A high contrast in fluidity is the norm in basaltic eruptions, which is why they commonly display compound morphology.

5.2.2 Tube formation

The development of tubes has long been documented in pāhoehoe flow fields (Peterson & Swanson 1974; Guest et al. 1980, 1984; Greeley 1987), and has been increasingly recognised in recent years as an important process in `a`ā flow fields (e.g. Calvari & Pinkerton 1998). The poor thermal conductivity of lava means that once the

tube is established, material within is very well insulated, and can flow far further than would be possible in a open channel. The subsurface distribution systems that develop in compound flows makes their activity more problematic to monitor.

Tubes form in pāhoehoe flows displaying any of the aforementioned morphologies (channelised, sheet, hummocky or toey), and are not limited to areas where active surface channels previously existed (Hon et al. 1994). In toey and hummocky flows, tube development is influenced by the distribution of the original cooling units, while in sheet flows, marginal cooling results in the gradual reduction of the cross-sectional area occupied by the fluid interior, eventually leading to the formation of tubes.

The development of tubes in `a`ā flows can occur by several different mechanisms, and on different timescales, as documented by Calvari & Pinkerton (1998) during the 1991-3 eruption of Etna. During the eruption, the earliest phase of tube development was seen to occur on shallow slopes in the distal flow field. In this region, following the cessation of a cooling-limited flow front, continued supply from upflow resulted in gradual inflation of the flow front. Eventually, the internal pressure in the inflating front caused a rupture in the chilled crust, allowing fluid lava from the flow interior to spill out and continue advancing downslope. If sufficient time had elapsed between cessation of the earlier flow unit and rupture of the carapace, the chilled surface was able to support its own weight, and it behaved as a tube. In this case, cycles of chilling and rupturing flow fronts could continue downslope, eventually resulting in a long continuous tube. Surveys of old, drained lava tubes have also provided evidence of this process (Calvari & Pinkerton 1999). The internal structure of the old tubes consists of large hemispherical or elongate chambers, with small, narrow passages at their distal ends. The large chambers represent inflated flow fronts, and the narrow passages the subsequent narrow stream of lava that emerged from the new ephemeral

vent (Calvari & Pinkerton 1999). This mechanism of tube formation was the most efficient, and could take as little as four days (Calvari & Pinkerton 1998). If, however, the elapsed time between cessation and rupture was not sufficient for the crust to develop a significant strength, then the roof collapsed upon partial drainage of the chamber. This often prevented the continued supply of lava through the ruptured front, and the freshly supplied lava broke out of the original channel somewhere above the constriction to form an overflow, or a new channel branch.

The second mechanism by which tubes formed occurred predominantly in the proximal flow field, in narrow channels on high slopes. Variations in the level of lava in the channel, either due to fluctuations in supply or transient blockages downstream, caused inward levée accretion, and the subsequent 'zipping up' of the roof over the channel (Calvari & Pinkerton 1998). Such a process took approximately two weeks to occur. The final mechanism of tube formation was observed in the medial flow field, on intermediate slopes. In this case, `a`ā clinkers gradually accumulated on the flow surface, and were welded together by fluctuating movement in the fluid interior, slowly increasing the crustal thickness. Eventually, after approximately one month, the thick crust adhered to the levées, and tube flow resulted.

Surveys of old tube systems (Calvari & Pinkerton 1999) indicate that where decreases in slope occur, master tubes break into many smaller, branching tubes, which form a network distributing lava throughout the flow field, and this agrees with the observations of Polacci & Papale (1999) who noted that breaks in slope result in an increase in the complexity of a flow field.

Mature tube systems can form complex three-dimensional tube networks as tubes within a branching system may subsequently coalesce, both vertically and horizontally. Coalescence plays an important role in prolonging and lengthening tube

systems on Etna. Monitoring the active tube system is important, as tube coalescence can rapidly divert lava to a previously inactive part of the flow field, through earlier drained tubes. This has implications in hazard assessment, as it may result in new breakouts of fresh, hot lava from unexpected regions of the flow, or the reactivation of stagnant flow fronts (Krauskopf 1948; Calvari & Pinkerton 1999). Tube systems commonly supply lava to the surface through ephemeral vents, which are abundant in compound flow fields (e.g. Polacci & Papale 1999), and these features are discussed below.

5.2.3 Ephemeral vent formation

Lava flows in tubes are very well insulated, and may cool by less than 1 °C km^{-1} (Peterson & Swanson 1974; Keszthelyi 1995), so the material supplied through ephemeral vents is often still very hot and fluid. In essence, the formation of an ephemeral vent downflow of the main eruptive fissure can have a similar effect to the opening of a new fissure in this location. As such, identifying the locations where an ephemeral vent might form is important in hazard assessment. Calvari & Pinkerton (1998) identified three major types of ephemeral vents during their study of the 1991-3 flow field on Etna.

First order ephemeral vents resulted from the inflation and rupture of cooling-limited flow fronts, when the normal stress at the flow front exceeded the tensile stress of the chilled carapace (Dragoni & Tallarico 1996). These vents commonly open at the boundary between the flow interior and the chilled basal crust, as the pressure is greatest at the base of the fluid. First order vents were observed to remain active for up to several months, and could feed `a`ā flows that attained a significant proportion (up to 50%) of the length of the original flow.

Second order vents opened in the surface of the flow field, above underlying tube systems, and were often found at breaks in slope where the pressure built up as supply exceeded drainage. Activity could persist at these vents for several months, feeding mainly `a`ā flows, though some pāhoehoe could be found very close to the vents. The development of second order vents provided an insight into the internal flow dynamics, and they acted as 'pressure release valves', indicating perturbations in the underlying tube system that resulted from either changes in effusion rate or blockages in the lower reaches of the tube system.

Third order vents developed around the margins of flow units that had ceased to advance, and resulted from the drainage of the flow interior. Such vents produced very small extrusions of pāhoehoe, or, more commonly, toothpaste lava (Rowland & Walker 1987), which were fed at a very low rate, and were usually only active for a short period of time.

The locations of first and second order vents can be useful in identifying the course of tube systems within a compound flow field, and their activity can provide information about the internal dynamics of the flow field. Perturbations in the internal flow can also result in inflationary features that do not necessarily involve the effusion of substantial volumes of lava, and so are not considered primarily as ephemeral vents. These are described in the following section, with specific reference to `a`ā flow fields.

5.2.4 Surface features resulting from inflation

The observation and interpretation of surface features can promote a better understanding of internal flow dynamics. One of the most important processes that can be observed through the study of surface features is inflation, which has already

been discussed with reference to the formation of first order ephemeral vents. Though first order vents develop as a result of inflation at the leading edges of flows, inflation can also occur within the flow field, as a result of changes in lava supply from upflow, or restrictions downflow. As such, the study of inflationary features in both active and inactive flows provides insights into the state of the system at the time that the features formed.

Inflation features are common in pāhoehoe and `a`ā flows, and have a wide range of morphologies and sizes that reflect the underlying supply system, the state of the crust, and the dynamics of the processes. The largest inflation features form on pāhoehoe sheet flows, as the magnitude of the internal fluid body is greatest in such flows, and were termed 'lava rises' by Walker (1991). Rises are regions where a large (up to hundreds of metres long and wide) area of the solidified flow surface is uniformly uplifted, forming a prominent flat-topped 'hill' within the lava flow. Smaller features, called 'lava rise pits' (Walker 1991), appear to be areas of collapse, but are in fact regions of no inflation, surrounded by flows which have inflated.

'Tumuli' are structures similar to lava rises in their mode of formation, but they are often smaller in size, and are distinct in morphology. The term tumulus, from the Latin for mound or small hill, was used by Daly (1914) to describe the steep-sided bulges that he observed on the surfaces of many pāhoehoe flows on Hawai'i, but such features are also commonly documented in `a`ā flow fields (e.g. Guest et al. 1984). The general morphology, in terms of size and shape, is similar in both types of basaltic flow field, consisting of a whale-back shaped area of positive relief resulting from the uplift of crustal plates without any shortening (Walker 1991). While there is no strict limit to their dimensions, these are influenced by the size of the underlying lava distributaries, and in pāhoehoe flows, large tumuli grade smoothly into lava rises.

Long-lived sheet flows are rare in `a`ā flow fields, and tumuli are therefore generally smaller.

Tumuli have been documented on flows in Hawai'i (e.g. Daly 1914; Macdonald 1972; Mattox et al. 1993; Hon et al. 1994), Etna (e.g. Duncan et al. 2004), Iceland (Rossi & Gudmundsson 1996), the Deccan flood basalts in India (Duraiswami et al. 2001) and Queensland, Australia (Whitehead & Stephenson 1998). They have been classified by different authors on the predominant basis of their morphology (e.g. Duraiswami et al. 2001), their location within the flow field (e.g. Walker 1991), their role within the distributary system (e.g. Duncan et al. 2004) or a combination of these factors (e.g. Rossi & Gudmundsson 1996). Despite these distinctions, the form of a tumulus is broadly similar in all cases, being modified only slightly by its location and the subsurface supply of lava.

Two views of tumuli are shown in figure 5.14, illustrating the whale-backed shape. Depending on the extent of the local inflation, tumuli can be equant or elongate, but in either case, surface fractures are ubiquitous. While these can be radial (similar to those seen in the analogue models of Buisson & Merle 2005, figure 2.9 a), there is commonly a clearly defined axial cleft (figure 5.14 b). The more elongate the tumulus, the more pronounced the axial cleft, which is usually intersected by the additional minor dilatational fractures (Duncan et al. 2004). Examination of axial 'inflation clefts' (Walker 1991) shows them to be v-shaped in cross section.

As previously mentioned, many examples of tumuli are observed to behave as ephemeral vents, feeding sustained flows (Calvari & Pinkerton 1998). In some cases, the flows that are fed by the tumulus may themselves undergo inflation, developing into 'satellite' tumuli, as described in the 1983 Etna flow by Duncan et al. (2004), who dubbed the main supply features 'focal' tumuli. In these cases, the amount of lava

supplied to the tumulus after its formation is quite substantial, but Duncan et al. (2004) also recognised 'distributary' tumuli, which were commonly short-lived, and associated only with the effusion of small amounts of lava. The 'squeeze up' of small amounts of material through the inflation clefts has frequently been observed (e.g. Walker 1991). The extruded lava often has a bulbous leading edge, indicating a high degree of fluidity, and extrusion has been inferred to occur during active growth of the cleft, as the squeeze up is sometimes observed adhering to only one of the walls of the cleft. In some cases, while large flows are not fed, enough lava is extruded through the tumulus to completely coat its outer walls. Examples of this process are described by Macdonald (1972), and dubbed 'lava coated tumuli' by Rossi & Gudmundsson (1996).

The formation of, and extrusion of lava through, a tumulus reflects the overpressure within the interior of a tube system. In some cases, the pressure exerted by the interior is sufficient to cause the updoming of the crust and viscoelastic layer, but not sufficient to cause an eruption of lava. At the other extreme, the pressure results in breaching of the crust, and a long-lived ephemeral vent is born. As for first order ephemeral vents, if pressure is not sustained during the early development of the tumulus, it may collapse, forming a blockage in the underlying tube system. Conversely, if pressure is maintained for long enough that the crust becomes self-supporting, then at the end of the eruption the underlying tube may drain, leaving a cave beneath the tumulus.

Inflation clefts commonly show three different surface textures on their inner surfaces. These have been documented by many authors (e.g. Hon et al. 1994; Anderson et al. 1999; Duncan et al. 2004) and can provide information about the way

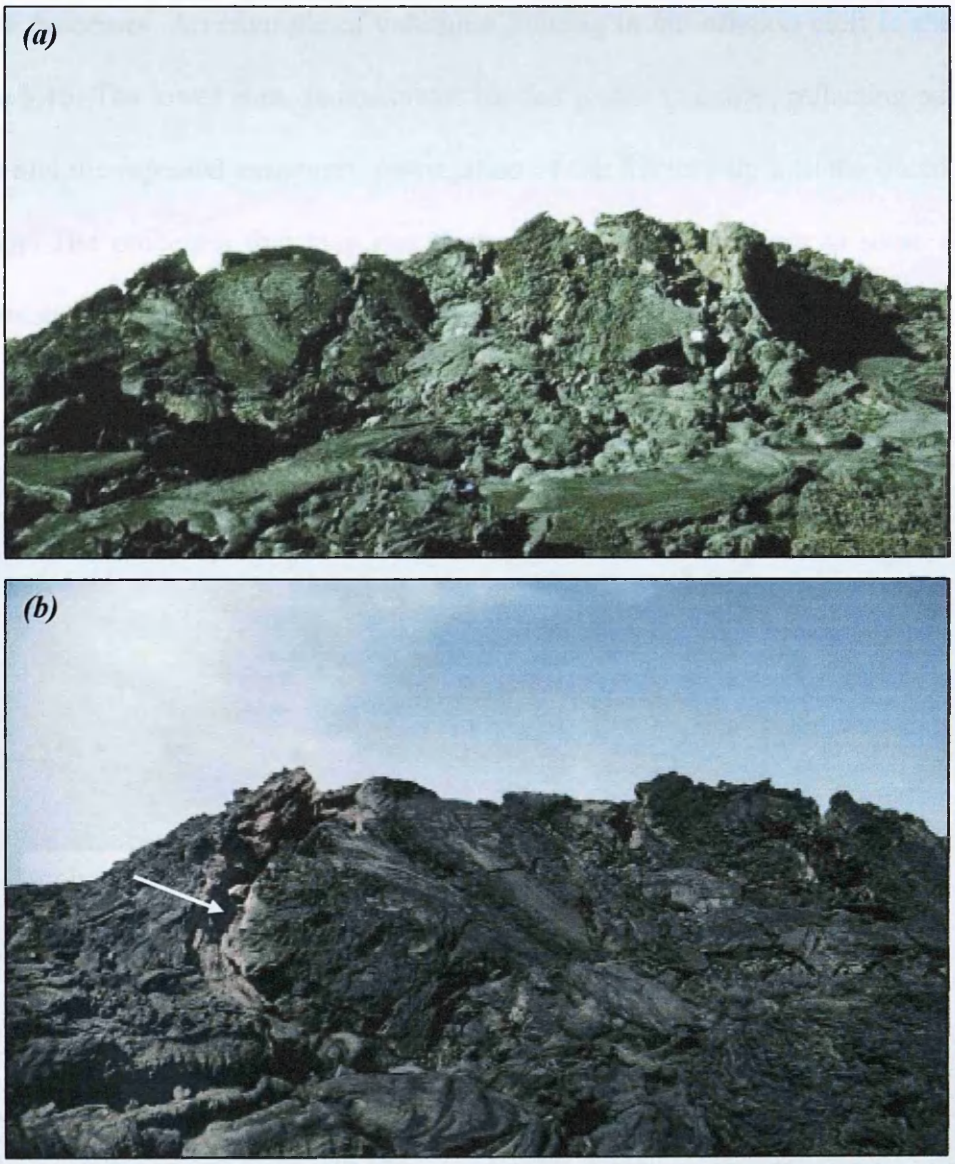

Figure 5.14. Two examples of tumuli in the 1983 `a`ā flow field, Mt. Etna. (a) Side view of an elongate tumulus, showing the whale-backed aspect. The structure is approximately 10 m in length. Note the mixture of `a`ā and pāhoehoe textures, as the fluid material newly extruded from the tumulus has formed small pāhoehoe flows, while the original flow had an `a`ā surface. Image: from Duncan et al. (2004); figure 3. (b) Oblique view of an elongate tumulus, showing the axial inflation cleft (arrowed), which is ~1 m wide. Image: from Duncan et al. (2004); figure 9.

in which tumuli grow. The upper part of the cleft is characterised by columnar jointing, and the middle part by planar fracture, which is consistent with a cooling model in which the crust undergoes thermal contraction before inflation, followed by tension during inflation (Duncan et al. 2004). These zones are indicative of brittle

failure processes. An example of columnar jointing in an inflation cleft is shown in figure 5.15. The lower zone demonstrates banded planar fractures, reflecting pulses of uplift and the repeated temporary propagation of the fracture-tip into the ductile flow interior. The processes that give rise to these fractures are subject to some debate. Anderson et al. (1999) suggest that the banded fractures in tumuli are analogous to

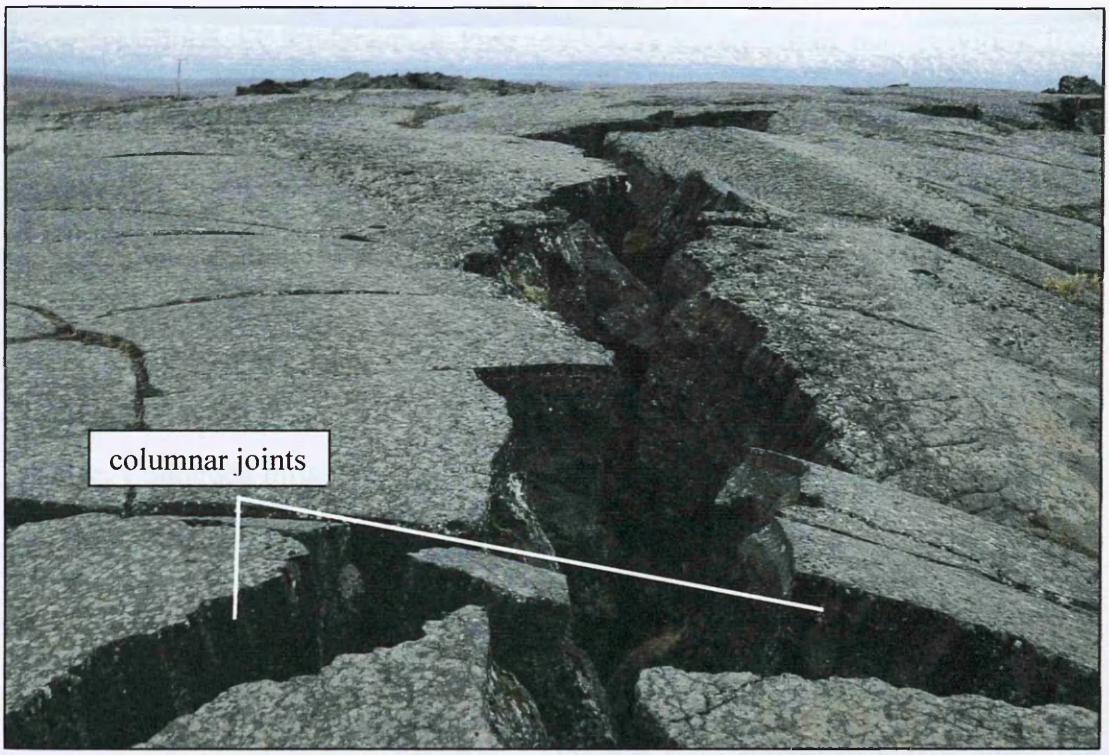

Figure 5.15. Columnar jointing exposed at the top of inflation clefts in a tumulus in Iceland, indicating the action of brittle fracture processes. Image: H. Pinkerton.

those commonly observed on crease structures (Anderson & Fink 1992), which correspond to alternate periods of brittle and ductile deformation (Hon et al. 1994). While Anderson et al. (1999) propose that the banding in tumuli requires periods of higher and lower strain rate, with a higher strain rate needed to force the crack tip into the fluid interior, strain rate variations are not mentioned by Anderson & Fink (1992) with reference to similar morphology. In order to achieve such cyclic variations in strain rate, Anderson et al. (1999) invoke pulsed inflation. This is refuted by Self et al.

(2000), who note that no such process has been observed in the field, though they concede that this does not categorically rule it out as a possibility. Nonetheless, the widespread nature of the texture suggests that the causal process is common, while the widespread observations of tumulus formation have not documented pulsed inflation, suggesting that it is not the dominant mechanism. It is plausible to explain the presence of fracture banding based only on steady inflation, as this was implied for crease structures by Anderson & Fink (1992). A steady strain rate, resulting from gradual inflation, causes an increase in the strain in the crust. When this reaches a threshold value, the brittle crust fractures, releasing the strain, reducing local pressure, and probably resulting in the fracture-tip propagating a short way into the ductile interior. The exposed interior cools and solidifies, preserving evidence both of the brittle fracture and a small amount of ductile 'spreading' that took place during the episode. Continued inflation results in repetition of this process, as the constant mass input again increases the local pressure.

Although pulsed inflation of tumuli need not be invoked to explain the texture in inflation clefts, evidence of cyclic inflation is preserved in 'shatter rings'. These are approximately circular rings of broken rubble that form directly over lava tubes, and appear to resemble collapsed tumuli (Kauahikaua et al. 1998). However, observations indicate that they form by the episodic, near constant flexing of the tube roof, causing repeated fracture around the edges of the uplifted area (Kauahikaua et al. 2003). One study has correlated observed cycles in the uplift of a shatter ring roof with tilt cycles of the volcano's flanks, finding that changes in supply in the tube system directly reflect variations in conduit processes (Orr 2008). As with tumuli, only vertical movement is observed to occur, but the roof of a shatter ring is not subjected to any tensile or compressive forces, unlike tumuli which are characterised by tensile clefts.

Tumuli are suggested to be areas where gas can escape from the underlying lava, or from where vesicle-rich lava can be extruded (Walker 1991). This may certainly be the case if overpressure in the system is low, as is inferred during early development. The upper part of the tumulus crust is usually highly vesicular, which has been interpreted to infer that overpressure in the system is low early in the eruption, allowing the exsolution of vesicles that rise to the surface and are preserved in the crust (Cashman & Kauahikaua 1997). Once the crust has developed, and overpressure is sufficient to cause inflation, exsolution is more difficult, so the number and size of vesicles incorporated into the downward growing crust decreases. If lava is stored within a tumulus, the vesicles that are present will (depending on the yield strength of the lava) rise to the top, as density-stable stratification occurs (Walker 1991). Unless the gas escapes through the crust, when rupture occurs along the inflation cleft, the resultant squeeze outs will be vesicle-rich. Storage of lava within tumuli is inferred by Duraiswami et al. (2001), who found that squeeze outs from tumuli could be rich in plagioclase phenocrysts, indicating that the lava must have resided in the tumulus for sufficient time to allow the rise of these crystals, which are less dense than the host fluid. Alternatively, squeeze outs from tumuli may be dense and vesicle-poor as a result of the resorption of gas due to very high overpressures, as suggested by Cashman & Kauahikaua (1997) and Hon et al. (1994). If the squeeze out initiates as vesicle-poor but volatile-rich lava, vesicularity increases with distance from the source, as the gas exsolves once more (Hon et al. 1994).

5.3 Summary and discussion

The evidence presented in the first part of this chapter has illustrated that structures which developed in the experiments presented in previous chapters are analogous to features commonly observed in natural flows of similar rheology. Due to necessary simplifications in the experiments, such as their isothermal nature and the absence of a viscoelastic layer, some of the structures do not appear identical, but their modes of formation are considered to be physically similar. Although clinker cover masks the surface features in lava flows, the rheological similarity between lavas and glaciers has also allowed comparison of the models with these flows of ice. In this way, all of the features produced in the models have been found to have natural counterparts, even if some have not yet been observed on clinker-covered lavas. This confirms the accuracy of the dynamic scaling between the natural and analogue systems, and justifies the use of simple analogue models to provide insights into processes that occur in lavas and glaciers. The analogue modelling approach is therefore of great use in the continuing attempts to improve our understanding of lava flow emplacement, as well as other natural processes.

The complex, cooling-dependent rheology of lava flows was highlighted in chapter two as one of the major difficulties in attempting to model their behaviour. The examination of field studies in this chapter has now illustrated that compound morphology, which is a common feature of basaltic eruptions, is also strongly dependent on other, extrinsic, parameters, the most important of which are effusion rate, eruption duration and local topography. Analogue models involving cooling have been able to replicate some of the morphologies observed during the emplacement of compound pāhoehoe flows, such as the formation of pillows, but scaling difficulties mean that a single analogue model is not capable of incorporating all rheological and

environmental parameters, and the reproduction of other complexities, including `a`ā surface texture and anastomosing tube systems, has not yet been achieved. While the use of analogue models certainly aids our understanding, it is not possible to overstate the importance of detailed field observations, both in validating experimental results, and in the study of processes that cannot be modelled.

The emplacement of simple flows is relatively easy to observe. However, as the eruption duration and the flow complexity increase, the growth of subsurface supply systems causes increasing difficulties in the observation and monitoring of flow field development. In order to track the evolution of such systems, it is necessary to observe the formation of tubes, and to be able to document changes in their distribution and behaviour during an eruption. Field studies can locate the presence of tubes by mapping such features as first and second order ephemeral vents, tumuli and shatter rings, and the behaviour of such features can also provide information about the state of flow within the supply system, which may reflect changes in conditions at the vent or the underlying supply system (e.g. Orr 2008).

Other difficulties that may be resolved through observations of active lavas include the role that stochastic processes can play in influencing structural development. While the formation and steady state behaviour of channels and tubes is broadly understood, collapses of tube roofs and/or levées may cause blockages and breakouts that have a significant effect on the subsequent paths taken by the lava. Such accidental breaches may cause flows to advance in greatly diverging directions, resulting in different areas coming under the threat of inundation without warning.

The importance of late-stage and post-emplacement processes has not been fully explored in the field studies discussed here. While the third order ephemeral vents described by Calvari & Pinkerton (1998) around the margins of stagnant flow lobes

only fed small volume, slow moving flows, the cessation of a flow lobe is not necessarily indicative of its inability to flow. The interior of a stationary flow retains heat for many months or years, depending on its thickness, and cessation of flow can reflect the development of a crustal, rather than an internal, yield strength. This was discussed during the formation of first order ephemeral vents, in which case continued supply to the front resulted in the rupture of the carapace in a matter of hours to days (e.g. Pinkerton & Sparks 1976; Calvari & Pinkerton 1998). Observations of lava flows during the eruption of Parícutin, Mexico, in the 1940s suggest that large-scale reactivation of a flow front can occur up to one month after it stops advancing (observations by Foshag and Gonzalez-Reyna, in Luhr & Simkin 1993). The emplacement of the San Juan Parangaricutiro basaltic andesite lava flow took place over several months, during which time several pauses in advance were recorded. Approximately six months after its initiation, following a pause in advance of one month, the front of the 8 km long flow again began to advance. Initially, the flow progressed as a series of lobes, from which lava in a highly plastic state broke out in tongues. These breakouts usually occurred approximately half way up the flow front, and advanced for no more than a day before congealing. Several days after this initial reactivation, a number of more fluid streams of lava broke out from the surface of the lava flow, close to the flow front, and advanced rapidly down the front as incandescent streams, covering 350,000 m^2 in one night.

These observations suggest that following the cessation of flow, the flow front remained inactive for several weeks before supply resumed from upflow. Initially, the increased pressure in the flow front caused material that had been stored for some time to be extruded from the front. This material had evidently undergone sufficient cooling and crystallisation to develop a yield strength, as demonstrated by the

plasticity, but was still able to advance several hundred metres. Eventually, the fresh, fluid supply from the vent arrived in the region of the flow front, emerging to rapidly inundate a significant area within a very short space of time. This observation indicates that reactivation of a flow front, and enforced drainage of the material contained within it, can occur on a large and devastating scale. The state of the material upon stagnation, and the processes that can lead to drainage, are therefore of great importance when considering lava flow emplacement. The products of squeeze ups from third order vents and tumuli can be useful indicators of conditions within the flow field at the time of their formation, and, if they are known to be late-stage features, may provide valuable information about the maximum crystallinity at which lava can flow. The value of this parameter is as yet unknown, but is vital in allowing the confident assessment of when a lava flow has ceased to pose a hazard.

The aim of this chapter has been to highlight the successes of analogue models, but also to demonstrate their shortcomings through illustrations of the high degree of complexity that lava flows may attain. The field studies discussed indicate that many difficulties remain when attempting to comprehensively describe the development of a compound flow field, and as such, the need for more work is clear. The following chapter considers the emplacement of a compound `a`ā flow field during the 2001 eruption of Etna, and attempts to provide insights into the factors governing the surface and structural morphologies observed in that example.

6. Etna 2001

The previous chapter illustrated that while analogue models are capable of reproducing many aspects of the emplacement of simple flows, the only way to gain a fuller understanding of the complexities that arise in long-lived compound flows is by studying them in the field. Valuable information on emplacement processes may be derived from the study of both active and inactive flows, though the data gleaned from inactive flows may be skewed towards the importance of late-stage processes. The observation of active flows, which allows insights to be gained into the processes prevailing during all stages of emplacement, is therefore a necessary part of fieldwork. Complex flow fields consist of many juxtaposed flow lobes, and contain tube systems, ephemeral vents and in many cases, surface features of uncertain origin. Elucidating the processes that result in such features will result in a clearer understanding of the dynamics of compound flow emplacement.

This chapter examines the development of the compound `a`ā lower flow field that was emplaced over a period of 23 days during the 2001 eruption of Etna. The eruption was monitored closely by the Istituto Nazionale di Geofisica e Vulcanologia (INGV), Catania, who collected many visible images of the flow field during its emplacement. Fieldwork was also carried out during the eruption by H. Pinkerton, who collected thermal images and video data over a period of several days. These data have been used, together with daily eruption reports published by INGV, detailed analysis of post-eruption aerial photographs, and my field observations to unravel the structural and temporal evolution of the flow field in a manner that has not previously been attempted. A large body of work has already been published on the lower flow field, and discussion of this is incorporated where relevant, but a detailed analysis of the

relatively small-scale and late-stage flow features has not been performed until now. These features can provide insights into the conditions prevailing during their formation, and help to broaden our understanding of the importance of processes that can occur once a flow unit has stopped advancing.

The following section provides some background on the recent eruptive history of Etna and the 2001 eruption, before presenting a chronological overview of the emplacement of the lower flow field. Following this introduction, a detailed description of the development of one part of the flow field is presented, in order to illustrate the complexities that can arise during emplacement. Subsequent sections discuss these various complex features, which are also observed in many other parts of the flow field, relating them to processes such as the emplacement, inflation, breaching and drainage of flow units. The final section considers the influence of effusion rate variations on flow morphology.

6.1 The 2001 eruption

Between 1971 and 1993, Etna produced frequent summit and flank eruptions, terminating with the voluminous outpourings of the 1991 to 1993 eruption, the largest for over 300 years. Following this eruption, the volcano entered a period of repose, which lasted for two years before activity resumed in the summit region. All four summit craters showed activity during the period from 1995 to 2001, sometimes individually and sometimes in concert, and periods of higher overall activity suggested the rise of pulses of magma from depth (Behncke & Neri 2003). The 2001 eruption was the first flank eruption since 1993, and marked the beginning of a new cycle of activity (Behncke & Neri 2003). The eruption, which was preceded by several months of intense summit activity, began on July 17th and lasted until August

9th. During this time, seven eruptive vents or fissures were active, and these were located on two different fissure systems (figure 6.1). The upper fissure system was active from July 17th to August 8th, and was host to five eruptive vents, while the lower fissure system, on the south flank of the volcano, was active from July 18th to August 9th, and fed two vents. The two fissure systems tapped different magma sources, with the upper vents producing trachybasalts that were compositionally comparable to the historic products of the volcano, while those produced by the lower fissure system were more primitive, consisting of plagioclase-poor, amphibole-bearing basalt (Métrich et al. 2004; Corsaro et al. 2007). The two magma supplies are not thought to have mixed during the eruption (Behncke & Neri 2003; Acocella & Neri 2003), and the activity of the lower fissure system is classed as an 'eccentric' eruption, i.e. one that tapped a magma source separate from that supplying the summit craters through the central conduit.

The lower fissure system vents, LFS1 and LFS2 following the notation of Coltelli et al. 2007 (figure 6.1), produced the longest flows of the eruption, with the lower flow field fed by LFS1 attaining a length of 6.4 km in the first nine days of activity. This flow field accounted for approximately half of the total erupted volume. Of the seven flow fields produced, only two remain largely intact: the lower flow field, and the flow emitted from the northernmost eruptive fissure in the Valle del Leone (figure 6.1). The others have been covered by the products of subsequent eruptions, or disturbed by road building activity. While the proximal part of the lower flow field has been thus affected, with the rebuilding of the SP92 road and some ash cover, the flow field to the south of the road remains perfectly exposed.

In the following summarised eruption chronology, only the activity of LFS1 and

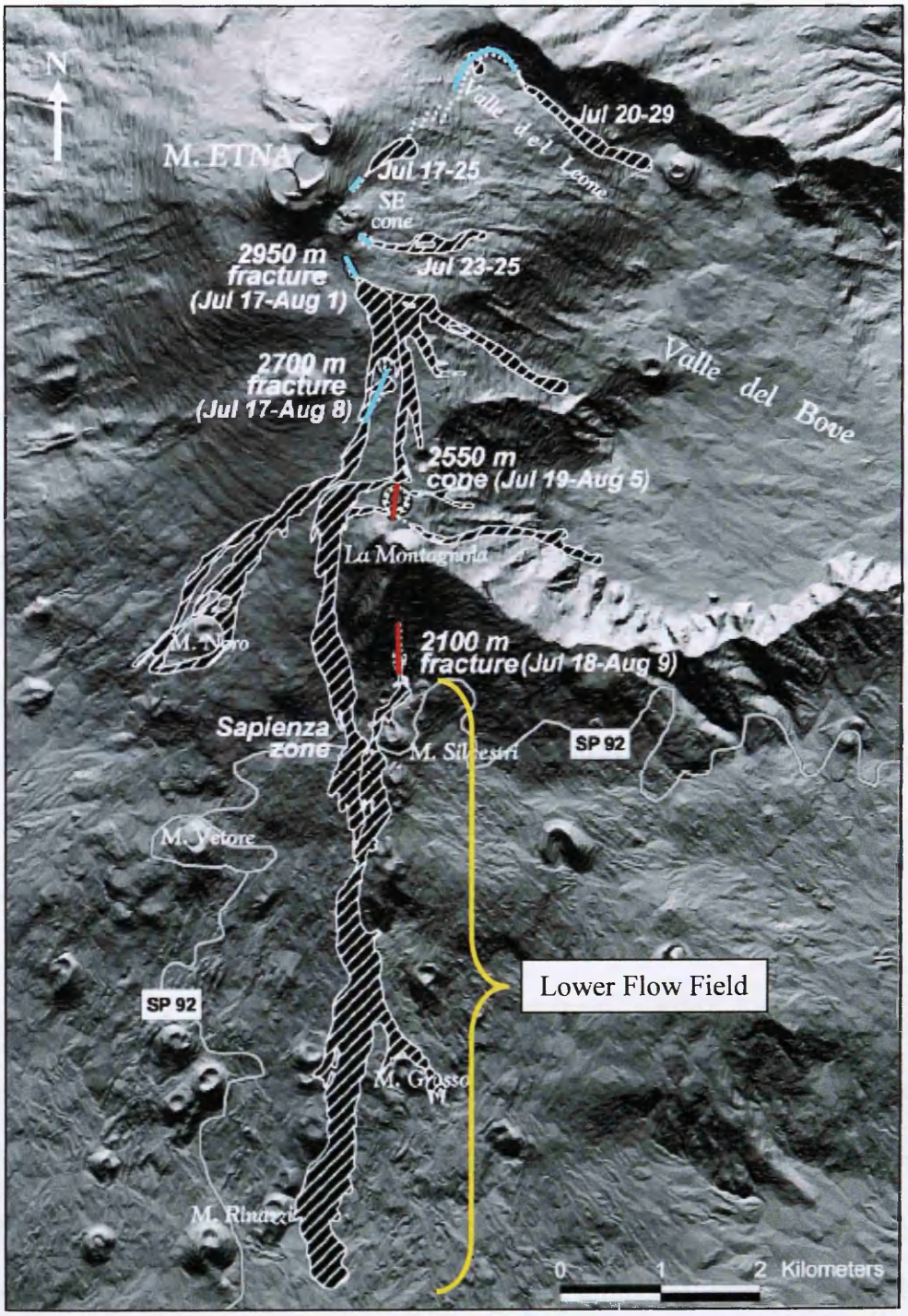

Figure 6.1. Map showing the lavas emplaced during the 2001 flank eruption of Mt. Etna, Sicily (cross-hatched areas). Vents and eruptive fissures on the upper fissure system are shown in blue; those on the lower fissure system are shown in red. The southernmost fracture, at 2100 m above sea level, is the LFS1 vent that gave rise to the lower flow field. LFS2 is the 2550 m cone. From Barberi et al. (2003); figure 1.

the development of the lower flow field is considered, save where changes in the behaviour of LFS2 had a direct effect on that of LFS1. The advance of the lower flow field was closely documented, as it flowed south towards the town of Nicolosi, and therefore posed a potential threat to human interests.

6.1.1 Eruption Chronology

The following description is divided into the early part of the eruption (until the end of July) and the late part of the eruption (August). This is because the available data only cover the later part of the eruption, and so the earlier chronology relies solely on published accounts. The earliest visible images from INGV were taken on August 1st, and although video and thermal image data are available from July 27th to August 4th, the July data concentrate on changes in activity at the LFS1 vent and the top ~2 km of the flow field, and do not provide information about the development of lower parts of the flow field. These data are discussed in section 6.3, where vent behaviour is considered in more detail.

The account of activity at LFS1 and LFS2 during July is compiled principally from the INGV daily eruption reports, but also draws on the eruption chronologies of Behncke & Neri (2003) and Coltelli et al. (2007). It is noted that there are some discrepancies between the reports regarding the timing of events (up to one day), and also in the quoted altitudes of certain features. The altitude differences are probably due to estimates being made by different people, possibly at different times on the same day and possibly by different methods. Behncke & Neri (2003) and Coltelli et al. (2007) state that field surveys were carried out several times during the eruption, and so positions were collected by GPS, but the INGV reports do not specify their methods. It is possible that the positions of active flow fronts were estimated from

aerial images, and so some error may have been incurred in this way. The quoted positions are therefore estimates.

The account of activity during August again draws on the INGV reports and the work of Behncke & Nero (2003) and Coltelli et al. (2007), but is largely based on a rigorous analysis of the visible images collected by INGV, and the thermal images collected by H. Pinkerton. Many of these images are used to illustrate the changes that took place in the lower flow field during this part of the eruption. A sketch of the lower flow field is provided in figure 6.2, which shows the main structural features of the flow, as well as contours and the names of the old cinder cones used in the text, while a detailed map of the post-eruption structure of the flow is provided in figure 6.4, and also in a larger version at the back of the thesis. Figure 6.3 shows sketches of the flow structure at several times during the later part of the eruption, with the active parts of the flow marked in red. Sketches of the active parts of the flow, before August 1st, have been made by Behncke & Neri (2003) and Coltelli et al. (2007) and are shown in figure 6.55. Figures 6.2 and 6.3 will be referred to when discussing the general development of the flow field during the remainder of this section, while the map in figure 6.4 is used during the more detailed analysis in section 6.2.

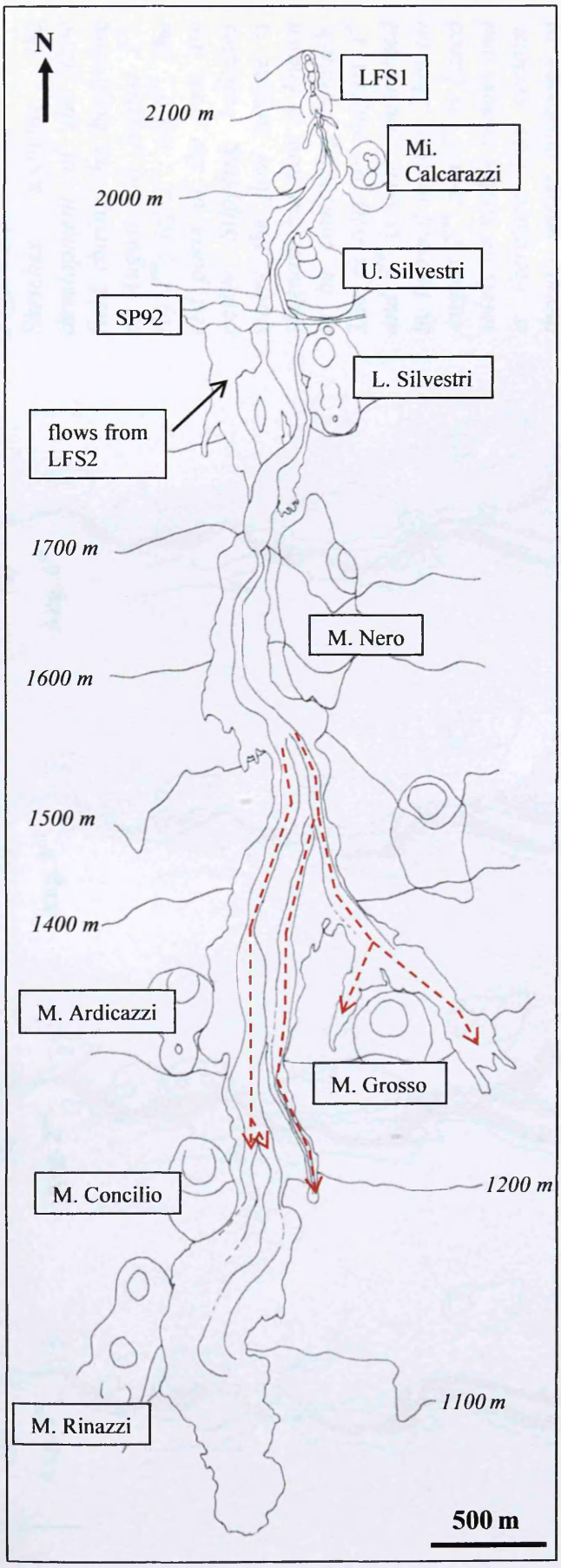

Figure 6.2.
Sketch showing the outline of the 2001 lower flow field, and its main structural features, as they appeared after the eruption. The flow field consists of a single main channel down to ~1500 m, where it branches. Three branches were active during the eruption, and these are indicated by the dashed red arrows. The western arrow indicates the main channel, which branches adjacent to M. Concilio, with the eastern branch being better developed. The central arrow is the secondary channel, which branched off from the main channel on July 30th. The eastern arrow is the M. Grosso channel, which initiated on August 2nd. The names of all the old cinder cones used in the text are indicated. Contour spacing is 100 m.

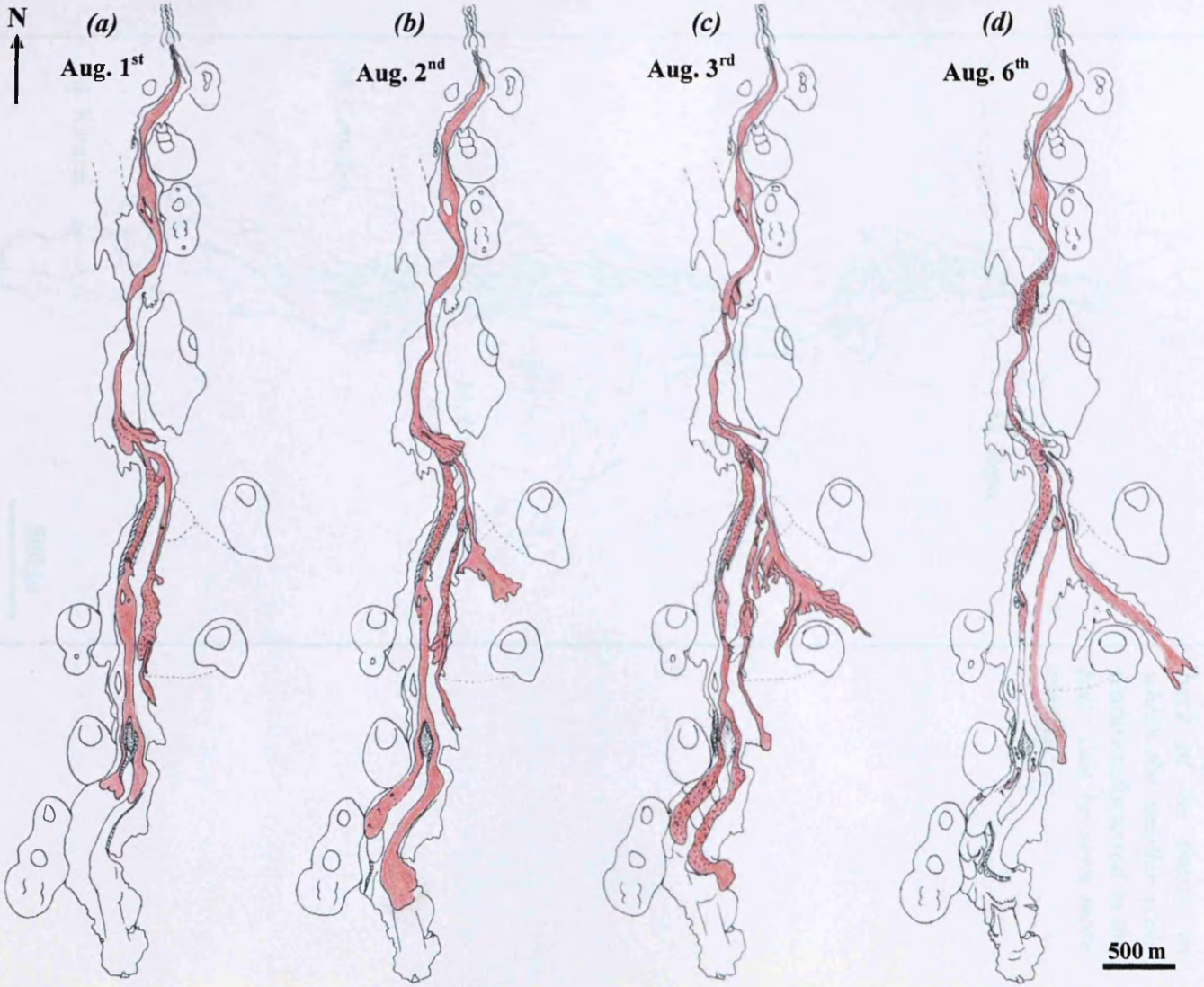

Figure 6.3.
Sketches showing the development of the flow field during the beginning of August. (a) August 1st; (b) 2nd; (c) 3rd; (d) 6th. The red parts of the flow are active. Stippling indicates where the flow surface is stagnant but flow is known to be continuing beneath. The activity on August 1st and 3rd is well constrained by thermal images. That on August 2nd and 6th is based solely on visible images and is therefore less certain, though image coverage of the flow is better on the 2nd than the 6th. The activity of the small squeeze ups in the distal flow field on the 6th is tentative, inferred from possible observations of gas. Dashed lines within the flow field indicate where channel boundaries are inferred; those outside the flow field are tracks.

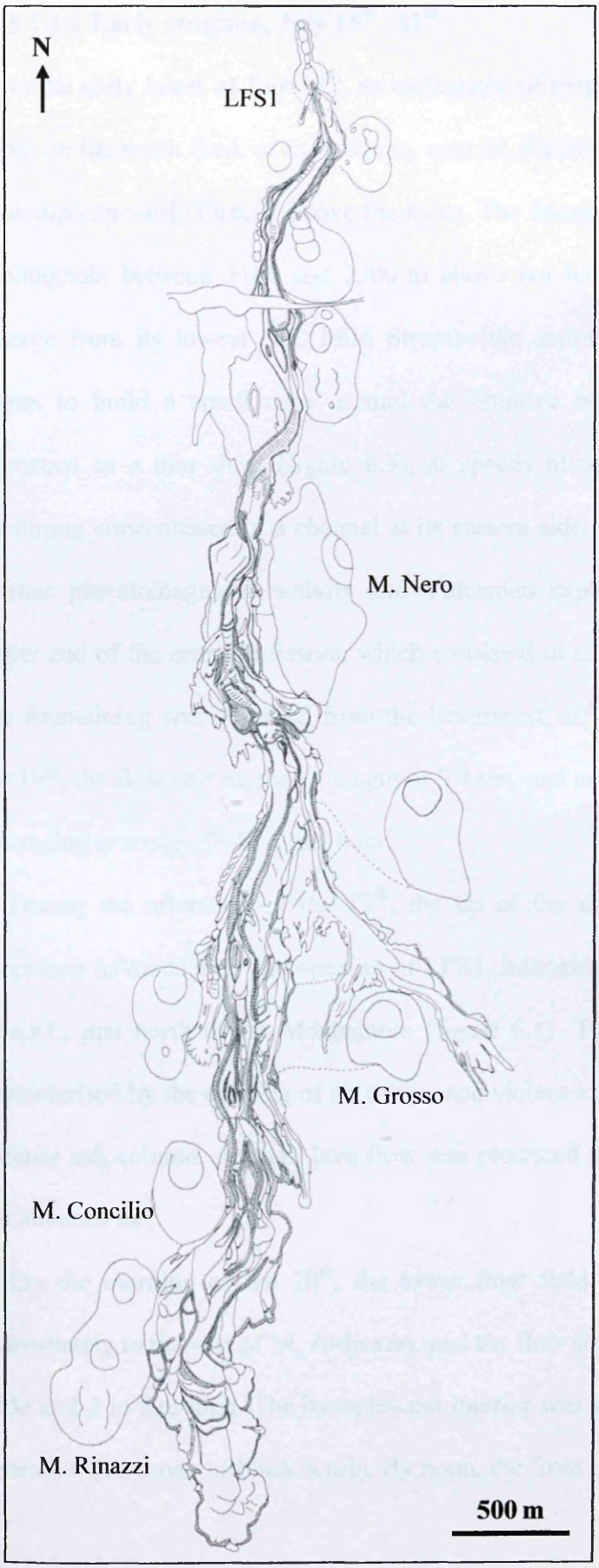

Figure 6.4.
Detailed post-eruption structure of the lower flow field. Even at such a small scale, the complexity is evident, and several generations of lobes can be seen both within and around the three main channels. A larger copy of this map is provided in the back of the thesis, in which the smaller scale features discussed in the text can be seen more clearly.

6.1.1.1 Early eruption, July 18th - 31st

In the early hours of July 18th, an earthquake of magnitude 2.7 occurred at 1.5 km depth on the south flank of the volcano, near M. Calcarazzi, and LFS1 opened almost contemporaneously directly above the focus. The fracture extended up the flank of La Montagnola between 2100 and 2300 m above sea level (a.s.l.), and lava began to emerge from its lowest end. Mild Strombolian activity was also observed, which began to build a small cone around the eruptive bocca. The lava flow initially advanced as a thin sheet (figure 6.5), at speeds of up to 150 m per hour, before becoming concentrated in a channel at its eastern side. Over the following few days, intense phreatomagmatic activity and Vulcanian explosions were observed at the upper end of the eruptive fissure, which consisted of at least three distinct vents, and fire fountaining was observed from the lowermost, effusive vent. By the evening of the 19th, the flow had reached a length of 3.4 km, and an altitude of ~1430 m, and was advancing at a rate of ~45 m per hour.

During the afternoon of the 19th, the tip of the dyke, which had continued to propagate upwards after the opening of LFS1, intersected the ground surface at 2550 m a.s.l., just north of La Montagnola (figure 6.1). This eruptive vent, LFS2, was characterised by the opening of pit craters and violent explosive activity that produced a dense ash column. A small lava flow was produced at the start of activity, but did not advance far.

On the morning of the 20th, the lower flow field had reached ~1350 m a.s.l., immediately to the east of M. Ardicazzi, and the flow front was estimated to be 100 m wide and 3 to 5 m high. The incandescent interior was visible through the flow front, beneath a thin cover of black scoria. By noon, the front had reached ~1300 m, and had

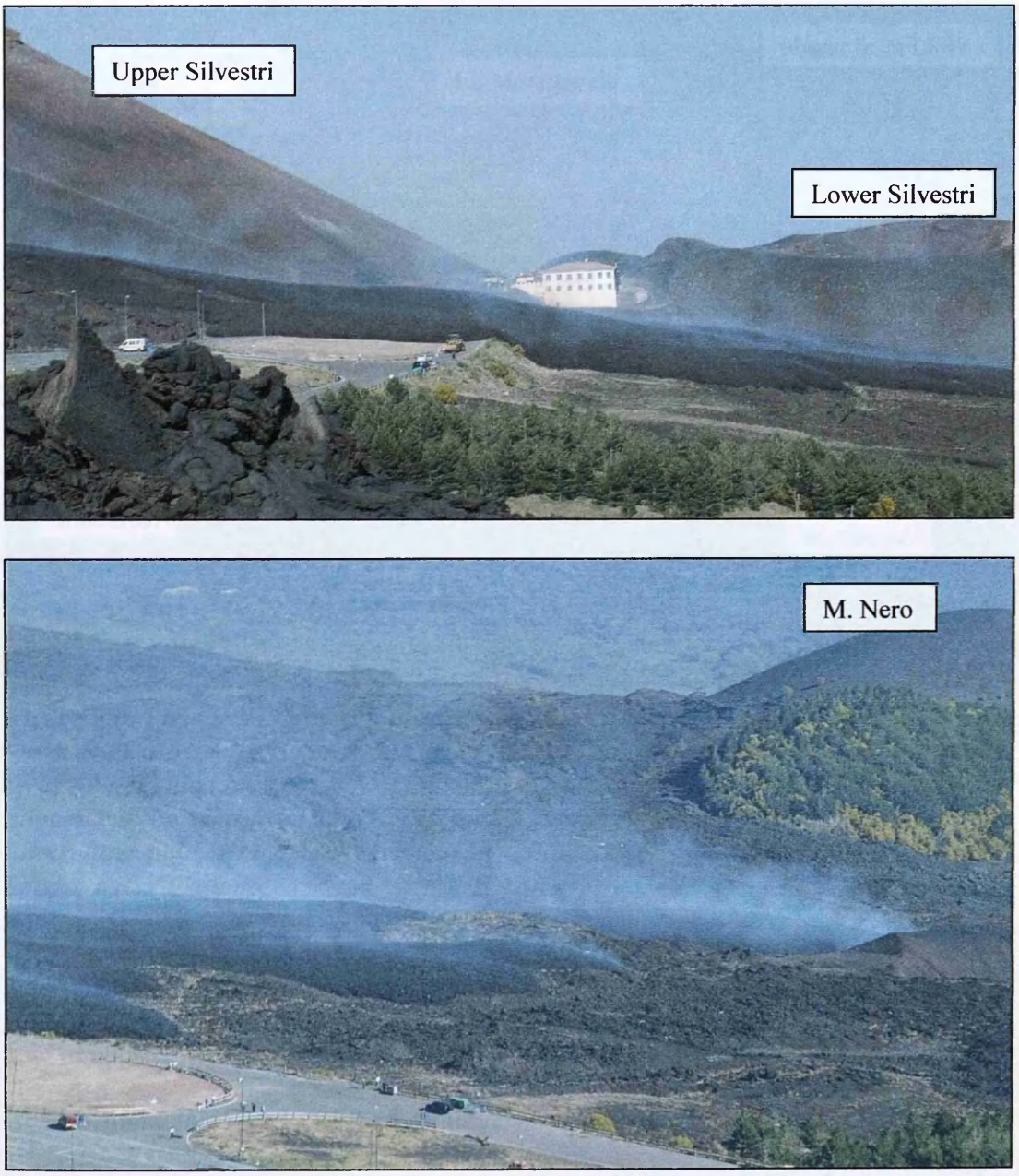

Figure 6.5. Views from the west of the advancing lava flow during the evening of July 18th 2001, showing its sheet-like character. The flow had reached a length of ~1.6 km in around 18 hours. Images: INGV Catania.

a width of 250 m (figure 6.6). Fire fountaining was observed at LFS1, and this continued until the 22nd, reaching heights of up to 200 m. By mid-afternoon on the 21st, the front had reached ~1070 m, and was 400 m wide, and by the morning of the 22nd, it had reached ~1060 m, south east of M. Rinazzi. Here, the flow front had split

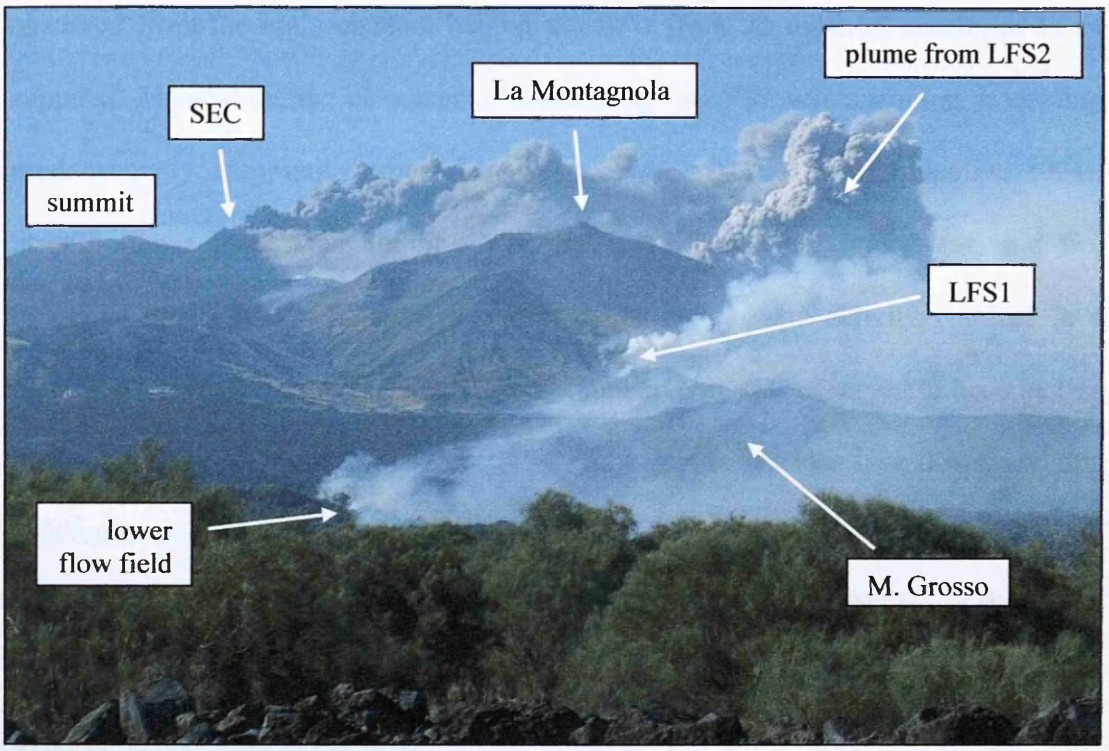

Figure 6.6. View from the south towards the summit on the evening of July 20th. Ash-laden plumes from the South East Crater and LFS2 are visible, though the vent region of LFS2 is hidden behind La Montagnola in the middle of the image. Ashy and steam plumes can be seen from LFS1. The gas in the foreground indicates the path of the lower flow field, which had reached an altitude of ~1300 m by noon on the 20th. Image: INGV Catania.

into tongues, the most advanced of which was around 150 m wide, and advancing at a rate of approximately 50 m per hour.

Fire fountaining at LFS1 had diminished considerably by the 23rd, and the flow front had reached an area of flatter topography at ~1055 m a.s.l. The flow appeared to be well supplied along its whole length, save for a few hundred metres immediately behind the flow front. The flow front, however, was still advancing slowly, and had spread out to form a fan shape with a width of around 100 m and a height of 10 m.

The lower flow field had reached 1048 m a.s.l. on the 24th, and 1035 m by the morning of the 25th. The front was 200 to 300 m wide, and 10 to 20 m high. This was the maximum extent reached by the lower flow field, and overflows were already

observed from the main channel behind the flow front, as material continued to be supplied. Meanwhile, the character of the activity at LFS2 was changing, becoming predominantly magmatic rather than ash-producing (Calvari & Pinkerton 2004). Strombolian activity was building a scoria cone around the main vent, and fire fountains up to 300 m high were observed. This magmatic activity resulted in a reduction in activity at LFS1, where Strombolian activity was observed to become less intense. During the night of the 25th-26th, LFS2 began to produce lava flows, and this resulted in a further reduction of activity at LFS1, where explosive activity was weak and the effusion rate had diminished significantly. The front of the lower flow field was observed to be stagnant, and the continued supply was resulting in overlapping lobes in medial parts of the flow.

Observations on the 27th indicated that continued activity in the lower flow field was resulting in widening and thickening due to the emplacement of juxtaposed lobes. The most advanced active flow front was seen to overlie the earlier flows, at around 1400 m a.s.l., and appeared to be poorly supplied. This active flow front slowly advanced on top of earlier flows over the next few days. Several effusive vents were active at LFS2, one of which produced flows that had advanced southwards towards the Sapienza tourist complex, and were abutting the main channel in the lower flow field. On the 30th, the main channel in the lower flow field branched at around 1500 m a.s.l., and a new, secondary, channel began flowing south alongside the main channel. This channel can be seen in the sketch (figure 6.3 a) and thermal image (figure 6.7) from August 1st.

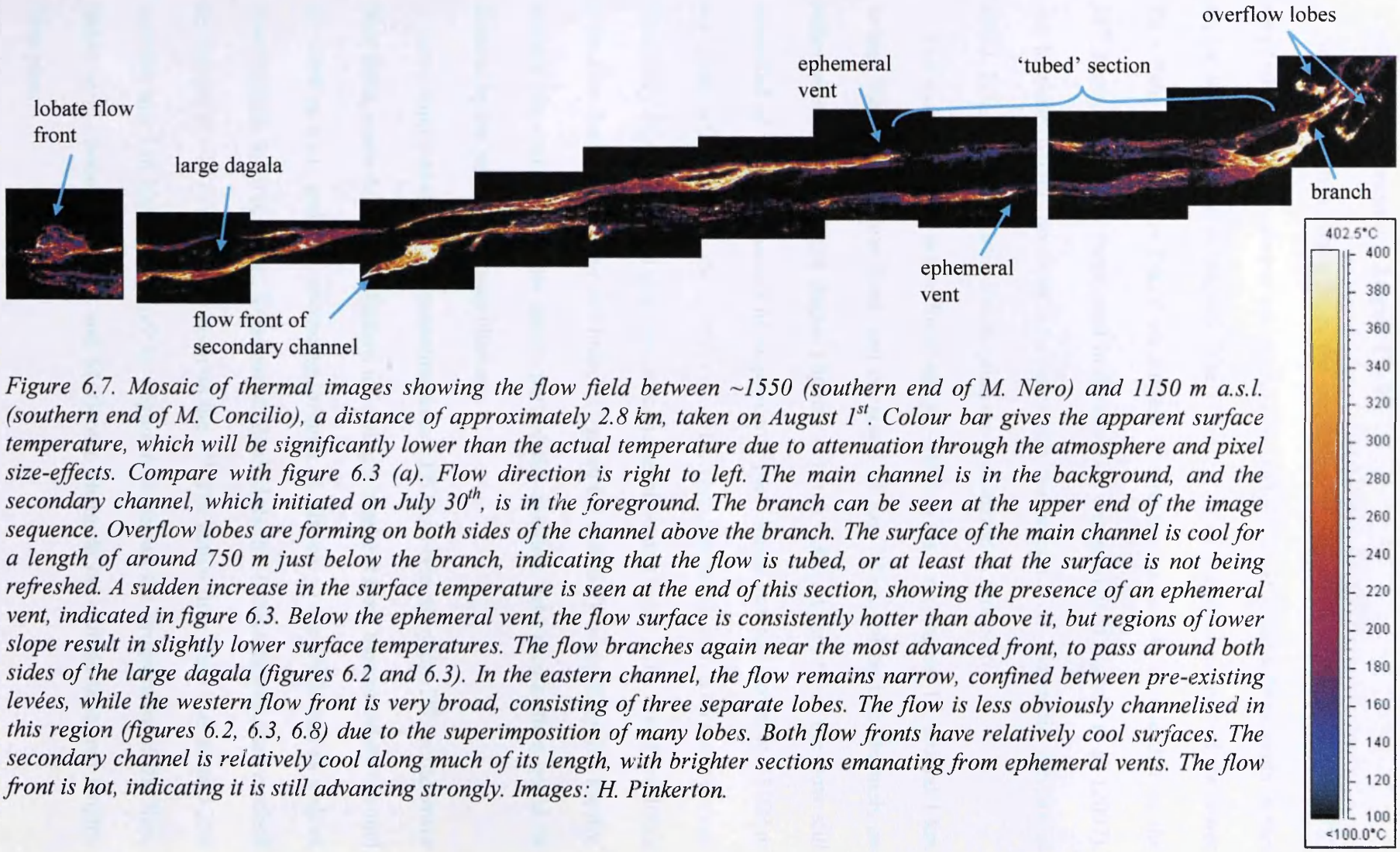

Figure 6.7. Mosaic of thermal images showing the flow field between ~1550 (southern end of M. Nero) and 1150 m a.s.l. (southern end of M. Concilio), a distance of approximately 2.8 km, taken on August 1st. Colour bar gives the apparent surface temperature, which will be significantly lower than the actual temperature due to attenuation through the atmosphere and pixel size-effects. Compare with figure 6.3 (a). Flow direction is right to left. The main channel is in the background, and the secondary channel, which initiated on July 30th, is in the foreground. The branch can be seen at the upper end of the image sequence. Overflow lobes are forming on both sides of the channel above the branch. The surface of the main channel is cool for a length of around 750 m just below the branch, indicating that the flow is tubed, or at least that the surface is not being refreshed. A sudden increase in the surface temperature is seen at the end of this section, showing the presence of an ephemeral vent, indicated in figure 6.3. Below the ephemeral vent, the flow surface is consistently hotter than above it, but regions of lower slope result in slightly lower surface temperatures. The flow branches again near the most advanced front, to pass around both sides of the large dagala (figures 6.2 and 6.3). In the eastern channel, the flow remains narrow, confined between pre-existing levées, while the western flow front is very broad, consisting of three separate lobes. The flow is less obviously channelised in this region (figures 6.2, 6.3, 6.8) due to the superimposition of many lobes. Both flow fronts have relatively cool surfaces. The secondary channel is relatively cool along much of its length, with brighter sections emanating from ephemeral vents. The flow front is hot, indicating it is still advancing strongly. Images: H. Pinkerton.

6.1.1.2 Late eruption, August 1st - 9th

Activity began to wane from the beginning of August. The behaviour of LFS2 reverted to mostly explosive ash production, and the flows issuing from vents in this region were observed to stagnate. The effusion rate in the proximal part of the lower flow field estimated by INGV on August 1st was approximately double that on the 31st, though this is not mentioned in the eruption chronology of Coltelli et al. (2007). An increase would, however, correlate with the reduction in magmatic activity at LFS2. Effusion rates during the eruption are considered in section 6.3.

The most advanced active front was at ~1080 m a.s.l. on August 1st, around 1 km behind the stagnant flow front, and consisted of two lobes, fed by two channels on either side of a prominent dagala (figures 6.3 a & 6.8). At this time, the flow still consisted of a single channel in its proximal part, which reached down to ~1500 m a.s.l. Below this altitude, the complexity of the flow increased, with both the main and secondary channels containing several ephemeral vents (figure 6.7). Overflow lobes were also developing above the branch (figures 6.3 a & 6.7), suggesting that supply, though low compared to the earlier part of the eruption, was greater than could be drained by the stagnating lower channels.

Lava supply to the flows emanating from LFS2 had ceased by the 2nd. In the lower flow field, a new branch had formed following a breakout from the secondary channel at ~1460 m a.s.l., and was advancing towards M. Grosso to the south east as a sheet flow (figures 6.3 b & 6.9 a). This branch, dubbed the M. Grosso branch, had reached an altitude of ~1375 m a.s.l. by noon on the 2nd. The active flow front was around 250 m wide and 3 m high (figure 6.9 b). Figure 6.10 shows the progression of the flow fronts of the main, secondary and M. Grosso channels on altitude-time and length-time plots.

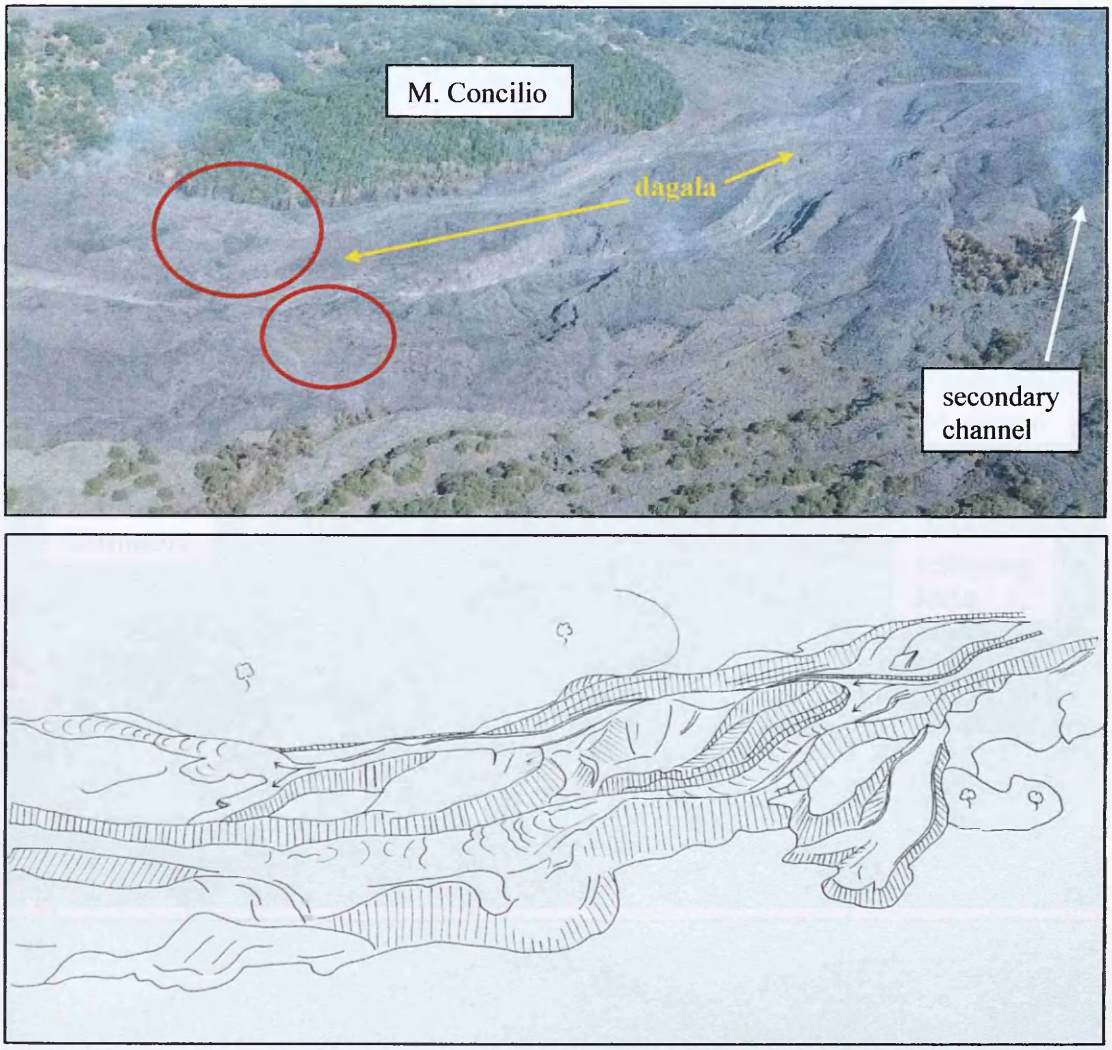

Figure 6.8. Image and sketch showing the active flow fronts (circled in red) in the main channel on 1st August, as seen in thermal images (figure 6.7). The main channel is split into two branches that are flowing around either side of a prominent dagala (indicated in the image). M. Concilio is in the background. The problem of determining where flow fronts are without the use of thermal imaging can be appreciated. While gas can be used to determine the parts of the flow that are active, this is not always precise. The haze seen downflow of the flow fronts in the image is from burning vegetation. The advancing front of the secondary branch can be seen to right hand side of image, and is very gassy. Image: INGV Catania.

Activity in the distal part of the main flow field continued, with the juxtaposition and superposition of lobes that seemed to be fed largely by the drainage of channels immediately upflow (INGV eruption reports). The M. Grosso branch had reached M. Grosso and bifurcated, with the eastern branch having attained an altitude of ~1320 m

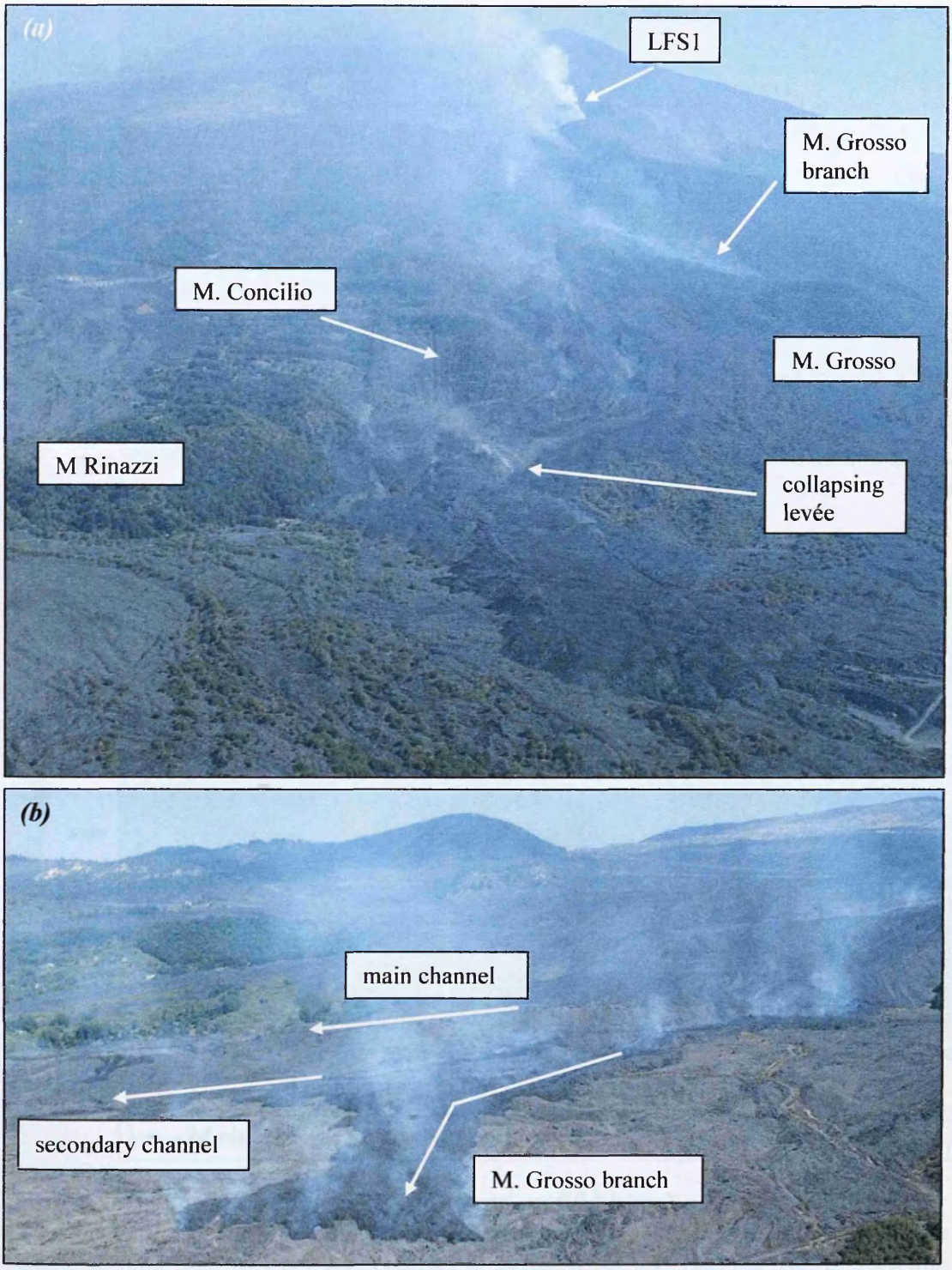

Figure 6.9. Images taken around noon on August 2nd. Compare figure 6.3. (a) View of the lower flow field from the south. Gas indicates where open channel flow is occurring. The M. Grosso branch can be seen heading south east in the upper right of the image, due to the presence of gas. Open channel flow is seen in the main channel only down to about the level of M. Concilio. The dusty plume arising from the east side of the flow beside M. Rinazzi is due to material collapsing from the levée of the main channel, which appears almost full. (b) Closer view, from the south east, of the front of the M. Grosso branch, which is advancing as a sheet. Images: INGV Catania.

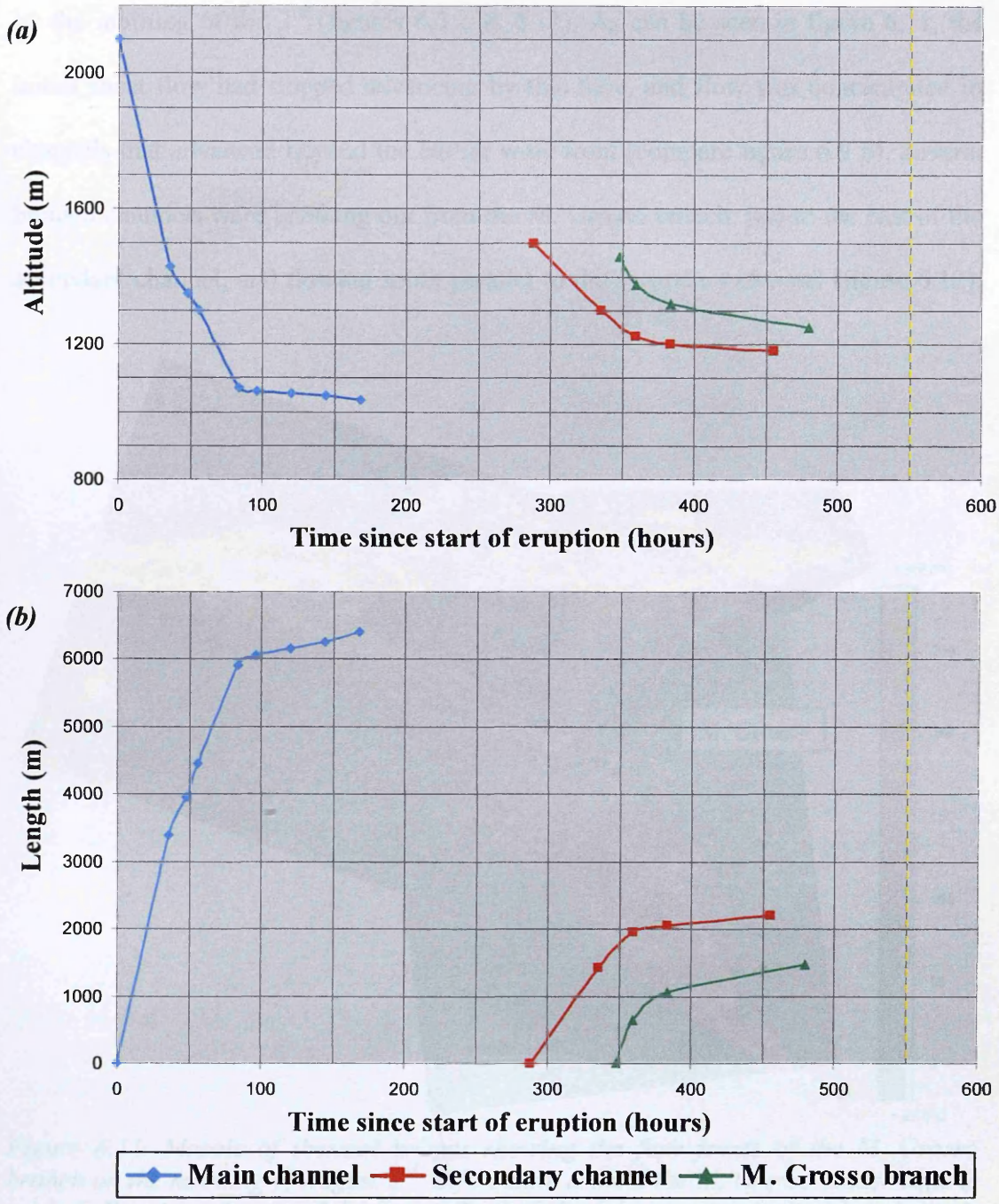

Figure 6.10. Plots of (a) altitude against time, and (b) length against time to show the advance of the three major channels in the lower flow field. The main channel is shown in blue, and was actively advancing between the 18th and the 26th of July, the secondary channel is shown in red (30th July to 6th August), and the M. Grosso branch in green (2nd to 7th August). It can be seen that in all cases, the flows initially advanced very rapidly, then slowed markedly before coming to rest. The dashed yellow lines indicate the end of the eruption.

by the morning of the 3rd (figures 6.3 c & 6.11). As can be seen in figure 6.11, the initial sheet flow had stopped advancing by this time, and flow was concentrated in channels that advanced beyond the earlier wide front (compare figure 6.9 b). Several braided channels were breaking out from the M. Grosso branch, just to the east of the secondary channel, and flowing south parallel to the secondary channel (figure 6.12).

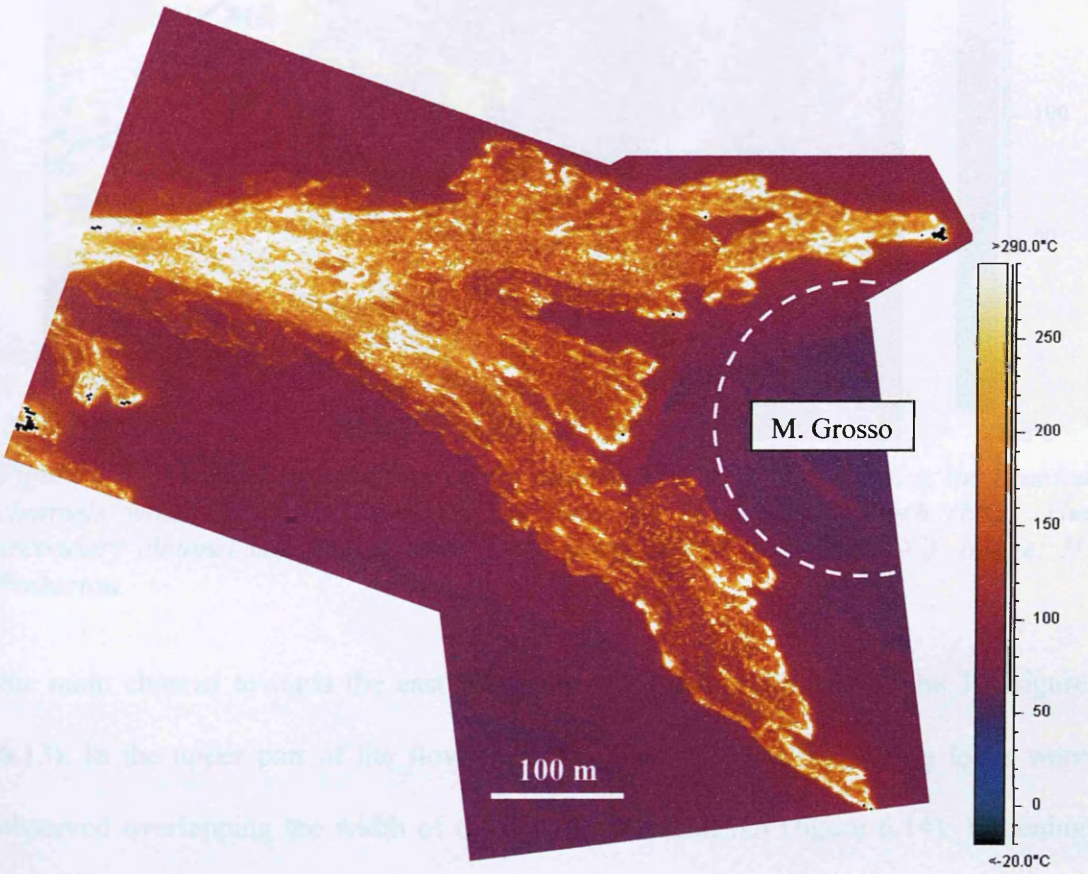

Figure 6.11. Mosaic of thermal images showing the flow fronts of the M. Grosso branch on the morning of August 3rd. Bifurcation around the M. Grosso cinder cone is evident. East is to the top of the figure. To the left of the mosaic, the braided channels can just be seen. See text for details. Images: H. Pinkerton.

These attained a length of around 500 m before stagnating. The secondary and main channels continued to be fed, with the secondary channel front still advancing slowly, though the majority of supply seemed to be feeding the M. Grosso branch. Lobes in the main channel continued to be active down to ~1060 m a.s.l., with a breakout from

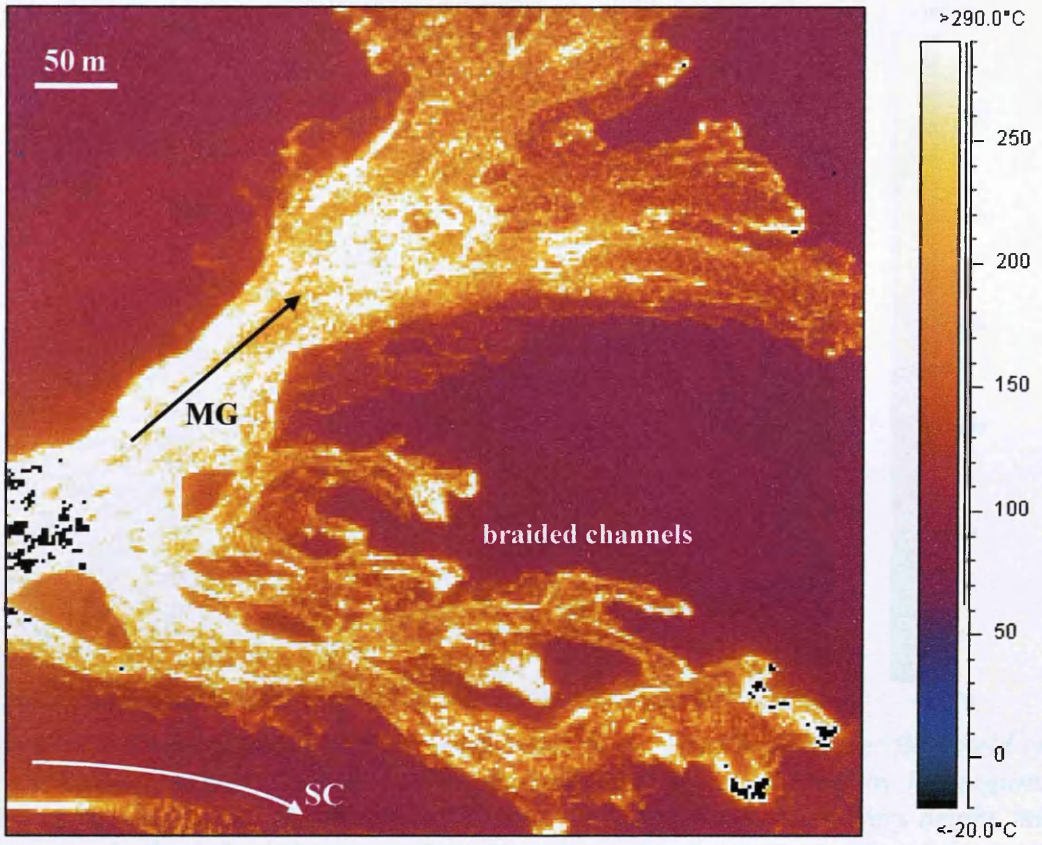

Figure 6.12. Thermal image taken on the morning of August 3rd, showing the braided channels which developed as overflows from the M. Grosso branch (MG). The secondary channel can just be seen in the lower left of the image (SC). Image: H. Pinkerton.

the main channel towards the east being observed at this altitude on the 3rd (figure 6.13). In the upper part of the flow field, at around 1750 m, stagnating lobes were observed overlapping the width of the earlier main channel (figure 6.14). Widening and thickening of the flow in this part of the channel was observed between August 1st and 2nd, in video footage taken by H. Pinkerton from Lower Silvestri, but the structure was not as clearly evident as in figure 6.14. Ogives were seen in this part of the channel on August 4th, suggesting slowing surface velocities.

From the 5th of August onwards, activity in the whole flow field was observed to reduce further. The main channel narrowed in the proximal parts as supply reduced, and the secondary channel reached its maximum length by the 6th, at ~1180 m a.s.l.

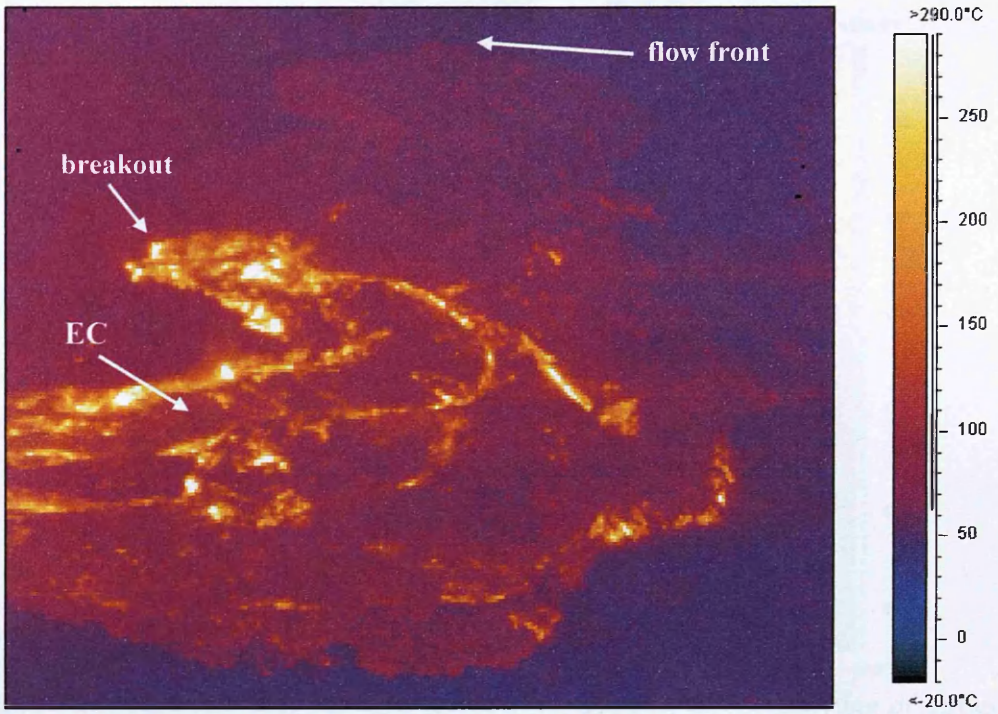

Figure 6.13. Thermal image looking south towards the front of the lower flow field on the morning of August 3rd. The eastern channel (EC) is well defined by hot regions along its margins, while the western side of the flow looks cooler. The very bright, hot lobe towards the left of the image is a breakout from the eastern side of the main channel close to where collapses of the levée were noted on the 2nd (figure 6.9 a). Image: H. Pinkerton.

(figure 6.3 d). Activity at LFS2 had completely ceased by the 6th. Flow fronts in the main channel appeared stagnant, and the effusion rate appeared substantially reduced compared to previous days. Overflows from the spillway channel just below the effusive bocca at LFS1 formed during the afternoon of the 6th, indicating either a late stage increase in effusion rate, or blockages in the proximal flow field (figure 6.15). The front of the M. Grosso branch had reached its maximum extent, at an altitude of around 1250 m a.s.l., by the 7th. While activity was still observed in the main and secondary channels, this was concentrated around ephemeral vents that were feeding small, sluggish flow lobes.

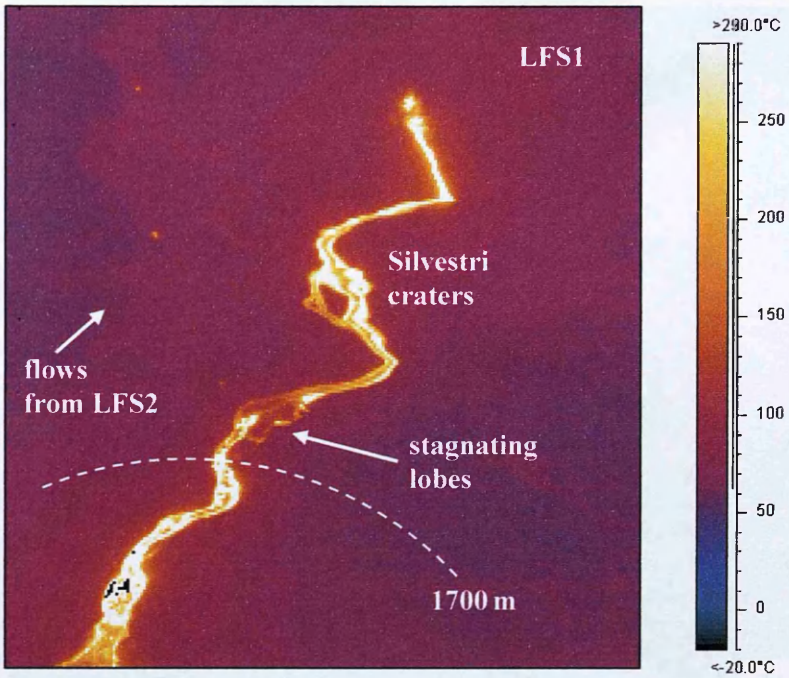

Figure 6.14. Thermal image looking north towards LFS1 on the morning of August 3rd. Open channel flow is occurring down to at least 1600 m a.s.l. (the lower edge of the image), save for three stagnating lobes that are developing just above 1700 m (contour given approximately by the dashed line). The higher flow surface temperature downstream of these stagnating lobes indicates that flow is continuing beneath the cooled lobe surfaces. The cooler surface of the flows originating from LFS2 can just be seen to the west, just encroaching on the lower flow field. Images: H. Pinkerton.

Explosive activity ceased at LFS1 on the 8th, though degassing was still observed. Effusive activity continued until the 9th, though flow lobes in the main channel extended no further than 1900 m a.s.l. Ephemeral vents were still active, including one that developed on the 8th, at ~1550 m, which fed a flow that reached approximately 100 m in length (figure 6.2). Although no further effusive activity was observed at the vent after the 9th, a few boccas continued to feed small, sluggish flows until the 12th, as they drained higher parts of the flow field. After this date, no further development of the flow field was observed, and vent activity was reduced to degassing at fumaroles.

Figure 6.15. View of the LFS1 vent region from the south after the eruption. The distance from the top to the base of the spillway channel is approximately 300 m. Late stage overflows are seen to both sides of the spillway channel, the longer of which formed on August 6th. The vent region can be seen to consist of at least five aligned cones, the largest of which is the lowest. This lower cone was the site of fire fountaining and Strombolian activity throughout the eruption, and also contained the effusive vent that fed the lower flow field. The higher cones resulted from vents that variably displayed Strombolian or more explosive activity. Image: INGV.

6.2 Surface features and processes

Although previous studies have attempted to reconstruct the general evolution of the flow, and documented the fact that the flow grew by juxtaposition and superimposition of younger flow lobes and breakouts from earlier channels once the final length had been reached (Calvari 2001; Behncke & Neri 2003; Coltelli et al. 2007), none have concentrated on understanding the manner in which the complex final flow structure arose (figure 6.4), or the development of small-scale surface features. As well as unravelling the structural development of the flow field (figure 6.3), the data collected have been used here to examine the many complex surface features which developed, often during the later part of the eruption. This work aims to distinguish between features related to emplacement processes, those related to inflation, to drainage, and to the breaching of stationary parts of the flow field. The morphology of these features is described in detail, and the possible processes that led to their formation are discussed.

To illustrate the complexity of the flow field, section 6.2.1 describes the structural evolution of the flow in the region to the south west of M. Nero (box in figure 6.16), in which the clear action of several of the above processes can be seen. It is evident, from detailed examination of the flow field, that the structures in this region are not isolated examples, but are common features of a compound `a`ā flow field. As such, the underlying processes responsible for them must also be common and repeatable, so need to be investigated before we can claim a comprehensive understanding of the emplacement of the flow. The description in section 6.2.1 is followed by an in-depth analysis of the morphology and development of such surface structures, in the subsequent sections. Figure 6.16 identifies the locations of all the small-scale features shown in images in this section.

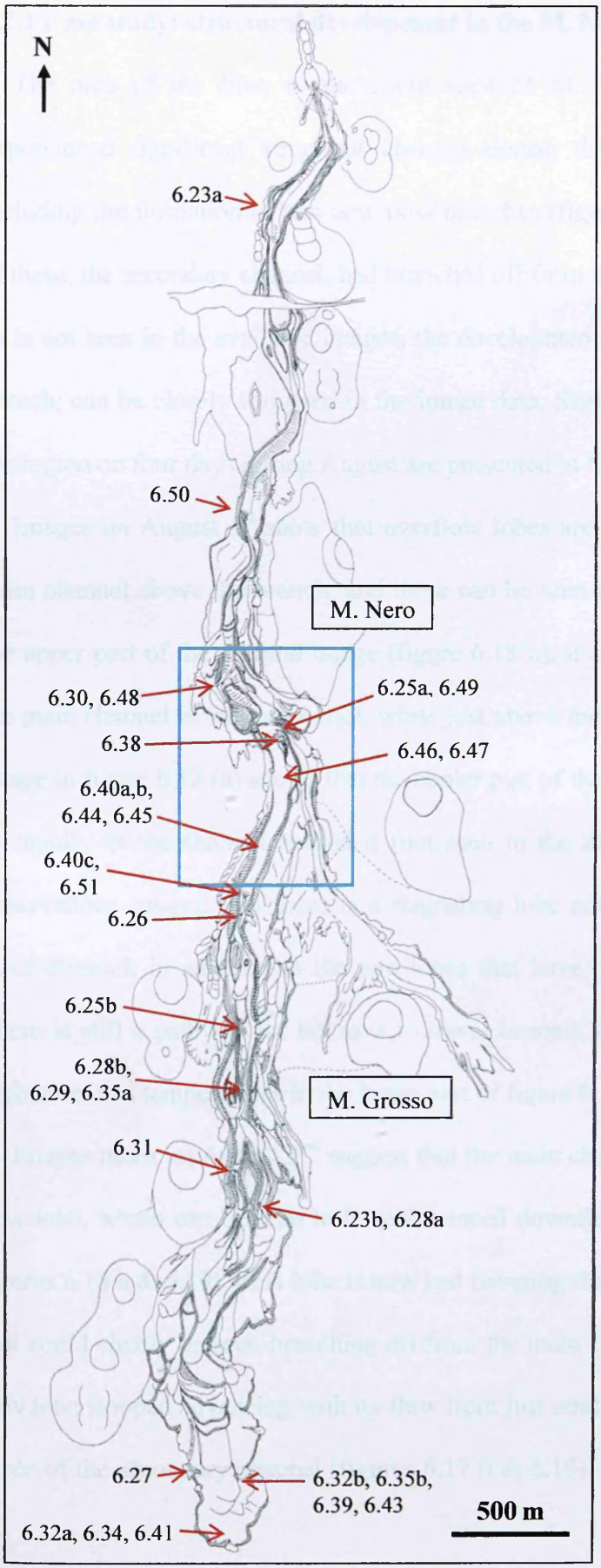

Figure 6.16.
Flow field map showing the location of the small scale features described in the text, according to the image in which they appear. The blue box indicates the region, to the south west of M. Nero, which is discussed in detail in section 6.2.1, and illustrated in figures 6.17 to 6.22.

6.2.1 Case study: structural development in the M. Nero region

The area of the flow to the south west of M. Nero (boxed in figure 6.16) experienced significant structural changes during the later part of the eruption, including the formation of two new flow branches (figures 6.2 & 6.3). While the first of these, the secondary channel, had branched off from the main flow on July 30th, and so is not seen in the available images, the development of the second, the M. Grosso branch, can be closely followed in the image data. Sketches showing the structure of the region on four days during August are presented in figure 6.17.

Images on August 1st show that overflow lobes are forming on either side of the main channel above the branch, and these can be seen in figure 6.17 (a) and 6.18. In the upper part of the thermal image (figure 6.18 b), it can be seen that the surface of the main channel is relatively cool, while just above the branch it is much hotter. The image in figure 6.18 (a) shows that the cooler part of the flow surface is not degassing as rapidly as the channel behind it (not seen in the thermal image), and these two observations suggest that there is a stagnating lobe advancing down the axis of the main channel, in addition to the two lobes that have overflowed from the channel. There is still a pathway for hot lava to travel beneath this lobe, as evidenced by the higher surface temperatures in the lower part of figure 6.18 (b).

Images taken on August 2nd suggest that the main channel is being overridden by a new lobe, which can be seen to have advanced downflow since August 1st (compare figures 6.18 a & 6.19). This lobe is now just covering the top of the secondary channel that could clearly be seen branching off from the main channel in figure 6.18 (a). The new lobe stopped advancing with its flow front just abutting against the south western levée of the secondary channel (figures 6.17 b & 6.19). This levée itself looks as if it

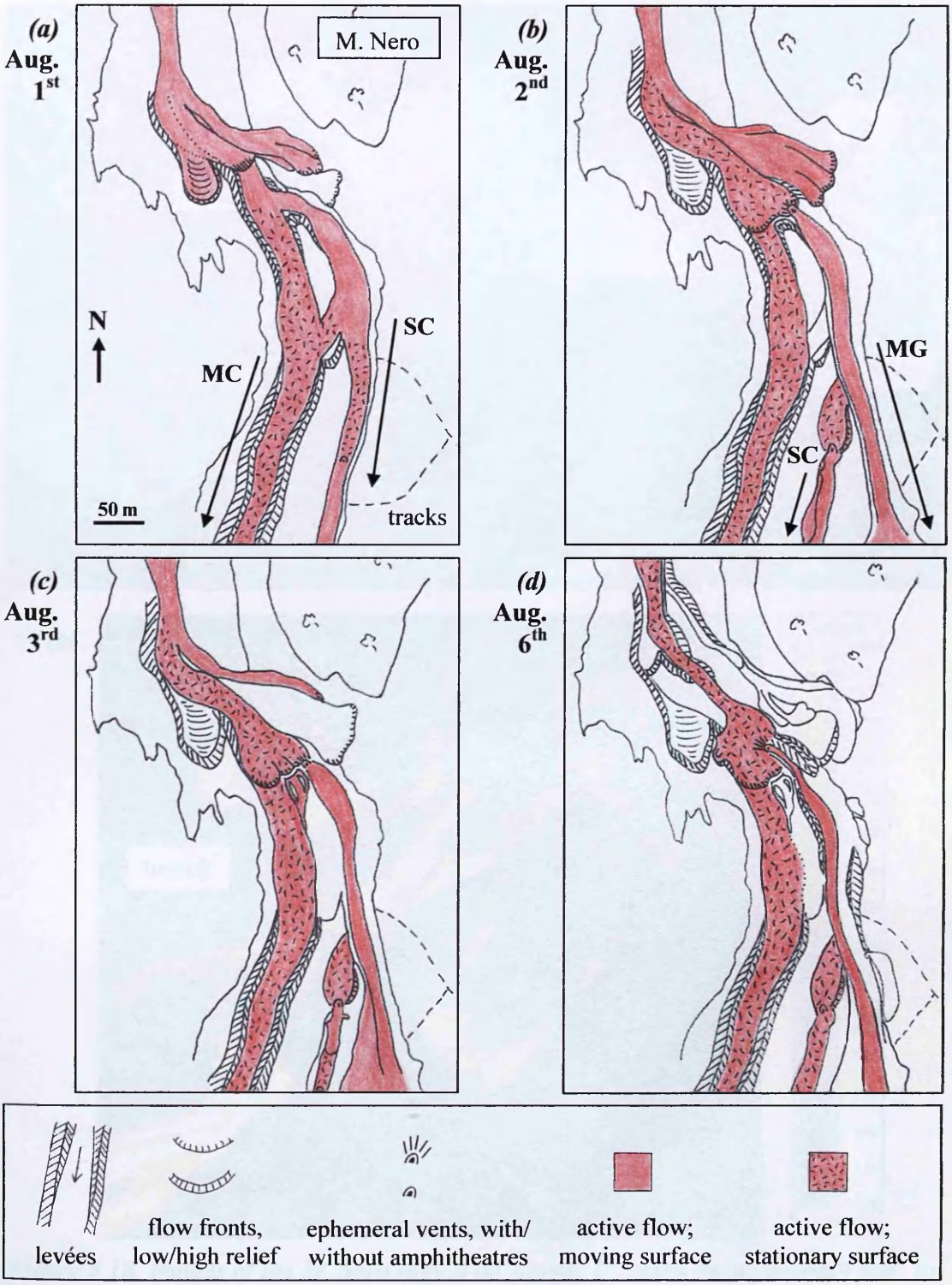

Figure 6.17. Schematic sketches showing the structural development of the M. Nero region during August. (a) August 1st. A new lobe is advancing down the main channel (MC). (b) August 2nd. The new lobe has stagnated, abutting against the levée of the secondary channel (SC). A blockage in the secondary channel has resulted in the development of the M. Grosso branch (MG). (c) August 3rd. A breakout has developed through the levée ahead of the stagnant flow lobe. (d) August 6th. The stagnant lobe has been 'eaten away' to form a deep, wide channel ending upflow in a steep amphitheatre. See text for details.

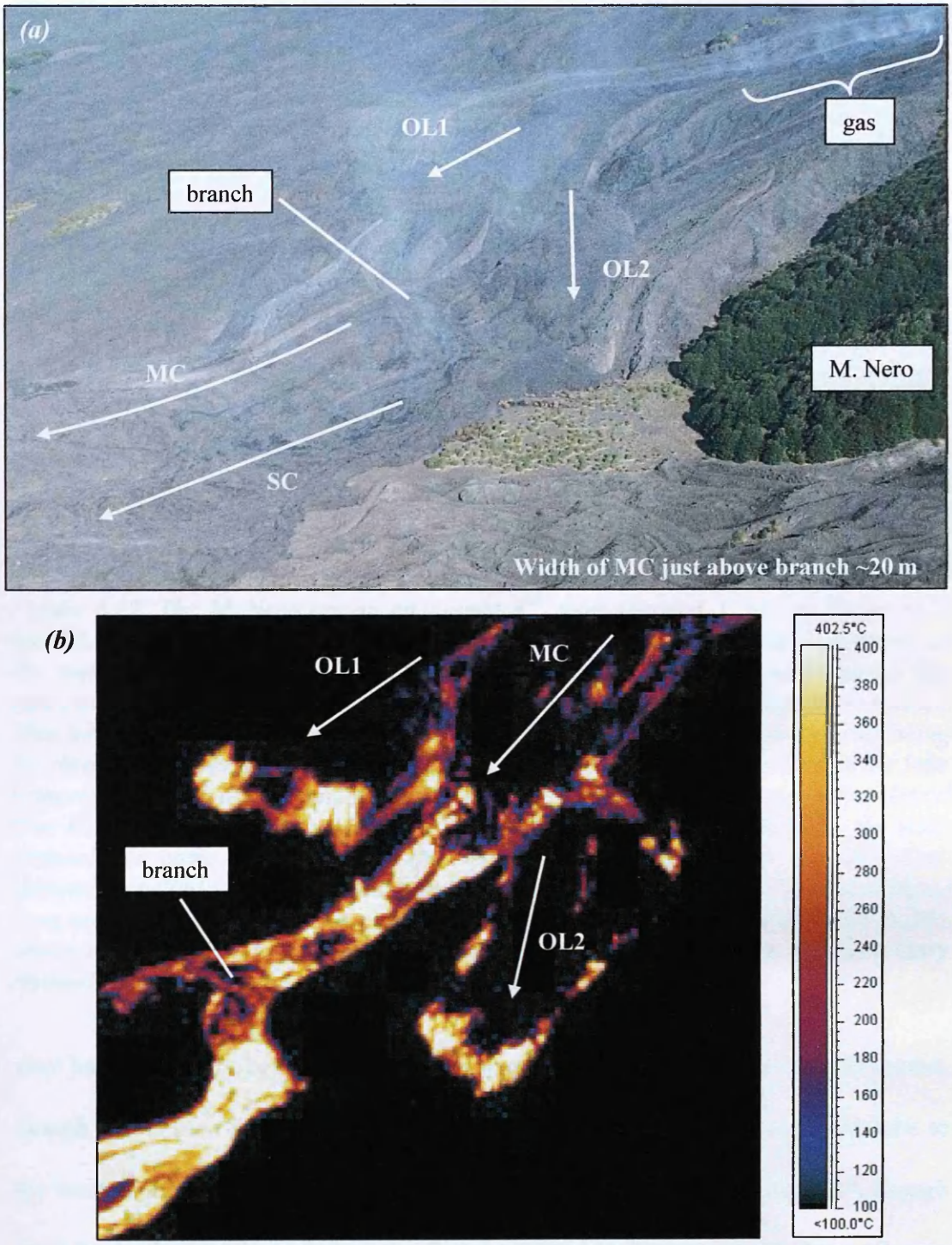

Figure 6.18. Images of the M. Nero region on August 1st, taken from the south east. (a) Visible image. The main channel (MC) is degassing strongly in the upper part of the image, but less obviously on the steeper ground where overflow lobes (OL1 & OL2) can be seen. The secondary channel (SC) branches off from the main channel below the lobes. Image : INGV. (b) Thermal image, with apparent surface temperature colour bar. The surface temperature in the main channel is relatively low in the upper part of the image, suggesting that a cooler lobe is propagating down this part of the channel. Flow is still occurring beneath this lobe, however, as evidenced by the higher surface temperatures downflow of the lobe. Image: H. Pinkerton.

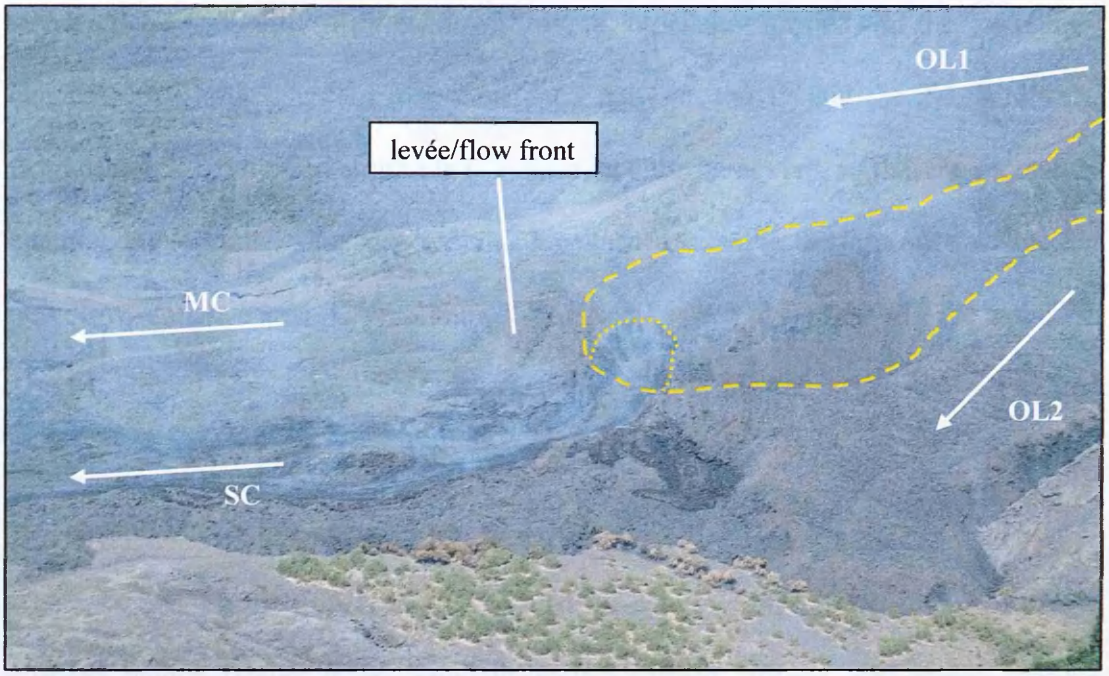

Figure 6.19. The M. Nero region on August 2nd, from the east. Compare figure 6.18 (a). OL1 has not advanced since the 1st, but OL2 has reached the flatter topography at the southern end of M. Nero. The lobe that was advancing down the main channel has now covered the place where the secondary channel broke out from the main channel. This lobe is roughly outlined by yellow dashes. The secondary channel is still being fed through the overlying lobe, and an arcuate collapse region has formed in the lobe front over the path of the channel. This collapse area is picked out by the yellow dotted line. Comparing this figure with 6.18 (a), it can be seen that the lobe in the main channel has come to rest against the original right hand levée of the secondary channel (labelled), whose arcuate morphology suggests that it may have developed from an earlier flow front. This morphology can be seen more clearly in figure (6.38), where the levée/flow front is viewed from the ground. In this figure, the secondary channel is approximately 20 m wide. Image: INGV.

may have originally been the front of an overflow lobe, as it has an arcuate aspect, though this is seen more clearly from the ground (figure 6.38). The overflow lobe to the west of the main channel has not advanced significantly since August 1st, though the lobe to the east has reached the flatter topography just below M. Nero (figures 6.17 b & 6.19). The secondary channel is now being supplied with lava through the overlying lobe, and an arcuate collapse region can be seen in the lobe flow front, above the path of this channel (figure 6.19).

Meanwhile, slightly further downflow, a blockage formed in the secondary channel, as a large stagnant lobe developed between the 1st and the 2nd. While the front of this lobe subsequently failed, to form an ephemeral vent, so that the secondary channel did continue to be supplied, this blockage resulted in the formation of another new flow branch, the M. Grosso branch. This can be seen in figures 6.17 (b) and 6.20. The M. Grosso branch broke out from the east side of the secondary channel behind the stagnant flow lobe, initially spreading as a sheet flow (figure 6.9 b), though subsequently becoming concentrated in a channel.

On August 3rd, the flow front that formed the south western levée of the secondary channel branch (figure 6.19) failed through its upper surface, and highly viscous material drained through this breach to form a short-lived flow (figures 6.17 c, 6.21 & 6.22). By August 6th, the lobe supplying the secondary and M. Grosso branches had largely disappeared, having been 'eaten away' from the flow front, forming a deep, wide channel ending upflow in an arcuate amphitheatre (figures 6.17 d & 6.22). All of the processes that contributed to the complexity of this region were widely observed acting throughout the flow, and these are discussed further in the following sections.

6.2.2 General features of emplacement

The general model for effusion rates encountered during effusive eruptions of lava is one of initially waxing flux, followed by a longer period of waning flux (Wadge 1981). As is discussed in section 6.3, this is a simplified version of events, but the general pattern of effusion rates documented during the emplacement of the lower flow field showed higher fluxes in the early part of the eruption, and lower fluxes towards the end of activity. As described in the eruption chronology, the initially high

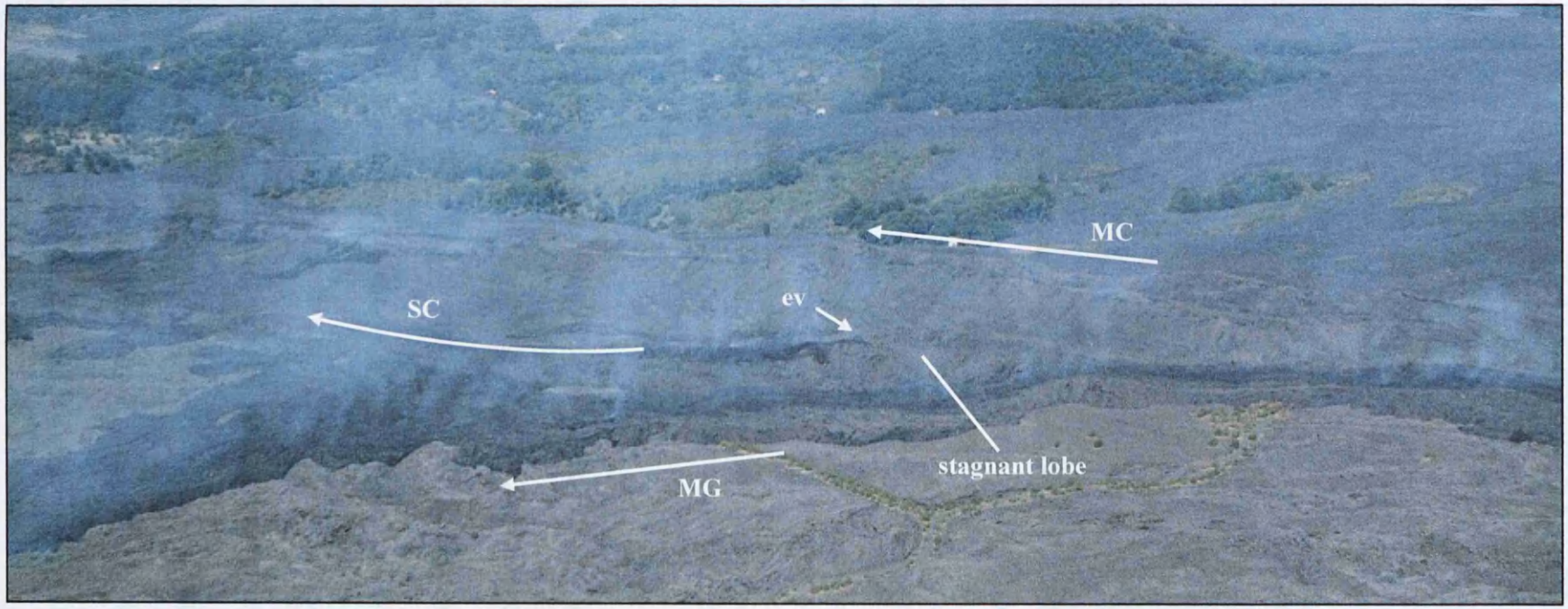

Figure 6.20. View from the east of the area downflow of M. Nero on August 2nd, showing the development of the M. Grosso branch. The main channel (MC) can be seen extending across the whole width of the image in the background. In the centre of the image, a thick flow lobe can be seen in the secondary channel (SC). The darker material downflow of this lobe indicates that the SC is still being fed through an ephemeral vent in this lobe front (labelled 'ev'). In the foreground, open channel flow is occurring in the higher reaches of the SC (to the right of the image), as indicated by the strong degassing, but the majority of this material is not being supplied to the SC. Instead, a new branch has formed, which is advancing to the south east (lower left of the image). This is the M. Grosso branch (MG). To the left of the image, the MG branch appears to be relatively thin, and is advancing as a sheet flow, having not yet formed levées. The structure of this part of the flow is shown schematically in figure 6.17 (b). Field of view is approximately 1 km wide in foreground. Image: INGV.

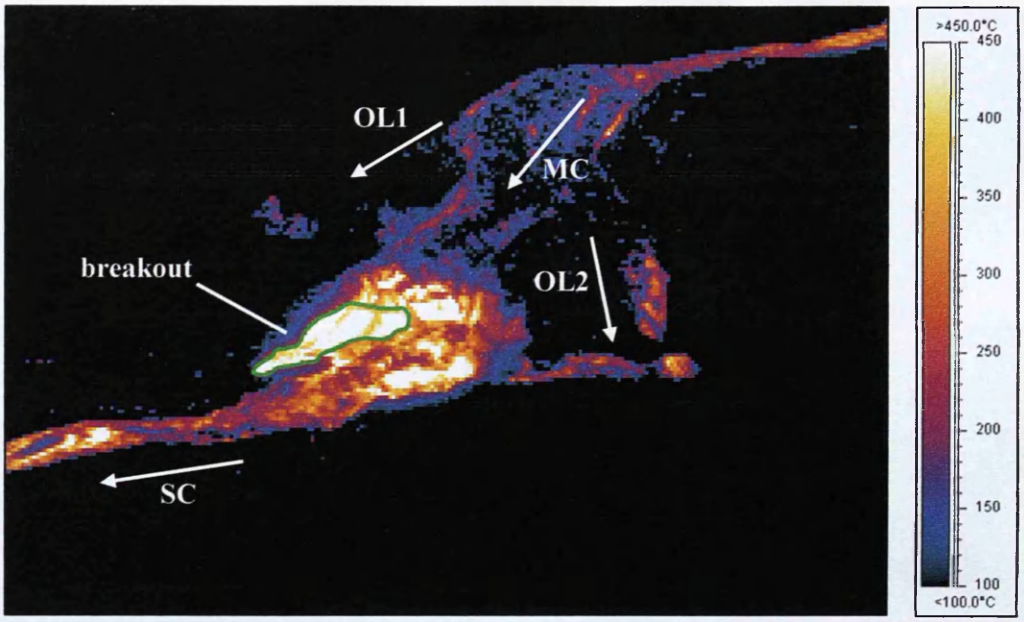

Figure 6.21. Thermal image of M. Nero region taken from the south east on August 3rd. Colour bar gives the apparent surface temperatures. The overflow lobes from the main channel (OL1 & OL2) can be seen. Towards the left hand side of the image, only the thermal signature of the secondary channel can be seen, suggesting the surface of the main channel is cooler than 100 °C. In the centre of the image, outlined in green, is a small area with a very high surface temperature, inferred to be a highly viscous, three-armed breakout from the surface of the flow front that formed the levée of the secondary channel (figure 6.19). The breakout can be seen in the visible image shown in figure 6.22, and the similarity in shape between the hot thermal signature in this image and the breakout as it appears in figure 6.22 suggests that its formation is being observed here. Image: H. Pinkerton.

effusion rate led to the flow being emplaced first as a sheet (figure 6.5), later becoming concentrated in a narrow stream within the inundated area, due to cooling of the sheet and possibly lowering effusion rate. The levées that grew as the flow stabilised as a narrow stream are well defined along the majority of the length of the flow (figure 6.4), though the flow margins are commonly marked by lobes that overflowed from the main channel. As is common in `a`ā flow fields (Lipman & Banks 1987), the stable channel does not reach all the way to the flow front, but passes into a transitional channel zone, and a zone of dispersed flow before reaching the flow toe (A. Harris, pers. comm.). The area behind the flow front is characterised

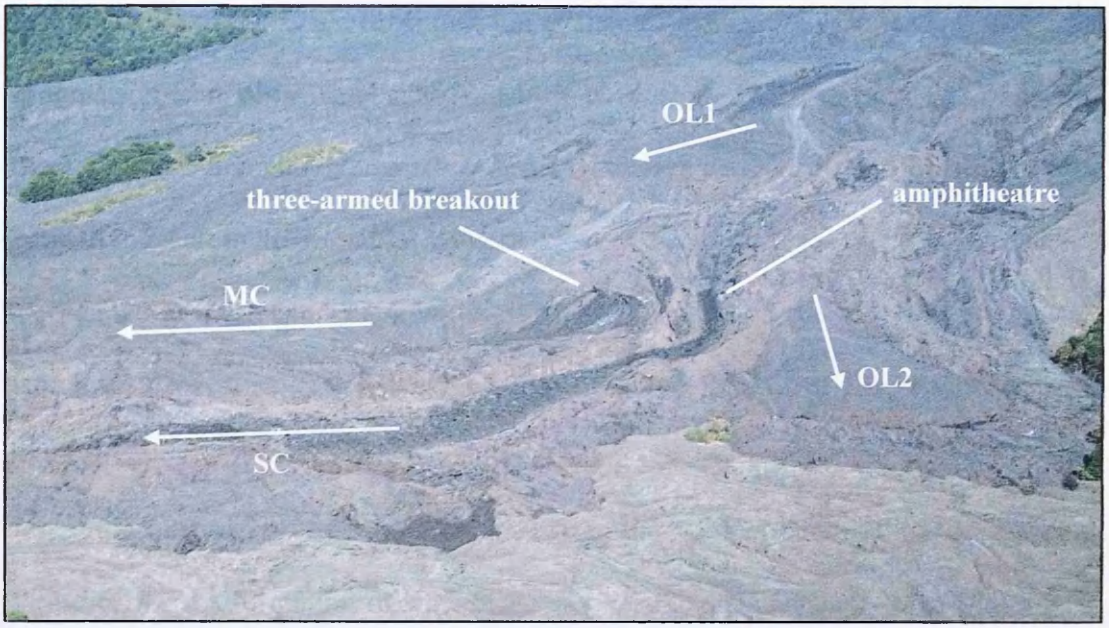

Figure 6.22. Post eruption image of the M. Nero region, from the south east. The overflow lobes (OL1 & OL2) are included for reference. OL1 has not changed significantly since August 1st (figure 6.18 a), while several younger lobes have been emplaced around and on top of OL2, which continued advancing till at least August 2nd. The main (MC) and secondary (SC) channels are visible to the left of the image. Comparing this image to that in figure 6.21, the shape of the three-armed breakout is very similar to that of the hot region outlined in that figure. The amphitheatre labelled in the centre of this image appears to have resulted from the original overflow lobe (figure 6.19) being 'eaten away' over time. This can be seen more clearly in the schematic sketch in figure 6.17 d. Field of view is approximately 380 m wide in the foreground. Image: INGV.

by many lobes that have been emplaced to the sides of the stable channel, as the front itself has stagnated, preventing free flow in this direction. As the eruption progressed and the effusion rate began to wane, the flux could no longer fill the initial main channel. This resulted in flow being concentrated in some parts of the initial channel, while others were cut off, forming dagalas, which are common in the flow field (figure 6.4). In addition to the isolation of parts of the original main channel, the lowering flux produced narrower flows that built new sets of levées within the original channel. Several regions of the flow field present spectacular examples of these nested

levées (figure 6.23), as a clear indication of many stages within the waning flow. The progression from sheet to channelised flow is illustrated well in the development of the M. Grosso branch (figures 6.9 b & 6.11), though activity did not persist for long enough to result in the formation of nested levées.

Stagnation was noted in many parts of the channel as the eruption progressed, which resulted in several processes being observed. If part of the channel became blocked by a stagnating lobe, continued supply from upflow could result in the formation of overflow lobes that escaped from the channel behind the blockage (e.g. figure 6.18), the formation of surface flows over the stagnant lobe, breaching of the levée behind the blockage to form a new branch (perhaps the process that led to the formation of the secondary channel) or continued flow into the stagnant lobe itself. If a stagnant lobe continues to be fed by lava from the vent, the rising pressure is transmitted to the cooled flow front, resulting in the formation of an ephemeral vent, as was observed in the secondary channel between August 1st and 2nd (figure 6.20). Once the front has ruptured, supply from upflow can continue through the stagnant lobe, in what could be the early stages of tube formation. The term tube is used here to mean an underground lava pathway with a self-supporting roof, which could drain to form the cave-like features commonly documented in both pāhoehoe (e.g. Hon et al. 1994) and `a`ā (Calvari & Pinkerton 1998) flows. The breaching of a flow front does not, however, always lead to tube formation, as the surface of the stagnant lobe can sag into the flow beneath, or collapse completely if steady supply is not maintained for long enough that the roof develops sufficient strength to support its own weight (Calvari & Pinkerton 1998). Where flow is observed to continue beneath a stagnant surface, but the surface is observed to be affected by this flow, the term 'preferential thermal pathway' is preferred to the term tube.

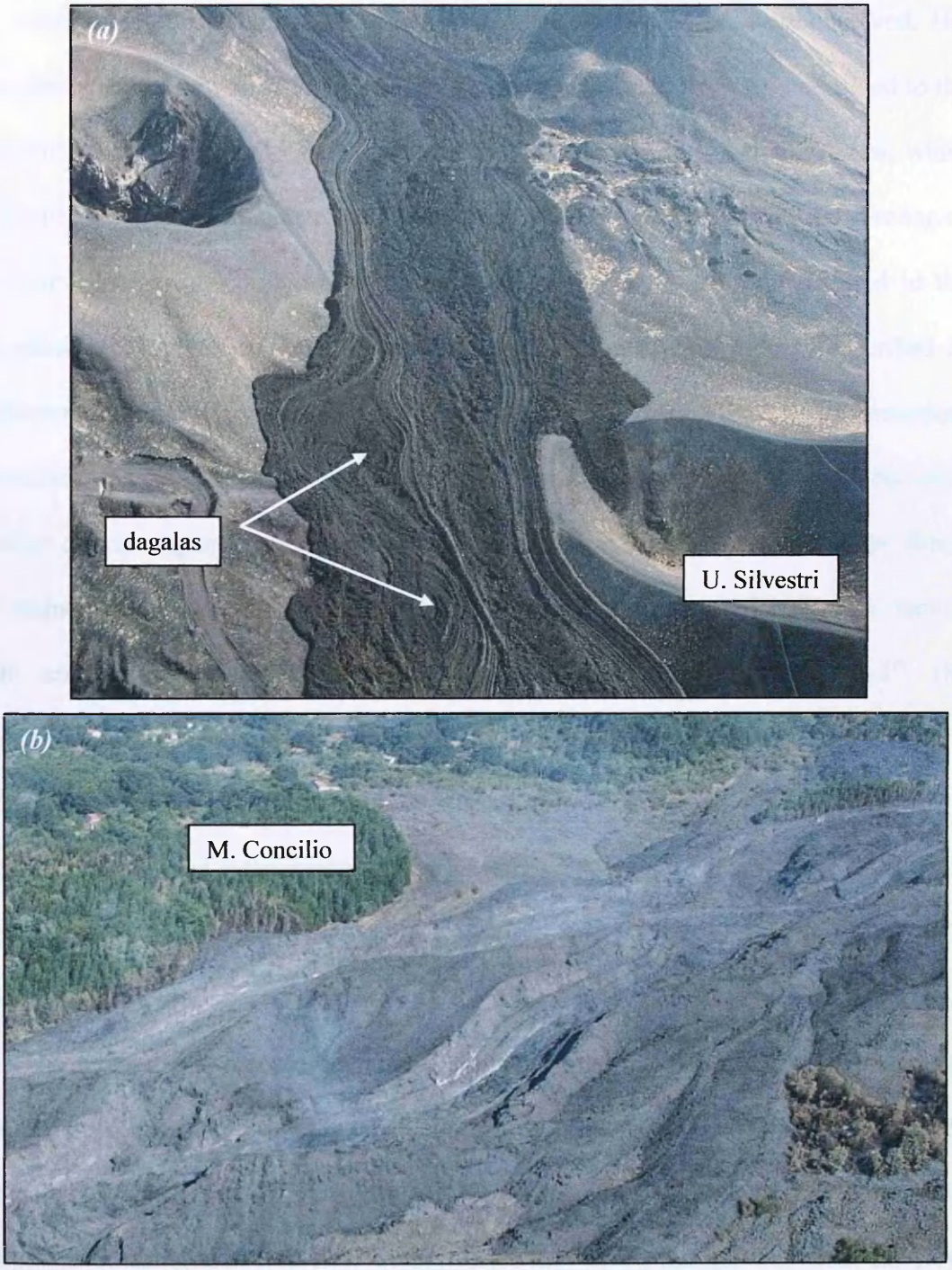

Figure 6.23. Examples of nested levées, indicative of waning flow. (a) Looking upflow towards LFS1 after the eruption. The flow originally advanced as a sheet in this area, and waning flow produced first small dagalas then several sets of low relief levées as the flow narrowed. (b) High relief nested levées in the lower part of the flow field on August 1st, viewed from the east. Flow is still occurring in the central part of the channel. Images: INGV.

During the 2001 eruption, all of the abovementioned processes were observed. The emplacement of new flow lobes on top of earlier ones could be largely confined to the original channel, or could spread beyond the original channel, forming a new, wider channelised area. In the latter case, as in cases of other overflow lobes, the slowing of the new lobe front combined with continued supply from the vent resulted in the formation of ogives on the flow surface, through the folding process described in chapters four and five. The presence of ogives indicates that, at the time of formation, material was being supplied at a greater rate than it could be removed from that area, either due to stagnation of downflow regions or decreasing topographic slope. Since sustained, healthy supply is inferred from the necessary compressional stress, ogives are considered to result from 'emplacement' processes. By August 1st, the combination of waning supply and cooling had resulted in the main and secondary channels containing many ephemeral vents, with flow proceeding through a number of preferential thermal pathways within earlier lobes.

6.2.3 Squeeze ups

The general processes associated with the formation and activity of ephemeral vents, or boccas, are well documented (e.g. Pinkerton & Sparks 1976; Polacci & Papale 1997; Calvari & Pinkerton 1998). Although such boccas are commonly observed forming at stalled flow fronts, where they allow hot material from the flow behind to continue advancing, Calvari & Pinkerton (1998) also noted that new flows could be fed by boccas forming in the roofs of established tube systems, or around the margins of flows. Flow front and tube roof boccas were often long lived, and were observed to feed flows that extended for several kilometres from source, while marginal boccas were only active for short periods of time, draining parent flows, and

feeding small extrusions. During the 2001 eruption, many boccas were observed, which were active for varying lengths of time. The longer-lived examples fed well developed flows that channelled material freshly supplied from the main vent, while other, shorter-lived boccas developed during the latter stages of activity and only extruded material which had been stored in the flow interior for some time.

The latest stages of development of all boccas involved the very slow extrusion of material that was either draining from higher parts of the flow, or was being forced out from the flow interior as changing local flow conditions pressurised parts of the flow that had been stagnant for some time. It is these final 'squeeze ups' that are of interest in this section, as they were observed to demonstrate marked morphological variation that reflects the rheology of the material being extruded, as well as the geometry of the source bocca. Examination of their morphology can therefore provide insights into the conditions prevailing in the flow at the time of formation, and the locations at which the squeeze ups occur give an indication of the structure of the flow beneath the clinker cover. The following sections provide descriptions and discussions of the varying morphologies that were observed, the locations at which squeeze ups were observed, and also the possible mechanisms that can result in the extrusion of material in a wide range of rheological states from the flow interior. Studying the squeeze up material could provide information about how the material was transported through the flow to the point of extrusion: was the transport system open or closed to the environment, and was the material stored for significant lengths of time before extrusion? Squeeze ups could also be used to determine the maximum crystallinity at which lava can be forced to flow, which is a critical parameter in flow modelling.

6.2.3.1 Squeeze-up morphologies

Squeeze ups have been described in both pāhoehoe and `a`ā flows, and show large variations in morphology. Macdonald (1972) described the squeeze up of pāhoehoe through fractured surface crust, to result in elongate bulbous ridges, the morphology of which clearly indicates that the lava was still fluid when the squeeze ups formed. At the other end of the morphological and rheological spectrum, the formation of crease structures on silicic flows and domes (Anderson & Fink 1992) results from the squeeze up of lava that has a considerable yield strength upon extrusion. A large number of squeeze ups are seen in the 2001 lower flow field, which show a range of morphologies, and which formed over a considerable proportion of the eruption: many had already been emplaced around the flow front area by August 1st. In some cases, squeeze ups can feed lava flows which are up to a few hundred metres long, in which case their sources can be regarded as ephemeral boccas, while in other cases the extruded material accumulates above the source, forming features more akin to tumuli.

Boccas

Ephemeral boccas are common within the flow field, forming at flow fronts, within established channels, and around flow margins, as described by Calvari & Pinkerton (1998). In many cases, the preserved solidified flows have the characteristic morphology described by Polacci & Papale (1997, 1999) for flows extruded by ephemeral vents on Etna. Commonly the bocca is arcuate in plan view, and the preserved flow can be divided longitudinally into three sections. If the emerging lava was still reasonably fluid when activity ceased, the central zone of the flow will be smooth, and this smooth zone grades laterally into two clinkery marginal zones, then

into the levées. The central zone is often thicker than the marginal zone. The central and marginal zones can be seen clearly in figure 6.24 (a), which shows a bocca that is supplying lava to an active flow. The curved opening has clearly migrated downflow over time, as can be seen by earlier frozen arcuate features behind the currently active bocca. In this example, the lava is hot and still fluid, evidenced both by the colour, and by the characteristic pāhoehoe folding of the flow surface just downflow from the bocca. Figure 6.24 (b) shows an example of a solidified flow, whose surface morphology indicates that the material had a yield strength when it was extruded. This can be seen by the grooves on the flow surface that formed as the lava flowed through the irregular bocca opening. Such lava is of the form known as 'toothpaste' lava (Macdonald 1972, Rowland & Walker 1987). The flow surface is seen to be fractured in several places, which may be due to discontinuous extrusion, whereby there is a decrease in the flux from the bocca, and the lava moving more quickly downslope fractures away from the bocca. Alternatively, the fractures may have resulted from tensile stresses developing as the flow moved away down the gradually steepening slope, and some of the lower fractures have an arcuate shape.

The two examples in figure 6.24 are taken from the effusive activity of Etna during 2006, and both boccas fed flows that maintained coherent, relatively smooth surfaces for at least ten metres beyond the vent. In figure 6.24 (b), the solidified flow surface can be seen breaking up beyond this distance, as the flow morphology grades into slabby pāhoehoe. The bocca that fed this flow was only active for around one day, and the flow solidified while viscosity-strain rate conditions still permitted the central portion of the lava to flow without fragmenting to form `a`ā. Activity during 2001 produced many ephemeral boccas, some of which were active for up to at least

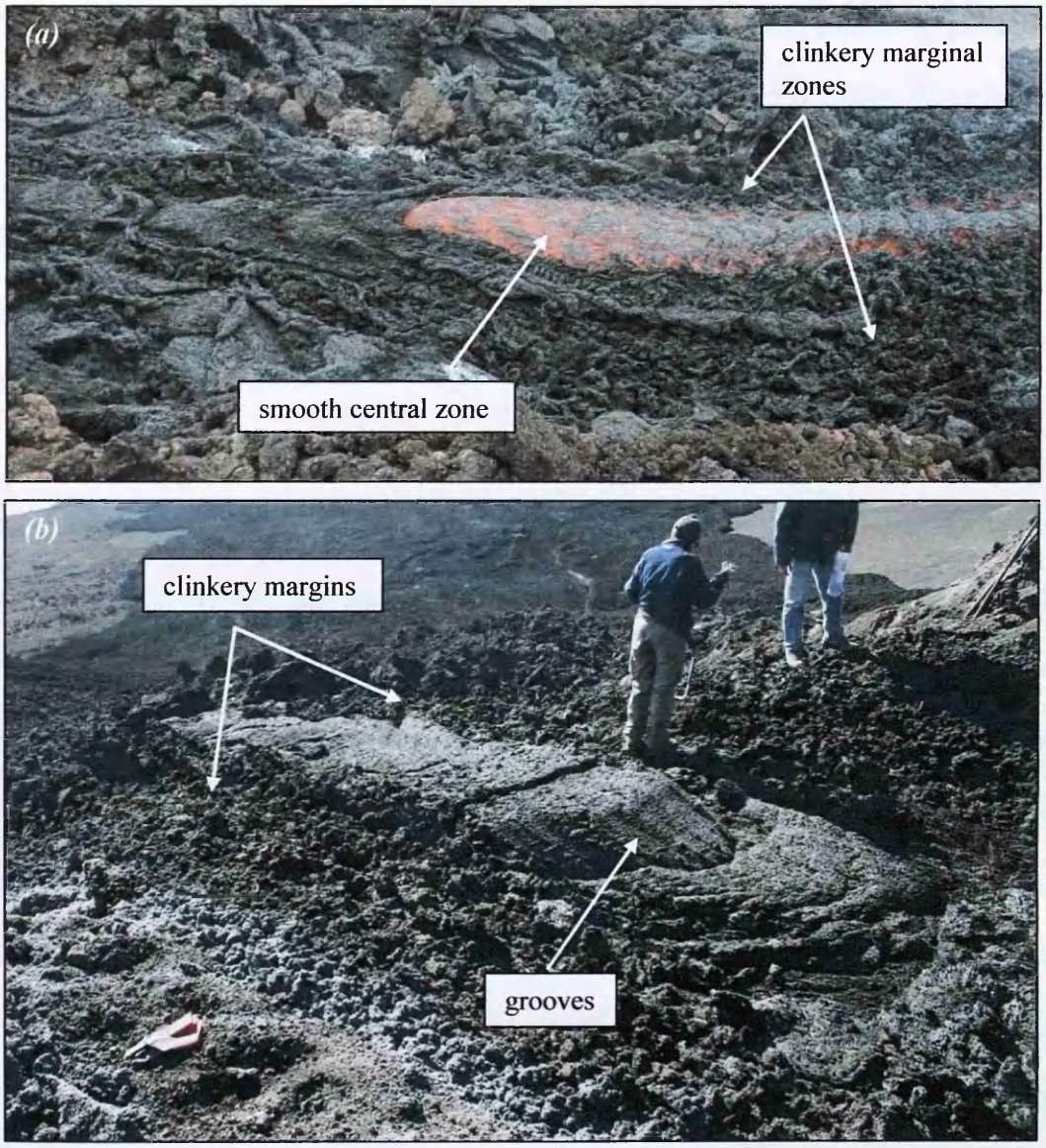

Figure 6.24. Ephemeral boccas that formed during the November 2006 activity at Mt. Etna, showing the smooth central zone and the clinkery margins as described by Polacci & Papale (1997, 1999). (a) Active bocca on the headwall of the Valle del Bove, showing pāhoehoe folding. Active channel is ~1 m wide. (b) Solidified flow from a bocca on the south west flank of the Bocca Nuova. Grooves on the flow surface identify this as toothpaste lava, which had a high yield strength upon eruption.

thirteen days. Clearly, only the final stages of activity are preserved in the solidified flow, but the varying morphology of the preserved flows emerging from these boccas indicates that material was extruded in a range of rheological states. In several cases, the material had been stored for some time within the flow, cooling and crystallising, and when it emerged produced surface textures very different to those seen in the two previous examples.

Figure 6.25 (a) shows the post-eruption morphology of the ephemeral bocca which fed the secondary and M. Grosso branches. The general morphology is similar to that previously described, in that an arcuate bocca has fed a flow with easily distinguishable central and lateral zones. In this case, however, the central zone looks very different to that in figure 6.24 (b), being largely covered in blade-like protrusions of lava, which clearly indicates that, at the end of activity, the extruded lava had a considerable yield strength. These protrusions did not break away from the massive interior to form `a`ā-like clinker, suggesting that although the yield strength is evident, and this central zone probably represented a region of plug flow, the strain rate during the final stages of extrusion was not sufficient to disrupt the plug. During extrusion, the flow fractured along the boundary between the central and marginal zones, and the central zone appears inflated, morphology that is observed in many of the flows described by Polacci & Papale (1997, 1999). Their explanation is that because more efficient cooling occurs in the marginal zone due to a greater exposure of the flow interior as the surface is continually sheared, the width of the actively flowing channel decreases. In order to conserve mass, the central part of the channel thickens, resulting in it decoupling from the marginal zones. In some cases, these fractures can be more than three metres deep (figure 6.25 b), and so allow the estimation of a minimum

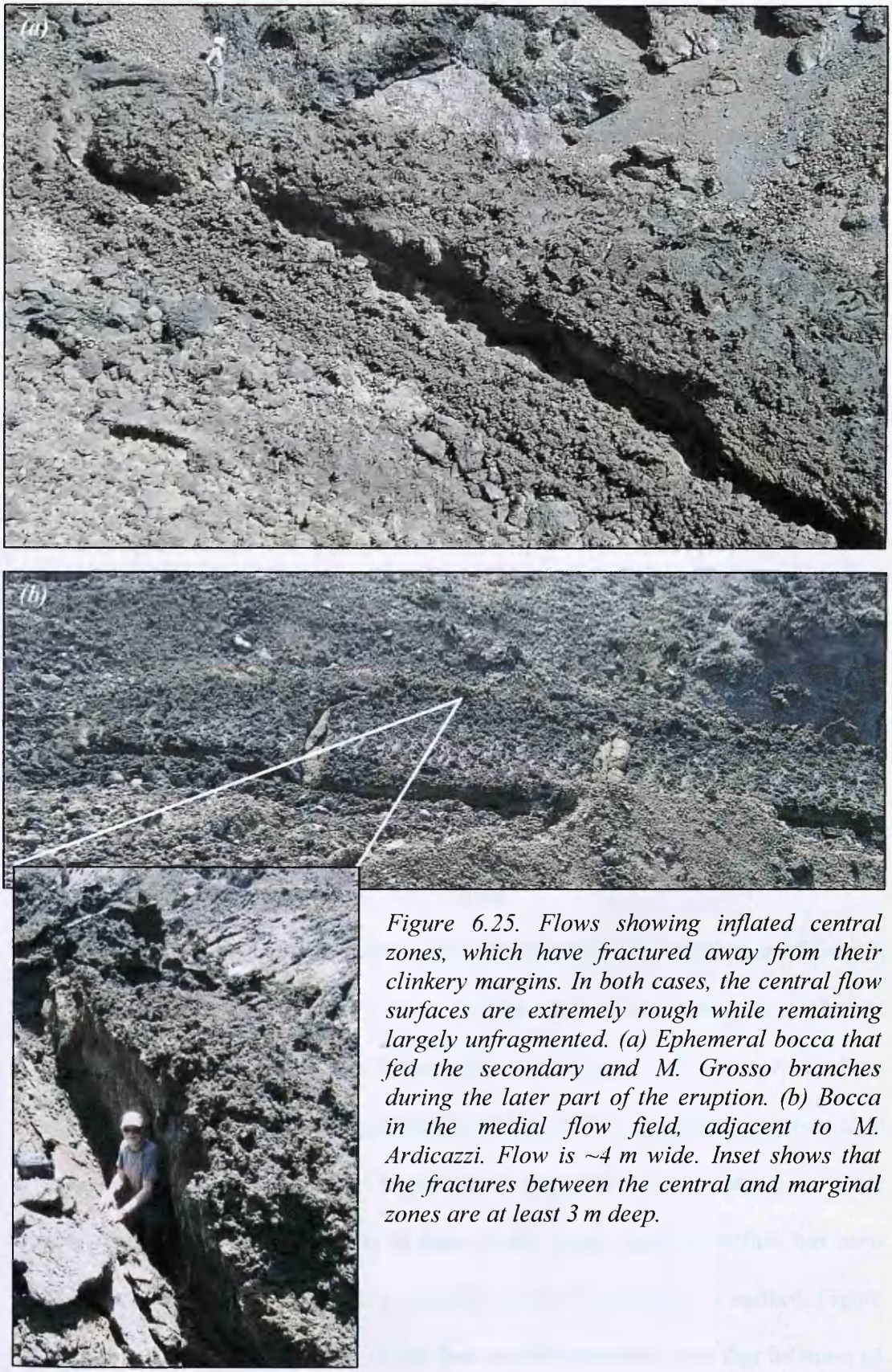

Figure 6.25. Flows showing inflated central zones, which have fractured away from their clinkery margins. In both cases, the central flow surfaces are extremely rough while remaining largely unfragmented. (a) Ephemeral bocca that fed the secondary and M. Grosso branches during the later part of the eruption. (b) Bocca in the medial flow field, adjacent to M. Ardicazzi. Flow is ~4 m wide. Inset shows that the fractures between the central and marginal zones are at least 3 m deep.

depth for the flow. Inflation may also be aided by the expansion of vesicles if the lava has travelled through preferential thermal pathways or tubes between being extruded from the main vent and emerging from the ephemeral bocca, and has thus been under pressure. This may have been the case for the bocca in figure 6.25 (a), as the majority of the flow surface above this region was observed to be stationary towards the end of the eruption.

If the supply of lava continues after the flow surface has solidified and ceased to advance, the new lava can be squeezed up through the marginal fractures rather than causing further inflation of the central zone. In the case that supply continues for long enough to extrude a significant volume of new material, then the solidified flow surface may be displaced by the squeeze ups from beneath. An example of this is shown in figure 6.26, where the upper ~1.5 m of the flow had solidified, and was tilted sideways as material forced its way up from beneath. The massive interior of the displaced crustal block is in marked contrast with the material that emerged from beneath, which was emplaced as thin, twisted sheets, the morphology of which is examined in more detail in the following section.

Other morphologies indicative of a high yield strength upon eruption are shown in figure 6.27. Figure 6.27 (a) shows a bocca feeding a flow which maintains a coherent surface for only about two metres beyond the vent. Beyond this distance, the flow conditions have resulted in the fragmentation of the surface, producing a texture akin to `a`ā, though the fragments are larger, more irregularly shaped and even more roughly textured. Even immediately in front of the bocca, the lava surface has been 'torn', as can be seen by the shallow, parallel tensile fractures on its surface. Figure 6.27 (b) shows that the lower part of the flow remains coherent, and that inflation of

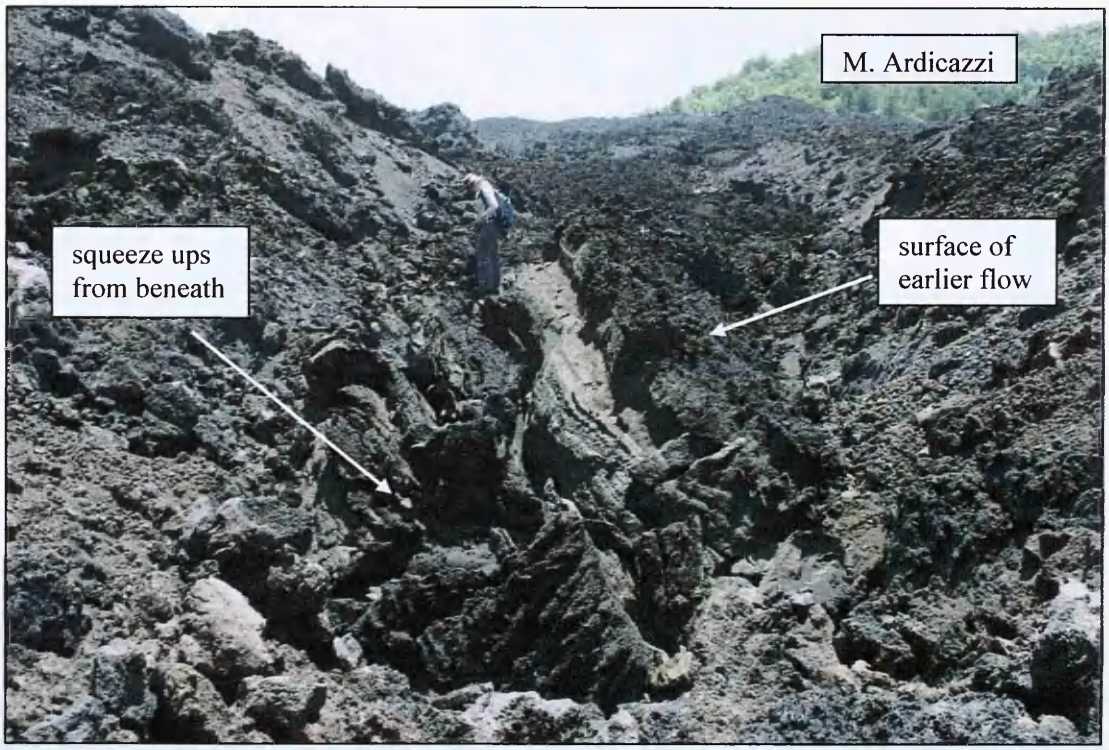

Figure 6.26. Ephemeral bocca in the main channel. Continued supply of lava towards the end of the eruption has displaced an earlier solidified flow. The newly extruded lava has been emplaced as twisted sheets that clearly indicate it to have had a high yield strength upon extrusion. Image: H. Pinkerton.

the flow has occurred. The texture of the fragmented flow surface can clearly be seen to differ from that of the surrounding clinkery `a`ā. Despite its considerable strength, the material advanced a few tens of metres before stopping, forming a flow with a low width/depth ratio that is largely comprised of the bladed fragments, but also contains some `a`ā clinker, probably carried on the surface from where the squeeze up emerged through the old flow surface.

In all of the above examples, material was extruded in a highly viscous or plastic state. In some cases, the combination of rheology and strain rate was not sufficient to cause fragmentation of the surface, which remained relatively coherent, if highly uneven (figures 6.25 & 6.26). In other cases, large-scale fragmentation of the surface did occur (figure 6.27), either because the viscosity and/or yield strength of the material was greater, or because the strain rate to which it was subjected was higher,

Figure 6.27. Squeeze-up through the flow surface near the flow front. (a) The lava surface tore as it emerged from the bocca, and began to fragment within ~2 m of the point of extrusion. Image: H. Pinkerton. (b) The lower part of the flow remained coherent. The central part of the flow inflated, and fractured away from the flow margins. It stands around 1 m above the surrounding flow surface. The texture of the squeeze-up flow is seen to be very different to that of the surrounding clinkery `a`ā.

or both. In all cases, however, the material was able to flow for some distance after leaving the bocca. Not all flows could be traced to a well defined front, but those that

could reached lengths of up to around 100 m. In all examples shown here, save that in figure 6.26, activity ceased when the material was still capable of moving away from the bocca after extrusion. In the following section, the case in which extrusion continues after the material has attained too high a strength to flow away from the bocca is considered.

Tumuli and crease structures

In several cases, the bocca which fed a flow cannot be seen, as it is covered by a high mound of locally accumulated squeeze up material. These mounds, dubbed tumuli as they are believed to result from inflation processes similar to those that give rise to the tumuli described in chapter five, are interpreted as the latest stages of activity of the ephemeral boccas with which they are associated.

Examples of tumuli are shown in figure 6.28. The morphology is usually a dome-shaped or elongate structure, up to around 5 m in height, consisting of a collection of many sheet-like protrusions or 'blades' of lava. In the easily observable (i.e. outer) parts of the tumulus, the blades can be seen to narrow towards their extremities, which are often curved over, presumably due to this lower thickness (figure 6.29 a). Although it is possible that the blades retain an almost uniform thickness along their whole length, as seen in the crease structure in figure 5.2 (b), it is more likely that they thicken towards the point of extrusion. While examining the lower ends of the blades is difficult, the presence of large, loose blocks around the base supports the latter theory. In many cases, the ends of the blades have vertical tears, transverse to the plane of the blade, and the torn parts can curve in different directions (figure 6.29 b). A common, though not ubiquitously observed feature is a wide, laterally continuous

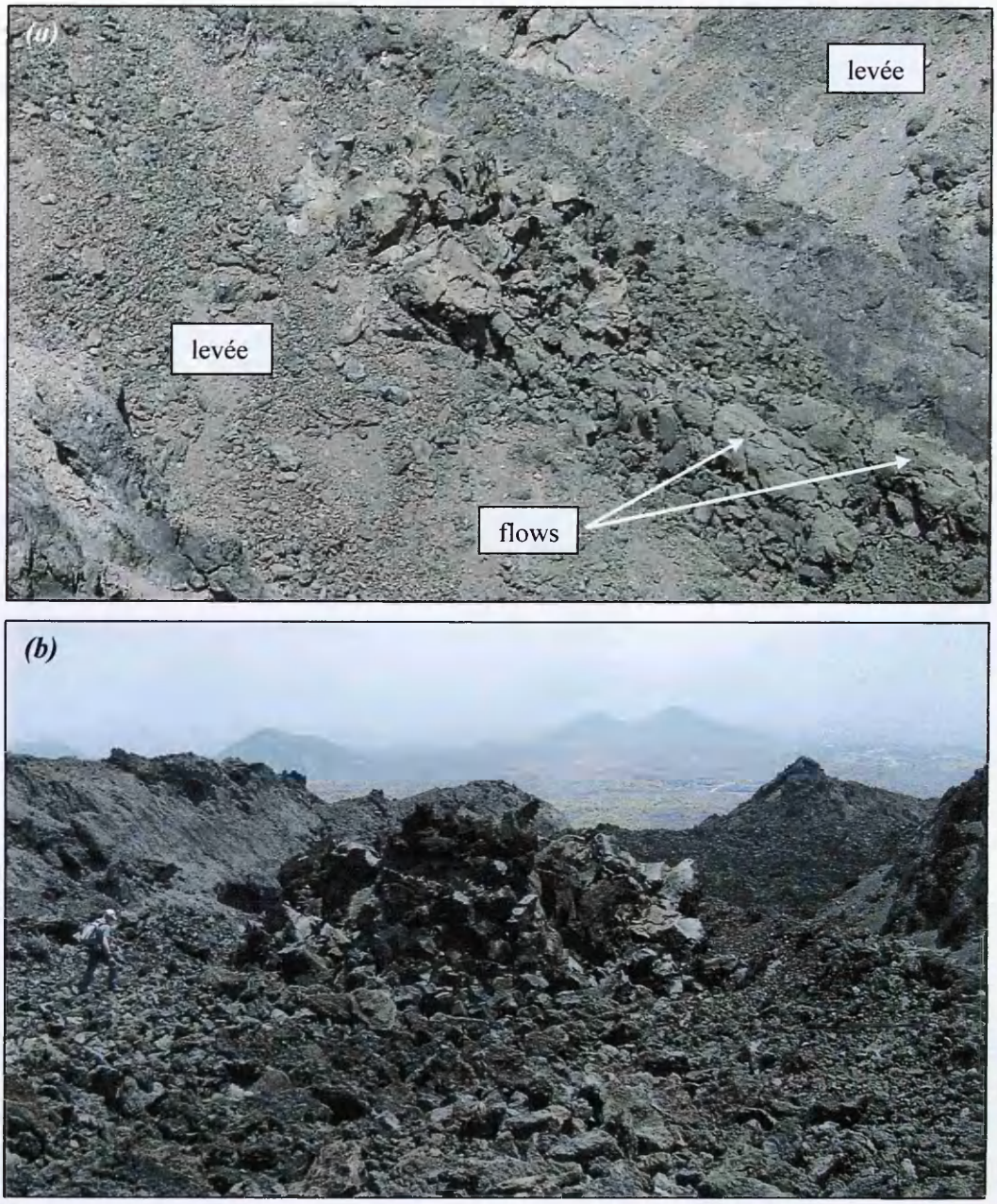

Figure 6.28. Two examples of tumuli. (a) Tumulus is ~5 m in height, and situated at a channel-levée boundary. Two short flows can be seen extending downslope from the tumulus, which have rough, platy surface morphology. (b) Tumulus is in the centre of a channel, at a break in slope. Locations are shown in figure 6.15.

central cleft that divides the tumulus into two halves (figure 6.30 a). Distribution of lava sheets on either side of this cleft is chaotic, as seen in figure 6.30 (b). This morphology is similar to that of crease structures (figure 5.2), and is also reminiscent of the surface morphology of the tumuli described in chapter five, which display

Figure 6.29. Detail of the tumulus shown in figure 6.21 (b). (a) The ends of the lava sheets are quite thin, of order centimetres, and can be highly curved. (b) Tears can form in the ends of the sheets, and the torn sections can fold in different directions. The curved sheet in the centre of the image is ~70 cm high. Image: H. Pinkerton.

prominent inflation clefts along their summits. The similarities to both of these types of features may provide a clue as to the mechanisms by which the bladed tumuli form. The simple crease structure seen in figure 5.2 (b) consists of two leaves of lava that have folded away from the axis of extrusion in opposite directions, leaving a well-

developed central cleft. While the quantity of material extruded in the tumuli is clearly greater, it is possible that in the early stages of formation, tumuli resemble crease structures. Though no evidence of localised inflation is seen in the flow underlying the crease in figure 5.2 (b), it is possible that in some cases inflation does occur before the extrusion of the highly plastic material. This early inflation may result in an inflation cleft, such as those described in chapter five, therefore providing an opening through which material can be extruded. If this is the case, crease structures and bladed tumuli could be thought of as 'exogenous' tumuli, as compared to the 'endogenous' examples discussed in the previous chapter. While the endogenous tumuli were often observed to be associated with squeeze ups, the underlying, domed inflation structure was always clearly visible indicating that inflation rather than extrusion processes dominated the developing morphology.

The development of the bladed morphology indicates that by the time it was extruded, the material was sufficiently strong that although it could be forced through the carapace, it did not flow away, and so accumulated above the vent. The example in figure 6.26 shows what may be the early stages of formation of a tumulus, as material with a considerable yield strength was forced up beneath a solidified flow, though not enough was extruded to obscure the bocca. However, as will be seen, the boccas over which tumuli develop are commonly associated with more fragmented flows, such as that seen in figure 6.27 (b), and, while this is likely to be a function of strain rate as well as rheology, it may also suggest that there was a pause in activity between the emplacement of the coherent flow in figure 6.26 and the extrusion of the squeeze up beneath.

Tumuli are commonly associated with ephemeral boccas that have previously fed rubbly flows, but their crease-like morphology suggests that the latest stages of

Figure 6.30. (a) The well-developed central cleft in an elongate tumulus. (b) The lava sheets on either side of this cleft are clearly much more closely spaced, and are chaotically oriented.

extrusion occurred through larger openings in the surface carapace than those which fed the earlier flows. If blockage of the earlier boccas resulted in localised inflation and the production of an endogenous tumulus complete with inflation clefts, this could

provide the opening through which the highly viscous material may be extruded. Such fractures would allow thin, laterally continuous sheets of lava to be extruded, if the lava had sufficient strength. If only a small amount of material is extruded, then a small feature, such as the crease in figure 5.2 (b) is formed, If, however, a large amount of material is available, then the complexity of the resulting feature can be far greater. As seen in figure 6.30 (a), the central sheets of lava can reach heights of up to at least three metres while remaining almost vertical, indicating that significant cooling of the lava occurred during extrusion, and thus implying a very low extrusion rate. Had extrusion occurred at a high rate, the sheets would probably have remained sufficiently fluid to collapse under their own weight.

Whether a single fracture produces the complex array of bladed sheets, or whether several fractures must be invoked is unclear. It is possible that, when the carapace fails, it does so in more than once place, and so several squeeze ups develop simultaneously. As discussed in chapter five, endogenous tumuli are often seen to have many fractures criss-crossing their surfaces, and while the central inflation cleft is the best developed, the others can develop in many different orientations, and so could give rise to the chaotic collection of bladed sheets as seen in figures 6.28 and 6.30 (b). An alternative mechanism is repeated cleaving of a single sheet as it is extruded through an inflation cleft. This mechanism was invoked by Krauskopf (1948), who observed similar morphology on lava flows and around fissures at Parícutin. While he did not witness the growth of the 'curved slabs' on the flows, the similarity in morphology with squeeze ups from fissures led him to infer a similar mode of growth, by which 'lava is pushed up slowly from beneath, splitting into slabs as it cools and contracts; then each slab grows as it is pushed outward, plastic at its base but cold and hard in its upper part'. However, the chaotic orientations of the

bladed sheets in the outer parts of the tumuli suggest that while this mechanism may explain the early development, it cannot account for all of the morphological complexities. A third possibility is that, following the initial stages of emplacement of the central crease structure, other squeeze ups begin to develop from the same fracture, outside of the solidifying central sheets. Whatever the mode of growth, the juxtaposition of well-defined, self-supporting sheets, that are in some cases arranged almost vertically, clearly indicate that the material was almost solid-like upon extrusion.

The height attained by a tumulus is a function of the pressure existing in the flow interior and the amount of material available to be extruded. In the early stages of extrusion, as long as the internal pressure is maintained, the tumulus will continue to grow. Once is has reached a certain height, or extruded a certain volume, its weight will be sufficient to prevent further material from being extruded. If material continues to be supplied to the area after this stage is reached, the build up of pressure may cause the process to be repeated nearby. This seems to have occurred in the western branch of the main channel adjacent to M. Concilio (figure 6.4), where three tumuli occur within 100 m. These are illustrated in figure 6.31. The lowest of these tumuli is around 5 m high with a well developed central cleft (figure 6.31 a), and is located over a bocca which fed a rubbly flow that reached a length of approximately 150 m. The middle tumulus is associated with a rubbly flow that reached only around 20 m in length. The amount of bladed material that built up to form this tumulus is smaller than for the lower tumulus, and from some angles, can be seen to be underlain by a smoother-surfaced bulge in the underlying flow (figure 6.31 b, c). The upper tumulus occurs with the shortest flow, and does not feature any bladed material (figure

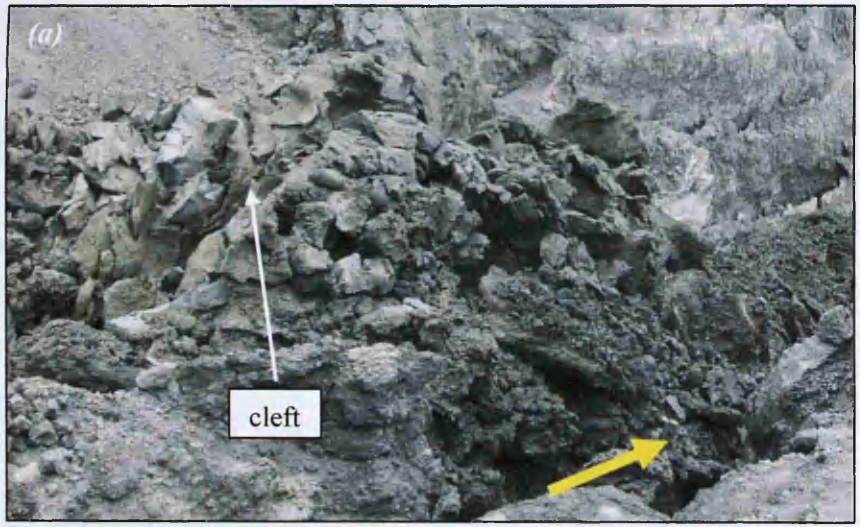

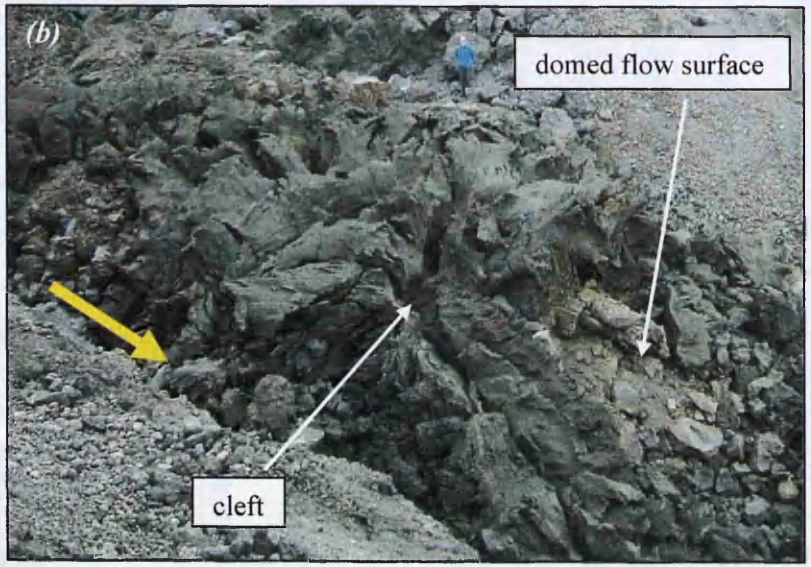

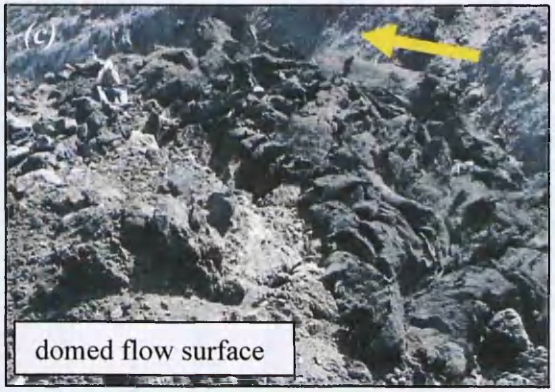

Figure 6.31. Three closely spaced tumuli in the main channel. (a) Lowest, ~5 m high, showing central cleft. (b) View of lower side, and (c) upper side, of the middle tumulus. Domed surface of underlying flow can be seen beneath bladed material. (d) Upper, 'failed' tumulus, that has fed a short, rubbly flow, but has not extruded any bladed material. Yellow colouration suggests that some degassing of material beneath has taken place in situ. In all cases, flow direction is indicated by the yellow arrow.

6.31 d). Assuming, due to the presence of the tumuli and other boccas in this part of the flow field, that flow in this region was tubed, or at least sealed within a preferential thermal pathway, a possible chronology for the development of these tumuli is as follows. The lowest ephemeral bocca developed first, and was active for sufficient time to produce the 150 m long rubbly flow. As time progressed, and perhaps due to waning flow, the material being supplied to the bocca became too plastic to flow, and the bocca became blocked. The continuing pressure of supply then resulted in the high yield strength material in the interior being extruded as a tumulus (figure 6.31 a), until the weight of this prevented any further extrusion at this locality. The thermal pathway was therefore blocked at this point. Continuing supply to the area resulted in a build up of pressure in the lowest part of the sealed system, which was now just above the lowest tumulus, and a ephemeral bocca developed at this point. In this case, again possibly due to waning flow, the material that could be extruded before this bocca became blocked was only sufficient to produce a short rubbly flow. Once this material had been exhausted, a second tumulus began to form. In this case, however, conditions in the underlying flow only allowed a relatively small quantity of bladed material to be extruded, and the underlying domed flow surface remained partially exposed (figure 6.31 b, c). Once activity ceased at this locality, the process was repeated again further upslope. The third bocca produced the shortest flow, which attained a length of only around 10 m (figure 6.31 d), and once effusive activity ceased the pressure in the flow interior was sufficient only to produce localised inflation, and no exogenous tumulus was formed. This may be due to a reduction in supply to this part of the flow field, as successive boccas extruded less and less material. The upper tumulus can be seen to be narrower than the underlying flow surface in the channel (figure 6.31 d), suggesting that by the latest stages of

activity, the thermal pathway was considerably narrower than earlier active flows. This would be expected to happen as flux wanes. The yellow colouration seen around the domed region may indicate that this area was underlain by a pocket of gas-rich lava, and that the gas was able to escape despite the fact that the carapace was not breached, resulting in the characteristic sulphurous hue. This hypothesis is in agreement with Walker (1991) who suggested that tumuli are areas where gas can escape from the underlying lava.

The tumuli shown in these examples have all been associated with short flows, indicating that extrusion in these areas commenced with more fluid material, before the highly plastic tumulus material was extruded. In other areas of the flow, there is evidence of the extrusion of material that was already in a highly plastic state when extrusion commenced, and so no flow was formed. One example of this is the crease that was shown in figure 5.2 (b). In this case, the material was still fluid enough to fold over to the sides. In other cases, the material is already very strong when it is extruded, and so does not form so smoothly symmetrical a structure, but a more chaotic collection of bladed sheets like those observed in the tumuli (figure 6.32 a). Elsewhere, mounds of material formed over boccas that produced short, rubbly flows, but did not develop the bladed morphology, retaining instead a more massive structure (figure 6.32 b), though the small-scale surface textures were very similar to those of the bladed tumuli. The precise morphology is likely to be a function of the lava rheology, the extrusion rate, the amount of material available and the geometry of the vent, thus allowing for many variations on a theme. Figure 6.33 gives a very general indication of the morphology an extrusion could be expected to develop, based on the volume of material, its rheology, and the strain rate it experiences.

Figure 6.32. (a) Squeeze-up that is not associated with any previous emission of more fluid lava. The extrusion is elongate in shape, which was probably determined by the source geometry, and is made up of bladed, twisted sheets as seen in exogenous tumuli. Again, the texture is seen to be very different to that of the surrounding `a`ā. (b) Mound of massive material that built up over an ephemeral bocca which earlier fed a flow that extended ~80 m from source (away from viewpoint). The morphology is clearly different to that in the bladed tumuli in previous figures. The mound stands ~5 m above the near lava surface.

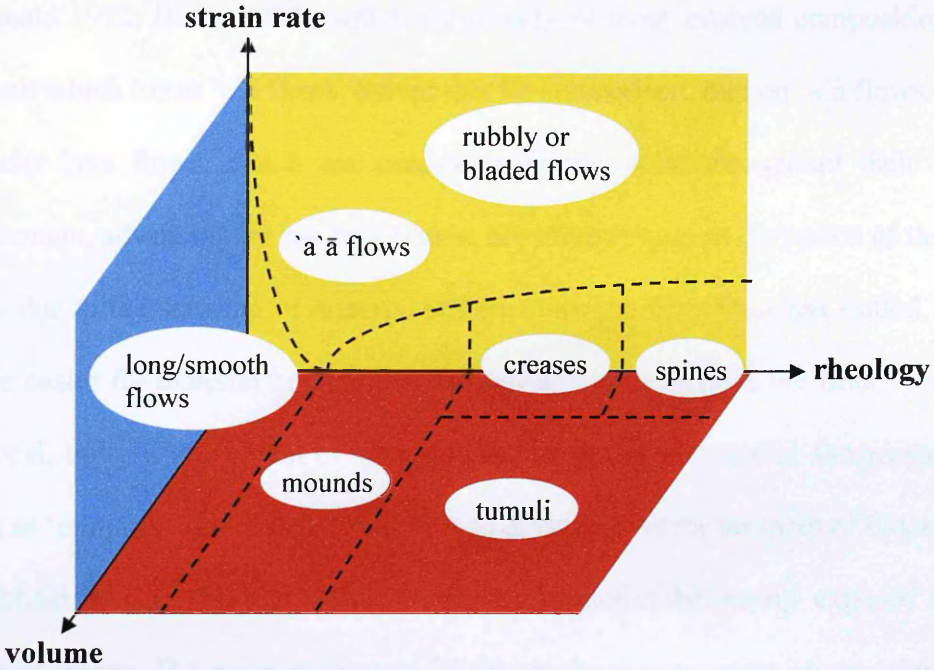

Figure 6.33. Sketch showing the morphology an extrusion would be expected to develop based on the volume of material, its rheology, and the strain rate to which it is subjected. At very low viscosities and/or yield strengths ('low' rheology), long, relatively coherent flows are likely to form even at significant strain rates. This is observed on Hawai'i, where channelised flows can retain pāhoehoe morphology even at very high velocities. As the viscosity and/or yield strength increases, it is more difficult for the material to flow. At high strain rates, the material will fragment, producing `a`ā or rubbly/bladed textures, while at low strain rates, material will accumulate over the point of extrusion. This accumulated material may produce massive mound structures, crease structures, bladed tumuli or spines, depending on its strength and the volume of the extrusion. Boundaries between the morphologies are arbitrary, and the sketch is intended only to give a very general indication of the probable morphology.

Spines

In the extreme end-member case, material which is almost completely solid may be extruded from the flow interior, resulting in spine-like features on the flow surface (figure 6.34 a). Several examples of this are seen on the 2001 flow, but these are exclusive to the region immediately behind the flow front. The material forming the spine extends vertically upwards from the flow surface, and commonly narrows from the base to the tip. These are well documented on lava domes and block lavas (e.g.

Macdonald 1972; Blake 1990), which are usually of more evolved composition than the basalt which forms `a`ā flows. Spines are, by comparison, rare on `a`ā flows.

Blocky lava flows, which are commonly almost solid throughout their whole emplacement, advancing by autobrecciation, are often subject to disruption of the flow surface due to the shearing of material within. Once the flow front has stalled, it can become easier for material behind to move upwards than to push the front forwards. This local, upward movement of lava, due to movement on internal shear planes, is known as 'ramping', and causes small hills to develop over the surfaces of block lavas (Macdonald 1972). This can result in the flow interior becoming exposed at the surface as spines. The spine in figure 6.34 (a) can be seen to occur on top of a small hillock that is elevated above the local flow surface, and figure 6.34 (b) shows another example of a locally uneven flow surface dotted with spines. This evidence suggests that the processes forming these features may be analogous to those described in block lavas by Macdonald (1972). If this is the case, these observations provide information about the state of the flow interior at the time of formation, indicating that at the very end of activity the flow interior may have cooled and degassed, at least in the surface regions, to the extent that the material inside was essentially solid. Increases in interior pressure, by mechanisms described in section 6.2.3.3, which in other regions have resulted in the extrusions of very viscous lava flows or plastic bladed sheets, have here resulted in almost solid parts of the flow interior ramping up through the fragmented clinker cover to extend above the flow surface. This material probably represents the most extreme condition in which lava can 'flow'.

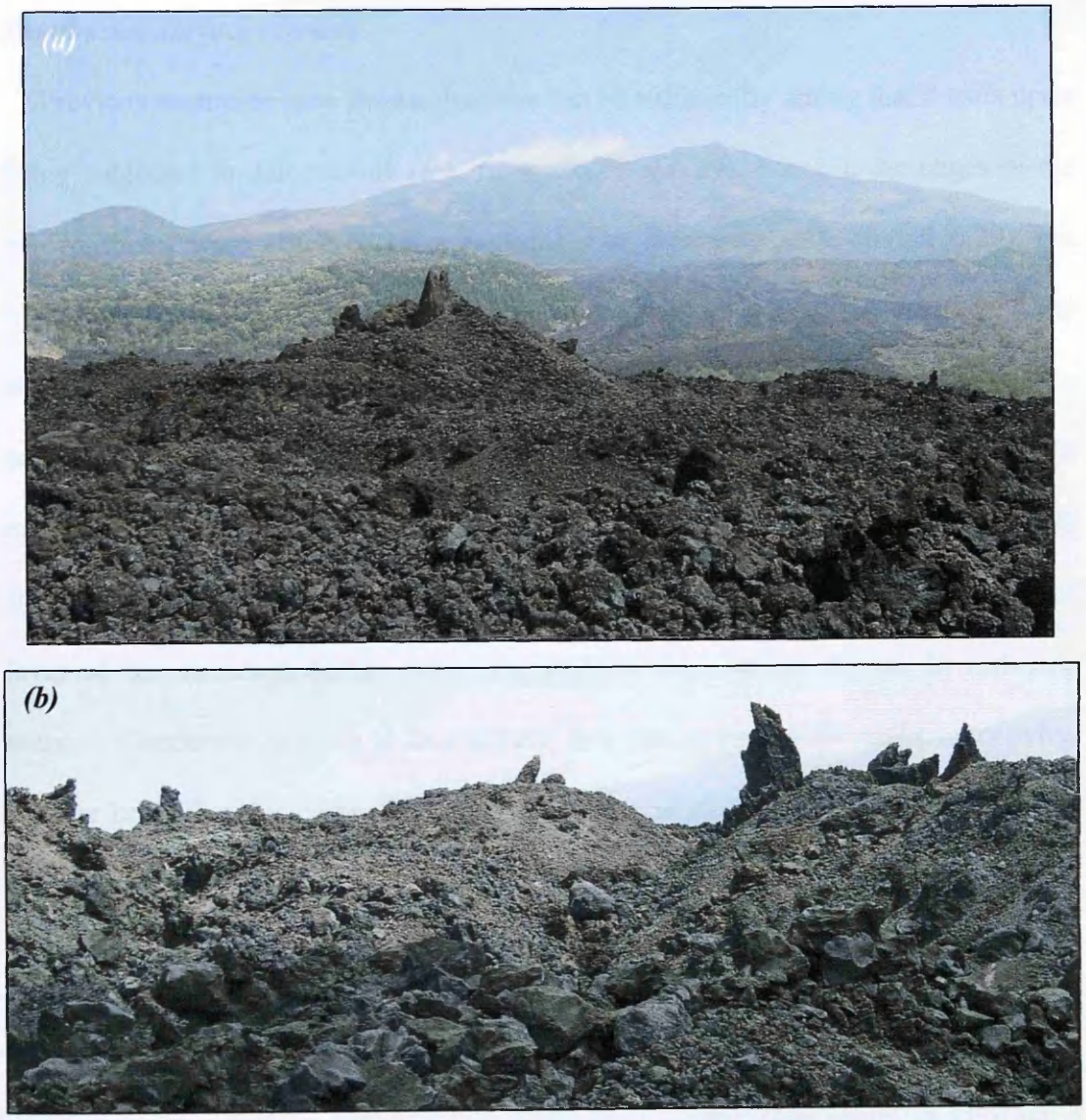

Figure 6.34. (a) Looking north up the flow from the flow front. Spine is protruding through the top of a small (~5 m high) hillock on the flow surface. (b) Just behind the flow front, the flow surface is uneven and hillocky, with several outcropping spines. Large spine in the mid-right of the image is ~2 m high.

Small-scale surface textures

Previous examples have shown that lava can be sufficiently strong that it tears upon being subjected to deformation (e.g. figures 6.27 a, 6.29). Tears in the edges of the bladed sheets were observed on a centimetre to decimetre scale (figure 6.29), but millimetre to centimetre scale tears were also observed across the surface of the sheets. This smaller-scale deformation resulted from the cleaving of the lava surface parallel to the plane of the sheet, with platy fragments 'peeling' away from the surface of the sheet as it folded over. This texture can be seen in figure 6.35 (a), and results from the surface cooling of the plastic lava upon extrusion, which renders the surface layer of the extrusion brittle, while the interior continues to deform in a ductile manner. Conductive cooling in lava is very slow due to its low thermal conductivity, and the brittle layer is commonly observed to extend only a few millimetres into the lava sheet.

Where lava was forced out of the flow interior in an almost solid-like state, the friction experienced along the interface between the squeeze up and the solid flow carapace was sufficient to produce fault gouge. This fine-grained material may be red or white in colour (figure 6.35 b), and its distribution may be used to determine the direction in which the squeeze up was travelling during extrusion, if it has remained in situ.

Vesicularity

While all of the squeeze-ups examined contained vesicles, the shape, size and proportion of these was found to vary greatly between-squeeze ups, as illustrated in figure 6.36. In the majority of examples, the interior of a squeeze-up was very similar

Figure 6.35. Squeeze-up surface textures. (a) Surface cooling upon extrusion can render the outer layer of lava brittle. This layer then fractures when subjected to deformation, producing platy, 'peeled' textures. (b) The friction between high yield strength material and the solid carapace can result in the formation of fault gouge. This is red or white in colour, and the distribution may indicate which direction the squeeze-up was travelling in during extrusion. Arrows show the possible directions in which the squeeze up was travelling as the two sets of gouge formed.

to that seen in figure 6.36 (a), being predominantly dense and crystalline, with a few large (up several cm long), irregular vesicles, and a fairly even, though sparse, distribution of smaller bubbles (a few mm across). In contrast, a small number of squeeze ups near the flow front consisted of much more vesicular material, like that shown in figure 6.36 (b). The vesicles in this sample fall within a narrower range of sizes ($\leq$ 0.5 cm), and, though more equant than the large vesicles in the denser examples, are again relatively angular in shape. The deformation of bubbles indicates that the lava in which they are trapped has a high yield strength, as has already been inferred from the larger-scale morphology of these features. The difference in vesicularity between these two examples suggests that they were extruded following different flow histories, and this may provide information about the transport of the material through the flow field prior to its extrusion.

Cross sections through basaltic flows commonly show that the flow interior is dense at depth, becoming more vesicular towards the surface, due to the rise of bubbles after their formation. As was noted in chapter five, the material extruded from tumuli can be highly vesicular, as a result of storage within the flow at low overpressures, which allows time for gas to exsolve and bubbles to rise. Alternatively, given high enough overpressures, the gas may be resorbed, resulting in the extrusion of very dense material (Walker 1991; Hon et al. 1994; Cashman & Kauahikaua 1997).

These observations suggest two possible explanations for the difference in vesicularity observed in the 2001 flow. Firstly, it is possible that the vesicular squeeze-up material was sourced from a shallow level in the flow, and the dense material from depth. Material from depth may be extruded if, prior to the extrusion, the flow had cooled sufficiently for the vesicular layer to solidify. This would imply

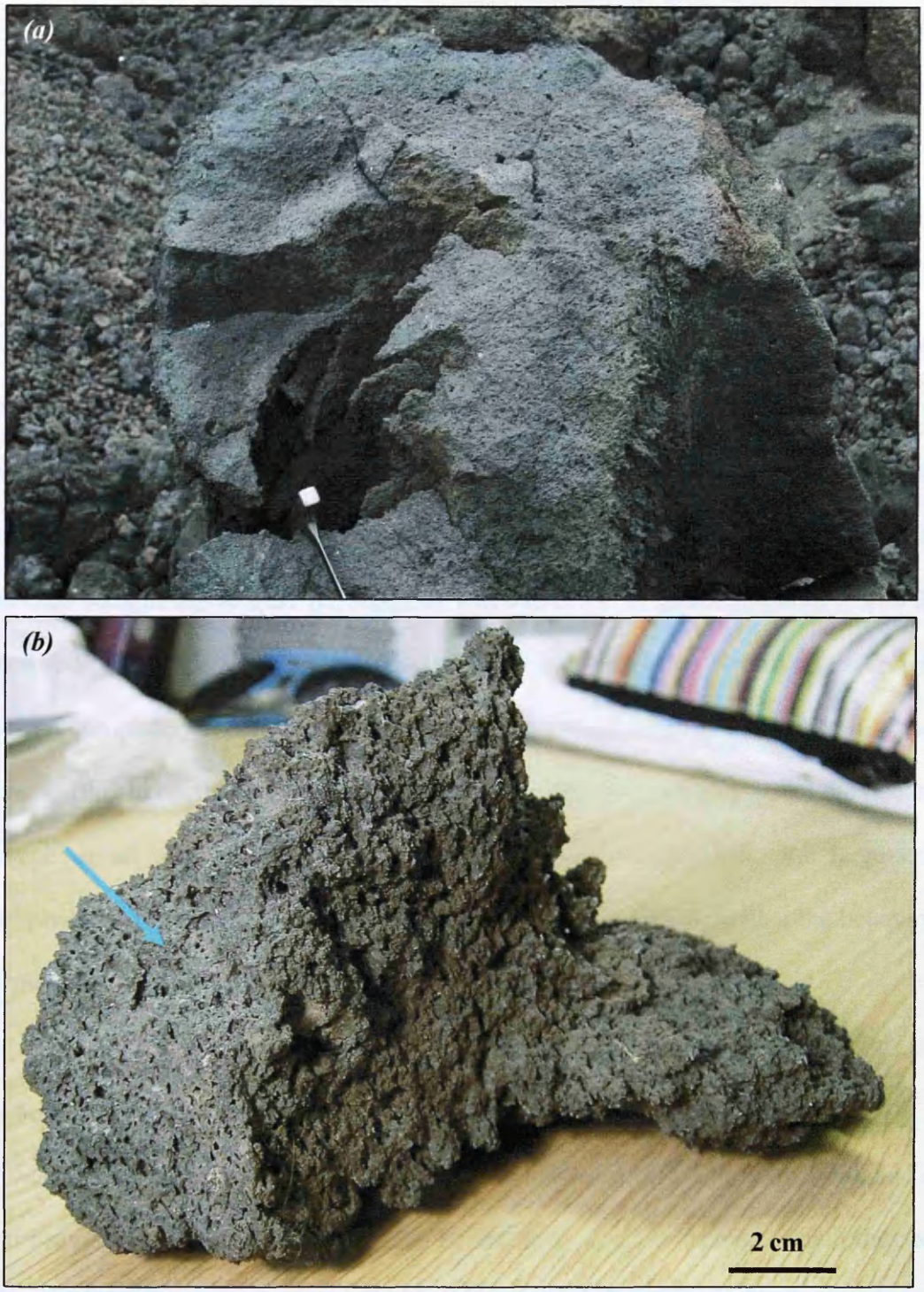

Figure 6.36. Variable vesicularity between squeeze-ups. (a) Relatively dense lava sheet. Some large, irregularly shaped vesicles are present indicating the high yield strength of the material. Note hammer for scale. Image: H. Pinkerton. (b) Sample taken from a highly vesicular squeeze-up. The surface representing the interior of the sample is indicated by the arrow. The vesicles are again irregular in shape, indicating a high yield strength, but are much smaller than those in (a). The difference in vesicularity between these two examples is indicative of different flow histories. See text for details.

that the vesicular squeeze ups result from processes occurring shortly after the flow has ceased advancing, while the denser squeeze ups are later-stage features. A second explanation, which would allow both types of material to be sourced from similar depths, is that the vesicular material was extruded relatively soon after emplacement, while the denser material was stored for some time within the flow prior to extrusion. Assuming the two bodies of material were identical upon emplacement, the longer storage time would have allowed more vesicles to rise and escape, thus resulting in denser lava, and may have allowed more coalescence of vesicles, resulting in the very large bubbles seen in figure 6.36 (a). The yellow colouration of the endogenous tumulus seen in figure 6.31 (d) suggests that degassing of stored material stored has occurred within this flow, and so this explanation is plausible. The fact that vesicles are not completely absent in the dense material may reflect either insufficient storage time for this to occur, or the high yield strength of the lava, which resisted the rise and escape of all gas bubbles. Despite the difference in vesicularity, the large-scale morphology of the two types of extrusion is very similar, indicating that the behaviour of the material and the squeeze-up processes were similar in both cases.

6.2.3.2 Squeeze-up locations

Squeeze ups are observed to exploit areas of weakness within the flow field, and so can provide information about the state of the flow carapace through which they are extruded. Ephemeral vents are commonly observed forming in flows fronts (e.g. Macdonald 1972; Pinkerton & Sparks 1976; Dragoni & Tallarico 1996), and have also been documented forming in the flow surface above established tube systems in long-lived flow fields (Calvari & Pinkerton 1998). During 2001, flows and squeeze ups were fed by ephemeral vents that formed in many locations, including flow fronts,

flow surfaces behind flow fronts and within channels, along channel-levée boundaries, and also possibly through levées. The localities of major squeeze ups are highlighted in figure 6.37, and are colour coded according to the part of the flow that they breach.

The continued supply of material to a flow front that has stalled can result in inflation of the front, followed by rupture on a relatively short timescale (hours to days). In cases where supply wanes after the lobe stalls, the flow front may have time to thicken sufficiently that if a new pulse of lava arrives, the front cannot be breached. In this case, the pressure building in the flow interior may cause rupture elsewhere within the lobe. An example of this is shown in figure 6.38, where a squeeze up has formed along a long curved fracture in the flow surface immediately behind the flow front, the geometry of which was clearly controlled by the internal structure of the lobe. In this case, while the opening of the bocca was controlled by the ramping of material within the lobe, as described in the context of spines, the squeeze up material was fluid enough to form a flow approximately 100 m in length, and so is not thought to have been stored for a great length of time before extrusion. These examples of ramping seem to have been controlled by the action of the flow interior, where the increase in pressure has caused the carapace to fail, then forced material up through the breach. An alternative possibility is that failure of the crust occurred for different reasons earlier in the flow history, and that these fractures were later exploited as the pressure in the flow interior increased. Such an example was discussed in relation to the possible formation of conjugate fractures in the carapace of the overflow lobe adjacent to M. Ardicazzi. In this lobe, the plastic squeeze ups were usually arranged along linear openings in the crust (figure 5.5).

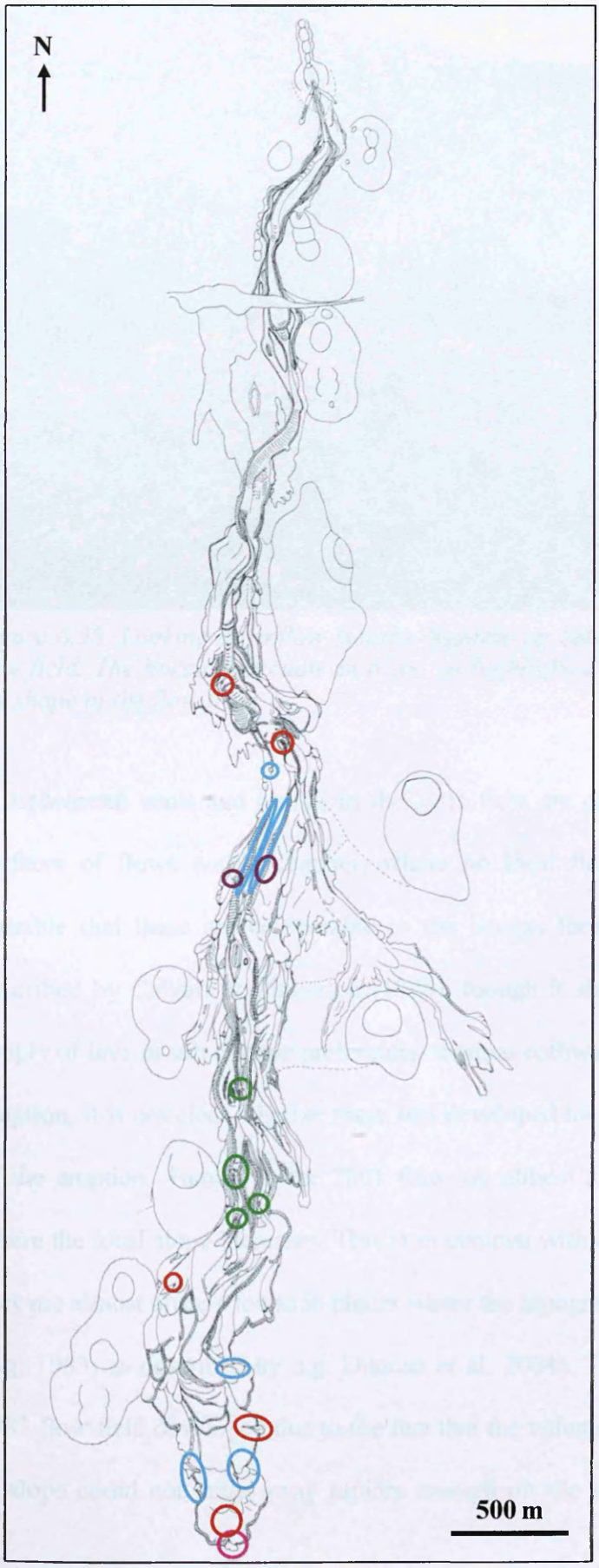

Figure 6.37.
Flow field map showing the locations of major squeeze ups discussed in the text, colour coded according to the part of the flow through which they were extruded. Ephemeral vents that formed in the fronts of stagnating lobes are not included.

***Blue**: along the channel-levée boundary*
***Green**: through the flow surface within the channel*
***Red**: through the flow surface behind flow fronts*
***Purple**: through levées*
***Pink**: between lobes*

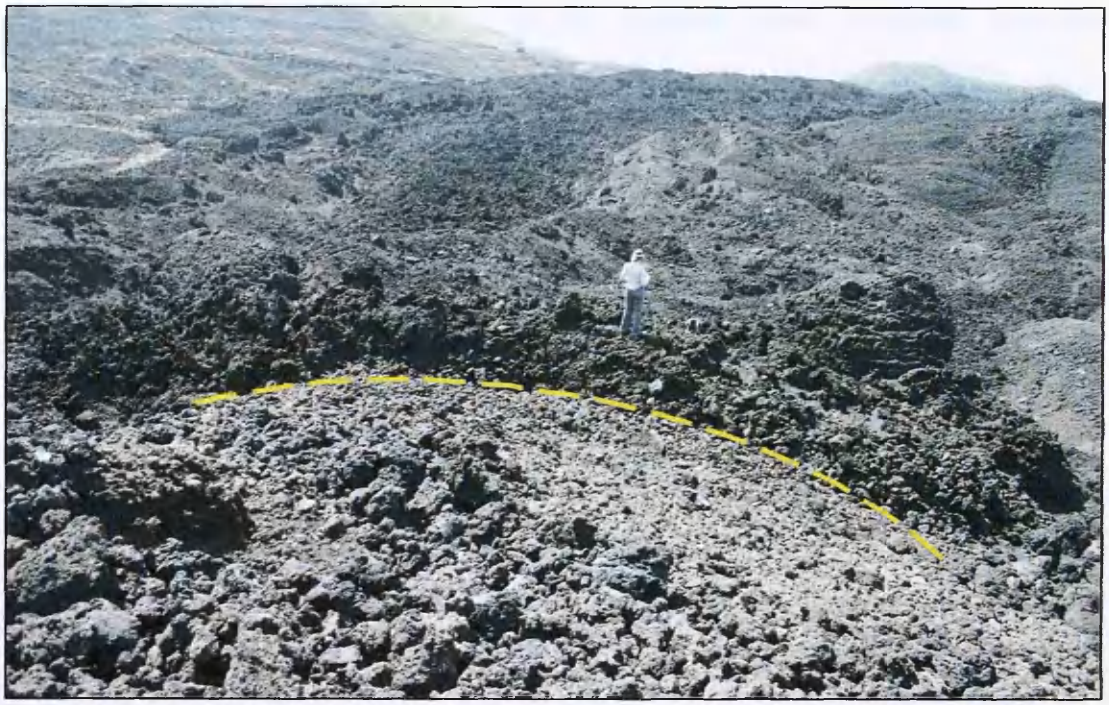

Figure 6.38. Looking downflow (south). Squeeze up behind a flow front in the medial flow field. The bocca is arcuate in trace, as highlighted by the dashed line, reflecting the shape of the flow front.

Ephemeral vents and tumuli in the 2001 flow are often observed to form on the surfaces of flows within channels where no local flow fronts are observed. It is possible that these are comparable to the boccas forming above tube systems, as described by Calvari & Pinkerton (1998), though it should be noted that while the supply of lava in sub-surface preferential thermal pathways was noted during the 2001 eruption, it is not clear whether these had developed into mature tubes before the end of the eruption. Tumuli in the 2001 flow are almost always associated with places where the local slope increases. This is in contrast with other flows on Etna, in which they are almost always found in places where the topographic slope abruptly decreases (e.g. 1983, as described by e.g. Duncan et al. 2004). The endogenous tumuli in the 1983 flow field developed due to the fact that the volume of lava arriving at the break in slope could not drain away rapidly enough on the shallower topography, and as

they were active for the majority of the eruption, were associated with the emplacement and transport of relatively fluid lava. By contrast, the exogenous tumuli in the 2001 flow represent the latest stages of activity, and as such are related to the movement of much more viscous material. An increase in slope would allow the more rapid drainage of fluid lava, so tumuli would not be expected to form in these regions during the early stages of an eruption. However, the rheological state of the material extruded as tumuli in the 2001 flow probably did not allow it to flow simply due to the action of gravity, and the extrusion of such material infers the action of high internal overpressures. The formation of exogenous tumuli in these locations may therefore reflect earlier emplacement processes. As observed in the analogue models described in chapters three and four, and in the field (chapter five), local acceleration of the flow, as induced by an increase in slope, commonly causes the brittle carapace to fracture (e.g. figure 5.3). This occurs while the flow surface is still moving. If the flow subsequently stagnates while supply continues to the area, and the interior becomes overpressured, the earlier surface fractures at the slope increase may provide a locus of weakness that can be exploited to produce an extrusion.

The location of squeeze ups along channel-levée boundaries is unsurprising, as this is a classic area of weakness due to the shearing of the flow surface crust against the levée. The most spectacular example of this occurs close to the flow front on the east side of the flow (figure 6.39 a). In this case, fluid material was extruded initially, probably from a small bocca, which fed a flow that drained over the levée down to the side. This flow reached a length of around 70 metres, and was formed of the very rough, rubbly material commonly associated with late-stage squeeze ups. Later, however, perhaps due to an increase in pressure within the flow interior, instead of

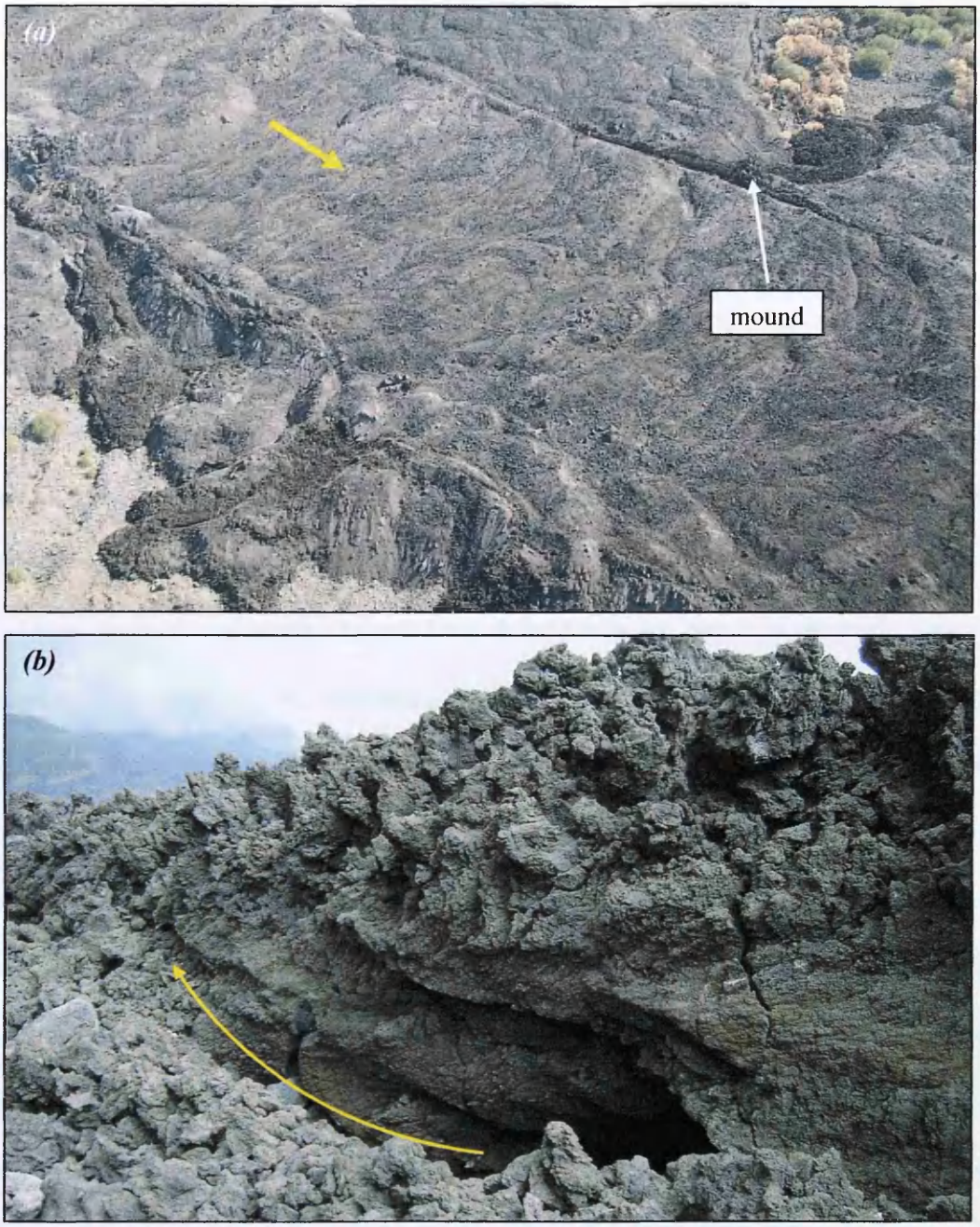

Figure 6.39. (a) View of the flow just behind the flow front, taken from the west. Flow direction is indicated by the yellow arrow. Late-stage squeeze ups can be seen along both margins of the flow, and appear a lot darker than the surrounding flow surface. On the far (eastern) margin, late-stage activity first fed a short rubbly flow, then the viscous squeeze up that extends along the channel-levée boundary for ~100 m. A mound (also seen in figure 6.32 b) covers the point of origin of the rubbly flow. (b) Close up of the squeeze up, upflow of the mound, which is 3 to 4 m high at this point. The grooves on the lava indicate that it was travelling both up and away from the point of origin, inferred to be below the mound, in the direction marked by the arrow.

being concentrated at a single point, material began to be squeezed up along the channel-levée boundary for a length of around 100 m. Field observations indicate that the extrusion was still concentrated at the early weak point, but perhaps the rheology of the material meant that it could not be released from this area as rapidly as it was supplied. As a result, material began to be squeezed to the side, where lateral as well as upward movement can be inferred from the deep grooves in the toothpaste lava extruded (figure 6.39 b), and from the fault gouge (figure 6.35 b). Many other squeeze ups also occur around the flow front margins, and these often have their sources in the channel-levée boundary region (figure 6.37, 6.39 a).

Other squeeze ups along channel-levée boundaries are found in the main channel between M. Nero and M. Ardicazzi, where the surface of the main channel was stationary for a large proportion of the eruption. Here, the squeeze ups are of rather lower volume than that described near the flow front, and commonly protrude only up to around 1 m above the flow surface (figure 6.40 a). They are widespread down both margins, suggesting that although the flow surface was stationary, it had not adhered to the margin completely. This, together with the general surface morphology as discussed in section 6.2.4, strongly suggests that tubed flow did not develop in this part of the channel during the eruption. Large blocks of massive material were also observed on the outer surface of the levées along this part of the channel, which may indicate that material was being forced through the levées (figure 6.40 b), though this could not be verified. Another possible squeeze-up is seen in figure 6.40 (c), where a short, dark lobe appears to emerge from the base of the levée. As noted, squeeze up material is commonly very dark in comparison to surrounding material, but the source vent of the material could not be identified, and so this remains speculative. If these squeeze ups are occurring through the levées, it suggests that the levées were not

Figure 6.40. Main channel below M. Nero. (a) In the channel, looking downstream. Squeeze ups can be seen along the channel-levée boundary. Such features are widespread down both sides of the channel. (b) Looking downstream. Features on the outer side of the left hand levée, which may or may not be squeeze ups through the levée. (c) Looking upflow. Squeeze up which may have been extruded through the levée. Channel is ~ 50 m wide. Image: INGV.

completely consolidated when the squeeze ups formed, perhaps having a rubbly structure as described by Sparks et al. (1976). Such behaviour was documented on active flows at Parícutin, by Krauskopf (1948), who noted that 'lava may ooze out at the base of the levées', suggesting that this is a plausible mechanism.

While breaching of the flow front has already been discussed, this has usually been reported, at least in the context of `a`ā flows, as single-lobed fronts rupturing somewhere around their convex margin. In the 2001 flow, however, one example of a squeeze up was seen at the boundary between two flow lobes. The mechanism of lobe development at the 2001 flow front is the subject of some debate, and this has bearing on the feature interpreted here as a squeeze up: the farthest advanced lobe, highlighted in figure 6.37 and shown in figure 6.41. A. Harris (pers. comm. 2008) favours the development of the flow front lobes one at a time, as they 'punched' through the stalled flow front. This is considered analogous to the inflating `a`ā advance mechanism reported by Calvari & Pinkerton (1998), in which a flow front stalls, inflates due to continued supply, then breaches. The process is then repeated, and is one method by which tubes can form. Harris invokes this process, but instead of the subsequent lobes developing in a linear array (which would form a lengthening tube), they all develop from the same stalled flow front, and are emplaced adjacent to one another, forming a fan-shaped array. The lobe inferred here to be a late stage squeeze up is inferred by Harris to be a 'failed' flow front lobe; an extrusion of low yield strength material that, had activity continued, would have developed into a feature similar to the surrounding flow front lobes. The lower thickness of this lobe compared to the rest of the flow front is cited as evidence of its lower yield strength.

This series of events is disputed here. Firstly, as demonstrated by the analogue experiments (chapters three and four), the formation of a lobate flow front does not require the breaching of a confining viscoelastic carapace. Secondly, if flow front breaching is invoked, and a new lobe first forms, then stalls, why should a subsequent breach take place in the original flow front rather than the new front which presumably has a thinner, more easily breached carapace? Thirdly, if subsequent

breaches do occur in the same flow front, resulting in the formation of lobes of different ages, it would seem remarkable that all of these lobes attained a very similar size before stalling, and that they lose the clarity of their margins so that the surface of the whole flow front looks very uniform (figure 6.41). Finally, the material forming the shallow lobe has been observed in the field to be largely made up of extremely rough fragments similar to those seen in other examples of late stage squeeze ups, and also appears darker than the surrounding lobes, as squeeze ups commonly do. The interpretation of it as an extrusion of *lower* yield strength material, based only on its thickness, is therefore rejected.

Figure 6.41. Flow front, showing the similarity of shape, size and colour of the thicker lobes, and the marked difference of the front lobe. This lobe appears darker in colour, as has been noted in earlier examples of squeeze ups (e.g. figure 6.39 a), and has a large proportion of very rough, bladed material on its surface. It is inferred here to be a late stage squeeze up of high yield strength lava, rather than a 'failed' lobe that was emplaced with low yield strength. Image: INGV.

The interpretation of the flow front morphology preferred here is as follows. During emplacement, the flow was, on at least one occasion before reaching its maximum length, observed to spread out to form a fan-shaped front upon reaching shallower topography. There appears to be no reason why this process could not be repeated during the final advance of the front, as the velocity decreased. Such lateral spreading was observed in the analogue experimental flows as they advanced beyond the channel, and resulted in fracturing of the flow crust due to a combination of transverse tensile and longitudinal compressional stresses. The uneven distribution of the crust led to an uneven distribution of weight on the flow surface, and so resulted in non-uniform advance of the flow front. It is possible that this could have occurred during the latest stages of emplacement of the 2001 flow front, causing the lobate flow front, though other mechanisms may also be important. Lobe structures can also arise due to the differential retardation of the flow by different amounts of crust avalanching down the flow front, as seen in the experiments, or as a result of small-scale topographic influences. In all of these cases, the fluid interior would remain continuous, allowing uniform inflation, so that the flow surface remained quite even. Whatever the mechanism by which the lobes form, once they developed, the lobate structure influenced the cooling of the flow front. The cuspate parts of the flow front were better insulated than the fronts of the lobes, and so did not thicken as quickly. This non-uniform thickening resulted in the cusps being weaker than other parts of the flow front. A subsequent increase in pressure in the interior caused the crust to breach in one of these weak spots, allowing the extrusion of highly viscous or plastic material between two lobes. In the field, the source of this squeeze up is difficult to locate. Although extrusion through the flow front as a result of the aforementioned processes is possible, it may instead have originated behind the flow front, through the flow

surface. In this case, it may provide some support for the experimental model of lobe formation by surface fracturing, as the development of fractures results in the formation of lobes to either side, by the loading of the interior by crustal plates. The presence of a squeeze up through the flow surface between two lobes may be evidence for this process, as extrusions exploit the weakest parts of the flow surface.

6.2.3.3 Processes leading to overpressure of the flow interior

Ephemeral vents result from the breaching of a flow carapace, due to overpressure in the flow interior. Previous studies of ephemeral vents have observed that this pressure increase results from the continued supply of material along the original flow path, as sketched in figure 6.42 (a). While this is certainly a viable mechanism for ephemeral vent formation in the 2001 flow, a second mechanism was also observed that directly resulted in the breaching of adjacent crust.

Once the flow field had reached its maximum length, the continued effusion of lava led to the flow field growing by the addition of overflow lobes along the flow margins, and also by the emplacement of new lobes on top of earlier lobes and channels. An excellent example of this is seen around 500 m behind the flow front, and this region is shown on August 1st, 2nd, and after the eruption in figure 6.43. The flow surface is seen to be uneven on the 1st (figure 6.43 a), and the image from the 2nd suggests that a new surface flow is developing on top of the original flow in the main channel (figure 6.43 b). In the post eruption image, stepped flow fronts can clearly be seen overlying the original flow (figure 6.43 c, compare with a). These stepped flow fronts appear to have been emplaced before the breakout channel, which was observed forming in a thermal image taken on August 3rd (figure 6.13), and probably

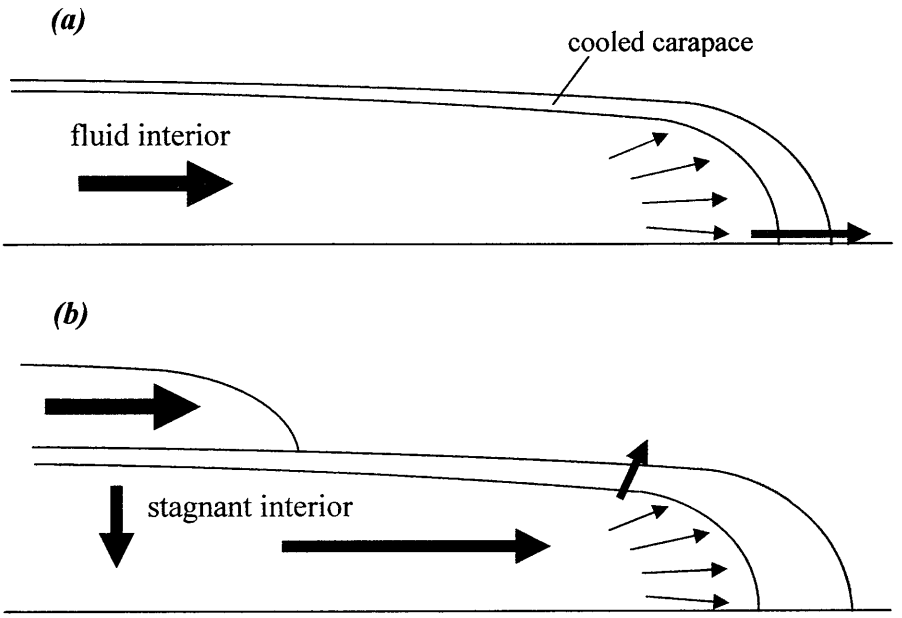

Figure 6.42. Schematic illustrations of two possible mechanisms whereby overpressure can develop in the flow front. (a) The continued supply of material from upslope results in inflation of a stalled flow front, and subsequent failure of the carapace at the base of the front. This is denoted by the arrow cross-cutting the carapace. (b) The cessation of a flow, without the continued supply of material, results in cooling and thickening of the carapace. If a second lobe (red arrow) is subsequently emplaced on top of the earlier lobe, the weight of the new lobe may squeeze material in the lower lobe towards the flow front, causing inflation. Due to cooling, the flow front is too thick to fail, and the overpressure results in a breach occurring in another, weaker part of the carapace, such as the flow surface (indicated). Due to the time elapsed between cessation of the original lobe and the formation of the breach, the material extruded may have developed a considerable yield strength before being forced out of the interior.

contributed to the breakout by further blocking the channel. As can be seen in figure 6.43 (c), the stepped flow fronts overtop the earlier channel-levée boundary, partially covering the marginal overflow lobes which probably developed around the same time as the flow front stopped advancing (July 25th). In the post eruption image, a dark squeeze up is observed at the front of this group of marginal lobes, that was not seen on August 2nd (figure 6.43 b). Since these lobes are clearly cut off from supply from behind by the levée, the mechanism for overpressuring this lobe cannot be by continued supply to the back of the lobe as shown in figure 6.42 (a). Instead, the loading of the back of the lobe from above by the overflowing superimposed stepped

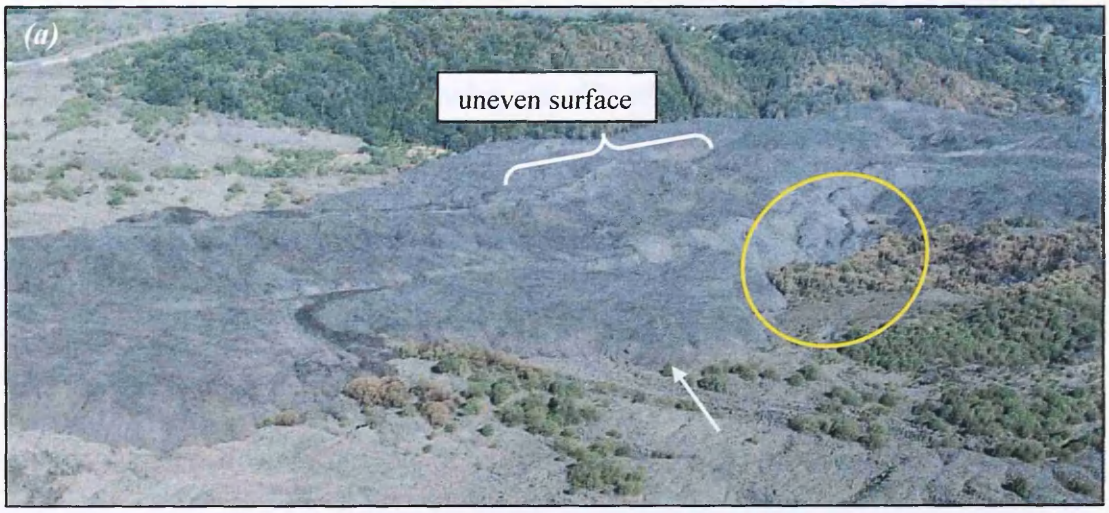

Figure 6.43. Views of the flow just behind the flow front. (a) August 1st. In the bracketed area, the channel can be seen to be very full, with an uneven surface. The area where the August 3rd breakout will form is ringed in yellow. (b) August 2nd. The stepped flow fronts seem to be forming in the main channel, indicated by the yellow arrow. (c) Post-eruption. Stepped flow fronts are obvious (bracketed), clearly overlying earlier flows, and the breakout to the east has formed (ringed). The viscous squeeze up through the front of an overflow lobe can be seen- this is not observed in (a) or (b), in which its future position is indicated by the white arrow. Images: INGV.

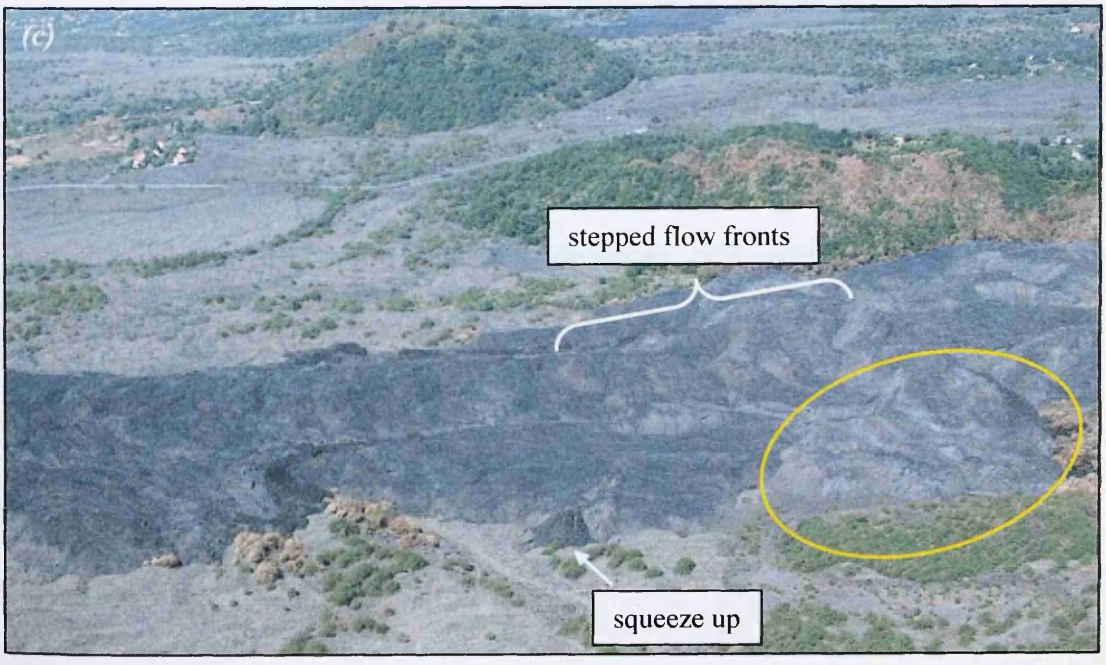

flow fronts must provide the required pressure. This mechanism, illustrated in figure 6.42 (b), is analogous to the squeezing out of toothpaste by pressing down on its tube and as such is dubbed the 'toothpaste mechanism'. Since the underlying flow has cooled for several days prior to pressurisation, any squeeze ups that form may well be of toothpaste texture, but the mechanism and the product are actually independent. This squeeze out is the only one observed to directly result from the superimposition of the stepped flow fronts, but it is possible that some of the other squeeze outs observed on the flow surface during field surveys, though which are too small to see in the aerial images, were also formed in this way. Others in the region clearly predate the emplacement of the stepped flow fronts (figure 6.43 a), and so probably result from the mechanism shown in figure 6.42 (a).

This mechanism provides an alternative theory for the development of the three closely spaced tumuli shown in figure 6.31. In section 6.2.3.1, these were inferred to propagate upslope, with the lowest one forming first. However, it is possible that the highest one developed first, and the material that it extruded loaded the underlying flow, thus forcing material to be extruded further downflow due to the toothpaste mechanism, and so on. While this is a plausible mechanism for the development of such a sequence of features, it is not the explanation favoured here. This is due to the fact that the lowest tumulus is associated with the largest volume of extruded material, and the volume of extruded material decreases progressively upslope. This is consistent with the earlier interpretation in which waning flow resulted in the gradual stagnation of the channel from the lowest part upwards, with a reduction in activity resulting in the progressively smaller volumes of material extruded from successive boccas.

6.2.4 Drainage features

6.2.4.1 Drained channels

Features have been identified in the flow field which are clearly indicative of the drainage of parts of the flow towards the end of effusive activity, and beyond. In long-lived basaltic eruptions, channelised lava flows commonly form tubes with self-supporting roofs, which are often drained to form caves at the end of an eruption (e.g. Calvari & Pinkerton 1998). During the 2001 eruption, the stagnation of flow units within the main channels was observed, and ephemeral vents and preferential pathways were observed to develop. However, after such pathways form, the stagnant flow surface is initially dependent on the flow interior for support, and any changes in flux can result in modification of the original flow surface (Calvari & Pinkerton 1998). Such surface modifications were observed within the 2001 flow field, and these may be linked with changes in flux and partial drainage of the interior of stagnant lobes.

Stagnation can result either from the development of an internal yield strength that prevents the whole unit from moving, by degassing, undercooling and crystallisation (Sparks & Pinkerton 1978), or through the cooling of the carapace to the extent that it can no longer advance, and prevents the material behind from doing so. In the former case, the large-scale drainage of the lobe would not be expected if the carapace were breached, while in the latter, the material behind the flow front could still be fluid enough to flow, and so drain through the developing preferential thermal pathway. Two different morphologies in partially drained channels suggest that both scenarios could have occurred in the 2001 flow field.

The two morphologies occur in adjacent parts of the main channel, in the area of the flow just south of M. Nero. Early in the eruption (before August 1st), the flow in

the main channel stagnated in this region, and an ephemeral vent developed at the front of the stagnant flow (thermal image, figure 6.7). Throughout the rest of the eruption, a preferential thermal pathway existed beneath the stationary channel surface, and the ephemeral vent continued to drain the flow behind until two days after the eruption ended. In this part of the flow, the main channel is approximately 30 to 40 m wide, and the levées are up to 20 m in height. Downflow of the ephemeral vent, the channel is largely drained, while immediately above the vent, the channel is almost completely full for a distance of around 100 m (figure 6.44). The morphology above the vent, however, indicates that the flow surface has sunk slightly over the expected trace of the thermal pathway, resulting in a shallow v-shaped profile (inset, figure 6.44). Further back, behind the full channel section, the flow has a similar v-shaped profile, but the central depression is seen to be much more pronounced. Field observations reveal marginal features within the channel that resemble rubbly levées, but are not inferred to be levées. No evidence of open channel flow is seen in the central depression between these marginal features (figure 6.45). The morphology of the channel as seen in figure 6.44 suggests that following the stagnation of the flow lobe and the establishment of the preferential thermal pathway, the more strongly cooled flow front region sagged slightly over the hot flux beneath, while further back up the channel, the flow interior was still fluid enough to flow, and so largely drained through the newly established ephemeral vent. While the central part of the channel drained substantially, the cooler margins had already stagnated to some extent, and these were left behind. The `a`ā surface texture gives these drainage features the appearance of rubbly levées.

Just upflow of this strongly drained channel section is another, fuller part of the channel, which has a rather different surface morphology. This part of the channel is

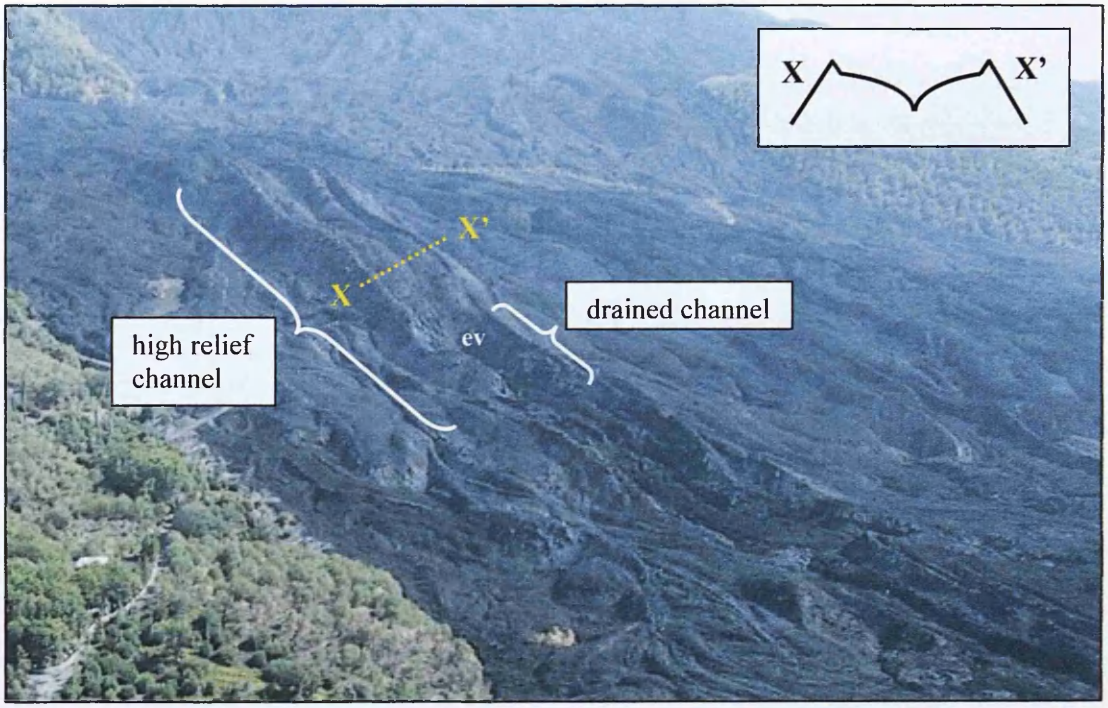

Figure 6.44. Post-eruption view up the main channel below M. Nero. The high relief part of the channel is indicated by the bracket. Along the majority of this length, the channel is still quite full, while it is almost completely drained at the downflow end. 'ev' indicates the location of the ephemeral bocca. The approximate cross-channel surface profile along the line X-X' is shown in the inset. Further back up the channel, the flow appears to be more drained, resulting in a profile with a deeper centre. Image: INGV.

wider and shallower than the downflow section, reaching ~50 m in width, with levées of 10 to 15 m in height, and the topographic slope is also shallower in this area. Instead of the v-shaped cross section, indicating large-scale drainage down the centre of the flow, the surface across the whole width of the channel has a 'hummocky' structure (figure 6.46). The hummocks are bulbous, hilly features, with an amplitude of up to five metres, and variable aerial extent. They appear to be aligned, forming bulbous ridges that extend across the width of the channel and are oblique to the flow direction (figure 6.47 b). The morphological development of this part of the channel can be followed through the syn-eruption images shown in figure 6.47. On August 1st, it is clear that this section of channel was slightly fuller than that immediately above,

Figure 6.45. In the upper part of the main channel visible in figure 6.44, looking downflow. The v-shaped profile across the channel due to drainage is evident, leaving features that resemble rubbly levées. No evidence of open channel flow is seen between these features, however, so they are not inferred to be levées, which are directly related to emplacement, but are thought to be drainage features. The distance between the top of the levée on the far side of the channel, and the lowest part of the drained section is ~15 m.

suggesting that lava was ponding as the topography shallows (figure 6.47 a). The levée, however, was still visible on the far side of the channel, showing that it was not completely full. The oblique angle from which the image was taken makes it difficult to be sure whether or not the hummocks had yet formed. Images on the 2nd were taken from a greater distance, and the presence of gas makes observations difficult. Figure 6.47 (b) shows the channel on August 6th, and is taken from the north west, looking across the flow field so that the main channel is in the foreground. In this image, the hummocks are clearly visible, and appear to have attained their final structure. An image from the 9th (figure 6.47 c), taken from a comparable angle to that on the 1st,

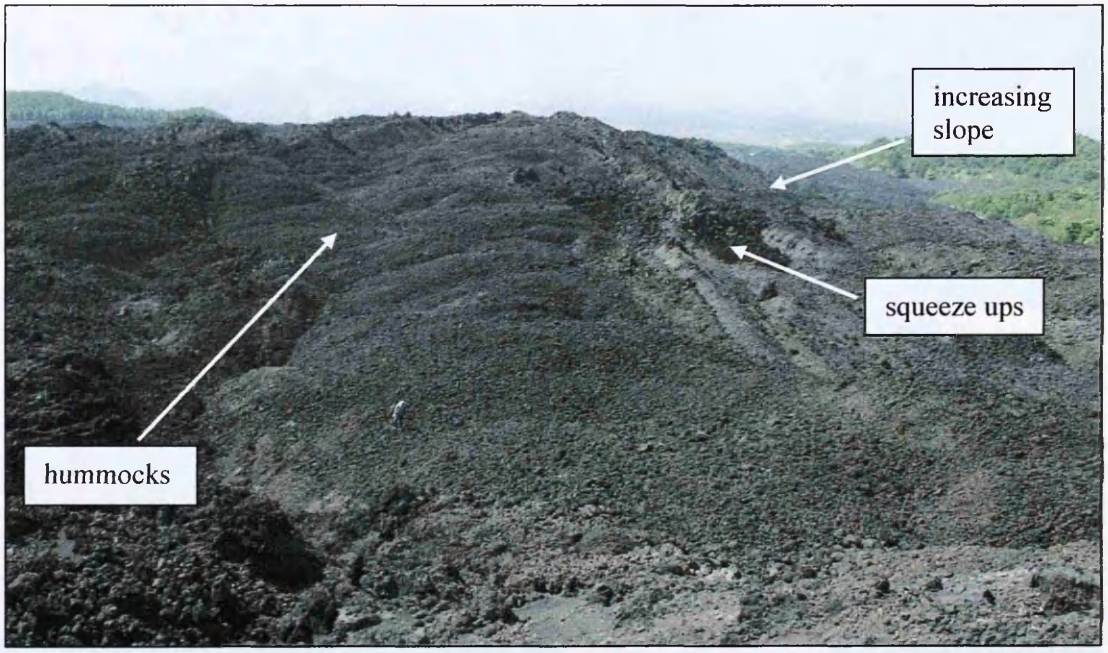

Figure 6.46. Looking downflow along the main channel just below M. Nero, showing the hummocky surface morphology. The topography is seen to become slightly steeper in the distance, and the part of the channel with the v-shaped cross section is just out of sight. Note figure for scale. Channel reaches ~50 m in width in the middle distance. Squeeze ups are discussed in the text. Image: H. Pinkerton.

shows that the hummocky part of the channel was fuller at the end of the eruption than it was on August 1st.

Between the 1st and the 9th, the net supply of material to the hummocky section was therefore greater than the net removal, which resulted in the channel becoming fuller. The hummocks may therefore result from processes related to the supply of material, to drainage, or to a combination of the two. The irregularity of the structures, and the fact that they are oriented at an oblique angle to the flow direction suggests that they are not large scale ogives, but they may initially have formed as such before being subsequently disrupted. Hummocks and hillocks are common on blocky basaltic flows, as discussed in the context of spines, resulting from the ramping of the flow interior up towards the surface. While extrusion of the flow interior has occurred in this part of the channel, as evidenced by the squeeze-ups along the channel-levée

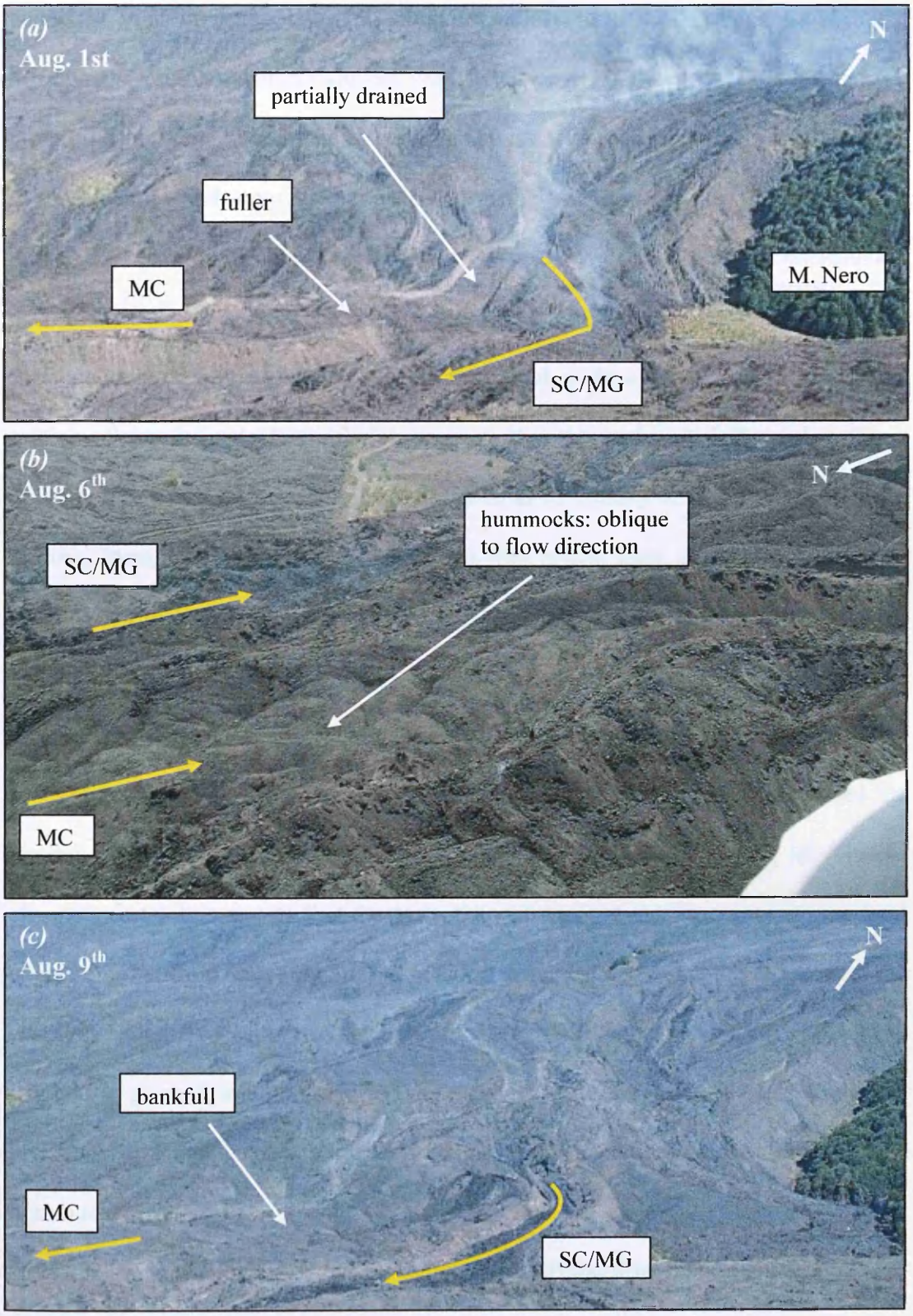

Figure 6.47. Development of the hummocky surface morphology. MC = main channel; SC/MG = branch leading to secondary and M. Grosso channels. (a) August 1st. Looking upflow. MC is fuller on the shallower topography. (b) August 6th. Looking across the flow to the SE. Hummocks have already developed. (c) August 9th. MC is fuller along more of its length than on August 1st. See text for details. Images: INGV.

boundary seen in figure 6.46, ramping commonly results in viscous squeeze-ups *through* the crust, and these are not seen in this part of the flow. For this reason, ramping is not thought to be the cause of the hummocky morphology.

One factor which may have contributed to the irregularity of the flow surface in this region is non-uniform drainage. Between August 1st and 9th, although net inflation occurred, as can be seen by comparison of figures 6.47 (a) and (c), it is known that supply continued to the lower part of the flow field, so lava was flowing through this section of the channel. The inflation suggests that the preferential thermal pathway downflow of this section could not drain material as quickly as it was supplied from upflow, though the shallow topography in this region may also have resulted in ponding of the lava. The v-section in the channel below (figure 6.45) is known to have developed before August 1st, perhaps indicating that the passage of material through this part of the channel was restricted. The collapse of the flow surface, which probably occurred due to waning flow, may have either resulted from or caused the ponding of material above. The development of the secondary and M. Grosso channels certainly suggests that the main channel was not able to cope with the total supply from upflow after July 30th, although it remained active for the duration of the eruption. Continued supply of lava to the shallower, stagnating section could have resulted in gradual inflation, and the maintenance of a hot interior, while continued low flux drainage caused disruption of the flow surface and the formation of hummocks.

While the initial formation of ogives in this part of the flow is speculative, drainage is inferred to have been an important factor contributing to the resultant surface morphology. From some angles (figures 6.46, 6.47 b), the hummocky ridges appear to be deeper towards the flow margins, which is in accordance with the expectation that

the centre of the flow remains hotter and more fluid, and so drains more easily than the cooler, slower moving margins. Hummocks are seen other parts of the flow, though on a smaller scale, in which they appear more similar in morphology to ogives, but are also clearly linked to drainage. Figure 6.48 shows an example of smaller-scale hummocks. In this case, the main channel was partially blocked by a stagnating flow front by August 6th (figure 6.48 a, b). Between August 6th and 9th, it is likely that flow through the remaining width of the active channel also became restricted, leading to inflation in the channel above. An ephemeral vent formed behind the stagnant flow front during this time (figure 6.48 c, d), which drained the channel behind, resulting in hummocky morphology. Again it can be seen that the channel is drained to a greater extent in the centre than at the margins, due to greater cooling in these marginal regions. The hummocks appear more regular, and are more nearly orthogonal to flow direction than those seen in figures 6.46 and 6.47, so a link to earlier ogives is more easily accepted in this case.

6.2.4.2 Drained flow fronts

In the previous examples, the morphology of drained channels behind ephemeral vents was considered, without reference to the structure that can develop immediately adjacent to the vent.

Once a flow unit has stopped moving, continued supply from upflow will result in pressurisation of the flow front. Assuming a uniform crustal thickness and tensile strength of the crust around the flow front (which is not always the case), Dragoni & Tallarico (1996) considered that the ephemeral vent is likely to open at the base of the flow front, where the pressure is slightly higher. However, they were considering the development of a vent in the most advanced front in a flow field; in contrast, most of

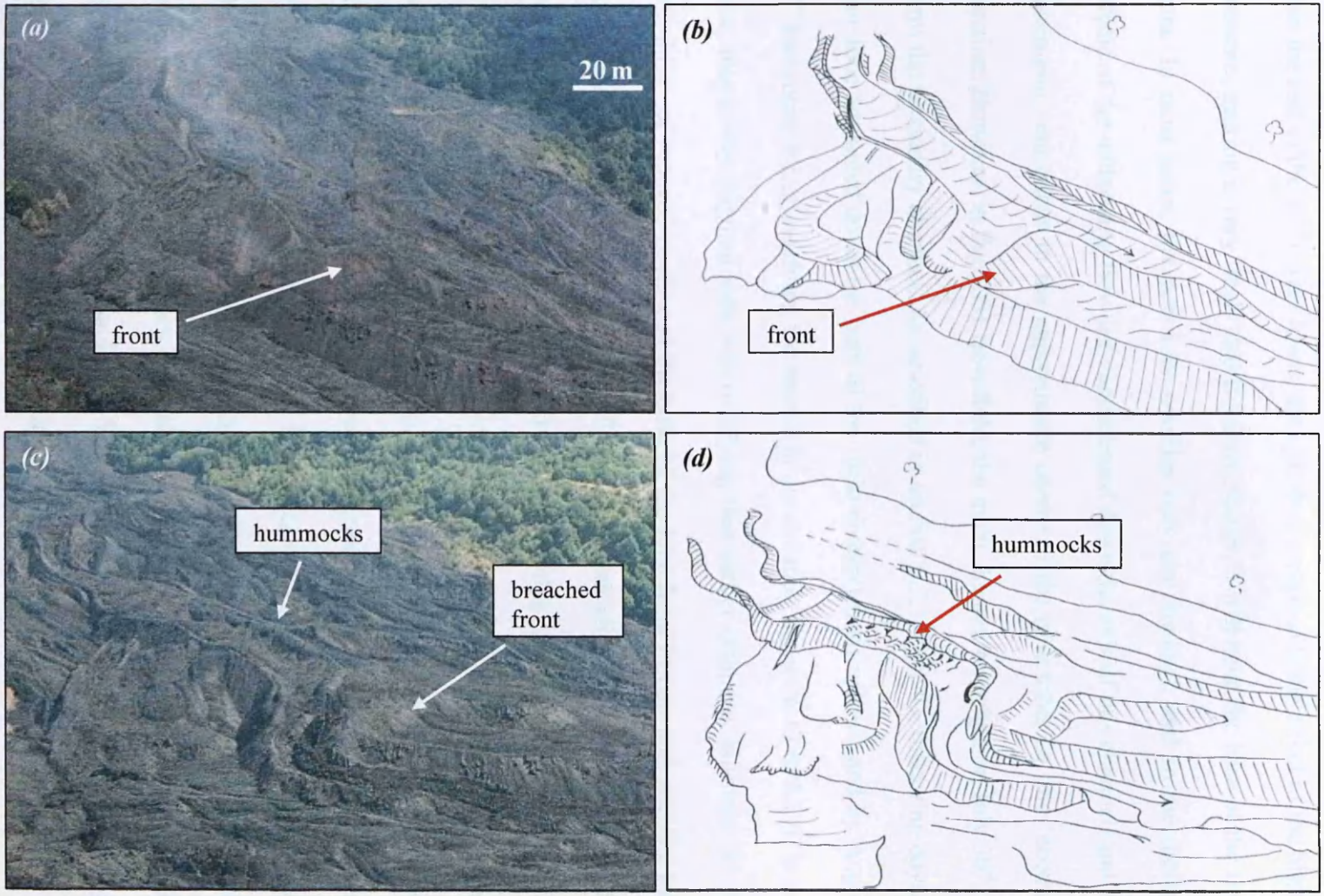

Figure 6.48. Formation of hummocky drainage features in the main channel adjacent to M. Nero.
(a & b) August 6th. Stagnating front has blocked part of the main channel, but lava continues to flow around the obstacle.
(c & d) After the eruption. Stagnant front has breached, causing drainage of the channel behind, and development of hummocky surface morphology (red arrows). The flow is deeper at the channel margins, indicating that only the channel centre has drained.
Images: INGV.

the ephemeral vents in the 2001 flow occurred in pre-existing channels. In this case, the newly stagnating lobe front is overlying an earlier flow, whose surface, though probably stagnant, will still be relatively hot. This will result in the crust around the base of the new lobe cooling more slowly, thus being thinner and therefore weaker than the rest of the front. This lower strength then compounds the effect of the higher pressure, making it very likely that if failure occurs, it will be at the base of the flow front. In most cases, the new lobe overlies only one channel, and so the thermal effects of the underlying flow are concentrated down the axis of this channel, and the ephemeral vent opens in the approximate centre of the new lobe, i.e. the 'normal' location. However, in the 2001 flow field, the main channel branched on July 30th, to form the secondary channel. As described in section 6.2.1, over the following days, a new lobe advanced down the path of the main channel from upflow, and by August 2nd had come to rest overlying the branch in the channel (figures 6.17 to 6.19). In this case, this newly stagnant lobe was overlying two earlier channels, allowing for the possibility of reduced cooling at the base of the lobe front in two regions. The lobe could have breached in either or both of these directions (figure 6.17 b). However, by this time, the main channel had cooled sufficiently that the surface was immobile, while open channel flow was occurring in the secondary channel. Although no thermal images were taken of this region on August 2nd, the branch is shown on August 1st in figure 6.7, where the surface temperature of the secondary channel (foreground) is seen to be higher. In figure 6.21, taken on August 3rd, the main channel cannot be seen, indicating that its surface temperature was considerably lower than that of the secondary channel, which is clearly visible. The lobe therefore breached over the path of the hotter, secondary channel, and the ephemeral vent supplied lava from upflow in this direction.

An interesting feature of this and at least one other ephemeral vent in the 2001 flow field, is that the vent did not remain in the same location throughout its life, but migrated back up through the lobe that it was draining, as was described in section 6.2.1. As can be seen in the image taken on August 2nd, the vent is established, and is draining the flow from the base (figure 6.49 a). An arcuate collapse region has already formed behind the vent, due to avalanching of the lobe material which is destabilised by the presence of the vent, although the appearance of the lobe behind suggests that it is well supplied with material. Over the remaining seven days of the eruption, this lobe, whilst continuing to be supplied, was progressively drained by the ephemeral vent, which migrated back up the trace of what was the original secondary channel, creating a large (~10 m high) amphitheatre-shaped drained section (figure 6.49 b). The scale of this can be seen more clearly in figure 6.49 (c). Field observations showed that behind the fully drained amphitheatre region, the surface of the flow was uneven, and possibly hummocky, suggesting that partial drainage had occurred.

A similar process was observed in the main channel between Lower Silvestri and M. Nero, just above 1700 m a.s.l. This wide channel was observed to develop from three initial lobes that were emplaced over the pre-existing main channel between the 2nd and 4th of August, as previously described (figure 6.3 c & 6.14). On August 6th, images suggest that the flow surface is stagnant in this region, while material continues to flow beneath, emerging from an ephemeral vent at the lobe front. This is evidenced by the fact that gas is present at the lobe front, and from the channel below, but none is seen above the surface of the lobe itself (figure 6.50 a). The surface immediately behind the vent can be seen to be sagging slightly in the centre, while further back the channel is full, with a fairly even surface. This suggests that the front of the lobe is beginning to drain. In post eruption images (figure 6.50 b), the vent can

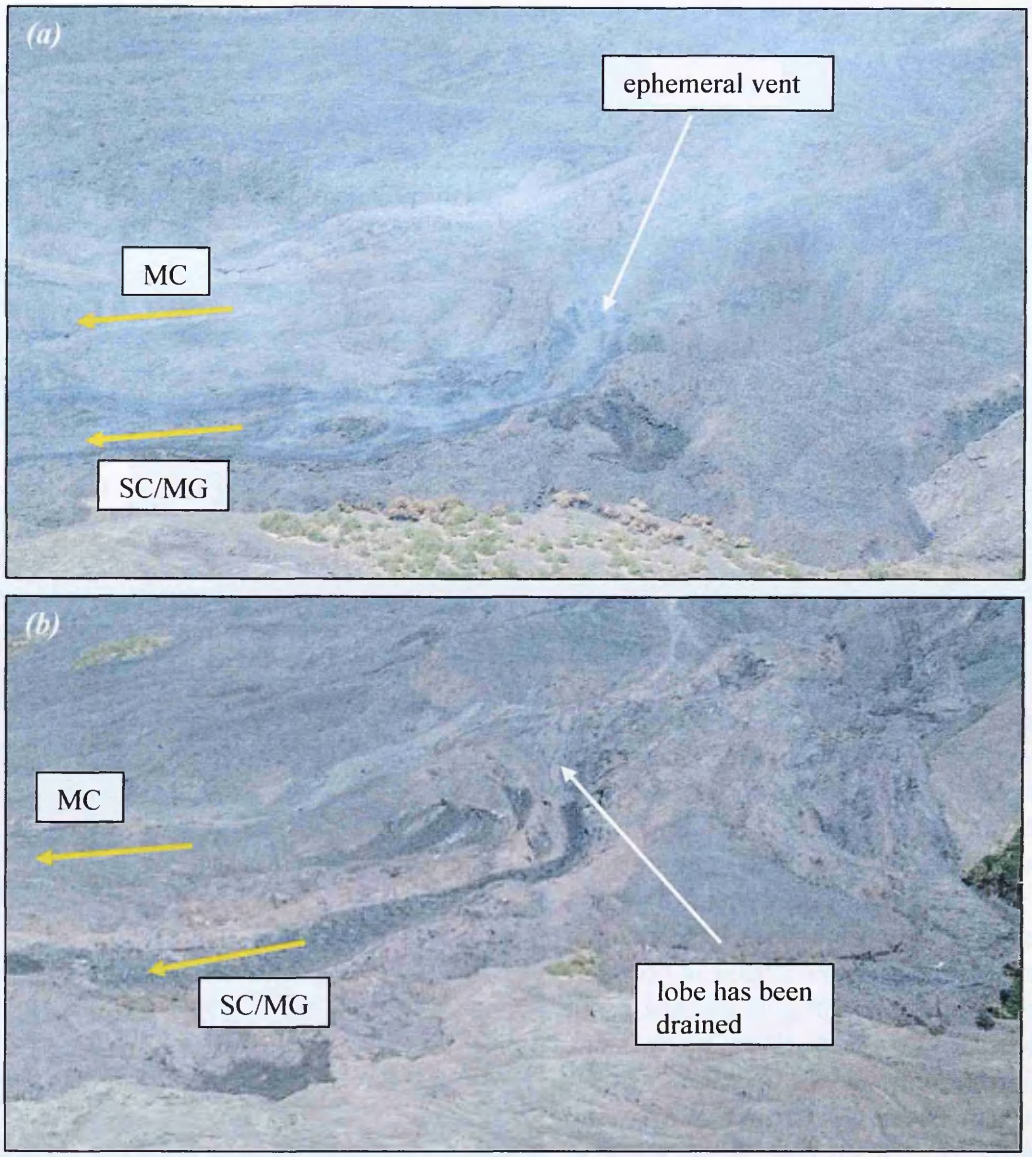

Figure 6.49. Development of the ephemeral vent feeding the secondary and M. Grosso channels (SC/MG). (a) August 2nd. The superimposed lobe that advanced down the main channel (MC) stagnated just after reaching the branch in the channel. An ephemeral vent developed above the path of the secondary channel, with an arcuate collapse zone behind. (b) Over the next seven days, the ephemeral vent migrated back into the overlying lobe, progressively draining both the lobe and the channel behind it. (c) The resultant amphitheatre behind the final vent location is ~10 m high.
Images (a) & (b): INGV.

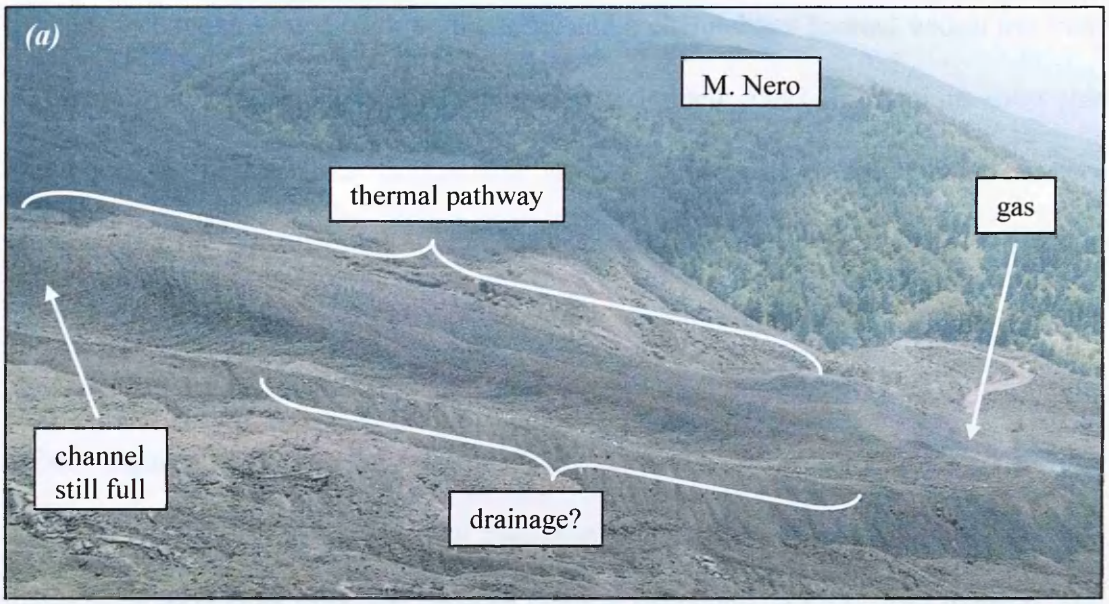

Figure 6.50. Wide channel between Lower Silvestri and M. Nero.
(a) August 6th. Channel surface has stagnated, though flow continues beneath in a preferential thermal pathway. The pathway ends at the front of the wide lobe, at which open channel flow resumes. The presence of gas indicates the location of the bocca. Behind the bocca, the surface appears to be sagging slightly, suggesting that some drainage is taking place, while further back the channel remains almost full. Ogives, observed to form between the 2nd and the 4th, are visible over the majority of the flow surface.
(b) Post-eruption morphology. The bocca that was originally at the flow front has migrated ~100 m back up the wide channel, and a narrow channel can be seen extending from the bocca to the front of the wide channel. The right hand side of the channel is drained, while the left hand side remains almost full.
Images: INGV.

be seen to have migrated back up the lobe, and a channel has formed within the front ~100 m of the lobe, which is almost completely drained. Field observations show that the boundary between the drained and undrained sections of the channel is very distinct, but the amphitheatre behind the ephemeral bocca is more shallow than that seen in figure 6.49 (c). In figure 6.50 (b) it can be seen that only the right hand side of the lobe has drained, which probably reflects its initial emplacement as three distinct lobes (figure 6.14) that subsequently coalesced. The final structure of the lobe suggests that its central spine may represent the margins of two of the coalescing lobes. The right hand lobe was situated directly above the original main channel, and so flow was favoured along this direction, due to the thermal effect of the underlying original flow, while the left hand side stagnated.

The ephemeral vent at ~1460 m a.s.l. (figure 6.44) is also framed by a steep amphitheatre. This vent was not observed forming, but its location is known not to have changed during August. Field observations, however, suggest that a similar upflow migration of the vent may have occurred before this date. As was seen in figure 6.44, the high levées in this part of the channel terminate approximately 50 m below the vent, giving way to lower relief levées. It is probable that when it was emplaced, the stagnant flow lobe extended to the end of the high relief channel, and that the flow front was subsequently drained, resulting in upflow migration of the ephemeral vent. Evidence for this can be seen in figure 6.51, which was taken within the channel, looking upflow at the amphitheatre. At either side of the channel, the massive flow interior is exposed, indicating that some collapse of the flow front has occurred. In this example, the ephemeral vent was active for at least nine days after the final structure was attained, suggesting that cooling of the flow behind eventually prevents further migration of the vent. In the previous examples, the vents are inferred

to have been migrating until the end of the eruption, suggesting that at that time, the lobes being drained had not cooled to this extent.

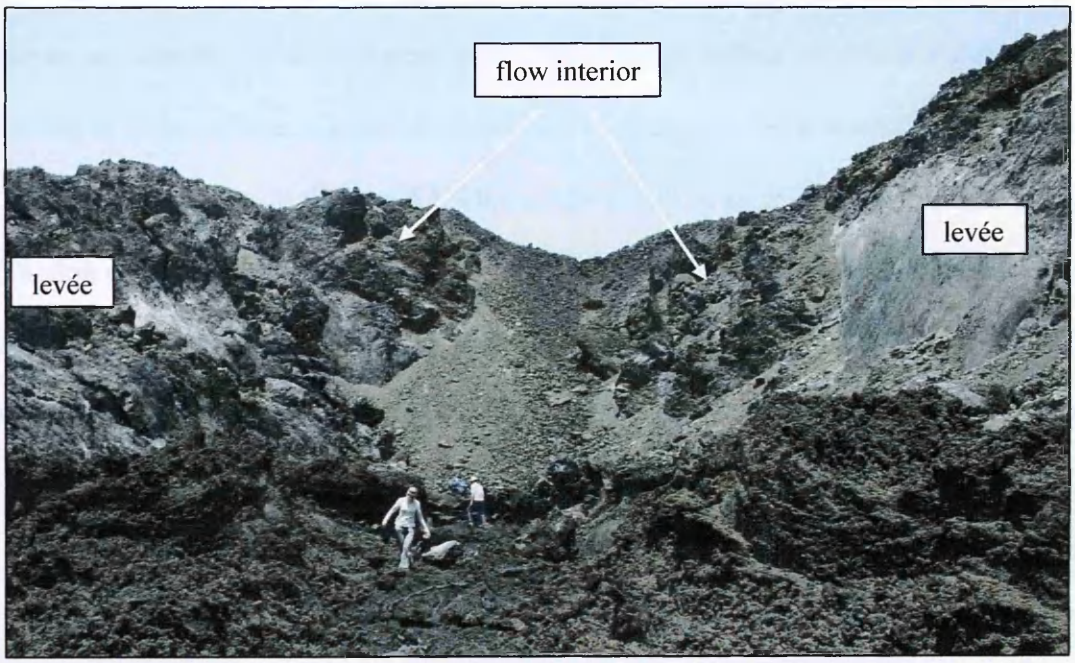

Figure 6.51. The amphitheatre that developed behind the ephemeral bocca shown in figure 6.44. In the centre, the amphitheatre is covered by clinkery scree, while to the margins the massive flow interior is exposed. This indicates that the margins of the channel were not drained, as inferred from figure 6.45, and that the ephemeral bocca has migrated back up the channel from its original location, which may have been at the end of the high relief channel (figure 6.44). Image: H. Pinkerton.

6.3 The influence of effusion rate on flow morphology

As noted in chapter one, effusion rate is one of many critical input parameters in numerical flow modelling, and so accurately estimating the instantaneous effusion rate during an eruption is an important task. The general pattern of effusion during the release of magma from a pressurised storage chamber has been modelled by Wadge (1981), and is shown in figure 6.52. This model involves an early period of increasing effusion rate, followed by a longer period in which flux dies off exponentially. While this general pattern is often observed, as during the 2001 eruption, it is not a precise representation of behaviour. It has long been observed that small-scale changes in

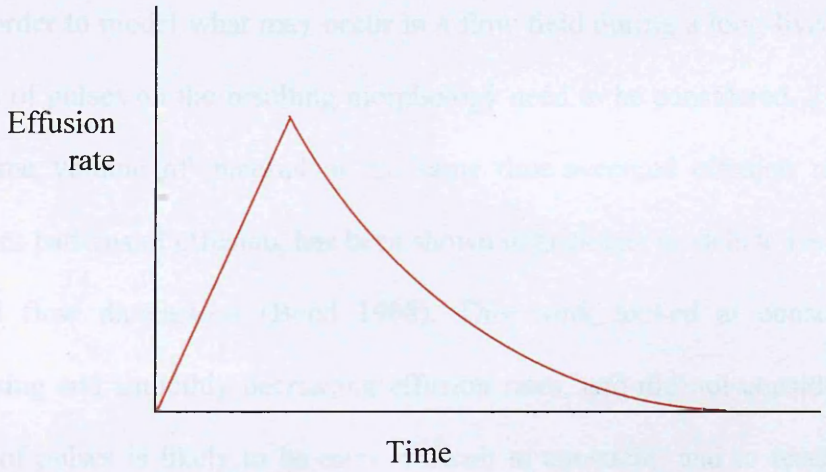

Figure 6.52. A generalised effusion rate pattern for basaltic eruptions from pressurised sources (Wadge 1981). A more realistic pattern will have a range of higher frequency changes superimposed on this general trend.

effusion occur on timescales of minutes to hours, which could result in an effusion rate pattern that has the same general trend as in figure 6.52, but which has smaller-scale oscillations superimposed. Such changes have been both inferred and observed during eruptions at many volcanoes, including Etna (e.g. Kauahikaua et al. 2003; Lautze et al. 2004; Bailey et al. 2006; Orr 2008; personal observations). Images showing the propagation of a lava pulse down a channel during the 2006 eruption of

Etna are shown in figure 6.53, and it can be seen that the pulse produces noticeable changes in the local flow morphology, including overflows from the established channel. Bailey et al. (2006) found that the activity of a flow during one of the 2001 summit eruptions of Etna progressed in a cyclic manner, with pulses occurring on scales of tens of minutes to hours, and producing predictable results in the channel. During periods of lower flux, surface velocities decreased, and the viscosity and yield strength of the lava were inferred to increase. This led to blockages in the channel, and the backing up of lava behind which often overflowed the levées. Periods of higher flux overwhelmed the channel, producing overflows and tending to clear blockages within the channel, thus resulting in increased channel efficiency (Bailey et al. 2006).

In order to model what may occur in a flow field during a long-lived eruption, the effects of pulses on the resulting morphology need to be considered. The eruption of the same volume of material at the same time-averaged effusion rates, but with different patterns of effusion, has been shown in analogue models to result in different overall flow dimensions (Bond 1988). This work looked at constant, smoothly increasing and smoothly decreasing effusion rates, and did not consider pulses. The effect of pulses is likely to be more difficult to constrain, and to result in increased complexity of the flow, as observed in the field by Bailey et al. (2006). One important consequence of effusion rate stability noted by Calvari & Pinkerton (1998) is the efficiency with which tubes systems can develop. The inflating `a`ā model of tube formation, in which the breaching of subsequent `a`ā lobes provides an internal pathway through which new material can travel, relies upon the maintenance of a steady effusion rate for some time after the inflated lobes have breached, so that the roofs have time to cool and solidify. A drop in effusion rate shortly after the initiation of a pathway is likely to result in the collapse of the roof.

Figure 6.53. Pulse of lava travelling down a channel during the 2006 eruption of Etna. In each image the front of the pulse is marker with an arrow. The channel is approximately 2 m wide. The time interval between the first two images is 10 seconds, and that between the second and third images is 30 seconds.

6.3.1 Estimating effusion rates

Monitoring the effusion rate during an eruption may allow more informed estimates to be made about how flux changes affect the development of the flow field. While the estimation of a time averaged effusion rate is relatively straightforward, involving measuring the difference between pre- and post-eruption DEMs and dividing the result by the emplacement time, the estimation of instantaneous syn-eruption effusion rates is not trivial. The estimation of syn-eruption rates for LFS1 was attempted by Behncke & Neri (2003) and Coltelli et al. (2007) (figure 6.54), whose results, while showing an overall similarity in pattern, varied considerably in absolute values. This is surprising, as the two methods employed were broadly similar.

Behncke & Neri (2003) mapped the daily active area of the lower flow field (figure 6.55), and multiplied this by the mean flow thickness estimated to have been emplaced during this time. They admit that thickness estimations are difficult due to the complexity of the flow, and attempted to maximise the accuracy by estimating the thickness of each active lobe along its whole length each day. It is interesting to note that they report an increase in the effusion rate noted at the vent on August 1st, but that this was not picked up in their results (figure 6.54, arrow). This suggests that the mapping method, which relies on daily measurements, is not sensitive to small changes in effusion rate, which nonetheless may have an influence on the flow field morphology.

The method of Coltelli et al. (2007) was similar, and their daily flow maps are also shown in figure 6.55. Comparing the flow maps of Behncke & Neri (2003) with those of Coltelli et al. (2007), it can be seen that there are some discrepancies. The work carried out here also suggests that, although these are probably low resolution

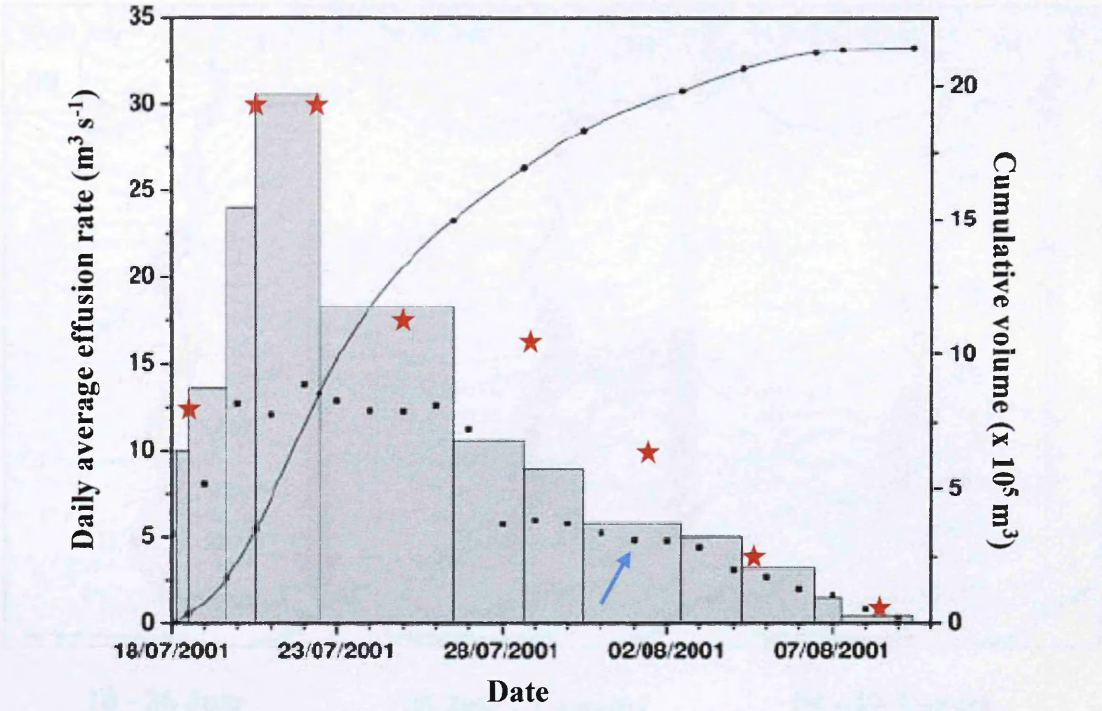

Figure 6.54. Syn-eruption effusion rate estimates for the 2001 lower flow field. Estimates are based on the planimetric method, with the results of Coltelli et al. (2007) shown by the grey bars, and those of Behncke & Neri (2003) by the black points. Arrow points to August 1st, where an increase in effusion rate is noted by Behncke & Neri (2003), but not picked up in their measurements. Estimates of instantaneous flux based on measurements at the vent by INGV are shown by the red stars. The curve gives the cumulative erupted volume based on the work of Coltelli et al. (2007). From Coltelli et al. (2007); figure 9.

reproductions of the maps from which areas were calculated, there are errors in both sets. This is illustrated by examining the active flow fronts at the beginning of August, which are mapped as stopping around 1 km behind the main flow front on the 2nd. The images used in this work suggest that they are, however, around 500 m more advanced than this (figure 6.3), and also that the breakout to the east of the main channel in this region occurred on August 3rd, while both published sets of maps include this area as if it had been emplaced before July 26th (indicated in the earliest figure of Coltelli et al. 2007).

Coltelli et al. (2007) estimated syn-eruption thicknesses using a laser range finder with an accuracy of 1 m, but their measurements were mainly confined to flow fronts.

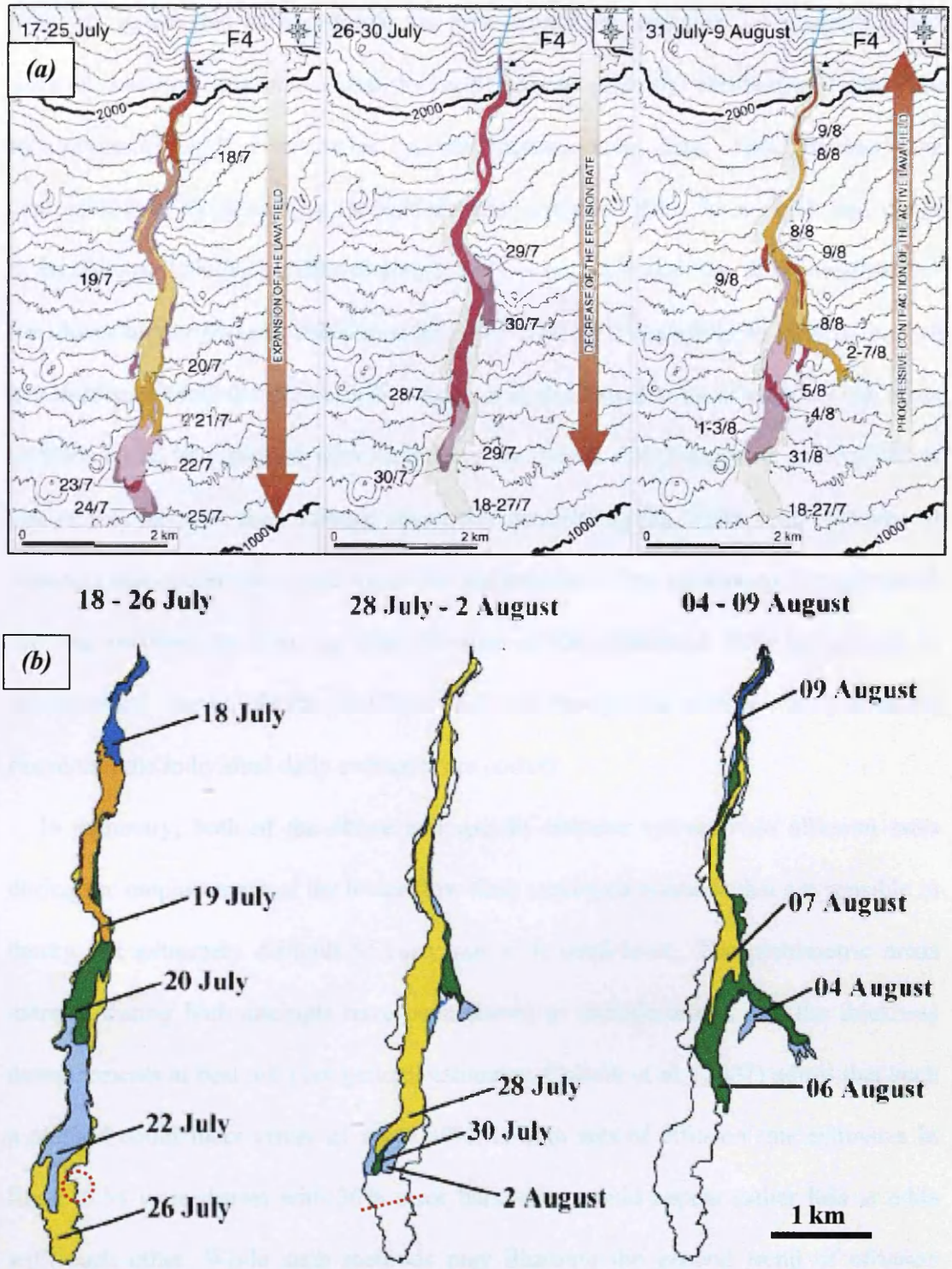

Figure 6.55. Daily flow field maps from (a) Behncke & Neri (2003), and (b) Coltelli et al. (2007). While these are likely to be low resolution versions of the maps actually used, discrepancies can be seen between the two sets of data. Furthermore, errors have been noted following the work presented in this chapter. As circled in the earliest of the lower maps, a part of the flow not emplaced until August 3rd is included in the earliest flow field outline. Active flow fronts on the 2nd were observed several hundred metres further towards the front than shown in the central lower map, indicated by the dashed line. From Behncke & Neri (2003); figure 6, and Coltelli et al. (2007) figure 6.

They recognise this as a problem, as flow fronts and margins are commonly the thickest parts of the flow, and try and address this by combining their field measurements with examination of the post-eruption data. This involved the examination of cross sections through the post-eruption DEM, from which they claim to be able to distinguish different stages of flow emplacement due to the tendency of the flows to narrow and thicken with time. While it is possible to discern such a general trend from the post-eruption data, it is questionable as to whether the cross sections could be dissected with such accuracy to pick out changes on a timescale of one or two days, as they attempt, especially considering the widespread drainage of channels that occurred towards the end of the eruption. They endeavour to cross check the two methods by ensuring that the sum of the calculated daily increments in thickness increase equals the total flow thickness, though this method clearly does not prove that the individual daily estimates are correct.

In summary, both of the above attempts to estimate syn-eruption effusion rates during the emplacement of the lower flow field employed methods that are sensible in theory but extremely difficult to carry out with confidence. The planimetric areas mapped during both attempts have been shown to include errors, and the thickness measurements at best are very general estimates. Coltelli et al. (2007) admit that such a method could incur errors of up to 30%. If both sets of effusion rate estimates in figure 6.54 were drawn with 30% error bars, they would appear rather less at odds with each other. While such methods may illustrate the general trend of effusion during the eruption, they produce estimates that are below the desired accuracy for input parameters in numerical models.

It is suggested here that, where possible, the most reliable method of estimating effusion rates during an eruption is by monitoring changes at the vent. This is

especially true during the emplacement of compound flow fields in which several channels are active at any one time, as small changes in the vent distributed between several channels are likely to produce changes that are not resolvable within the margins of error of the planimetric method. Monitoring the vent allows changes in effusion rate to be observed as soon as they occur, and so are more useful in providing information for real time modelling. Coltelli et al. (2007) carried out seven estimates of effusion rate close to the vent during the eruption, by measuring the width of the active channel (w) and the maximum flow surface velocity (v), and estimating the channel depth (d). Effusion rate can be estimated by $\frac{2}{3} w d v$. While these estimates of instantaneous effusion rate do generally agree with estimates using the planimetric method, the two estimates for August 1st differ substantially. As noted by Behncke & Neri (2003), though not by Coltelli et al. (2007), in the eruption chronologies, the change in activity from magmatic to explosive at LFS2 on August 1st resulted in a small increase in the effusion rate at LFS1. This is picked up in neither set of results by the planimetric method, but is suggested by the instantaneous method.

A more intensive monitoring of changes in vent behaviour was carried out during the eruption by Pinkerton, who spent many hours observing changes in the proximal channel between July 26th and August 4th. Five hours of video footage were taken during this time, as well as many thermal images, and several estimates of the instantaneous flux were made. During this period, the general trend was one of waning flux, as universally reported for the end of the eruption, but two notable exceptions occur. These are two short-lived increases in flux, noted during the afternoon of July 31st and on the evening of August 2nd. Observations during the 1st did not detect a pulse, though this is not surprising if it was short-lived, as monitoring was not carried out for the whole of each day. The problem with both instantaneous

and planimetric estimates is that widely spaced measurements are likely to miss short-lived pulses.

Previous observations of varying flux have only observed changes close to the vent, and have not attempted to correlate these with what is happening in the more distal parts of the flow field. This is of course not a trivial matter, requiring widespread observation of the flow field over considerable periods of time. This could not be done with the available data for the emplacement of the lower flow field, but observations of structures in the 2001 flow field suggest that the recorded pulses, despite their short-lived nature, may have had a significant influence on the flow field. For example, the M. Grosso branch of the flow was observed for the first time on the morning of August 2nd. This may have been linked with the observed pulse on August 1st. The secondary channel was observed on the 1st to be stagnating in many parts, and a slight increase in the flux supplied could have resulted in a breakout that then formed the new branch. This pulse may also have been associated with the widening of the channel below L. Silvestri, which was observed by H. Pinkerton between the 1st and the 2nd.

The observations of the proximal channel makes it clear that small, short-lived changes in effusion rate occurred during the emplacement of the lower flow field, though, due to the relatively sporadic coverage, it is uncertain whether the changes were cyclic, as observed by Bailey et al. (2006). These observations, together with the demonstrated problems with the planimetric method of estimating effusion rate, suggest that close monitoring of changes at the vent should be carried out during an eruption.

6.3.2 Estimating viscosities

Monitoring of the flow close to the vent can also allow viscosity estimates to be made, using Jeffrey's equation (Jeffrey 1925):

$$u_{max} = \rho g h^2 \sin\alpha / n\eta \qquad (6.1)$$

where u_{max} is the centreline velocity of the flow surface, ρ is the density, g the gravitational acceleration, h the flow depth, α the slope, η the fluid viscosity and n is a constant whose value is taken as 3. Estimates of the local topographic slope, the maximum surface velocity and the flow depth are needed, of which depth is the most difficult to estimate. The viscosity was estimated from video footage recorded on August 4th, which shows the flow adjacent to Lower Silvestri. The DEM subtraction of Coltelli et al. (2007) suggests that the final depth of this part of the flow was less than 8 m, and the video data suggest that the depth on the August 4th was very similar to the post eruption depth. The calculation is therefore performed using depths of 2 and 8 m, to give a range of viscosity estimates. The local slope was measured from a topographic map as ~5.7° and a density of 2700 kg m^{-3} was used. Estimating the surface velocity from the video gives a value of 0.1 m s^{-1}. Using the two values of depth, the estimated viscosity falls in the range 3.5×10^4 and 5.6×10^5 Pa s. While these estimates are fairly crude, they are very similar to the viscosity estimate obtained from the folding analysis in chapter five, which gave values of between 3.9×10^4 and 9.4×10^5 Pa s. The fact that similar values were obtained using two different methods suggests that these are plausible estimates of the viscosity.

6.4 Discussion

This chapter has presented a comprehensive set of observations of the surface and structural morphology of the 2001 flow field, and of the processes that can give rise to such morphology. These observations have implications for our understanding of the emplacement of compound flow fields, and for the assessment of potential hazards. Although this eruption was short-lived, lasting only 23 days, the action of such processes as were observed during the emplacement of the lower flow field could have more serious consequences in longer-lived flow fields. The main conclusions of this work, regarding the importance of squeeze ups, tube systems and effusion rates, are summarised below.

The squeeze up features in the 2001 flow field demonstrated morphologies and textures that differ greatly from typical `a`ā surface textures. While 'normal' `a`ā is clinkery and fragmented, and the fragments have a very pronounced surface roughness on a scale of millimetres to centimetres, the late-stage squeeze up material that was extruded in the 2001 flow to form 'rubbly' flows (figure 6.27) was even more extreme in its surface roughness. Toothpaste lava, as described in the 1991-1993 Etna flows by Calvari & Pinkerton (1998), is inferred to be a transitional form between pāhoehoe and `a`ā, extruded at a high viscosity and significant crystallinity, but not subjected to a high enough strain rate to produce `a`ā (Rowland & Walker 1987). The material that formed the rubbly flows in the 2001 flow may represent a part of the rheological spectrum between `a`ā and blocky lavas. While `a`ā has sufficient strength to deform in a brittle manner under certain conditions, it is still sufficiently fluid to 'tear' rather than fracture. This results in the rough, spinose surface texture. Blocky lava, by contrast, has a very high strength and flows by autobrecciation, fracturing cleanly to produce more smoothly surfaced fragments. The fact that the rubbly lava had a higher

strength than `a`ā is evidenced by figure 6.27 (a), in which it can be seen that the flow has fragmented over most of its depth very shortly after extrusion. However, the roughness of the surface texture indicates that it is being torn, rather than fracturing cleanly, so it is also still akin to `a`ā. The strain rate during the extrusion of the rubbly flows was high enough to cause large-scale fragmentation, while that during the formation of tumuli was not, The lower strain rate may have been accompanied by a yet higher strength, as the tumulus material was the very last to be extruded. The surface roughness of the tumulus material was less pronounced than that of the rubbly flows, perhaps indicating that it rheology was approaching that of blocky lavas.

The squeeze ups of toothpaste lava described in the 1991-1993 Etna flow field by Calvari & Pinkerton (1998) were small in volume, while the rubbly squeeze ups in the 2001 flow could produce flows that were up to ~100 m in length. While insignificant in comparison to the volume of the whole flow, the fact that such squeeze ups are common throughout the flow suggests that they should not be ignored in a comprehensive analysis of the flow dynamics. The wide range of squeeze up morphologies has been inferred to mean that a number of different conditions, such as rheology, strain rate, vent geometry and the volume of material extruded played important roles in controlling the final form of the extrusion (figure 6.33). The effects of rheology are perhaps the most interesting. To recap, if material extruded from an ephemeral bocca is relatively fluid, it will form smooth pāhoehoe flows. With increasing viscosity and/or yield strength, it will develop first `a`ā then rubbly flows, then, as it becomes incapable of flowing away from the vent, may form a mound over the point of extrusion. Under the most extreme rheological conditions, material may be extruded in the manner of crease structures, having sufficient strength to preserve evidence of the bocca geometry, producing what have been termed here exogenous

tumuli (figures 6.38 to 6.31). The formation of these structures is also probably strongly dependent on the conditions in the flow interior, as the extrusion of material in such a rheological state requires significant overpressures.

Exogenous tumuli appear very different to the endogenous tumulus structures described in chapter five, and this morphological difference reflects both the rheological contrast and the relative importance of the flow interior and the surface crust at the time of formation. Endogenous tumuli form due to flow inflation, which often occurs in areas of shallowing local slope, where material cannot be drained as rapidly as it is supplied. This inflation causes deformation of the overlying crust, resulting in updoming and the eventual formation of inflation clefts as the crust fails (Walker 1991). The fluid interior may then drain through the surface fractures. In this case, the conditions in the flow interior are the primary controls on the formation and location of the tumulus. Exogenous tumuli, though still resulting from overpressure in the flow interior, are observed to form in areas where the local slope is increasing. Due to the fact that they are late-stage features, it is likely that cooling of the surface carapace has resulted in its having a considerable strength. In this case, the overpressure in the interior may not be able to cause deformation and updoming of the carapace in areas where it is coherent, and the location of a tumulus will be controlled by the presence of pre-existing weaknesses in the surface crust. As seen in the analogue experiments, and in the field (figure 5.3), the surface carapace may be disrupted by the action of tensile stresses, which develop primarily in regions of increasing slope. The formation of surface fractures earlier in the history of a flow may therefore provide the necessary weaknesses that can be exploited by these late stage processes. Doming of the crust in the 2001 flow was observed in two tumuli, one solely endogenous and one also demonstrating exogenous morphology (figure

6.31), suggesting that the thick crust can be deformed, but tumulus-forming activity in these areas may still have been influenced by pre-existing weakness in the crust. The contrast between endogenous and exogenous tumuli represents a transition from interior-controlled to crust-controlled dynamics as the eruption progresses and the flow cools.

The rheological state of the squeeze up material also has implications for numerical modelling and hazard assessment. As mentioned in chapter one, it is probable that the increase in crystallinity eventually results in lava ceasing to flow (e.g. Marsh 1981; Lejeune & Richet 1995), but the precise value of this critical crystallinity threshold is not yet known. This parameter is of vital importance when modelling lava flows numerically, as it is necessary to be able to determine with confidence when a flow will no longer be capable of advancing. It seems likely that the material forming the exogenous tumuli has a crystallinity that is close to this critical threshold. The fact that flow conditions can force material in this state out of the flow interior is important, as it indicates that even several days after the flow has stopped advancing, the material in the interior is clearly still able to 'flow'. In chapter five, it was noted that the San Juan Parangaricutiro flow at Parícutin was reactivated one month after it ceased to advance. Krauskopf (1948) made a detailed survey of this flow after it had truly come to rest, noting that the entire lower half of the 10 km long flow was made up of the 'curved slabs' that seem to be analogous to the tumuli-forming material of the 2001 flow. The volume of such material in the San Juan flow is clearly far greater than that observed in the 2001 Etna flow. As noted in chapter five, the reactivation of the flow resulted in the extrusion of these curved slabs of plastic lava, before fresh material was extruded at the flow front, covering a large area of terrain very rapidly. The initial stagnation of the San Juan flow may have resulted from a pause in activity at the vent, the

temporary diversion of lava in a different direction, or inflation of higher parts of the flow, but when supply continued it was able to cause extrusion at the flow front by the transmission of fluid pressure via the mechanism shown in figure 6.42. This has significant implications for hazard assessment in lava flows, as forced drainage of a stagnant flow results in the formation of a tube system, whereby fresh material can be transported, well-insulated, to the flow front. While the formation of tube systems has been closely observed, and the hazards posed by ephemeral vents are well understood, the development of ephemeral vents in stagnant flow fronts on Etna usually occurs on a time scale of hours to a few days (Pinkerton & Sparks 1976). There is no precedent for reactivation of a lobe following a month of inactivity, as observed on Parícutin, but, similarly, there is no reason to assume that it could not happen on Etna.

Krauskopf (1948) observed that the squeeze ups in the San Juan flow were of 'normal' temperature but 'abnormally' low gas content. While no measurements were taken, and so these inferences are speculative, Krauskopf's observations suggest that the extremely high viscosity could have arisen from the growth of quench crystals as the result of degassing-induced undercooling (Sparks & Pinkerton 1978), without the need for significant surface cooling. It is possible that the examination of squeeze up material may provide information about degassing processes, as suggested with reference to the variable vesicularities of squeeze ups noted in the 2001 flow. The action of degassing through the course of an eruption is currently not well enough constrained to be incorporated into numerical flow models, so the study of squeeze ups may aid progress in this area, as well as in the consideration of critical crystallinities.

One final observation of interest regarding squeeze ups was their formation as a result of the 'toothpaste' mechanism (figure 6.42), whereby the superposition of lobes

can result in the extrusion of the material stored in the underlying lobe. This process is also of potential importance in considering the possibility of ephemeral vent formation, and the drainage of lobes to form new flows.

While the presence of mature, self-supporting tubes cannot be confirmed in the 2001 flow, there is clear evidence of preferential thermal pathways. These are subsurface routes though which lava is transported, as in tubes, but which lack mechanically and structurally stable roofs. This is evidenced by the widespread occurrence of drainage surface morphologies. Preferential thermal pathways are very important in the development of flow fields, as they represent the early stages of tube formation, and they were observed forming in new lobes that were emplaced over earlier channels during the latter part of the 2001 eruption. The formation of ephemeral vents is closely linked to that of thermal pathways. As noted previously, the formation of ephemeral vents depends, among other factors, on the local topography, in a similar manner to the formation of endogenous tumuli (e.g. Polacci & Papale 1999). In the 2001 flow, the importance of underlying earlier flows was also noted in the formation of new boccas. This was illustrated in the M. Nero region, where a new lobe was emplaced over two earlier channels, and an ephemeral vent formed in the new lobe front directly overlying the hotter of the two channels. These two factors, shallowing slope, and the possible influence of earlier flows, could be used as preliminary, qualitative predictive tools when attempting to forecast where ephemeral vents may form in complex flow fields.

The importance of effusion rate variations in influencing the development of compound morphology has been documented (e.g. Polacci & Papale 1999), and has been considered here in the context of the 2001 flow field. It was seen that even small and transient changes in effusion rate can have major effects on the morphology of a

flow field. A possible example of this, though unconfirmed, was the development of the M. Grosso branch, which formed shortly (< 1 day) after a small increase in effusion rate was noted at the vent. As discussed, flow in the main and secondary channels is this region was sluggish, probably due to shallowing of the local topography, and a small increase in the flux of material supplied to the secondary channel, which was partially blocked by a lobe front (figure 6.20), may have raised the level in this channel, increasing stress on the levées sufficiently to cause failure, and resulting in the new branch. Subsequent material was drained mostly through the new M. Grosso branch, as it presented the path of least resistance. Similar processes probably led to the development of the secondary channel, though this was not observed, and while the secondary channel propagated parallel to the main channel, the M. Grosso branch advanced in a direction around 40° removed from that of the earlier flow field. These observations suggest that in addition to constant monitoring of the effusion rate at the vent, the effects of any changes should be tracked throughout the flow field, though this task becomes more and more difficult as the size and complexity of a flow field increases.

The observations presented indicate that syn-eruption monitoring of flow field emplacement can produce a wealth of information about many aspects of flow dynamics. As noted in chapter one, while numerical modelling of lava flows is desirable as a tool for forecasting the manner in which emplacement will progress, difficulties arise due to uncertainties in many of the input parameters, including effusion rate and the rheological properties of the lava, and due to the development of structural complexities. This work has presented evidence of lava flowing in a highly evolved rheological state, which could be examined further to provide information

about the critical crystallinity and possibly about degassing. The investigation of increasing structural complexity has provided new insights into the controls on ephemeral vent location, which had previously been linked primarily to the importance of conditions in the flow interior. Here it has been seen that in the context of late-stage processes, the role that the crust plays becomes increasingly important, and the formation of vents is controlled by pre-existing crustal weaknesses. It is concluded that syn-eruption monitoring is a vital tool in our quest to understand the complexities of compound flow field emplacement, and that the investigation of small-scale features and processes can be as important to this understanding as the consideration of the larger-scale structural development.

7. Conclusions

7.1 Summary of main findings

The aim of this research was to investigate complexity in lava flows. The study included both small-scale surface features that form in individual flow units, and larger-scale structures that are the result of interactions between flow units in compound flow fields. Laboratory analogue models were used to study the emplacement of single flow lobes, and explored the effects of crustal thickness and topographic slope on surface morphology. These experiments also allowed the interactions between a brittle crust and a viscous flow interior to be examined; this is a difficult process to study by any other means. In addition to the experimental work, a comprehensive analysis of the emplacement of the compound lower flow field on Etna during the 2001 eruption was undertaken. This extended the study of complexity to include the assessment of parameters that could not be examined experimentally, including interactions between flow units, the formation of subsurface thermal pathways, the effects of effusion rate variations on flow field morphology, and the importance of rheological changes and late-stage squeeze ups. The main findings of this work, reviewed below, have raised some interesting suggestions for further work, which are discussed in section 7.2, together with a more general survey of the challenges that remain in understanding the evolution of complex lava flow fields.

7.1.1 Experimental work

The surface morphology of the experimental flows was found to depend strongly on crustal thickness, and only weakly on topographic slope. Despite representing a significant simplification of the conditions prevailing in lava flows, all of the

morphologies observed in the experiments were found to have analogues on natural flows of similar rheology, either of lava, ice or debris. This similarity indicates that the dynamics of the analogue flows scaled to those of the natural flows, and demonstrates the success of the simulations. Scaling analysis showed that the experimental flows could be considered representative of lavas over a wide range of compositions, from basaltic `a`ā to rhyolite. The results can therefore be applied to the interpretation of structures seen on lavas that fall within this compositional range.

The structures that formed in the surface crust were a function of the stress distribution in the flow, and one of the key outcomes of the simulations was the observation of significant variations in the response of crusts of different thicknesses to similar stress regimes. This observation is very important when considering the behaviour of lava at different stages in its emplacement, and infers that surface morphology can be used as an indicator of syn-emplacement changes in flow dynamics. Thin crust flows correspond to the conditions prevailing in proximal channels, before a flow has undergone significant cooling. When subjected to compressional stress, thin crusts deform easily, producing surface ridges or ogives which propagate down the flow, eventually resulting in the entire carapace being deformed. In this case, the crust is inferred to rest passively on the flow interior, with little or no shear occurring between the two layers, and the fluid interior is dominating the behaviour. Thick crusts, by contrast, are resistant to compressive deformation and shearing, and do not initially respond to the flow of the viscous interior beneath. Shear between the crust and the flow interior is therefore inferred for thick crust flows during the early stages of an experiment. This initial resistance to movement suggests that although self-supporting roofs do not develop in any of the experiments, due to insufficient cohesion, increasing crustal thickness, corresponding to increasingly distal

channels, leads to conditions that are closer to tube flow. The increasing thickness resulted in increasing strength of the carapace under compression. As a consequence of this, the crust increasingly influenced the behaviour of the flow, especially in the upper part of the channel. At the flow front, however, the fluid interior dominated behaviour in the early stages of all experiments, as evidenced by the ubiquitous tensile fractures. This suggests that varying the crustal thickness does not cause significant variation in the tensile strength of the carapace.

The similarity of the experimental morphologies to those observed in a range of natural flows indicates that a two-layer rheological structure is capable of reproducing the behaviour of flows with more complex rheologies. If the crust is considered as a plug, increasing the crustal thickness results in an increased plug thickness, thus representing a greater yield strength. In this way, the two-layer structure can simulate flows with either stratified rheologies, such as lavas with crusts, or with viscoplastic rheologies, such as glaciers. As discussed in chapter two, the importance of a viscoelastic layer between the brittle surface layer and the fluid interior of lava flows has been noted in the field (e.g. Hon et al. 1994; Cashman et al. 2006). Such a layer was not included in the experiments, and would prove difficult to scale. Since the tensile strength of a brittle carapace is negligible in comparison with that of a viscoelastic layer, limited attention has sometimes been paid to the importance of the brittle crust in influencing flow behaviour. However, the success of the analogue experiments in reproducing flow structures suggests that the influence of a purely brittle crust cannot be overlooked. One interesting outcome of the experiments is the production of lobe structures at the flow front without a viscoelastic layer, simply as a result of crustal fracturing and/or avalanching at the flow front.

The results indicate that as the thickness of the crust increases, it plays an increasingly important role in controlling flow advance. The greater degree of interaction between the crust and the flow interior in thicker crust flows, due to the more permanent disruption of the crust at the flow front, resulted in upwelling of the flow interior and the entrainment of crustal material. The structure of the flow front was observed to become increasingly complex as the crustal thickness increased. While it might appear logical that thicker crusts should lead to more efficient insulation of a flow, and thus a lower cooling rate, the experimental results suggest that a positive feedback mechanism may be operating. In this case, fractures in thicker crusts are more difficult to heal, so result in more exposure of the flow interior than occurs in thin crust flows. In addition to this, the greater amount of entrainment of crustal material observed in thicker crusts could lead to an increased rate of cooling by advection, therefore reinforcing the tendency of the flow front to cease advancing. This process may be important in the cessation of cooling-limited lava flows.

In conclusion, the experiments successfully reproduced surface features observed in natural flows, and provided insights into how these develop. Similar features on inactive flows may be used as indicators of the flow dynamics or flow structure at the time of their formation.

7.1.2 Fieldwork

The second part of the thesis examined the development of the complex surface and structural morphologies that develop during the emplacement of a compound flow field, and the processes responsible for their formation. While commonly observed larger-scale structural complexities, such as the stacking and overlapping of flow units and the formation of tubes and ephemeral boccas, have been well documented by

previous studies (e.g. Calvari & Pinkerton 1998; Polacci & Papale 1997, 1999; Calvari et al. 2002), smaller-scale and late-stage features have received less attention. The present study has confirmed the importance of thermal pathways in the development of the flow field, and the effects of effusion rate changes on flow field morphology. The study has also examined the formation of smaller-scale features, such as tumuli and squeeze ups. These are interpreted to represent the very last stages of lava flow emplacement.

Squeeze up morphology is inferred to depend on the rheology of the material being extruded from the flow, its volume, the vent geometry, and strain rate. The rheology can be used as an indicator of both the emplacement history of the material being extruded, and of the conditions prevailing in the flow interior at the time of formation. It can provide information on how the material has been transported through the flow, as a very high crystallinity and viscosity may indicate that it has been stored for some time within the flow interior, cooling and degassing, before extrusion. The gas content may give an indication of the state of the supply system: has the material been able to degas before extrusion, or has it been stored in a closed system under pressure? Rheology can also be indicative of conditions within the flow at the time of extrusion, specifically the overpressures experienced, as, while very fluid material may be extruded easily, the lava which formed the exogenous tumuli that are so common in the 2001 flow could only have been forced out of the flow interior at very high pressures, as the pressure gradient needed is that to overcome the yield strength. The wide range of squeeze up morphologies observed in the flow indicate that a wide range of conditions must have been experienced.

The fieldwork also presented a further opportunity to support the outcomes of the experimental work, such as the increasing influence of the crust as it thickened. This

can be illustrated by comparison of the exogenous tumuli seen in the 2001 flow with the endogenous tumuli described in chapter five. While endogenous tumuli occurred in places where the local slope decreased, exogenous features developed in areas of steep or increasing slope. The endogenous examples are inferred to develop while the crust is relatively thin, and the material in the flow interior is relatively fluid. The pressure in the flow interior governs the location in which the tumulus develops. In contrast, by the time that exogenous tumuli begin to form, the crust is thought to be much thicker. While overpressures in the flow interior are necessary for the extrusion of material, due to the high yield strength, it is possible that the locality in which the extrusion develops may be influenced more by the state of the crust than by conditions in the interior. Pre-existing weaknesses that resulted from earlier processes such as tensile fracturing on steep slopes may provide loci which can be exploited by the squeeze ups. The overpressures needed to produce such squeeze ups were found to result from at least two mechanisms. One, which has long been observed, is the continuing supply of material to a stalled lobe, causing inflation and pressurisation of the lobe front which can eventually result in rupture. The second, however, is difficult to infer without observing it occurring, and has been dubbed the 'toothpaste' mechanism. This was observed within the 2001 flow, and involves the superposition of a new lobe on top of an earlier one, squeezing the material out of the underlying lobe, in the same manner that applying pressure to an open toothpaste tube results in toothpaste being squeezed out of the tube. The importance of crustal control was also discussed with relation to the locations of other squeeze ups and ephemeral vents.

Despite the widespread nature of the squeeze ups in the 2001 flow, their combined volume was insignificant in comparison with the volume of the whole flow. However, observations of such squeeze ups on other volcanoes, namely Parícutin, suggest that

they should not be overlooked in a comprehensive consideration of lava flow dynamics. The discussion of the San Juan flow on Parícutin illustrates that such late stage processes merit attention, as they may herald the onset of large-scale drainage, and the possible reactivation of a flow. While such events may be uncommon, they are clearly a possibility. Squeeze ups may be important for other reasons too. Since they represent the latest stages of activity, textural characterisation could provide information about properties such as the maximum crystallinity at which lava can flow, as will be discussed in section 7.2.

7.2 Future directions

One of the principal aims of studying lava flows is the development of a robust numerical model that is capable of accurately predicting the temporal and spatial evolution of a lava flow, for the purposes of hazard assessment. In order to achieve this aim, accurate measurements of the intrinsic properties of the lava are needed, coupled with an understanding of the structural complexities that can arise during long-lived eruptions. While the work presented in chapter six has addressed the latter of these problems, illustrating that by observing the emplacement of compound flow fields, a good qualitative understanding of the structural evolution of a flow can be acquired, this resultant morphology needs to be linked to the lava properties. However, at present, the primary problem facing modellers is the lack of robust data available on the physical properties of lava. This is a fundamental limitation, as uncertainties in the inputs significantly increases uncertainty in the output. Uncertainties in the estimation of initial effusion rates, eruption temperatures and rheological parameters, including viscosity, yield strength, crystallinity and gas

content, all contribute, and the current inability to predict with confidence how these parameters change with time also needs to be addressed.

Since effusion rate is one of the most important parameters in determining the maximum length to which a cooling-limited flow unit can advance (Walker 1973; Guest et al. 1987), accurate measurement of this parameter, especially in the early stages of flow emplacement, is a highly important task. While complex flow models, such as MAGFLOW (Del Negro et al. 2008), are capable of accounting for variable effusion rates, the problem of characterising any variations in flux is not trivial. The model of Wadge (1981), in which an initial period of rapid increase is followed by a longer period of waning flux (figure 6.52) is known to be a considerable simplification of the behaviour often observed during eruptions, which are usually characterised by smaller-scale oscillations. In order to provide a realistic pattern of effusion rates, behaviour at the vent should ideally be monitored continually during an eruption. Following initial measurements or estimations of the channel dimensions in the vent region, subsequent changes in surface velocity and the level in the channel could be monitored with cameras, and the use of stereo pairs could allow changes in channel geometry to be accounted for. The conflict between the need for frequent data and the problem of limited data storage, or constant retrieval then needs to be resolved. If instantaneous effusion rates can be estimated frequently, these could be used as inputs in syn-eruption model runs, to assess the hazards posed by flux changes. In addition to monitoring vent changes, the effect of these changes on the flow field needs to be considered. Even in a simple channelised flow, the advance rate of the flow front is significantly lower than the surface velocities measured in proximal parts of the channel, suggesting the need for observation along the entire length of the flow in

order to monitor the way in which lava is distributed. Variations in effusion rate and compound flow morphology will result in this task being even more complex.

The other important inputs to lava flow models are temperature, crystallinity, gas content, and the various rheological parameters that depend on these quantities. The need for accurate initial values of these parameters is evident, but an equally vital requirement is the ability to robustly characterise the way in which these vary spatially. While measurement of the initial temperature is achievable, accurately modelling the heat loss downflow is more challenging. Recent models, such as FLOWGO (Harris & Rowland 2001) have attempted a comprehensive description of the heat budget by including heat loss due to radiative, convective and conductive cooling, and heat gain through the release of latent heat during crystallisation and viscous heating. FLOWGO also tried to include the problem of variable crustal coverage, hence variable surface cooling (Crisp & Baloga 1990), though this is very difficult to characterise. The problem of entrainment related cooling has not yet been tackled (Crisp & Baloga 1994), nor has that of variable surface texture. As noted by Ball (2006), the emissivity of Etnaean basalt varies between 0.973 and 0.984 depending on whether the surface texture is smooth or rough, and this affects the efficiency with which the crust can lose heat by radiation. The measurement of interior temperatures along a channel, coupled with observations of surface conditions, and the comparisons of these with modelled temperature changes may provide some insight into the relative importance of the many factors that contribute to the heat budget.

Flow cooling results in rheological changes, including the increase of viscosity of the liquid phase, and the nucleation and growth of crystals. Crystallisation, as well as releasing latent heat, also contributes to the viscosity, and eventually to the yield

strength due to crystal-crystal interactions. Current models of downflow changes in rheological parameters rely on empirical temperature-viscosity and temperature-yield strength relations. These relationships are commonly derived from the consideration of non-vesicular melts, and also rely on approximations of the effects that crystals have on rheology. As noted in chapter one, the application of MAGFLOW to the 2004-5 eruption of Etna (Del Negro et al. 2008) illustrated that the outcome of the model was strongly dependent on which empirical relation is used. The need for a more accurate characterisation of the effect of temperature changes on crystallinity and rheology again depends on downflow sampling and measurements during active flow.

In addition to these problems, no current flow models have attempted to address the effects of degassing, which can have a significant impact on the bulk rheology of a flow (Sparks & Pinkerton 1978). Degassing, leading to undercooling, can trigger the pervasive nucleation of quench crystals, thus potentially leading to rapid changes in the rheological properties of the flow. The sudden increase in crystallinity may lead to a substantial increase in viscosity and yield strength, or, alternatively, the release of large quantities of latent heat could result in quite the opposite effect. The need to link degassing processes to changes in crystallinity and rheological properties again requires that active lavas be studied and sampled in the field. The additional problem of the way in which vesicles affect rheology is also in need of attention.

Assumptions regarding rheology are important when considering the conditions under which a flow can be considered to have ceased advancing permanently. The initial cessation of a flow lobe may reflect the development of a crustal, rather than an internal yield strength, and continued supply of material may allow rupture of the carapace, followed by drainage of the lobe. As was found at Parícutin, a flow may

retain its internal heat for many months, or even years, depending on its thickness, and, given suitable conditions, may be reactivated following a considerable period of rest. The ability to determine when a lava is incapable of flowing is therefore important. In many numerical models, cessation of a flow lobe is dependent on one of two conditions: either cooling of the flow interior to the solidus temperature, or the increase of the yield strength to the point where it equals the basal shear stress. In the former case, reactivation would not be expected, but in the latter, a change in flow conditions, such as an increase in the pressure exerted from upflow, may result in the resumption of advance. This is evidenced by the widespread, late-stage squeeze ups in the 2001 flow on Etna. Yield strength is commonly calculated from crystallinity, with observations of Hawai'ian basaltic flows suggesting that a yield strength develops at a crystal volume fraction of approximately 45% (Cashman et al. 1999b). Experimental results suggest that lava becomes incapable of flowing once the crystal volume fraction reaches 55 to 60% (Marsh 1981; Lejeune & Richet 1995), but this is subject to debate due to the variability of crystal shapes, which will affect how individual crystals interact within a host fluid. The determination of the threshold crystallinity beyond which a lava is incapable of flowing has yet to be achieved for any flow, and is critical when considering the problem of flow modelling. As discussed in chapter six, the late stage tumuli that developed in the 2001 flow are probably representative of lava close to the critical crystallinity threshold, and the examination of material taken from these features may help to constrain this value, which is a critical parameter in flow modelling.

Finally, the problem of accurately representing topography within a model needs to be considered closely. While the local topography can be represented by DEMs, in some cases the spatial resolution of these may be insufficient for the accurate

prediction of behaviour. Microtopography (on scales of centimetres) may be sufficient to limit the coalescence of pāhoehoe toes to produce a sheet flow, and so can fundamentally alter the characteristics of the resultant flow. Other topographic effects may have major consequences for the thermal evolution of the flow, as exemplified by the fact that flows captured in small topographic channels are often observed to advance further than predicted maximum cooling-limited lengths based on flow on an inclined plane, as their lateral spreading is limited (Parfitt & Wilson 2008). During long-lived flows, the modification of topography by the extruded lava may be important in the subsequent structural development of the flow, and the creation of syn-eruption DEMs may vastly improve the accuracy of models being run during eruptive crises.

The development of a reliable model that is capable of accurately forecasting lava flow emplacement processes relies on the input of volcanologists, fluid dynamicists and computer modellers. The majority of the problems discussed above relate to the lack of robust data on lava, and therefore fall within the domain of the volcanologists, but further difficulties relating to the accurate simulation of emplacement processes within numerical models also need to be considered. Although forecasting every aspect of lava flow emplacement accurately may ultimately prove impossible, the identification and inclusion of the most important parameters influencing the potential hazard will result in a very useful predictive tool. Significant steps have already been made towards this aim, though room for improvement certainly remains.

The most important parameter in hazard assessment is the maximum length that a lava flow can reach, hence the most important improvements that need to be made to models are those that have the greatest effect on this quantity. The accurate

characterisation of effusion rate, plus the ability to incorporate measured changes into a syn-eruption model is clearly a fundamental requirement. As has been observed during many eruptions, whether or not lava tubes develop is also a major control on the final length of a lava flow (e.g. Peterson & Swanson 1974; Guest 1980; Greeley 1987). Hidaka et al. (2005) have made the first steps towards including the formation of tubes, but have not yet been able to simulate mechanical stability. Variations in flux therefore result in the collapse of these features. This is clearly not always the case in lava flows, as tubes are often observed to run partially full (e.g. Keszthelyi 1995). The development of mechanically stable tubes is therefore one aspect of emplacement that needs to be tackled.

A second major problem is that of breaching, either accidentally, leading to the formation of overflows and/or new flow branches (Pinkerton & Wilson 1994), or through the inflation and rupture of stationary flow fronts, resulting in ephemeral vents. Breaching events are fundamental in controlling the development of compound and long-lived flow fields. Many authors have noted that breaks in topographic slope commonly lead to the formation of tubes and ephemeral vents (e.g. Polacci & Papale 1997; Calvari & Pinkerton 1998). This has been confirmed here in the study of the 2001 flow field, in which two new flow branches developed where the slope shallowed below M. Nero. In addition to the break in slope, the direction of flow of the main channel changed in this area, bending around towards the west (figure 6.4). The two new branches originated on the eastern side of the main channel, which was the outside of the bend. These observations suggest that both the channel geometry and the topography could be used in attempts to predict where breaches may occur during emplacement. Although ephemeral vent formation has been successfully modelled in stationary flow fronts (Dragoni & Tallarico 1996), the breach that led to

the M. Grosso branch did not form in this way. While a stationary flow front did develop, and subsequently breached, in the secondary channel, the M. Grosso branch originated from a different, accidental, breach in the levée behind the stationary front.

It is likely that the prediction of accidental breaching events within a numerical model will prove difficult or impossible, as the factors contributing to such events are difficult to constrain. In order to predict where a levée is likely to fail, it would be necessary to have data on the integrity of levées throughout the flow field. In addition, the processes occurring in the channel are likely to contribute, such as variations in flux, leading to changes in the lava velocity and depth, and hence the pressure exerted on the levées. Any solid debris being transported in the flow may also cause abrasion and damage to the levées, thus contributing to the possibility of failure. It may be necessary to choose potential sites of accidental breaching manually, using these as the start points for the simulations of new flows. The need to accurately simulate small changes in effusion rate can be seen from the fact that the M. Grosso branch in the 2001 flow originated at a similar time to a small increase in effusion rate. Overflows in the M. Nero region preceded the formation of the M. Grosso branch, and field observations such as these may contribute to the choice of breaching locations. Places where earlier overflows from a channel developed may show where levées have been, or are prone to be, affected by increased stresses.

At present, the most important improvements to be made to numerical models include the accurate simulation of complex effusion rate patterns over a range of scales, the formulation of mechanically stable tubes, and the predication of sites at which breaching may occur. Effusion rate variations contribute both to the ability of stable tubes to develop, and to breaching events, as well as having a direct effect on many of the important rheological and physical parameters. The incorporation of syn-

eruption effusion rate measurements, as well as the informed choice of sites of potential breaches and ephemeral vent formation that can be included in syn-eruption model runs, will aid the creation of more comprehensive hazard assessments.

All of the above factors, relating both to data collection and model development, represent major challenges in the field of lava flow study, which need to be addressed before we can claim a full understanding of the complexities that arise during effusive volcanic eruptions.

References

Acocella, V., and M. Neri (2003), What makes flank eruptions? The 2001 Etna eruption and its possible triggering mechanisms, *Bulletin of Volcanology, 65*, 517-529.

Allen, J.R.L. (1970), Physical processes of sedimentation. Elsevier Publishing, New York, 248pp.

Anderson, S.W., and J.H. Fink (1987), Modelling crease structures on the surfaces of silicic lava flows, *EOS Transactions AGU, 68*, 1545.

Anderson, S.W., and J.H. Fink (1990), The development and distribution of surface textures at the Mount St. Helens dome, *in* Fink, J.H., ed., *Lava flows and domes: emplacement mechanisms and hazard implications*, IAVCEI Proceedings in Volcanology 2. Springer-Verlag, New York, IUGG Congress, Vancouver, B.C., 25-46.

Anderson, S.W., and J.H. Fink (1992), Crease structures: indicators of emplacement rates and surface stress regimes of lava flows, *Geological Society of America Bulletin, 104*, 615-625.

Anderson, S.W., E.R. Stofan, S.E. Smrekar, J.E. Guest, and B. Wood (1999), Pulsed inflation of pāhoehoe lava flows: implications for flood basalt emplacement, *Earth and Planetary Science Letters, 168*, 7-18.

Anderson, S.W., S.M. McColley, J.H. Fink, and R.K. Hudson (2005), The development of fluid instabilities and preferred pathways in lava flow interiors: insights from analogue experiments and fractal analysis, *in* Manga, M., and G. Ventura, eds., *Kinematics and dynamics of lava flows*, Geological Society of America Special Paper 396, 147-161.

Atkinson, K. (1996), Close range photogrammetry and machine vision. Whittles Publishing, Scotland, 384pp.

Avolio, M.V., G.M. Crisci, S. DiGregorio, R. Rongo, W. Spataro, and G.A. Trunfio (2006), SCIARA γ2: an improved cellular automata model for lava flows and applications to the 2002 Etnaean crisis, *Computers and Geosciences, 32*, 876-889.

Bailey, J.E., A.J.L. Harris, J. Dehn, S. Calvari, and S.K. Rowland (2006), The changing morphology of an open lava channel on Mt. Etna, *Bulletin of Volcanology, 68*, 497-515.

Ball, M.D. (2006), The validation and use of thermal imaging cameras for quantitative temperature measurements of lava flows, unpublished Ph.D. thesis, Lancaster University, UK.

Balmforth, N.J., and R.V. Craster (1999), A consistent thin-layer theory for Bingham plastics, *Journal of Non-Newtonian Fluid Mechanics, 84*, 65-81.

Balmforth, N.J., A.S. Burbidge, R.V. Craster, J. Salzig, and A. Shen (2000), Viscoplastic models of isothermal lava domes, *Journal of Fluid Mechanics, 403*, 37-65.

Balmforth, N.J., R.V. Craster, A.C. Rust, and R. Sassi (2006), Viscoplastic flow over an inclined surface, *Journal of Non-Newtonian Fluid Mechanics, 139*, 103-127.

Barberi, F., and M.L. Carapezza (2004), The control of lava flows at Mt. Etna, *in* Bonaccorso, A., S. Calvari, M. Coltelli, C. Del Negro, and S. Falsaperla, eds., *Mt. Etna: Volcano Laboratory*, Geophysical Monograph Series 143, American Geophysical Union, Washington D.C., 357-369.

Barberi, F., F. Brondi, M.L. Carapezza, L. Cavarra, and C. Murgia (2003), Earthen barriers to control lava flows in the 2001 eruption of Mt. Etna, *Journal of Volcanology and Geothermal Research, 123*, 231-243.

Barca, D. G.M. Crisci, S. DiGregorio, and F.P. Nicoletta (1987), Lava flow simulation be cellular automata: Pantelleria's examples, *Proceedings of the International Conference of Applied Modelling and Simulation, Cairo, Egypt, 4A*, 9-15.

Barca, D. G.M. Crisci, S. DiGregorio, and F.P. Nicoletta (1993), Cellular automata methods for modelling lava flow: simulation of the 1986-1987 Etnaean eruption, *in* Kilburn, C.R.J., and G. Luongo, eds., *Active Lavas*, University College London, UK, 283-301.

Behncke, B., and M. Neri (2003), The July-August 2001 eruption of Mt. Etna (Sicily), *Bulletin of Volcanology, 65*, 461-476.

Biot, M.A. (1961), Instability of a continuously inhomogeneous half space under initial stress, *Journal of the Franklin Institute, 270*, 190-201.

Blake, S. (1990), Viscoplastic models of lava domes, *in* Fink, J.H., ed., *Lava flows and domes: emplacement mechanisms and hazard implications*, IAVCEI Proceedings in Volcanology 2. Springer-Verlag, New York, IUGG Congress, Vancouver, B.C., 88-126.

Blake, S., and B.C. Bruno (2000), Modelling the emplacement of compound lava flows, *Earth and Planetary Science Letters, 184*, 181-197.

Booth, B., and S. Self (1973), Rheological features of 1971 Mount Etna lavas, *Philosophical Transactions of the Royal Society of London, A274*, 99-106.

Bond, A.J. (1988), The simulation of lava flows with small-scale models, unpublished Ph.D. thesis, Lancaster University, UK.

Brun, J.P., and O. Merle (1985), Strain patterns in models of spreading-gliding nappes, *Tectonics, 4*, 705-719.

Bruno, B.C., G.J. Taylor, S.K. Rowland, P.G. Lucey, and S. Self (1992), Lava flows are fractals, *Geophysical Research Letters, 19*, 305-308.

Bruno, B.C., G.J. Taylor, S.K. Rowland, and S.M. Baloga (1994), Quantifying the effect of rheology on lava-flow margins using fractal geometry, *Bulletin of Volcanology, 56*, 193-206.

Buisson, C., and O. Merle (2002), Experiments on internal strain in lava dome cross sections, *Bulletin of Volcanology, 64*, 363-371.

Buisson, C., and O. Merle (2005), Influence of crustal thickness of dome destabilisation, *in* Manga, M., and G. Ventura, eds., *Kinematics and dynamics of lava flows,* Geological Society of America Special Paper 396, 181-188.

Calvari, S. (2001), Multidisciplinary approach yields insight into Mt. Etna 2001 eruption, *EOS Transactions AGU, 82*(52), 653.

Calvari, S., and H. Pinkerton (1998), Formation of lava tubes and extensive flow field during the 1991-1993 eruption of Mount Etna, *Journal of Geophysical Research, 103: B11*, 27291-27301.

Calvari, S., and H. Pinkerton (1999), Lava tube morphology on Etna, and evidence for lava flow emplacement mechanisms, *Journal of Volcanology and Geothermal Research, 90*, 263-280.

Calvari, S., and H. Pinkerton (2004), Birth, growth and morphologic evolution of the 'Laghetto' cinder cone during the 2001 Etna eruption, *Journal of Volcanology and Geothermal Research, 132*, 225-239.

Calvari, S., M. Coltelli, M. Neri, M. Pompilio, and V. Scribano (1994), The 1991-1993 Etna eruption: chronology and lava flow field evolution, *Acta Vulcanologia, 4*, 1-14.

Calvari, S., M. Neri, and H. Pinkerton (2002), Effusion rate estimations during the 1999 summit eruption on Mount Etna, and the growth of two distinct lava flow fields, *Journal of Volcanology & Geothermal Research, 119*, 107-123.

Carrigy, M.A. (1970), Experiments of angles of repose of granular materials, *Sedimentology, 14*, 147-158.

Cashman, K.V., and J.P. Kauahikaua (1997), Re-evaluation of vesicle distributions in basaltic lava flows, *Geology, 25*, 419-422.

Cashman, K.V., B. Sturtevant, P. Papale, and O. Navon (1999a), Magmatic fragmentation, *in* Sigurdsson, H., B.F. Houghton, S.R. McNutt., H. Rymer, and J. Stix, eds., *Encyclopaedia of Volcanoes*, Academic Press, San Diego, California, 2421-430.

Cashman, K.V., C. Thornber, and J.P. Kauahikaua (1999b), Cooling and crystallisation of lava in open channels, and the transition of pāhoehoe lava to `a`ā, *Bulletin of Volcanology, 61*, 306-323.

Cashman, K. V., R.C. Kerr, and R.W. Griffiths (2006), A laboratory model of surface crust formation and disruption on lava flows through non-uniform channels, *Bulletin of Volcanology, 68*, 753-770.

Cioni, R., and A. Funedda (2005), Structural geology of crystal-rich, silicic lava flows: a case study from San Pietro Island (Sardinia, Italy), *in* Manga, M., and G. Ventura, eds., *Kinematics and dynamics of lava flows*, Geological Society of America Special Paper 396, 1-14.

Coltelli, M., C. Proietti, S. Branca, M. Marsella, D. Andronico, and L. Lodato (2007), Analysis of the 2001 lava flow eruption of Mt. Etna from three-dimensional mapping, *Journal of Geophysical Research, 112*, F02029.

Corsaro, R.A., L. Miraglia, and M. Pompilio (2007), Petrologic evidence of a complex plumbing system feeding the July-August 2001 eruption of My. Etna, Sicily, Italy, *Bulletin of Volcanology, 69*, 401-421.

Costa, A., and G. Macedonio (2005), Computational modelling of lava flows: a review, *in* Manga, M., and G. Ventura, eds., *Kinematics and dynamics of lava flows,* Geological Society of America Special Paper 396, 209-218.

Coussot, P. (1999), Saffman-Taylor instability for yield stress fluids, *Journal of Fluid Mechanics, 380*, 363-376.

Coward, M.P., and G.J. Potts (1983), Complex strain patterns developed at frontal and lateral tips to shear zones and thrust zones, *Journal of Structural Geology, 5*, 383-399.

Crisci, G.M., S. DiGregorio, and G. Ranieri (1982), A cellular space model of basaltic lava flow, *Proceedings of the International Conference of Applied Modelling and Simulation, Paris, France, 11*, 65-67.

Crisci, G.M., S. DiGregorio, O. Pindaro, and G. Ranieri (1986), Lava flow simulation by a discrete cellular model: first implementation, *International Journal of Modelling and Simulation, 6*, 137-140.

Crisp, J., and S. Baloga (1990), A model for lava flows with two thermal components, *Journal of Geophysical Research, 95*, 1255-1270.

Crisp, J., and S. Baloga (1994), Influence of crystallisation and entrainment of cooler material on the emplacement of basaltic `a`ā lava flows, *Journal of Geophysical Research, 99*, 11819-11832.

Daag, A.S., M.T. Dolan, E.P. Laguerta, G.P. Meeker, C.G. Newhall, J.S. Pallister and R.U. Solidum (1996), Growth of a postclimactic lava dome at Mount Pinatubo, July-October 1992: fire and mud, *in* Newhall, C. G., and R.S. Punongbayan, eds., *Fire and*

mud: eruptions and lahars of Mount Pinatubo, Philippines, Seattle, University of Washington Press, 647-664.

Daly, R.A. (1914), Igneous rocks and their origin. McGraw Hill, New York.

de Silva, S. L., S. Self, P.W. Francis, R.E. Drake, and R. Carlos Ramirez (1994), Effusive silicic volcanism in the Central Andes: the Chao dacite and other young lavas of the Altiplano-Puna Volcanic Complex, *Journal of Geophysical Research, 99: B9*, 17805-17825.

Del Negro, C., L. Fortuna, A. Herault, and A. Vicari (2008), Simulations of the 2004 lava flow at Etna volcano using the MAGFLOW cellular automata model, *Bulletin of Volcanology, 70*, 805-812.

Denlinger, R. P. (1990), A model for dome eruptions at Mount St. Helens, Washington, based on subcritical crack growth, *in* Fink, J.H., ed., *Lava flows and domes: emplacement mechanisms and hazard implications*, IAVCEI Proceedings in Volcanology 2. Springer-Verlag, New York, IUGG Congress, Vancouver, B.C., 70-87.

Donnadieu, F., and O. Merle (1998), Experiments on the indentation process during cryptodome intrusions: new insights into Mount St. Helens deformation, *Geology, 26*(1), 17-82.

Doppler, D., P. Gondret, T. Loiseleux, S. Meyer, and M. Rabaudi (2007), Relaxation dynamics of water-immersed granular avalanches, *Journal of Fluid Mechanics, 577*, 161-181.

Dragoni, M., and A. Tallarico (1994), The effect of crystallisation on the rheology and dynamics of lava flows, *Journal of Volcanology and Geothermal Research, 59*, 241-252.

Dragoni, M., and A. Tallarico (1996), A model for the opening of ephemeral vents in a stationary lava flow, *Journal of Volcanology and Geothermal Research, 74*, 39-47.

Dragoni, M., S. Pondrelli, and A. Tallarico (1992), Longitudinal deformation of a lava flow- the influence of Bingham rheology, *Journal of Volcanology and Geothermal Research, 52*, 247-254.

Dragoni, M., A. Piombo, and A. Tallarico (1995), A model for the formation of lava tubes by roofing over a channel, *Journal of Geophysical Research, 100: B5, 8435-8447.*

Dragoni, M., F. D'Onza, and A. Tallarico (2002), Temperature distribution inside and around a lava tube, *Journal of Volcanology and Geothermal Research, 115*, 43-51.

Duncan, A.M., J.E. Guest, E.R. Stofan, S.W. Anderson, H. Pinkerton, and S. Calvari (2004), Development of tumuli in the medial portion of the 1983 `a`ā flow field, Mount Etna, Sicily, *Journal of Volcanology and Geothermal Research, 132*, 173-187.

Duraiswami, R.A., N.R. Bondre, G. Dole, V.M. Phadnis, and V.S. Kale (2001), Tumuli and associated features from the western Deccan Volcanic Province, India, *Bulletin of Volcanology, 63*, 435-442.

Eirich, F.R. (1960), Rheology: theory and applications, volume 3. Academic Press, New York, 680pp.

Favalli, M., M.T. Pareschi, M. Neri, and I. Isola (2005), Forecasting lava flow paths by a stochastic approach, *Geophysical Research Letters,3*, L03305.

Fink, J.H. (1978), Surface structures on obsidian flows, unpublished Ph.D. thesis, Stanford University, Palo Alto, California.

Fink, J.H. (1980), Surface folding and viscosity of rhyolite flows, *Geology, 8*, 250-254.

Fink, J. H. , and R.C. Fletcher (1978), Ropy pāhoehoe: surface folding of a viscous fluid, *Journal of Volcanology and Geothermal Research, 4*, 151-170.

Fink, J.H., and R.W. Griffiths (1990), Radial spreading of viscous gravity currents with solidifying crust, *Journal of Fluid Mechanics, 221*, 485-509.

Fink, J.H., and R.W. Griffiths (1992), A laboratory analogue study of the morphology of lava flows extruded from point and line sources, *Journal of Volcanology and Geothermal Research, 54*, 19-32.

Fink, J.H., and R.W. Griffiths (1998), Morphology, eruption rates and rheology of lava domes: insights from laboratory models, *Journal of Geophysical Research, 103*, 527-546.

Fink, J.H., and J. Zimbelman (1990), Longitudinal variations in rheological properties of lavas: Pu`u `Ō`ō basalt flows, Kīlauea Volcano, Hawai'i, *in* Fink, J.H., ed., *Lava flows and domes: emplacement mechanisms and hazard implications*, IAVCEI Proceedings in Volcanology 2. Springer-Verlag, New York, IUGG Congress, Vancouver, B.C., 157-173.

Fletcher, B. (1976), Incipient motion of granular materials, *Journal of Physics (D), 9*, 2471-2478.

Frazzetta, G., and R. Romano (1984), The 1983 Etna eruption: event chronology and morphological evolution of the lava flow, *Bulletin of Volcanology, 47*, 1079-1096.

Friedman, I., W. Long, and R.L. Smith (1963), Viscosity and water content of rhyolite glass, *Journal of Geophysical Research 68*, 6523-6535.

Girolami, L., T.H. Druitt, O. Roche, and Z. Khrabrykh (2008), Propagation and hindered settling of laboratory ash flows, *Journal of Geophysical Research, 113: B2*, B02202.

Greeley, R. (1987), The role of lava tubes in Hawai'ian volcanoes, *in* Decker, R.W., T.L. Wright, and P.H. Stauffer, eds., *Volcanism in Hawai'i*, U.S. Geological Survey Professional Paper 1350, 1589-1602.

Greeley, R. and M.B. Womer (1981), Mare Basin filling on the Moon: laboratory simulations, *Proceedings of the Lunar and Planetary Sciences, 12B*, 651-663.

Gregg, T.K.P., and J.H. Fink (1995), Quantification of submarine lava-flow morphology through analogue experiments, *Geology, 23*, 73-76.

Gregg, T.K.P., and J.H. Fink (1996), Quantification of extraterrestrial lava flow effusion rates through laboratory simulations, *Journal of Geophysical Research, 101: E7*, 16891-16900.

Gregg, T.K.P., and J.H. Fink (2000), A laboratory investigation into the effects of slop on lava flow morphology, *Journal of Volcanology and Geothermal Research, 96*, 145-159.

Gregg, T.K.P., and L.P. Keszthelyi (2004), The emplacement of pāhoehoe toes: field observations and comparison to laboratory simulations, *Bulletin of Volcanology, 66*, 381-391.

Gregg, T.K.P., and D.K. Smith (2003), Volcanic investigations of the Puna Ridge, Hawai'i: relations of lava flow morphologies and underlying slopes, *Journal of Volcanology and Geothermal Research, 126*, 63-77.

Gregg, T.K.P., J.H. Fink, and R.W. Griffiths (1998), Formation of multiple fold generations on lava flow surfaces: influence of strain rate, cooling rate and lava flow composition, *Journal of Volcanology and Geothermal Research, 80*, 281-292.

Griffiths, R.W. (2000), The dynamics of lava flows, *Annual Review of Fluid Mechanics, 32*, 477-518.

Griffiths, R.W., and Fink, J.H. (1992a), Solidification and morphology of submarine lavas: a dependence on extrusion rate, *Journal of Geophysical Research, 97*, 19729-19737.

Griffiths, R.W., and Fink, J.H. (1992b), The morphology of lava flows under planetary environments: predictions from analogue experiments, *Journal of Geophysical Research, 97*, 19739-19748.

Griffiths, R.W., and Fink, J.H. (1993), Effects of surface cooling on the spreading of lava flows and domes, *Journal of Fluid Mechanics, 252*, 667-702.

Griffiths, R.W., and Fink, J.H. (1997), Solidifying Bingham extrusions: a model for the growth of silicic lava flows, *Journal of Fluid Mechanics, 347*, 13-36.

Guest, J.E., J.R. Underwood, and R. Greeley (1980), Role of lava tubes in flows from the observatory vent, 1971 eruption on Mount Etna, *Geological Magazine, 117*, 601-606.

Guest, J.E., D.K. Chester, and A. M. Duncan (1984), The Valle del Bove, Mount Etna- its origin and relation to the stratigraphy and structure of the volcano, *Journal of Volcanology and Geothermal Research, 21*, 1-23.

Guest, J.E., C.R.J. Kilburn, H. Pinkerton, and A.M. Duncan (1987), The evolution of lava flow-fields: observations of the 1981 and 1983 eruptions of Mount Etna, Sicily, *Bulletin of Volcanology, 49*, 527-540.

Guest, J.E., A. Duncan, P. Cole, and D. Chester (2003), Volcanoes of Southern Italy. The Geological Society, Bath, UK, 284pp.

Hallworth, M.A., H.E. Huppert, and R.S.J. Sparks (1987), A laboratory simulation of basaltic lava flows, *Modern Geology, 11*, 93-107.

Handin, J. (1966), Strength and ductility, *in* Clarck, S.P.J., ed., *Handbook of physical constants*, Geological Society of America Memoir 97, 223-298.

Harris, A.J.L., and S.K. Rowland (2001), FLOWGO: A kinematic thermo-rheological model for lava flowing in a channel, *Bulletin of Volcanology, 63*, 20-44.

Harris, C., and M. Stephens (1988), A combined corner and edge detector, *Proceedings of the Fourth Alvey Vision Conference, Manchester*, 147-151.

Herault, A., A. Vicari, A. Ciraudo, and C. Del Negro, Forecasting lava flow hazards during the 2006 Etna eruption: using the MAGFLOW cellular automata model, *Computers & Geosciences, in press, 2008.*

Heslop, S.E. (1987), Aspects of volcanic fluid dynamics, unpublished Ph.D. thesis, Lancaster University, UK.

Hess, K.U., and D.B. Dingwell (1996), Viscosities of hydrous leucogranitic melts- a non-Arrhenian model, *American Mineralogist, 81*, 1297-1300.

Hidaka, M., A. Goto, S. Umino, and E. Fujita (2005), VTFS project: Development of the lava flow simulation code LavaSIM with a model for three-dimensional convection, spreading and solidification, *Geochemistry, Geophysics, Geosystems, 6*, QO7008.

Hodgson, G.W. (1969), An experimental investigation of simulated lava flows using carbowax material, unpublished M.S. thesis, Wright-Patterson A.F.B., Air Force Institute of Technology, Ohio.

Hoek, E., P.K. Kaiser, and W.F. Bawden (1995), Support of underground excavation, *in* Balkema, A.A., ed., *Hard Rock*, Rotterdam, Netherlands, 215pp.

Hon, K., J.P. Kauahikaua, R.P. Denlinger, and K. Mackay (1994), Emplacement and inflation of pāhoehoe sheet flows: observations and measurements of active lava flows on Kīlauea Volcano, Hawai'i, *Geological Society of America Bulletin, 106*, 351-370.

Hopkins, W. (1862), On the theory of the motion of glaciers, *Philosophical Transactions, 152*, 677-745.

Hoshino, K., H. Koide, K. Inami, S. Iwamura, and S. Mitsui (1972), Mechanical properties of Japanese Tertiary sedimentary rocks under high confining pressures, *Geological Survey of Japan Report 244*, 200pp.

Hubbert, M.K. (1937), Theory of scale models as applied to the study of geologic structures, *Geological Society of America Bulletin, 48*, 1459-1520.

Hubbert, M.K. (1951), Mechanical basis for certain familiar geologic structures, *Geological Society of America Bulletin, 61*, 355-372.

Hulme, G. (1974), The interpretation of lava flow morphology, *Geophysical Journal of the Royal Astronomical Society, 39*, 361-383.

Hulme, G. (1976), The determination of the rheological properties and effusion rate of an Olympus Mons lava, *Icarus, 27*, 207-213.

Huppert, H.E. (1982), Flow and instability of a viscous current down a slope, *Nature, 300*, 427-429.

Huppert, H.E., J.B. Shepherd, H. Sigurdsson, and R.S.J. Sparks (1982), On lava dome growth, with application to the 1979 lava extrusion of the Soufriere of St. Vincent, *Journal of Volcanology and Geothermal Research, 14*, 199-222.

Hurwitz, S., and O. Navon (1994), Bubble nucleation in rhyolitic melts- experiments at high pressure, temperature and water content, *Earth and Planetary Science Letters, 122*, 267-280.

Hutter, K., T. Koch, C. Pluss, and S.B. Savage (1995), The dynamics of avalanches of granular materials from initiation to runout. 2. Experiments, *Acta Mechanica, 109*, 127-165.

Ishihara, K., M. Iguchi, and K. Kamo (1990), Numerical simulation of lava flows on some volcanoes in Japan, *in* Fink, J.H., ed., *Lava flows and domes: emplacement mechanisms and hazard implications*, IAVCEI Proceedings in Volcanology 2. Springer-Verlag, New York, IUGG Congress, Vancouver, B.C., 174-207.

Iverson, R.M. (1990), Lava domes modelled as brittle shells that enclose pressurised magma, with application to Mount St. Helens, *in* Fink, J.H., ed., *Lava flows and domes: emplacement mechanisms and hazard implications*, IAVCEI Proceedings in Volcanology 2. Springer-Verlag, New York, IUGG Congress, Vancouver, B.C., 47-69.

Jaeger, J.C., and N.G.W. Cook (1969), Fundamentals of rock mechanics. Methuen, London, UK, 513pp.

James, M.R., S.J. Lane, and B.A. Chouet (2006), Gas slug ascent through changes in conduit diameter: laboratory insights into a volcano-seismic source process in low-viscosity magmas, *Journal of Geophysical Research, 111: B5*, B05201.

Jeffreys, H. (1925), The flow of water in an inclined channel of rectangular section, *Philosophical Magazine, 6*(49), 794-807.

Johnson, A.M. (1970), Physical processes in geology. Freeman, Cooper, San Francisco, 577pp.

Kauahikaua, J.P., K.V. Cashman, T.N. Mattox, C.C. Heliker, K. Hon, M.T. Mangan, and C.R. Thornber (1998), Observations on basaltic lava streams in tubes from Kīlauea Volcano, island of Hawai'i, *Journal of Geophysical Research, 103: B11*, 27303-27323.

Kauahikaua, J.P., D.R. Sherrod, K.V. Cashman, C.C. Heliker, K. Hon, T.N. Mattox, and J.A. Johnson (2003), Hawai'ian lava-flow dynamics during the Pu`u `Ō`ō-Kūpaianaha eruption: a tale of two decades, *in* Heliker, C.C., D.A. Swanson, and T.J. Takahashi, eds., *The Pu`u-`O`o-Kūpaianaha eruption of Kīlauea Volcano, Hawai'i: the first 20 years*, U.S. Geological Survey Professional Paper 1676, 63-87.

Kerr, R.C., and J.R. Lister (1991), The effects of shape on crystal settling and on the rheology of magmas, *Journal of Geology, 99*, 457-467.

Kerr, R.C., R.W. Griffiths, and K.V. Cashman (2006), Formation of channelised lava flows on an unconfined slope, *Journal of Geophysical Research, 111: B10*, B10206.

Keszthelyi, L. (1995), A preliminary thermal budget for lava tubes on the Earth and planets, *Journal of Geophysical Research, 100: B10*, 20411-20420.

Keszthelyi, L., and S. Self (1998), Some physical requirements for the emplacement of long basaltic lava flows, *Journal of Geophysical Research, 103: B11*, 27447-27464.

Kilburn, C. R. J. (1990), Surfaces of `a`ā flow-fields on Mount Etna, Sicily: morphology, rheology, crystallisation and scaling phenomena, *in* Fink, J.H., ed., *Lava flows and domes: emplacement mechanisms and hazard implications*, IAVCEI Proceedings in Volcanology 2. Springer-Verlag, New York, IUGG Congress, Vancouver, B.C., 129-156.

Kilburn, C.R.J. (1993), Lava crusts, `a`ā flow lengthening and the pāhoehoe-`a`ā transition, *in* Kilburn, C.R.J., and G. Luongo, eds., *Active Lavas*, University College London, UK, 263-280.

Kilburn, C.R.J. (2000), Lava flows and flow fields, *in* Sigurdsson, H., B.F. Houghton, S.R. McNutt., H. Rymer, and J. Stix, eds., *Encyclopaedia of Volcanoes*, Academic Press, San Diego, California, 346-368.

Kilburn, C.R.J. (2004), Fracturing as a quantitative indicator of lava flow dynamics, *Journal of Volcanology and Geothermal Research, 132*, 209-224.

Knudsen, J.G., and D.L. Katz (1958), Fluid dynamics and heat transfer. McGraw-Hill, New York 576pp.

Krauskopf, K.B. (1948), Lava movement at Parícutin Volcano, Mexico, *Bulletin of the Geological Society of America, 59*, 1267-1284.

Lane, S.J., B.A. Chouet, J.C. Phillips, P. Dawson, G.A. Ryan, and E. Hurst (2001), Experimental observations of pressure oscillations and flow regimes in an analogue volcanic system, *Journal of Geophysical Research, 106: B4*, 6461-6476.

Lautze, N.C., A.J.L. Harris, J.E. Bailey, M. Ripepe, S. Calvari, J. Dehn, S.K. Rowland, and K. Evans-Jones (2004), Pulsed lava effusion at Mount Etna during 2001, *Journal of Volcanology and Geothermal Research, 137*, 231-246.

Lejeune, A., and P. Richet (1995), Rheology of crystal-bearing silicate melts: an experimental study at high viscosities, *Journal of Geophysical Research, 100*, 4215-4229.

Lescinsky, D.T., and O. Merle (2005), Extensional and compressional strain in lava flows and the formation of fractures in surface crust, *in* Manga, M., and G. Ventura, eds., *Kinematics and dynamics of lava flows,* Geological Society of America Special Paper 396, 163-179.

Lipkaman, L.J., and T.K.P. Gregg (2003), `A`ā versus pāhoehoe on Mars, Venus, and Earth: what do fractal dimensions actually reveal? Lunar and Planetary Science XXXIV, Houston, Abstract 1389.

Lipman, P.W., and N.G. Banks (1987), `A`ā flow dynamics, Mauna Loa, 1984, *in* Decker, R.W., T.L. Wright, and P.H. Stauffer, eds., *Volcanism in Hawai'i*, U.S. Geological Survey Professional Paper 1350, 1527-1567.

Luhr, J.F. and T. Simkin (1993), Paricutin, the volcano born in a Mexican cornfield. Geoscience Press, Phoenix, Arizona, 427pp.

Lyman, A.W., and R.C. Kerr (2006), Effect of surface solidification on the emplacement of lava flows on a slope, *Journal of Geophysical Research, 111*, B05206.

Lyman, A.W., R.C. Kerr, and R.W. Griffiths (2005), Effects of internal rheology and surface cooling on the emplacement of lava flows, *Journal of Geophysical Research, 110*, B08207.

Macdonald, G.A. (1972), Volcanoes. Prentice-Hall, New Jersey, 510pp.

Macedonio, G., M.T. Pareschi, and R. Santacroce (1990), A simple model for lava hazard assessment: Mount Etna, IAVCEI, Mainz, Germany, Abstract.

Mader, H.M., M. Manga, and T. Koyaguchi (2004), The role of laboratory experiments in volcanology, *Journal of Volcanology and Geothermal Research, 129*, 1-5.

Malin, M.C. (1980), Lengths of Hawai'ian lava flows, *Geology, 8*, 306-308.

Mandelbrot, B.B. (1967), How long is the coast of Britain? Statistical self-similarity and fractal dimension, *Science, 156*, 636-638.

Manga, M., and H.A. Stone (1994), Interactions between bubbles in magmas and lavas- effects of bubble deformation, *Journal of Volcanology and Geothermal Research, 63*, 267-279.

Manga, M., J. Castro, K.V. Cashman, and M. Loewenberg (1998), Rheology of bubble-bearing magmas: theoretical results, *Journal of Volcanology and Geothermal Research, 87*, 15-28.

Mangan, M., and T. Sisson (2000), Delayed, disequilibrium degassing in rhyolite magma: decompression experiments and implications for explosive volcanism, *Earth and Planetary Science Letters, 183*, 441-455.

Marsh, B.D. (1981), On the crystallinity, probability of occurrence, and rheology of lava and magma, *Contributions to Mineralogy and Petrology, 78*, 85-98.

Mattox, T.N., C.C. Heliker, J.P. Kauahikaua, and K.A. Hon (1993), Development of the 1990 Kalapana flow field, Kīlauea Volcano, Hawai'i, *Bulletin of Volcanology, 55*, 407-413.

McBirney, A.R., and T. Murase (1984), Rheological properties of magmas, *Annual Reviews of Earth and Planetary Sciences, 12*, 337-357.

Merle, O. (1998), Internal strain within lava flows from analogue modelling, *Journal of Volcanology and Geothermal Research, 81*, 189-206.

Merle, O., and A. Borgia (1996), Scaled experiments of volcanic spreading, *Journal of Geophysical Research, 101: B6*, 13805-13817.

Merle, O., and F. Donnadieu (2000), Indentation of volcanic edifices by the ascending magma, *in* Vendeville, B., Y. Mart, and J.-L. Vigneresse, eds., *From the Arctic to the Mediterranean: salt, shale and igneous diapirs in and around Europe*, Geological Society of London Special Publication 174, 43-53.

Métrich, N., P. Allard, N. Spilliaert, D. Andronico, and M. Burton (2004), 2001 flank eruption of the alkali- and volatile-rich primitive basalt responsible for Mount Etna's evolution in the last three decades, *Earth and Planetary Science Letters, 228*, 1-17.

Middleton, G.V., and P.R. Wilcock (1996), Mechanics in the earth and environmental sciences. Cambridge University Press, UK, 459pp.

Mikhail, E.M., J.S. Bethel, and J.C. McGlone (2001), Introduction to modern photogrammetry. John Wiley & Sons Inc., New York, 479pp.

Miyamoto, H., and S. Sasaki (1997), Simulating lava flows by an improved cellular automata method, *Computers and Geosciences, 23*, 283-292.

Mourgues, R. and P.R. Cobbold (2003), Some tectonic consequences of fluid overpressures and seepage forces as demonstrated by sandbox modelling, *Tectonophysics, 376*, 75-97.

Murase, T., and A.R. McBirney (1973), Properties of some common igneous rocks and their melts at high temperatures, *Geological Society of America Bulletin, 84*, 3563-3592.

Nadai, A. (1950), Theory of flow and fracture of solids. McGraw-Hill, New York, 572pp.

Nakada, S., Y. Miyake, H. Sato, O. Oshima, and A. Fujinawa (1995), Endogenous growth of dacite dome at Unzen Volcano (Japan), 1993-1994, *Geology, 23*, 157-160.

Nichols, R.L. (1936), Flow-units in basalt, *Journal of Geology, 44*, 617-630.

Nye, J.F. (1952a), The mechanics of glacier flow, *Journal of Glaciology, 2*(12), 82-93.

Odonne, F., and P. Vialon (1983), Analogue models of folds above a wrench fault, *Tectonophysics, 99*, 31-46.

Olleveant, A.S. (1983), The simulation of lava flows, unpublished B.Sc. thesis, Lancaster University, UK.

Orr, T. (2008), Lava flux variations and the development of shatter rings, IAVCEI, Reykjavik, Iceland, Abstract.

Osmond, D.W., and R.W. Griffiths (1998), Silicic lava domes on slopes, *in* Thomson, M.C., and K. Hourigan, eds., *Proceedings of the 13th Australian Fluid Mechanics Conference*, Monash University, Melbourne, Australia, 827-830.

Osmond, D.W., and R.W. Griffiths (2001), the static shape of yield strength fluids slowly emplaced on slopes, *Journal of Geophysical Research, 106: B8*, 16241-16250.

Parfitt, E.A., and L. Wilson (2008), Fundamentals of physical volcanology. Blackwell Publishing, Oxford, UK, 230pp.

Paterson, W.S.B. (1981), The physics of glaciers. Pergamon Press, Oxford, UK, 380pp.

Peterson, D.W., and D.A. Swanson (1974), Observed formation of lava tubes, *Studies in Speleology, 2*(6), 209-222.

Peterson, D.W., and R.I. Tilling (1980), Transition of basaltic lava from pāhoehoe to ʻaʻā, Kīlauea Volcano, Hawaiʻi- field observations and key factors, *Journal of Volcanology and Geothermal Research, 7*, 271-293.

Pinkerton, H. (1987), Factors affecting the morphology of lava flows, *Endeavour, 11*, 73-79.

Pinkerton, H., and G. Norton (1995), Rheological properties of basaltic lavas at sub-liquidus temperatures: laboratory and field measurements on lavas from Mount Etna, *Journal of Volcanology and Geothermal Research, 68*, 307-323.

Pinkerton, H., and R.S.J. Sparks (1976), The 1975 sub-terminal lavas, Mount Etna-case history of formation of a compound lava field, *Journal of Volcanology and Geothermal Research, 1*, 167-182.

Pinkerton, H., and R.S.J. Sparks (1978), Field measurements of rheology of lava, *Nature, 276*, 383-385.

Pinkerton, H., and R.J. Stevenson (1992), Methods of determining the rheological properties of magmas at sub-liquidus temperatures, *Journal of Volcanology and Geothermal Research, 53*, 47-66.

Pinkerton, H., and L. Wilson (1994), Factors controlling the length of channel-fed lava flows, *Bulletin of Volcanology, 56*, 108-120.

Polacci, M., and P. Papale (1997), The evolution of lava flows from ephemeral vents at Mount Etna: insights from vesicle distribution and morphological studies, *Journal of Volcanology and Geothermal Research, 76*, 1-17.

Polacci, M. and P. Papale (1999), The development of compound of lava fields ay Mount Etna, *Physics and Chemistry of the Earth (A), 24*, 193-205.

Reiner, M. (1969), Deformation, strain and flow. H.K. Lewis & Co., London, UK, 347pp.

Ridley, J., and M. Casey (1989), Numerical modelling of folding in rotational strain histories: strain regime expected in thrust belts and shear zones, *Geology, 17*, 875-878.

Robson, G.R. (1967), thickness of Etnaean lavas, *Nature, 216*, 251-252.

Rocchi, V., P.R. Sammonds, and C.R.J. Kilburn (2004), Fracturing of Etnaean and Vesuvian rocks at high temperatures and low pressures, *Journal of Volcanology and Geothermal Research, 132*, 137-157.

Roche, O., M. Gilbertson, J.C. Phillips, and R.S.J. Sparks (2002), Experiments on de-aerating granular flows and implications for pyroclastic flow mobility, *Geophysical Research Letters, 29*, 1792.

Roche, O., M. Gilbertson, J.C. Phillips, and R.S.J. Sparks (2004), Experimental study of gas-fluidised granular flows with implications for pyroclastic flow emplacement, *Journal of Geophysical Research, 109:B10*, B10201.

Roche, O., M. Gilbertson, J.C. Phillips, and R.S.J. Sparks (2006), The influence of particle size on the flow of initially fluidised powders, *Powder Technology, 166*, 167-174.

Rossi, M.J., and A. Gudmundsson (1996), The morphology and formation of flow-lobe tumuli on Icelandic shield volcanoes, *Journal of Volcanology and Geothermal Research, 72*, 291-308.

Rowland, S.K., and G.P.L. Walker (1987), Toothpaste lava: characteristics and origin of a lava structural type transitional between pāhoehoe and `a`ā, *Bulletin of Volcanology, 49*, 631-641.

Rowland, S.K., and G.P.L. Walker (1988), Mafic-crystal distributions, viscosities, and lava structures of some Hawai'ian lava flows, *Journal of Volcanology and Geothermal Research, 35*, 55-66.

Rowland, S.K., H. Garbeil, and A.J.L. Harris (2005), Lengths and hazards from channel-fed lava flows on Mauna Loa, Hawai'i, determined from thermal and downslope modelling with FLOWGO, *Bulletin of Volcanology, 67*, 634-647.

Saemundsson, K. (1992), Geology of the Þingvallavatn area, *Oikos, 64*, 40-68.

Saffman, P.G., and G. Taylor (1958), The penetration of a fluid into a porous medium or Hele-Shaw cell containing a more viscous liquid, *Proceedings of the Royal Society of London, A245*, 312-329.

Sakimoto, S.E.H., and M.T. Zuber (1998), Flow and convective cooling in lava tubes, *Journal of Geophysical Research, 103: B11*, 27465-27487.

Savage, J.C., and W.S.B. Paterson (1963), Borehole measurements in the Athabasca Glacier, *Journal of Geophysical Research, 68*, 4521-4536.

Schultz, R.A. (1996), Relative scale and the strength and deformability of rock masses, *Journal of Structural Geology, 18*, 1139-1149.

Scott Blair, G.W. (1969), Elementary rheology. Academic Press, London, UK,158pp.

Self, S., L. Keszthelyi, and T. Thordarson (1998), The importance of pāhoehoe, *Annual Review of Earth and Planetary Sciences, 26*, 81-110.

Self, S., L.P. Keszthelyi, and T. Thordarson (2000), Discussion of: 'Pulsed inflation of pāhoehoe lava flows: implications for flood basalt emplacement' by Anderson, S.W., E.R. Stofan, S.E. Smrekar, J.E. Guest, and B. Wood (1999), [Earth and Planetary Science Letters, 168, 7-18], *Earth and Planetary Science Letters, 179*, 421-423.

Shaw, H.R. (1969), Rheology of basalt in the melting range, *Journal of Petrology, 10*, 510-535.

Shaw, H.R. (1972), Viscosities of magmatic silicate liquids: an empirical method of prediction, *American Journal of Science, 272*, 870-893.

Shaw, H.R., T.L. Wright, D.L. Peck, and R. Okamura (1968), The viscosity of basaltic magma: an analysis of field measurements in Makaopuhi lava lake, Hawai'i, *American Journal of Science, 266*, 255-264.

Shea, T., and B. van Wyk de Vries (2008), Structural analysis and analogue modelling of the kinematics and dynamics of rockslide-avalanches, *Geosphere, 4*, 657-686.

Sigurdsson, H. (2000), The history of volcanology, *in* Sigurdsson, H., B.F. Houghton, S.R. McNutt., H. Rymer, and J. Stix, eds., *Encyclopaedia of Volcanoes*, Academic Press, San Diego, California, 15-37.

Soule, S.A., and K.V. Cashman (2004), The mechanical properties of solidified polyethylene glycol 600, an analogue for lava crust, *Journal of Volcanology and Geothermal Research, 129*, 139-153.

Sparks, R.S.J., and H. Pinkerton (1978), Effect of degassing on rheology of basaltic lava, *Nature, 276*, 385-386.

Sparks, R.S.J., H. Pinkerton, and G. Hulme (1976), Classification and formation of lava levées on Mount Etna, *Geology, 4*, 269-271.

Stasiuk, M.V., C. Jaupart, and R.S.J. Sparks (1993), Influence of cooling on lava flow dynamics, *Geology, 21*, 335-338.

Tanguy, J.C. (1973), The 1971 Etna eruption: petrography of the lavas, *Philosophical Transactions of the Royal Society of London, A274*, 45-53.

Thorarinsson, S. (1953), Ogives in lava streams, *Journal of Glaciology, 2*, 295.

Valentino, R., G. Barla, and L. Montrasio (2008), Experimental analysis and micro-mechanical modelling of dry granular flow and impacts in laboratory flume tests, *Rock Mechanics and Rock Engineering, 41*, 153-177.

Van Wyk de Vries, B., and O. Merle (1998), Extension induced by volcanic loading in regional strike-slip zones, *Geology, 26*, 983-986.

Vicari, A., A. Herault, C. Del Negro, M. Coltelli, M. Marsella, and C. Proietti (2007), modelling of the 2001 lava flow at Etna volcano by a cellular automata approach, *Environmental Modelling and Software, 22*, 1465-1471.

Wadge, G. (1978), Effusion rate and shape of `a`ā lava flow-fields on Mount Etna, *Geology, 6*, 503-506.

Wadge, G. (1981), The variation of magma discharge during basaltic eruptions, *Journal of Volcanology and Geothermal Research, 11*, 139-168.

Walker, G.P.L. (1967), Thickness and viscosity of Etnaean lavas, *Nature, 213*, 484-485.

Walker, G.P.L. (1971), Compound and simple lava flows and flood basalts, *Bulletin of Volcanology, 35*, 579-590.

Walker, G.P.L. (1973), Lengths of lava flows, *Philosophical Transactions of the Royal Society of London, A274*, 147-151.

Walker, G.P.L. (1989), Spongy pāhoehoe in Hawai'i- a study of vesicle distribution patterns on basalt and their significance, *Bulletin of Volcanology, 51*, 199-209.

Walker, G.P.L. (1991), Structure, and origin by injection of lava under surface crust, of tumuli, lava rises, lava-rise pits, and lava-inflation clefts in Hawai'i, *Bulletin of Volcanology, 53*, 546-558.

Wentworth, C.K., and G.A. Macdonald (1953), Structures and forms of basaltic rocks in Hawai'i, *U.S. Geological Survey Bulletin 994*, 98pp.

Williams, H. (1932), The history and character of volcanic domes, *Bulletin of the Department of Geological Sciences, University of California Publications, 21*, 51-146.

Appendix A: Camera specifications

	Olympus E-20	Canon EOS 300D/Rebel
Image size (px)	2560 x 1920	3072 x 2048
Effective pixels (M px)	4.92	6.3
Image format	JPEG	JPEG
Lens aperture range	f/2.0 - f/11	f/1.8 - f/22
Focal length (mm)	35 - 140	28 and 50
Shutter speed (s)	2 - 1/640	30 - 1/4000

Appendix B: Individual camera calibration data

VMS Project: Camera data

Wednesday, May 16, 2007

Project name: cam cal expts

This file contains information on 2 cameras

Parameters: 1 = PPx; 2 = PPy; 3 = PD; 4-6 = radial; 7-8 = decentring; 9 = orthogonality; 10 = affinity.

1: Calibration parameters for camera 1 left (Canon EOS digital rebel)

1	0.1200	0.0031
2	-0.0483	0.0034
3	28.9608	0.0030
4	-1.2226e-004	1.2521e-006
5	3.5589e-008	1.7825e-008
6	6.3007e-010	7.5487e-011
7	2.0497e-006	1.2622e-006
8	-1.1952e-005	1.3498e-006
9	-5.3778e-005	1.7243e-005
10	4.1515e-005	1.8282e-005

x and y pixel size in mm and x, y image size in pixels

0.00740	0.00740	3072	2048

Fiducial Mark Data

Camera	Point	Ref X	Ref Y	Std X	Std Y	Obs X	Obs Y	Std X	Std Y

No fiducial information for this camera

2: Calibration parameters for camera 2 right (Canon EOS 300D)

1	0.0725	0.0046
2	-0.0122	0.0049
3	28.8541	0.0045
4	-1.4597e-004	2.1239e-006
5	3.2864e-007	2.9287e-008
6	-5.6251e-010	1.2189e-010
7	1.8535e-006	1.8892e-006
8	1.9378e-005	1.8532e-006
9	-1.0700e-004	1.8881e-005
10	1.3875e-004	2.0507e-005

x and y pixel size in mm and x, y image size in pixels

0.00740	0.00740	3072	2048

Fiducial Mark Data

Camera	Point	Ref X	Ref Y	Std X	Std Y	Obs X	Obs Y	Std X	Std Y

No fiducial information for this camera

*** End of file ***

Appendix C: Dual calibration data, .pho file, Lancaster

*** VMS Project: Photo data ***
Thursday, June 07, 2007

Project name: dual calib Lancaster

This file contains information on 42 photos
Exterior orientation parameters for photo: 1000

Photo	X	Y	Z	Omega	Phi	Kappa	Camera
1000	-269.1706	-199.6242	1076.5967	8.2462	-17.0539	98.4097	1
1001	32.6485	-566.8903	1142.6351	27.4921	-1.3955	90.1291	1
1002	276.7357	-569.8278	1058.5427	28.0386	9.6526	84.2092	1
1003	428.6872	-549.4528	980.2661	28.0249	18.5408	78.5572	1
1004	581.2154	-545.4603	850.9540	29.8415	27.8367	72.7789	1
1005	-135.1234	-573.9374	1077.8101	27.8937	-8.9882	95.2703	1
1006	-275.4153	-581.9638	992.7589	28.7694	-16.5445	100.9808	1
1007	-438.0458	-575.7891	870.4982	30.4277	-25.2016	105.6732	1
1008	-439.2539	-565.2517	880.7534	29.6717	-25.2882	103.9523	1
1009	-515.3062	-534.6781	798.9251	29.8001	-31.9633	109.1776	1
1010	16.5132	-362.9662	1208.4628	16.6273	-2.1939	91.6113	1
1011	17.8499	-141.7588	1210.0293	5.0248	-2.1498	91.6928	1
1012	17.9965	83.0289	1163.9959	-5.8121	-2.1975	91.5872	1
1013	26.4682	-703.1885	1009.2489	34.8438	-1.4796	90.2539	1
1014	34.7580	-856.1985	765.0237	47.1069	-1.0702	91.1675	1
1015	33.5145	-961.0025	470.7477	61.0053	-1.1248	90.9842	1
1016	-34.5743	-679.4453	1003.2865	34.0320	-4.6283	94.9310	1
1017	-118.5752	-786.4285	823.6085	41.6483	-8.8778	97.8956	1
1018	-181.2876	-858.9437	619.5798	49.9566	-13.1471	100.9983	1
1019	-81.8075	-347.9276	1173.6679	17.1022	-6.5358	93.9426	1
1020	-202.9401	-268.3552	1119.3599	12.9718	-12.0289	96.7263	1
2000	-252.5555	579.0895	778.7089	-32.0212	-16.3779	85.9537	2
2001	44.2785	266.4117	1133.0853	-10.9090	0.8774	89.5149	2
2002	286.3791	263.0753	1048.6077	-11.0541	13.1318	91.8007	2
2003	444.9364	282.5865	947.4883	-12.9398	23.5018	93.3901	2
2004	592.9502	286.0034	808.5263	-14.7107	33.9490	96.1269	2
2005	-135.6571	258.4399	1068.7161	-10.9707	-8.1924	88.7982	2
2006	-293.7928	249.5732	976.3528	-11.4496	-17.5956	88.2662	2
2007	-446.9569	256.2992	851.2502	-12.5045	-26.9927	85.5978	2
2008	-428.3967	266.5249	861.1519	-13.1080	-26.0102	84.2554	2
2009	-509.3706	296.1588	745.5246	-16.3231	-34.0075	82.6289	2
2010	14.6655	453.2732	1041.4569	-21.8052	-0.6627	90.1835	2
2011	15.2246	624.4494	882.0415	-33.4286	-0.6477	90.2975	2
2012	16.7699	773.7509	697.8730	-44.2541	-0.6316	90.1814	2
2013	35.8694	124.7792	1106.2055	-3.5721	0.6758	89.5412	2
2014	31.3197	-68.0324	1035.3339	8.6865	0.5185	90.5071	2
2015	33.2334	-260.8981	922.2619	22.5998	0.6166	90.3091	2
2016	-62.9845	150.0792	1083.9999	-4.5869	-4.6791	91.2389	2
2017	-153.9495	26.4829	1005.8969	2.6406	-9.7872	90.8666	2
2018	-225.0497	-76.7739	905.7248	10.2604	-15.0358	90.5131	2
2019	-82.0278	469.3522	1011.1272	-21.5689	-5.4320	89.3240	2
2020	-200.0455	533.7488	892.2426	-26.3681	-11.4177	88.0001	2

*** End of photo orientation file ***

Appendix D: Dual calibration data, .pho file, Clermont

*** VMS Project: Photo data ***
Friday, October 12, 2007

Project name: dual calib france

This file contains information on 54 photos
Exterior orientation parameters for photo: 1000

Photo	X	Y	Z	Omega	Phi	Kappa	Camera
1000	-331.8694	114.4054	1075.8489	9.4022	-19.8158	-94.7708	1
1001	26.2936	425.0727	1336.8179	-10.7091	0.0204	-92.1684	1
1002	31.4156	563.2999	1241.4171	-17.2660	-0.0985	-92.3621	1
1003	38.1977	793.6085	1037.5660	-28.5515	0.0141	-92.8002	1
1004	36.4938	931.8805	863.9247	-36.7267	0.0034	-92.6342	1
1005	46.5846	1086.3988	583.1250	-48.4591	0.2206	-93.1586	1
1006	-177.6746	416.1336	1249.1826	-11.1690	-9.1844	-94.3021	1
1007	-371.9883	419.0840	1130.9245	-11.6627	-18.3027	-96.4754	1
1008	-546.0177	419.3373	983.1982	-12.5465	-27.3206	-98.4628	1
1009	-688.2442	420.2754	816.3763	-13.9151	-35.9129	-100.7143	1
1010	35.3343	300.8530	1324.3912	-5.8030	-0.1016	-91.4661	1
1011	35.6324	23.0768	1252.1256	6.3943	-0.0449	-91.6824	1
1012	35.6465	-217.8869	1133.4599	17.9292	-0.2510	-91.0176	1
1013	35.8013	-470.4509	930.2232	31.6071	-0.4192	-90.3536	1
1014	189.6957	425.8038	1284.5470	-10.5661	6.7921	-90.6559	1
1015	385.9040	418.6600	1186.0729	-10.7750	15.7424	-89.6292	1
1016	595.7821	415.3000	1031.5532	-11.5138	26.2554	-87.7722	1
1017	785.8462	431.7901	818.7861	-13.1655	38.1397	-84.4292	1
1018	237.7271	307.3533	1247.4108	-4.6412	9.5554	-90.1797	1
1019	330.1238	205.7555	1181.2763	0.0997	13.7936	-89.8025	1
1020	448.7081	103.5917	1076.3411	5.1121	19.8173	-90.6218	1
1021	-119.2226	553.2893	1190.6421	-16.7949	-6.8216	-95.3665	1
1022	-163.7775	824.5679	896.9133	-31.4480	-9.3765	-97.1044	1
1023	-245.3565	862.8479	698.7330	-38.7560	-16.9861	-103.6693	1
1024	175.5068	543.6637	1204.9473	-16.1479	7.1539	-90.1485	1
1025	345.9628	728.2785	879.8852	-30.4339	17.4425	-87.1954	1
1026	-272.8254	261.9274	1176.9847	-1.4899	-13.2484	-96.4755	1
2000	-360.6587	-784.6853	742.5530	53.7074	-18.9487	-79.6740	2
2001	-19.6565	-534.4811	1353.3976	30.9893	-2.6109	-91.5422	2
2002	-15.0444	-389.2507	1366.9343	24.4826	-2.7392	-91.6452	2
2003	-17.5077	-117.0312	1346.9274	13.2430	-3.0157	-92.0408	2
2004	-15.4488	77.3213	1299.6807	4.9501	-2.8726	-91.9211	2
2005	-14.4146	340.3593	1182.9342	-6.8905	-3.0480	-92.4440	2
2006	-231.5809	-542.6187	1262.4841	31.2188	-10.8664	-86.9360	2
2007	-431.3160	-539.6405	1134.1953	32.5114	-18.9470	-82.0741	2
2008	-603.5581	-539.3479	979.2812	34.5582	-26.5613	-76.4871	2
2009	-743.4621	-539.1907	806.6347	37.4810	-33.6413	-70.3989	2
2010	4.3961	-660.5897	1256.0466	36.0915	-2.1169	-90.9868	2
2011	-2.0596	-900.6677	984.8257	48.1740	-2.3340	-91.1122	2
2012	10.9196	-1068.6601	688.6099	59.6333	-1.9916	-90.5322	2
2013	22.4935	-1192.4220	296.3270	73.3476	-1.6776	-89.9373	2
2014	148.7415	-536.4761	1301.1190	31.3633	3.4115	-94.8764	2
2015	339.9141	-540.7041	1210.6734	31.9036	10.8224	-100.2796	2
2016	550.6920	-543.8468	1065.2229	33.4952	19.6617	-106.5536	2
2017	751.7204	-527.8249	858.8638	36.7937	29.7636	-114.0493	2
2018	196.5044	-652.0555	1165.6389	37.4915	5.7596	-96.3610	2
2019	285.0401	-742.5530	1022.9607	42.5978	9.2066	-99.0281	2
2020	377.0375	-825.4861	846.8136	48.1782	13.2031	-103.8674	2
2021	-196.0157	-400.1678	1297.1521	25.4117	-9.7679	-89.3843	2
2022	-261.7580	-71.6074	1232.4571	11.0799	-12.8498	-88.9113	2
2023	-419.6905	6.6906	1099.8226	5.4074	-22.7308	-88.3163	2
2024	145.6313	-410.9951	1314.6489	25.7545	4.1563	-94.8571	2
2025	334.5567	-173.1953	1215.0619	12.9060	13.6993	-99.7351	2
2026	-348.9485	-682.1653	1017.0252	41.6129	-15.2934	-85.7047	2

*** End of photo orientation file ***

Appendix E: Dual calibration data, network log file, Lancaster

```
*** Vision Measurement System (VMS) ***
Self-calibrating Photogrammetric Network Solution

Version 7.6 - Mark Shortis and Stuart Robson - August
2003


Project name:  dual calib lancaster

VMS bundle adjustment log file:    dual calib
lancaster_network.log written on Thu Jun 07 14:24:03 2007


<<< Program control variables >>>

Network datum definition type:        external
constraints on targets

Additional parameter set type:        all parameters
fixed

Maximum iterations for a solution:    10

Default target image precision:       1.66

Minimum images for a network target:  4

Rejection criterion for image errors: 5.0


<<< Initial Camera Calibration Sets >>>

Units : millimetres

Calibration set : 1

Parameter       Value              Precision

    1            0.120
    2           -0.048
    3           28.961
    4    -1.2226e-004
    5     3.5589e-008
    6     6.3007e-010
    7     2.0497e-006
    8    -1.1952e-005
    9    -5.3778e-005
   10     4.1515e-005

Pixel size in mm     Format size in pixels

   x          y          x          y
0.0074     0.0074       3072       2048
```

Calibration set : 2

Parameter	Value	Precision
1	0.072	
2	-0.012	
3	28.854	
4	-1.4597e-004	
5	3.2864e-007	
6	-5.6251e-010	
7	1.8535e-006	
8	1.9378e-005	
9	-1.0700e-004	
10	1.3875e-004	

Pixel size in mm		Format size in pixels	
x	y	x	y
0.0074	0.0074	3072	2048

<<< Initial Camera Locations >>>

Photo	Cal Set	X	Y	Z	Omega	Phi	Kappa	#Images
			(millimetres)			(degrees)		
1000	1	-269.171	-199.624	1076.597	8.25	-17.05	98.41	50
1001	1	32.648	-566.890	1142.635	27.49	-1.40	90.13	38
1002	1	276.736	-569.828	1058.543	28.04	9.65	84.21	42
1003	1	428.687	-549.453	980.266	28.02	18.54	78.56	47
1004	1	581.215	-545.460	850.954	29.84	27.84	72.78	38
1005	1	-135.123	-573.937	1077.810	27.89	-8.99	95.27	40
1006	1	-275.415	-581.964	992.759	28.77	-16.54	100.98	40
1007	1	-438.046	-575.789	870.498	30.43	-25.20	105.67	37
1008	1	-439.254	-565.252	880.753	29.67	-25.29	103.95	39
1009	1	-515.306	-534.678	798.925	29.80	-31.96	109.18	35
1010	1	16.513	-362.966	1208.463	16.63	-2.19	91.61	45
1011	1	17.850	-141.759	1210.029	5.02	-2.15	91.69	43
1012	1	17.996	83.029	1163.996	-5.81	-2.20	91.59	36
1013	1	26.468	-703.189	1009.249	34.84	-1.48	90.25	35
1014	1	34.758	-856.199	765.024	47.11	-1.07	91.17	36
1015	1	33.515	-961.002	470.748	61.01	-1.12	90.98	26
1016	1	-34.574	-679.445	1003.286	34.03	-4.63	94.93	33
1017	1	-118.575	-786.428	823.608	41.65	-8.88	97.90	30
1018	1	-181.288	-858.944	619.580	49.96	-13.15	101.00	31
1019	1	-81.807	-347.928	1173.668	17.10	-6.54	93.94	47
1020	1	-202.940	-268.355	1119.360	12.97	-12.03	96.73	45
2000	2	-252.556	579.089	778.709	-32.02	-16.38	85.95	38
2001	2	44.279	266.412	1133.085	-10.91	0.88	89.51	44
2002	2	286.379	263.075	1048.608	-11.05	13.13	91.80	44
2003	2	444.936	282.587	947.488	-12.94	23.50	93.39	47
2004	2	592.950	286.003	808.526	-14.71	33.95	96.13	46
2005	2	-135.657	258.440	1068.716	-10.97	-8.19	88.80	43
2006	2	-293.793	249.573	976.353	-11.45	-17.60	88.27	46
2007	2	-446.957	256.299	851.250	-12.50	-26.99	85.60	45
2008	2	-428.397	266.525	861.152	-13.11	-26.01	84.26	45
2009	2	-509.371	296.159	745.525	-16.32	-34.01	82.63	43

2010	2	14.665	453.273	1041.457	-21.81	-0.66	90.18	44
2011	2	15.225	624.449	882.042	-33.43	-0.65	90.30	40
2012	2	16.770	773.751	697.873	-44.25	-0.63	90.18	33
2013	2	35.869	124.779	1106.205	-3.57	0.68	89.54	44
2014	2	31.320	-68.032	1035.334	8.69	0.52	90.51	43
2015	2	33.233	-260.898	922.262	22.60	0.62	90.31	40
2016	2	-62.985	150.079	1084.000	-4.59	-4.68	91.24	45
2017	2	-153.950	26.483	1005.897	2.64	-9.79	90.87	45
2018	2	-225.050	-76.774	905.725	10.26	-15.04	90.51	39
2019	2	-82.028	469.352	1011.127	-21.57	-5.43	89.32	43
2020	2	-200.046	533.749	892.243	-26.37	-11.42	88.00	37

<<< Initial Targets >>>

Target	X	Y	Z	Index	sX	sY	sZ	#Images
		(millimetres)				(microns)		
1	-0.0103	0.1284	-0.0136	7	336.9	336.9	9.1	41
5	95.5989	0.2034	-0.0290	7	320.6	320.6	9.1	42
7	95.9393	96.1560	0.0048	7	303.6	303.7	9.2	42
9	-0.0355	96.0929	0.0183	7	320.7	320.7	9.2	41
28	96.0562	-95.9732	0.0061	7	383.9	383.8	9.4	40
34	-0.2417	192.0562	0.0047	7	354.9	355.0	9.6	30
36	268.7090	192.4125	-0.0056	7	425.6	425.9	9.7	25
37	383.4083	383.1276	-0.0035	7	656.7	657.8	10.0	4
64	-287.5714	384.0000	0.0000	7	-1.0	-1.0	-1.0	0
	(insufficient images)							
70	-172.8929	191.8780	0.0055	7	479.8	479.7	9.7	25
76	-172.8718	-96.1804	-0.0050	7	512.2	512.2	9.6	37
90	-287.5714	-249.0000	0.0000	7	-1.0	-1.0	-1.0	0
	(insufficient images)							
100	383.4286	-249.0000	0.0000	7	-1.0	-1.0	-1.0	0
	(insufficient images)							
113	269.0548	-95.9013	0.0173	7	462.1	461.8	9.7	19
1000	-288.1453	-192.2992	0.1071	0				5
1001	-192.1533	-192.2636	-0.3520	0				29
1002	-95.9254	-192.1186	0.4258	0				40
1003	0.0965	-192.0342	0.2744	0				37
1004	96.1247	-191.9464	0.5201	0				41
1005	192.3512	-191.8713	0.4807	0				35
1006	288.2675	-191.7851	0.3990	0				24
1007	384.0967	-191.6836	0.8155	0				7
1008	-287.5714	-96.0000	0.0000	0				0
	(insufficient images)							
1009	-192.2058	-96.0774	-0.1672	0				40
1010	-95.9699	-96.0038	0.0006	0				39
1011	0.0383	-95.9307	0.1826	0				39
1012	192.2445	-95.7862	0.1060	0				37

1013	288.2134	-95.7244	0.4522	0	29
1014	384.0190	-95.6868	0.4323	0	4
1015	-288.2343	0.0101	-0.0106	0	4
1016	-192.2254	-0.0063	-0.0653	0	40
1017	-96.0054	0.0559	0.0354	0	40
1018	192.1664	0.2596	-0.1521	0	41
1019	288.0892	0.3100	-0.1260	0	40
1020	383.9733	0.4073	0.0455	0	10
1021	-288.1946	95.9707	-0.0375	0	4
1022	-192.2222	95.9601	0.1802	0	40
1023	-96.0253	96.0236	0.4480	0	41
1024	192.0989	96.2110	-0.0435	0	41
1025	288.0165	96.2579	0.7125	0	36
1026	383.8916	96.2587	-0.0177	0	9
1027	-288.1306	191.9547	-0.0857	0	7
1028	-192.2183	191.9934	0.0269	0	35
1029	-96.0456	192.0710	0.1007	0	38
1030	95.8634	192.2159	-0.0683	0	40
1031	192.0586	192.2758	-0.0517	0	38
1032	287.9526	192.3034	-0.0467	0	34
1033	383.7817	192.2812	-0.0549	0	12
1034	-288.1358	288.0410	-0.3861	0	11
1035	-192.2214	288.0586	-0.2816	0	34
1036	-96.0546	288.1129	-0.4543	0	35
1037	-0.0968	288.1753	-0.5163	0	34
1038	95.8217	288.2362	-0.6144	0	37
1039	191.9754	288.2794	-0.5668	0	38
1040	287.8457	288.2944	-0.4187	0	31
1041	383.6664	288.0064	-0.0780	0	5
1042	-192.2628	383.9645	-1.2453	0	21
1043	-96.0758	383.9606	-1.2480	0	30
1044	-0.1465	383.9935	-1.3609	0	35
1045	95.7826	384.0504	-1.3410	0	37
1046	191.9134	384.0898	-1.4524	0	33
1047	287.8100	384.1539	-1.6137	0	24

<<< Input Summary >>>

Number of camera calibration sets:	2
Number of target image observations:	1707
Total number of exposures:	42
Number of exposures in the network:	42
Total number of targets:	62
Number of targets in the network:	58
Total number of survey measurements:	0
Number of survey measurements in the network:	0

*** Results for the Calibration Solution ***

Solution completed successfully after 3 iteration(s)

Unit weight estimate (sigma zero):	1.00
RMS image residual (microns):	1.54
Number of rejected target images:	0
Number of observables in the network:	3467
Number of unknowns in the network:	426
Number of redundancies in the network:	3041

<<< Fixed Camera Calibration Sets >>>

Parameter	Value
Units : millimetres	
1	0.1200
2	-0.0483
3	28.9608
4	-1.2226e-004
5	3.5589e-008
6	6.3007e-010
7	2.0497e-006
8	-1.1952e-005
9	-5.3778e-005
10	4.1515e-005

Lens Distortion Profiles for Camera Calibration Set: 1

Units : microns

Radius	Radial Distortion		Decentring Distortion	
	Value	Precision	Value	Precision
0.0	0.00	0.00	0.00	0.00
2.0	-0.98	0.00	0.05	0.00
4.0	-7.78	0.00	0.19	0.00
6.0	-25.96	0.00	0.44	0.00
8.0	-60.11	0.00	0.78	0.00
10.0	-112.40	0.00	1.21	0.00
12.0	-179.83	0.00	1.75	0.00
14.0	-249.92	0.00	2.38	0.00

<<< Fixed Camera Calibration Sets >>>

Parameter	Value
Units : millimetres	
1	0.0725
2	-0.0122
3	28.8541
4	-1.4597e-004
5	3.2864e-007
6	-5.6251e-010
7	1.8535e-006
8	1.9378e-005
9	-1.0700e-004
10	1.3875e-004

Lens Distortion Profiles for Camera Calibration Set: 2

Units : microns

Radius	Radial Distortion Value	Radial Distortion Precision	Decentring Distortion Value	Decentring Distortion Precision
0.0	0.00	0.00	0.00	0.00
2.0	-1.16	0.00	0.08	0.00
4.0	-9.01	0.00	0.31	0.00
6.0	-29.13	0.00	0.70	0.00
8.0	-65.15	0.00	1.25	0.00
10.0	-118.73	0.00	1.95	0.00
12.0	-190.62	0.00	2.80	0.00
14.0	-283.09	0.00	3.82	0.00

<<< Updated Camera Location Values and Precisions >>>

Photo	Cal Set	X	Y	Z	Omega	Phi	Kappa	sX	sY	sZ	sO	sP	sK
		(millimetres)			(degrees)			(microns)			(seconds of arc)		
1000	1	-269.1616	-199.6365	1076.5808	8.247	-17.054	98.410	359.4	360.7	725.6	55.7	41.3	142.0
1001	1	32.6539	-566.9053	1142.6067	27.493	-1.395	90.129	498.4	472.7	778.3	37.1	73.7	122.3
1002	1	276.7356	-569.8396	1058.5141	28.040	9.653	84.209	494.0	482.8	720.1	38.9	71.1	123.2
1003	1	428.6834	-549.4632	980.2390	28.026	18.541	78.557	512.2	504.4	665.5	50.6	70.0	128.0
1004	1	581.2079	-545.4680	850.9286	29.843	27.837	72.779	557.3	555.9	581.3	69.7	72.5	135.0
1005	1	-135.1165	-573.9506	1077.7840	27.895	-8.988	95.270	503.1	487.5	733.8	39.6	72.7	123.2
1006	1	-275.4076	-581.9750	992.7345	28.771	-16.544	100.981	524.6	517.5	678.0	48.0	72.3	125.9
1007	1	-438.0369	-575.7980	870.4759	30.429	-25.201	105.673	565.6	564.8	596.5	62.7	73.7	131.2
1008	1	-439.2451	-565.2609	880.7310	29.673	-25.288	103.952	561.7	561.3	604.8	64.3	72.5	132.3
1009	1	-515.2970	-534.6859	798.9046	29.801	-31.963	109.177	576.1	576.6	549.9	80.4	72.5	141.0
1010	1	16.5210	-362.9821	1208.4392	16.628	-2.194	91.611	425.4	389.4	815.5	42.6	61.0	131.7
1011	1	17.8582	-141.7783	1210.0095	5.026	-2.149	91.693	399.2	368.7	811.2	54.8	59.9	136.8
1012	1	17.9982	83.0094	1163.9801	-5.811	-2.197	91.587	470.7	450.3	775.2	75.7	80.0	136.9
1013	1	26.4726	-703.1992	1009.2193	34.845	-1.479	90.254	559.7	541.3	692.0	33.0	84.7	113.4
1014	1	34.7618	-856.2015	764.9949	47.108	-1.070	91.167	637.2	628.0	530.0	26.1	103.1	94.6
1015	1	33.5151	-960.9978	470.7212	61.006	-1.125	90.984	700.1	695.7	342.8	25.3	121.7	69.6
1016	1	-34.5686	-679.4563	1003.2579	34.033	-4.628	94.931	555.0	532.4	690.2	35.9	84.6	114.9
1017	1	-118.5683	-786.4337	823.5821	41.649	-8.878	97.895	611.4	601.5	574.0	36.3	95.8	104.9
1018	1	-181.2813	-858.9442	619.5542	49.958	-13.147	100.998	653.8	650.2	434.9	32.0	107.0	92.0
1019	1	-81.7983	-347.9440	1173.6457	17.103	-6.535	93.942	396.9	386.7	792.0	44.1	56.8	132.1
1020	1	-202.9303	-268.3704	1119.3411	12.973	-12.029	96.726	378.5	378.0	755.6	50.6	50.0	136.8
2000	2	-252.5488	579.0670	778.7081	-32.020	-16.378	85.954	431.9	430.3	527.3	44.6	76.8	121.8
2001	2	44.2732	266.3896	1133.0732	-10.908	0.877	89.515	367.6	342.9	756.3	52.5	62.1	134.9
2002	2	286.3743	263.0491	1048.5988	-11.053	13.132	91.801	313.2	328.2	701.8	55.1	48.6	138.4
2003	2	444.9313	282.5615	947.4811	-12.938	23.502	93.390	340.9	352.9	635.6	67.7	42.2	146.0
2004	2	592.9437	285.9828	808.5205	-14.709	33.949	96.127	407.7	415.6	543.9	94.2	41.8	160.2
2005	2	-135.6596	258.4232	1068.7025	-10.970	-8.193	88.798	340.6	325.3	715.5	49.6	55.7	136.2
2006	2	-293.7897	249.5584	976.3405	-11.449	-17.596	88.266	333.8	342.1	655.1	56.2	43.7	141.2
2007	2	-446.9502	256.2856	851.2401	-12.504	-26.993	85.598	394.1	402.7	572.8	74.7	39.2	150.5
2008	2	-428.3906	266.5114	861.1415	-13.107	-26.010	84.255	387.4	396.5	579.5	72.4	40.9	148.9
2009	2	-509.3605	296.1423	745.5194	-16.322	-34.007	82.629	433.9	440.3	502.7	93.3	44.4	159.1
2010	2	14.6602	453.2505	1041.4488	-21.804	-0.663	90.183	369.5	345.0	698.7	38.8	66.5	127.9
2011	2	15.2271	624.4230	882.0408	-33.427	-0.648	90.298	417.0	409.6	595.8	30.2	80.5	115.2
2012	2	16.7726	773.7255	697.8790	-44.253	-0.632	90.181	497.3	493.2	476.4	26.0	98.1	99.5
2013	2	35.8679	124.7606	1106.1913	-3.571	0.676	89.541	356.3	329.1	736.1	55.4	61.4	136.9
2014	2	31.3258	-68.0483	1035.3179	8.687	0.519	90.507	311.2	281.5	690.4	47.0	56.7	135.6
2015	2	33.2404	-260.9130	922.2425	22.601	0.617	90.309	302.6	294.7	620.6	37.6	63.6	127.0
2016	2	-62.9858	150.0631	1083.9859	-4.586	-4.679	91.239	331.5	310.9	722.7	51.2	55.8	137.2
2017	2	-153.9459	26.4710	1005.8833	2.641	-9.787	90.867	290.1	282.2	672.4	48.1	45.5	139.0
2018	2	-225.0455	-76.7819	905.7120	10.261	-15.036	90.513	301.6	298.5	608.6	52.7	47.2	139.9
2019	2	-82.0258	469.3277	1011.1201	-21.568	-5.432	89.324	369.5	359.8	680.4	40.3	63.2	128.6
2020	2	-200.0399	533.7250	892.2388	-26.367	-11.418	88.000	406.2	402.8	604.1	42.8	68.7	126.0

<<< Target Image Precisions and Residuals >>>

Units : microns

Photo	#Targets	#Rej	Mean Precision x	Mean Precision y	Mean Residual x	Mean Residual y	Max Residual x	Max Residual y
1000	50	0	1.65	1.65	1.49	1.24	3.16	4.09
1001	38	0	1.65	1.65	1.05	0.89	2.30	2.72
1002	42	0	1.65	1.65	2.27	0.87	6.10	1.93
1003	47	0	1.65	1.65	1.63	1.18	4.82	3.42
1004	38	0	1.65	1.65	1.45	1.93	3.15	4.73
1005	40	0	1.65	1.65	2.81	1.01	6.54	2.69
1006	40	0	1.65	1.65	3.02	1.33	6.21	3.12
1007	37	0	1.65	1.65	2.65	1.79	6.00	3.62
1008	39	0	1.65	1.65	2.22	1.49	4.90	2.92
1009	35	0	1.65	1.65	1.78	2.24	3.73	6.32
1010	45	0	1.65	1.65	1.00	0.72	3.65	2.43
1011	43	0	1.65	1.65	0.56	0.80	1.65	2.12
1012	36	0	1.65	1.65	0.70	0.85	3.05	2.53
1013	35	0	1.65	1.65	2.95	1.06	6.81	2.30
1014	36	0	1.65	1.65	2.70	0.83	7.00	2.52
1015	26	0	1.65	1.65	2.61	0.58	6.03	1.34
1016	33	0	1.65	1.65	2.38	1.17	5.72	2.75
1017	30	0	1.65	1.65	2.37	1.24	5.26	2.99
1018	31	0	1.65	1.65	2.68	1.59	6.11	3.33
1019	47	0	1.65	1.65	1.47	0.92	3.41	2.61
1020	45	0	1.65	1.65	1.82	1.10	4.25	3.56
2000	38	0	1.65	1.65	2.13	1.01	5.53	2.79
2001	44	0	1.65	1.65	0.70	0.72	1.72	2.10
2002	44	0	1.65	1.65	1.11	0.84	3.30	2.56
2003	47	0	1.65	1.65	1.36	1.21	5.30	3.78
2004	46	0	1.65	1.65	1.44	2.44	2.91	6.31
2005	43	0	1.65	1.65	1.08	1.04	3.01	2.42
2006	46	0	1.65	1.65	1.27	1.28	3.34	4.09
2007	45	0	1.65	1.65	1.33	2.17	3.26	6.96
2008	45	0	1.65	1.65	1.29	1.86	3.12	6.77

2009	43	0	1.65	1.65	1.17	2.12	2.64	6.48
2010	44	0	1.65	1.65	0.83	0.81	3.04	1.78
2011	40	0	1.65	1.65	0.78	1.07	2.83	2.2
2012	33	0	1.65	1.65	1.01	1.18	3.54	2.33
2013	44	0	1.65	1.65	1.23	1.17	3.67	3.14
2014	43	0	1.65	1.65	1.37	1.21	5.37	3.41
2015	40	0	1.65	1.65	1.92	1.17	6.03	3.11
2016	45	0	1.65	1.65	1.51	1.36	4.86	4.70
2017	45	0	1.65	1.65	1.72	1.66	5.04	5.52
2018	39	0	1.65	1.65	1.43	1.99	4.01	5.74
2019	43	0	1.65	1.65	1.07	1.01	2.84	2.10
2020	37	0	1.65	1.65	1.94	1.13	4.61	2.91
Mean	40.6	0.0	1.65	1.65	1.73	1.35		
All	1707	0					7.00	6.96

<<< Updated Targets >>>

Target (y=yes, n=no, R=rejected)	Coordinates X (millimetres)	Y	Z	Index	Precisions sX (microns)	sY	sZ	Mean Residuals x (microns)	y	Max Residuals x	y	#Ims
1 yyyyyyyyyyyyyyyyyyyyyyyyynyyyyyyyyyyyyyyyy	-0.0089	0.1296	-0.0233	7	131.1	131.2	8.4	0.73	0.76	1.56	1.76	41
5 yyyyyyyyyyyyyyyyyyyyyyyyyyyyyyyyyyyyyyyyy	95.6007	0.2048	-0.0494	7	125.5	125.5	8.4	1.15	0.95	3.08	2.66	42
7 yyyyyyyyyyyyyyyyyyyyyyyyyyyyyyyyyyyyyyyyy	95.9384	96.1550	0.0081	7	119.9	120.0	8.5	0.49	0.37	0.94	0.84	42
9 yyyyyyyyyyyyyyynyyyyyyyyyyyyyyyyyyyyyyyyy	-0.0356	96.0913	0.0314	7	125.7	125.8	8.5	0.99	0.67	1.90	1.42	41
28 yyyyyyyyyyyyyyyyyyyyyyyyyyyyyyyyynnyyyyyyyy	96.0546	-95.9719	0.0098	7	159.1	159.1	8.8	1.13	0.81	2.75	1.89	40
34 ynyynynnnnyyynnnnnnyyyyyyyyyyyyyyyyyyyyyyy	-0.2409	192.0544	0.0089	7	150.2	150.2	9.2	0.54	0.75	1.07	1.81	30
36 ynnnnnnnnnyyynnnnnnnyyyyyyyyyyyynyynyyyyyyyy	268.7080	192.4102	-0.0104	7	197.5	197.8	9.5	1.20	1.15	3.11	2.40	25
37 nnnynnnnnnnnnnynnyynnnnnnnnnnnnnnnnnnnnnnnn	383.4058	383.1282	-0.0069	7	322.2	326.4	9.9	1.55	2.85	2.45	3.42	4
64	Indeterminate - invalid or insufficient target images											
70 ynnnynnnnnnynnnnnnnyyyyyyynyyyyyyyyyyyyyyyy	-172.8896	191.8766	0.0105	7	213.6	213.5	9.4	1.44	0.79	2.60	1.85	25
76 yyyynyyyyyyyyyynyyyyyyyyynyyyyynynyyyyyyyy	-172.8690	-96.1781	-0.0095	7	223.1	223.3	9.3	2.59	1.36	5.11	3.38	37
90	Indeterminate - invalid or insufficient target images											
100	Indeterminate - invalid or insufficient target images											
113 ynyyynnnnnynnnnnnnnnnnyyyyyyyynynnyynyyynn	269.0489	-95.8979	0.0324	7	208.3	208.0	9.5	1.51	2.88	3.16	6.96	19
1000 nnnyynnnnnnnnnnnnnnnnnnyyynnnnnnnnnnnnnnn	-288.1154	-192.2866	0.1166	0	319.0	314.4	83.9	0.89	1.87	1.56	2.68	5
1001 yynnnyyyyynyynnnnnnyyyynnnyyyyyyyyyyyyyyyy	-192.1608	-192.2518	-0.3313	0	267.8	268.1	36.1	2.41	1.36	4.86	3.34	29
1002 yyyyyyynyyyyyyyyyynyyyyyyyyyyyyyyyyyyyyyy	-95.9309	-192.0938	0.4753	0	232.3	232.5	28.4	2.40	1.94	4.84	4.07	40
1003 yyyyyyyyyyynyyyyyyyyynynyyyyyyyyynyyyyyyyn	0.0954	-192.0271	0.2873	0	210.8	210.9	27.8	1.09	1.65	2.13	3.01	37

1004	96.1339	-191.9553	0.4858	0	207.4	207.3	27.2	1.54	1.29	3.74	2.86	41
yyyyyyyyyyyyyyyynyyyyyyyyyyyyyyyyyyyyyyy												
1005	192.3606	-191.8842	0.4351	0	223.2	222.9	30.6	2.13	1.69	5.43	6.32	35
yyyyyyynnyyyyyyyyyyyynnyyyyyyyynyyyyyyyyynn												
1006	288.2913	-191.8058	0.3406	0	254.6	254.1	41.1	3.09	2.56	6.81	6.48	24
ynyynynnnnyynynnnnnyyyyyynyyynynyyyynyynyn												
1007	384.1032	-191.6729	0.7925	0	302.1	296.9	82.1	1.80	1.42	3.65	2.43	7
ynnnnnyyyyynnnnnnnnnnnnnnnnnnnynnnnnnnnnnn												
1008	Indeterminate - invalid or insufficient target images											
1009	-192.2085	-96.0542	-0.1125	0	232.4	232.6	27.4	2.82	1.71	6.00	4.86	40
yyyyyyyyynyyyyyyyyyyyyyynyyyyyyyyyyyyyyyy												
1010	-95.9734	-95.9935	0.0355	0	190.5	190.7	25.1	1.50	1.36	3.00	2.67	39
yyyyyyyyyyyyyyyyyyynynyyyyyyyyyyynyyyyyyyy												
1011	0.0363	-95.9241	0.1982	0	163.6	163.6	24.2	0.74	1.10	1.70	1.85	39
yyyynyyyyyyyyyyyyyyyyyyyyyyyyyyynyyyyyyyn												
1012	192.2573	-95.7958	0.0594	0	179.2	179.0	26.9	1.99	1.36	4.11	3.48	37
yyyyyyyyyyyynyyyyynyyyyyyyyynynyyyyyyyyy												
1013	288.2226	-95.7387	0.4139	0	216.9	216.5	33.0	2.39	1.83	5.97	3.44	29
yyyyyyynnnynyyynyynynnyyyynyyynyynyynyyny												
1014	384.0143	-95.6860	0.4309	0	286.0	272.1	236.6	1.29	0.66	2.16	0.83	4
ynnnnynnnnynnnnnnnnnynnnnnnnnnnnnnnnnnnnn												
1015	-288.2260	0.0097	-0.0065	0	276.5	267.9	89.9	0.27	0.61	0.47	1.01	4
nnnyynnnnnnnnnnnnnnnnnnnyynnnnnnnnnnnnnnnn												
1016	-192.2251	-0.0014	-0.0414	0	211.0	211.0	26.1	1.84	0.93	3.40	3.44	40
yynynyyyyyyyyyyyyyyyyyyyyyyyyyyyyyyyyyyyy												
1017	-96.0053	0.0572	0.0426	0	163.7	163.7	23.1	1.10	0.69	2.42	1.74	40
yynyyyyyyyyyynyyyyyyyyyyyyyyyyyyyyyyyyyyy												
1018	192.1702	0.2553	-0.1699	0	150.2	150.1	23.9	1.06	0.78	3.40	1.93	41
yyyyyyyyynyyyyyyyyyyyyyyyyyyyyyyyyyyyyyyy												
1019	288.1004	0.3044	-0.1626	0	193.4	193.2	27.5	1.69	1.41	3.42	3.32	40
yyyyyyyyyyyyyyyyyynyyyyyyyyyyyyyyyynyyyyy												
1020	383.9901	0.3948	-0.0132	0	250.0	247.9	71.0	2.24	1.18	5.72	2.23	10
yynnnyyyyynnnnnnynnynnnnnnnnnnnynnnnnnnnnn												
1021	-288.1934	95.9677	-0.0347	0	274.6	265.4	91.6	0.35	0.68	0.46	1.01	4
nnnyynnnnnnnnnnnnnnnnnnnyynnnnnnnnnnnnnnnn												
1022	-192.2179	95.9542	0.1571	0	207.7	207.6	26.8	1.88	0.70	4.03	1.73	40
yynyyyyyyyyyyyyynyyyyyyyyyyyyyyyyyyyyyyyy												
1023	-96.0219	96.0212	0.4333	0	159.4	159.4	23.8	1.24	0.51	2.97	1.56	41
yyyynyyyyyyyyyyyyyyyyyyyyyyyyyyyyyyyyyyyy												

```
 1024    192.0955     96.2096    -0.0388    0    145.4   145.4    24.2    0.68   0.45   1.84   0.89  41
yyyyyyynyyyyyyyyyyyyyyyyyyyyyyyyyyyyyyyyyy
 1025    288.0124     96.2589     0.7168    0    189.7   189.7    28.7    1.01   0.78   2.10   1.56  36
yyyyyyyyynyyyyyynyyyyyyyyynyyyyyynyynyyyyn
 1026    383.8937     96.2581    -0.0279    0    244.7   246.7    67.1    1.23   0.55   2.34   0.79   9
yyynynnyynynnnnnynynnnnnnnnnnnnnnnnnnnnnnn
 1027   -288.1175    191.9549    -0.1186    0    276.6   278.1    58.0    2.82   1.68   6.53   2.95   7
nnynynnyyynnnynnnnnnnnnnnynnnnnnnnnnnnnnnn
 1028   -192.2099    191.9853    -0.0074    0    223.4   223.2    30.6    2.17   1.22   5.99   2.57  35
ynnyyyyyyyyynnynynyyyyyynyyyyyyyyyyyyyyyyy
 1029    -96.0412    192.0646     0.0683    0    179.3   179.2    27.6    1.45   0.92   5.26   2.25  38
ynyynyyyyyyyynnyyyyyyyyyyyyyyyyyyyyyyyyyyy
 1030     95.8602    192.2150    -0.0594    0    145.4   145.6    25.2    0.58   0.59   1.29   1.48  40
ynyyyyyyyyyyynyyyyyyyyyyyyyyyyyyyyyyyyyyyy
 1031    192.0489    192.2764    -0.0248    0    166.9   167.1    27.7    1.10   0.69   2.93   1.72  38
yyyyynynyyyyyyyyynnyyyyyyyyyyyyyyyyyyyyyyy
 1032    287.9372    192.3037    -0.0071    0    206.7   206.9    32.9    1.63   1.40   3.45   2.88  34
ynynyyynyyyyyyynyyyyynyyyyyyyyyynnyyyyyyyn
 1033    383.7592    192.2653    -0.0005    0    257.4   260.4    60.5    1.63   2.03   2.59   4.77  12
ynyyynnynynnnyynyyyynnnnnnnnnnnnnnnnnnnnnn
 1034   -288.1236    288.0770    -0.4582    0    302.0   302.7    58.2    2.88   2.46   4.82   4.75  11
nyyynyyyynnnnnnnnnyynnnyynnnnnnnnnnnnnnnnn
 1035   -192.2108    288.0554    -0.3022    0    254.5   254.3    35.1    1.99   1.75   3.44   4.08  34
yyyyyyyyyynyynnnnnnyyyyyyyyyyyyyyyyyyyynyy
 1036    -96.0496    288.1092    -0.4974    0    216.9   216.8    32.3    1.76   1.39   6.03   2.45  35
ynnyyyynyyyyyynyynnyyyyyyyyyyyyyyyyyyyynyy
 1037     -0.0948    288.1729    -0.5282    0    193.5   193.6    31.0    0.67   1.19   1.68   2.94  34
yynynnynyyyyyynyynnyyyyyyyyyyyyyyyyyyyynyy
 1038     95.8145    288.2336    -0.5940    0    189.7   190.0    31.0    0.99   0.88   2.56   1.76  37
yyyynynyyyyyyyynynnyyyyyyyyyyyyyyyynyyyyyy
 1039    191.9603    288.2808    -0.5149    0    206.6   207.0    31.1    2.04   1.16   5.05   2.92  38
yyyyynyyynnyyyyynyyyyyyyyyyyyyyyyyyyyyyyyy
 1040    287.8294    288.2909    -0.3800    0    239.8   240.2    38.2    2.26   2.16   5.37   4.73  31
yyyyyyyynnnyyynnnynyynyyyyyyyyynnyyyyyyn
 1041    383.6599    287.9880    -0.0513    0    285.1   302.2   120.1    0.67   0.66   1.02   1.23   5
nnyyynnnnynnnynnnnnnnnnnnnnnnnnnnnnnnnnnnn
 1042   -192.2528    383.9562    -1.2757    0    296.4   296.1    45.9    3.06   2.18   6.21   5.67  21
nyynnnynnnyynnnnnnnyyyynyynyyyyynnyynnnnyy
 1043    -96.0660    383.9595    -1.2923    0    264.6   264.5    38.3    2.81   1.76   7.00   3.37  30
yyyynynyyyyyynyynnnnnnyynyyyyyyyyynynyynyy
```

1044	-0.1449	383.9926	-1.3725	0	245.7	245.9	36.1	1.41	1.73	4.01	3.38	35
yyyyynnnnyyynyynynyyyyyyyyyyyyyyyyyyyyyyyy												
1045	95.7747	384.0482	-1.3117	0	242.7	243.1	35.3	1.60	1.07	4.10	2.10	37
yyyyyyyyynyynnyyynyyyyyyyyyyyyyyyyyyyyynyy												
1046	191.8938	384.0851	-1.3994	0	256.1	256.6	37.8	2.49	1.50	6.11	3.09	33
yyyynnyynnyynynnynyyyyyyyyyyyyyyyyyynyyyyyy												
1047	287.7797	384.1355	-1.5567	0	283.7	284.2	47.0	2.83	2.91	6.54	6.31	24
ynynnynynnyyynnnnnnyynyyyyyyyyyynnynyyyynn												
Mean												
29.4												

<<< Target Precision Summary >>>

Units: microns

	Target	sX	sY	sZ
Minimum	7	119.86	119.97	8.50
Mean		218.30	218.07	38.51
Maximum	1014	285.96	272.10	236.62

Mean precision of target coordinates: 158.29

Relative precision for the network 1: 5000

<<< Target Coordinate Corrections >>>

Units : microns

Target	Corrections			Precisions			Significance		
	x	y	z	x	y	z	x	y	z
1	1.4	1.2	-9.7	131.1	131.2	8.4	0.0	0.0	1.2
5	1.8	1.5	-20.4	125.5	125.5	8.4	0.0	0.0	2.4
7	-0.9	-1.1	3.3	119.9	120.0	8.5	0.0	0.0	0.4
9	-0.1	-1.6	13.1	125.7	125.8	8.5	0.0	0.0	1.5
28	-1.6	1.4	3.8	159.1	159.1	8.8	0.0	0.0	0.4
34	0.7	-1.9	4.1	150.2	150.2	9.2	0.0	0.0	0.5
36	-1.1	-2.3	-4.8	197.5	197.8	9.5	0.0	0.0	0.5
37	-2.5	0.6	-3.4	322.2	326.4	9.9	0.0	0.0	0.3
64	0.0	0.0	0.0	-1.0	-1.0	-1.0			
70	3.3	-1.4	5.0	213.6	213.5	9.4	0.0	0.0	0.5
76	2.8	2.3	-4.5	223.1	223.3	9.3	0.0	0.0	0.5
90	0.0	0.0	0.0	-1.0	-1.0	-1.0			
100	0.0	0.0	0.0	-1.0	-1.0	-1.0			
113	-5.9	3.4	15.1	208.3	208.0	9.5	0.0	0.0	1.6
RMS	2.24	1.63	8.59						

*** End of VMS calibration log file ***

Appendix F: Dual calibration data, network log file, Clermont

```
*** Vision Measurement System (VMS) ***
Self-calibrating Photogrammetric Network Solution

Version 7.6 - Mark Shortis and Stuart Robson - August
2003


Project name:  dual calib france

VMS bundle adjustment log file:     dual calib
france_network.log written on Fri Oct 12 22:19:46 2007


<<< Program control variables >>>

Network datum definition type:         external
constraints on targets

Additional parameter set type:         all parameters
fixed

Maximum iterations for a solution:     10

Default target image precision:        1.28

Minimum images for a network target:   4

Rejection criterion for image errors: 5.0


<<< Initial Camera Calibration Sets >>>

Units: millimetres

Calibration set: 1

Parameter        Value              Precision

    1             0.120
    2            -0.048
    3            28.961
    4    -1.2226e-004
    5     3.5589e-008
    6     6.3007e-010
    7     2.0497e-006
    8    -1.1952e-005
    9    -5.3778e-005
   10     4.1515e-005

Pixel size in mm      Format size in pixels

   x          y          x          y
0.0074     0.0074       3072       2048
```

Calibration set : 2

Parameter	Value	Precision
1	0.072	
2	-0.012	
3	28.854	
4	-1.4597e-004	
5	3.2864e-007	
6	-5.6251e-010	
7	1.8535e-006	
8	1.9378e-005	
9	-1.0700e-004	
10	1.3875e-004	

Pixel size in mm		Format size in pixels	
x	y	x	y
0.0074	0.0074	3072	2048

<<< Initial Camera Locations >>>

Photo	Cal Set	X	Y (millimetres)	Z	Omega	Phi (degrees)	Kappa	#Images
1000	1	-331.916	117.192	1075.505	9.25	-19.83	-94.78	34
1001	1	23.857	425.983	1336.567	-10.75	-0.08	-92.18	41
1002	1	30.576	562.515	1241.812	-17.23	-0.13	-92.37	39
1003	1	38.421	793.591	1037.650	-28.55	0.03	-92.80	41
1004	1	37.226	932.783	863.057	-36.79	0.04	-92.61	34
1005	1	46.823	1087.389	581.545	-48.56	0.24	-93.14	31
1006	1	-178.113	416.569	1248.777	-11.19	-9.21	-94.31	56
1007	1	-372.067	419.505	1130.474	-11.69	-18.31	-96.48	52
1008	1	-546.037	419.317	982.970	-12.55	-27.33	-98.47	46
1009	1	-688.824	419.706	816.305	-13.88	-35.95	-100.72	46
1010	1	34.755	300.587	1324.395	-5.79	-0.13	-91.46	53
1011	1	35.645	22.229	1252.108	6.43	-0.04	-91.68	50
1012	1	36.279	-217.650	1133.470	17.92	-0.22	-91.02	43
1013	1	36.196	-470.359	930.208	31.60	-0.40	-90.36	42
1014	1	188.435	425.714	1284.782	-10.56	6.74	-90.66	46
1015	1	386.757	419.762	1185.376	-10.83	15.79	-89.62	50
1016	1	596.325	416.028	1030.923	-11.56	26.29	-87.76	47
1017	1	785.709	431.418	818.849	-13.14	38.14	-84.44	39
1018	1	236.772	306.803	1247.667	-4.61	9.51	-90.18	51
1019	1	329.134	205.172	1181.624	0.13	13.75	-89.80	53
1020	1	449.387	104.880	1076.062	5.05	19.85	-90.62	47
1021	1	-118.081	553.460	1190.689	-16.80	-6.77	-95.35	46
1022	1	-162.517	825.855	896.484	-31.52	-9.31	-97.08	44
1023	1	-245.542	862.769	698.274	-38.77	-17.00	-103.67	45
1024	1	175.380	542.975	1205.057	-16.12	7.15	-90.16	45
1025	1	346.204	728.241	879.747	-30.44	17.46	-87.18	39
1026	1	-272.804	262.233	1176.865	-1.50	-13.25	-96.48	50
2000	2	-360.573	-784.504	742.759	53.69	-18.94	-79.67	38
2001	2	-18.174	-534.642	1353.457	31.00	-2.56	-91.55	53
2002	2	-17.515	-389.696	1366.819	24.50	-2.83	-91.61	57
2003	2	-17.226	-115.531	1347.059	13.18	-3.00	-92.04	60

2004	2	-15.149	77.531	1299.609	4.94	-2.86	-91.92	56
2005	2	-14.522	340.211	1182.952	-6.88	-3.05	-92.45	48
2006	2	-231.809	-543.103	1261.943	31.25	-10.88	-86.92	54
2007	2	-431.196	-539.751	1134.198	32.51	-18.94	-82.07	54
2008	2	-603.323	-539.748	978.997	34.58	-26.55	-76.48	51
2009	2	-743.362	-539.315	806.178	37.50	-33.65	-70.39	51
2010	2	3.690	-658.896	1257.840	36.00	-2.14	-90.98	52
2011	2	-1.063	-900.527	984.464	48.18	-2.30	-91.14	44
2012	2	11.148	-1068.558	688.000	59.66	-1.98	-90.55	41
2013	2	22.707	-1192.176	295.759	73.37	-1.67	-89.96	38
2014	2	149.196	-535.330	1301.970	31.31	3.43	-94.90	51
2015	2	340.028	-540.550	1210.578	31.90	10.83	-100.29	53
2016	2	549.907	-543.608	1065.725	33.47	19.63	-106.53	52
2017	2	750.982	-528.272	859.039	36.81	29.72	-114.04	56
2018	2	197.619	-651.265	1165.854	37.46	5.80	-96.41	50
2019	2	285.017	-742.995	1022.376	42.63	9.21	-99.02	49
2020	2	376.673	-826.276	846.412	48.22	13.18	-103.86	46
2021	2	-196.790	-399.106	1297.192	25.37	-9.80	-89.36	55
2022	2	-260.901	-69.752	1232.963	10.99	-12.81	-88.92	57
2023	2	-420.547	6.717	1099.185	5.41	-22.78	-88.32	51
2024	2	146.243	-411.832	1313.962	25.80	4.18	-94.87	51
2025	2	334.809	-173.302	1215.103	12.91	13.71	-99.74	53
2026	2	-347.716	-683.113	1016.917	41.65	-15.24	-85.74	44

<<< Initial Targets >>>

Target	X	Y (millimetres)	Z	Index	sX	sY (microns)	sZ	#Images
1	0.0831	0.1747	0.0390	7	15.7	15.8	7.2	41
5	95.5153	0.1803	0.0418	7	15.5	15.6	7.0	48
7	95.9197	96.0883	0.0362	7	15.7	15.9	7.2	41
9	-0.0304	96.0785	0.0559	7	15.8	16.1	7.4	36
28	95.9012	-95.7389	0.0325	7	18.2	18.3	7.7	37
34	-0.0494	191.9780	0.0466	7	18.0	18.2	7.5	38
36	268.6190	192.0729	-0.1641	7	23.2	23.4	8.2	31
37	383.5069	383.4507	-0.0136	7	42.6	46.7	9.8	5
64	-287.7761	383.5221	-0.0125	7	36.1	35.9	9.0	17
70	-172.6964	191.8822	0.0419	7	22.8	22.9	8.0	33
76	-172.6831	-95.6803	-0.1102	7	22.9	23.1	8.2	30
90	-287.7886	-249.0049	-0.0477	7	35.7	35.4	9.5	10
100	383.8858	-249.3583	0.0148	7	38.7	38.1	9.6	6
113	268.6324	-95.7921	0.0163	7	23.1	23.1	8.0	34
1000	-287.8376	-191.5832	-0.9600	0				32
1001	-191.9443	-191.5974	-0.6470	0				40
1002	-96.0148	-191.5810	-0.2385	0				47
1003	-0.0766	-191.6216	-0.0589	0				50
1004	95.8631	-191.6628	0.0686	0				50
1005	191.8113	-191.7194	0.1608	0				49
1006	287.8016	-191.7310	0.1590	0				44
1007	383.8584	-191.7492	-0.0905	0				15
1008	-287.7632	-95.7272	-0.7569	0				35
1009	-191.8879	-95.7064	-0.1980	0				48
1010	-95.9707	-95.7167	-0.1475	0				52
1011	-0.0449	-95.7298	-0.0029	0				53
1012	191.8358	-95.7791	0.1039	0				51
1013	287.8279	-95.7940	-0.0499	0				49
1014	383.8506	-95.7788	-0.2269	0				19
1015	-287.7412	0.1207	-0.5160	0				38
1016	-191.8716	0.1533	-0.2731	0				52

1018	191.8437	0.1745	0.0237	0			50
1019	287.8368	0.1625	-0.1660	0			49
1020	383.8483	0.1672	-0.4224	0			23
1021	-287.7227	95.9603	-0.4300	0			40
1022	-191.8560	96.0042	-0.1480	0			51
1023	-95.9629	96.0379	0.0805	0			51
1024	191.8534	96.1041	-0.0170	0			53
1025	287.8479	96.1135	-0.2857	0			52
1026	383.8798	96.1238	-0.6749	0			28
1027	-287.7305	191.8155	-0.3182	0			41
1028	-191.8674	191.8683	-0.0368	0			49
1029	-95.9689	191.9215	0.1312	0			52
1030	95.8920	192.0146	-0.0084	0			53
1031	191.8397	192.0475	-0.0970	0			51
1032	287.8371	192.0621	-0.4093	0			52
1033	383.8426	192.0788	-0.8799	0			28
1034	-287.7350	287.6834	-0.1643	0			34
1035	-191.8823	287.7518	-0.0656	0			47
1036	-95.9956	287.8166	-0.0005	0			53
1037	-0.0683	287.8815	-0.0915	0			54
1038	95.8677	287.9342	-0.2013	0			54
1039	191.8219	287.9896	-0.3183	0			53
1040	287.8175	288.0334	-0.7031	0			50
1041	383.8038	287.9907	-1.1917	0			26
1042	-191.9168	383.6142	-0.1125	0			48
1043	-96.0261	383.7141	-0.1541	0			52
1044	-0.0935	383.8008	-0.3043	0			53
1045	95.8445	383.8739	-0.4327	0			53
1046	191.8020	383.9334	-0.5818	0			51
1047	287.8201	383.9773	-1.1467	0	-1.0	-1.0	41
2	47.9286	81.7742	0.0000	-1	-1.0	-1.0	0 (not yet
intersected)							

<<< Input Summary >>>

Number of camera calibration sets:	2
Number of target image observations:	2575
Total number of exposures:	54
Number of exposures in the network:	54
Total number of targets:	63
Number of targets in the network:	62
Total number of survey measurements:	0
Number of survey measurements in the network:	0

*** Results for the Calibration Solution ***

Solution completed successfully after 5 iteration(s)

Unit weight estimate (sigma zero):	1.00
RMS image residual (microns):	1.17
Number of rejected target images:	3
Number of observables in the network:	5206
Number of unknowns in the network:	510
Number of redundancies in the network:	4696

<<< Fixed Camera Calibration Sets >>>

Parameter	Value
Units : millimetres	
1	0.1200
2	-0.0483
3	28.9608
4	-1.2226e-004
5	3.5589e-008
6	6.3007e-010
7	2.0497e-006
8	-1.1952e-005
9	-5.3778e-005
10	4.1515e-005

Lens Distortion Profiles for Camera Calibration Set: 1

Units : microns

Radius	Radial Distortion		Decentring Distortion	
	Value	Precision	Value	Precision
0.0	0.00	0.00	0.00	0.00
2.0	-0.98	0.00	0.05	0.00
4.0	-7.78	0.00	0.19	0.00
6.0	-25.96	0.00	0.44	0.00
8.0	-60.11	0.00	0.78	0.00
10.0	-112.40	0.00	1.21	0.00
12.0	-179.83	0.00	1.75	0.00
14.0	-249.92	0.00	2.38	0.00

<<< Fixed Camera Calibration Sets >>>

Parameter	Value
Units : millimetres	
1	0.0725
2	-0.0122
3	28.8541
4	-1.4597e-004
5	3.2864e-007
6	-5.6251e-010
7	1.8535e-006
8	1.9378e-005
9	-1.0700e-004
10	1.3875e-004

Lens Distortion Profiles for Camera Calibration Set: 2

Units : microns

Radius	Radial Distortion Value	Radial Distortion Precision	Decentring Distortion Value	Decentring Distortion Precision
0.0	0.00	0.00	0.00	0.00
2.0	-1.16	0.00	0.08	0.00
4.0	-9.01	0.00	0.31	0.00
6.0	-29.13	0.00	0.70	0.00
8.0	-65.15	0.00	1.25	0.00
10.0	-118.73	0.00	1.95	0.00
12.0	-190.62	0.00	2.80	0.00
14.0	-283.09	0.00	3.82	0.00

<<< Updated Camera Location Values and Precisions >>>

Photo	Cal Set	X	Y	Z	Omega	Phi	Kappa	sX	sY	sZ	sO	sP	sK
		(millimetres)			(degrees)			(microns)			(seconds of arc)		
1000	1	-331.8953	117.2272	1075.5059	9.253	-19.825	-94.784	161.1	224.2	100.3	42.2	31.6	12.4
1001	1	23.8565	425.9653	1336.5666	-10.748	-0.080	-92.179	242.8	291.0	127.7	45.4	35.9	9.9
1002	1	30.5720	562.5153	1241.8054	-17.230	-0.135	-92.373	199.4	210.9	126.6	36.1	30.7	10.3
1003	1	38.4280	793.5925	1037.6441	-28.550	0.025	-92.798	135.5	108.4	114.2	23.3	22.5	10.8
1004	1	37.2336	932.7843	863.0488	-36.786	0.042	-92.614	106.7	75.2	103.2	18.8	18.8	11.1
1005	1	46.8323	1087.3878	581.5347	-48.557	0.237	-93.137	85.9	62.5	92.7	16.0	16.0	11.9
1006	1	-178.1117	416.5908	1248.7605	-11.193	-9.205	-94.308	167.6	182.4	92.6	30.0	26.5	8.8
1007	1	-372.0598	419.5230	1130.4587	-11.690	-18.311	-96.483	128.0	137.2	90.1	24.7	22.7	9.5
1008	1	-546.0206	419.3279	982.9630	-12.550	-27.327	-98.469	95.2	110.2	93.1	22.7	19.9	10.9
1009	1	-688.8091	419.7125	816.3020	-13.879	-35.947	-100.725	64.0	82.4	81.9	19.7	15.6	11.7
1010	1	34.7627	300.5829	1324.3898	-5.792	-0.125	-91.464	225.3	262.5	85.8	40.6	33.8	8.5
1011	1	35.6818	22.2355	1252.1015	6.433	-0.043	-91.680	261.9	254.0	54.8	40.9	42.0	9.4
1012	1	36.3113	-217.6410	1133.4666	17.917	-0.219	-91.025	231.6	187.1	87.1	34.2	39.6	12.1
1013	1	36.2268	-470.3513	930.2070	31.603	-0.397	-90.364	121.5	91.2	89.0	21.7	22.6	11.4
1014	1	188.4380	425.6957	1284.7841	-10.559	6.738	-90.655	229.4	216.6	105.9	34.9	35.5	9.6
1015	1	386.7690	419.7479	1185.3750	-10.831	15.786	-89.621	154.9	165.8	105.6	28.9	26.5	10.0
1016	1	596.3463	416.0219	1030.9099	-11.559	26.289	-87.764	99.5	120.5	99.6	23.9	20.0	11.1
1017	1	785.7192	431.4211	818.8293	-13.144	38.137	-84.445	67.1	85.9	90.7	20.8	16.3	12.3
1018	1	236.7801	306.7878	1247.6636	-4.614	9.513	-90.178	203.6	218.7	92.4	35.8	33.0	9.1
1019	1	329.1503	205.1511	1181.6167	0.130	13.747	-89.798	166.3	182.7	83.8	31.2	29.0	9.5
1020	1	449.4176	104.8752	1076.0427	5.046	19.857	-90.620	135.6	154.9	87.8	28.7	26.6	10.5
1021	1	-118.0793	553.4676	1190.6771	-16.803	-6.769	-95.354	178.5	165.1	108.2	29.4	28.6	9.9
1022	1	-162.5109	825.8575	896.4725	-31.517	-9.308	-97.076	95.7	76.2	90.8	18.0	17.2	9.8
1023	1	-245.5327	862.7714	698.2638	-38.774	-16.999	-103.671	69.8	58.2	75.7	14.7	14.4	10.4
1024	1	175.2973	543.1274	1204.9751	-16.124	7.144	-90.159	194.3	181.7	114.4	31.9	31.1	9.9
1025	1	346.1574	728.3064	879.6885	-30.441	17.454	-87.186	97.4	83.2	99.8	20.5	18.7	11.0
1026	1	-272.7934	262.2493	1176.8569	-1.505	-13.248	-96.481	174.4	195.0	85.6	33.7	30.1	9.5
2000	2	-360.5660	-784.4923	742.7688	53.693	-18.944	-79.675	89.0	73.3	105.4	18.1	16.0	13.9
2001	2	-18.1411	-534.6374	1353.4558	30.995	-2.554	-91.553	217.1	174.0	121.2	27.6	28.9	12.7
2002	2	-17.4733	-389.6779	1366.8242	24.503	-2.832	-91.610	222.2	185.9	101.2	28.5	30.5	11.4
2003	2	-17.1923	-115.5233	1347.0552	13.180	-3.003	-92.042	235.9	246.8	76.3	37.4	34.6	9.7
2004	2	-15.1197	77.5448	1299.6037	4.940	-2.858	-91.919	253.7	280.3	54.4	43.6	39.2	9.0
2005	2	-14.5199	340.2192	1182.9428	-6.883	-3.054	-92.447	198.5	203.1	85.0	35.4	33.3	8.7
2006	2	-231.7738	-543.0883	1261.9533	31.245	-10.875	-86.925	162.7	141.0	119.2	24.2	23.3	11.4
2007	2	-431.1680	-539.7387	1134.2139	32.514	-18.939	-82.071	121.3	115.3	115.4	21.6	19.6	11.3
2008	2	-603.3014	-539.7394	979.0150	34.583	-26.552	-76.484	91.1	97.3	111.6	20.4	16.7	12.0
2009	2	-743.3457	-539.3092	806.1959	37.503	-33.645	-70.395	70.1	80.4	99.4	18.9	14.1	12.6
2010	2	3.6337	-659.0071	1257.7553	36.004	-2.146	-90.974	165.8	135.1	126.5	23.8	22.4	11.8
2011	2	-1.0448	-900.5157	984.4665	48.182	-2.295	-91.143	128.2	90.2	131.7	20.4	18.3	12.7
2012	2	11.1608	-1068.5475	688.0065	59.655	-1.982	-90.547	98.3	71.9	114.5	16.8	14.8	13.1
2013	2	22.7158	-1192.1703	295.7612	73.367	-1.666	-89.963	82.4	77.1	94.7	14.5	12.8	13.0
2014	2	149.2308	-535.3187	1301.9642	31.308	3.428	-94.903	188.3	159.9	120.6	26.4	25.8	11.9
2015	2	340.0547	-540.5384	1210.5673	31.901	10.829	-100.288	150.5	131.7	113.9	23.1	22.3	11.4

2016	2	549.9256	-543.5966	1065.7113	33.474	19.627	-106.533	108.4	103.9	108.2	20.2	18.4	11.4
2017	2	750.9925	-528.2623	859.0262	36.809	29.726	-114.043	70.0	76.8	92.0	17.2	13.9	11.7
2018	2	197.6469	-651.2526	1165.8490	37.460	5.804	-96.406	145.5	117.6	114.5	21.9	20.9	11.7
2019	2	285.0425	-742.9762	1022.3766	42.627	9.208	-99.022	114.9	91.7	110.0	19.3	17.5	11.3
2020	2	376.6929	-826.2604	846.4123	48.218	13.184	-103.863	95.6	74.4	101.3	17.2	15.5	11.8
2021	2	-196.7509	-399.0892	1297.2018	25.367	-9.796	-89.364	190.0	170.4	113.7	27.8	27.7	11.5
2022	2	-260.8669	-69.7237	1232.9717	10.992	-12.809	-88.924	170.1	203.1	80.9	33.5	27.9	9.6
2023	2	-420.5251	6.7515	1099.1920	5.408	-22.780	-88.318	120.5	144.6	92.8	26.5	23.5	10.6
2024	2	146.3099	-411.6261	1314.0646	25.786	4.182	-94.868	219.7	188.3	112.2	30.2	31.2	12.0
2025	2	334.7267	-173.3674	1215.1116	12.913	13.705	-99.737	171.8	182.8	96.3	31.0	28.5	10.0
2026	2	-347.8800	-682.8857	1016.9887	41.641	-15.247	-85.739	126.9	108.2	123.3	22.2	20.4	13.0

<<< Target Image Precisions and Residuals >>>

Units : microns

Photo	#Targets	#Rej	Mean Precision x	Mean Precision y	Mean Residual x	Mean Residual y	Max Residual x	Max Residual y
1000	34	0	1.24	1.24	1.04	2.32	2.13	4.89
1001	41	0	1.24	1.24	1.09	0.85	2.92	2.98
1002	39	0	1.24	1.24	0.72	0.47	2.21	1.10
1003	41	0	1.24	1.24	1.02	0.45	2.46	1.24
1004	34	0	1.24	1.24	1.17	0.46	3.65	1.48
1005	31	0	1.24	1.24	1.63	0.42	4.24	1.21
1006	56	0	1.24	1.24	0.50	0.41	1.20	1.35
1007	52	0	1.24	1.24	0.79	0.59	2.56	2.58
1008	46	0	1.24	1.24	0.86	0.79	2.11	2.19
1009	46	0	1.24	1.24	0.93	1.00	2.55	3.74
1010	53	0	1.24	1.24	1.08	0.88	3.45	2.83
1011	50	0	1.24	1.24	0.97	0.93	4.18	2.83
1012	43	0	1.24	1.24	1.20	0.78	3.27	1.85
1013	42	0	1.24	1.24	2.17	0.86	5.42	1.65
1014	46	0	1.24	1.24	0.53	0.50	1.46	1.16
1015	50	0	1.24	1.24	0.74	0.73	1.72	1.71
1016	47	0	1.24	1.24	0.76	1.00	1.79	2.21
1017	39	0	1.24	1.24	0.76	1.03	1.78	3.03
1018	51	0	1.24	1.24	0.77	0.62	2.36	1.86
1019	53	0	1.24	1.24	0.84	0.75	1.99	1.84
1020	47	0	1.24	1.24	0.83	1.08	2.02	2.13
1021	46	0	1.24	1.24	0.85	0.58	1.91	1.59
1022	44	0	1.24	1.24	1.89	0.73	3.54	1.77
1023	45	0	1.24	1.24	1.80	0.69	3.54	1.52
1024	45	0	1.24	1.24	2.04	1.35	5.35	3.93
1025	39	0	1.24	1.24	2.74	1.38	4.90	3.63
1026	50	0	1.24	1.24	1.40	1.88	3.66	4.81
2000	38	0	1.24	1.24	2.84	1.33	5.30	3.12
2001	53	0	1.24	1.24	1.97	0.98	5.11	2.75

2002	57	0	1.24	1.24	1.09	0.47	5.02	1.49
2003	60	0	1.24	1.24	0.74	0.60	2.11	3.54
2004	56	0	1.24	1.24	0.46	0.39	1.94	1.33
2005	48	0	1.24	1.24	0.93	0.53	4.44	1.58
2006	54	0	1.24	1.24	1.04	0.60	4.03	1.40
2007	54	0	1.24	1.24	1.13	0.74	3.48	2.11
2008	51	0	1.24	1.24	0.94	0.66	2.36	1.71
2009	51	0	1.24	1.24	1.02	1.04	3.28	2.57
2010	51	1	1.24	1.24	1.90	0.87	4.73	2.65
2011	44	0	1.24	1.24	2.12	0.47	5.34	1.21
2012	41	0	1.24	1.24	2.59	0.51	4.91	1.17
2013	38	0	1.24	1.24	2.68	0.77	5.24	2.05
2014	51	0	1.24	1.24	1.03	0.49	2.20	1.18
2015	53	0	1.24	1.24	1.05	0.58	2.37	1.29
2016	52	0	1.24	1.24	0.99	0.60	2.31	1.90
2017	56	0	1.24	1.24	0.86	0.85	1.93	2.81
2018	50	0	1.24	1.24	1.73	0.60	3.59	1.51
2019	49	0	1.24	1.24	1.94	0.63	3.67	2.05
2020	46	0	1.24	1.24	1.92	0.72	4.09	1.63
2021	55	0	1.24	1.24	1.19	0.81	3.47	2.35
2022	57	0	1.24	1.24	0.93	0.87	4.77	2.37
2023	51	0	1.24	1.24	0.65	1.02	1.65	2.16
2024	51	0	1.24	1.24	1.87	1.29	4.42	3.62
2025	53	0	1.24	1.24	1.14	1.75	2.56	4.76
2026	42	2	1.24	1.24	2.55	1.25	4.87	2.87
Mean	47.6	0.1	1.24	1.24	1.40	0.90		
All	2572	3					5.42	4.89

<<< Updated Targets >>>

Target	Coordinates X	Y	Z	Index	Precisions sX	sY	sZ	Mean Residuals x	y	Max Residuals x	y	#Ims
Photo List (y=yes, n=no, R=rejected)	(millimetres)				(microns)			(microns)				
1	0.0834	0.1753	0.0417	7	9.1	9.3	6.7	0.51	0.55	1.15	1.74	41
yyyynnyyyyyyyynyyyyyyynyynyyynyyynyyyyynnnnyynnyyyyyyy												
5	95.5150	0.1809	0.0458	7	8.9	9.1	6.5	0.52	0.51	1.54	1.03	48
yyyyynyynyyyyyyyyyyyyynyyyyyyyyyyyynyyynynyyyyyyyyyyyy												
7	95.9191	96.0881	0.0399	7	9.2	9.4	6.7	0.59	0.31	1.52	1.01	41
yyyynyyyynyyyyyyyyyyyyynyyyyyyyyyyynnyynynnnynynyyyynyy												
9	-0.0305	96.0784	0.0621	7	9.4	9.6	6.9	0.57	0.50	1.15	0.91	36
yyyynnyyyyyyyyyyynyyyynynyyyynyyynnyynnyynnnynnnnyynyy												
28	95.9013	-95.7377	0.0364	7	10.3	10.5	7.3	1.03	0.97	4.77	2.35	37
nnnnnnynnnyyyyyyyyyyynnnnyyyyyyyyyyynnyyyyyyyyynnyyyyyy												
34	-0.0492	191.9778	0.0516	7	10.2	10.4	7.0	0.61	0.57	2.18	1.53	38
yyyynyyyyynyyyyyyyyyyyyyyyynnnyyynnnnnyynyynyynynyynyn												
36	268.6195	192.0710	-0.1852	7	12.8	13.1	7.9	1.81	1.01	4.24	2.13	31
yynnyyyyynynyyyyynyyynynyyynnnyyyyynnnnnynnnnnynyynyyn												
37	383.5046	383.4530	-0.0161	7	27.6	31.9	9.7	1.48	2.37	2.34	3.54	5
nnnnnnnnnnnnnnnnnnnnnnnnnnnnnnynnynnnnnnynnnnnnnnnnnnnnyy												
64	-287.7760	383.5211	-0.0122	7	20.1	19.9	8.8	2.06	0.80	4.73	1.88	17
nnnnnnnnnynnnnyyyyyyynnnnnnnnnyynnynnnynnnyynnyynnnnnn												
70	-172.6946	191.8823	0.0461	7	12.3	12.5	7.6	1.25	1.03	3.23	3.93	33
yyynyyyyyynyyyyynnyyyyyyyyyynnyyyyynynnnynnnnnnnnnnyyyyn												
76	-172.6821	-95.6796	-0.1236	7	12.5	12.7	7.9	1.59	1.35	4.03	4.03	30
yyynnnyyyyyyyyynnnyynnnnynyynyyyyyynnynnynnnnnnnnyynyyy												
90	-287.7922	-249.0099	-0.0555	7	20.7	20.3	9.4	3.37	1.47	5.11	2.37	10
nnnnnnnnnnyynnnnnnnnnnnnnnynnyynyynnnnnnnnnnnnnnnnnnynyyn												
100	383.8887	-249.3628	0.0182	7	24.0	23.3	9.3	1.12	0.81	2.23	1.56	6
nnnnnnyynnnnnnnnnnnnnnynnnnnynnnnnnnnnnnnnnnnynnnnnynnn												
113	268.6313	-95.7910	0.0192	7	12.6	12.6	7.6	1.68	0.91	4.42	2.36	34
nnnnynnyyyyyyyynyynyyynyyyyynnyyyyyynnnnnnnnyyynynyyyyyy												
1000	-287.8302	-191.5893	-0.9656	0	17.8	17.7	29.9	1.50	1.45	3.82	4.67	32
nyynynyynnyynnyynyyynyynnnynyyyyyyyyyynnnyyyyynnyynnnn												
1001	-191.9426	-191.5965	-0.6419	0	15.3	15.2	25.8	1.84	1.09	5.35	3.88	40
nynynnyyynyyynynyyyyyyynynynyyyyyyyyyynnnyyyyyyyyyyyyn												

```
  1002    -96.0136   -191.5798      -0.2338    0      13.4     13.5     20.5       2.35     1.19     4.79     3.12  47
nnnnynnyyyyyyynyyyyyyyyyyyyyyyyyyyyyyyyyyyyyyyyyyyyyyyy
  1003     -0.0757   -191.6202      -0.0549    0      12.6     12.8     18.9       1.30     1.10     3.35     2.26  50
nnyynyyyyyyyyyyyyyyyyyyyynyyyyyyyyyyyyyyyyyyyyyyyyyyyyy
  1004     95.8635   -191.6616       0.0724    0      12.7     12.8     18.4       1.10     1.07     3.84     2.29  50
nynnnyyyyyyyyyyyyyyyyyyyyyyyyyyyyyyyyyyyyyyyyyyyyyyyyyy
  1005    191.8113   -191.7182       0.1645    0      13.6     13.5     19.1       1.95     1.01     4.91     2.44  49
nnnyyyyyyyyyyyyyynyyyyyyyyyyyyyyyyyyyyyyynyyyyyyyyyyyyy
  1006    287.8012   -191.7299       0.1587    0      15.4     15.1     21.6       1.87     0.89     5.42     4.60  44
nyyyyyyyyyyyyyyyynyynyyynnynyyyyyyyyyyynnnyyyyyyyyyyyyn
  1007    383.8577   -191.7485      -0.0912    0      22.5     21.1     33.8       2.04     1.23     4.88     2.75  15
nynynnyynnynnnnnnnnnnnnnynnnnyyynnyynnnnnnnnyynnnynynnn
  1008   -287.7611    -95.7266      -0.7524    0      16.3     16.3     27.0       1.24     1.25     3.75     4.76  35
nyynnnyyyyyynnyyynyynyynynynyyyynyyyyyynnnyyyyynnyynyyn
  1009   -191.8865    -95.7058      -0.1940    0      13.3     13.7     20.0       2.04     0.87     4.87     2.21  48
nynnyyyyyyynyynyynyyyyyyyyyyyyyyyyyyyyyyyyyyyyyyyyyyyyy
  1010    -95.9697    -95.7159      -0.1441    0      11.7     12.1     18.1       1.37     0.93     2.95     4.17  52
yyyyyyyyynyyyyyynyyyyyyyyyyyyyyyyyyyyyyyyyyyyyyyyyyyyyy
  1011     -0.0442    -95.7291      -0.0001    0      10.9     11.3     16.7       0.76     0.87     1.63     2.94  53
yyyyyyyyyyyyyyyyynyyyyyyyyyyyyyyyyyyyyyyyyyyyyyyyyyyyyy
  1012    191.8355    -95.7784       0.1060    0      12.0     12.2     17.2       1.31     0.80     4.14     2.14  51
yyyyyyyynyyyyyyyyyyyyyyyyynyyyyyyyyyyyyyynyyyyyyyyyyyyy
  1013    287.8270    -95.7934      -0.0481    0      13.8     13.7     19.0       2.10     1.17     5.34     4.89  49
yyyynyyynyyynyyyyyyyyyyyyyyyyyyyyyyyyyynnyyyyyyyyyyyyyy
  1014    383.8496    -95.7787      -0.2292    0      19.9     19.0     29.0       1.27     0.82     4.38     1.77  19
nyynnnynnnynnnnnnynnnnnnynnnnyyynnyyyynnnnyyyynnnynynnn
  1015   -287.7397      0.1208      -0.5147    0      15.5     15.6     23.6       1.33     0.76     4.38     2.35  38
nnyynnyyyynynnnyyyyynyynyyynyyyyynyyyyyynnyyyyyynyynyyy
  1016   -191.8703      0.1534      -0.2704    0      12.5     12.8     18.4       1.02     0.61     2.58     2.17  52
yyyyyyyyyyyyynyyynyyyyyyyyyyyyyyyyyyyyyyyyyyyyyyyyyyyyy
  1017    -95.9626      0.1687      -0.0313    0      11.0     11.3     16.7       0.79     0.59     1.97     2.18  52
yynyynyyyyyyyyyyyyyyyyyyyyyyyyyyyyyyyyyyyyyyyyyyyyyyyyy
  1018    191.8432      0.1746       0.0237    0      11.4     11.7     16.6       0.99     0.50     3.75     1.16  50
nynynyyyyyyyyyyyyyyyyyyyynyyyyyyyyyyyyyyyyyyyyyyyyyyyyy
  1019    287.8359      0.1627      -0.1668    0      13.1     13.2     18.4       1.48     0.58     4.44     1.52  49
nyyyyyynyynyyyyyyyyyyyyyynyyyyyyyyyyyyyynyyyyyyyyyyyyyy
  1020    383.8471      0.1671      -0.4251    0      18.5     19.1     29.0       1.64     0.75     4.06     1.59  23
nnnnnnynnnynnnnnnynnnnnnnnnnyyyynyyyyynnnyyyyyyyyynyynn
  1021   -287.7215     95.9591      -0.4272    0      15.4     15.6     22.7       1.16     0.56     3.66     2.05  40
nnyynnyyyyyynnyyyyyynyynnnynyyyynyyyyyyyynyyyyyyyyynyyy
```

```
  1022   -191.8549     96.0040     -0.1465    0     12.5    12.9    17.8     0.88    0.47    2.28    1.52  51
ynnyyyyyyyyyyyyyynyyyyyyyyyyyyyyyyyyyyyyyyyyyyyyyyyyyy
  1023    -95.9623     96.0377      0.0812    0     11.1    11.6    16.4     0.48    0.52    1.59    1.10  51
nyyynyyyyyyyyyyynyyyyyyyyyyyyyyyyyyyyyyyyyyyyyyyyyyyyy
  1024    191.8526     96.1037     -0.0184    0     11.2    11.6    16.6     0.66    0.37    1.69    0.96  53
yyyyyyyyyyyyyyyyyyyyynyyyyyyyyyyyyyyyyyyyyyyyyyyyyyyyy
  1025    287.8466     96.1129     -0.2878    0     13.0    13.2    18.7     1.08    0.55    2.47    1.40  52
ynyyyyyyyyyyyyyyynyyyyyyyyyyyyyyyyyyyyyyyyyyyyyyyyyyyy
  1026    383.8784     96.1233     -0.6779    0     18.0    19.5    27.1     1.65    0.80    5.24    2.22  28
nnnnnnynnnynnnnnynnnnnnnnnnyyyyynyyyyyyyyyyyyyyyyyyyny
  1027   -287.7291    191.8151     -0.3195    0     16.1    16.3    22.9     1.88    1.09    4.76    3.63  41
nnynnnyyyyyyynnyynyyyynnyyynyyyynyyyyyyyyyyyyyyyyynyyy
  1028   -191.8663    191.8677     -0.0372    0     13.3    13.8    19.0     1.46    0.80    4.76    2.39  49
ynyyynyyyyyyyynynnyyyyyyyyyyyyyyyyyyyyyyyyyyyyyyyyyyyy
  1029    -95.9684    191.9207      0.1307    0     11.8    12.3    17.1     0.87    0.66    3.25    1.96  52
yyyyyyyyyyyyyyynynyyyyyyyyyyyyyyyyyyyyyyyyyyyyyyyyyyyy
  1030     95.8915    192.0138     -0.0106    0     11.2    11.7    17.3     0.48    0.46    1.18    1.76  53
yyyyynyyyyyyyyyyyyyyyyyyyyyyyyyyyyyyyyyyyyyyyyyyyyyyyy
  1031    191.8387    192.0466     -0.0999    0     12.1    12.7    18.3     0.93    0.49    3.13    1.03  51
yynyyyyynyyyyynyyyyyyyyyyyyyyyyyyyyyyyyyyyyyyyyyyyyyyy
  1032    287.8356    192.0610     -0.4128    0     13.7    14.0    20.8     1.45    0.86    5.03    2.99  52
yyyynnyyyyyyyyyyyyyyyyyyyyyyyyyyyyyyyyyyyyyyyyyyyyyyyy
  1033    383.8409    192.0775     -0.8847    0     18.7    20.5    29.0     1.19    0.81    4.67    2.64  28
ynnnnnynnnynnnnnnynnnnnnnnnyyyyynyyyyyyyyyyyyyyyyyyyny
  1034   -287.7369    287.6744     -0.1475    0     18.0    18.3    25.7     2.01    1.25    5.15    3.70  34
nynnnnnyyyyyynnyyyyyynnnnynyyynnyyyyynnyyyyyyyyyyynyyn
  1035   -191.8814    287.7481     -0.0359    0     14.8    15.3    20.5     1.63    0.90    3.82    2.76  46
yynyyyyyyyynnyyyynnyyyyynynyyyyyyyyyyyyyyyyyyyyyyyyyyR
  1036    -95.9952    287.8152     -0.0023    0     13.2    13.7    18.8     1.37    0.86    5.30    2.39  53
yyyyyyyyyyyyynyyyyyyyyyyyyyyyyyyyyyyyyyyyyyyyyyyyyyyyy
  1037     -0.0684    287.8803     -0.0940    0     12.5    13.1    18.5     0.64    0.76    2.09    2.08  54
yyyyyyyyyyyyyyyyyyyyyyyyyyyyyyyyyyyyyyyyyyyyyyyyyyyyyy
  1038     95.8671    287.9329     -0.2047    0     12.6    13.2    19.2     0.72    0.73    1.52    2.15  54
yyyyyyyyyyyyyyyyyyyyyyyyyyyyyyyyyyyyyyyyyyyyyyyyyyyyyy
  1039    191.8208    287.9883     -0.3227    0     13.5    14.0    20.6     1.50    0.85    4.42    2.28  53
nyyyyyyyyyyyyyyyyyyyyyyyyyyyyyyyyyyyyyyyyyyyyyyyyyyyyy
  1040    287.8159    288.0321     -0.7077    0     15.1    15.5    23.2     1.75    1.16    4.46    4.81  50
ynyyyyyyyyyyyyyyyyyyyyyynynyyyyyyyyyyyyyyyyyyyyyyyyyyn
  1041    383.8013    287.9907     -1.1973    0     20.0    22.8    32.0     1.96    1.38    4.23    4.02  26
ynnnnynnnnnnnnnnnynnnnnnnnnnyyyynyyyyyyyyyyyyyyyyyynyn
```

```
  1042   -191.9158    383.6123     -0.1098     0       16.5    16.9    22.3     2.24    1.22    4.65    3.57  48
ynyyyyyyyynyyyyyyynyyyy,ynynyyyyyyyyyyyyyyyyyyyyyyyn
  1043    -96.0239    383.7149     -0.1438     0       15.2    15.7    21.8     1.38    1.07    4.42    3.68  51
yyyyyyyyyyyyyyyyynyyyyyyyynyyyyyyyyyyyyyyyyyyyyyyyyR
  1044     -0.0937    383.7990     -0.3081     0       14.6    15.2    21.6     1.06    1.03    3.02    2.76  53
yyyyyyyyyyyyyyyyynyyyyyyyyyyyyyyyyyyyyyyyyyyyyyyyyy
  1045     95.8438    383.8722     -0.4378     0       14.7    15.3    22.7     1.33    1.10    4.50    3.05  53
yyyyynyyyyyyyyyyyyyyyyyyyyyyyyyyyyyyyyyyyyyyyyyyyyy
  1046    191.8008    383.9318     -0.5878     0       15.5    16.1    24.4     2.27    1.23    5.23    3.46  51
nyyyynyyynyyyyyyyyyyyyyyyyyyyyyyyyyyyyyyyyyyyyyyyyy
  1047    287.8289    383.9675     -1.1770     0       17.5    17.5    28.3     1.01    1.15    2.90    4.63  40
yyyyynyyyyyynnyyyyyyyyyyynnnnyyyyyyyyRnnnyyyyyyyyyynnn
     2    Indeterminate - invalid or insufficient target images
Mean
41.5
```

<<< Target Precision Summary >>>

Units: microns

	Target	sX	sY	sZ
Minimum	5	8.89	9.07	6.45
Mean		14.44	14.79	18.55
Maximum	1007	22.51	21.07	33.76

Mean precision of target coordinates: 15.92

Relative precision for the network 1: 59000

<<< Target Coordinate Corrections >>>

Units : microns

Target	Corrections			Precisions			Significance		
	x	y	z	x	y	z	x	y	z
1	0.3	0.6	2.7	9.1	9.3	6.7	0.0	0.1	0.4
5	-0.3	0.6	4.0	8.9	9.1	6.5	0.0	0.1	0.6
7	-0.7	-0.1	3.7	9.2	9.4	6.7	0.1	0.0	0.6
9	-0.1	-0.1	6.2	9.4	9.6	6.9	0.0	0.0	0.9
28	0.1	1.2	3.9	10.3	10.5	7.3	0.0	0.1	0.5
34	0.2	-0.2	5.0	10.2	10.4	7.0	0.0	0.0	0.7
36	0.5	-1.9	-21.1	12.8	13.1	7.9	0.0	0.1	2.7
37	-2.3	2.3	-2.5	27.6	31.9	9.7	0.1	0.1	0.3
64	0.1	-1.0	0.2	20.1	19.9	8.8	0.0	0.1	0.0
70	1.8	0.1	4.3	12.3	12.5	7.6	0.1	0.0	0.6
76	1.0	0.7	-13.5	12.5	12.7	7.9	0.1	0.1	1.7
90	-3.6	-5.0	-7.7	20.7	20.3	9.4	0.2	0.2	0.8
100	3.0	-4.5	3.4	24.0	23.3	9.3	0.1	0.2	0.4
113	-1.0	1.0	2.9	12.6	12.6	7.6	0.1	0.1	0.4
RMS		1.55	2.05	7.78					

*** End of VMS calibration log file ***

Appendix G: Residual histograms

For the experiments that were monitored using stereo imaging, post-experiment data processing needed to be carried out in order to calculate the positions of the marker points in space. As discussed in chapter three, this was achieved using the two sets of 'points' outputs from *Pointcatcher*, and the exterior orientation data from the dual camera calibration. The intersections were performed in MATLAB. Error assessment at this stage allowed the calculation of the residuals associated with the point position data. These are presented in the figure below.

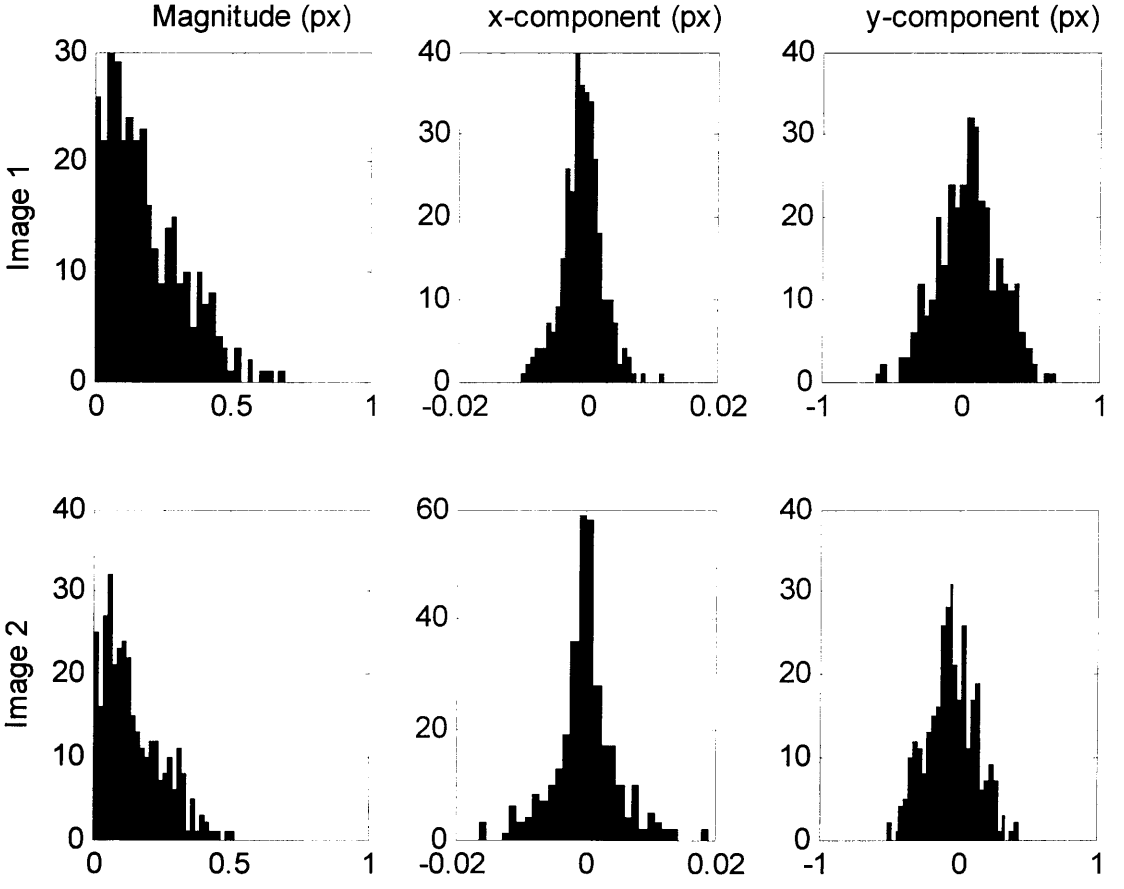

Figure G1. Histograms of the residuals associated with the point position data, calculated during the stereo image processing. The results shown are those from experiment 38.

The figure shows the total magnitude of the residuals in pixels, and the x- and y-components of the residuals, also in pixels, for each image in a stereo pair. As was noted in chapter three, the calculation of the x-coordinate of a marker is very accurate, as the x-vectors are in the plane of the optic axes of the cameras. The residuals in x are less than ± 0.02 pixels. In y, however, the vectors are orthogonal to the plane of the optic axes, and are therefore more difficult to calculate. Nonetheless, the residuals are generally less than ± 0.5 pixels. This is considered to be an acceptable level of accuracy.

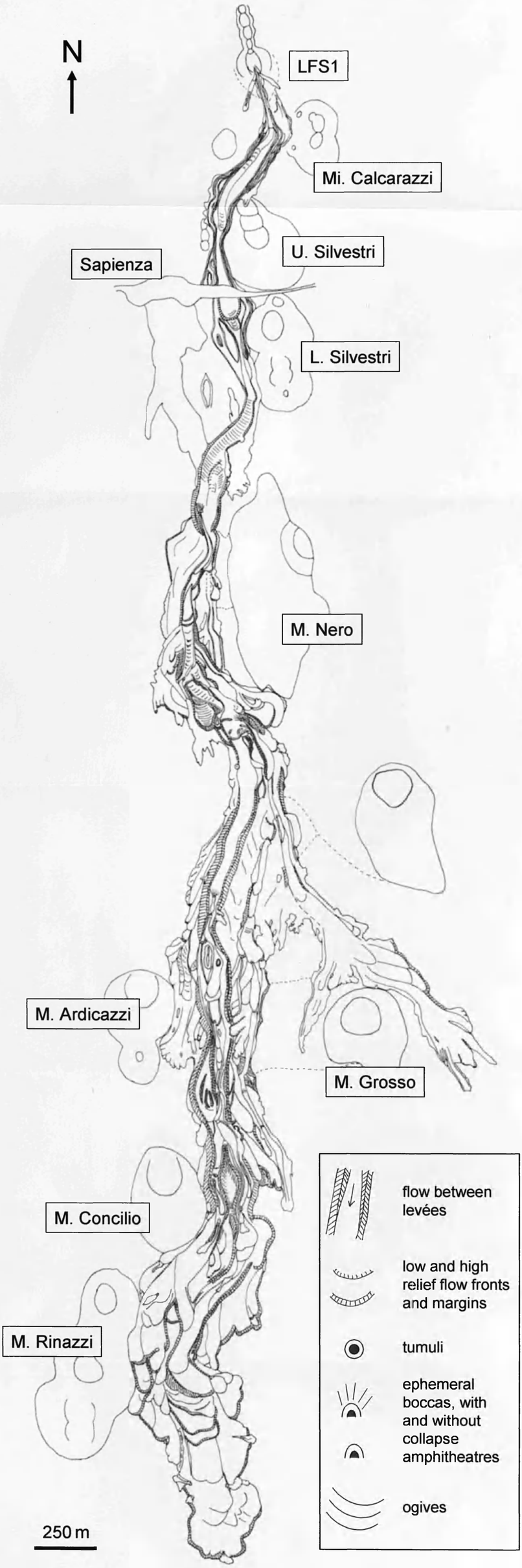
N
LFS1
Mi. Calcarazzi
U. Silvestri
Sapienza
L. Silvestri
M. Nero
M. Ardicazzi
M. Grosso
M. Concilio
M. Rinazzi
250 m
flow between levées
low and high relief flow fronts and margins
tumuli
ephemeral boccas, with and without collapse amphitheatres
ogives